CATALYTIC CONSEQUENCES OF ACTIVE SITE SPECIATION, DENSITY, MOBILITY AND STABILITY ON SELECTIVE CATALYTIC REDUCTION OF NO$_X$ WITH AMMONIA OVER CU-EXCHANGED ZEOLITES

by

Ishant Khurana

A Dissertation

Submitted to the Faculty of Purdue University

In Partial Fulfillment of the Requirements for the degree of

Doctor of Philosophy

Davidson School of Chemical Engineering

West Lafayette, Indiana

December 2019

THE PURDUE UNIVERSITY GRADUATE SCHOOL
STATEMENT OF COMMITTEE APPROVAL

Dr. Fabio H. Ribeiro, Chair

    Department of Chemical Engineering

Dr. Rajamani Gounder

    Department of Chemical Engineering

Dr. Jeffrey T. Miller

    Department of Chemical Engineering

Dr. Krishna Kamasamudram

    Cummins Inc., Technical Advisor – Catalyst Technology & Integration Group

Approved by:

    Dr. John A. Morgan

        Head of the Graduate Program

ACKNOWLEDGMENTS

First and foremost, I am very thankful to my advisor Prof. Fabio H. Ribeiro for constant encouragement and support throughout my time at Purdue. He offered me lots of independence and freedom to pursue research problems. His advice and guidance immensely helped me in becoming a better researcher. I am grateful to Prof. Rajamani Gounder for his persisting involvement and unflagging willingness in helping guide the project. Even though he is officially not my co-advisor, I have always considered him my co-advisor. I have been truly impressed by his hard work, unwavering passion and work ethics. I learnt a lot from him in terms of generating and refining ideas, planning smart experiments, being more meticulous, rigorous and critical in thinking, analyzing and technical writing. I am thankful to my committee member, Prof. Jeffrey T. Miller, for all the help during the trips to Advanced Photon Source in Argonne National Lab, Chicago. He has been very kind and generous in offering his time to help me analyze lots of data.

I am also thankful to my committee members from Cummins, Inc., Dr. Aleksey Yezerets and Dr. Krishna Kamasamudram, for giving their valuable time to be on my thesis committee, and also helping me gain an industrial perspective towards fundamental problems in academic research. I would also like to acknowledge Dr. Ashok Kumar, Dr. Saurabh Joshi, Dr. Yadan Tang and their colleagues for very fruitful and stimulating discussions during in-person meetings with Cummins, Inc.

I would like to thank Prof. William Schneider and his research group at the University of Notre Dame for a fruitful and exciting collaboration with our team at Purdue. I enjoyed discussions with him and his group, which really helped me gain a lot of fundamental insights on the research findings. I really admire Prof. Schneider's skill of paraphrasing a complex problem in simple terms and breaking it down to small tangible components. I am very grateful to Dr. Yury Zvinevich for all of his help with the instrumentation in lab. He has always been willing and prompt in helping me with any type of instrument repair in lab, which saved me a lot of time and effort.

I thoroughly enjoyed working closely with Dr. (Prof.) Christopher Paolucci from Prof. William Schneider's research group. His ability to rigorously interpret experimental results and critically couple them with theoretical results to derive meaningful conclusions helped in shaping me as a researcher.

TABLE OF CONTENTS

LIST OF TABLES

LIST OF FIGURES

ABSTRACT

Author: Khurana, Ishant. PhD
Institution: Purdue University
Degree Received: December 2019
Title: Catalytic Consequences of Active Site Speciation, Spatial Distribution, Mobility, and
Stability on Ammonia Selective Catalytic Reduction over Cu-Zeolites.
Committee Chair: Fabio H. Ribeiro

Selective catalytic reduction (SCR) of NO_x using NH_3 as a reductant ($4NH_3 + 4NO + O_2 \rightarrow 6H_2O + 4N_2$) over Cu-SSZ-13 zeolites is a commercial technology used to meet emissions targets in lean-burn and diesel engine exhaust. Optimization of catalyst design parameters to improve catalyst reactivity and stability against deactivation (hydrothermal and sulfur poisoning) necessitates detailed molecular level understanding of structurally different active Cu sites and the reaction mechanism. With the help of synthetic, titrimetric, spectroscopic, kinetic and computational techniques, we established new molecular level details regarding 1) active Cu site speciation in monomeric and dimeric complexes in Cu-SSZ-13, 2) elementary steps in the catalytic reaction mechanism, 3) and deactivation mechanisms upon hydrothermal treatment and sulfur poisoning.

We have demonstrated that Cu in Cu-SSZ-13 speciates as two distinct isolated sites, nominally divalent Cu^{II} and monovalent $[Cu^{II}(OH)]^+$ complexes exchanged at paired Al and isolated Al sites, respectively. This Cu site model accurately described a wide range of zeolite chemical composition, as evidenced by spectroscopic (Infrared and X-ray absorption) and titrimetric characterization of Cu sites under *ex situ* conditions and *in situ* and *operando* SCR reaction conditions. Monovalent $[Cu^{II}(OH)]^+$ complexes have been further found to condense to form multinuclear Cu-oxo complexes upon high temperature oxidative treatment, which have been characterized using UV-visible spectroscopy, CO-temperature programmed reduction and dry NO oxidation as a probe reaction. Structurally different isolated Cu sites have different susceptibilities to H_2 and He reductions, but are similarly susceptible to $NO + NH_3$ reduction and have been found to catalyze NO_x SCR reaction at similar turnover rates (per Cu^{II}; 473 K) via a Cu^{II}/Cu^{I} redox cycle, as their structurally different identities are masked by NH_3 solvation during reaction.

Molecular level insights on the low temperature Cu^{II}/Cu^{I} redox mechanism have been obtained using experiments performed *in situ* and *in operando* coupled with theory. Evidence has been provided to show that the $Cu^{II} \rightarrow Cu^{I}$ reduction half-cycle involves single-site Cu reduction of isolated Cu^{II} sites with $NO+NH_3$, which is independent of Cu spatial density. In contrast, the $Cu^{I} \rightarrow Cu^{II}$ oxidation half-cycle involves dual-site Cu oxidation with O_2 to form dimeric Cu-oxo complexes, which is dependent on Cu spatial density. Such dual-site oxidation during the SCR Cu^{II}/Cu^{I} redox cycle requires two $Cu^{I}(NH_3)_2$ sites, which is enabled by NH_3 solvation that confers mobility to isolated Cu^{I} sites and allows reactions between two $Cu^{I}(NH_3)_2$ species and O_2. As a result, standard SCR rates depend on Cu proximity in Cu-SSZ-13 zeolites when Cu^{I} oxidation steps are kinetically relevant. Additional unresolved pieces of mechanism have been investigated, such as the reactivity of Cu dimers, the types of reaction intermediates involved, and the debated role of Brønsted acid sites in the SCR cycle, to postulate a detailed reaction mechanism. A strategy has been discussed to operate either in oxidation or reduction-limited kinetic regimes, to extract oxidation and reduction rate constants, and better interpret the kinetic differences among Cu-SSZ-13 catalysts.

The stability of active Cu sites upon sulfur oxide poisoning has been assessed by exposing model Cu-zeolite samples to dry SO_2 and O_2 streams at 473 and 673 K, and then analyzing the surface intermediates formed via spectroscopic and kinetic assessments. Model Cu-SSZ-13 zeolites were synthesized to contain distinct Cu active site types, predominantly either divalent Cu^{II} ions exchanged at proximal framework Al (Z_2Cu), or monovalent $[Cu^{II}OH]^+$ complexes exchanged at isolated framework Al (ZCuOH). SCR turnover rates (473 K, per Cu) decreased linearly with increasing S content to undetectable values at equimolar S:Cu ratios, consistent with poisoning of each Cu site with one SO_2-derived intermediate. Cu and S K-edge X-ray absorption spectroscopy and density functional theory calculations were used to identify the structures and binding energies of different SO_2-derived intermediates at Z_2Cu and ZCuOH sites, revealing that bisulfates are particularly low in energy, and residual Brønsted protons are liberated at Z_2Cu sites as bisulfates are formed. Molecular dynamics simulations also show that Cu sites bound to one HSO_4^- are immobile, but become liberated from the framework and more mobile when bound to two HSO_4^-. These findings indicate that Z_2Cu sites are more resistant to SO_2 poisoning than ZCuOH sites, and are easier to regenerate once poisoned.

The stability of active Cu sites on various small-pore Cu-zeolites during hydrothermal deactivation (high temperature steaming conditions) has also been assessed by probing the structural and kinetic changes to active Cu sites. Three small-pore, eight-membered ring (8-MR) zeolites of different cage-based topology (CHA, AEI, RTH) have been investigated. With the help of UV-visible spectroscopy to probe the Cu structure, in conjunction with measuring differential reaction kinetics before and after subsequent treatments, it has been suggested that the RTH framework imposes internal transport restrictions, effectively functioning as a 1-D framework during SCR catalysis. Hydrothermal aging of Cu-RTH results in complete deactivation and undetectable SCR rates, despite no changes in long-range structure or micropore volume after hydrothermal aging treatments and subsequent SCR exposure, highlighting beneficial properties conferred by double six-membered ring (D6R) composite building units. Exposure aging conditions and SCR reactants resulted in deleterious structural changes to Cu sites, likely reflecting the formation of inactive copper-aluminate domains. Therefore, the viability of Cu-zeolites for practical low temperature NO_x SCR catalysis cannot be inferred solely from assessments of framework structural integrity after aging treatments, but also require Cu active site and kinetic characterization after aged zeolites are exposed to low temperature SCR conditions.

1.   INTRODUCTION

1.1   Reliance on Fossil Fuels

Fossil fuels continue to be a major contributor to global energy production, with fossil fuels contributing to over 80% of global and US energy needs, as of 2010.[1,2] With the current policy commitments, the global energy demands have been predicted to rise by 40% in 2035, which would result in continued reliance on fossil fuels to account for increased energy demand, projected to contribute 75% of global energy demand by 2035.[1,3] Current diversification in fossil fuel global consumption comes from crude oil (39%), coal (33%) and natural gas (28%).[2,4] Each of these fossil fuels (oil, coal and natural gas) have different energy efficiencies (to usable forms like electric power, etc.) and environmental footprint/emissions. Different applications of fossil fuel-derived energy include transportation fuels (oil and natural gas), electricity (oil, coal and natural gas), heating systems (natural gas), etc.[1,2] Despite heavy reliance on fossil fuels for energy production, the degree of dependence on fossil fuels has to eventually decline due to 1) non-renewable nature of fossil fuels, 2) difficulty and expensiveness in extracting remaining reserves, and 3) negative impact on the environment/pollution during extraction, transportation and use of fossil fuels.[5]

1.2   Pollution from Consumption of Fossil Fuels

A major drawback/cost of heavy reliance on fossil fuels is their environmental footprint/pollution. Extraction of coal from the ground, via mining, negatively affects neighboring surface and subsurface water bodies polluting the water with toxic chemicals like selenium, arsenic, manganese, lead, iron, and hydrogen sulfide (water pollution), adversely affects soil quality (soil pollution) and also alters the surrounding ecosystem.[5] On the other hand, extraction of oil and gas, via drilling, involves large volumes of water and diverse chemical usage, contamination of surfaced water (with harmful solids, heavy metals, hydrocarbons and radioactive materials) (water pollution), land degradation, alteration of ecosystem, along with greenhouse gas (methane) emissions.[3,5] Additionally, the transportation of coal, oil and gas poses human health risks, and other safety concerns like oil spills and gas leaks. Most significant impact occurs from air emissions during burning of fossil fuels. [3,5] Various types of emitted air

pollutants include carbon dioxide (CO_2), carbon monoxide (CO), sulfur dioxide (SO_2), nitrogen oxides (NO_x), particulate matter/soot (PM), volatile organic compounds (VOCs), ozone (O_3), ammonia (NH_3), benzene, ethylene oxide, formaldehyde, etc.[6] Amongst various public health and environmental concerns (Figure 1), the most serious one is universal and irreversible global warming effects caused by these air pollutants. United States Environmental Protection Agency (EPA) classified air pollution emission sources as stationary sources (electric power generation, residential, industrial and commercial fuel combustion), mobile sources (aircraft, locomotives, non-road equipment and on-road vehicles), fires (agricultural field burning, wildfires) and biogenics (naturally occurring emissions – vegetation and soil).[7] Mobile sources contribute to majority of nitrogen oxides (NO_x) and carbon monoxide (CO) emissions in the US.[8] Among mobile sources, on-road vehicles (fossil fuel transportation) emissions alone contribute to about 30% of total global warming emissions (surpassing the power sector)[9]. More specifically, these on-road vehicles (fossil fuel transportation) contribute more than 33% to total nitrogen oxides (NO_x) (and carbon monoxide - CO) emissions, making them the single largest source of toxic air pollution (Figure 1 and 2).
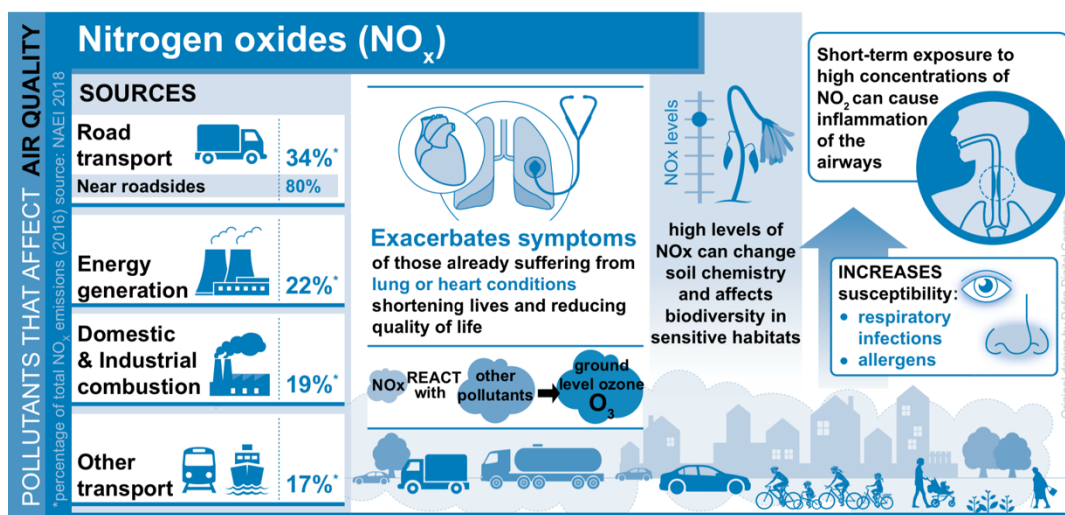
Figure 1.1 Anthropogenic NO_x emission sources and their impact on public health and environment (NAEI 2018)

In the light of this increasing pollution from use of fossil fuels in transportation (and power sector), there is an ongoing shift to new cleaner renewable energy sources (water, biomass, wind, geothermal and solar energy) to replace non-renewable fossil fuel energy resources (coal, oil and natural gas). However, complete transition from fossil fuels to renewable energy sources will

require substantial time, which necessitates the use fossil fuels in the most environmentally responsible way in the meantime. One of the important strategies to use transportation fossil fuels in environmentally friendly manner (without substantial reduction in consumption) is to have emission controls for the abatement of emitted air pollutants like particulate matter (PM), carbon monoxide (CO), nitrogen oxides (NO_x), etc., specifically from on-road vehicles i.e. gasoline and diesel engine exhausts, as these mobile sources has been found to a dominant contributor to total air pollutant emissions.[11]
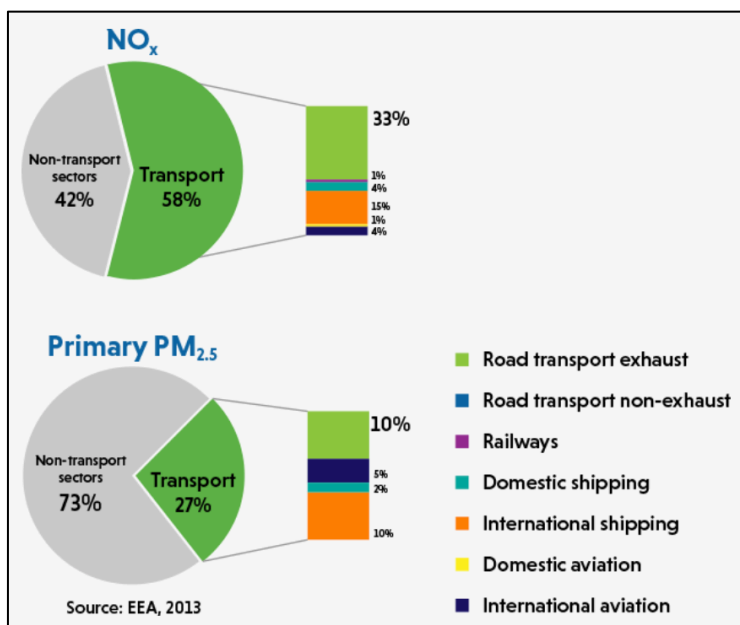
Figure 1.2 Anthropogenic PM and NO_x emission sources, with a detailed breakdown of dominant mobile/transport pollutant sources (2013)

1.3 Emission Aftertreatment Systems for Gasoline and Diesel Engine Exhaust

About 80% of transportation fuels are derived from petroleum (fossil fuels), which includes gasoline, diesel, liquified petroleum gas (LPG), jet fuel and marine fuel[12]. About 92% of transportation fuels include gasoline and diesel, which upon combustion emits carbon dioxide (CO_2), particulate matter (PM), nitrogen oxides (NO_x), carbon monoxide (CO) and unburnt hydrocarbons (uHC).[12,13] Both gasoline and diesel are internal, intermittent combustion engines, but have a fundamental difference in their mixture preparation and ignition, which subsequently results in different exhaust chemical composition requiring different emission control/aftertreatment system designs.

In gasoline engines, air and fuel are mixed prior to entering the cylinder followed by compression of the mixture. In order to prevent auto-ignition, compression ratio is much lower compared to diesel engine, resulting in slightly reduced fuel-efficiency.[14] This is followed by igniting the mixture with a spark, and propagation of flame across the combustion chamber.[14] Minimization of local fuel-rich conditions (due to premixing) produces a little soot, high temperatures in the flame zone results in the formation of CO and NO_x, and flame quenching near the walls results in partially oxidized and unburned HC.[14,15] Therefore, pollutants from gasoline engine exhaust include unburnt hydrocarbon (uHC), carbon monoxide (CO), particulate mater (PM) and nitrogen oxides (NO_x). Overall emission abatement strategy involves combination of advanced engine control strategies (to design efficient and cleaner engines) and emission control strategies (aftertreatment system for emission abatement).[13] Emission control system includes oxidation catalyst (OC), three-way catalyst (TWC), NO_x absorber catalyst and gasoline particulate filter (GPF). [13,16,17]

On the other hand, in diesel engines, air is first introduced into the engine cylinder followed by compression heating to temperatures above 700 K.[18] The fuel is then introduced into the combustion chamber via a high-pressure injection system to be mixed with the hot air until the fuel jet becomes hot enough for auto-ignition.[18] Fuel-rich center of burning jet results in formation of partially burnt or unburnt fuel, polycyclic aromatic HC (PAHs) and CO, whereas excess air at the outer edges of burning jet results in high temperatures and the formation of NO_x.[18] Diesel engines are the preferred power systems, especially for heavy-duty trucks and buses, due to their long record of reliability, durability, high torque output and fuel-efficiency.[18] While such lean-burn diesel engine-powered vehicles have advantage of having 30-40% higher fuel economy and about 20% reduction in CO and CO_2 emissions (as compared to gasoline engine), there are some disadvantages in the form of significantly higher particulate matter (PM) and NO_x emissions, along with some unburnt HC, CO and CO_2 emissions, in the atmosphere.[18,19] In the wake of various health and environmental concerns posed by such diesel engine emissions, a number of countries worldwide have established substantially lower emission limits, with US EPA imposing new regulations for on-highway diesel tracks and passenger cars to further reduce diesel engine exhaust emissions starting with 2007 model year.

Reducing diesel emissions to achieve ultra-low emission targets requires a systems engineering approach[20,21], which combines the use of ultra low sulfur diesel (ULSD)[22] with

advanced engine control technologies and advanced exhaust emission control technologies (aftertreatment systems). Engine control technologies involve developing cleaner diesel engines by engine manufacturer with an ultimate aim to reduce engine-out emission to as low as possible in order to reduce the burden on exhaust emission control. These engine control approaches/strategies include reduced oil consumption, advanced common rail fuel injection, electronic engine controls, combustion chamber modifications, intake temperature management, air boosting, improved air/fuel mixing and exhaust gas recirculation (EGR).[20,21] Advanced viable emission control technologies (aftertreatment system) aim to reduce gaseous tailpipe emissions including unburnt hydrocarbon (HC), carbon monoxide (CO), particulate matter (PM) and Nitrogen oxides (NO_x). Designed technologies to control HC, CO and PM emissions include Diesel oxidation catalysts (DOCs), Diesel particulate filters (DPFs) and Closed crankcase ventilation (CCV), and technologies designed to control NO_x emissions include Exhaust gas recirculation (EGR), Selective catalytic reduction (SCR), Lean NOx catalysts (LNCs) and Lean NOx traps (LNTs).[20,21] As the diesel emission standards and diesel engine technology are closely linked, currently stringent diesel emission standards are driving the emission technology. While the combination of engine control/management (combustion) and emission control/aftertreatment system (post-combustion) have sufficed to abate engine emissions meeting current emission regulations. As legislations become more stringent in future, engine control/management strategy alone will not be sufficient for compliance with stringent NO_x limits, making the emission control (i.e. technology to treat exhaust emissions) more critical. Figure 3 shows a typical diesel aftertreatment/emission control system.
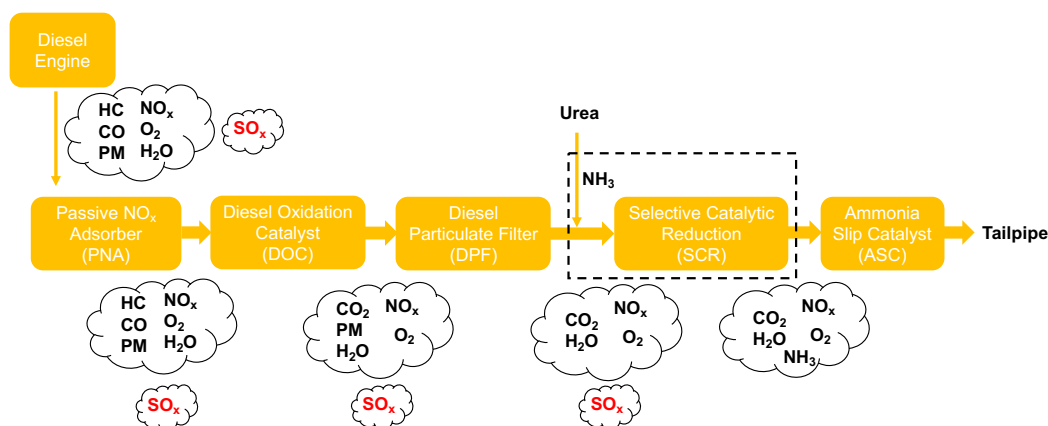
Figure 1.3 Block diagram representation of a typical Diesel Aftertreatment system (HC: Unburnt Hydrocarbon, PM: Particulate Matter, NO_x: NO and NO_2, SO_x: SO_2 and SO_3)

This work focusses on selective catalytic reduction (NO_x SCR) component of diesel aftertreatment/emission control system. The following section discusses the basics of SCR.

1.4 Selective Catalytic Reduction (SCR) of NO_x with Ammonia

Nitrogen oxides (NO_x, x=1,2) are a family of poisonous gases, which upon reaction with volatile organic compounds (VOC) produces ozone (smog) in the atmosphere and are a dominant source of air pollution[3]. As discussed above, most of the NO_x emissions (~60% in Europe) results from combustion engines[23], via high temperature oxidation of atmospheric nitrogen, even though there has been a significant decline in nitrogen content in gasoline and diesel. Among NO_x emission from all combustion engines, diesel engines contribute to about 75% of total NO_x emissions[23].

$$N_2 + O_2 \xrightarrow{\Delta T} 2NO \tag{1.1}$$

Due to their high efficiency and low costs, catalytic technologies are preferred (over emission abatement) for NO_x emission abatement[24]. The importance of catalyst becomes even more apparent in this case, where NO reduction (to N_2 and O_2) is thermodynamically favored, but kinetically difficult, which necessitates the discovery of catalytic technology to accelerate NO reduction kinetics. This has been a very difficult problem to solve, and to date no catalyst has been found that can achieve appreciable NO_x conversions under relevant operating conditions[25]. Though NO_x can be efficiently reduced using a three-way catalyst in gasoline engine exhaust[25,26], this three-way catalyst technology cannot be extrapolated to diesel engine exhaust due to operation under excess oxygen. This further led the way to a discovery of a very elegant reaction to reduce NO_x from lean exhaust conditions (excess oxygen) - selective catalytic reduction of NO_x with NH_3 to nitrogen (NH_3-SCR). As the current diesel exhaust gas contains dominantly nitrogen oxides (NO), with a minor fraction is nitrogen dioxide (NO_2)[27], the basic and dominant reaction on SCR catalysts is referred to as standard SCR, as shown below[27–29].

$$4NO + 4NH_3 + O_2 \rightarrow 4N_2 + 2H_2O \tag{1.2}$$

This SCR process has been applied to abatement of NO_x from stationary power plants for last few decades[30], and has been developed enough to be applied for NO_x reduction in diesel engine exhaust[31,32], wherein reducing agent (NH_3) results from decomposition of non-toxic urea in presence of water (hydrothermal conditions). It is worthwhile to note that, SCR process has also been previously used with other reducing agents like hydrocarbons (HC-SCR) and hydrogen (H_2-SCR). However, standard NH_3-SCR is unique, as it involves stoichiometric dosage of NH_3 to reduce NO_x, as opposed to HC- and H_2-SCR, where the reducing agents are used in stoichiometric manner. This standard SCR is the leading emissions control strategy for the abatement of hazardous nitrogen oxide pollutants (NO_x, x = 1, 2) in lean-burn and diesel engine exhaust.
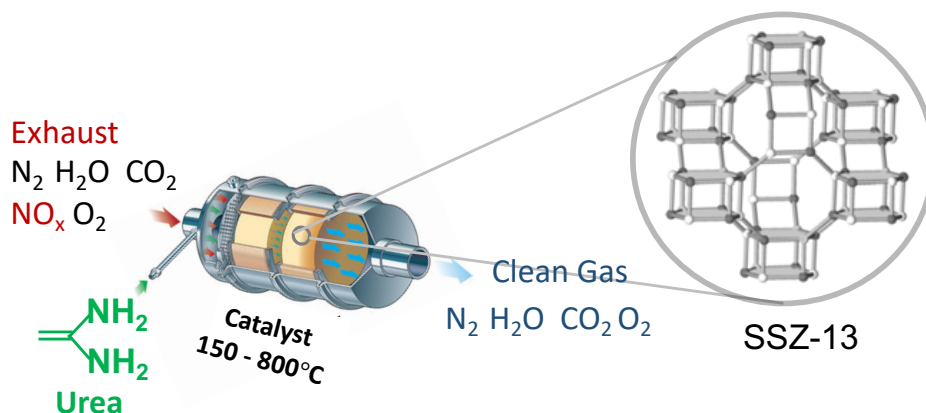
Figure 1.4 Representation of a typical Standard SCR catalytic system (Images from Johnson Matthey and International Zeolite Association)

In case there is an increase in NO_2 share of NO_x emissions, or NO is pre-oxidized to NO_2, and NO and NO_2 are both present as 1:1 mixture, then the NO reduction reaction becomes faster the standard SCR, and is referred to as fast SCR, as shown below[28,29,33]:

$$4NH_3 + 2NO + 2NO_2 + O_2 \rightarrow 4N_2 + 6H_2O \qquad \textbf{(1.3)}$$

Thus, such involvement of NO_2 increases the reaction rate, precludes the participation of O_2 in the SCR reaction, and therefore, simultaneously broadens the operating temperature window of catalysts at lower temperatures[34]. However, feeding significant amounts of NO_2 to SCR catalyst results in formation of ammonium nitrate, an undesired byproduct, which can build

up, accumulate and further block the catalytic active sites for low temperature SCR as indicated by infrared spectroscopy, and can also decompose to N_2O, an unwanted potent greenhouse gas.[35]

In case NO_2 exceeds NO in the mixture, SCR reaction occur with pure NO_2 via. slow SCR, as shown below[29,36]:

$$4NH_3 + 3NO_2 \rightarrow 3.5N_2 + 6H_2O \tag{1.4}$$

Even though NH_3 (reducing agent) should ideally selectively react and reduce NO_x without reacting with excess oxygen, NH_3 can undergo oxidation unselectively to give N_2, NO, N_2O or NO_2 as follows:

$$4NH_3 + 3O_2 \rightarrow 2N_2 + 6H_2O \tag{1.5}$$

$$4NH_3 + 5O_2 \rightarrow 4NO + 6H_2O \tag{1.6}$$

$$2NH_3 + 2O_2 \rightarrow N_2O + 3H_2O \tag{1.7}$$

$$4NH_3 + 7O_2 \rightarrow 4NO_2 + 6H_2O \tag{1.8}$$

NH_3 can react selectively with NO_x via. standard, slow and fast SCR, or react non-selectively via. side reaction NH_3 oxidation to give N_2, NO, N_2O or NO_2 depending on catalyst composition, surrounding gas conditions and temperature.[37] All these possible undesirable and competitive side reactions add complexity to SCR chemistry and hence, the reaction mechanism has been studied extensively on SCR catalysts, as will be discussed in introduction sections of subsequent chapters.

1.5   Standard SCR Catalysts

Standard SCR of NO_x (using urea/ammonia as the reducing agent) in lean-burn diesel engine exhaust has been studied over a wide variety of catalysts including precious (Ag) and noble metal (Pt) based catalysts, transition and base metal oxides (like vanadium, manganese, tungsten, molybdenum, titanium, cerium, zirconium, iron)[38], spinel-based oxides, zeolites (framework with narrow pores like ZSM-5, BEA, FER, MOR and CHA)[37] as well as activated carbon-based catalysts. Vanadia based catalyst (TiO_2-supported V_2O_5, promoted with WO_3, with V acting as the active redox center)[39], which are a common choice for non-road applications, found commercial application as standard SCR catalyst for heavy duty diesel vehicles in 2005 in Europe[39]. Despite commercialization of such vanadia based catalysts, there were some associated

problems including poor low temperature standard SCR performance, decrease in reactivity and selectivity at high temperatures (>550^0C), volatility (>650^0C) and toxicity of vanadia species, and ability to oxidize SO_2 to SO_3 (more potent catalyst poison than SO_2)[40–42]. These disadvantages with vanadia based catalysts resulted in exploration of other catalysts, including metal-exchanged zeolites in the recent years, which can operate over a wide temperature range, while retaining the stability in SO_2 and H_2O at high temperatures (>873 K).

1.6   Cu-exchanged Zeolite as Standard SCR Catalyst

Cu/Fe-exchanged zeolites are the most preferred set of standard SCR catalysts, as they offer higher NO_x conversion efficiencies over a wide temperature range and better hydrothermal stability, as compared to traditional vanadia based catalysts, with some drawbacks of limited sulfur tolerance and hydrocarbon poisoning. [43–45] Cu-exchanged zeolites are more popular and widely used due to higher activity at low temperatures (~473 K) and low sensitivity to NO_2/NO_x ratio[46], as compared to Fe-zeolites, which exhibit appreciable activity at higher temperatures (>573 K)[37] and higher sensitivity to NO_2/NO_x ratio. Therefore, this work is centered around Cu-exchanged zeolites as the standard SCR catalyst. With respect to the choice of zeolite support, the attention has been shifted recently to the use of small-pore zeolite supports (specifically CHA framework zeolites – Cu-SAPO-34 and Cu-SSZ-13) because of their excellent hydrothermal stability and resistance to hydrocarbon poisoning, as compared to medium- (MFI and FER) and large-pore (BEA and FAU) zeolites.[43,44]

In spite of commercialization of Cu-SSZ-13 as a standard NH_3-SCR catalyst, there are many challenges to further improve Cu-SSZ-13 SCR performance, including the reactivity, selectivity and stability, especially the SCR performance in low temperature regime (373-573 K) during the cold start and short distance travel[47]. Additionally, there are quite a bit of unknowns with Cu-SSZ-13, which hamper the development of new strategies to design more active and stable Cu-SSZ-13 catalysts. Their structure (nature of Cu active sites) and function (catalytic SCR performance) changes unpredictably with operating conditions (hydrating conditions, dehydrating conditions, SCR gas conditions), sulfur poisoning and hydrothermal treatment. Further development of more reactive and stable Cu-SSZ-13 catalysts would require fundamental molecular level understanding of nature of Cu active sites under different operating conditions and reaction pathways/mechanism.

1.7 Zeolites → Transition Metal-Exchanged Zeolite → Cu-SSZ-13

Zeolites are crystalline aluminosilicates composed of elementary building units of corner-sharing SiO_4 and AlO_4 tetrahedra and can be arranged to create molecular sieve frameworks that vary in crystalline topology, pore size, channel dimensionality (0D-3D) and interconnectivity[48], pockets, cages and other structural characteristics. This diversity in structural features resulted in over 230 zeolite frameworks/topologies listed in the Zeolite Structures Database[49]. From the perspective of catalysis, all these zeolite structural features are critical in influencing the chemical reactions taking place in pores and voids, due to 1) shape-selectivity effects, 2) confinement effects due to stabilization by van der Waals interactions, and 3) coordination of active metal centers to the zeolite involving covalent and electrostatic interactions of cationic metal species with conjugate anions[50,51]. These shape-selectivity effects, confinement effects as well as metal-zeolite interactions could be advantageously tailored for a specific application.
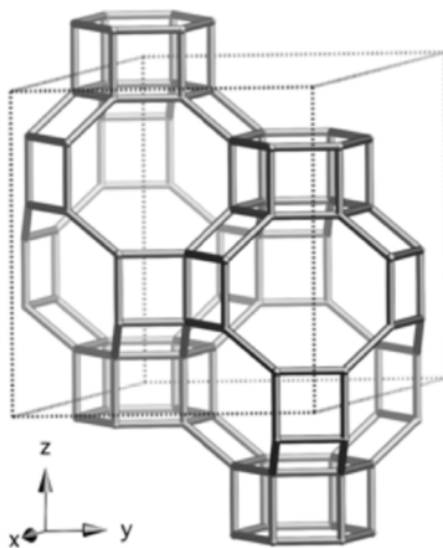
Figure 1.5. Zeolite unit cell with chabazite (CHA) topology from International Zeolite Association

There are various types of transition metal-zeolite interactions, depending on the way in which transition metal active site is incorporated into the zeolite, as follows[52]:

1. Metal centers could be stabilized chemically via. strong basic lattice sites ligation: Substitution of quadri-charged silicon cations (Si^{4+}) by triply-charged aluminum cations (Al^{3+}) generate anionic charges that are compensated by either a proton/Bronsted acid sites (H^+) or monovalent/multivalent extralattice/extraframework cations (e.g. Na^+, Cu^{2+}, etc.)

resulting in isolated single-site transition metal-exchanged catalyst

2. Metal centers could be stabilized mechanically via. encapsulation within the zeolite pores. For example, Pt nanoparticles dispersed inside MFI zeolite nanoshells

3. Metal centers could be directly isomorphously substituted into the zeolite framework as single framework heteroatom

Out of various transition metals for application in catalysis, most prominent elements include Cu, Fe, Ni, Pt, Ti, Pd, Mo, and Co.[52] Among these prominent transition metals, Cu exchanged as divalent extraframework cations (Cu-zeolite) has received substantial attention in the past 40 years for the removal of nitrogen oxides from lean combustion gases (diesel and lean-burn exhaust aftertreatment), as standard NH_3-SCR catalyst [53,54]. And among various Cu ion-exchanged zeolites, Cu exchanged on small-pore CHA zeolites (specifically, SSZ-13) have received a lot of importance due to their excellent hydrothermal stability and activity for NO_x SCR and methanol conversion to light olefins, commonly assigned to their unique 8 membered ring cage structure, pore size, and channel connectivity. Therefore, this work is focused around Cu-exchanged on small-pore zeolite catalysts (specifically, Cu-SSZ-13) for NH_3-SCR of NO_x.

1.8   Cu Site Speciation in SSZ-13 Zeolite

Due to structural heterogeneity at the molecular scale, most of the heterogenous solids contain distribution of active sites with varying reactivity, local environment, coordination and interaction with surrounding gas conditions. Similarly, Cu cations exchanged in SSZ-13 zeolite have also been reported to exhibit structural and chemical heterogeneity, as Z_2Cu (+2 oxidation state, 4-fold coordination and 2:1 H^+:Cu exchange stoichiometry) and ZCuOH (+2 oxidation state, 3-fold Cu coordination and 1:1 H^+:Cu exchange stoichiometry)[55–58]. There remain a lot of unknowns in the understanding Cu cation speciation in SSZ-13, including the exact nature, number, and reactivity of different Cu cationic species, as a function of zeolite composition (Si/Al and Cu/Al ratios), framework topology, pretreatment and operating gas conditions, their spectroscopic assignments, and their catalytic consequences on standard SCR kinetics. More detailed literature review and specific details will be discussed in the introduction section of chapter 2.

1.9 Standard SCR Reaction Mechanism

It has been widely accepted that low temperature standard SCR proceeds via. Cu^{II}-Cu^I redox cycle, as seen from prevalence of a mixture of Cu^I and Cu^{II} with *operando* x-ray absorption spectroscopy (XAS) experiments under steady-state SCR catalysis and no observed correlation of standard SCR rate with either Cu^I or Cu^{II} fraction [59–62]. With the help of reactant O_2 cutoff experiments, it was previously shown that a combination of NO and NH_3 is necessary for the $Cu^{II} \rightarrow Cu^I$ reduction half-cycle, which was shown to occur via NO assisted dissociation of N-H bond of a Cu-bound NH_3 ligand along with generation of a proximal Brønsted acid site[61]. $Cu^I \rightarrow Cu^{II}$ re-oxidation was hypothesized to occur via. *in-situ* reaction of NO and O_2 to yield nitrite ion (NO_2^-) on Cu, which could react with proximal NH_4^+ ions to produce N_2 and H_2O and close the catalytic cycle (Figure 5)[61].
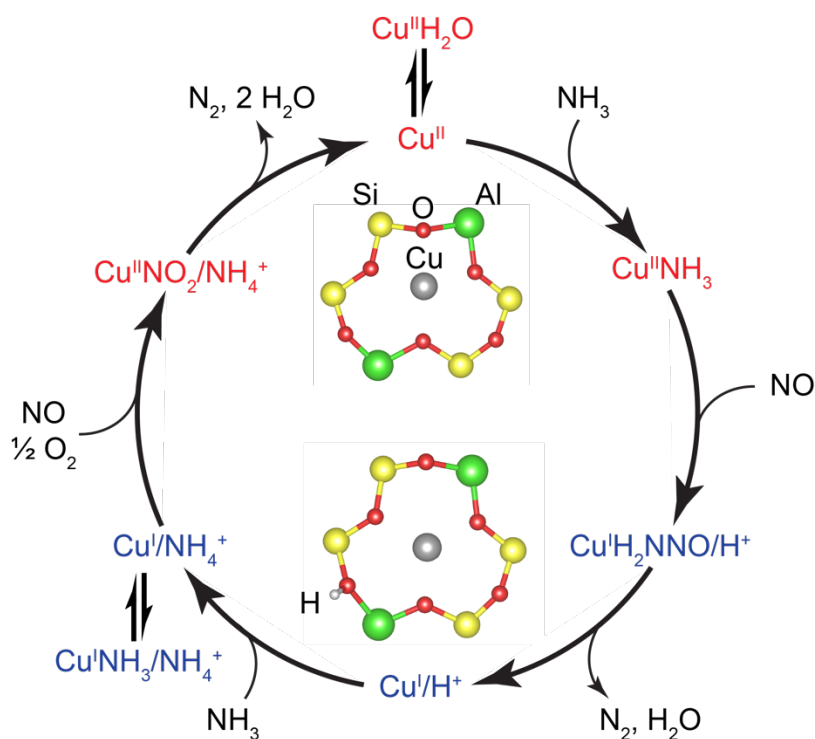
Figure 1.6 Proposed low temperature standard SCR Cu^{II}-Cu^I redox mechanism on isolated Cu^{II} on paired Al sites in six-membered ring[61]

This proposed reaction pathway was expanded further by Janssens et al.[62] to suggest that the $Cu^I \rightarrow Cu^{II}$ re-oxidation occurred via a termolecular *in-situ* reaction of Cu^I, NO and O_2 to form

Cu^{II}-nitrate ($Cu^{II}NO_3^-$), which is further reduced by another NO to form Cu^{II}-nitrite ($Cu^{II}NO_2^-$) and release NO_2 molecule to participate in a parallel fast SCR cycle, thus coupling standard and fast SCR reactions (Figure 6). Both of these redox reaction pathways (Figure 5 and 6) were proposed to occur on a single and isolated Cu cationic site, which is consistent with observed standard SCR reaction rate varying linearly with the catalyst Cu content (Cu/Al = 0-0.2, Si/Al = 4.5)[56]. However, this linear dependence is not observed at low Cu loadings (Si/Al = 6, Cu/Al < 0.02)[63] and in fact, the standard SCR rate (473 K) was found to show a quadratic dependence on total Cu content. This observation was reconciled by proposing the formation of transient Cu dimers ([Cu-O-Cu]$^{2+}$) as the active site at low Cu loadings (Si/Al = 6, Cu/Al < 0.02), while single and isolated Cu cationic site (Cu^{II}) became the predominant active sites at higher Cu loadings (Si/Al = 6, Cu/Al > 0.02) [63]. But preferential formation of Cu dimers at low Cu loadings seems unlikely as opposed to high Cu loadings, along with the fact that single and isolated Cu^{II} at paired framework Al sites are the energetically preferred sites at low Cu loadings.
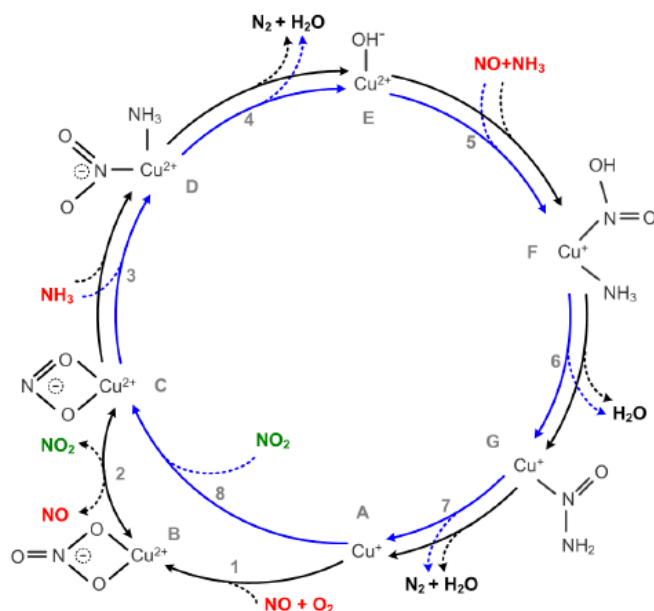
Figure 1.7 Proposed coupled standard SCR (black) and fast SCR (blue) redox reaction pathways on isolated [$Cu^{II}OH$]$^+$ sites on isolated Al sites[62]

Therefore, there is a need to resolve this discrepancy and propose a fully consistent $Cu^I \rightarrow Cu^{II}$ re-oxidation reaction pathway. Furthermore, as discussed in section 1.8, Cu cations exchanged in SSZ-13 zeolite have been reported to exist as single and isolated Z_2Cu (Cu^{II})

and/or ZCuOH ($[Cu^{II}OH]^+$), depending on sample composition (Si/Al and Cu/Al ratios), but how these structurally different Cu^{II} sites will behave under SCR conditions, and whether they have the same reaction mechanism/pathway is not clear.

In summary, some of the unresolved pieces in the standard SCR mechanism includes, 1) unknown active site requirements and reactivity of different single and isolated Cu^{II} and Cu^{I} cationic sites, 2) elementary steps and reaction intermediates, and 3) unrecognized role of Bronsted acid sites (H^+) during low temperature (473 K) standard SCR reaction. Detailed literature review and more specific details will be discussed in the subsequent chapters 3 and 4.

1.10 Challenges with interpretation of differences in SCR Kinetics

Under conventional standard SCR conditions, fractional reaction orders with respect to reactants (NO, NH_3 and O_2) are observed. Such fractional orders are difficult to interpret and could be indicative of mixed kinetic relevance of various reaction steps (mixed kinetic regime), involvement of the same reactant in multiple reaction steps, and multiple adsorbed reaction intermediates. This makes it difficult to interpret SCR kinetics differences with change in catalyst structural features like Cu spatial density (Cu/Al), framework Al density (Si/Al), etc.

1.11 Stability of Cu-SSZ-13 against Hydrothermal Deactivation

Cu-SSZ-13 catalysts are required to retain sufficient SCR performance upon exposure to high temperatures (>923 K) in the presence of steam (~7% H2O (v/v))[45,64,65], conditions experienced during regeneration of particulate filters. It has been previously established that hydrothermal deactivation results in, 1) dealumination of framework Al (which anchors extraframework Cu cations and ammonium species during SCR reaction), and 2) structural and chemical changes to extraframework Cu cations (aggregation into larger Cu oxide species - Cu_xO_y). Such structural changes are shown to be more severe in medium-pore and large-pore Cu-exchanged zeolites (e.g., Cu-MFI, Cu-BEA) than in small-pore zeolites (e.g., Cu-CHA, Cu-AEI)[66–68]. As a result, more hydrothermally stable small-pore zeolites (Cu-CHA, Cu-AEI, Cu-RTH) have been used in this work to identify various structural descriptors like support zeolite framework type, dimensionality, pore size, pore and channel interconnectivity, exchanged Cu speciation that dictate the hydrothermal stability. There have been instances where structural

integrity of zeolite has been maintained, despite the loss in SCR performance[69]. This necessitates the need to use a detailed step-wise approach on model Cu-zeolite catalysts to study atomic level deactivation mechanism, which would further aid in development of more hydrothermal stable catalysts.

1.12 Stability of Cu-SSZ-13 against Sulfur Poisoning

In spite of regulation of diesel sulfur levels from "low-sulfur" contents (500 ppm in 1993) to "ultra-low sulfur" (15 ppm in 2006) by the Environmental Protection Agency [70](EPA), amounts of sulfur oxides (SO$_x$, x = 2, 3) formed during the diesel combustion are enough to deactivate Cu-SSZ-13 zeolite catalysts, which are used for NH$_3$-SCR. Even though high temperature (673-1073 K) regeneration is a typical strategy used to reverse the deactivation of SO$_x$-poisoned Cu-SSZ-13 zeolites, further improvement in strategies to regenerate sulfur-poisoned catalysts and develop more sulfur-tolerant catalysts could be made by gaining molecular understanding of stability of different Cu site types to sulfur exposure in Cu-SSZ-13[71,72]. Cu-SSZ-13 catalyst deactivation with sulfur has been previously shown to occur via. physical (sulfur-derived species causing pore-blocking)[73–76] and chemical[77,78] (sulfur-derived species adsorbed on Cu sites causing deactivation or inhibition) mechanisms. In the subsequent chapters, effects of SO$_2$ poisoning on different types of Cu sites in Cu-SSZ-13 zeolites will be studied.

1.13 Thesis Overview

As discussed in the above introduction sections, there are many opportunities and challenges to further improve Cu-zeolite catalysts SCR performance, including reactivity, selectivity and stability. With the general objective of improving the low temperature standard SCR performance of Cu-zeolite catalysts, especially the SCR performance in low temperature regime (373-573 K), this work specifically aims to:

1. Understand the nature of active Cu sites as a function of zeolite support framework type, framework Al density (Si/Al), Cu exchange levels (Cu/Al) and gas conditions,

2. Study the role played by zeolitic support, other than stabilizing the Cu active species,

3. Investigate detailed reaction mechanism for low temperature NH$_3$-SCR (443 – 503 K) on Cu-SSZ-13 catalysts to enable future development of microkinetic and/or global kinetic model,

4. Investigate hydrothermal deactivation mechanisms of various small-pore zeolite catalysts (Cu-CHA, Cu-AEI and Cu-RTH) in order to identify structural descriptors (support zeolite framework type, dimensionality, pore size, pore and channel interconnectivity, exchanged Cu speciation) that dictate the hydrothermal stability of a given Cu-zeolite catalyst,

5. Investigate Cu-SSZ-13 catalyst deactivation mechanisms upon sulfur poisoning to develop more efficient catalyst regeneration strategies and synthesize more sulfur-tolerant catalysts

Relevant detailed literature review and specific details will be discussed in the introduction section of subsequent chapters.

Chapter 2 elaborates on how the surrounding conditions and bulk zeolite composition play crucial roles in determining Cu speciation (type and number) and reactivity (chemical characteristics). It combines experimental (synthetic, titrimetric, spectroscopic and kinetic characterization) and computational (stochastic simulations, *ab initio* dynamics and free energy calculations) approaches to elucidate Cu speciation under different operating conditions as a function of catalyst composition over a wide range of zeolite chemical composition space. Catalytic consequences of structurally and chemically different Cu sites on standard SCR kinetics are also discussed.

Chapter 3 serves a dual purpose of proposing a fully consistent $Cu^I \rightarrow Cu^{II}$ oxidation cycle reaction pathway as well as investigating the consequences of Cu active site spatial density and mobility on standard SCR kinetics, by integrating computational (*ab initio* dynamics and free energy) and experimental (synthesis, spectroscopic, kinetic and titrimetric analysis) approach.

Chapter 4 interrogates the catalytic function of Cu-CHA zeolites under SCR reaction conditions that enable isolating quantitative kinetic parameters that reflect rate constants in which Cu^{II} reduction or Cu^I oxidation become the dominant kinetically relevant processes. Operating at dilute O_2 pressures enable accessing conditions in which Cu^I oxidation becomes the dominant kinetically relevant step, and excess O_2 pressures enable accessing conditions in which Cu^I oxidation steps appear to become kinetically irrelevant. This approach enables more accurately quantifying the influence of Cu ion spatial density in Cu-CHA on the kinetics of oxidation and reduction processes in the SCR redox cycle, and can be extended to quantitatively determine how changes to catalyst properties, including zeolite topology and framework Al

density and arrangement, influence the fraction of active Cu ion sites and the rate constants of different elementary steps in the SCR cycle.

Chapter 5 explores the effects of commonly observed NH_3 inhibition during low temperature standard SCR, different parameters influencing NH_3 inhibition and its origin in the reaction mechanism.

Chapter 6 picks up from chapter 3 to further investigate low temperature standard SCR reaction mechanism, specifically investigating the mechanistic pathways of mononuclear and binuclear copper complexes in Cu-SSZ-13. The combination of steady state distribution of different Cu oxidation states as a function of sample composition, and non-steady state temporal changes to Cu oxidation state and coordination number during various sequential transient reaction steps enabled to reveal the nature (active site requirements and kinetics) of various reaction steps. Further with the aid of vibrational spectroscopy, attempts are made to identify reaction intermediates during such reaction steps. Additionally, the previously unestablished connection between Cu-SSZ-13 catalyst composition, nature of active site (s), operating reaction conditions and reaction pathway has been discovered in this work.

Chapter 7 investigates the effects of zeolite support framework Al density on standard SCR kinetics, and eventually decouples different intrinsic effects of framework Al density on measured steady state standard SCR kinetics.

Chapter 8 studies the stability of three different small-pore Cu-exchanged zeolites (Cu-CHA – Cu-SSZ-13, Cu-AEI – Cu-SSZ-39, Cu-RTH) upon hydrothermal aging and subsequent exposure to standard SCR reactants at low temperatures (473 K) via. monitoring the structural and active site changes in these three different small-pore Cu-exchanged zeolites. Bulk characterization techniques (XRD and micropore volumes) were found to divulge only subtle differences between fresh, hydrothermally aged and SCR gas mixture-exposed aged Cu-zeolites, and therefore, fail to provide direct insights into decreases in SCR reactivity measured on hydrothermally aged, small-pore Cu-zeolites. However, this decrease in SCR reactivity was further explained using UV-Visible spectroscopy, wherein structural changes to active Cu sites were detected upon exposure of hydrothermally aged catalysts to SCR reaction conditions at low temperature. These structural changes to active Cu sites were consistent with the formation of mixed copper-aluminate domains via reaction with extraframework Al species formed upon dealumination during hydrothermal aging.

Chapter 9 aims to study the stability of Cu-SSZ-13 against sulfur poisoning. Specifically, it decouples the effects of SO_2 poisoning on different types of Cu sites (ZCuOH and Z_2Cu) in Cu-SSZ-13 zeolites to further build upon the prior literature work. We use a combination of detailed kinetic (reaction rate, orders and activation energies), spectroscopic (XAS, UV-Visible, FTIR), Brønsted acid site titration (NH_3) methods, and density functional theory (DFT) calculations measurements to show that sulfur transforms both ZCuOH and Z_2Cu sites to inactive states, resulting in a constant SCR turnover rate when normalized by the number of residual Cu sites that are not poisoned by sulfur. Effect of exposure conditions on poisoning intermediates further highlights chemical differences between the two Cu site types, including differences in the number of titratable Brønsted acid sites.

Chapter 10 deals studies Ultraviolet-visible (UV-Vis) spectra of Cu-SSZ-13 zeolites synthesized to contain specific Cu site motifs, together with ab initio molecular dynamics and time-dependent density functional theory calculations, were used to test the ability to relate specific spectroscopic signatures to specific site motifs.

Chapter 11 deals with identification and quantification of multinuclear Cu-oxo complexes evolved from mononuclear Cu cations, and their relevancy for SCR and NO oxidation reactions.

1.14 References

1   EPA, in Inventory of U.S. Greenhouse Gas Emissions and Sinks: 1990–2012, 2012.
2   A. F. Armor, R. D. Srivastava, H. G. McIlvried, T. D. Marshall and S. I. Plasynski, in Energy Efficiency and Renewable Energy: Handbook, Second Edition, 2015.
3   Z. Wang, in Comprehensive Energy Systems, 2018.
4   J. Woodcock, D. Banister, P. Edwards, A. M. Prentice and I. Roberts, Lancet, 2007.
5   P. R. Epstein, J. J. Buonocore, K. Eckerle, M. Hendryx, B. M. Stout, R. Heinberg, R. W. Clapp, B. May, N. L. Reinhart, M. M. Ahern, S. K. Doshi and L. Glustrom, Ann. N. Y. Acad. Sci., 2011.
6   C. Dore, T. Murrells, N. Passant, M. Hobson, G. Thistlethwaite, a Wagner, Y. Li, T. Bush, K. King, J. Norris, P. Coleman, C. Walker, R. Stewart, I. Tsagatakis, C. Conolly, N. Brophy and M. Hann, AEA Energy, 2008.
7   EPA, The Clean Air Act in a Nutshell : How It Works, 2013.
8   EPA, Energy Econ., 2008.
9   U.S. Environmental Protection Agency - Office of Transportation and Air Quality, EPA-420-F-14-040a, 2014.
10   M. V Twigg, 2007, **70**, 2–15.
11   United States Environmental Protection Agency, Diesel Fuel Stand., 2017.
12   P. H. Abelson, Science (80-.)., 1990.
13   T. Johnson, SAE Int. J. Engines, 2016.

14   Gasoline Engine Management, 2014.
15   A. C. Alkidas, Energy Convers. Manag., 2007.
16   T. Johnson and A. Joshi, in SAE Technical Paper Series, 2018.
17   S. Matsumoto, Catal. Today, 2004, **90**, 183–190.
18   V. Badescu, in Studies in Systems, Decision and Control, 2017.
19   I. A. Reşitoğlu, K. Altinişik and A. Keskin, Clean Technol. Environ. Policy, 2015.
20   T. V. Johnson, SAE Int. J. Engines, 2011, **4**, 143–157.
21   T. V. Johnson, Int. J. Engine Res., 2009.
22   C. Song, Catal. Today, 2003.
23   H. Peace, B. Owen and D. W. Raper, Sci. Total Environ., 2004.
24   R. M. Heck, R. J. Farrauto and S. T. Gulati, Catalytic Air Pollution Control: Commercial Technology: Third Edition, 2012.
25   M. Fernandez-García, A. Martínez-Arias, J. A. Anderson, J. C. Conesa and J. Soria, 2009.
26   P. L. T. Gabrielsson, Top. Catal., 2004.
27   M. Koebel, M. Elsener and M. Kleemann, Catal. Today, 2000, **59**, 335–345.
28   M. Devadas, O. Kröcher, M. Elsener, A. Wokaun, N. Söger, M. Pfeifer, Y. Demel and L. Mussmann, Appl. Catal. B Environ., 2006.
29   M. Koebel, M. Elsener and G. Madia, in SAE Technical Paper Series, 2010.
30   Catal. Today, 1988.
31   M. Devadas, O. Kröcher, M. Elsener, A. Wokaun, G. Mitrikas, N. Söger, M. Pfeifer, Y. Demel and L. Mussmann, Catal. Today, 2007.
32   G. Busca, L. Lietti, G. Ramis and F. Berti, Appl. Catal. B Environ., 1998.
33   G. Tuenter, W. F. van Leeuwen and L. J. M. Snepvangers, Ind. Eng. Chem. Prod. Res. Dev., 1986.
34   M. Colombo, I. Nova, E. Tronconi, V. Schmeißer, B. Bandl-Konrad and L. Zimmermann, Appl. Catal. B Environ., 2012.
35   C. Ciardelli, I. Nova, E. Tronconi, D. Chatterjee, B. Bandl-Konrad, M. Weibel and B. Krutzsch, Appl. Catal. B Environ., 2007.
36   M. Koebel, M. Elsener and M. Kleemann, Catal. Today, 2000.
37   S. Brandenberger, O. Kröcher, A. Tissler and R. Althoff, The State of the Art in Selective Catalytic Reduction of NOx by Ammonia Using Metal-Exchanged Zeolite Catalysts, 2008, **50**, 492-531.
38   D. Yadav and R. Prasad, Procedia Technol., 2016, **24**, 639–644.
39   V. Narkhede, D. Kumar, R. M. Cursetji and T. A. Sidiquie, SAE Int. J., 2015, **8**, 380-385.
40   R. Q. Long and R. T. Yang, J. Catal., 1999.
41   K. Rahkamaa-Tolonen, T. Maunula, M. Lomma, M. Huuhtanen and R. L. Keiski, Catal. Today, 2005, **100**, 217–222.
42   R. Q. Long and R. T. Yang, J. Am. Chem. Soc., 1999.
43   Y. Xin, Q. Li and Z. Zhang, ChemCatChem, 2018.
44   W. Shan and H. Song, Catal. Sci. Technol., 2015.
45   A. M. Beale, F. Gao, I. Lezcano-Gonzalez, C. H. F. Peden and J. Szanyi, Chem. Soc. Rev., 2015, **44**, 7371–7405.
46   M. Colombo, I. Nova and E. Tronconi, in Catalysis Today, 2010.
47   P. Forzatti, L. Castoldi, I. Nova, L. Lietti and E. Tronconi, Catal. Today, 2006, **117**, 316–320.
48   Ch. Baerlocher and L.B. McCusker, 1996.

49   C. Baerlocher and L. B. McCusker, 2013.

50   R. Gounder and E. Iglesia, J. Am. Chem. Soc., 2009, **131**, 1958–71.

51   R. Gounder and E. Iglesia, Chem. Commun. (Camb)., 2013, **49**, 3491–509.

52   N. Kosinov, C. Liu, E. J. M. Hensen and E. A. Pidko, Chem. Mater., 2018, **30**, 3177-3198.

53   H.-Y. Chen, eds. I. Nova and E. Tronconi, Springer New York, New York, NY, 2014, 123–147.

54   S. Brandenberger, O. Kröcher, A. Tissler and R. Althoff, The State of the Art in Selective Catalytic Reduction of NOx by Ammonia Using Metal-Exchanged Zeolite Catalysts, 2008, **50**, 492-531.

55   F. Giordanino, P. N. R. Vennestrøm, L. F. Lundegaard, F. N. Stappen, S. Mossin, P. Beato, S. Bordiga and C. Lamberti, Dalt. Trans., 2013, **42**, 12741–61.

56   S. A. Bates, A. a. Verma, C. Paolucci, A. a. Parekh, T. Anggara, A. Yezerets, W. F. Schneider, J. T. Miller, W. N. Delgass and F. H. Ribeiro, J. Catal., 2014, **312**, 87–97.

57   F. Gao, N. M. Washton, Y. Wang, M. Kollár, J. Szanyi and C. H. F. Peden, J. Catal., 2015, **331**, 25–38.

58   E. Borfecchia, K. a. Lomachenko, F. Giordanino, H. Falsig, P. Beato, a. V. Soldatov, S. Bordiga and C. Lamberti, Chem. Sci., 2015, **6**, 548–563.

59   J. S. McEwen, T. Anggara, W. F. Schneider, V. F. Kispersky, J. T. Miller, W. N. Delgass and F. H. Ribeiro, Catal. Today, 2012, **184**, 129–144.

60   V. F. Kispersky, J. Kropf, F. H. Ribeiro and J. T. Miller, Phys. Chem. Chem. Phys., 2012, **14**, 2229-2238.

61   C. Paolucci, A. A. Verma, S. A. Bates, V. F. Kispersky, J. T. Miller, R. Gounder, W. N. Delgass, F. H. Ribeiro and W. F. Schneider, 2014, **53**, 11828–11833.

62   T. V. W. Janssens, H. Falsig, L. F. Lundegaard, P. N. R. Vennestrøm, S. Rasmussen, P. G. Moses, F. Giordanino, E. Borfecchia, K. a. Lomachenko, C. Lamberti, S. Bordiga, A. Godiksen, S. Mossin and P. Beato, ACS Catal., 2015, **5**, 2832-2845.

63   F. Gao, E. D. Walter, M. Kollar, Y. Wang, J. Szanyi and C. H. F. Peden, J. Catal., 2014, **319**, 1–14.

64   K. Kamasamudram, N. W. Currier and X. Chen, Catal. Today, 2010, **151**, 212–222.

65   J. H. Kwak, R. G. Tonkyn, D. H. Kim, J. Szanyi and C. H. F. Peden, Excellent activity and selectivity of Cu-SSZ-13 in the selective catalytic reduction of NOx with NH3, 2010, **275**, 197-190.

66   W. Su, Z. Li, Y. Peng and J. Li, Phys. Chem. Chem. Phys., 2015, **17**, 29142–29149.

67   M. Dusselier, M. A. Deimund, J. E. Schmidt and M. E. Davis, ACS Catal., 2015, 6078–6085.

68   F. Gao, Y. Wang, N. M. Washton, M. Kollár, J. Szanyi and C. H. F. Peden, ACS Catal., 2015, **5**, 6780–6791.

69   A. Wang, Y. Chen, E. D. Walter, N. M. Washton, D. Mei, T. Varga, Y. Wang, J. Szanyi, Y. Wang, C. H. F. Peden and F. Gao, Nat. Commun., 2019, **10**, 1137.

70   C. P. Generation, Power, 2007.

71   S. Dahlin, C. Lantto, J. Englund, B. Westerberg, F. Regali, M. Skoglundh and L. J. Pettersson, Catal. Today, 2019, **320**, 72–83.

72   J. Luo, K. Kamasamudram, N. Currier and A. Yezerets, Chem. Eng. Sci., 2018, **190**, 60–67.

73   S. W. Ham, H. Choi, I. S. Nam and Y. G. Kim, Ind. Eng. Chem. Res., 1995, **34**, 1616–

1623.

74   S.-W. Ham, I.-S. Nam and Y. G. Kim, Korean J. Chem. Eng., 2000, **17**, 318–324.

75   K. Wijayanti, S. Andonova, A. Kumar, J. Li, K. Kamasamudram, N. W. Currier, A. Yezerets and L. Olsson, Appl. Catal. B Environ., 2015, **166**–**167**, 568–579.

76   D. W. Brookshear, J. G. Nam, K. Nguyen, T. J. Toops and A. Binder, Catal. Today, 2015, **258**, 359–366.

77   L. Zhang, D. Wang, Y. Liu, K. Kamasamudram, J. Li and W. Epling, Appl. Catal. B Environ., 2014, **156**–**157**, 371–377.

78   A. Kumar, K. Kamasamudram, N. Currier and A. Yezerets, SAE Int. J. Engines, 2017, **10**, 1604-1612.

2. CATALYTIC CONSEQUENCES OF CONDITION-DEPENDENT CU SITE SPECIATION IN SSZ-13 ZEOLITE ON STANDARD SCR KINETICS

2.1 Preface

Chapter 2 reflects the reproduction of my first coauthored article published in The Journal of the American Chemical Society, 138 (18), 6028-6048, 2016, titled "Catalysis in a Cage: Condition-Dependent Speciation and Dynamics of Exchanged Cu Cations in SSZ-13 Zeolites". This chapter not only contains a good amount of experimental work (synthetic, titrimetric, spectroscopic and kinetic characterization), but also includes a lot of theory and computation results (stochastic simulations, *ab initio* dynamics and free energy calculations) from our collaborators. The contents of this chapter serve to combine experimental and computational approach to elaborate on Cu cation speciation dependency on different catalyst operating conditions as a function of catalyst composition over a wide range of zeolite chemical composition space. This chapter also reveals how structurally different Cu^{II} cationic sites will behave under SCR conditions, and whether they have the same low temperature reaction mechanism/pathway or not.

2.2 Abstract

The relationships among the macroscopic compositional parameters of a Cu-exchanged SSZ-13 zeolite, the types and numbers of Cu active sites, and activity for the selective catalytic reduction (SCR) of NO_x by NH_3 are established through experimental interrogation and computational analysis of materials across the catalyst composition space. Density functional theory, stochastic models, and experimental characterizations demonstrate that under the synthetic conditions applied here, Al randomly distribute on the SSZ-13 lattice subject to

Löwenstein's rule and that exchanged Cu^{II} ions first populate 2 Al sites within six-membered-rings before populating remaining 1 Al sites as $[Cu^{II}OH]^+$. These sites are distinguished and enumerated *ex situ* through vibrational and x-ray absorption spectroscopies (XAS) and chemical titrations. *In situ* and *operando* XAS follow Cu oxidation state and coordination environment as a function of environmental conditions including low temperature (473 K) SCR catalysis and are rationalized through first-principles thermodynamics and *ab initio* molecular dynamics. Experiment and theory together reveal that the Cu sites respond sensitively to exposure conditions, and in particular that Cu species are solvated and mobilized by NH_3 under SCR conditions. While Cu sites are spectroscopically and chemically distinct away from these conditions, they exhibit the same turnover rates, apparent activation energies and apparent reaction orders at the SCR conditions, even on zeolite frameworks other than SSZ-13.

2.3   Introduction

In 1925,[1] Hugh Stott Taylor theorized that specific groups of atoms were responsible for the rate enhancing capacity of heterogeneous catalyst surfaces, from which he coined the phrase "active site." This concept has become ubiquitous in modern catalysis science and has proven indispensable to the emergence of rational catalyst design. Most catalytic solids, however, are structurally heterogeneous at the molecular scale. They contain a distribution of active sites of different catalytic reactivity,[2–4] reflecting non-uniformities in active site coordination and local environment,[5,6] response to external stimuli,[7,8] and interactions with reacting molecules.[9–12] The integration of density functional theory (DFT) computational models and experimental operando spectroscopies that interrogate active sites during catalysis can provide powerful insights into the coupling between active site composition, reaction environment, and reaction mechanism.[13,14] In this work, we demonstrate how this approach enables the identification, quantification, and characterization of distinctly different active sites in a macro- and microscopically heterogeneous zeolite catalyst. We show through operando characterization that the composition and structure of active sites changes dynamically during reaction, differs from their ex situ states, and that such reaction-environment-induced modifications are integral to observed catalytic performance.

We demonstrate this capability in the context of Cu-exchanged zeolite catalysts. Zeolites are crystalline, nanoporous aluminosilicates constructed of corner-sharing SiO_4 and AlO_4 tetrahedra, or T-sites. Framework substitution of Si^{4+} by Al^{3+} introduces an anionic charge into

the oxide lattice that must be charge-compensated by extralattice cations. The Al sites are in general not ordered, so that at a given Si:Al ratio a zeolite presents a distribution of local Al environments.[15–19] The common oxidation states of Cu are 1+ and 2+, and thus a single Cu ion can in principle charge-compensate one or two Al T-sites.[20–27] The exact form of this exchange and charge compensation can depend on Cu oxidation state, overall framework structure, and local Al siting. In addition, Cu is observed to form multinuclear oxo-complexes and oxide clusters that further enrich its exchange chemistry and catalysis.[28–33]

Cu-exchanged zeolites have been explored for a variety of hydrocarbon partial oxidations [31,32,34–44] and NO_x reduction and decomposition chemistries.[45–47] Cu-zeolites have long been known to be active for the selective catalytic reduction (SCR) of NO_x with NH_3.[13,48–56] SCR catalysts promote the reduction of NO_x by NH_3:

$$4NO + 4NH_3 + O_2 \rightarrow 4N_2 + 2H_2O \tag{2.1}$$

over the competing and undesired oxidation of NH_3:

$$4NH_3 + 3O_2 \rightarrow 2N_2 + 6H_2O \tag{2.2}$$

Small pore Cu-exchanged SSZ-13, in particular, is able to satisfy all the practical requirements of an SCR catalyst and is now in commercial use.[57–60] However, the relationships between zeolite composition, reaction conditions, active site(s), and mechanism remain to be elucidated.
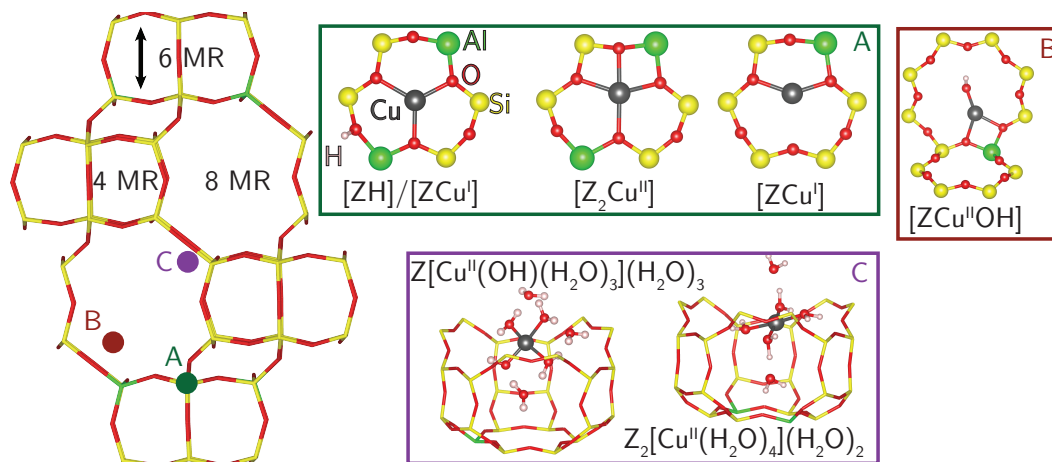
Figure 2.1 (left) side view of the chabazite cage. (right) HSE06-optimized structures of (A, B) dehydrated oxidized and reduced Cu sites and (C) hydrated oxidized sites. Label indicates location of Cu ion within the chabazite cage.

SSZ-13 has the chabazite topology. The single symmetry distinct T-site organizes into four-, six-, and eight membered rings (Figure 2.1, left) that form a cage ~8 Å in diameter.[61] SSZ-13 can be prepared in elemental compositions from highly enriched (Si:Al = 2) to infinitely dilute (Si:Al = ∞) in Al sites. The H-form (i.e., Al charge-compensated by H+) can be exchanged to various Cu:Al ratios, and the locations and forms of these exchanged Cu ions have received considerable attention.[28,62,63,65–79] X-ray absorption (XAS), UV−visible (UV−vis) , and infrared (IR) spectra of zeolites[28,42,66,70,71,80,81] all suggest exchanged Cu ions are present as hydrated and oxidized $Cu^{II}(H_2O)_6$ [82] at ambient conditions regardless of zeolite composition and topology.

The homogeneity of Cu sites under ambient conditions gives way to a rich variety of Cu species after high temperature and oxidative removal of H_2O. X-ray diffraction (XRD) reveals monomeric Cu ions in SSZ-13 that occupy either 6MR (A) sites[63,69] or both (A) and (B) sites[62,75] (Figure 2.1). We have reported that high Al content Cu SSZ-13 zeolites (Si:Al = 5) contain exclusively Cu^{II} in the (A) site under dry oxidizing conditions up to a Cu:Al = 0.20,[66,83] as demonstrated through the 4-fold coordination of Cu with zeolitic oxygen in extended X-ray absorption fine structure spectra (EXAFS) and titrations of residual Brønsted acid sites that reveal a 2:1 H^+:Cu^{2+} exchange stoichiometry. In contrast, Borfecchia et al. report 3-fold Cu coordination under similar conditions[64] on a Si:Al = 13, Cu:Al = 0.44 sample. Giordanino et al. report IR features attributable to Cu hydroxyl ($[Cu^{II}OH]^+$)[64,71] on Si:Al = 13, Cu:Al = 0.44, whereas Gao et al. only observe this band on a subset of Si:Al = 6 samples.[76] DFT calculations generally indicate that isolated, unligated Cu^I and Cu^{II} ions prefer the A site (Figure 2.1, left) regardless of the location of Al.[64,66,68,83–88]

H_2 temperature programmed reduction (TPR)[76,89] experiments are consistent with the existence of at least two types of exchanged Cu^{II} with differing susceptibility to reduction. Borffecchia et al. similarly observe only a fraction of Cu^{II} ions to reduce in He at 673 K. Chemical probes including NO, NO_2 and CO[73,89–94] will thus see a different mixture of Cu sites depending on sample history. For instance, NO adsorbs strongly on vacuum-reduced $Cu^{II} \rightarrow Cu^I$ sites[89,90] but more weakly and dynamically on Cu^{II} sites.[65,83] The relevance of these ex situ probes to catalytic conditions has yet to be established. Standard SCR is a redox reaction, as evidenced by the observation of both Cu^I and Cu^{II} in operando experiments,[73,84,95] and thus the ex situ reducibility of catalysts might be expected to correlate with observed activity. However, catalysts with different ex situ properties exhibit similar SCR characteristics. Reactant cutoff

experiments demonstrate that both NO and NH$_3$ are necessary for the Cu^{II} → Cu^{I} reduction half-cycle across samples of various compositions.[73,83] Apparent activation energies are the same (≈70 kJ mol^{-1}) and 473 K SCR turnover rates are linear in Cu content (Cu:Al = 0.08 − 0.20) on Si:Al = 5 samples.[66,83,96] Samples with compositions nearer to those studied by Borfecchia et al. present the same Cu^{I}/Cu^{II} fractions in operando XAS[73] and similar apparent activation energies[76] as the Si:Al = 5 samples but different susceptibilities to Cu reduction in H$_2$ TPR.[76] Thus, while there is general agreement that various isolated, exchanged Cu ions are present and contribute to the SCR catalysis, the precise nature, number, and reactivity of different cationic species, their dependence on zeolite composition (Si:Al and Cu:Al ratios) and framework topology, sample treatment history and environment, and their spectroscopic signatures under ex situ vs. in situ conditions, remain unknown. Here, we report a coordinated computational (stochastic simulation, ab initio dynamics, and free energy) and experimental (synthetic, spectroscopic and titrimetric) analysis of Cu speciation under ex situ conditions and in situ and operando SCR conditions as a function of catalyst composition over a wide range of zeolite chemical composition space. We demonstrate that the types, numbers, and chemical characteristics of Cu sites depend on bulk composition of the zeolite, can be predicted through first-principles-based models, can be distinguished in the laboratory, and depend strongly on the environmental conditions. Environmental conditions have a profound impact on Cu ion siting, coordination, and mobility, resulting in SCR turnover rates (473 K) that are independent of the initial Cu cation site and the zeolite framework type. The results rationalize a large body of literature, resolve contradictory findings regarding the active sites for NO$_x$ SCR, and consolidate the understanding of Cu cation speciation in zeolites.

2.4   Results

2.4.1   Cu Cation Speciation in Cu-SSZ-13

2.4.1.1   First-principles Speciation of Cationic Cu Complexes

We first created molecular models for isolated Cu exchange sites in SSZ-13 and established their relative free energies under wet and oxidizing conditions relevant to Cu exchange and catalyst treatment. We used a 12 T-site supercell[66,83,84] with a single Al substitution to represent an isolated Al atom in the CHA framework. Charge-compensating Cu^{I} ions prefer to sit in the plane

of the 6MR,[66,83,84,86] and we label this structure as [ZCu^I] in Figure 2.1A to denote charge-compensation of a single Al (Z) by Cu. This notation also emphasizes the formal 1+ oxidation state of Cu, and this structure is used as the Cu^I reference in relating computed Bader charges to effective Cu oxidation states. An oxidized form of the Cu site compensating a single framework Al atom has been proposed[64,73,97] to be formed by addition of an extra-lattice OH ligand, which redirects the Cu into the 8MR according to the optimized [ZCu^{II}OH] structure shown in Figure 2.1B. Similarly, two proximal framework Al atoms (2Al sites) can be charge compensated by a single Cu^{II} ion. The exchange energies of Cu^{II} at different potential 2Al sites were previously computed using a 2 × 1 × 1 24 T-site supercells containing 4 Al atoms distributed to place 2Al sites in each of the 4, 6, and 8MR:[66]

$$Z_2H_4 + Cu^{II}_{(aq)} \rightarrow Z_4H_2Cu^{II} + 2H^+_{(aq)} \tag{2.3}$$

Cu^{II} exchange at 2Al sites in the 6MR ring is 108 and 145 kJ mol^{-1} more exothermic than exchange at 2Al sites in the 4MR and 8MR, respectively. We adopt a model with 2Al at third-nearest-neighbor (3NN) positions in a 6MR for Cu near 2Al. Cu exchange at the 2NN Al 6MR is coordinatively similar and the exchange energy more endothermic by 22 kJ mol^{-1}. The 3NN Al 6MR structure is labeled [Z$_2$Cu^{II}] in Figure 1A and is taken as the Bader charge standard for the Cu^{II} oxidation state. We previously found that this [Z$_2$Cu^{II}] site can be reduced by addition of H to an Al site proximal to Cu,[83] which is the [ZH]/[ZCu^I] species shown in Figure 2.1A. The forward slash emphasizes that these two sites are proximal. Reduction to Cu^I decreases Cu coordination to the lattice but preserves Cu location within the 6MR.

Motivated by XAS[20,66,70] and molecular dynamics[98] evidence that exchanged Cu^{II} ions are hydrated under ambient conditions, we first explored H$_2$O coordination to the [Z$_2$Cu^{II}] and [ZCu^{II}OH] ions by computing the structures and successive adsorption energies of H$_2$O ligands (x = 1 to 6):

$$1Al: \quad ZCu^{II}(OH)(H_2O)_{x-1} + H_2O \xrightarrow{\Delta E_{ads}} ZCu^{II}(OH)(H_2O)_x \tag{2.4}$$

$$2Al: \quad Z_2Cu^{II}(H_2O)_{x-1} + H_2O \xrightarrow{\Delta E_{ads}} Z_2Cu^{II}(H_2O)_x$$
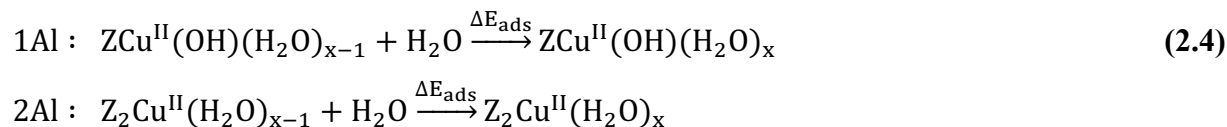
Table 2.1 H_2O adsorption energies (ΔE_{ads}) on Cu sites computed using HSE06-TSvdw. Cage location referenced to Figure 2.1. CN and O_f indicate total Cu coordination number and number of close framework O contacts, respectively.

	$+ xH_2O$	1	2	3	4	5	6
	ΔE_{ads} (kJ mol^{-1})	−84	−94	−108	−84	−90	−73
Z_2Cu	Cage Location	A	A	B	C	C	C
	O_f/total CN	3/4	3/4	2/4	0/4	0/4	0/4
	ΔE_{ads} (kJ mol^{-1})	−75	−67	−76	−63	−95	−56
ZCuOH	Cage Location	B	C	C	C	C	C
	O_f/total CN	2/4	0/3	0/3	0/4	0/4	0/4

In each simulation, we started from the equilibrated (x − 1) H_2O structure, added another H_2O molecule, annealed for 150 ps at 473 K using NVT ab initio molecular dynamics (AIMD) at the GGA level, then subsequently optimized the geometry and evaluated the energy with the HSE06 functional including Tkatchenko Scheffier van der Waals (TSvdw) corrections, and zero-point vibrational energies (ZPE) (supplementary information section 2.1.1-1 of Paolucci et al.[177]). Energy and Cu coordination number (CN) results are summarized in Table 2.1, where CN is defined as the number of heavy atoms within 2.3 Å of Cu. H_2O adsorption energies are on the order of −70 to −90 kJ mol^{-1} and are generally more exothermic on [Z_2Cu^{II}] than on [$ZCu^{II}OH$] sites. The computed Cu oxidation state is insensitive to added H_2O. On [Z_2Cu^{II}], successive H_2O ligands generally displace framework oxygen (O_f) from the first coordination sphere, until at x = 4 the Cu^{II} ion is fully coordinated by H_2O; additional H_2O molecules form a second coordination sphere through hydrogen bonds to first shell H_2O. With hydration, the Cu ion moves from within the 6MR (site A, Figure 2.1) to the 8MR (site B) to the cage center (site C). The final optimized x = 6 structure is shown in Figure 2.1C. The [$ZCu^{II}OH$] site behaves similarly with added H_2O; the fully hydrated complex is shown in Figure 2.1C.

Exchanged Cu may lose waters of hydration and acquire other ligands during synthesis and after oxidation or reduction treatments. We computed the structures and energies of various combinations of O, OH, H_2O, and O_2 ligands on both the 1Al and 2Al models in the nominally oxidized and reduced states. The list of candidate structures was guided by chemical plausibility and includes proposed intermediate species reported elsewhere (e.g., $Cu^{II}O$, $Cu^{II}(OH)_2$).[84,99] Optimized structures, energies, and ZPE's, of all 26 species are tabulated in SI 2.1.1-1. We applied a first-principles thermodynamic analysis to rank the stability of this library of Cu-bound

H_xO_y species as a function of temperature and hydrogen and oxygen potentials. We take O_2 and H_2O as the oxygen and hydrogen references, respectively:

$$Z_*Cu + \frac{x}{2}\left(H_2O - \frac{1}{2}O_2\right) + \frac{y}{2}O_2 \xrightarrow{\Delta G_{form}} Z_*CuH_xO_y \qquad (2.5)$$
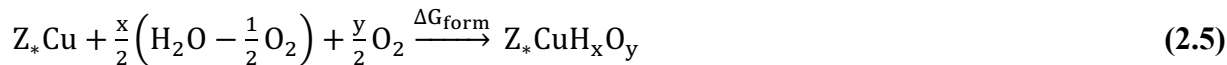
used the HSE06-TSvdw energies and applied previously developed correlations[83] to estimate adsorbate entropies. The formation free energies (ΔG_{form}) are computed according to Section 5.2 and the μH_2O and μO_2 related to T and P through the ideal gas relation. Results for an ambient condition (Condition 1, 298 K, 2% H_2O, and 20% O_2) representative of an air- exposed catalyst, and an elevated temperature condition (Condition 2, 673 K, 2% H_2O, and 20% O_2) representative of an oxidation pretreatment are summarized in Figure 2.2. For clarity, species with $\Delta G_{form} >$ +200 kJ mol^{-1} are not shown in Condition 2.

At the high temperatures (673 K) and high oxygen potentials (20% O_2) of Condition 2, the lowest free energy structure near the 2Al site is the isolated [Z_2Cu^{II}] ion. At these conditions, adsorption of a single H_2O ligand is endergonic by 15 kJ mol^{-1}, and the reduced form of the Cu site ([ZCu^I]/[ZH]) is endergonic by another 15 kJ mol^{-1}. Other adsorbates on Cu sites near 2Al lead to complexes much higher in free energy, including adsorbed molecular O_2. Similarly, on Cu sites near 1Al, the lowest free energy structure is oxidized [$ZCu^{II}OH$] with normalized Bader charge (SI 2.1.1-1) of +1.8, slightly less than [Z_2Cu^{II}]. The reduced form of the site, [ZCu^I], and its hydrated form, [$ZCu^I(H_2O)$], are very close in free energy to the oxidized [$ZCu^{II}OH$] state. Molecular O_2 adsorption on the [ZCu^I] site is endergonic by 50 kJ mol^{-1} relative to [$ZCu^{II}OH$], and even higher in free energy are other oxidized forms, including [$ZCu^{II}O$][99] and [$ZCu^{II}(OH)_2$].[84] The primary effect of decreasing temperatures to ambient (Condition 1) is a significant decrease in the free energies of all hydrated Cu states, which causes the most stable species to become the fully hydrated $Z_2[Cu^{II}(H_2O)_4](H_2O)_2$ and $Z[Cu^{II}(OH)(H_2O)_3](H_2O)_3$ complexes at 2Al and 1Al sites, respectively.
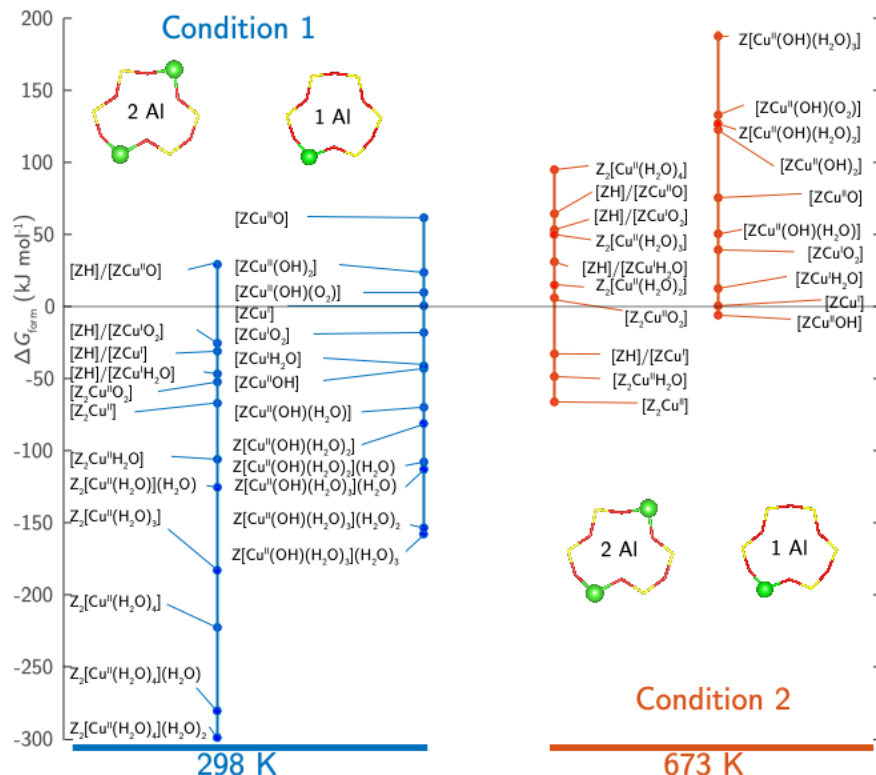
Figure 2.2 Formation free energies (ΔG_{form}) CuH_xO_y species at (left) 298 K, 2% H_2O, 20% O_2 and at (right) 673 K, 2% H_2O, 20% O_2 on the 2Al (Z_2Cu) and 1Al (ZCu) sites. Common energy reference set through Equation 2.6.

We generalize the analysis in Figure 2.2 to a range of temperatures and O_2 pressures at fixed H_2O partial pressure (2%) and plot the lowest free energy species at each set of conditions in Figure 2.3 in the form of a phase diagram. For reference, Conditions 1 and 2 of Figure 2.2 are labeled with red boxes on Figure 2.3. The phase diagrams are insensitive to the H_2O pressure over the range of experimental interest. For comparison, we report the corresponding T-P_{H2O} diagram in supplementary information section 2.1.1-2 of Paolucci et al.[177]. As discussed below, these diagrams indicate that the stable Cu state (CN, O_f, and oxidation state) depend sensitively on the environmental conditions over ranges of experimental interest and that the lowest free energy species differ for Cu complexes that charge compensate 1Al or 2Al sites.
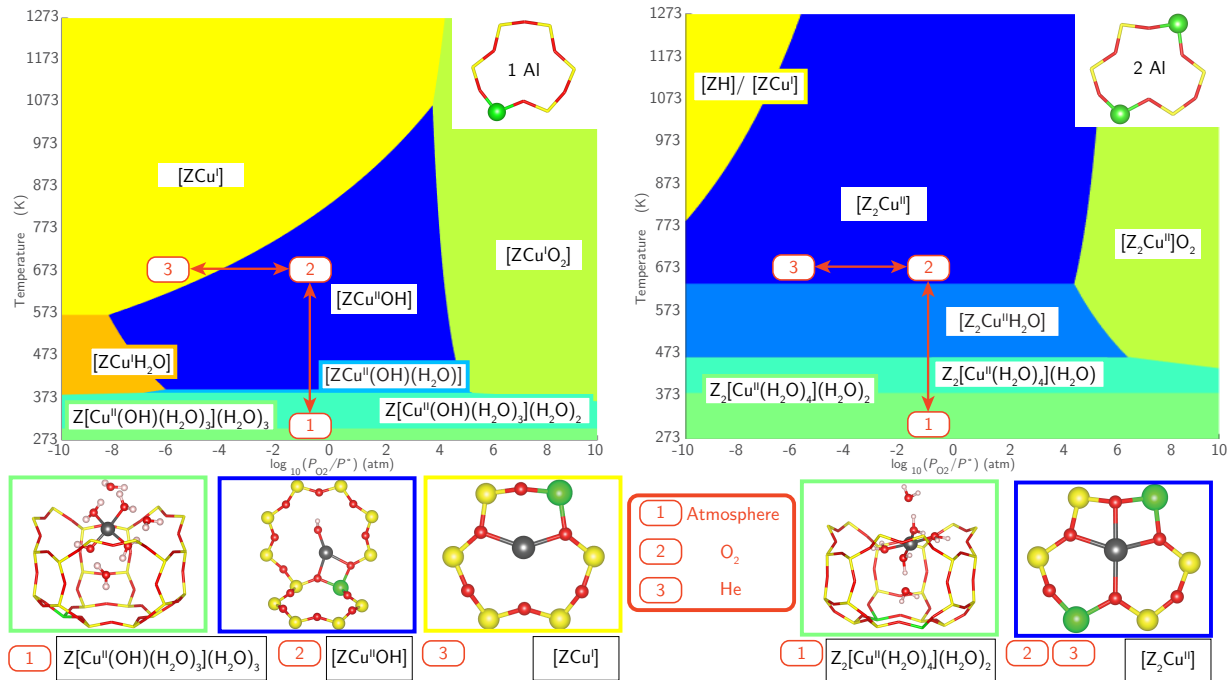
Figure 2.3 Ex situ Cu speciation phase diagrams based on HSE06-Tsvdw calculations on 1Al (left) and 2Al (right) Cu exchange sites. Regions indicate site composition that minimizes free energy at 2% H_2O and given T and PO_2. Labeled on the phase diagram and illustrated below are minimum free energy species at (1) ambient (298 K, 20% O_2), (2) oxidizing (673 K, 20% O_2) and (3) inert (673 K, 10^{-6} atm O_2 in He).

2.4.1.2   1Al and 2Al Cu Exchange Populations

To this point, we have treated the 1Al and 2Al sites independently. To place these two on a common energy scale, we computed the Cu exchange energy between the two sites:

$$[Z_2CuH_2O] + [ZH] \rightarrow ZH/ZH + [ZCuOH] \quad \Delta E = +66\text{ kJ mol}^{-1} \tag{2.6}$$
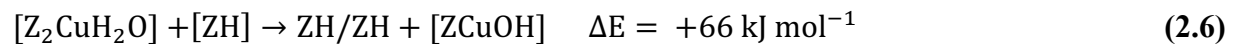
We evaluated this energy in a large supercell containing separated Z_2 and Z sites as well as in separate supercells constructed to conserve atomic numbers; results are in close agreement (+66 vs. +69 kJ mol^{-1}) and structures are given in supplementary information section 2.1.2 of Paolucci et al.[177] . We used the +66 kJ mol^{-1} result to offset the 0 K energies of $[Z_2Cu^{II}H_2O]$ and $[ZCu^{II}OH]$ and thus place the two site types on the same free energy y-axis shown in Figure 2.2. The zero of energy is defined as $[ZCu^{I}]$. The free energy associated with Cu near 2Al is substantially lower than Cu near 1Al at both 298 K (-142 kJ mol^{-1}) and at 673 K (-55 kJ mol^{-1}).

These results indicate that Cu ions prefer to segregate to 6MR 2Al exchange sites over a wide range of conditions.

The relative density of Cu ions in 6MR 2Al sites and in 8MR 1Al sites will depend on the total Cu content and the number of such 2Al and 1Al sites present in a given SSZ-13 sample. We determined the Al distribution as a function of Si:Al ratio by numerical simulation[17,66] assuming random Al distribution subject to Löwenstein's rule,[100] which prohibits 1NN Al pairs. We then assume that exchanged Cu ions populate all available 2NN and 3NN 2Al sites as [Z_2Cu^{II}] before occupying 1Al sites as [$ZCu^{II}OH$]. Figure 2.4 reports the computed fraction of Cu present as [$ZCu^{II}OH$] as a function of Si:Al and Cu:Al ratios. The region below the white line corresponds to a composition space containing exclusively Cu species near 2Al, while the region above the white line contains gradually increasing [$ZCu^{II}OH$] fractions that become the dominant species in the upper right red area. To ensure 2Al 6MR stay charge compensated by a single Cu past the saturation point we computed the energy of two [$ZCu^{II}OH$] in a 6MR (supplementary information section 2.1.2 of Paolucci et al.[177]):

$$[Z_2CuH_2O] + [ZCuOH] \rightarrow ZCuOH/ZCuOH + [ZH] \qquad \Delta E = +81 \text{ kJ mol}^{-1} \qquad \textbf{(2.7)}$$
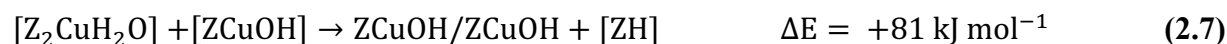
Thus, these 6MR 2Al sites will remain populated by [Z_2Cu^{II}] as additional Cu is exchanged in the form of [$ZCu^{II}OH$].

To test these model predications, we prepared and analyzed a series of SSZ-13 catalysts of varying Si:Al and Cu:Al ratio (samples represented by white circles in Figure 2.4). An Al-rich SSZ-13 sample (Si:Al = 5) was synthesized using high Al FAU zeolite as the Al source[101] and characterized as reported previously,[28,66,83,102,103] while lower Al content SSZ-13 samples (Si:Al = 15, 25) were synthesized using $Al(OH)_3$ as the Al source.[104] Powder XRD patterns (Supplementary Information section 2.1.3-1 of Paolucci et al.[177]), and Ar adsorption isotherms (87 K, SI Supplementary Information section 5.3-2 of Paolucci et al.[177]) were consistent with the CHA topology on all H-form SSZ-13 samples. The number of H^+ sites on each H-SSZ-13 sample was quantified from the NH_3 evolved during TPD of NH_4-form samples, and were 0.65, 1.02, and 0.98 H^+:Al for the Si:Al ratios of 5, 15, and 25, respectively. The high Al H-SSZ-13 sample (Si:Al=5) contained fewer H^+ sites than its number of framework Al atoms (H^+:Al_f = 0.76),[103] reflecting the imprecision with which ex situ methods such as 27Al MAS NMR

spectroscopy may characterize structural surrogates for H^+ sites. It also reflects the non-uniformity of SSZ-13 samples prepared using FAU to CHA interconversion methods,[101] for which repeat synthesis experiments on crystallized samples that contained H^+: Al ratios that varied between 0.45-0.85 were observed (Supplementary Information section 2.1.3-4 of Paolucci et al.[177]).
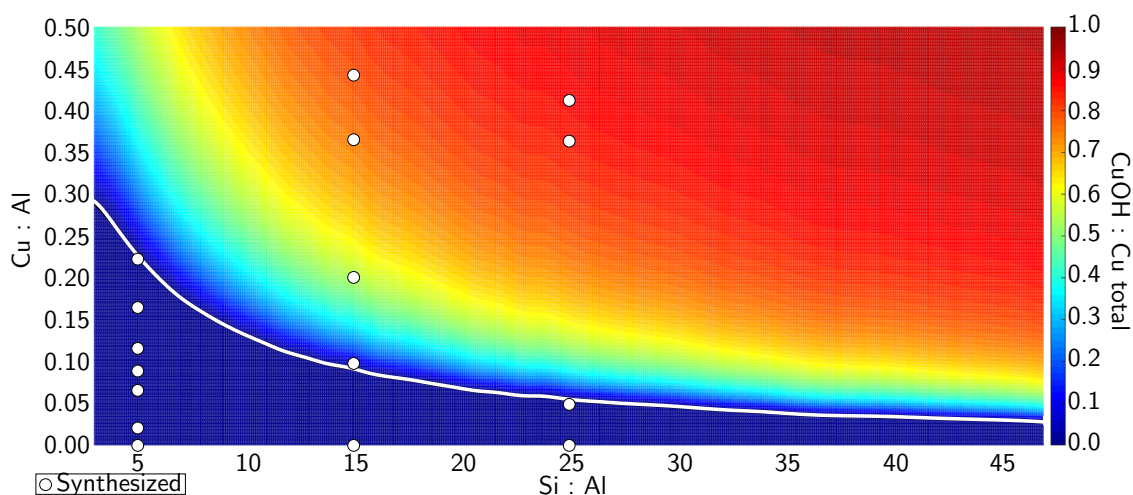
Figure 2.4 Predicted Cu site compositional phase diagram vs. Si:Al and Cu:Al ratios. Color scales indicates predicted fraction of CuOH. White line demarcates transition from [Z2Cu^{II}]-only region to mixed [Z2Cu^{II}]/[ZCu^{II}OH] region. White circles indicated compositions of synthesized Cu-SSZ-13 samples.

Increasing amounts of Cu were exchanged into these three (Si:Al = 5,15,25) H-SSZ-13 samples from aqueous-phase Cu^{II}(NO$_3$)$_2$. The number of residual H+ sites was quantified using NH$_3$ TPD, which was performed after samples were saturated with gaseous NH$_3$ (433 K) and purged in wet helium (3% H$_2$O, 433 K) to desorb Lewis acid-bound NH$_3$ and selectively retain NH$_4^+$ species,[102] as illustrated by Equation 2.8:

$$Z_*CuNH_3 + H_2O \rightarrow Z_*CuH_2O + NH_3 \tag{2.8}$$

$$Z_*CuNH_3 + H_2O \rightarrow Z_*CuH_2O + NH_3$$

Figure 2.5 shows the number of residual H^+ sites present on each Cu-SSZ-13 sample after oxidative treatment in flowing air (773 K), normalized by the number of H^+ sites quantified on their respective H-SSZ-13 parent samples after the same oxidative treatment, as a function of Cu:Al ratio. The dashed lines in Figure 2.5 represent the number of residual H^+ sites as a

function of Cu:Al ratio predicted from the simulation results in Figure 2.4. At a Si:Al ratio of 5, each exchanged Cu cation decreased the number of residual H^+ sites by two (on average) up to a Cu:Al ratio of 0.20 (Figure 2.5),[102,103] consistent with the exchange stoichiometry:

$$Z_2H_2 + Cu^{II} \rightarrow Z_2Cu^{II} + 2H^+ \tag{2.9}$$

On samples with Si:Al ratios of 15 and 25, each exchanged Cu exchanged two H^+ sites until Cu:Al ratios of 0.10 and 0.04, respectively, but only one additional H^+ site beyond this limit (Figure 2.5), consistent with the exchange reaction:

$$ZH + Cu^{II}H_2O \rightarrow ZCuOH + 2H^+ \tag{2.10}$$

These Cu:H^+ exchange stoichiometries provide experimental evidence that cationic Cu species exchange sequentially as [Z_2Cu^{II}] sites until saturation and then as [$ZCu^{II}OH$] sites (Figure 2.2).

Figure 2.6 shows FTIR quantification of the disappearance of Brønsted ZH species and the appearance of [$ZCu^{II}OH$] as a function of Cu density on the series of Cu-SSZ-13 samples with Si:Al= 15. The H-SSZ-13 spectrum includes four features in the O–H region, including modes at 3605 and 3580 cm^{-1} [105,106] from Brønsted sites, at 3732 cm^{-1} from isolated silanols, and at 3700 cm^{-1} from vicinal silanols.[107] The integrated area of the Brønsted ZH peaks of the Cu:Al 0.12 sample, taking that of the H-SSZ-13 sample as the baseline, decreased with a 2:1 H^+:Cu ratio (supplementary information section 2.1.3-3 of Paolucci et al.[177]), consistent with Equation 2.9. A new, fifth feature appears at 3660 cm^{-1} in Cu:Al > 0.21 samples, at a location consistent with previous assignment to[64] and the computed harmonic O–H stretch frequency of [$ZCu^{II}OH$]. The integrated area of this 3660 cm^{-1} band increases linearly across the range Cu:Al = 0.21-0.44 (Figure 2.6 inset), and the integrated areas of the Brønsted OH stretches decrease concurrently in a 1:1 H^+:Cu ratio, consistent with Equation 2.10. These vibrational data provide strong additional support for the sequential population of [Z_2Cu^{II}] followed by [$ZCu^{II}OH$] sites.
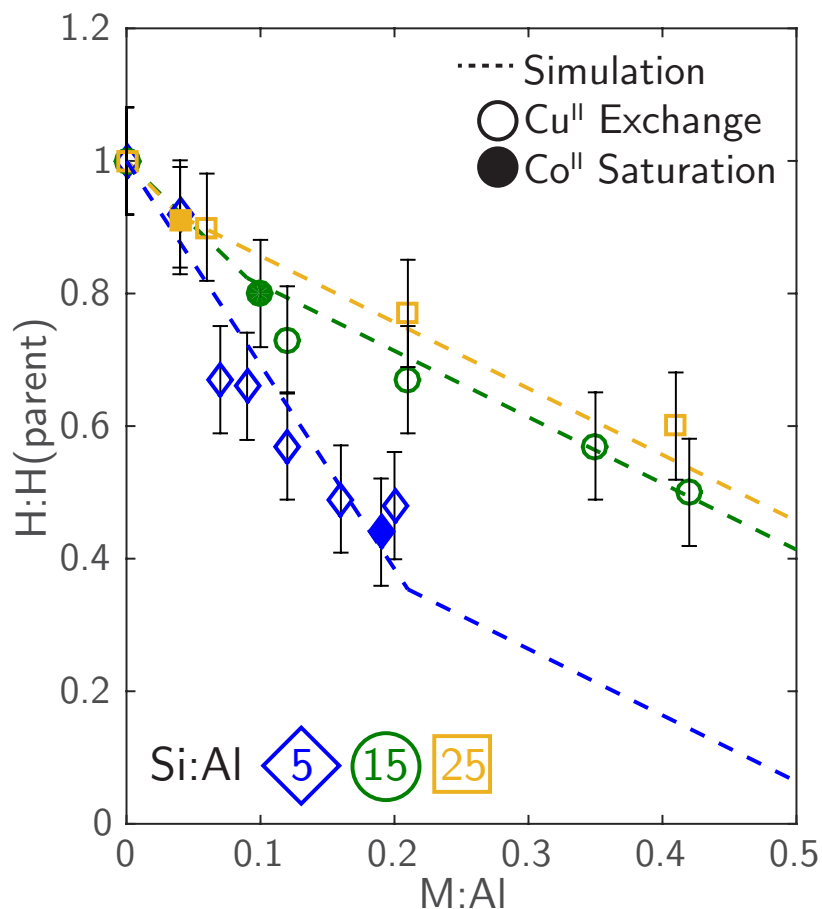
Figure 2.5 Residual H$^+$ sites per parent sample H$^+$ from NH$_3$ titrations on oxidized M-SSZ-13 samples vs. extent of M/Al exchange for Si:Al = 5 (blue diamonds), 15 (green circles) and 25 (orange squares). Open and filled symbols denote CuII and saturated CoII exchange, respectively. Dashed lines are model predictions

Co^{II} exchange provides a third independent enumeration of the number of 2Al 6MR sites on each sample, because Co^{II} does not exchange at single Al sites as [ZCo^{II}OH] at the exchange pH used here (pH ≈3.2).[108] Samples with Si:Al ratios 5, 15, and 25 were saturated with Co^{II} and the Co:Al contents were determined by atomic absorption (supplementary information section 2.1.3-2 of Paolucci et al.[177]) to be 0.19, 0.10, and 0.04, respectively. These values agree quantitatively with the maximum number of 2Al 6MR sites predicted for each Si:Al ratio in Figure 2.4 for a random Al distribution in SSZ-13. Furthermore, the numbers of residual of H$^+$ sites on Co-saturated SSZ-13 samples were quantified by NH$_3$ titration and are plotted on Figure 2.5 as filled symbols, and agree quantitatively with the transition Cu:Al ratios between exchange of [Z$_2$Cu^{II}] and [ZCu^{II}OH] species. These results indicate that isolated Co^{II} and Cu^{II} exhibit

identical preferences for 2Al 6MR sites and that both cations replace two Brønsted sites via Equation 9 when exchanged at these sites.
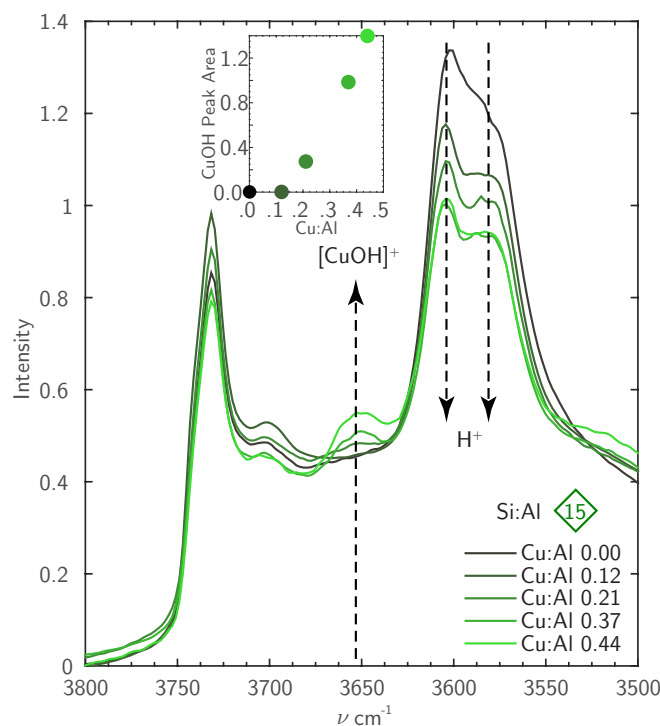
Figure 2.6 FTIR spectra of oxidized Cu-SSZ-13 samples (Cu:Al = 0–0.44, Si:Al=15). Inset: Integrated 3660 cm^{-1} CuO-H area as a function of Cu:Al ratio.

The Cu:Al values that demarcate the transition between formation of [Z$_2$Cu^{II}] sites and [ZCu^{II}OH] sites are 0.20, 0.10 and 0.04 for the H-SSZ-13 samples with Si:Al ratios of 5, 15 and 25, respectively (Figure 2.5). These Cu:Al values are identical, within error, to the fraction of 2Al 6MR sites predicted from simulation of Al distribution in CHA frameworks at these Si:Al ratios (Figure 2.4). Taken together, these experimental and computational findings indicate that under the conditions of synthesis applied here,[109] the concentration of 2Al 6MR sites are in agreement with a random Al distribution in SSZ-13 subject to Löwenstein's rule, that 2Al 6MR are the preferred sites for Cu^{II} exchange, and that these sites saturate before remaining 1Al sites are populated with [ZCu^{II}OH]. This quantification allows us to identify and contrast the structures, properties and catalytic performance under low temperature (473 K) standard SCR conditions of samples that contain predominantly [Z$_2$Cu^{II}] or [ZCu^{II}OH] sites. We choose a sample with Si:Al=5 and Cu:Al=0.08 to represent a [Z$_2$Cu^{II}] site and a sample with Si:Al=15 and Cu:Al=0.44,

similar in composition to that explored by others,[64,71,73] to represent [ZCu^{II}OH]. We refer to these as the "2Al" and "1Al" samples, respectively. While the 1Al sample contains ≈20% [Z$_2$Cu^{II}] sites, they are in the minority and the bulk spectroscopic techniques applied here are primarily sensitive to the majority [ZCu^{II}OH] site.

2.4.2   Copper Cation Structure under *ex situ* Conditions

We next combined XAS and AIMD simulations to explore the molecular and electronic structures of both the model 1Al and 2Al samples as a function of the conditions represented in Figure 2.3. Results are summarized in Figure 2.7 and 2.8 and in Table 2.2. We expect the framework composition to be robust to the conditions studied here. Significant dealumination of SSZ-13 is observed only after several hours of exposure to 10% H$_2$O at ≈1000 K.[60,79,110,111]

2.4.2.1   Condition 1: Ambient Atmosphere (XAS/AIMD)

First, both 1Al and 2Al samples were subjected to high temperature oxidative treatments and then exposed to ambient atmosphere at 298 K, corresponding to Condition 1 of Figure 2.3. The Cu K-edge X-ray absorption near edge spectra (XANES) collected on both samples were indistinguishable, as shown in Figure 2.7, left. A single edge at 8.988 keV corresponds to the 1s→4p transitions of a Cu^{II} ion in a distorted square-planar or octahedral coordination.[82] EXAFS spectra of both samples from the same energy scan (Figure 2.7, middle) exhibited a high intensity first coordination shell peak at ≈ 1.5 Å. The spectra were fitted using a Cu$_2$O(s) experimental reference to estimate 4.0 Cu-O bonds (1.94 Å average distance), and 4.2 Cu-O bonds (1.93 Å average distance) respectively on the 2Al and 1Al samples, which are identical within the ±5% error of the fit (details in supplementary information section 2.2.1-1 of Paolucci et al.[177]). Higher coordination shells beyond 2.0 Å appear with low intensity on both samples and indicate Cu-O bonds with extra- framework O species, as evidenced by the absence of scattering from Si or Al atoms bound to O$_f$. The XANES and EXAFS spectra are indistinguishable from each other and that of aqueous Cu^{II} complexes,[82] which are also known to form a square-planar tetraaquo complex. These observations are in agreement with the phase diagram Condition 1 predictions shown in Figure 2.3.

The EXAFS provides an ensemble average of the Cu coordination environment. To extract comparable information from simulation, we performed 298 K AIMD simulations (50 ps

of equilibration followed by 90 ps of sampling) on the lowest free energy hydrated forms of [Z_2Cu^{II}] and [$ZCu^{II}OH$].
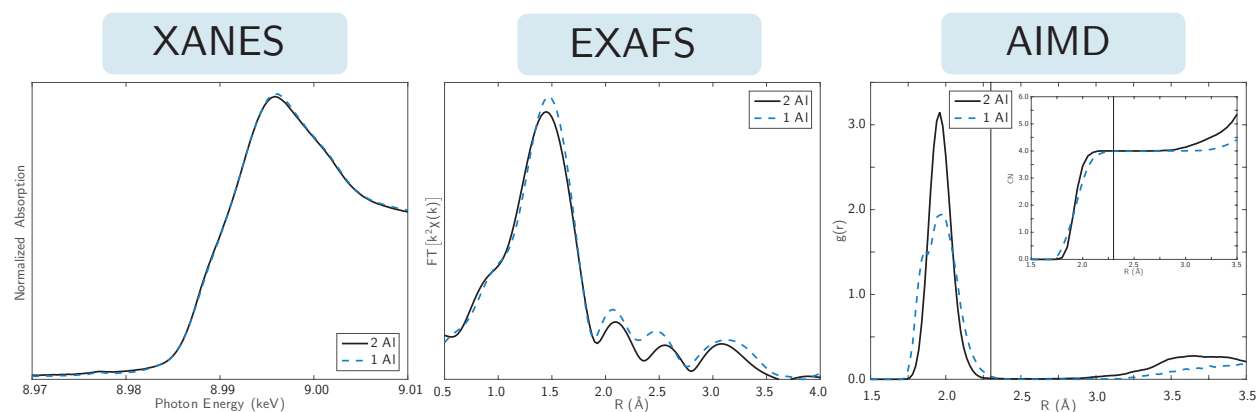
Figure 2.7 Left: XANES spectra collected on the 1Al (teal dashes) and 2Al (black lines) Cu-SSZ-13 samples under treatment in 2% H_2O 20% O_2 at 298 K Middle: EXAFS spectra at same conditions. Right: 298 K AIMD RDFs and integrated RDFs (inset)

In both cases, Cu remained near the center of the cage (Figure 2,1C) and were dynamic. Figure 2.8 superimposes the Cu positions relative to the zeolite cage during the 90 ps sampling. To quantify Cu mobility, we discretized the supercell into 0:2×0:2×0:2 Å cubes, counted the cubes visited at least once during the simulation, scaled by the cube volume, and normalized to the volume visited by $Z_2[Cu^{II}(H_2O)_4(H_2O)_2]$. Results are summarized in Table 2.2 and further detailed in supplementary information section 2.2.1-2 of Paolucci et al.[177]. $Z[Cu^{II}OH(H_2O)_3](H_2O)_3$ is estimated to be 1.38 times as mobile as $[Z_2Cu^{II}(H_2O)_4](H_2O)_2$, consistent with the weaker electrostatic attraction to a single Al compared to two proximal Al atoms. Throughout the $Z[Cu^{II}OH(H_2O)_3](H_2O)_3$ simulation, H atoms are observed to hop between non-framework O with a barrier of ~20 kJ mol^{-1}, causing O bound to Cu to spend time as both OH and H_2O. The right panel of Figure 2.7 shows the computed radial distribution functions (RDFs) between Cu and all heavy atoms. Both RDFs show a prominent peak near 2 Å corresponding to the first coordination shell with peak area corresponding to four O atoms. This first RDF peaks correspond with the first EXAFS peak (the RDF and EXAFS are offset due to the difference between electron scattering and interatomic distances). The 1Al RDF is broadened in comparison to the 2Al due to the presence of both shorter Cu-OH and longer Cu-H_2O bonds that are not resolvable by EXAFS. The RDFs are near-zero between 2.2- 3.0 Å; structure appears

beyond 3.0 Å. The results are consistent with the observation of only low intensity peaks beyond the first major one in the EXAFS and H_2O solvated Cu complexes.

Table 2.2 Comparison of AIMD (blue, left) and EXAFS (black, right) characterization of 2Al and 1Al sites, including Cu-X (X = O, N) coordination number (CN), average Cu-X distances, and whether second-shell features appear.

Gas Condition	Sample	CN	Avg. Bond Dist.	2nd Shell	Cu mobility[c]
			AIMD | EXAFS		
Condition 1 (Ambient)	1Al	4.0|4.2	1.96|1.93	N|N	1.38
	2Al	4.0|4.0	1.96|1.94	N|N	1.00
Condition 2 (O_2)	1Al	3.0|3.0	1.89|1.91	Y|Y	0.11
	2Al	3.9|3.8	2.02|1.94	Y|Y	0.14
Condition 3 (He)	1Al	2.5[a]|2.4	1.92[a]|1.92	Y|Y	0.14[a]
	2Al	3.7[a]|3.6	2.50[a]|2.40	Y|Y	0.14[a]
$NO + NH_3$ 473 K	1Al	2.0|2.2	1.89|1.88	N|N	3.26
	2Al	2.0|2.1	1.89|1.88	N|N	1.83
$O_2 + NH_3$ 473 K	1Al	3.3[b]|3.2	1.97[b]|1.92	N|N	2.21[b]
	2Al	3.6[b]|3.5	2.00[b]|1.92	N|N	1.31[b]

[a] XANES weighted average of Cu^I (ZCu^I) and Cu^{II} (Z_2Cu and $ZCuOH$) structures obtained from AIMD.
[b] XANES weighted average of Cu^I ($ZCu^I(NH_3)_2$ and $ZNH_4/ZCu^I(NH_3)_2$) and Cu^{II} ($Z_2Cu(NH_3)_4$ and $ZCu(OH)(NH_3)_3$) structures obtained from AIMD.
[c] Volume visited by the minimum free energy forms of Cu^I and Cu^{II} (Fig. 3) during 90 ps AIMD, normalized to the volume of hydrated Z_2Cu (1.00).

2.4.2.2 Condition 2: 20% O_2, 673 K (XAS/AIMD)

Next, we collected XANES spectra at 298 K on both samples after 1 hour treatment at 673 K in O_2, corresponding to Condition 2 in Figure 2.3. The vessels were sealed before cooling to prevent rehydration of Cu. Resultant XANES and EXAFS are shown in Figure 2.9. In addition to the 8.988 keV CuII edge feature found observed in Figure 2.7, an additional feature appears at 8.987 keV that reflects Cu^{II} present in a lower than octahedral coordination environment.[20] Further, on the 1Al sample a low intensity peak appears at 8.983 keV that we assign to 5% Cu^I based on a fit using Cu^I and Cu^{II} references (supplementary information section 2.2.2-1 of Paolucci et al.[177]).
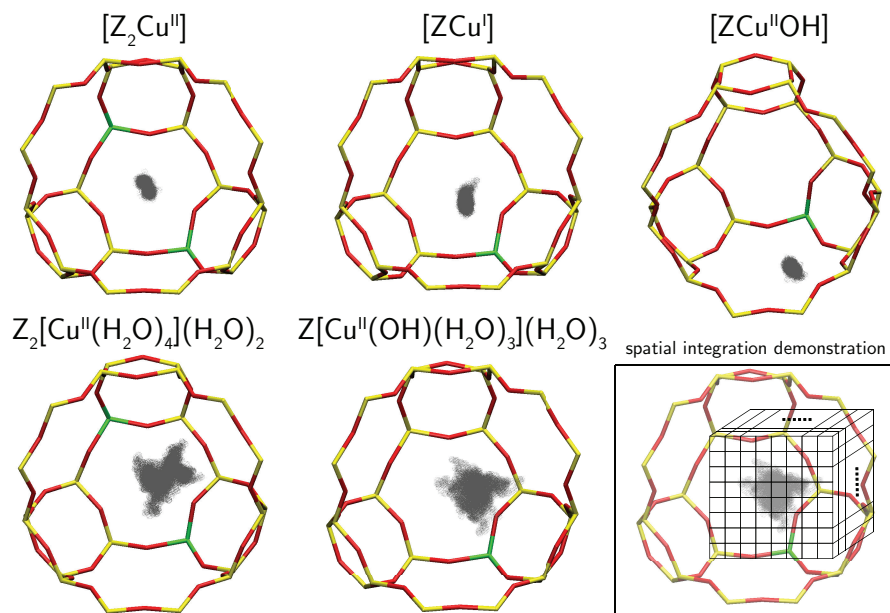
Figure 2.8 Cu positions (grey balls) visited during 90 ps of NVT AIMD at 298 K. Fixed zeolite framework shown for ease of visualization; framework was unconstrained during dynamics. Inset illustrates discretization used to compute relative Cu mobilities.

The EXAFS (Figure 2.9, middle) exhibit high intensity peaks at ≈1.5 Å that fit to 3.0 Cu-O bonds at 1.91 Å and 3.8 Cu-O bonds at 1.94 Å on the 1Al and 2Al samples, respectively (Table 2.2). Consistent with the higher first-shell coordination and closer proximity to multiple Si/Al, the 2Al sample also exhibits a more distinct second shell peak at ≈2.4 Å than that on the 1Al sample. To ensure reversibility, we cycled samples between Condition 1 and Condition 2 and confirmed that XAS spectra were identical to those shown in Figure 2.7.

These EXAFS features are consistent with those expected for the $[Z_2Cu^{II}]$ and $[ZCu^{II}OH]$ species predicted to predominate at Condition 2. Cu remain bound to multiple O_f for the duration of AIMD simulations on each, and each are computed to be about 8 times less mobile than the $Z_2[Cu^{II}(H_2O)_4](H_2O)_2$ reference. The $[Z_2Cu^{II}]$ site oscillates between three nearly isoenergetic minima (Supplementary Information section 2.2.2-2 of Paolucci et al.[177]) that differ in the O_f nearest-neighbor to Cu. The 1st shell in the RDF (Figure 2.9, bottom right) convolutes these three and integrates to a CN 3.9. By deconvolution of the RDF, we assign the second feature at ≈2.8 Å to one Al and one Si atom nearest Cu (Supplementary Information section 2.2.2-3 of Paolucci et al.[177]). The AIMD CN is consistent with the EXAFS fit.

In contrast, [ZCu^{II}OH] only exhibits a "wagging" into and out of the 8MR plane during AIMD. The Cu-Of and Cu-OH pairs appear as sharp features in the RDF (Figure 2.9, top right). The integrated RDF and fitted CN are identical. The slightly broad second shell feature at ≈2.75 Å arises from the Al nearest Cu (Figure 2.1B). This second shell feature is at 0.25 Å shorter distance and half the integrated area of the [Z$_2$Cu^{II}] second shell, consistent with both the location and magnitude of the EXAFS second shell features.
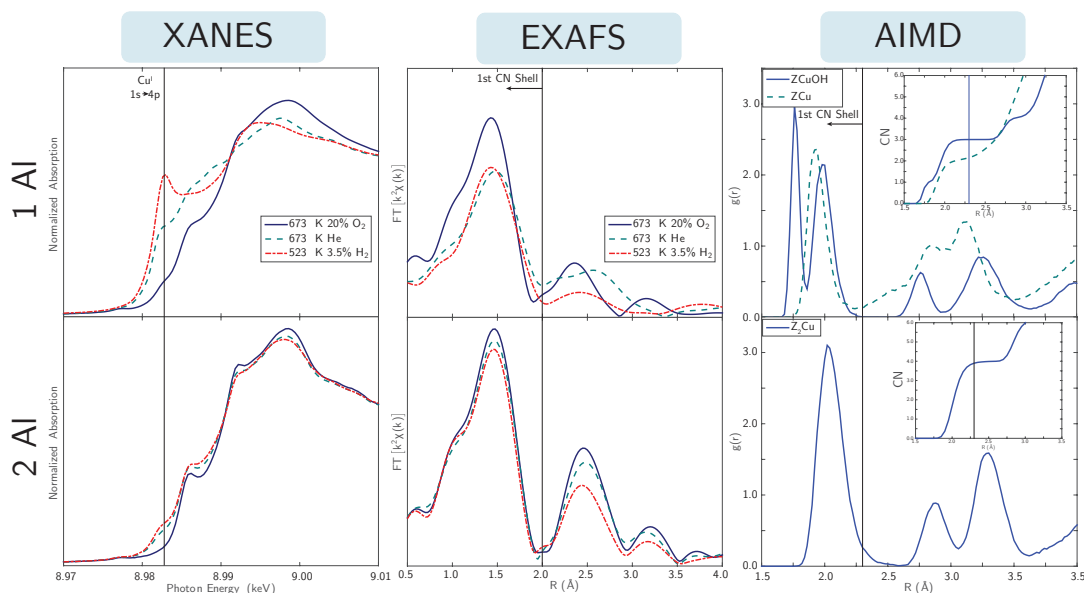
Figure 2.9 Left: XANES spectra collected on the 1Al (top) and 2Al (bottom) samples after treatment in 20% O$_2$ at 673 K (solid blue lines), He at 673 K (dashed teal lines) and in 3% H$_2$ at 523 K (dot-dashed red lines). Middle: Corresponding EXAFS spectra. Right: AIMD Cu-Si/O/Al RDFs for ZCuOH (top) and Z$_2$Cu (bottom). Insets show integrated RDFs.

2.4.2.3   Condition 3: He, 673 K (XAS/AIMD)

As noted above, a small amount of Cu^I appears in the XANES of the calcined 1Al sample. This auto-reduction feature[64,71], becomes more prominent after treating the 1Al sample in flowing helium at 673 K for 1 hr following the calcining treatment (Figure 2.9, left panel). From spectral deconvolution and EXAFS fitting, we infer 55% of the Cu to be present as Cu^I and the mean Cu-O coordination number to decrease to 2.4 (Table 2.2). In contrast, only 10% Cu^I is observed on the 2Al sample following the same helium treatment, and the coordination number is unchanged. The Cu^I feature becomes even more pronounced and the Cu^I fraction increases to 65% on the 1Al sample treated in 3% H$_2$ at 523 K [76,77]; the 2Al sample is changed negligibly by H$_2$ reduction.

These observations of autoreduction in the 1Al but not 2Al samples are consistent with the predictions for Condition 3 in Figure 2.3. That reduction is not complete on the 1Al sample suggests some kinetic as well as thermodynamic contribution to the autoreduction process, possibly associated with the mobility of the [ZCu^{II}OH]. Re-oxidation of samples after the He purge or H$_2$ treatment returns the XANES and EXAFS spectra to their post-calcination forms (additional details in supplementary information section 2.2.3-1 of Paolucci et al.[177]), indicating that reduction and re-oxidation are reversible. To interpret the observed EXAFS, we used 298 K AIMD to compute the dynamics of the reduced [ZCu^{I}] site. The Cu ion stays within the 6MR and retains coordination to the same two O$_f$ atoms; the computed RDF (Figure 2.9) is dominated by a Cu-O$_f$ feature at 1.93 Å that integrates to CN 2.1. The Cu mobility is enhanced by about 20% compared to [ZCu^{II}OH] and [Z$_2$Cu^{II}], but still roughly 8 times less than hydrated [Z$_2$Cu^{II}]. The second shell feature in EXAFS, spanning from roughly 2-3 Å, is echoed in the broad AIMD RDF past the first coordination shell, a consequence of [ZCu^{I}] mobility within the 6MR.

2.4.3   Copper Speciation At SCR Conditions

The ex situ characterizations above show that Cu in the 1Al and 2Al samples are identical under ambient and hydrated conditions, exhibit different coordination after high temperature oxidation, and respond differently to high temperature reduction. We next explore the implications under catalytic conditions relevant to low-temperature NO$_x$ SCR.

2.4.3.1   *Operando* XAS spectra and SCR Kinetics

We used a custom-built reactor[112] designed to collect XAS spectra in operando to determine the Cu oxidation states of the 2Al and 1Al samples during steady-state SCR (300 ppm NO, 300 ppm NH$_3$, 10% O$_2$, 2% H$_2$O) at 473 K under differential and plug-flow conditions (<20% NO conversion). Observed SCR turnover rates (TOR, mol NO s^{-1} mol Cu^{-1}), apparent NO, O$_2$ and NH$_3$ reaction orders, and apparent activation energies (E$_{app}$) (Table 2.3) were identical on the 2Al and 1Al samples, within experimental error, and identical to values measured on these samples in a different plug-flow reactor. *Operando* XANES spectra for the two samples (Figure 2.10, left, black traces) indicate the presence of 50% and 55% Cu^{I} (8.983 keV peak), respectively, that are identical within fitting error (5%). Although the presence of both Cu^{II} and Cu^{I} species during standard SCR redox cycles is not surprising[53,73,83,84,95], the identical Cu^{I} fractions and kinetic

parameters (Table 2.3) are unexpected given the different structures, dynamics and reducibility of [Z_2Cu^{II}] and [$ZCu^{II}OH$] species in He and H_2. These operando characterization results suggest that cationic copper sites are functionally equivalent during low temperature standard SCR at 473 K.

Table 2.3 Characterization of 2Al and 1Al Cu-SSZ-13 catalysts during low temperature (473 K) standard SCR: XANES Cu^I/Cu^{II} fraction, SCR rates (per Cu and mol NO) in the operando reactor/plug-flow reactor, apparent activation energies, and apparent NO, O_2, and NH_3 orders.

	Cu^I | Cu^{II}	TOR[a]	E_{app} (kJ mol^{-1})	NO Order	O_2 Order	NH_3 Order
2Al	50|50 ±5	8.3/7.3	60 ±10	0.8/0.8	0.3/0.3	-0.2/-0.1
1Al	55|45 ±5	9.9/8.0	74 ±10	n.m./0.7[b]	n.m./0.3[b]	n.m./0.0[b]

[a](s^{-1}mol Cu^{-1} mol NO $^{-1}$)×10^{-3} [b]n.m. = not measured, 1Al orders were measured only in PFR.
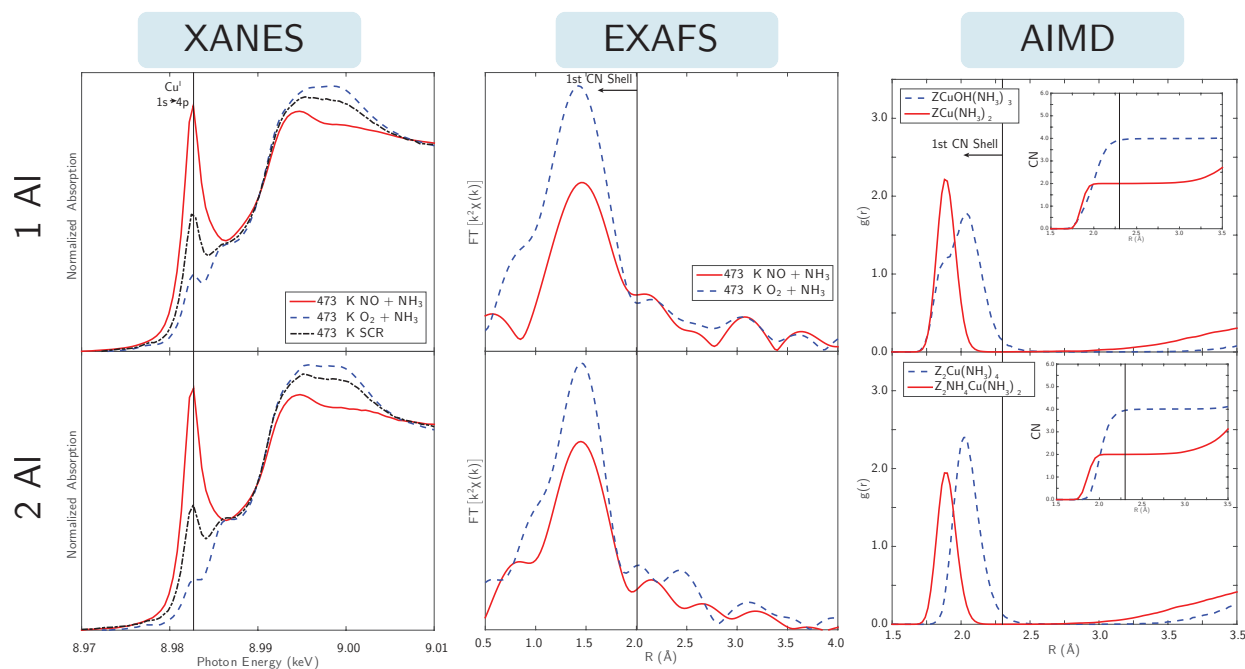
Figure 2.10 Left: XANES spectra of the 1Al (top) and 2Al (bottom) Cu-SSZ-13 samples under treatment in 2% H_2O, 10% O_2, 300 ppm NH_3 at 473 K (O_2 + NH_3, blue traces), 2% H_2O and 300 ppm NO/NH_3 at 473 K (NO + NH_3, red lines) and in 2% H_2O, 10% O_2, 300 ppm NO/NH_3 at 473 K (black traces). Middle: EXAFS collected under same conditions. Right: AIMD Cu-Si/O/Al RDFs for the most stable Cu^I (red lines) and Cu^{II} (blue traces) species on the 1Al and 2Al sites in the presence of NH_3. Insets: Integrated RDFs

2.4.3.2 SCR gas species binding energies

To understand Cu coordination in the SCR gas mixture (H_2O, N_2, NH_3, NO, O_2), we first computed adsorption energies of these species as well as NO_2, which is often proposed as an SCR intermediate,[73,91–94] on the oxidized and reduced forms of the 1Al and 2Al Cu sites using the same AIMD and HSE06-TSvdw optimization protocol. The computed NH_3 binding energy to the [ZH]/[ZCu^I] Brønsted site is -151 kJ mol^{-1}, quantitatively consistent with NH_3 differential heats observed via microcalorimetery on zeolitic H$^+$ sites:[113–117]

$$[ZH]/[ZCu^I] + NH_3 \rightarrow [ZNH_4]/Z[Cu^I] \tag{2.11}$$

Thus, the NH_4^+ form of this site prevails under SCR conditions, and we used the [ZNH$_4$]/[ZCu^I] structure shown in Figure 2.11 as the model for a reduced 2Al site.

Computed 1Al site binding energies are plotted against 2Al sites in Figure 2.11. Binding energies without the TSvdw correction are approximately 20 kJ mol^{-1} more positive. Binding energies (supplementary information section 2.3.2-1 of Paolucci et al.[177]) and structures on the [Z$_2$Cu^{II}] and [ZCu^{II}OH] sites are generally consistent with those for H_2O, NO, and NH_3 reported elsewhere,[67,73,86–88] although the inclusion of hybrid exchange significantly decreases the NO binding relative to the GGA values.[67,83,86–88] The 1Al and 2Al binding energies are roughly linearly correlated, although deviations as large as 50 kJ mol^{-1} are evident. O_2 interacts weakly with all sites; H_2O and NO exhibit intermediate binding strengths. NH_3 binds by -120 to -140 kJ mol^{-1} on all four Cu adsorption sites and does not significantly alter the Cu oxidation state. NO_2 binds strongly to reduced sites (oxidizing the Cu center to form a nitrite) but interacts weakly with oxidized Cu. NO is a notable outlier from the linear correlation: the HSE calculations predict NO to bind weakly to [Z$_2$Cu^{II}] (-25 kJ mol^{-1}) but with intermediate strengths on [ZCu^{II}OH] (-75 kJ mol^{-1}). NO locates near the OH ligand rather than Cu, similar to structures for this species reported elsewhere,[67] but does not form a HONO-like structure. N_2 more strongly adsorbs to [ZCu^I] than to other sites.
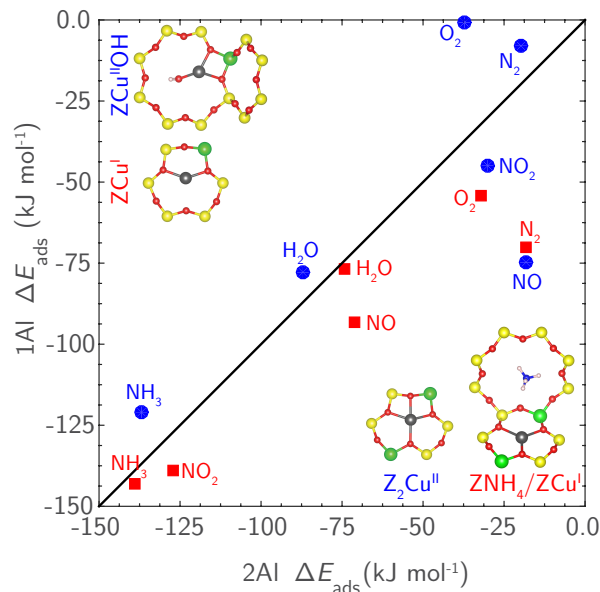
Figure 2.11 Parity plot of HSE06-TSvdw-computed binding energies of gaseous species relevant to SCR on 2Al oxidized (Z_2Cu, blue) and reduced (ZNH_4/ZCu, red) vs. corresponding oxidized (ZCuOH, blue) and reduced (ZCu, red) 1Al sites.

Because NH_3 out-binds all other species and is similar in its coordination behavior to H_2O, we explored the sequential binding of additional NH_3 on all four sites:

$$* (NH_3)_{x-1} + NH_3 \xrightarrow{\Delta E_{form}} * (NH_3)_x \tag{2.12}$$

using an AIMD anneal at 473 K followed by HSE06-TSvdw optimization. Results are summarized in Table 2.4; structures and normalized Cu Bader charges are detailed in supplementary information section 2.1.1-1 of Paolucci et al.[177]. Binding energies are roughly constant as NH_3 displaces O_f from the Cu coordination sphere.

Table 2.4 HSE06-TSvdw-computed sequential NH_3 adsorption structures and energies. Cage location indicates optimized ion location referenced to Figure 2.1. CN and O_f indicate total Cu coordination number and number of close framework O contacts, respectively.

	$+ \, x NH_3$	1	2	3	4
	ΔE_{ads} (kJ mol^{-1})	-132	-136	-123	-132
$[Z_2 Cu^{II}]$	Cage Location	A	A	B	C
	O_f/total CN	3/4	2/4	1/4	0/4
	ΔE_{ads} (kJ mol^{-1})	-134	-150	-72	-73
$[ZNH_4]/[ZCu^I]$	Cage Location	B	C	C	C
	O_f/total CN	1/2	0/2	0/2	0/2
	ΔE_{ads} (kJ mol^{-1})	-117	-119	-116	-47
$[ZCu^{II}OH]$	Cage Location	B	C, B^a	C	C
	O_f/total CN	2/4	0/3, 1/4^a	0/4	0/4
	ΔE_{ads} (kJ mol-1)	-137	-151	-75	-41
$[ZCu^I]$	Cage Location	B	C	C	C
	O_f/total CN	1/2	0/2	0/2	0/2

^{a}Trigonal planar, square planar values.

Cu^I and Cu^{II} retain 2-fold and 4-fold coordination, respectively; additional NH_3 beyond these limits are more weakly bound and not directly associated with Cu, instead forming hydrogen bonds with NH_3 in the first coordination sphere. The only exception is $ZCu^{II}OH(NH_3)_2$; this species adopts a square-planar conformation including a single O_f ligand at 0 K, but in the finite T dynamics adopts a trigonal planar form, free from O_f, for $\approx$90% of the trajectory. Energy and entropy are evidently closely balanced between the two configurations.

2.4.3.3   NH$_3$ Phase Diagrams

We used a first-principles thermodynamic analysis to rank the free energies of the NH_3 species in Table 2.4 and $H_x O_y$ structures from Figure 2.2,[42] species in total, taking O_2, H_2O, and NH_3 as oxygen, hydrogen, and nitrogen references, respectively:

$$Z_* Cu + \frac{x}{2}\left(H_2 O - \frac{1}{2} O_2\right) + \frac{y}{2} O_2 + z\left(NH_3 - \frac{3}{2} H_2 O + \frac{3}{4} O_2\right) \xrightarrow{\Delta G_{form}} Z_* Cu H_x O_y N_z \qquad (2.13)$$
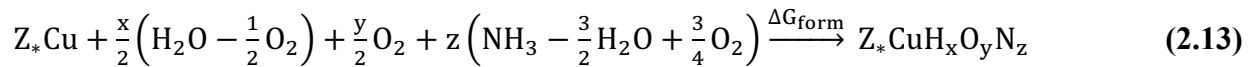
Figure 2.12 reports the lowest free energy 1Al and 2Al species as a function of T and O_2 partial pressure at H_2O and NH_3 concentrations of 2%, and 300 ppm, respectively, representative of the experimental conditions shown in Figure 2.10. We chose O_2 pressure as an independent variable for direct comparison to the experimental results detailed in the proceding section. The resultant

phase diagrams are substantially different from the H_xO_y ones in Figure 2.3; NH_3-containing species dominate the diagrams up to 773 K, and H_2O is an unimportant adsorbate. The most prominent species in the 1Al and 2Al diagrams are reduced CuI species and oxidized Cu^{II} species, respectively, although both oxidized and reduced forms of Cu appear on both diagrams. Both sites are saturated with NH_3 at 473 K and successively lose NH_3 ligands with increasing temperature. At 473 K, the 2Al phase diagram (Figure 2.12 right) shows Cu preferring $Cu^I(NH_3)_2$ as the O_2 concentration decreases, and $Cu^{II}(NH_3)_4$ species as the O_2 concentration increases. The $Cu^I(NH_3)_2$ complex is the most stable 1Al species over the entire O_2 range examined here.
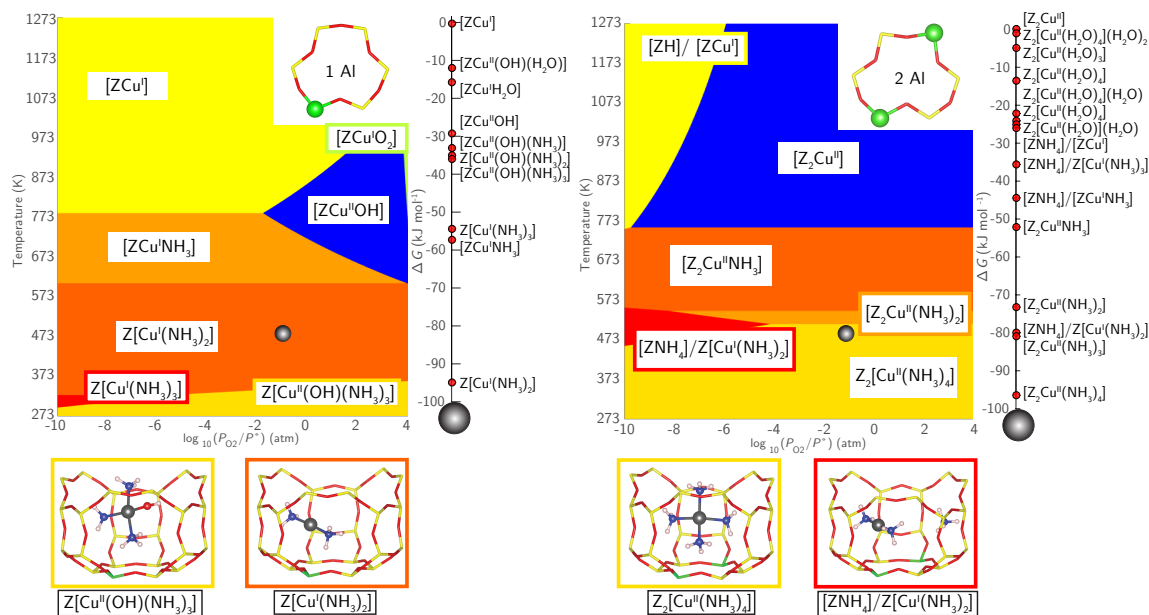
Figure 2.12 Phase diagrams for 1Al (left) and 2Al (right) sites with varying T and PO_2 at 300 ppm NH_3 and 2% H_2O. Relative rankings for all species $\Delta G_{form} < 0$ at 473 K and 10% O_2 (chrome spheres on the phase diagrams) are given to the right of each phase diagram. The structures shown on the bottom are the most stable Cu^I (red) and Cu^{II} (golden) under these conditions.

Sidebars in Figure 2.12 rank the relative free energies of intermediates at the condition indicated by the chrome spheres in the phase diagrams (473 K and 10% O_2), equivalent to those in Figure 2.10. Species with $\Delta G_{form} > 0$ kJ mol^{-1} are excluded for clarity; full results are tabulated in supplementary information section 2.3.4-1 of Paolucci et al.[177]. The analysis predicts a reduced and NH_3-saturated Cu^I to be most stable 1Al species at these conditions. Cu^I

complexes with one or three NH_3 ligands are higher in free energy, and the first Cu^{II} species to appear is $Z[Cu^{II}OH(NH_3)_3]$ at 50 kJ mol^{-1} higher free energy than the most stable species. Thus, these two NH_3-saturated and O_f-liberated complexes are the most likely dominant forms of Cu^I and Cu^{II} under SCR conditions in the 1Al catalyst. The Cu^I/Cu^{II} ordering is reversed at the 2Al site, where the most stable complex is an oxidized and NH_3-saturated $Z_2[Cu^{II}(NH_3)_4]$ at 16 kJ mol^{-1} below the reduced and NH_3-saturated $[ZNH_4]$ / $Z[Cu^I(NH_3)_2]$. The Cu^I/Cu^{II} fractions are the same in the operando XANES (Figure 2.10) on the 1Al and 2Al samples and likely kinetically rather than thermodynamically controlled. The thermodynamic screening identifies the species most relevant to catalysis and highlights the importance of NH_3 coordination under SCR conditions.

2.4.3.4   XAS/AIMD for Cu^I/Cu^{II} with NH_3

To explore Cu structure and dynamics under SCR conditions, we collected XAS and AIMD information on both 1Al and 2Al samples prepared with subsets of SCR gas mixtures that place them primarily in the Cu^I and Cu^{II} states.

Figure 2.10 shows the XANES and EXAFS at 473 K of 1Al and 2Al samples treated in 300 ppm of NO and NH_3. Consistent with previous reports,[73,83,95] this treatment reduces Cu. In fact, the XANES and the EXAFS on both samples are indistinguishable and the XANES fit to a CuI fraction of 100%. A prominent first shell peak at 1.88 Å in the EXAFS fits to 2.1 CN, which EXAFS cannot distinguish between O and N. The EXAFS is absent of longer-range structure.

These XAS results are consistent with the reduced Cu forms highlighted in Figure 2.12.
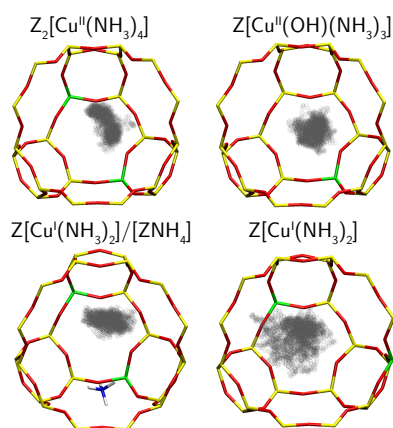
Figure 2.13 Cu positions (grey balls) sampled inside the zeolite cage during 90 ps of equilibrated NVT AIMD at 473 K for the most stable NH_3 solvated Cu^I and Cu^{II} species.

We performed 473 K AIMD simulations on $[ZNH_4]/Z[Cu^I(NH_3)_2]$ and $[Z[Cu^I(NH_3)_2]$ for the 2Al and 1Al sites, respectively. The linear $Cu^I(NH_3)_2$ species are identical in structure and, as evidenced in the dynamics trajectory (Figure 2.13) and the volume visited (Table 2.2), highly mobile. Computed RDFs between Cu and other heavy atoms are shown in Figure 2.10. As in the EXAFS, the lone peak at 1.89 Å integrates to 2.0 CN; the Cu location is completely disordered with respect to the zeolite lattice. To probe the ability of this NH_3-mobilized Cu^I to diffuse between cages, we used the climbing image nudged elastic band (CI-NEB, appendix A) method to compute the energy to thread a $Cu^I(NH_3)_2$ ion through the 8MR. The path starts with one NH_3 in the plane of the 8MR, passes over a 37 kJ mol^{-1} transition state in which the Cu is centered within the ring, and ends with the other NH_3 in the 8MR. This modest barrier suggests rather facile transport of reduced NH_3 within the SSZ-13 lattice, as has been inferred from the NH_3-facilitated exchange of Cu^I.[118]

Figure 2.10 similarly shows XAS spectra collected on the same samples during exposure to an oxidizing mixture of NH_3 (300 ppm) and O_2 (10%) at 473 K. The XANES are again similar to one another but markedly different from those at the reducing condition. Both samples exhibit a peak at 8.983 keV corresponding to a Cu^I species, 27% and 17% on the 1Al and 2Al samples, respectively, and a balance of Cu^{II} species. EXAFS show prominent first coordination shells at 1.5 Å (not phase-corrected) that fit to 3.2 and 3.5 O or N around Cu at 1.92 Å. Neither EXAFS exhibit second shell coordination in the 2.5-3 Å range. RDFs and AIMD performed at 473 K on $Z[Cu^{II}(OH)(NH_3)_3]$ and $Z_2[Cu^{II}(NH_3)_4]$, corresponding to the oxidized 1Al and 2Al species at SCR conditions, are also shown in Figure 2.10. As with Cu^I, both are free from framework oxygen and remain fully coordinated to NH_3 through the course of the dynamics. RDFs integrate to ≈3.9 CN; weighting the AIMD RDFs by the XANES-observed fractions of Cu^I and Cu^{II} recovers average coordination numbers of 3.2 and 3.6, close to the EXAFS-fitted values. These species were roughly 50% less mobile than their $Cu^I(NH_3)_2$ counterparts (Table 2.2), and 30% more mobile than their hydrated forms (Table 2.2). Finally, to confirm the transferability of EXAFS spectra collected under the non-catalytic NO + NH_3 and O_2 + NH_3 conditions to catalytic ones, we obtained 473 K SCR operando EXAFS on the recently enhanced APS Sector 10-ID beam line on a Si:Al = 25, Cu:Al = 0.42 sample similar to the 1Al catalyst (Figure 2.4), kinetic details and spectra provided in SI 2.3.5-2. This catalyst has a 60/40 Cu^I/Cu^{II} ratio, a fit CN of 3.1, and no second shell structure. The CN is consistent with a 60/40 weighted average of

2CN Cu^I and 4CN Cu^{II}. The lack of second shell character demonstrates all Cu are NH$_3$ solvated under *operando* conditions.

2.4.4   SCR Mechanism

2.4.4.1   Cu$^{II} \rightarrow$ Cu^I half-cycle

We previously proposed an NO-assisted NH$_3$ dissociation to be responsible for the Cu^{II} to Cu^I reduction during SCR.[83] We report in Figure 2.14 (and supplementary information section 2.4.1-1 of Paolucci et al.[177]) the computed CI-NEB pathways for such a step starting from NH$_3$-saturated Cu^{II} identified in the XAS and DFT here. Both reactions proceed by attack of NO on a Cu-bound NH$_3$ to form an N–N bond. In the process, a proton is transferred to an acceptor and an electron to Cu, leaving an H$_2$NNO intermediate that can decompose via proton transfers to N$_2$ and H$_2$O.[83,119] In the 1Al case,
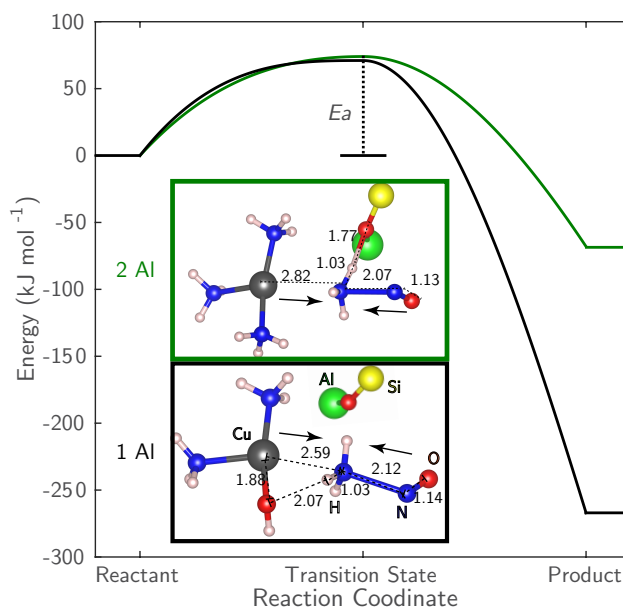
Figure 2.14 HSE06 CI-NEB calculated activation (E$_a$) and reaction energies for NO assisted reduction of NH$_3$ solvated Cu^{II} 1Al (black) and 2Al (green) sites. Transition state structures are shown boxed. For ease of visualization, most of the zeolite framework is hidden.

the Cu-OH ligand acts as the proton acceptor, to form water

$$[ZCu^{II}(OH)(NH_3)_3] + NO \rightarrow Z[Cu^I(NH_3)_3(H_2NNO)] + H_2O \qquad \text{(2.14)}$$
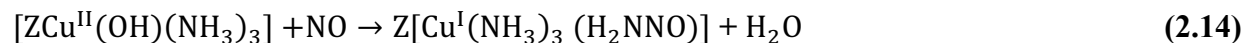
In the 2Al case, an Of plays the role of the acceptor, to form a new, proximal Brønsted site: $Z_2[Cu^{II}(NH_3)_4]$

$$[ZCu^{II}(NH_3)_4] + NO \rightarrow [ZH]/Z[Cu^I(NH_3)_3\,(H_2NNO)] \tag{2.15}$$
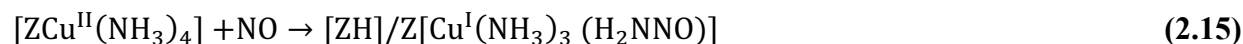
The first path is much more exothermic than the second (-267 vs. -68 kJ mol^{-1}), reflecting the strong driving force for creating H_2O. Nonetheless, the computed barriers for these two paths are a similar 71 and 74 kJ mol^{-1}, respectively, within the HSE06 model. These similarities reflect an early transition state dominated primarily by the partial desorption of NH_3 from Cu to accommodate the attacking NO. The N–N separations at the transition states are over 2 Å and N–H bonds only slightly elongated.
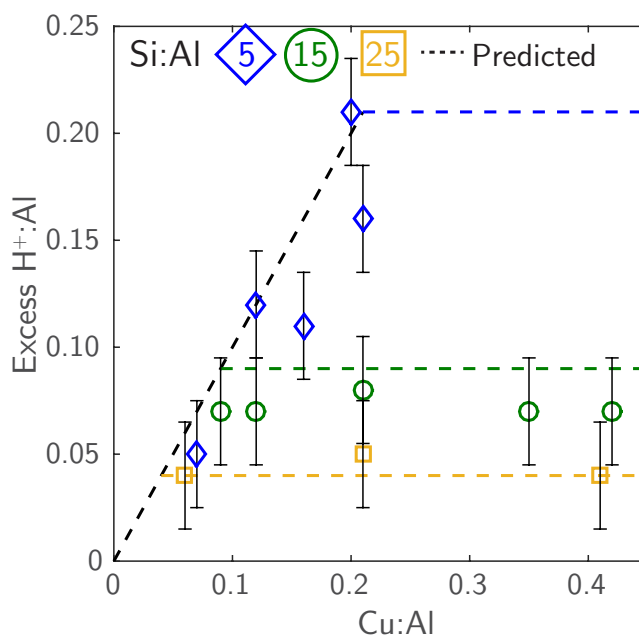
Figure 2.15 The number of extra H^+ sites (per Al) formed after reduction of Cu^{II} to Cu^I in flowing NO and NH_3 (473 K) as measured by NH_3 titration and TPD. Dashed lines represent the predicted number of H^+ formed based on the assumption that reduction of only Cu^{II} at 2Al sites form a Cu^I/H^+ site pair.

The key difference between the 1Al and 2Al paths is that NH_3/NO reduction of 2Al Cu^{II} should produce new Brønsted sites while 1Al Cu^{II} should not. The number of NH_4^+ species on samples treated in flowing NO and NH_3 (473 K) were counted by TPD performed after purging physisorbed and Cu^I-bound NH_3 species in flowing wet helium (3% H_2O, 433 K).[102] On all Cu-

SSZ-13 samples, a larger number of NH$_4^+$ species were present after reduction treatments than after oxidation treatments (supplementary information section 2.4.1-2 of Paolucci et al.[177]). Figure 2.15 shows the number of additional H$^+$ sites present after reduction of Cu sites to Cu^I as a function of the Cu:Al ratio on the Si:Al = 5 (blue diamonds), 15 (green circles), and 25 (orange squares) samples. The dashed lines indicate the excess H$^+$ expected from the theoretical enumeration of 1Al and 2Al sites (Figure 2.4). In line with predictions, one additional H$^+$ site is formed per Cu formed until all the 2Al sites are filled, beyond which point no additional H$^+$ sites were formed. Re-oxidation in NO and O$_2$ (supplementary information section 2.4.1-2 of Paolucci et al.[177]) returns the samples to the state shown in Figure 2.5. The catalytic cycle can thus be closed on both 2Al and 1Al sites.
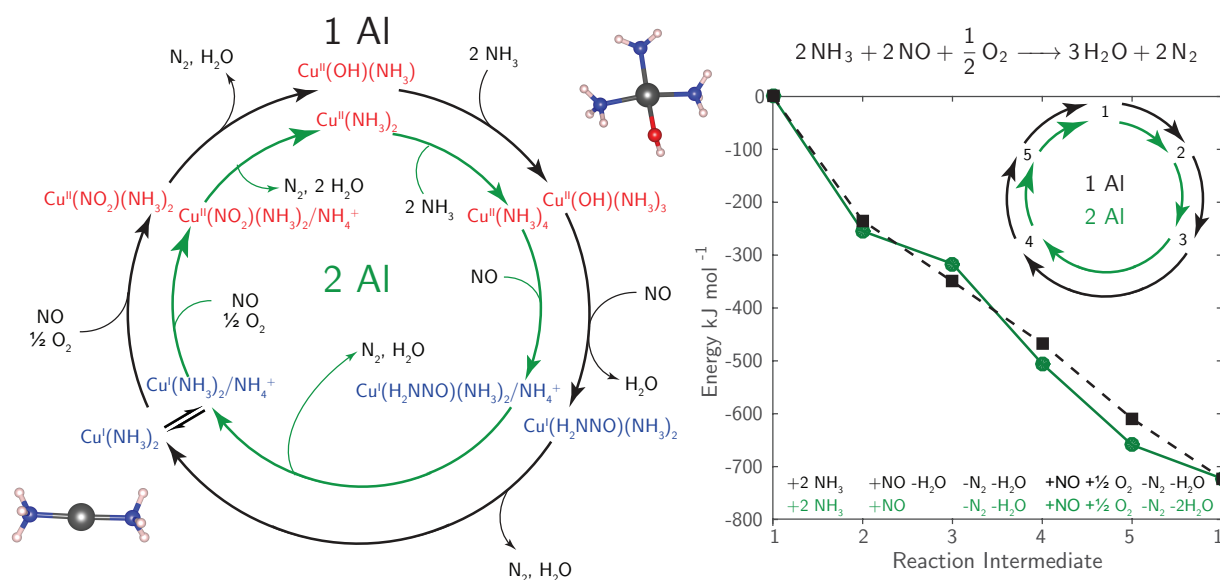
Figure 2.16 (Left) Proposed parallel standard SCR cycles for NH$_3$-solvated Cu ions near 1Al (black) or 2Al (green). (Right) HSE06-TSvdw-computed reaction energies along each step of the proposed cycles. 1–5 correspond to the intermediates in the left panel. Listed are the molecules consumed (+) and generated (-) between each intermediate.

2.4.4.2   SCR Cycle Energies

The results above highlight the importance of NH$_3$ coordination during 473 K SCR. We previously proposed an SCR cycle on [Z$_2$Cu^{II}] sites that accounts for the observed Cu redox.[83] Figure 2.16 shows an elaboration of that cycle that incorporates NH$_3$-solvation inferred from the thermodynamic analysis and EXAFS on 1Al and 2Al sites. The mechanism includes five primary

steps, starting from the 12 o'clock position: (1) NH_3 adsorption on Cu^{II}; (2) NO- assisted NH_3 dissociation concurrent with Cu^{II} reduction to Cu^{I}; (3) N_2 and H_2O desorption from Cu^{I}; (4) Cu^{I} reoxidation to Cu^{II} by NO and O_2 (a non-elementary step); and (5) reaction of adsorbed NO_2 with NH_3 or NH_4^+ to desorb N_2 and H_2O. Figure 2.16 (right) compares the computed reaction energies for each step (supplementary information section 2.4.2-1 of Paolucci et al.[177]). The similar energetics are consistent with the similar standard SCR turnover rates (473 K) measured on the two site types (Table 2.3).

2.4.5 SCR Rates on Other Cu-Zeolites

All the cationic Cu species in these cycles are NH_3-solvated and thus not sensitive to the location of charge-compensating framework Al. To test the generality of this observation, standard SCR rates were measured on synthesized and commercial Cu-ZSM-5 and Cu-BEA samples of compositions similar to the Si:Al = 15 SSZ-13 samples. Standard SCR rates (per g, 473 K) on Cu-exchanged MFI (Si:Al = 13), BEA (Si:Al = 13) (sample preparation and characterization described in supplementary information section 5.3-1, 5.3-2 and 2.1.3-1 of Paolucci et al.[177]), and Cu-CHA (Si:Al = 5, 15) are shown in Figure 2.17 as a function of the Cu density (per g). The error was calculated by replicate experiments under the same conditions. These SCR rates were measured in a regime uncorrupted by mass or heat transfer artifacts (Koros-Nowak test[96]) and in a kinetic regime characterized by similar apparent reaction orders and apparent activation energies (supplementary information section 2.5-1 of Paolucci et al.[177]). Standard SCR rates (per g, 473 K) increased linearly with Cu density (per g) on the Cu-CHA samples of different Si:Al ratio (5, 15), as expected from the similar turnover rate measured for Cu at 1Al and at 2Al sites (supplementary information section 2.3.1 of Paolucci et al.[177]). Turnover rates for Cu-ZSM-5 and Cu-BEA samples are of the same magnitude and exhibit a similar dependence on Cu density. A linear fit to the entire dataset has a correlation coefficient $R^2 = 0.86$. The Cu speciation was not determined on the Cu-ZSM-5 and Cu-BEA samples, and thus the observed scatter may have contributions from discrepancies between Cu weight % and isolated Cu ion density on these samples. These data suggest that both turnover rates and SCR mechanisms are independent of zeolite support at these conditions and in this kinetic regime. We surmise that this insensitivity to zeolite framework arises from NH_3 solvation of both Cu^{II} and Cu^{I} species at 473 K, and that these NH_3-covered ions are responsible for observed SCR turnover.
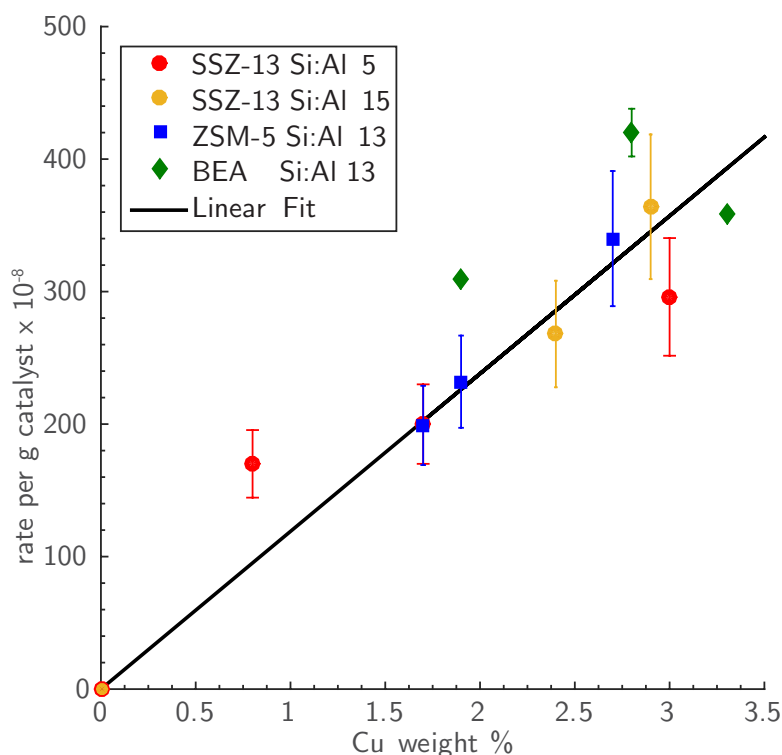
Figure 2.17 Standard SCR rates per g catalyst at 473 K on Cu-exchanged SSZ-13, ZSM-5, and BEA vs. Cu mass density

2.5 Discussion

2.5.1 Al distribution and Cu speciation *ex-situ*

While the apparent macroscopic composition of a heterogeneous catalyst is typically simple to determine, relating that composition to the molecular-scale, functional composition of an active site remains a major challenge. The relevant macroscopic composition variables for the Cu-SSZ-13 materials are the Si:Al and Cu:Al ratio. As reported in Figure 2.4 and the supporting experimental results, two types of Cu sites are present over the composition ranges studied here, and the relative densities of each type of Cu site are a function of both composition variables. Figure 2.4 is based on two assumptions: first, that framework Al atoms are randomly sited during zeolite crystallization modulo Löwenstein's rule, and second, that 6MR 2Al sites are populated by Cu^{II} cations to saturation before 1Al sites are populated with $Cu^{II}OH$. The close correspondence between these predictions and the experimental characterizations support the

model. Synthesis conditions are well known to influence Al siting in zeolites,[18,19,120–126,126–131] and specifically in SSZ-13[109] and thus the conclusions drawn from the synthetic conditions here cannot be extended to all Cu-zeolites or even to all Cu-SSZ-13 materials. We can, however, compare our findings to SSZ-13 zeolites prepared via procedures equivalent to those used here.[66,69,101,104,132,133,133–136] Fickel et al.[104] concluded, based on XRD and EXAFS, that an SSZ-13 sample with Si:Al = 9 and Cu:Al = 0.18 contained predominantly Cu in the 6MR, in agreement with the models here that predict 80% of $[Z_2Cu^{II}]$ in such sites. Gao et al. compared the H_2 TPR of SSZ-13 zeolites with Si:Al = 6 and 12 and Cu:Al=0.10-0.50.[76,77,137] Samples we predict to contain $[Z_2Cu^{II}]$ show only a 653 K TPR feature, while samples in the range expected to contain $[ZCu^{II}OH]$ also exhibit a 503 K TPR feature, consistent with the readier reducibility of $[ZCu^{II}OH]$ sites demonstrated here (Figure 2.3 and 2.9). FTIR similarly shows only a 895 cm^{-1} Cu-perturbed T-O-T vibration in the composition range dominated by $[Z_2Cu^{II}]$, supplemented by a 940 cm^{-1} feature in the range containing $[ZCu^{II}OH]$.[137] Davis and co-workers recently showed that these 2Al 6MR sites can be selectively protected against dealumination and deactivated for methanol-to-olefins (MTO) activity by preferential exchange of Cu^{II} ions[110,138,139] and Gao et al. used an analogous concept to exchange 2Al 6MR sites with alkaline earth cations.[110]

While this partitioning and counting of $[Z_2Cu^{II}]$ and $[ZCu^{II}OH]$ sites is successful, these sites themselves are not monolithic. A 6MR ring can have 2Al in 2NN or 3NN relative positions, and even for given positions, at finite temperature an exchanged ion is quite dynamic within the site, as illustrated by the AIMD simulations. Coordination numbers and bond distances from the HSE06 optimizations are similar to those extracted from the AIMD trajectories, but only the latter captures the contributions of dynamics to the EXAFS. For example, even for given Al positions within a 6MR, $[Z_2Cu^{II}]$ samples several local minima (supplementary information section 2.2.2-3 of Paolucci et al.[177]) during the AIMD, broadening the RDF (Figure 2.9) and reducing CN< 4. Thus, finite temperatures and Cu dynamics are important considerations in DFT models of these systems.

2.5.2   Cu speciation *in situ*

Once microscopic sites are identified and enumerated, a second key challenge is to determine how they respond to environmental, in situ conditions. We find from the first-principles thermodynamics and spectroscopies that ambient conditions cause both the $[Z_2Cu^{II}]$ and

[ZCu^{II}OH] species to exist as hydrated ions, liberated from coordination to zeolite framework oxygens, differing in composition by only a single proton, and differing only slightly in mobility (Figure 2.8). These observations are consistent with a large body of literature on Cu-zeolites. XAS and UV-vis spectroscopies of Cu^{II}-exchanged SSZ-13,[28,71,81,112,140] ZSM- 5 and BEA zeolites under ambient conditions are identical to the corresponding spectra of aqueous CuII complexes, demonstrating the insensitivity of zeolite topology to solvated ions.[71,82] Similarly, the perturbed T-O-T vibrations in IR spectra due to framework-bound Cu^{II} disappear upon hydration of Cu^{II} under ambient conditions.[70] Electron paramagnetic resonance (EPR) spectra at ambient observed for predominantly [Z$_2$Cu^{II}] samples have been taken as evidence of hydrated and mobile CuII;[77] broadening at 155 K is attributed to loss of that Cu^{II} ion mobility[24,141] and coalescence into a single sharp signal at 523 K to loss of the hydration sphere.[80]

The first-principles thermodynamics and XAS spectroscopies are consistent with the loss of water ligands at high temperature in O$_2$. Similarly, Borfecchia et al.[64] infer this loss from observed changes in EXAFS to a 3CN Cu species, the same behavior the Si:Al=15, Cu:Al=0.44 catalyst exhibits (Figure 2.9) after dehydration. We and Borfecchia et al. also observe the appearance of Cu^I under more reducing conditions. We assign this reduced fraction to [ZCu^{II}OH] species, based on the comparisons between the 1Al and 2Al samples. The autoreduction is not complete on any sample, suggesting some kinetic in addition to thermodynamic control of the reduction process. The nominal autoreduction stoichiometry:

$$4[ZCu^{II}OH] \rightarrow 4[ZCu^{I}] + 2H_2O + O_2 \qquad\qquad (2.16)$$

implies a complicated, multi-step process likely involving Cu dimer or higher-order intermediates[28,77,97] and thus a sensitivity to spatial Cu–Cu (and hence Al–Al) separations. Consistent with this inference, Gao et al.[76] report that the fraction of reducible [ZCu^{II}OH] at constant Cu:Al ratio decreases with increasing Si:Al ratio, or equivalently, increasing mean [ZCu^{II}OH] separation.

Under standard SCR conditions at 473 K, Cu^I and Cu^{II} ions near 1Al or 2Al are all predicted and observed to be fully solvated by NH$_3$, and further all Brønsted sites are present as NH$_4^+$. Both NH$_4^+$ and Cu-NH$_3$ are observed in DRIFTS spectra at similar conditions[142–144] on Cu-SSZ-13 samples. In fact, both vibrational and XAS spectra of NH$_3$ dosed to a number of Cu-

exchanged zeolites are similar to those of aqueous $Cu^I(NH_3)_2$ and $Cu^{II}(NH_3)_4$.[66,73,112,143,145–149] The standard SCR active sites at 473 K are NH_3-solvated Cu ions.

NH_3 solvation influences Cu mobility as well as structure, and this effect is insensitive to zeolite topology. NH_3 is observed to promote the exchange of Cu^{II} from CuO(s) into a number of zeolite frameworks, and this process is further promoted by in situ reduction of Cu^{II} to Cu^I by NH_3 and NO mixtures.[118]

2.5.3 Mechanistic Implications for SCR

The SCR reaction is well established to involve $Cu^I \to Cu^{II}$ redox cycles.[53,73,83,95] There has been some controversy regarding the species responsible for reduction.[56,73,83,90,94] Exposure to NO alone at 473 K does not reduce either the 1Al [ZCu^{II}OH] (Supplementary information section 3.4.1-1 of Paolucci et al.[177]) or 2 Al ([Z$_2$Cu^{II}])[83] samples, and the hybrid-exchange DFT results do not predict NO to strongly bind to or reduce either Cu^{II} site. We thus find no evidence to support the elementary mechanistic steps:

$$[Z_2Cu^{II}] + NO \to 4[Z_2Cu^INO^+] \qquad \text{or} \qquad (2.17)$$

$$[ZCu^{II}OH] + NO \to [ZCu^IHONO] \qquad (2.18)$$

Rather, NO and NH_3 together are necessary to reduce either of these sites. The reaction pathways and activation barriers for these reductions are computed to be similar on the [ZCu^{II}OH] and [Z$_2$Cu^{II}] sites in the presence of solvating NH_3. These barriers are also similar to the experimental apparent activation energies, although direct comparison of the experiment and computations is only possible through a kinetic model. The presence of both Cu oxidation states during standard SCR likely indicates that neither oxidation nor reduction alone is rate-limiting,[83] and thus a satisfactory kinetic model would require kinetic details on both half-cycles. Reduction rates on the [ZCu^{II}OH] and [Z$_2$Cu^{II}] may differ at temperatures at which NH_3 ligands are lost.

While NO and NH_3 are most effective at reducing Cu^{II}, we and others[95,150] also observe a partial reduction of $Cu^{II} \to Cu^I$ in flowing NH_3 and O_2. DFT calculations identified an O_2-assisted NH_3 dissociation pathway that parallels but has much higher barrier than the NO-assisted NH_3 dissociation reaction.[83] This pathway is unlikely to be catalytically relevant but could be responsible for this reduction. The results presented here provide indirect mechanistic

information about the SCR oxidation half-cycle. We find adsorbed NO_2 to oxidize Cu^I to Cu^{II} as Cu-bound nitrite:

$$[Cu^I] + NO \rightarrow 4[Z_2Cu^INO^+] \tag{2.19}$$

consistent with many proposals.[56,73,91–94] The source of NO_2 and even its presence as a free intermediate during standard SCR is less clear. Janssens et al.[73] proposed NO oxidation to nitrite to occur on a single, reduced Cu site through the intermediacy of a nitrate with the initial step as rate-determining (RDS):

$$[ZCu(O_2)(NO)] \rightarrow [ZCuNO_3] \xrightarrow{+NO} [ZCuNO_2] + NO_2 \xrightarrow{+NH_3} [ZCuOH] + H_2O + N_2 \tag{2.20}$$
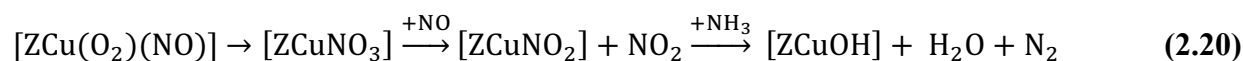
However, computed activation energies and the RDS assumption are inconsistent with experimental activation energies and the observed 50/50 mixture of Cu^I/Cu^{II} for SCR.[66,76,77,83]. Rather, as with autoreduction, NO oxidation may involve participation of more than one Cu species, facilitated by the solvation and high mobility of $Cu^I(NH_3)_2$ and its low diffusion barrier between CHA cages. Solvated Cu^I ions are well known to participate in dimeric Cu oxidation chemistries,[20,151–153] and a second-order dependence of SCR rate on Cu concentration has been observed on an Si:Al = 6 Cu-SSZ-13 catalyst at Cu:Al ratios ≤ 0.03.[80] At higher temperatures Cu is expected to desolvate (Figure 2.12), consistent with the FTIR findings of Giordanino et al.[142] In sharp contrast to the 473 K spectra (Figure 2.10), EXAFS collected at 673 K in NH_3 and O_2 demonstrate similar second shell character (supplementary information section 3.3.3- 1 of Paolucci et al.[177]) to the dry-oxidized framework bound Cu (Figure 2.9). Concurrent with this desolvation, apparent activation energies increase from 70 kJ mol^{-1} at 473 K to 140 kJ mol^{-1} [76] at 623 K, consistent with the dip in NO conversion observed[89] in non-differential measurements. Thus, NH_3 (de)solvation likely has a large impact on SCR oxidation half cycle rates.

2.5.4 Implications for partial methane oxidation

The results and approach described here are useful for the interpretation of the recently observed[43] non-catalytic, stoichiometric partial oxidation of methane (PMO) on Cu-SSZ-13:

$$2CH_4 + O_2 \rightarrow 2CH_3OH \tag{2.21}$$
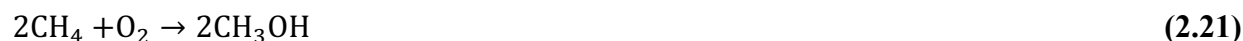
PMO is carried out in a three step sequence[38–41,43] that can be understood in part through reference to Figure 2.3. In a first step, the Cu-SSZ-13 material is brought to ≈ 673 K in O2 (≈20%) and balance inert, corresponding to Condition 2 in the figure. O_2 is then purged by inert, bringing the material to Condition 3. We observe a subset of sites to reduce under these conditions, consistent with the participation of only a fraction of exchanged Cu in PMO.[39] Subsequent introduction of CH4 at 473 K results in the production of methanol, which is liberated by returning to percent level H_2O pressures, between Conditions 1 and 2 of Figure 2.3.

Wulfers et al. demonstrated[43] PMO on Si:Al = 6 and 12, Cu:Al = 0.35 SSZ-13 materials. The Si:Al = 12 sample has roughly double (mol methanol per mol Cu) the performance of the Si:Al= 6 sample, in precise correlation with the predicted increase in [ZCu^{II}OH] sites (Figure 2.4). We conclude [ZCu^{II}OH] sites are likely precursors to ZCuOCuZ sites proposed to be responsible for PMO activity[32,35,36,40,42] and [Z$_2$Cu^{II}] are inactive.

$$2ZCuOH \rightarrow ZCuOCuZ + H_2O \qquad\qquad (2.22)$$

2.6 Conclusions

While the macroscopic composition of a solid catalyst is generally straightforward to measure and control, the relationship between this apparent composition and the number and type of catalytically relevant active sites is generally difficult to infer. We illustrate here an example of a non-trivial catalytic system in which it is possible to determine through theory and experiment both the speciation and number density of active sites as a function of the relevant synthetic compositional variables. Further, we show that these distinct active sites can be tracked as they evolve under different exposure conditions, from ambient characterization, to dry and inert high temperature, to operando reaction conditions. This enumeration and tracking is enabled by site-sensitive spectroscopies that are able to interrogate the catalyst under working conditions and computational approaches that treat the catalyst in a "operando" fashion, incorporating reaction conditions and effective estimates of free energies avoiding the standard harmonic approximations into the predictions of site structure and composition.

We show that exchanged, atomically dispersed and isolated Cu ions within the SSZ-13 cages populate two distinct types of sites, distinguished by the number of charge-compensating Al T-sites, and that the structure and dynamics of these two Cu types are strongly influence by

the environment they experience. H_2O solvates both Cu types at ambient conditions, is lost at higher temperatures, and is replaced by NH_3 reactant at the 473 K SCR conditions. This NH_3 liberates Cu from the framework, greatly enhances Cu mobility, and masks some of the differences between the two site types. The sites remain distinct, however; while both Cu sites undergo similar redox cycles at similar rates under the conditions studied here, the mechanisms differ in detail, as illustrated by the intermediacy of transient Brønsted sites on one but not the other Cu site type (Figure 2.15).

These findings underscore the need for caution in extrapolating from ex situ characterizations to catalytic conditions. Reaction conditions can and in this example do have a substantial influence on active site structure and properties. These environment-induced modifications need not be limited to reactants. Surrogate "promoters" that modify active sites (e.g., by mobilizing at different conditions, or that modify redox properties) could provide an an alternative to traditional catalytic material modifications for tuning catalytic activity.

2.7   Methods

2.7.1   DFT and AIMD Details

Plane-wave, supercell DFT supercell calculations employed a triclinic SSZ-13 supercell containing 12 T-sites84 and Si:Al ratios of either 11:1 or 10:2. The first Brillouin zone was sampled at the Γ point only, as appropriate for this insulator. Many of the adsorbate structures considered here have multiple local minima. To identify representative structures for subsequent optimizations, initial structures were first annealed non-spin-polarized at 473 K in five independent simulations of 30 ps each starting from different initial guess structures, for 150 ps total using the Car-Parrinello molecular dynamics software154(CPMD), version 3.17.1, the Perdew-Becke-Erzenhof155 generalized gradient approximation (GGA) exchange-correlation functional, and ultrasoft psuedopotentials.[156–158] These Born-Oppenheimer molecular dynamics simulations were run in the NVT ensemble using a Nose-Hoover thermostat with a timestep of 0.6 fs. RDFs from the final 90 of 150 ps simulations were constructed from the trajectories of a subset of these species for comparison to EXAFS results.

Low energy structures visited during the AIMD simulations were subsequently optimized using the Vienna Ab initio Simulation Package (VASP)[159,159] version 5.3.5. Calculations were performed spin-polarized using the projector augmented wave (PAW) treatment of core-valence interactions[160,161] and a plane wave cut off of 400 eV. For computational efficiency, structures were first relaxed within the GGA of Perdew et al.[155] and subsequently relaxed using the hybrid screened-exchange method of Heyd-Scuseria-Ernzerhof (HSE06)[162–165] and the Tkatchenko Scheffier method for van der Waals interactions (TS-vdW).[166] We con- verged self-consistent-field (SCF) electronic energies to 10^{-6} eV and atomic forces to less than 0.03 eV/Å. Charge analysis was performed through the method of Bader.[167–171] Cu charges are reported normalized to Cu^{II} and Cu^{I} references ($[Z_2Cu^{II}]$ and $[ZCu^{I}]$, respectively), then rounded to I or II reported as a superscript on Cu. Harmonic vibrational frequencies of adsorbed species were calculated at the HSE06-TSvdW level by numerical differentiation of atomic forces with 0.01 Å displacements on the adsorbate atoms and used to compute zero-point vibrational energies (ZPE). All structures can be found in the sites CONTCARS attachment SI file.

2.7.2 *Ab initio* Free Energies

Details can be found in Paolucci et al.[177].

2.7.3 Zeolite Synthesis and Characterization

Synthesis methods for all zeolites (SSZ-13, BEA, ZSM-5) can be found in SI 5.3-1. The crystal topologies of H-zeolites were confirmed from powder X-ray diffraction (XRD) patterns collected on a Rigaku Smartlab X-ray diffractometer equipped with a Cu K x-ray source (1.76 kW), and measured from 4-40° at a scan rate of 0.00833° s^{-1} with a step size of 0.01° (supplementary information section 2.1.3- 1 of Paolucci et al.[177]). Micropore volumes of H-SSZ-13 zeolites were determined from Ar adsorption isotherms (87 K), and for H-BEA and H-ZSM-5 zeolites were determined from N2 adsorption isotherms (77 K), using a Micromeritics ASAP 2020 Surface Area and Porosity Analyzer, and were in reasonable agreement with the values expected for the CHA, BEA, and MFI frameworks and can be found in supplementary information section 5.3-2 of Paolucci et al.[177]. Solid-state ^{27}Al magic angle spinning nuclear magnetic resonance (^{27}Al MAS NMR) spectroscopy was used to estimate the fraction of framework and extraframework Al on H-form zeolites. SS NMR spectra were collected using a

Chemagnetics CMX400 400 MHz spectrometer in a wide-bore 9.4 Tesla magnet at ambient conditions from 456 scans with 12.5 µs pulses and a 2 s delay and were measured at 104.24 MHz and MAS rate of 5 kHz. Prior to packing in a 4mm ZrO2 rotor, zeolite samples were hydrated by holding for >48 h in a desiccator containing a saturated potassium chloride (KCl) solution. All 27Al MAS NMR spectra are referenced to an aqueous 1.0M $Al(NO_3)_3$ solution. NMR spectra and quantification of extraframework Al for all H-zeolite samples can be found in supplementary information section 5.3-3 of Paolucci et al.[177].

Cu-zeolites were prepared by aqueous-phase Cu ion exchange of H-form zeolites with a $Cu^{II}(NO_3)_2$ solution (0.001M-0.1M, 100 cm^3 g catalyst^{-1}; 99.999 wt%, Sigma Aldrich) for 4 h and 300 RPM at ambient conditions, during which the pH was controlled to 4.9 ± 0.1 through dropwise addition of a 1.0M NH_4OH solution (Sigma Aldrich). Co-SSZ-13 zeolites were prepared by ion exchange of H-SSZ-13 with an aqueous 0.25M $Co^{II}(NO_3)_2$ solution (150 ml g catalyst^{-1}) for 4 h at ambient conditions, during which the pH was not controlled (pH stabilized between 3.2-3.6 after 4 h). Metal-exchanged zeolites were recovered by centrifugation and washed with deionized water six times (70 ml g catalyst^{-1} per wash), dried at ambient temperature under flowing air, and then treated in flowing dry air (100 ml g catalyst^{-1}) to 773 K (0.0167 K s^{-1}) for 4h. Elemental composition (Si, Al, Cu, Co) was determined using atomic absorption spectroscopy (AAS) on a Perkin-Elmer AAnalyst 300.

2.7.4   NH₃ Temperature Programmed Desorption

Residual H$^+$ sites on H-zeolites, on Cu- and Co-exchanged zeolites after oxidation treatments in air (20% O_2, balance N2, 773 K, 4 h), and on Cu-zeolites after reduction treatments (500 ppm NO + 500 ppm NH_3, balance He, 473 K, 2 hr) were titrated using the procedure described by Di Iorio et al.[102] This titration method involves saturation of zeolites (≈0.03- 0.05 g) with NH_3 at 433 K (500 ppm, balance He, 2 h, 350 mL min^{-1}), followed by removal of physisorbed and Cu-bound NH_3 by treatment in wet helium (2.5-3.0% H_2O/He, 8 h, 350 mL min^{-1}), in order to selectively retain surface NH_4^+ species.[102,103] NH_3 was then evolved in a subsequent TPD in flowing He (350 ml min^{-1}) to 823 K (0.083 K s^{-1}), and quantified using on-board calibrations in a MKS Multigas 2030 gas-phase FT-IR spectrometer. Further details can be found in supplementary information section 5.4-1 of Paolucci et al.[177].

2.7.5   Kinetics

Standard selective catalytic reduction (SCR) kinetics were measured on a bench-top tubular glass reactor described elsewhere.[66] All samples were sieved to a nominal size of 125-250 µm and diluted with silica gel to obtain a bed height of ≈2.5 cm. Steady-state kinetic data was collected at NO conversions below 20%, so that the entire bed was exposed to approximately the same gas concentrations, using a reactant gas mixture of 300 ppm NO (3.6% NO/Ar, Praxair), 300 ppm NH_3 (3.0% NH_3/Ar, Paxair), 5% CO_2 (liquid, Indiana Oxygen), 10% O_2 (99.5%, Indiana Oxygen), 2.5% H_2O (deionized, 18.2 MΩ, introduced through saturator), and balance N_2 (99.999% UHP, Indiana Oxygen) at 473K and 1 atm. The total gas flow rate was maintained at 1.5 L min^{-1}. Outlet gas concentrations were analyzed using on-board gas calibrations on an MKS MultigasTM 2030 gas-phase Fourier Transform Infrared (FTIR) spectrometer and NO, NO_2, NH_3, CO_2, and H_2O concentration data was recorded every 0.95s.

2.7.6   Spectroscopic Methods (XAS, FTIR)

XAS experiments were carried out on the insertion device (ID) and bending magnet (BM) beam lines of the Materials Research Collaborative Access Team (MRCAT, Sector 10) at the Advanced Photon Source (APS) at Argonne National Laboratory. A cryogenically cooled double-crystal Si(111) monochromator was used with an uncoated glass mirror to minimize the presence of harmonics. Spectra were recorded in transmission mode with the ionization chambers optimized for the maximum current with linear response (≈1010 photons s^{-1}) using gas mixtures to give 10% absorption in the incident X-ray detector and 70% absorption in the transmission X-ray detector. A Cu metal foil spectrum were simultaneously collected while measuring sample spectra to calibrate the Cu K-edge to 8979 eV. Operando experiments were performed at the 10-ID line in a special glassy carbon tube reactor described by Kispersky et al.,[112] in which XAS spectra were collected simultaneously with steady-state standard SCR rate measurements to verify that rates were identical to those measured in separate differential plug-flow reactor experiments. XAS spectra were collected in an energy range between 8700 and 9890 eV for samples held under different gas conditions, and between 8700 eV and 9780 eV for operando experiments (additional details in supplementary information section 2.2.1-1 of Paolucci et al.[177]). Multiple energy scans were taken to ensure the absence of time-dependent

change or beam damage to the sample. Spectra were collected under isothermal conditions and normalized using a first- order polynomial in the pre-edge region and a third-order polynomial in the post-edge region. XANES spectra were fitted using a linear combination of Cu^I and Cu^{II} references[66,83,84] to determine the fractions of Cu^I and Cu^{II} in certain gas environments and under operando conditions. EXAFS data were fit from k = 2.7 to ≈11 Å^{-1} (details of the fitting procedure in supplementary information section 2.2.1-1 of Paolucci et al.[177]).

FTIR data were collected on zeolite samples using a Nicolet 6700 FTIR spectrometer equipped with a liquid nitrogen-cooled mercury cadmium telluride (MCT) detector. Catalyst samples (≈35-40 mg) were pressed into a self-supporting wafer (≈2 cm in diameter) and placed in a custom-built FTIR cell that has been described elsewhere.[176] Wafers were treated in flowing oxygen (10% O_2, balance He) to 673 K for 30 min and then cooled to 473 K, prior to collecting spectra. Spectra were collected with a resolution of 4 cm^{-1} and averaged over 1000 scans, baseline corrected, and normalized to the framework Si-O-Si combination/overtone band between 2100-1750 cm^{-1}. Additional details can be found in supplementary information section 2.1.3-3 of Paolucci et al.[177].

2.8   Acknowledgements

2.9   References

(1) Taylor, H. S. Proceedings of the Royal Society A: Mathematical, Physical and Engineering Sciences 1925, 108, 105–111.

(2) Behrens, M.; Studt, F.; Kasatkin, I.; Kuhl, S.; Havecker, M.; Abild-Pedersen, F.; Zan- der, S.; Girgsdies, F.; Kurr, P.; Kniep, B.-L.; Tovar, M.; Fischer, R. W.; Norskov, J. K.; Schlogl, R. Science 2012, 336, 893–897.

(3) Zambelli, T.; Wintterlin, J.; Trost, J.; Ertl, G. Science 1996, 273, 1688–1690.

(4) Jaramillo, T. F.; Jørgensen, K. P.; Bonde, J.; Nielsen, J. H.; Horch, S.; Chorkendorff, I. Science 2007, 317, 100–102.

(5) Thomas, J. M. Angewandte Chemie International Edition 1999, 38, 3588–3628. (6) Kim, Y. D.; Seitsonen, A. P.; Wendt, S.; Wang, J.; Fan, C.; Jacobi, K.; Over, H.; Ertl, G. The Journal of Physical Chemistry B 2001, 105, 3752–3758.

(7) Tyo, E. C. et al. ACS Catalysis 2012, 2, 2409–2423.

(8) Hwang, T.; Goldsmith, B. R.; Peters, B.; Scott, S. L. Inorganic Chemistry 2013, 52, 13904–13917.

(9) Beale, A. M.; van der Eerden, A. M. J.; Kervinen, K.; Newton, M. a.; Weckhuy- sen, B. M. Chemical Communications 2005, 3015–3017.

(10) Topsøe, H. Journal of Catalysis 2003, 216, 155–164. (11) Weckhuysen, B. M. Physical Chemistry Chemical Physics 2003, 5, 4351–4360. (12) Green, I. X.; Tang, W.; Neurock, M.; Yates, J. T. Science 2011, 333, 736–739.

(13) Boubnov, A.; Carvalho, H. W. P.; Doronkin, D. E.; Günter, T.; Gallo, E.; Atkins, A. J.; Jacob, C. R.; Grunwaldt, J.-D. Journal of the American Chemical Society 2014, 136, 13006–13015.

(14) Peterson, E. J.; DeLaRiva, A. T.; Lin, S.; Johnson, R. S.; Guo, H.; Miller, J. T.; Hun Kwak, J.; Peden, C. H. F.; Kiefer, B.; Allard, L. F.; Ribeiro, F. H.; Datye, A. K. Nature Communications 2014, 5, 4885.

(15) Rice, M. J.; Chakraborty, A. K.; Bell, A. T. Journal of Catalysis 2000, 194, 278–285. (16) Rice, M. J.; Chakraborty, A. K.; Bell, A. T. Journal of Catalysis 1999, 186, 222–227.

(17) Goodman, B. R.; Hass, K. C.; Schneider, W. F.; Adams, J. B. Catalysis Letters 2000, 68, 85–93.

(18) Sarv, P.; Fernandez, C.; Amoureux, J.-P.; Keskinen, K. Journal of Physical Chemistry 1996, 100, 19223–19226.

(19) Perea, D. E.; Arslan, I.; Liu, J.; Ristanović, Z.; Kovarik, L.; Arey, B. W.; Lercher, J. A.; Bare, S. R.; Weckhuysen, B. M. Nature Communications 2015, 6, 7589.

(20) Vanelderen, P.; Vancauwenbergh, J.; Sels, B. F.; Schoonheydt, R. A. Coordination Chemistry Reviews 2013, 257, 483–494.

(21) Rice, M. J.; Chakraborty, A. K.; Bell, A. T. Journal of Physical Chemistry B 2000, 104, 9987–9992.

(22) Hass, K. C.; Schneider, W. F. The Journal of Physical Chemistry 1996, 100, 9292–9301.

(23) Trout, B. L.; Chakraborty, A. K.; Bell, A. T. The Journal of Physical Chemistry 1996, 100, 4173–4179.

(24) Kucherov, A. V.; Slinkin, A. A.; Kondrat'ev, D. A.; Bondarenko, T. N.; Rubin- stein, A. M.; Minachev, K. Zeolites 1985, 5, 320–324.

(25) Spoto, G.; Zecchina, A.; Bordiga, S.; Ricchiardi, G.; Martra, G.; Leofanti, G.; Petrini, G. Applied Catalysis B: Environmental 1994, 3, 151–172.

(26) Palomino, G. T.; Fisicaro, P.; Bordiga, S.; Zecchina, A.; Giamello, E.; Lamberti, C. The Journal of Physical Chemistry B 2000, 104, 4064–4073.

(27) Nachtigallová, D.; Nachtigall, P.; Sierka, M.; Sauer, J. Physical Chemistry Chemical Physics 1999, 1, 2019–2026.

(28) Verma, A. A.; Bates, S. A.; Anggara, T.; Paolucci, C.; Parekh, A. A.; Kamasamu- dram, K.; Yezerets, A.; Miller, J. T.; Delgass, W. N.; Schneider, W. F.; Ribeiro, F. H. Journal of Catalysis 2014, 312, 179–190.

(29) Da Costa, P.; Moden, B.; Meitzner, G. D.; Lee, D. K.; Iglesia, E. Physical Chemistry Chemical Physics 2002, 4, 4590–4601.

(30) Goodman, B. R.; Hass, K. C.; Schneider, W. F.; Adams, J. B. The Journal of Physical Chemistry B 1999, 103, 10452–10460.

(31) Smeets, P. J.; Hadt, R. G.; Woertink, J. S.; Vanelderen, P.; Schoonheydt, R. A.; Sels, B. F.; Solomon, E. I. Journal of the American Chemical Society 2010, 132, 14736–14738.

(32) Woertink, J. S.; Smeets, P. J.; Groothaert, M. H.; Vance, M. A.; Sels, B. F.; Schoonheydt, R. A.; Solomon, E. I. Proceedings of the National Academy of Sciences of the United States of America 2009, 106, 18908–18913.

(33) Groothaert, M. H.; van Bokhoven, J. A.; Battiston, A. A.; Weckhuysen, B. M.; Schoonheydt, R. A. Journal of the American Chemical Society 2003, 125, 7629–7640.

(34) Balasubramanian, R.; Smith, S. M.; Rawat, S.; Yatsunyk, L. A.; Stemmler, T. L.; Rosenzweig, A. C. Nature 2010, 465, 115–119.

(35) Groothaert, M. H.; Smeets, P. J.; Sels, B. F.; Jacobs, P. A.; Schoonheydt, R. A. Journal of the American Chemical Society 2005, 127, 1394–1395.

(36) Vanelderen, P.; Hadt, R. G.; Smeets, P. J.; Solomon, E. I.; Schoonheydt, R. A.; Sels, B. F. Journal of Catalysis 2011, 284, 157–164.

(37) Beznis, N. V.; Weckhuysen, B. M.; Bitter, J. H. Catalysis Letters 2010, 138, 14–22.

(38) Alayon, E. M. C.; Nachtegaal, M.; Bodi, A.; van Bokhoven, J. A. ACS Catalysis 2014, 4, 16–22.

(39) Alayon, E. M. C.; Nachtegaal, M.; Kleymenov, E.; van Bokhoven, J. A. Microporous and Mesoporous Materials 2013, 166, 131–136.

(40) Alayon, E. M. C.; Nachtegaal, M.; Bodi, A.; Ranocchiari, M.; van Bokhoven, J. A. Physical Chemistry Chemical Physics 2015, 17, 7681–7693.

(41) Grundner, S.; Markovits, M. A.; Li, G.; Tromp, M.; Pidko, E. A.; Hensen, E. J.; Jentys, A.; Sanchez-Sanchez, M.; Lercher, J. A. Nature Communications 2015, 6, 7546.

(42) Smeets, P. J.; Groothaert, M. H.; Schoonheydt, R. A. Catalysis Today 2005, 110, 303–309.

(43) Wulfers, M. J.; Lobo, R. F.; Ipek, B.; Teketel, S. Chemical Communications 2015, 51, 4447–4450.

(44) King, S. Journal of Catalysis 1996, 161, 530 – 538.

(45) Dědeček, J.; Čapek, L.; Sazama, P.; Sobalík, Z.; Wichterlová, B. Applied Catalysis A: General 2011, 391, 244–253.

(46) Smeets, P. J.; Sels, B. F.; van Teeffelen, R.; Leeman, H.; Hensen, E. J.; Schoonheydt, R. A. Journal of Catalysis 2008, 256, 183–191.

(47) Modén, B.; Da Costa, P.; Fonfé, B.; Lee, D. K.; Iglesia, E. Journal of Catalysis 2002, 209, 75–86.

(48) Iwamoto, M.; Furukawa, H.; Mine, Y.; Uemura, F.; Mikuriya, S.-i.; Kagawa, S. Journal of the Chemical Society, Chemical Communications 1986, 1272–1273.

(49) Kamasamudram, K.; Currier, N. W.; Chen, X.; Yezerets, A. Catalysis Today 2010, 151, 212–222.

(50) Grossale, A.; Nova, I.; Tronconi, E.; Chatterjee, D.; Weibel, M. Journal of Catalysis 2008, 256, 312–322.

(51) Colombo, M.; Nova, I.; Tronconi, E. Catalysis Today 2010, 151, 223–230.

(52) Shishkin, A.; Kannisto, H.; Carlsson, P.-A.; Harelind, H.; Skoglundh, M. Catalysis Science and Technology 2014, 4, 3917–3926.

(53) Doronkin, D. E.; Casapu, M.; Günter, T.; Müller, O.; Frahm, R.; Grunwaldt, J.-D. The Journal of Physical Chemistry C 2014, 118, 10204–10212.

(54) Cavataio, G.; Girard, J.; Patterson, J. E.; Montreuil, C.; Cheng, Y.; Lambert, C. K. SAE Tehcnical Paper 2007-01-1575 2007, 2007, 776–790.

(55) Koebel, M.; Elsener, M.; Kleemann, M. Catalysis Today 2000, 59, 335–345.

(56) Brandenberger, S.; Kröcher, O.; Tissler, A.; Althoff, R. Catalysis Reviews 2008, 50, 492–531.

(57) Kwak, J. H.; Tonkyn, R. G.; Kim, D. H.; Szanyi, J.; Peden, C. H. F. Journal of Catalysis 2010, 275, 187–190.

(58) Ye, Q.; Wang, L.; Yang, R. T. Applied Catalysis A: General 2012, 427-428, 24–34.

(59) Luo, J.; Wang, D.; Kumar, A.; Li, J.; Kamasamudram, K.; Currier, N.; Yezerets, A. Catalysis Today 2015, in press, 10.1016/j.cattod.2015.12.002.

(60) Chen, H.-Y. In Urea-SCR Technology for deNOx After Treatment of Diesel Exhausts; Nova, I., Tronconi, E., Eds.; Fundamental and Applied Catalysis; Springer New York, 2014; pp 123–147.

(61) Baerlocher, C.; McCusker, L. B. Database of Zeolite Structures. 2016; http://www. iza-structure.org/databases/.

(62) Deka, U.; Lezcano-Gonzalez, I.; Warrender, S. J.; Lorena Picone, A.; Wright, P. A.; Weckhuysen, B. M.; Beale, A. M. Microporous and Mesoporous Materials 2013, 166, 144–152.

(63) Deka, U.; Juhin, A.; Eilertsen, E. A.; Emerich, H.; Green, M. A.; Korhonen, S. T.; Weckhuysen, B. M.; Beale, A. M. The Journal of Physical Chemistry C 2012, 116, 4809–4818.

(64) Borfecchia, E.; Lomachenko, K. A.; Giordanino, F.; Falsig, H.; Beato, P.; Solda- tov, A. V.; Bordiga, S.; Lamberti, C. Chemical Science 2015, 6, 548–563.

(65) Göltl, F.; Sautet, P.; Hermans, I. Angewandte Chemie International Edition 2015, 54, 7799–7804.

(66) Bates, S. A.; Verma, A. A.; Paolucci, C.; Parekh, A. A.; Anggara, T.; Yezerets, A.; Schneider, W. F.; Miller, J. T.; Delgass, W. N.; Ribeiro, F. H. Journal of Catalysis 2014, 312, 87–97.

(67) Zhang, R.; McEwen, J.-S.; Kollár, M.; Gao, F.; Wang, Y.; Szanyi, J.; Peden, C. H. ACS Catalysis 2014, 4, 4093–4105.

(68) Göltl, F.; Sautet, P.; Hermans, I. Catalysis Today 2015, in press, 10.1016/j.cattod.2015.10.028.

(69) Fickel, D. W.; Lobo, R. F. The Journal of Physical Chemistry C 2010, 114, 1633– 1640. 54.

(70) Kwak, J. H.; Varga, T.; Peden, C. H. F.; Gao, F.; Hanson, J. C.; Szanyi, J. Journal of Catalysis 2014, 314, 83–93.

(71) Giordanino, F.; Vennestrøm, P. N. R.; Lundegaard, L. F.; Stappen, F. N.; Mossin, S.; Beato, P.; Bordiga, S.; Lamberti, C. Dalton Transactions 2013, 42, 12741–61.

(72) Godiksen, A.; Stappen, F. N.; Vennestrøm, P. N. R.; Giordanino, F.; Rasmussen, S. B.; Lundegaard, L. F.; Mossin, S. The Journal ofPhysical Chemistry C 2014, 118, 23126–23138.

(73) Janssens, T. V. W.; Falsig, H.; Lundegaard, L. F.; Vennestrøm, P. N. R.; Ras- mussen, S. B.; Moses, P. G.; Giordanino, F.; Borfecchia, E.; Lomachenko, K. A.; Lamberti, C.; Bordiga, S.; Godiksen, A.; Mossin, S.; Beato, P. ACS Catalysis 2015, 5, 2832–2845.

(74) Vennestrøm, P. N. R.; Katerinopoulou, A.; Tiruvalam, R. R.; Kustov, A.; Moses, P. G.; Concepcion, P.; Corma, A. ACS Catalysis 2013, 3, 2158–2161.

(75) Andersen, C. W.; Bremholm, M.; Vennestrøm, P. N. R.; Blichfeld, A. B.; Lunde- gaard, L. F.; Iversen, B. B. IUCrJ 2014, 1, 382–386.

(76) Gao, F.; Washton, N. M.; Wang, Y.; Kollár, M.; Szanyi, J.; Peden, C. H. Journal of Catalysis 2015, 331, 25–38.

(77) Gao, F.; Walter, E. D.; Karp, E. M.; Luo, J.; Tonkyn, R. G.; Kwak, J. H.; Szanyi, J.; Peden, C. H. F. Journal of Catalysis 2013, 300, 20–29.

(78) Kwak, J. H.; Tran, D.; Szanyi, J.; Peden, C. H. F.; Lee, J. H. Catalysis Letters 2012, 142, 295–301.

(79) Kwak, J. H.; Tran, D.; Burton, S. D.; Szanyi, J.; Lee, J. H.; Peden, C. H. Journal of Catalysis 2012, 287, 203–209.

(80) Gao, F.; Walter, E. D.; Kollar, M.; Wang, Y.; Szanyi, J.; Peden, C. H. Journal of Catalysis 2014, 319, 1–14.

(81) Dědeček, J.; Wichterlová, B. The Journal of Physical Chemistry B 1997, 101, 10233–10240.

(82) Fulton, J. L.; Hoffmann, M. M.; Darab, J. G.; Palmer, B. J.; Stern, E. A. Journal of Physical Chemistry 2000, 104, 11651–11663.

(83) Paolucci, C.; Verma, A. A.; Bates, S. A.; Kispersky, V. F.; Miller, J. T.; Gounder, R.; Delgass, W. N.; Ribeiro, F. H.; Schneider, W. F. Angewandte Chemie International Edition 2014, 53, 11828–11833.

(84) McEwen, J.-S.; Anggara, T.; Schneider, W.; Kispersky, V.; Miller, J.; Delgass, W.; Ribeiro, F. Catalysis Today 2012, 184, 129–144.

(85) Göltl, F.; Bulo, R. E.; Hafner, J. The Journal of Physical Chemistry Letters 2013, 4, 2244–2249.

(86) Göltl, F.; Hafner, J. The Journal of Chemical Physics 2012, 136, 064501. (87) Göltl, F.; Hafner, J. The Journal of Chemical Physics 2012, 136, 064502. (88) Göltl, F.; Hafner, J. The Journal of Chemical Physics 2012, 136, 064503.

(89) Beale, A. M.; Gao, F.; Lezcano-Gonzalez, I.; Peden, C. H. F.; Szanyi, J. Chem. Soc. Rev. 2015, 44, 7371–7405.

(90) Kwak, J. H.; Lee, J. H.; Burton, S. D.; Lipton, A. S.; Peden, C. H. F.; Szanyi, J. Angewandte Chemie International Edition 2013, 52, 9985–9989.

(91) Forzatti, P.; Lietti, L.; Nova, I.; Tronconi, E. Catalysis Today 2010, 151, 202–211. (92) Colombo, M.; Nova, I.; Tronconi, E. Catalysis Today 2012, 197, 243–255.

(92) Colombo, M.; Nova, I.; Tronconi, E. Catalysis Today 2012, 197, 243–255.

(93) Ruggeri, M. P.; Selleri, T.; Colombo, M.; Nova, I.; Tronconi, E. Journal of Catalysis 2014, 311, 266–270.

(94) Ruggeri, M. P.; Nova, I.; Tronconi, E.; Pihl, J. A.; Toops, T. J.; Partridge, W. P. Applied Catalysis B 2014, 166, 181–192.

(95) Günter, T.; Carvalho, H. W. P.; Doronkin, D. E.; Sheppard, T.; Glatzel, P.; Atkins, A. J.; Rudolph, J.; Jacob, C. R.; Casapu, M.; Grunwaldt, J.-D. Chemical Communications 2015, 51, 9227–9230.

(96) Koros, R. M.; Nowak, E. J. Chemical Engineering Science 1967, 22, 470.

(97) Godiksen, A.; Stappen, F. N.; Vennestrøm, P. N. R.; Giordanino, F.; Rasmussen, S. B.; Lundegaard, L. F.; Mossin, S. The Journal ofPhysical Chemistry C 2014, 118, 23126–23138.

(98) Psofogiannakis, G. M.; McCleerey, J. F.; Jaramillo, E.; van Duin, A. C. T. The Journal of Physical Chemistry C 2015, 119, 6678–6686.

(99) Clemens, A. K. S.; Shishkin, A.; Carlsson, P.-A.; Skoglundh, M.; Martínez- Casado, F. J.; Matĕҭj, Z.; Balmes, O.; Härelind, H. ACS Catalysis 2015, 5, 6209– 6218.

(100) Löwenstein, W. American Mineralogist 1954, 39, 92–96. (101) Zones, S. I. Zeolite SSZ-13 and its method of preparation. US Patent 4544538A, 1985.

(102) Di Iorio, J. R.; Bates, S. A.; Verma, A. A.; Delgass, W. N.; Ribeiro, F. H.; Miller, J. T.; Gounder, R. Topics in Catalysis 2015, 58, 424–434.

(103) Bates, S. A.; Delgass, W. N.; Ribeiro, F. H.; Miller, J. T.; Gounder, R. Journal of Catalysis 2014, 312, 26–36.

(104) Fickel, D. W.; Lobo, R. F. Journal of Physical Chemistry C 2010, 114, 1633–1640.

(105) Sierka, M.; Sauer, J. The Journal of Physical Chemistry B 2001, 105, 1603–1613. (106) Smith, L.; Davidson, A.; Cheetham, A. Catalysis Letters 1997, 49, 143–146.

(107) Bordiga, S.; Vitillo, J. G.; Ricchiardi, G.; Regli, L.; Cocina, D.; Zecchina, A.; Ar- stad, B.; Bjørgen, M.; Hafizovic, J.; Lillerud, K. F. Journal of Physical Chemistry B 2005, 109, 18237–18242.

(108) Baes, C. F.; Mesmer, R. E. Hydrolysis of cations; Wiley New York, 1976. (109) Di Iorio, J.R.; Gounder, R. Chemistry of Materials 2016, in press, 10.1021/acs.chemmater.6b00181.

(110) Gao, F.; Wang, Y.; Washton, N. M.; Kollár, M.; Szanyi, J.; Peden, C. H. F. ACS Catalysis 2015, 5, 6780–6791.

(111) Wang, D.; Jangjou, Y.; Liu, Y.; Sharma, M. K.; Luo, J.; Li, J.; Kamasamudram, K.; Epling, W. S. Applied Catalysis B: Environmental 2015, 165, 438–445.

(112) Kispersky, V. F.; Kropf, A. J.; Ribeiro, F. H.; Miller, J. T. Physical Chemistry Chem- ical Physics 2012, 14, 2229–2238.

(113) Auroux, A.; Bolis, V.; Wierzchowski, P.; Gravelle, P. C.; Vedrine, J. C. Journal of the Chemical Society, Faraday Transactions 1: Physical Chemistry in Condensed Phases 1979, 75, 2544.

(114) Auroux, A. Calorimetry and Thermal Methods in Catalysis; Springer, 2013; Vol. 154; pp 1– 561.

(115) Sharma, S.; Meyers, B.; Chen, D.; Miller, J.; Dumesic, J. Applied Catalysis A: General 1993, 102, 253–265.

(116) Lee, C.; Parrillo, D. J.; Gorte, R. J.; Farneth, W. E. Journal of the American Chemical Society 1996, 118, 3262–3268.

(117) Brandle, M.; Sauer, J.; Dovesi, R.; Harrison, N. The Journal of Chemical Physics 1998, 109, 10379.

(118) Shwan, S.; Skoglundh, M.; Lundegaard, L. F.; Tiruvalam, R. R.; Janssens, T. V.; Carlsson, A.; Vennestrøm, P. N. ACS Catalysis 2014, 5, 16–19.

(119) Sun, D.; Schneider, W. F.; Adams, J. B.; Sengupta, D. Journal of Physical Chemistry A 2004, 108, 9365–9374.

(120) Dĕdeček, J.; Čapek, L.; Sazama, P.; Sobalík, Z.; Wichterlová, B. Applied Catalysis A: General 2011, 391, 244–253.

(121) Dedecek, J.; Sobalik, Z.; Wichterlova, B. Catalysis Reviews-Science and Engineering 2012, 54, 135–223.

(122) Pashkova, V.; Klein, P.; Dedecek, J.; Tokarová, V.; Wichterlová, B. Microporous and Mesoporous Materials 2015, 202, 138–146.

(123) Sklenak, S.; Dědeček, J.; Li, C.; Wichterlová, B.; Gábová, V.; Sierka, M.; Sauer, J. Physical Chemistry Chemical Physics 2009, 11, 1237–1247.

(124) Sklenak, S.; Dědeček, J.; Li, C.; Wichterlová, B.; Gábová, V.; Sierka, M.; Sauer, J. Angewandte Chemie - International Edition 2007, 46, 7286–7289.

(125) Dědeček, J.; Kaucký, D.; Wichterlová, B.; Gonsiorová, O. Physical Chemistry Chem- ical Physics 2002, 4, 5406–5413.

(126) Gábová, V.; Dědeček, J.; Čejka, J. Chemical Communications 2003, 1196–1197.

(127) Vjunov, A.; Fulton, J. L.; Huthwelker, T.; Pin, S.; Mei, D.; Schenter, G. K.; Govind, N.; Camaioni, D. M.; Hu, J. Z.; Lercher, J. A. Journal of the American Chemical Society 2014, 136, 8296–306.

(128) Akporiaye, D. E.; Dahl, I. M.; Mostad, H. B.; Wendelbo, R. The Journal of Physical Chemistry 1996, 100, 4148–4153.

(129) Prasad, S.; Petrov, M. Solid state nuclear magnetic resonance 2013, 54, 26–31.

(130) Han, O. H.; Kim, C. S.; Hong, S. B. Angewandte Chemie - International Edition 2002, 41, 469–472.

(131) Yokoi, T.; Mochizuki, H.; Namba, S.; Kondo, J. N.; Tatsumi, T. The Journal of Physical Chemistry C 2015, 119, 15303–15315.

(132) Eilertsen, E. A.; Arstad, B.; Svelle, S.; Lillerud, K. P. Microporous and Mesoporous Materials 2012, 153, 94–99.

(133) Fickel, D. W.; D'addio, E.; Lauterbach, J. A.; Lobo, R. F. Applied Catalysis B: Envi- ronmental 2011, 102, 441–448.

(134) Zones, S. I. Journal of the Chemical Society, Faraday Transactions 1991, 87, 3709– 3716.

(135) Zones, S.; Van Nordstrand, R. Zeolites 1988, 8, 166–174.

(136) Chang, C.-C.; Wang, Z.; Dornath, P.; Je Cho, H.; Fan, W. RSC Advances 2012, 2, 10475.

(137) Kwak, J. H.; Zhu, H.; Lee, J. H.; Peden, C. H. F.; Szanyi, J. Chemical Communications 2012, 48, 4758.

(138) Dusselier, M.; Deimund, M. A.; Schmidt, J. E.; Davis, M. E. ACS Catalysis 2015, 5, 6078–6085.

(139) Deimund, M. A.; Harrison, L.; Lunn, J. D.; Liu, Y.; Malek, A.; Shayib, R.; Davis, M. E. ACS Catalysis 2016, 6, 542–550.

(140) Groothaert, M.; Lievens, K.; Van Bokhoven, J.; Battiston, A.; Weckhuysen, B.; Pier- loot, K.; Schoonheydt, R. Studies in Surface Science and Catalysis 2004, 154 C, 2449–2457.

(141) Kucherov, A. V.; Slinkin, A. A. Zeolites 1986, 6, 175–180.

(142) Giordanino, F.; Borfecchia, E.; Lomachenko, K. A.; Lazzarini, A.; Agostini, G.; Gallo, E.; Soldatov, A. V.; Beato, P.; Bordiga, S.; Lamberti, C. The Journal ofPhysical Chemistry Letters 2014, 5, 1552–1559.

(143) Zhu, H.; Kwak, J. H.; Peden, C. H. F.; Szanyi, J. Catalysis Today 2013, 205, 16–23.

(144) Szanyi, J.; Kwak, J. H.; Zhu, H.; Peden, C. H. F. Physical Chemistry Chemical Com- munications 2013, 15, 2368–2380.

(145) Lamble, G.; Moen, A.; Nicholson, D. G. Journal of the Chemical Society, Faraday Transactions 1994, 90, 2211–2213.

(146) Wang, D.; Zhang, L.; Kamasamudram, K.; Epling, W. S. ACS Catalysis 2013, 3, 871–881.

(147) Sjövall, H.; Fridell, E.; Blint, R. J.; Olsson, L. Topics in Catalysis 2007, 42, 113–117.

(148) Lezcano-Gonzalez, I.; Deka, U.; Arstad, B.; Van Yperen-De Deyne, A.; Hemelsoet, K.; Waroquier, M.; Van Speybroeck, V.; Weckhuysen, B. M.; Beale, A. M. Physical Chemistry Chemical Physics 2014, 16, 1639–1650.

(149) Gomez-Lor, B.; Iglesias, M.; Cascales, C.; Gutierrez-Puebla, E.; and Monge, M A, Chemistry of Materials 2001, 13, 1364–1368.

(150) Moreno-González, M.; Hueso, B.; Boronat, M.; Blasco, T.; Corma, A. The Journal of Physical Chemistry Letters 2015, 6, 1011–1017.

(151) Hoover, J. M.; Ryland, B. L.; Stahl, S. S. Journal of the American Chemical Society 2013, 135, 2357–67.

(152) Chen, P.; Solomon, E. I. Proceedings of the National Academy of Sciences of the United States of America 2004, 101, 13105–13110.

(153) Solomon, E. I.; Heppner, D. E.; Johnston, E. M.; Ginsbach, J. W.; Cirera, J.; Qayyum, M. F.; Kieber-Emmons, M. T.; Kjaergaard, C. H.; Hadt, R. G.; Tian, L. Chemical Reviews 2014, 114, 3659–3853.

(154) Corp., I. Carr-Parrinello Molecular Dynamics Code. 2016; http://www.cpmd.org/.

(155) Perdew, J. P.; Wang, Y. Physical Review B 1992, 45, 13244–13249.

(156) Vanderbilt, D. Physical Review B 1990, 41, 7892–7895.

(157) Laasonen, K.; Car, R.; Lee, C.; Vanderbilt, D. Physical Review B 1991, 43, 6796–6799.

(158) Laasonen, K.; Pasquarello, A.; Car, R.; Lee, C.; Vanderbilt, D. Physical Review B 1993, 47, 10142–10153.

(159) Kresse, G.; Furthmüller, J. Physical Review B 1996, 54, 11169–11186.

(160) Blöchl, P. E. Physical Review B 1994, 50, 17953–17979. (161) Kresse, G. Physical Review B 1999, 59, 1758–1775.

(162) Heyd, J.; Scuseria, G. E.; Ernzerhof, M. The Journal of Chemical Physics 2003, 118, 8207.

(163) Heyd, J.; Scuseria, G. E. The Journal of Chemical Physics 2004, 121, 1187.

(164) Heyd, J.; Scuseria, G. E.; Ernzerhof, M. The Journal of Chemical Physics 2006, 124, 219906.

(165) Krukau, A. V.; Vydrov, O. A.; Izmaylov, A. F.; Scuseria, G. E. The Journal of Chemical Physics 2006, 125, 224106.

(166) Tkatchenko, A.; Scheffler, M. Physical Review Letters 2009, 102, 73005. (167) Bader, R. F. W. Oxford University Press 1990, 36, 354–360.

(168) Tang, W.; Sanville, E.; Henkelman, G. Journal of Physics: Condensed Matter 2009, 21, 084204.

(169) Sanville, E.; Kenny, S. D.; Smith, R.; Henkelman, G. Journal ofComputational Chem- istry 2007, 28, 899–908.

(170) Henkelman, G.; Arnaldsson, A.; Jónsson, H. Computational Materials Science 2006, 36, 354–360.

(171) Yu, M.; Trinkle, D. R. Journal of Chemical Physics 2011, 134, 1–8.

(172) Bray, J. M.; Schneider, W. F. In CHAPTER 2. First-principles Thermodynamic Mod- els in Heterogeneous Catalysis; Asthagiri, A., Janik, M., Eds.; Royal Society of Chem- istry, 2013; pp 59–115.

(173) Penninger, M. W.; Kim, C. H.; Thompson, L. T.; Schneider, W. F. The Journal of Physical Chemistry C 2015, 119, 20488–20494.

(174) Piccini, G.; Sauer, J. Journal of Chemical Theory and Computation 2014, 10, 2479– 2487.

(175) Campbell, C. T.; Sellers, J. R. V. Journal of the American Chemical Society 2012, 134, 18109–18115.

(176) Wang, J.; Kispersky, V. F.; Nicholas Delgass, W.; Ribeiro, F. H. Journal of Catalysis 2012, 289, 171–178.

(177) Paolucci, C.; Parekh, A. A.; Khurana, I.; Iorio, J. R. Di; Albarracin, J.; Shih, A.; Anggara, T.; Nicholas, W.; Miller, J. T.; Ribeiro, F. H.; Gounder,. Journal of the American Chemical Society 2016**,** 138**,** 6028-6048.

3.   CATALYTIC CONSEQUENCES OF CU SPATIAL DENSITY AND MOBILITY IN CU-SSZ-13 ZEOLITE ON STANDARD SCR KINETICS

3.1   Preface

Chapter 3 reflects the reproduction of my coauthored article published in Science, 357 (6354), 898-903, 2017, titled "Dynamic multinuclear sites formed by mobilized copper ions in NO$_x$ selective catalytic reduction". This chapter contains integrates the experimental work (primarily led by me) with computation results (from our collaborators). The contents of this chapter serve a dual purpose of proposing fully consistent $Cu^I \rightarrow Cu^{II}$ oxidation cycle reaction pathway as well as investigating the consequences of Cu active site spatial distribution and dynamics on standard SCR kinetics. This work not only resolves many questions about standard SCR, but also demonstrates how metal-exchanged zeolites can behave in ways that resemble homogenous catalysis, with the addition of non-mean-field effects.

3.2   Abstract

Copper ions exchanged into zeolites are active for the selective catalytic reduction (SCR) of NO$_x$ with NH$_3$, but the low temperature rate dependence on Cu volumetric density is inconsistent with reaction at single sites. We combine steady-state and transient kinetic measurements, x-ray absorption spectroscopy, and first-principles calculations to demonstrate that under reaction conditions, mobilized Cu ions can travel through zeolite windows and form transient ion pairs that participate in an O$_2$-mediated $Cu^I \rightarrow Cu^{II}$ redox step integral to SCR. Electrostatic tethering to framework Al centers limits the volume that each ion can explore and thus its capacity to form an ion pair. The dynamic, reversible formation of multinuclear sites from mobilized single atoms represents a distinct phenomenon that falls outside the conventional boundaries of a heterogeneous or homogeneous catalyst.

3.3   Introduction

Single-site heterogeneous catalysts promise to combine the attractive features of homogeneous and heterogeneous catalysts: active sites of regular and tunable architecture that provide precise catalytic function, integrated into a thermally-stable, porous solid host that facilitates access of substrates to those sites and separation of products from the catalyst[1]. In the conventional definition, a single-site catalyst contains functionally isolated active sites, such that reaction rates per active site are independent of their spatial proximity[2]. Single metal atoms incorporated into solid oxide supports are reported to follow this conventional single-site behavior in catalytic CO oxidation to CO_2[3-5], selective hydrogenation[6,7], and water-gas shift[8,9]. Here, we report that a nominally single-site catalyst[10] operates by dynamic, reversible, and density-dependent (non-mean-field) interaction of multiple ionically tethered single sites, a behavior that lies outside the canonical definition of a single-site heterogeneous catalyst[11].

We discovered this phenomenon in the quest for a molecularly detailed model to unify the seemingly disparate observations of the catalytic function of copper-exchanged chabazite (Cu-CHA) zeolites, materials used in emissions control for the standard selective catalytic reduction (SCR) of nitrogen oxides (NO_x, x = 1, 2) with ammonia[12]:

$$4NO + 4NH_3 + O_2 \rightarrow 4N_2 + 2H_2O \tag{3.1}$$

Chabazite is a small-pore zeolite composed of cages (8 × 8 × 12 Å) interconnected by 6-membered-ring (6-MR) prisms and 8-membered ring (8-MR) windows (Figure X). Substitution of Si^{4+} by Al^{3+} within the framework introduces an anionic charge that is balanced by extra-lattice cations. After Cu ion exchange and high temperature oxidation treatment, two isolated Cu site motifs are present: discrete Cu^{II} ions that balance two proximal Al centers and $[Cu^{II}OH]^+$ ions that balance single Al centers[10,13,14]. Under low temperature (<523 K) standard SCR conditions, ammonia coordinates to and liberates Cu ions from direct association with the zeolite support, and these solvated Cu ions act as the redox-active catalytic sites[15]. At typical Cu ion volumetric densities, standard SCR rates increase linearly with Cu density, as expected for a single-site catalyst. As shown below, however, experimental observations in the low-Cu-density limit reveal a portion of the catalytic cycle in which O_2 activation by transiently formed Cu pairs becomes rate-limiting. These Cu pairs form from NH_3-solvated Cu ions with mobilities restricted

by electrostatic attraction to charge-compensating framework Al centers, leading to catalytic function that is neither single-site nor homogeneous.

Recognizing the intermediacy of this distinct catalytic state reconciles a number of controversies in Cu-zeolite SCR catalysis, including the role of the zeolite support in the catalytic mechanism, the sensitivity of SCR rates to Cu density under different conditions of observation, the extent to which standard and the closely-related fast SCR cycles[16] are connected via common intermediates, the chemical processes that limit low-temperature NO_x SCR reactivity, and the origins of the apparent change in mechanism at elevated temperatures. These observations provide insight into the design of improved catalysts for SCR. More broadly, they reveal a distinct class of catalytic materials characterized by partially mobile ions that dynamically and reversibly form multinuclear active sites, a concept that may be exploited for a wide variety of reactions.

3.4   Results and Discussions

3.4.1   Turnover Rates Depend on the Spatial Density of Single Cu Sites

In order to assess the catalytic consequences of Cu ion density, we prepared a series of Cu-CHA samples with fixed framework Al composition (Si/Al = 15) and Cu/Al content ranging from 0.04 to 0.44 (synthesis methods and characterization data in appendix B section B1, figures B1-B4, and tables B1-B2), corresponding to Cu volumetric densities (ρ_{Cu}) from (0.3 to 4.2) × 10^{-4} Cu $Å^{-3}$. We denote samples as Cu-CHA-X, where X indicates the mean Cu-Cu distance (in Å) assuming a homogeneous Cu distribution (appendix B, table B2). Mean Cu-Cu distances vary from 40.7 to 16.6 Å from the least to most heavily Cu-exchanged samples, and the highest Cu loading corresponds to approximately one Cu ion per three chabazite cages (Figure 3.1A).

We observed that SCR rates increased linearly with Cu density at ρ_{Cu} >1.9 × 10^{-4} $Å^{-3}$ (Figure 3.1B), as would be expected for a reaction catalyzed by isolated Cu sites. Turnover rates, apparent reaction orders and apparent activation energies (appendix B, table B3) are consistent with values reported for high Cu density Cu-CHA samples[17,18]. In contrast, standard SCR rates vary quadratically with Cu density below ρ_{Cu} < 1.13 × 10^{-4} $Å^{-3}$. All kinetic quantities are consistent with those reported for Cu-dilute Cu-CHA samples (Si/Al = 4.5, Cu/Al < 0.02[17]; Si/Al = 6, Cu/Al < 0.03[18]). We show below that these two kinetic regimes, characterized by distinct

kinetic parameters, reflect different rate-controlling elementary steps and prevalent reactive intermediates during steady-state NO_x SCR.
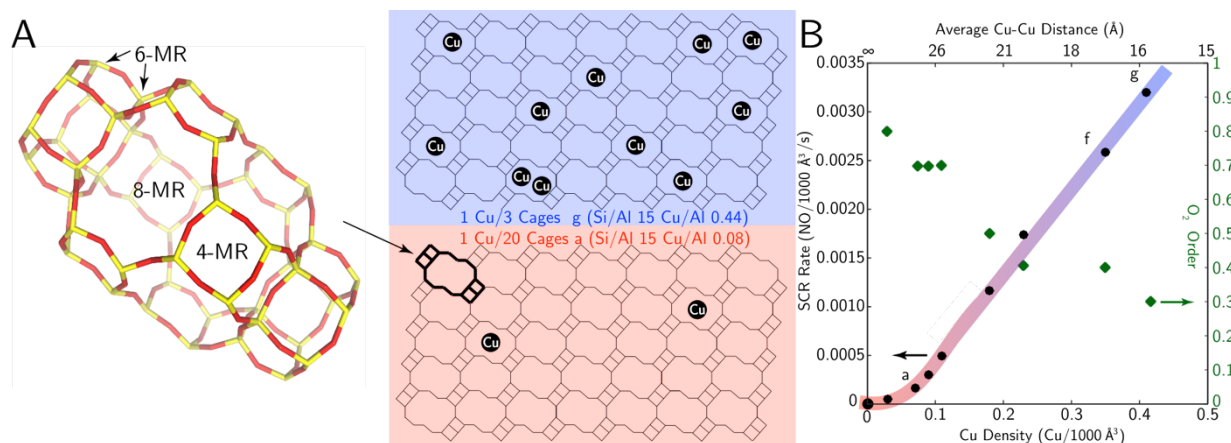
Figure 3.1 Cu-density dependence of SCR rates. (A) The CHA cage and schematic representation of the Cu ion densities per CHA cage in samples a and g. (B) Standard NO_x SCR rates (per volume catalyst, 473 K, measured in a differential reactor using a gas mixture representative of practical low-temperature application, including 2.5% H_2O, details in appendix B section B2) and apparent O_2 orders measured on Cu-CHA-X samples (Si/Al = 15, table B3) of increasing Cu ion density. Colored line is a visual guide; regression fits to the quadratic (R^2=0.99) and linear (R^2=0.99) kinetic regimes are detailed in appendix B section B2.

To probe the mechanistic origins of this change in kinetic behavior, we used x-ray absorption near-edge structure (XANES) spectroscopy to quantify Cu oxidation state during steady-state standard SCR *in operando*. Figure 3.2 and table B4 (appendix B) report the steady-state Cu^I fraction obtained by XANES fitting (procedure detailed in appendix B section B3) as a function of Cu density for three samples in Figure 3.1 (Si/Al = 15) and seven other Cu-CHA zeolites (Si/Al = 4.5, 15, 25, table B4 in appendix B). Consistent with prior observation, the site-isolated Cu^{II} ions observed *ex situ* evolve into a mixture of Cu^I and Cu^{II} ions during standard SCR catalysis, indicative of redox cycling between Cu^I and Cu^{II} oxidation states coupled with the SCR catalytic cycle[12]. The $Cu^{II} \rightarrow Cu^I$ half-cycle (Figure 3.2, inset) is accepted to occur on site-isolated Cu^{II}, to consume one equivalent of NO and NH_3 per Cu^{II}, and to produce N_2 and H_2O[15,16].

The inverse relationship between steady-state Cu^I fraction and Cu volumetric density (Figure 3.2) is inconsistent with the behavior expected of a single-site catalyst, for which the active site oxidation state should depend only on the reaction conditions and temperature. The

XANES data show that Cu^I is the minority oxidation state at the highest Cu density and smallest mean Cu-Cu separations ($< \sim$15 Å) during steady-state catalytic operation, but that its proportion increases with decreasing Cu density to the point that it becomes the majority oxidation state in the most dilute sample (mean Cu-Cu distance $\sim$29 Å). In this dilute limit, the *operando* XANES and extended X-ray absorption fine structure (EXAFS) spectra become indistinguishable from those of a Cu^I-CHA sample reduced *in situ* or of $Cu^I(NH_3)_2$ in aqueous solution (figure B5, table B4 in appendix B)[10]. This observation suggests that $Cu^I \rightarrow Cu^{II}$ oxidation rates increase with Cu ion density and implies non-single-site behavior in the oxidation half-cycle, a process that is not well understood mechanistically beyond the observation that it consumes O_2[12].
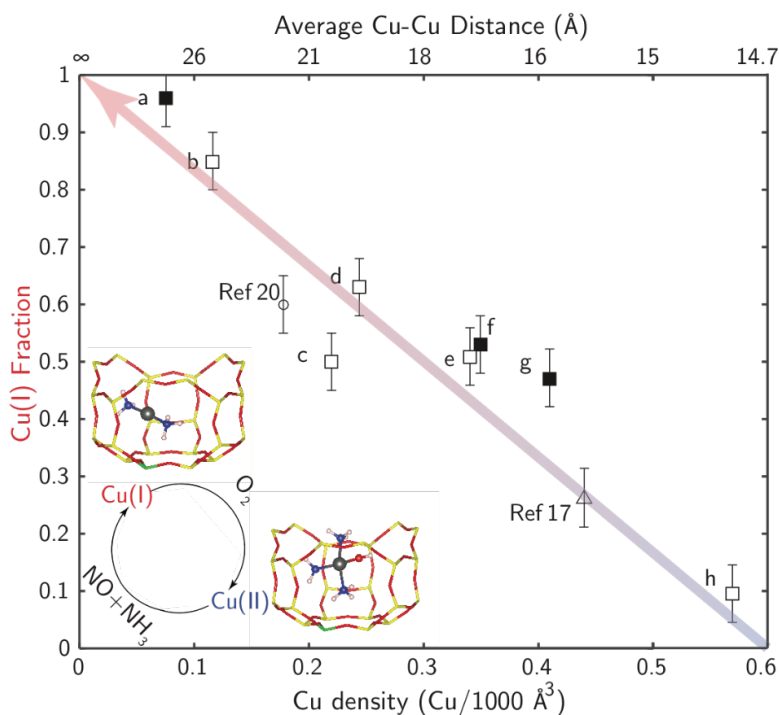
Figure 3.2 Cu-density dependence of *operando* Cu oxidation state. The dependence of Cu^I fraction on Cu ion volumetric density during steady-state standard SCR at 473 K was measured by XANES (details in appendix section B3). Data points include samples a, f and g shown in Fig. 1 (Si/Al = 15, filled squares), samples at Si/Al = 4.5 and Si/Al = 25 (open squares), and comparable literature data (open circle[21], Si/Al = 16, and open triangle Ref[17], Si/Al = 4.5). Inset shows NH_3-solvated, isolated Cu^I and Cu^{II} species previously observed and computed[10] to be present during standard SCR at 473 K. Grey = Cu, green = Al, yellow = Si, red = O, blue = N and white = H. The colored arrow is a visual guide; error bars represent the absolute 5% uncertainty from linear combination XANES fitting (details in appendix section B3).

The coordination states of site-isolated Cu^I and Cu^{II} ions under standard SCR conditions at 473 K have been explored previously in detail[10]. X-ray absorption[10] and emission[20,21] spectroscopy and density functional theory (DFT)-based models[10] (including *ab initio* thermodynamic phase diagrams in figures B17-B18, appendix B) show that NH_3 outcompetes other gases present under standard SCR conditions, including H_2O, for binding at both Cu^I and Cu^{II} ions, which are respectively two- and four-fold coordinated. Consistent with these findings, the standard SCR reaction rate is zero-order with respect to water pressure (1%-10% atm; figure B19 in appendix B). Schematic illustrations of the most probable coordination states of Cu^I and Cu^{II} ions under these conditions are shown in the inset to Figure 3.2.

In the high Cu-density samples (Figure 3.2, c - g), the first-shell Cu coordination number (CN) derived from *operando* EXAFS is three, consistent with the expectation for a nearly equimolar mixture of Cu^I and Cu^{II} [10](appendix B, table B4). The CN decreases to two in the fully reduced (Figure 3.2, a - b), lowest Cu-density samples, consistent with site-isolated $Cu^I(NH_3)_2$ as the most abundant reactive intermediate present during steady-state standard SCR. In this limit, the SCR turnover rate is solely limited by the $Cu^I \rightarrow Cu^{II}$ half-reaction. The increase in apparent O_2 reaction order from 0.3 to 0.8 with decreasing Cu density reinforces the increasing kinetic relevance of the $Cu^I \rightarrow Cu^{II}$ half-cycle as Cu becomes more dilute (Figure 3.1). This change also corresponds with the transition from a first-order to a second-order dependence of SCR rate on Cu ion density (Figure 3.1,[18]). From these observations, we conclude that the kinetically relevant O_2-consuming step in the oxidation half-cycle is sensitive to Cu density.

3.4.2 Cu^I Site Density Requirements Differ for Oxidation with O_2 and NO_2.

To probe the coupled roles of O_2 and Cu density in the oxidation half-cycle, Cu-CHA-15, Cu-CHA-20, and Cu-CHA-29 (Figure 3.2, h, c, a) were first reduced to the Cu^I state in flowing NO and NH_3 (details in appendix B section B3, figures B6-8)[10]. Then, samples were held under flowing O_2 and the transient evolution of the Cu oxidation state was monitored using XANES. The Cu^I fraction decayed in the presence of O_2 at different rates on the three samples (Figure 3.3 A), and significant and different fractions of Cu^I persisted at steady-state (appendix B, table B6).

The dependence of the transient oxidation state response on Cu density suggests some underlying spatial requirements for $Cu^I(NH_3)_2$ ions to react with O_2. After exploring various rate

laws, we found that an expression that is second-order in total Cu^I density $[Cu^I](t)$ and offset by a recalcitrant fraction of Cu^I, $[Cu^I]_\infty$, fits the data most satisfactorily ($R^2 = 0.99$ (a), 0.98 (c), and 0.99 (h); details in appendix B section B4). Normalizing to the initial Cu^I density, $[Cu^I]_0$, the integrated rate law becomes:

$$Cu^I \text{ Fraction} = \frac{[Cu^I](t)}{[Cu^I]_0} = \frac{1 - [Cu^I]_\infty/[Cu^I]_0}{1 + 2k\left([Cu^I]_0 - [Cu^I]_\infty\right)t} + \frac{[Cu^I]_\infty}{[Cu^I]_0} \tag{3.2}$$

where k is a pseudo-homogeneous second-order rate constant for disappearance of Cu^I. Solid lines in Figure 3.3 A denote best fit regressions of the data to equation 3.2. Fitted k values of $(1.0, 1.7, 8.2) \times 10^{-4}$ m^3 mol Cu^{-1} s^{-1} for Cu-CHA-29, Cu-CHA-20 and Cu-CHA-15, respectively increased systematically with Cu density. The variation in k demonstrates that all the reaction sites are not kinetically equivalent. Further analysis below suggests that the oxidation kinetics cannot be faithfully captured by a mean field model.
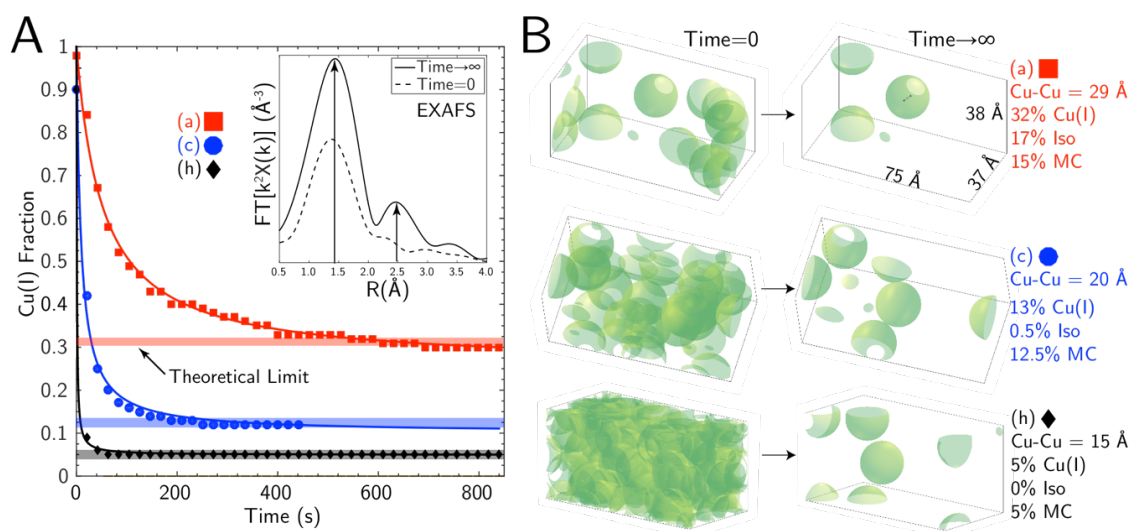
Figure 3.3 Kinetics of Cu^I oxidation by O_2 (A) Temporal evolution of the XANES-measured Cu^I fraction is plotted for the Cu-CHA-29 (a, red) Cu-CHA-20 (c, blue) and Cu-CHA-15 (h, black) samples during transient oxidation in 10% O_2 at 473 K. Least-squares fit to equation 3.2 is shown by solid lines and predicted recalcitrant Cu^I fractions shown as horizontal bars. $[Cu^I]_\infty$ was set by forcing the fit through the last (longest time) data point; $[Cu^I]_0$ was set to 1 (full details in appendix B section B4). The Cu^I fractions reported contain an absolute 5% error from linear combination XANES fits (details in appendix B section B3) Left inset: EXAFS spectra of Cu-CHA-15 collected before O_2 exposure and after the transient experiment. (B) Snapshots taken from simulated initial (Time = 0) and final (Time $\rightarrow \infty$) Cu^I spatial distributions corresponding to the three samples (a, c, h) in panel (A). Cu^I volumetric footprints denoted by 9 Å radius green spheres. Simulation results include decomposition of unoxidized Cu^I fraction into physically isolated (Iso) and functionally isolated (MC) components.

This second-order Cu dependence suggests a pseudo-bimolecular reaction between two $Cu^I(NH_3)_2$ ions and O_2 during the transient experiment:

$$2\,[Cu^I(NH_3)_2] + O_2 \longrightarrow [(NH_3)_2\,Cu^{II}-O_2-Cu^{II}(NH_3)_2] \qquad\qquad \textbf{(3.3)}$$
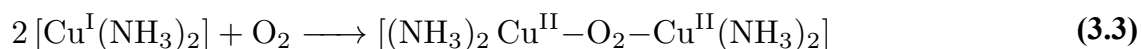
Oxygen-bridged Cu dimers are well known in Cu-zeolite chemistry[22-24] and find analogies in the biological chemistry of Cu that prevails at lower temperatures[25-30]. These dimers can adopt various oxygen-bridging configurations[26,31]. To probe the plausibility of this reaction between two caged $Cu^I(NH_3)_2$ centers, we turned to DFT (computational details in appendix B section B5).

We first considered the energy landscape for two $Cu^I(NH_3)_2$ ions to occupy the same CHA cage. Starting from two $Cu^I(NH_3)_2$ ions in adjacent cages that share an Al T-site vertex (Figure 3.4 (A)), the computed barrier for one $Cu^I(NH_3)_2$ to diffuse through an 8-MR window into the adjacent $Cu^I(NH_3)_2$-containing cage (B) is 35 kJ mol^{-1}, consistent with prior estimates of $Cu^I(NH_3)_2$ diffusion barriers into an empty cage[10,32]. The net pairing cost is 23 kJ mol^{-1}. Thus, transport between adjacent Al-sharing cages is expected to be facile at temperatures of catalytic interest. Two $Cu^I(NH_3)_2$ ions bind O_2 more effectively (-59 kJ mol^{-1}) than does an isolated $Cu^I(NH_3)_2$ (-26 kJ mol^{-1}) (table B10, figure B14 in appendix B), and the O_2 binding energy more than offsets the energy cost for two $Cu^I(NH_3)_2$ to cohabit the same cage. Initial reaction likely generates the end-on spin triplet species shown in Figure 3.4 (C), and further rearrangement and dissociation of O_2 across two Cu^I centers ultimately leads to the di-oxo structure E, containing two four-fold-coordinated Cu^{II} centers. Conversion of structure (C) into (D) is spin-forbidden; the effective barrier in similar ligand environments is estimated to be 20 kJ mol^{-1} [25]. Subsequent conversion of (D) to (E) occurs with a modest barrier. The rate-limiting process across this entire cascade (A to E, Table B9 in appendix B) is the migration of Cu^I through the 8-MR; beyond that point, reaction energies are computed to be independent of the zeolite cage. Thus, the primary role of the zeolite support in this oxidation process is to regulate Cu^I mobility.
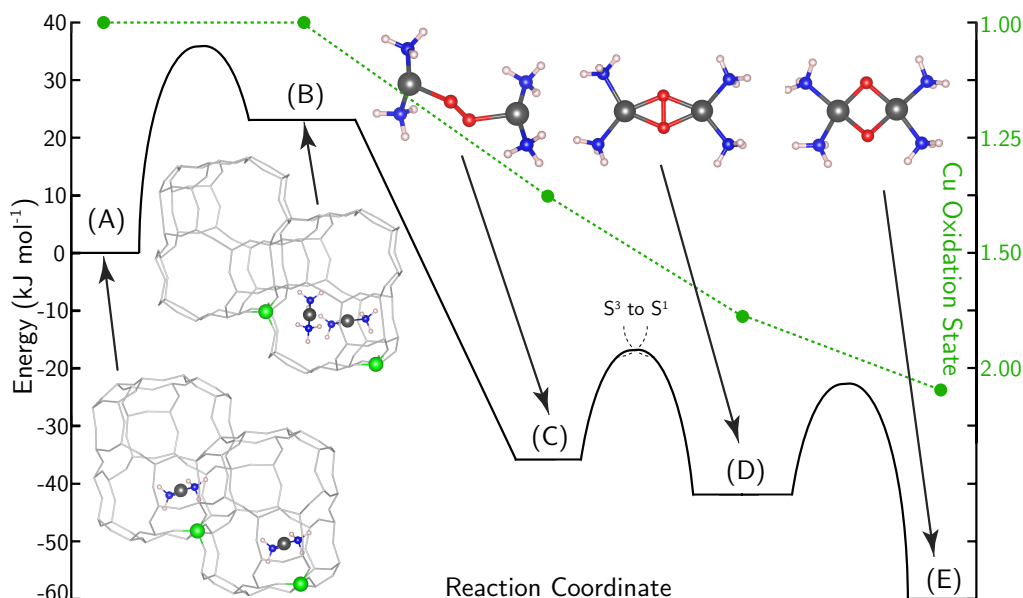
Figure 3.4 Simulation of O_2 adsorption and oxidation of 2 $Cu^I(NH_3)_2$ equivalents. DFT-computed energy landscape is shown for the diffusion of $Cu^I(NH_3)_2$ through an 8-MR CHA window into an adjacent cage and subsequent bimolecular reaction with O_2. All minima and transition states were computed here, except C to D, which is taken from[25]. Grey = Cu, green = Al, red = O, blue = N and white = H.

Structure E is consistent both with XANES-observed Cu^{II} oxidation state and with the first and second-shell features extracted from EXAFS (Figure 3.3A, inset, appendix B figures B9-11) at the end of the transient O_2 oxidation experiment. Thus, experiment and computation both reveal a second Cu^{II} state of the catalyst, distinct from framework-bound Cu^{II} observed after oxidative treatments and from NH_3-solvated Cu^{II} detected during low temperature standard SCR[10,21]. Exposure of samples to NO and NH_3 at 473 K following the transient O_2 oxidation experiments reduces all sites to the original mononuclear Cu^I state, demonstrating that the SCR redox cycle can be closed through sequential stoichiometric reactions (section B6, figure B12 in appendix B). Further, subsequent O_2 treatment recovers the same transient response and the same fraction of Cu^I sites that are unresponsive to O_2 exposure (appendix B, table B7), indicating that Cu^I ions do not irreversibly aggregate during O_2 exposure, but return to their original site-isolated state after each reduction step.

To verify that the residual Cu^I fraction did not represent a physically inaccessible or chemically distinct site, transient O_2 experiments were compared with an analogous transient NO_2 experiment (details in appendix B, section B3) on reduced forms of the same three samples

(appendix B, figures B6-8). After NO_2 exposure at 473 K, the Cu^I fraction decayed with time as in the O_2 experiment, but the Cu^I absorption edges disappeared completely after ~300 s. Further, the decrease in Cu^I fraction with time is best described ($R^2 = 0.98$ (a), 0.98 (c), and 0.89 (h); details in appendix B, section B4) by a pseudo-first order rate expression with apparent rate constants (0.030 s^{-1}) that are independent of Cu density (appendix B section B4, figure B13). Thus, all Cu^I sites are equivalently susceptible to oxidation by NO_2. We compute the reaction energy for NO_2 binding to $Cu^I(NH_3)_2$ to be -46 kJ mol^{-1} and to generate a Cu^{II} center (section B5, figure B14, table B10 in appendix B).

We conclude that the spatial proximity of isolated Cu^I ions, and not the presence of minority dimeric Cu species at low Cu densities, is responsible for the transition in the standard SCR turnover rate from a quadratic to linear dependence on Cu ion loading with increasing Cu density (Figure 3.1B). The steady-state and transient experiments and DFT models are consistent with a $Cu^I \rightarrow Cu^{II}$ half-cycle that combines two $Cu^I(NH_3)_2$ complexes with one O_2 molecule to create a previously unobserved binuclear Cu^{II} intermediate (equation 3.3, Figure 3.4).

The available data exclude the possibility that O_2 activation occurs on a persistent minority fraction of Cu ion pairs within single zeolite cages[33]. First, the fraction of isolated $Cu^I(NH_3)_2$ complexes that could be reversibly oxidized with O_2 (Figure 3.3A) exceeds by 10-fold the fraction of Cu pairs within a single cage if Cu were randomly dispersed on the zeolite support (section B7, figure B15 in appendix B). Second, steady-state and transient rates of Cu^I oxidation with O_2 would exhibit a first-order dependence on Cu density, as observed with NO_2 as the oxidant. Rather, these results imply a pseudo-homogeneous reaction between equivalent site-isolated Cu^I ions with mobilities constrained in a manner that limits the total fraction of sites reactive toward O_2.

3.4.3   Solvation by Ammonia Confers Mobility to Single Cu Ions

To assess the mobility of $Cu^I(NH_3)_2$ complexes over timescales inaccessible to conventional *ab initio* molecular dynamics, we turned to *ab initio* metadynamics (appendix B section B8), taking Cu-Al coordination distance as the collective variable, employing a supercell with a minimum image distance of >10 Å (appendix B, section B8), and sampling at 473 K. Free energy was minimized at a Cu-Al distance of 4.7 Å and increased with Cu-Al separation until the

Cu ion entered an 8-MR window separating two cages, at 8 Å (Figure 3.5). Free energy decreased as the Cu ion moved into the adjacent cage, before increasing again as the Cu-Al distance exceeded 9 Å. Comparison with a point-charge model indicates that electrostatics dominate this distance-dependent free energy (section B9 in appendix B, Figure 3.5). From the computed free energy landscape, we estimate the hopping rate for a $Cu^I(NH_3)_2$ to leave its resting cage to be 6×10^6 s^{-1} at 473 K, much faster than steady-state SCR turnover rates (appendix B, table B3), and the equilibrium fraction of Cu ions outside their resting cage to be 1.4×10^{-5} at 473 K.
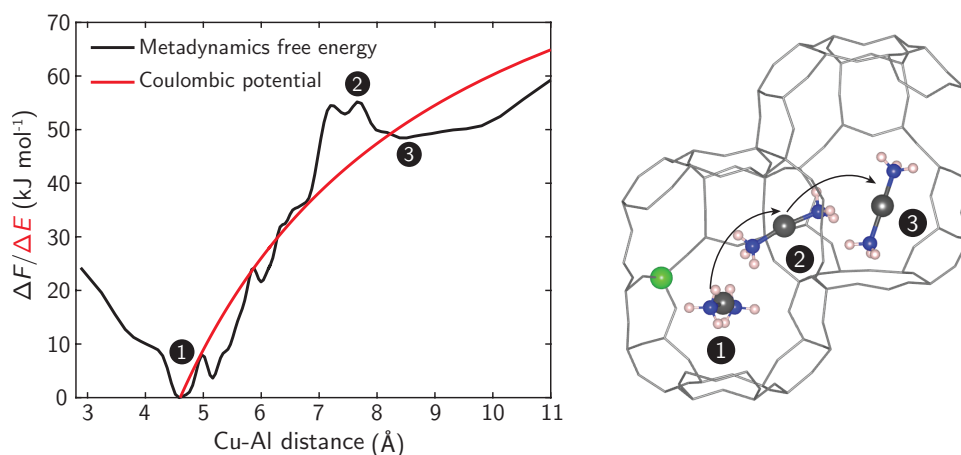
Figure 3.5 Simulated $Cu^I(NH_3)_2$ diffusion up to 11 Å from charge-compensating Al. The free energy profile is projected on the Cu-Al distance of $Cu^I(NH_3)_2$ in the 72-T-site CHA supercell for reactant state ($Cu^I(NH_3)_2$ in the same cage as Al) **(1)**, transition state ($Cu^I(NH_3)_2$ diffusion through 8-MR) **(2)** and product state ($Cu^I(NH_3)_2$ in the neighboring cage without Al) **(3)**. $Cu^I(NH_3)_2$ configurations at different states are superimposed in the inset. Grey = Cu, green = Al, blue = N and white = H. The red line is the energy profile predicted from a point-charge electrostatic model, described in appendix B section B9.

$Cu^I(NH_3)_2$ migration is thus rapid at 473 K, but constrained by electrostatic tethering to charge-compensating framework Al sites. We next used this concept to predict the unoxidized fraction of $Cu^I(NH_3)_2$ in the transient O_2 experiments (Figure 3.3A), assuming that Cu ions are randomly associated with Al in the CHA lattice, that each Cu can access a limited diffusion volume, and that only Cu^I ions with overlapping diffusion volumes can form an O_2-bridged Cu pair (Figure 3.4). To exercise the model, we distributed Al onto a periodic super-cell of the CHA lattice following Löwenstein's rule[34], occupied sites with Cu following previously validated rules[10] , counted the number of overlapping diffusion spheres at a given radius (Figure 3.3B, t =

0) permitting each Cu to be counted only once, and repeated until the average unoxidized Cu^I fraction converged (section B10 in appendix B and figure B16). At the end of a single simulation, the unoxidized Cu^I fraction consisted of Cu ions that were either initially physically isolated from all other Cu (Iso) or were functionally isolated because they shared overlapping diffusion volumes with Cu ions that had more than one potential partner, the losers in a molecular game of musical chairs (MC). Representative initial and final simulation snapshots are shown in Figure 3.3B, for Cu densities corresponding to Cu-CHA-15, Cu-CHA-20 and Cu-CHA-29, and the predicted fraction of unoxidized Cu^I assuming a diffusion radius of 9 Å are plotted as solid horizontal bars in Figure 3A. Model results agree quantitatively with both experimental observation and the metadynamics observation of a ~9 Å maximum diffusion distance, implying that the Cu sites are neither conventionally heterogeneous (immobile) or homogenous (mobility governed by molecular diffusion), and demonstrating that the fraction of spectator $[Cu^I]_\infty$ sites is a consequence of regulated and localized mobility due to electrostatic tethering.

These observations resolve the outstanding issues regarding SCR catalysis raised in the introduction. NH_3 solvates and mobilizes discrete Cu active sites under low temperature SCR conditions. When the activation of O_2 is not rate-controlling, NH_3-solvated Cu ions appear catalytically equivalent, such that rates increase linearly with their number density. In this regime the zeolite framework itself has only a weak influence on the SCR turnover rate[10], because it functions primarily as an ionic host for homogeneous-like NH_3-ligated Cu^{II} complexes. Experiments performed on samples with low Cu density revealed, however, that a homogeneous picture of the SCR mechanism is incomplete.
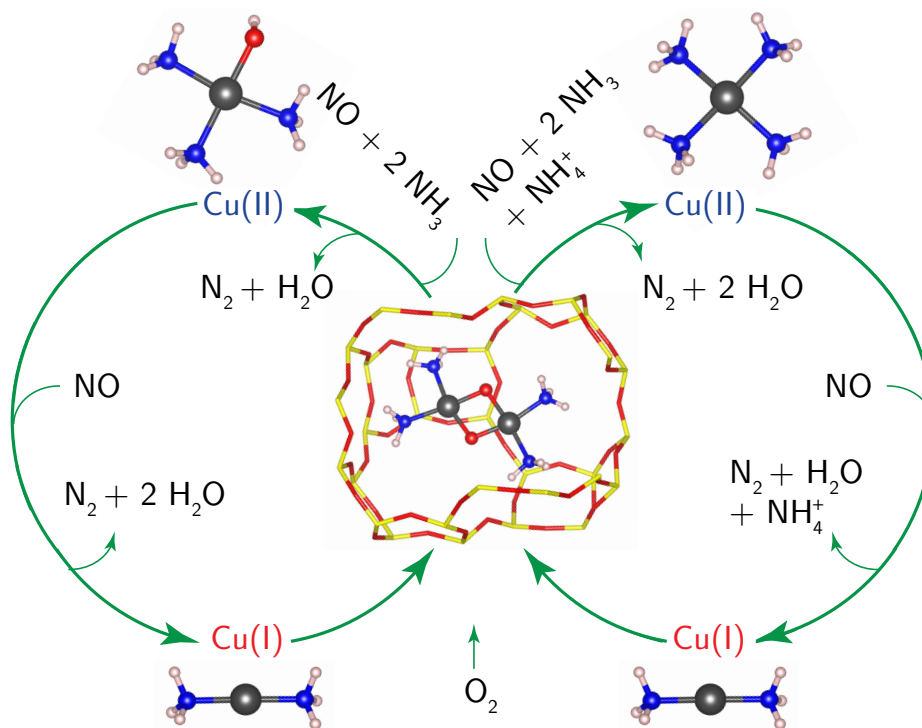
Figure 3.6. Proposed low-temperature SCR catalytic cycle. Reduction steps proceed on site-isolated Cu^{II} ions residing near one (left outer circle) or two (right outer cycle) framework Al centers with constrained diffusion of Cu^I ions into single cages and oxidation by O_2 (inner step). NH_4^+ is formed and consumed in the right-hand cycle to maintain stoichiometry and charge balance. Grey = Cu, yellow = Si, red = O, blue = N and white = H.

Simulations reveal that NH_3-solvated Cu^I ions have sufficient mobility to travel through 8-MR CHA windows, to visit adjacent cages, and to form Cu site pairs that activate O_2 via equation 3.3. Because of this requirement for dynamic Cu pairing, SCR rates scale approximately second-order with Cu density under conditions in which the $Cu^I \rightarrow Cu^{II}$ oxidation by O_2 is rate-determining, consistent with quantitative analysis of the transient oxidation of Cu^I with O_2. In contrast with previous assertions[35], binuclear Cu^{II} intermediates can be detected experimentally and are structurally distinct from the mononuclear NH_3-solvated Cu^{II} observed *in operando*[10,21], and the number of such binuclear sites that can form on a given Cu-CHA sample can be quantitatively predicted. These results motivate a revision of previous mechanisms to incorporate this dynamic coupling of isolated Cu ions, as illustrated in Figure 3.6. Isolated, NH_3-solvated Cu^{II} ions charge-compensating either one (left cycle) or two (right cycle) framework Al sites are reduced by NO and NH_3 to produce N_2, H_2O, and $Cu^I(NH_3)_2$. These two paths are distinguished only by the fate of the proton that is also generated[10]. Mobile $Cu^I(NH_3)_2$ species

can diffuse and combine in a reaction that consumes O_2 and generates the Cu^{II} dimer intermediate observed here. We confirmed that this binuclear Cu^{II} complex reacts with two equivalents of NO per Cu (section B6 and figure B12 in appendix B) to regenerate $Cu^{I}(NH_3)_2$ and close the SCR cycle.

A key aspect of our model is that Cu ions supported on the zeolite are neither mobile as prescribed by molecular diffusion processes, as in a homogeneous catalyst, nor segregated into separate ensembles of active and inactive sites, as in a heterogeneous catalyst. Rather, all Cu ions located within diffusion distances of other ions can potentially form Cu pairs dynamically and reversibly during the SCR cycle, at rates influenced by the mobility and effective diffusion distances of Cu ions. Thus, rates of O_2-assisted oxidations are sensitive to Cu proximity and could also be sensitive to the zeolite support composition and topology. In contrast, all NH_3-solvated Cu^{I} sites are equivalently susceptible to first-order oxidation by NO_2, independent of Cu spatial density, and are subsequently reducible by NO and NH_3. These observations demonstrate that fast SCR, in which oxidation capacity is provided by NO_2 rather than O_2 (equation 3.4)

$$NO + NO_2 + 2NH_3 \rightarrow 2N_2 + 3H_2O \tag{3.4}$$

is not linked through a common intermediate to standard SCR under conditions in which Cu sites are NH_3-solvated[16]. NO_2 oxidants accelerate SCR rates both by accelerating Cu^{I} oxidation kinetics and by engaging a larger fraction of Cu sites in the catalyst.

At higher temperatures (>523 K), standard SCR rates are independent of Cu density[12,18], the apparent activation energy increases to 140 kJ mol^{-1} [18] , and Cu ions lose their NH_3 solvation shell[12], implicating the involvement of different O_2 activation steps that do not occur at the Cu ion pairs formed dynamically at lower temperatures (<523 K). Of greater practical importance to NO_x emissions control is to increase SCR rates at even lower temperatures (<473 K)[12]. The results here imply that standard SCR onset ("light-off") temperatures, which are observed to depend on zeolite composition, topology, and Cu distribution[36], are sensitive to changes in rate-determining O_2 activation steps Thus, optimization of Cu spatial distribution or promotion of Cu mobility are promising strategies for accelerating Cu^{I} oxidation rates and improving low-temperature SCR catalysts.

3.5 Conclusions

Some vital details related to low temperature NH_3-SCR of NO_x are seemingly elusive and controversial, including and a molecular-level detailed reaction mechanism, which could reconcile seemingly disparate observations. These observations include the role of the zeolite support topology and composition in the catalytic cycle, the different sensitivity of SCR rates to Cu concentration under different conditions, if standard and fast SCR cycles are connected via some common intermediates, reaction steps that limit low-temperature SCR reactivity, and the reasons behind apparent change in reaction mechanism at high temperatures. In chapter 2, we demonstrated that NH_3 solvates and mobilizes Cu active sites at low temperature (473 K) SCR conditions. In the kinetic regime, when the $Cu^{II} \rightarrow Cu^{I}$ reduction half-cycle is rate-limiting, NH_3-solvation leads to all Cu ions appearing catalytically equivalent, and as a consequence, observed rates vary linearly with the concentration of Cu sites, as expected for a single-site reaction. In this $Cu^{II} \rightarrow Cu^{I}$ reduction-limited kinetic regime, the primary role of zeolite support is to ionically tether NH_3-solvated Cu^{II} complexes (homogenous-like), as the zeolite structure was found to only weakly influence the SCR turnover rate (per Cu)[10]. In this chapter, the experiments on samples with low Cu density showed that homogenous type behavior ($[Cu^{II}OH](NH_3)_3$ near 1 Al or $Cu^{II}(NH_3)_4$ near 2Al) is insufficient in explain the low Cu density observation. We showed that NH_3-solvated Cu^{I} sites have sufficient mobility to travel through windows, visit adjacent cages, and form the Cu^{II}-dimer pairs, which is a prerequisite for activation with O_2. When such Cu^{II}-dimer formation is difficult, $Cu^{I} \rightarrow Cu^{II}$ oxidation becomes rate-limiting, as substantiated by observed second-order dependence of SCR turnover rate on Cu spatial density, second-order transient oxidation of Cu^{I} with O_2 and spectroscopic identification of this dimeric Cu intermediate. Additionally, it can be concluded that NH_3-solvated Cu^{I} sites are neither infinitely mobile, as in a homogeneous catalyst, nor segregated into separate ensembles of active and inactive sites, as might be expected in a heterogeneous catalyst. Cu sites are required to be within diffusion distances of another Cu to be able to pair dynamically and reversibly during the SCR cycle, at rates that are influenced by the mobility and effective diffusion distances of Cu ions. Therefore, the rates of such dynamic oxidation processes are sensitive to Cu spatial density and would be expected to be sensitive to the zeolite support composition and topology.

3.6   Outlook

The results here point to a previously unrecognized catalytic mechanism that embodies salient features of homogeneous and heterogeneous catalysts. This mechanism encompasses solvent mobilization of discrete active site precursors (e.g., single metal ions) and ionic bonds to the support that limit their mobility. The active site precursor has an effective diffusion distance and occupies a volumetric footprint that restricts its interactions only to other precursors within overlapping volumes; such catalytic behavior cannot be described by mean-field, Langmuir kinetics. The ionic tethering motif provides opportunities to confer catalytic benefits beyond immobilization strategies based on covalent anchors or tethers. This motif enables the *in situ* dynamic generation of multinuclear complexes implicated as active sites in O_2 activation, and therefore could also apply to other reactions, such as the partial oxidation of methane to methanol on Cu-zeolites**.** We expect that design parameters to regulate the mobility of active sites and their precursors would include the structure, composition and electronic conductivity of the support, and the molecules that solvate such sites to promote their mobility. Manipulating these variables could open approaches to catalyst design for a wide variety of reactions by combining knowledge from homogeneous and heterogeneous catalysis.

3.7   Acknowledgements

3.8 References

1. J. M. Thomas, The societal significance of catalysis and the growing practical importance of single-site heterogeneous catalysts. *Proc. R. Soc. A* **468**, 1884-1903 (2012).
2. M. Boudart, Turnover Rates in Heterogeneous Catalysis. *Chemical Reviews* **95**, 661-666 (1995).
3. K. Ding *et al.*, Identification of active sites in CO oxidation and water-gas shift over supported Pt catalysts. *Science* **350**, 189-192 (2015).
4. J. Jones *et al.*, Thermally stable single-atom platinum-on-ceria catalysts via atom trapping. *Science* **353**, 150-154 (2016).
5. E. J. Peterson *et al.*, Low-temperature carbon monoxide oxidation catalysed by regenerable atomically dispersed palladium on alumina. *Nature Communications* **5**, 4885 (2014).
6. G. Kyriakou *et al.*, Isolated Metal Atom Geometries as a Strategy for Selective Heterogeneous Hydrogenations. *Science* **335**, 1209-1212 (2012).
7. H. Wei *et al.*, FeOx-supported platinum single-atom and pseudo-single-atom catalysts for chemoselective hydrogenation of functionalized nitroarenes. *Nature Communications* **5**, 5634 (2014).
8. M. Yang *et al.*, Catalytically active Au-O(OH)x- species stabilized by alkali ions on zeolites and mesoporous oxides. *Science* **346**, 1498-1501 (2014).
9. M. Yang *et al.*, A Common Single-Site Pt(II)–O(OH) x – Species Stabilized by Sodium on "Active" and "Inert" Supports Catalyzes the Water-Gas Shift Reaction. *Journal of the American Chemical Society* **137**, 3470-3473 (2015).
10. C. Paolucci *et al.*, Catalysis in a Cage: Condition-Dependent Speciation and Dynamics of Exchanged Cu Cations in SSZ-13 Zeolites. *Journal of the American Chemical Society* **138**, 6028-6048 (2016).
11. J. M. Thomas, R. Raja, D. W. Lewis, Single-Site Heterogeneous Catalysts. *Angewandte Chemie International Edition* **44**, 6456-6482 (2005).
12. C. Paolucci, J. Di Iorio, F. Ribeiro, R. Gounder, W. Schneider, Chapter One-Catalysis Science of NOx Selective Catalytic Reduction With Ammonia Over Cu-SSZ-13 and Cu-SAPO-34. *Advances in Catalysis* **59**, 1-107 (2016).
13. S. T. Korhonen, D. W. Fickel, R. F. Lobo, B. M. Weckhuysen, A. M. Beale, Isolated Cu^{2+} ions: active sites for selective catalytic reduction of NO. *Chemical Communications* **47**, 800-802 (2011).
14. E. Borfecchia *et al.*, Revisiting the nature of Cu sites in the activated Cu-SSZ-13 catalyst for SCR reaction. *Chemical Science* **6**, 548-563 (2015).
15. C. Paolucci *et al.*, Isolation of the Copper Redox Steps in the Standard Selective Catalytic Reduction on Cu-SSZ-13. *Angewandte Chemie International Edition* **53**, 11828-11833 (2014).
16. T. V. W. Janssens *et al.*, A Consistent Reaction Scheme for the Selective Catalytic Reduction of Nitrogen Oxides with Ammonia. *ACS Catalysis* **5**, 2832-2845 (2015).
17. S. A. Bates *et al.*, Identification of the active Cu site in standard selective catalytic reduction with ammonia on Cu-SSZ-13. *Journal of Catalysis* **312**, 87-97 (2014).
18. F. Gao *et al.*, Understanding ammonia selective catalytic reduction kinetics over Cu/SSZ-13 from motion of the Cu ions. *Journal of Catalysis* **319**, 1-14 (2014).
19. C. Baerlocher, L. B. McCusker, Database of Zeolite Structures. (2017).

20. T. Günter *et al.*, Structural snapshots of the SCR reaction mechanism on Cu-SSZ-13. *Chemical Communications* **51**, 9227-9230 (2015).

21. K. A. Lomachenko *et al.*, The Cu-CHA deNO x Catalyst in Action: Temperature-Dependent NH₃ -Assisted Selective Catalytic Reduction Monitored by Operando XAS and XES. *Journal of the American Chemical Society* **138**, 12025-12028 (2016).

22. P. J. Smeets *et al.*, Oxygen Precursor to the Reactive Intermediate in Methanol Synthesis by Cu-ZSM-5. *Journal of the American Chemical Society* **132**, 14736-14738 (2010).

23. P. Vanelderen *et al.*, Spectroscopic Definition of the Copper Active Sites in Mordenite: Selective Methane Oxidation. *Journal of the American Chemical Society* **137**, 6383-6392 (2015).

24. J. S. Woertink *et al.*, A [Cu2O]2+ core in Cu-ZSM-5, the active site in the oxidation of methane to methanol. *Proceedings of the National Academy of Sciences of the United States of America* **106**, 18908-18913 (2009).

25. M. Metz, E. I. Solomon, Dioxygen Binding to Deoxyhemocyanin: Electronic Structure and Mechanism of the Spin-Forbidden Two-Electron Reduction of O_2. *Journal of the American Chemical Society* **123**, 4938-4950 (2001).

26. L. M. Mirica, X. Ottenwaelder, T. D. P. Stack, Structure and Spectroscopy of Copper−Dioxygen Complexes. *Chemical Reviews* **104**, 1013-1046 (2004).

27. L. M. Mirica *et al.*, Tyrosinase reactivity in a model complex: an alternative hydroxylation mechanism. *Science* **308**, 1890-1892 (2005).

28. P. Chen, E. I. Solomon, O_2 activation by binuclear Cu sites: noncoupled versus exchange coupled reaction mechanisms. *Proceedings of the National Academy of Sciences of the United States of America* **101**, 13105-13110 (2004).

29. S. D. McCann, S. S. Stahl, Copper-Catalyzed Aerobic Oxidations of Organic Molecules: Pathways for Two-Electron Oxidation with a Four-Electron Oxidant and a One-Electron Redox-Active Catalyst. *Accounts of Chemical Research* **48**, 1756-1766 (2015).

30. B. R. Goodman, K. C. Hass, W. F. Schneider, J. B. Adams, Cluster Model Studies of Oxygen-Bridged Cu Pairs in Cu−ZSM-5 Catalysts. *The Journal of Physical Chemistry B* **103**, 10452-10460 (1999).

31. E. I. Solomon *et al.*, Copper active sites in biology. *Chemical Reviews* **114**, 3659-3853 (2014).

32. L. Chen, J. Jansson, M. Skoglundh, H. Grönbeck, Mechanism for Solid-State Ion Exchange of Cu+ into Zeolites. *The Journal of Physical Chemistry C* **120**, 29182-29189 (2016).

33. H. Falsig, P. N. R. Vennestrøm, P. G. Moses, T. V. W. Janssens, Activation of Oxygen and NO in NH3-SCR over Cu-CHA Catalysts Evaluated by Density Functional Theory. *Topics in Catalysis* **59**, 861-865 (2016).

34. W. Lowenstein, The distribution of aluminium in the tetrahedra of silicates and aluminates. *American Mineralogist* **39**, 92-96 (1954).

35. F. Gao, D. Mei, Y. Wang, J. Szanyi, C. H. F. Peden, Selective Catalytic Reduction over Cu/SSZ-13: Linking Homo- and Heterogeneous Catalysis. *Journal of the American Chemical Society* **139**, 4935-4942 (2017).

36. J. H. Kwak, R. G. Tonkyn, D. H. Kim, J. Szanyi, C. H. F. Peden, Excellent activity and selectivity of Cu-SSZ-13 in the selective catalytic reduction of NOx with NH3. *Journal of Catalysis* **275**, 187-190 (2010).

37. G. Lamble, A. Moen, D. G. Nicholson, Structure of the diamminecopper (I) ion in solution. An X-ray absorption spectroscopic study. *Journal of the Chemical Society, Faraday Transactions* **90**, 2211-2213 (1994).

38. L.-S. Kau, D. J. Spira-Solomon, J. E. Penner-Hahn, K. O. Hodgson, E. I. Solomon, X-ray absorption edge determination of the oxidation state and coordination number of copper: application to the type 3 site in Rhus vernicifera laccase and its reaction with oxygen. *Journal of the American Chemical Society* **109**, 6433-6442 (1987).

39. V. F. Kispersky, A. J. Kropf, F. H. Ribeiro, J. T. Miller, Low absorption vitreous carbon reactors for operandoXAS: a case study on Cu/Zeolites for selective catalytic reduction of NOx by NH3. *Physical Chemistry Chemical Physics.* **14**, 2229-2238 (2012).

40. A. A. Verma *et al.*, NO oxidation: A probe reaction on Cu-SSZ-13. *Journal of Catalysis* **312**, 179-190 (2014).

41. M. H. Groothaert *et al.*, Bis (μ-oxo) dicopper as Key Intermediate in the Catalytic Decomposition of Nitric Oxide. *ChemPhysChem* **4**, 626-630 (2003).

42. J. R. Di Iorio *et al.*, The Dynamic Nature of Brønsted Acid Sites in Cu–Zeolites During NOx Selective Catalytic Reduction: Quantification by Gas-Phase Ammonia Titration. *Topics in Catalysis* **58**, 424-434 (2015).

43. S. Bordiga, E. Groppo, G. Agostini, J. A. van Bokhoven, C. Lamberti, Reactivity of surface species in heterogeneous catalysts probed by in situ X-ray absorption techniques. *Chemical reviews* **113**, 1736-1850 (2013).

44. J. A. Van Bokhoven, C. Lamberti, *X-ray absorption and X-ray emission spectroscopy: theory and applications.* (Wiley, 2016), vol. 1.

45. C. Lamberti *et al.*, Determination of the oxidation and coordination state of copper on different Cu-based catalysts by XANES spectroscopy in situ or in operando conditions. *Physical Chemistry Chemical Physics* **5**, 4502-4509 (2003).

46. F. Giordanino *et al.*, Characterization of Cu-exchanged SSZ-13: a comparative FTIR, UV-Vis, and EPR study with Cu-ZSM-5 and Cu-BETA with similar Si/Al and Cu/Al ratios. *Dalton Transactions* **42**, 12741-12761 (2013).

47. G. Shulman, Y. Yafet, P. Eisenberger, W. Blumberg, Observations and interpretation of X-ray absorption edges in iron compounds and proteins. *Proceedings of the National Academy of Sciences* **73**, 1384-1388 (1976).

48. J. E. Hahn *et al.*, Observation of an electric quadrupole transition in the X-ray absorption spectrum of a Cu (II) complex. *Chemical Physics Letters* **88**, 595-598 (1982).

49. F. Giordanino *et al.*, Interaction of NH 3 with Cu-SSZ-13 Catalyst: A Complementary FTIR, XANES, and XES Study. *The Journal of Physical Chemistry Letters* **5**, 1552-1559 (2014).

50. P. N. Vennestrøm *et al.*, Influence of lattice stability on hydrothermal deactivation of Cu-ZSM-5 and Cu-IM-5 zeolites for selective catalytic reduction of NOx by NH3. *Journal of Catalysis* **309**, 477-490 (2014).

51. D.-J. Liu, H. J. Robota, On the mechanism of NO selective catalytic reduction by hydrocarbons over Cu-ZSM-5 via X-ray absorption spectroscopic study. *The Journal of Physical Chemistry B* **103**, 2755-2765 (1999).

52. D.-J. Liu, H. J. Robota, In situ XANES characterization of the Cu oxidation state in Cu-ZSM-5 during NO decomposition catalysis. *Catalysis letters* **21**, 291-301 (1993).

53. Y. Kuroda *et al.*, Specific feature of copper ion-exchanged mordenite for dinitrogen adsorption at room-temperature. *Journal of Physical Chemistry* **99**, 10621-10628 (1995).

54. C. Lamberti *et al.*, Cu I-Y and Cu II-Y zeolites: a XANES, EXAFS and visible-NIR study. *Chemical Physics Letters* **269**, 500-508 (1997).

55. K. Mathisen, M. Stockenhuber, D. G. Nicholson, In situ XAS and IR studies on Cu: SAPO-5 and Cu: SAPO-11: the contributory role of monomeric linear copper (i) species in the selective catalytic reduction of NO x by propene. *Physical Chemistry Chemical Physics* **11**, 5476-5488 (2009).

56. A. Moen, D. G. Nicholson, M. Rønning, Studies on the pre-edge region of the X-ray absorption spectra of copper (I) oxide and the diamminecopper (I) ion. *Journal of the Chemical Society, Faraday Transactions* **91**, 3189-3194 (1995).

57. R. Car, M. Parrinello, Unified approach for molecular dynamics and density-functional theory. *Physical Review Letters* **55**, 2471 (1985).

58. J. P. Perdew, K. Burke, M. Ernzerhof, Generalized gradient approximation made simple. *Physical Review Letters* **77**, 3865 (1996).

59. D. Vanderbilt, Soft self-consistent pseudopotentials in a generalized eigenvalue formalism. *Physical Review B* **41**, 7892-7895 (1990).

60. G. Kresse, J. Furthmüller, Efficient iterative schemes for ab initio total-energy calculations using a plane-wave basis set. *J. Phys. Rev. B: Condens. Matter Mater. Phys.*, **54**, 11169−11186 (1996)..

61. S. Grimme, Semiempirical GGA-type density functional constructed with a long-range dispersion correction. *Journal of Computational Chemistry* **27**, 1787-1799 (2006).

62. G. Henkelman, B. P. Uberuaga, H. Jónsson, A climbing image nudged elastic band method for finding saddle points and minimum energy paths. *The Journal of Chemical Physics* **113**, 9901-9904 (2000).

63. J. Heyd, G. E. Scuseria, M. Ernzerhof, Erratum: "Hybrid functionals based on a screened Coulomb potential" [J. Chem. Phys. 118, 8207 (2003)]. *The Journal of Chemical Physics* **124**, 219906 (2006).

64. A. Tkatchenko, M. Scheffler, Accurate Molecular Van Der Waals Interactions from Ground-State Electron Density and Free-Atom Reference Data. *Phys. Rev. Lett.* **102**, 73005 (2009).

65. M. Iannuzzi, A. Laio, M. Parrinello, Efficient Exploration of Reactive Potential Energy Surfaces Using Car-Parrinello Molecular Dynamics. *Physical Review Letters* **90**, 238302 (2003).

66. A. Barducci, M. Bonomi, M. Parrinello, Metadynamics. *Wiley Interdisciplinary Reviews: Computational Molecular Science* **1**, 826-843 (2011).

67. M. Rybicki, J. Sauer, Acidity of two-dimensional zeolites. *Physical Chemistry Chemical Physics* **17**, 27873-27882 (2015).

68. J. D. Albarracin-Caballero *et al.*, Structural and kinetic changes to small-pore Cu-zeolites after hydrothermal aging treatments and selective catalytic reduction of NO x with ammonia. *Reaction Chemistry & Engineering* **2**, 168-179 (2017).

4. CATALYTIC CONSEQUENCES OF REACTANT DIOXYGEN PRESSURE ON STANDARD SCR KINETICS OVER CU-SSZ-13

4.1 Preface

Chapter 4 contains the most recent draft of a manuscript in preparation. This chapter explore varying reactant gas pressures to yield non-fractional orders and compare samples in the same kinetic regime. This approach allows for decoupling of various effects on measured overall SCR kinetics and isolate different active site requirements of various reaction steps during SCR reaction, enabling better interpretation of kinetic differences.

4.2 Abstract

The low-temperature (<573 K) selective catalytic reduction (SCR) of NO with NH_3 on Cu-exchanged zeolites occurs via reactions catalyzed by NH_3-solvated Cu ions, which are intermediates in a Cu^{II}/Cu^{I} redox cycle. SCR turnover rates are often measured under "standard" reaction conditions, in which O_2 is used as the oxidant and present in concentrations (typically 3-20% (v/v)) that cause both single Cu^{II}-site reduction and dual Cu^{I}-site oxidation steps to become kinetically relevant. As a result, "standard" SCR turnover rates on Cu-exchanged zeolites, normalized per isolated Cu ion, show a complex dependence on the spatial density of Cu ions, depending on the extent to which Cu^{I} oxidation and Cu^{II} reduction steps limit rates of the overall SCR cycle. Here, SCR kinetic parameters (apparent rate constants, activation energies, reaction orders) and *in operando* X-ray absorption spectra are measured on a suite of model Cu-CHA zeolites (Si/Al = 15) of varying extraframework Cu ion spatial density (Cu/Al = 0.08-0.44; ρ_{Cu} = 0.07-0.42 per 1000 Å), under widely varying dioxygen pressures (0-70 kPa) in order to perturb the Cu^{II}/Cu^{I} redox cycle to operate in kinetic regimes limited predominantly by Cu^{I} oxidation and Cu^{II} reduction steps. SCR turnover rates show a Langmuirian dependence on dioxygen pressure, allowing estimation of apparent rate constants in first-order and zero-order kinetic regimes with respect to dioxygen. Apparent zero-order rate constants (per Cu) increase with Cu density up to a point, beyond which they become essentially invariant with Cu density, as increasing fractions of Cu ions are able to catalyze SCR redox cycles. Apparent first-order rate constants (per Cu) increase linearly with Cu density, consistent with the quadratic dependence of

O_2-assisted Cu^I oxidation rates on Cu density. The combination of steady-state kinetic measurements with *in operando* spectroscopy provides a methodology to precisely quantify the dependences of SCR reduction and oxidation half-cycle rates on Cu-zeolite material properties, including the spatial density of extraframework Cu ions as shown here, and also the zeolite pore connectivity and its density and distribution of framework Al atoms.

4.3   Introduction

Selective catalytic reduction (SCR) using ammonia is a strategy used for nitrogen oxides (NO_X, x=1,2) abatement in diesel and lean-burn engine emissions control, in which Cu-CHA zeolite catalysts were implemented commercially a decade ago. Fundamental catalysis research has since focused on elucidating the kinetic and mechanistic details of NO_X SCR with NH_3 on Cu-zeolites to determine the underlying factors that become manifested as macroscopic observables in NO_X conversion profiles with temperature [1], including the onset of the "light-off" in NO_X conversion at low temperatures (<473 K) and the "seagull" phenomenon describing the decrease in NO_X conversion at intermediate temperatures (~623 K) [2–5]. SCR active sites are derived from isolated Cu cations that are exchanged at anionic framework sites introduced by Al substitution, including those present nominally as monovalent $[Cu^{II}OH]^+$ (ZCuOH) and divalent Cu^{II} (Z_2Cu) sites that respectively charge-compensate one and two framework Al sites [1,6–8]. At low temperatures (<573 K) and SCR-relevant reaction conditions, ZCuOH and Z_2Cu sites are fully solvated by NH_3 ligands, as evidenced by phase diagrams constructed from first-principles thermodynamic analyses of DFT-computed free energies of Cu-ligand complexes [6], by *in situ* X-ray emission spectra (XES) that show Cu-N coordination in both their oxidized (Cu^{II}) and reduced (Cu^I) states [7,9], and by *in situ* X-ray absorption near edge spectroscopy (XANES) and extended X-ray absorption fine structure (EXAFS) spectra of oxidized and reduced states of Cu-CHA samples that are indistinguishable from those for four-fold and two-fold Cu-amine complexes [6,10], respectively.

NH_3-solvated Cu ions are reactive intermediates that propagate the Cu^I/Cu^{II} SCR redox cycle, and are present as cationic complexes that are bonded ionically to anionic framework centers, evident in the absence of coherent second-shell Cu-T (T = Si, Al) scattering in EXAFS spectra collected *in operando* [6] and of perturbations of zeolite framework T-O-T vibrations in diffuse reflectance IR (DRIFTS) spectra collected *in situ* [11]. NH_3-solvated mononuclear Cu^{II}-

amine complexes ($Cu^{II}(NH_3)_4$, $Cu^{II}(OH)(NH_3)_3$) are reduced by NO and NH_3 via nitrosamine-like transition states to form mononuclear Cu^I-amine complexes ($Cu^I(NH_3)_2$) according to DFT calculations of Cu^{II} reduction pathways, which are consistent with experimental observations such as the complete reduction of Cu^{II} ions upon exposure of Cu-CHA to flowing NO and NH_3 after O_2 is removed from SCR reactant feeds [6,12]. Two mononuclear Cu^I-amine complexes ($Cu^I(NH_3)_2$) are subsequently oxidized with O_2 to form NH_3-solvated binuclear Cu^{II}-oxo complexes (e.g., $(NH_3)_2Cu^{II}(O_2)Cu^{II}(NH_3)_2$) [2,13], consistent with DFT calculations of plausible dual-site Cu^I oxidation pathways with O_2, and EXAFS spectra collected after the transient oxidation of $Cu^I(NH_3)_2$ sites with O_2 that show second-shell Cu-Cu scattering at distances characteristic of binuclear Cu-oxo complexes [13]. Finally, NH_3-solvated binuclear Cu^{II}-oxo complexes react with NO and NH_3, via elementary steps whose details remain incompletely understood, to close the SCR catalytic cycle [13].

Rates of NOx SCR reactions are often measured under "standard" conditions using dioxygen as the oxidant, the only practical option in automotive exhaust aftertreatment given its ubiquity in the ambient atmosphere, in which dioxygen is present in feed streams in amounts representative of those commonly present in diesel exhaust (3-20% (v/v)) [14]. SCR rates are also measured under "fast" conditions in which NO_2 is present in equimolar amounts to NO, which allows bypassing O_2-assisted oxidation steps involving two $Cu^I(NH_3)_2$ complexes with NO_2-assisted oxidation steps of single $Cu^I(NH_3)_2$ complexes to form $(NH_3)_2Cu^{II}(NO_2^-)$ [13], as often practiced to accelerate low-temperature "light-off" behavior [15–19]. Under "standard" SCR conditions, reaction rates (per volume catalyst) show a complex dependence on the spatial density of isolated Cu sites (per volume catalyst), increasing with a pseudo-quadratic dependence on Cu density at low Cu densities, and with a pseudo-linear dependence on Cu density at high Cu densities [20,21]. *In operando* X-ray absorption spectra (XAS) provide direct evidence that $Cu^I(NH_3)_2$ is the most abundant reactive intermediate (MARI), and in turn that $Cu^I(NH_3)_2$ oxidation with dioxygen is the sole kinetically-relevant process in the kinetic regime wherein SCR rates increase quadratically with Cu density [13]. Quantitative modeling of stoichiometric O_2-assisted oxidation of $Cu^I(NH_3)_2$ show that transient Cu^I oxidation are best described by a pseudo-second-order dependence on Cu density, and that the fraction of oxidizable $Cu^I(NH_3)_2$ sites (in the asymptotic limit of long reaction times) increase systematically with Cu spatial density, implicating the involvement of two $Cu^I(NH_3)_2$ sites in O_2-assisted oxidation steps [13].

These findings suggest that two $Cu^I(NH_3)_2$ sites must be located within a given CHA cage in order for O_2-assisted oxidation steps to occur, and are consistent with metadynamics simulations indicating that transport of $Cu^I(NH_3)_2$ species into an adjacent CHA cage through connecting 8-MR windows is energetically feasible (<50 kJ/mol) with respect to apparent activation energies measured during steady-state SCR (50-70 kJ/mol) [13]. Yet, quantitative measurements that are able to distinguish between the number of Cu sites that participate in the Cu^{II}/Cu^I redox cycle, and the kinetics of elementary steps propagated by such Cu sites, is difficult when measured reaction rates are convoluted by the kinetic contributions of multiple elementary steps in the catalytic cycle, as is the case during "standard" SCR conditions [10,12,13,22].

Here, the catalytic function of Cu-CHA zeolites is interrogated under SCR reaction conditions that enable isolating quantitative kinetic parameters that reflect rate constants in which Cu^{II} reduction or Cu^I oxidation become the dominant kinetically relevant processes. Since dioxygen is only involved in the Cu^I oxidation step of the SCR redox cycle, operating at dilute O_2 pressures enable accessing conditions in which Cu^I oxidation becomes the dominant kinetically relevant step, and excess O_2 pressures enable accessing conditions in which Cu^I oxidation steps appear to become kinetically irrelevant. As a result, steady-state SCR rates measured at conditions perturbed far from "standard" reaction conditions, in combination with *in operando* XAS to quantify the prevalence of Cu^{II} and Cu^I sites present during catalytic turnover under these conditions, enables measuring turnover rates in Cu^I oxidation-limited (i.e., dilute O_2 pressure) and Cu^{II} reduction-limited (i.e., excess O_2 pressure) kinetic regimes. Apparent reduction and oxidation rate constants are determined from regression of rate data to an empirical model that describes the observed Langmuirian dependence on O_2 pressure, and are compared to a kinetic rate equation derived from a simplified mechanistic model for the SCR reaction. This approach enables more accurately quantifying the influence of Cu ion spatial density in Cu-CHA on the kinetics of oxidation and reduction processes in the SCR redox cycle, and can be extended to quantitatively determine how changes to catalyst properties, including zeolite topology and framework Al density and arrangement, influence the fraction of active Cu ion sites and the rate constants of different elementary steps in the SCR cycle.

4.4 Results and Discussion

4.4.1 Evidence that both Cu^I oxidation and Cu^{II} reduction processes are kinetically relevant during steady-state SCR turnover

In order to study the effects of Cu ion density on the Cu^I oxidation and Cu^{II} reduction processes that occur during steady-state SCR turnover, a series of Cu-CHA samples with fixed framework Al content (Si/Al = 15) and varied concentration of exchanged extraframework Cu ions (Cu/Al = 0.03 to 0.44) were synthesized, as done in our previous study [13]. The samples used in this study are summarized in Table 4.1 (synthesis methods and characterization data are reported in Appendix B: Supplementary Materials to Chapter 3). Cu-CHA samples are denoted as Cu-CHA-X-Y, where X indicates the Si/Al ratio, and Y indicates the mean Cu volumetric density (per 1000 Å^3) assuming a homogeneous Cu distribution throughout the crystallite volume (Appendix B: Supplementary Materials to Chapter 3). Mean Cu volumetric densities vary from 0.07-0.42$\times$ 10^{-3} Cu Å^{-3} from the least to most heavily Cu-exchanged samples, corresponding respectively to approximately one Cu ion per sixteen to three chabazite cages.

Table 4.1 Characterization data of the Cu-CHA samples used in this study.

Cu-CHA-X-Y	Si/Al	Cu/Al	Cu wt%	Cu volumetric density (per 1000 Å^3)	Cu per CHA cage	Number of cages per Cu
Cu-CHA-15-0.07	15	0.08	0.5	0.07	0.06	17.3
Cu-CHA-15-0.09	15	0.10	0.7	0.09	0.07	13.8
Cu-CHA-15-0.11	15	0.12	0.8	0.11	0.09	11.5
Cu-CHA-15-0.16	15	0.17	1.1	0.16	0.12	8.1
Cu-CHA-15-0.18	15	0.19	1.3	0.18	0.14	7.3
Cu-CHA-15-0.23	15	0.25	1.7	0.23	0.18	5.5
Cu-CHA-15-0.30	15	0.32	2.0	0.30	0.23	4.3
Cu-CHA-15-0.34	15	0.37	2.4	0.34	0.27	3.7
Cu-CHA-15-0.42	15	0.44	2.9	0.42	0.32	3.1

SCR reaction rates (per 1000 Å^3, 473 K) measured at 1, 10 and 70 kPa O$_2$ on these model Cu-CHA zeolites are shown in Figure 4.1a, with the corresponding Cu^I fraction measured during *in operando* XAS experiments at these O$_2$ pressures shown in Figure 4.1b. SCR rates measured at 10 kPa O$_2$ (Fig. 4.1a, blue circles), which are representative of typical "standard" SCR conditions, increase quadratically with Cu density at low ρ_{Cu} values (<0.2 Cu per 1000 A^3), and gradually transition to increasing linearly with Cu density at high ρ_{Cu} values (>0.3 Cu per 1000

A^3), consistent with prior reports [13,20]. The fraction of Cu^I present during steady-state SCR turnover at 10 kPa O_2 (Fig. 4.1b, blue circles) decreases systematically with increasing Cu density, as dual-site Cu^I oxidation processes become less kinetically relevant and single-site Cu^{II} reduction processes become more kinetically relevant, as also reported previously [13]. At dilute ρ_{Cu} (<0.1 Cu per 1000 A^3), *in operando* XANES and EXAFS spectra indicate that $Cu^I(NH_3)_2$ is the sole most abundant reactive intermediate (MARI). At these operating conditions and catalyst compositions, Cu^I oxidation with O_2 becomes the dominant kinetically relevant step and thus SCR turnover rates depend quadratically on Cu density, as expected from dual-site requirement of Cu^I oxidation with O_2 [13]. Taken together, these data indicate that low-temperature SCR reaction rates measured under "standard" reaction conditions (e.g., 10 kPa O_2) are influenced by kinetics of both single-site Cu^{II} reduction and dual-site Cu^I oxidation processes, and become more sensitive to the kinetics of Cu^I oxidation with O_2 with decreasing Cu density, because of the Cu spatial density requirements of this dual-site step in the SCR redox cycle.
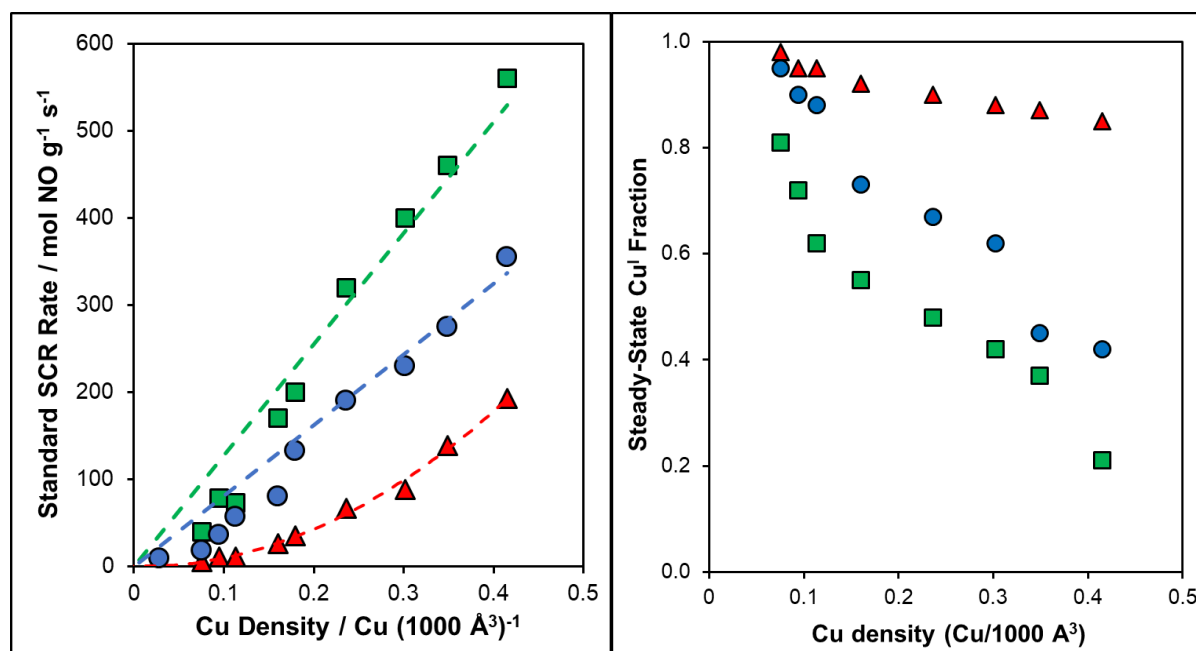
Figure 4.1 Left (a): Standard NO_x SCR rates (mol NO per g catalyst, 473 K) measured on Cu-CHA-X-Y samples under 1 kPa (red triangles), 10 kPa (blue circles) and 70 kPa O_2 (green squares). Right (b): Steady state Cu^I coverage under 1 kPa (red triangles), 10 kPa (blue circles) and 70 kPa O_2 (green squares) obtained from *operando* XAS as a function of Cu spatial density on a series of model Cu-CHA-15-Y samples. (Conditions: 300 ppm NO, 300 ppm NH_3, 1/10/70% O_2, 7% CO_2, 3% H_2O and balance He at 473 K)

The rates of Cu^{II} reduction and Cu^I oxidation in the SCR redox cycle, which must be equal during steady-state turnover, also depend on the apparent rate constants for these processes and the pressures of gaseous reactants involved. Since current mechanistic proposals involve dioxygen as a reactant only in the Cu^I oxidation step, varying the dioxygen pressure should enable changing the relative rates of Cu^{II} reduction and Cu^I oxidation processes, and in turn the extent to which they limit rates of the SCR redox cycle. Low-temperature SCR reaction rates (per 1000 Å^3, 473 K) measured at 70 kPa O_2 (Fig. 4.1a, green squares) are systematically higher than those measured at 10 kPa O_2, and the fraction of Cu^I present *in operando* is systematically lower at 70 kPa O_2 (Fig. 4.1b, green sqaures) than at 10 kPa O_2, in the entire range of ρ_{Cu} on the Cu-CHA zeolites studied here, consistent with the preferential acceleration of rates of Cu^I oxidation steps over those of Cu^{II} reduction steps at higher O_2 pressures. Furthermore, low-temperature SCR reaction rates (per 1000 Å^3, 473 K) measured at 1 kPa O_2 on Cu-CHA zeolites (Fig. 4.1a, red triangles) are systematically lower than those measured at 10 kPa O_2, and the fraction of Cu^I present *in operando* is systematically higher at 1 kPa O_2 (Fig. 4.1b, red triangles; >0.85 among all samples) than at 10 kPa O_2, in the entire range of ρ_{Cu} on the Cu-CHA zeolites studied here, consistent with the preferential deceleration of rates of Cu^I oxidation steps compared to those of Cu^{II} reduction steps at lower O_2 pressures. SCR rates on Cu-CHA show a quadratic dependence on Cu density in a much wider composition range (ρ_{Cu} = 0.07-0.42 Cu per 1000 Å^3) at dilute O_2 pressures (1 kPa O_2) than at those typical of "standard" SCR conditions (10 kPa O_2) or excess O_2 pressures (70 kPa O_2).

These data provide yet another reminder that the rate-limiting nature of Cu^I oxidation steps depend both on sample composition and reaction conditions, given the different kinetic and site requirements of dual-site Cu^i oxidation and single-site Cu^{II} reduction processes in the SCR redox cycle. Cu^I oxidation steps become increasingly kinetically relevant both as Cu ion density becomes more dilute, and as O_2 pressure decreases. Yet, even at dilute but fixed (1 kPa) O_2 pressure, SCR rates are not solely limited by the rates of Cu^I oxidation steps, evident by the finite but small Cu^{II} fraction quantified by *in operando* XANES that also increases systematically with Cu spatial density (Fig. 4.1b). Thus, we next investigate the steady-state catalytic function of Cu-CHA zeolites under widely varying O_2 pressures, in order to isolate limiting kinetic behavior that allows decoupling the influence of Cu^I oxidation and Cu^{II} reduction on SCR redox cycles.

4.4.2   Dependence on SCR turnover rates on dioxygen pressure

The SCR turnover rate (per Cu) on a representative Cu-CHA sample (Cu-CHA-15-0.23) as a function of dioxygen pressure is shown in Figure 4.2a, along with the corresponding fraction of Cu^I present at steady state measured using *in operando* XAS spectroscopy. Apparent reaction orders in dioxygen approach unity at low dioxygen pressures (<5 kPa), decrease systematically with increasing dioxygen pressure, and approach zero at high dioxygen pressures (>50 kPa). SCR turnover rates (per Cu) show a Langmuirian dependence on dioxygen pressure, according to the following empirical rate expression:

$$\frac{-r_{NO}}{[Cu]} = \frac{k_1 k_0 [O_2]}{k_0 + k_1 [O_2]} \qquad \textbf{(4.0)}$$

where k_1 is the apparent rate constant in the limiting kinetic regime that is first-order in dioxygen pressure, and k_0 is the apparent rate constant in the limiting kinetic regime that is zero-order in dioxygen pressure. The corresponding fraction of Cu^I present at steady-state, measured *in operando* by XAS, is shown on the secondary axis in Figure 4.2a. In the first-order dioxygen pressure limit, Cu is present solely as Cu^I, consistent with dual-site oxidation of $Cu^I(NH_3)_2$ with dioxygen becoming the sole kinetically relevant process in this regime. The steady-state fraction of Cu^I decreases systematically with increasing dioxygen pressure, and asymptotically approaches a non-zero value in the zero-order dioxygen pressure limit. In this limit, Cu^{II} reduction processes, which are insensitive to the presence of dioxygen, are expected to be the sole kinetically relevant step. The presence of a finite fraction of Cu^I in the zero-order dioxygen pressure limit can be rationalized from our prior work [13], in which exposure of Cu-CHA samples in their $Cu^I(NH_3)_2$ states to dioxygen resulted in oxidation of only a fraction of the $Cu^I(NH_3)_2$ species present. The remaining fraction of $Cu^I(NH_3)_2$ complexes remained unoxidized either because they were physically or functionally isolated from other $Cu^I(NH_3)_2$ complexes, and thus unable to oxidize because of the dual-site requirement of this elementary step; in turn, such stranded $Cu^I(NH_3)_2$ complexes would nominally be unable to contribute to steady-state SCR catalytic turnover.
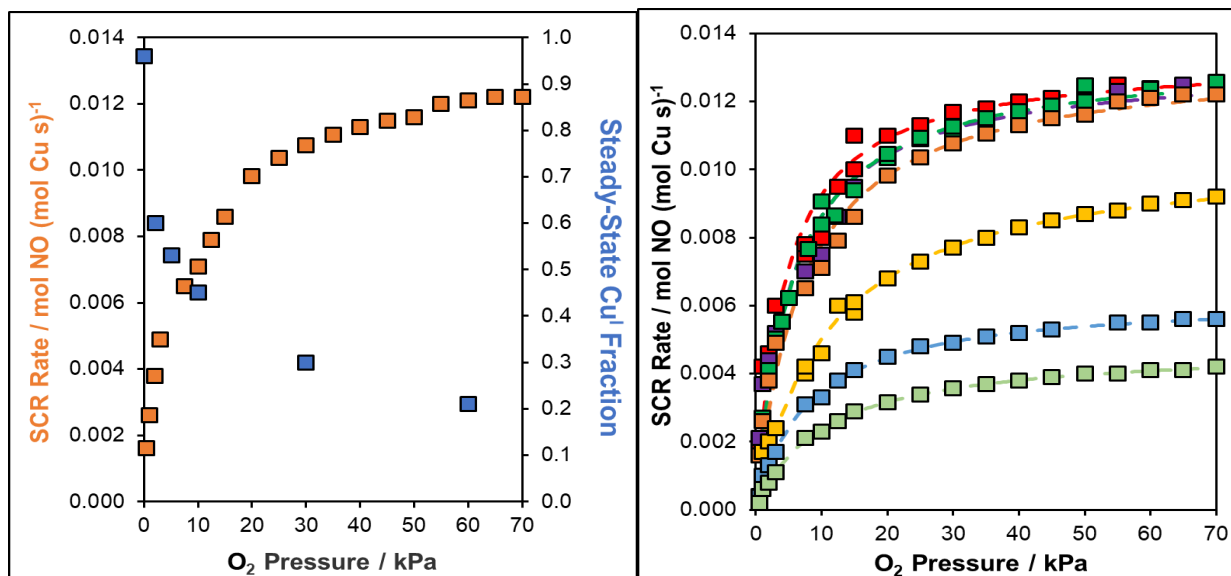
Figure 4.2 Left (a): Steady-state SCR rate (per mol Cu) and Cu^I coverage as a function of O_2 pressure on Cu-CHA-15-0.23 sample. Right (b): Steady-state SCR rate (per mol Cu) as a function of O_2 pressure on a series of model Cu-CHA-15-Y samples (light green: Cu-CHA-15-0.07, blue: Cu-CHA-15-0.11, yellow: Cu-CHA-15-0.16, orange: Cu-CHA-15-0.42, purple: Cu-CHA-15-0.34, dark green: Cu-CHA-15-0.30, red: Cu-CHA-15-0.23), along with best-fit regressions of Eq. (4.0) to the data.

SCR rates (per Cu) as a function of dioxygen pressure on a series of model Cu-CHA samples with increasing volumetric Cu density (Table 4.1) are shown in Figure 4.2b. For all Cu-CHA samples, SCR rates show a Langmuirian dependence on dioxygen pressure, according to Eq. (4.0). Apparent reaction orders and activation energies measured at fixed dioxygen pressure in the low (1 kPa O_2) and high (70 kPa O_2) dioxygen pressure limits are shown in Table 4.2. Measured kinetic parameters are consistent with previously reported values [6,13,20] that dual-site Cu^I oxidation being the step that predominantly limits rates at 1 kPa O_2 and Cu^{II} reduction being step that predominantly limits rates at 70 kPa O_2. At low ρ_{Cu} (<0.25 Cu per 1000 A^3), SCR rates in both the first-order and zero-order kinetic regimes increase systematically with Cu volumetric density. Above this threshold ρ_{Cu} value (>0.25 Cu per 1000 A^3), SCR rates in both the first-order and zero-order kinetic regimes become invariant with Cu density. The similar values for apparent reaction orders and activation energies measured across the series of Cu-CHA samples of varying Cu ion density (Table 4.2) indicate that all samples operate in similar kinetic regimes in the low and high O_2 pressure limit, which are directly linked to Cu^I oxidation

and Cu^{II} reduction processes being steps that limit rates from *in operando* XAS spectra measured on Cu-CHA-15-0.23 (Fig. 4.2b).

Table 4.2 SCR kinetic parameters measured on Cu-CHA-X-Y samples at low (1 kPa O_2) and high (70 kPa O_2) dioxygen pressures.

Cu-CHA-X-Y	1 kPa O_2[a]				70 kPa O_2[a]			
	O_2 order[b]	NO order[b]	NH_3 order[b]	E_{app}[c] (kJ mol^{-1})	O_2 order[b]	NO order[b]	NH_3 order[b]	E_{app}[c] (kJ mol^{-1})
Cu-CHA-15-0.07	0.9	0.1	-0.6	43	0.2	0.7	-0.2	65
Cu-CHA-15-0.09	0.9	0.2	-0.5	45	0.1	0.8	-0.1	63
Cu-CHA-15-0.11	0.9	0.2	-0.5	44	0.0	0.8	-0.1	64
Cu-CHA-15-0.16	0.8	0.2	-0.5	48	0.2	0.8	-0.1	63
Cu-CHA-15-0.18	0.8	0.2	-0.5	42	0.1	0.8	-0.1	66
Cu-CHA-15-0.23	0.8	0.2	-0.5	50	0.0	0.8	-0.1	67
Cu-CHA-15-0.30	0.7	0.2	-0.4	50	0.0	0.9	-0.1	65
Cu-CHA-15-0.34	0.8	0.3	-0.4	52	0.0	0.9	0.0	65
Cu-CHA-15-0.42	0.7	0.3	-0.5	50	0.0	1.0	0.0	75

[a]Other reaction conditions: 0.03 kPa NO, 0.03 kPa NH_3, 7 kPa CO_2, 3 kPa H_2O and balance He at 473 K.
[b]Errors are $\pm$ 0.1.
[c]Errors are $\pm$ 7 kJ/mol.

4.4.3   A simplified kinetic model to identify the factors that influence apparent rate constants

A complete set of elementary steps that describe the low temperature SCR mechanism is currently unknown, specifically those steps involving reactions of binuclear NH_3-solvated Cu^{II}-oxo complexes with NO and NH_3 to form mononuclear NH_3-solvated Cu^{II} complexes [13]. Thus, here we derive a simplified kinetic model for the SCR reaction rate based on lumped reaction steps that describe Cu^I oxidation and Cu^{II} reduction processes (Scheme 1), in order to determine how macroscopic properties (e.g., Cu spatial density, reactant pressures, temperatures) influence apparent first-order and zero-order rate constants. In the lumped Cu^I oxidation process, two mononuclear Cu^I species react with O_2 to form a binuclear Cu^{II}-oxo complex ($Cu_2O_2^{2+}$), at a rate given by r_o. In the lumped Cu^{II} reduction process, a binuclear Cu^{II}-oxo complex reacts with four equivalents of NO and NH_3 to produce four and six equivalents of N_2 and H_2O, respectively, and two mononuclear Cu^I species at a rate given by r_r.
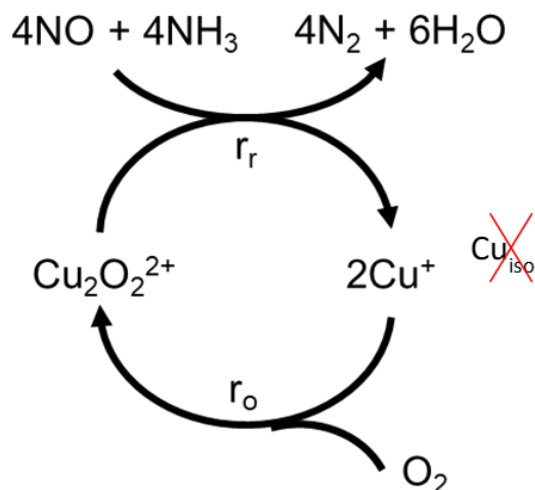
Scheme 4.1 Simplified scheme for low-temperature SCR mechanism in which Cu^I oxidation and Cu^{II} reduction are modeled as lumped processes. Solvating ammonia ligands on active Cu intermediates not shown for simplicity.

On a given Cu-zeolite sample prepared to contain nominally isolated ion-exchanged Cu sites, a site balance describing the Cu inventory during steady state catalysis can be written as:

$$[Cu_{tot}] = [Cu^+] + 2[Cu_2O_2^{2+}] + [Cu_{iso}] \tag{4.1}$$

where $[Cu_{tot}]$ describes the total Cu concentration (per unit volume catalyst), $[Cu^+]$ and $[Cu_2O_2^{2+}]$ the concentrations of mononuclear Cu^I and binuclear Cu^{II} sites that participate in the SCR cycle, and $[Cu_{iso}]$ is the concentration of Cu atoms that are physically or functionally isolated so as not to participate in the SCR cycle. A given Cu site can be physically isolated if there are no other Cu sites located within diffusion distances, which would preclude the formation of binuclear intermediates ($Cu_2O_2^{2+}$) altogether, or functionally isolated if an even number of Cu sites are located within diffusion distances, in which case not all Cu sites contained within this volume will be able to form binuclear intermediates during steady-state turnover of the SCR cycle [13].

From this Cu site balance, ρ can be defined as concentration of Cu sites that are able to form binuclear $Cu_2O_2^{2+}$ intermediates during steady-state turnover of the SCR cycle:

$$\rho = [Cu^+] + 2[Cu_2O_2^{2+}] \tag{4.2}$$

Eq. (4.2) can be rearranged to obtain an expression for the concentrations of mononuclear Cu^+ and binuclear $Cu_2O_2^{2+}$ intermediates and present within the pool of reactive Cu intermediates:

$$[Cu^+] = \rho - 2[Cu_2O_2^{2+}] \tag{4.3}$$

$$[Cu_2O_2^{2+}] = \frac{1}{2}\rho - \frac{1}{2}[Cu^+] \qquad (4.4)$$

Since ρ accounts for the total number of Cu sites that participate in the SCR cycle, and the fraction of Cu^+ sites that are already located within diffusion distances of each other so as to be able to form binuclear Cu intermediates, we can define γ as the concentration of possible binuclear complexes that can form from Cu^+ intermediates:

$$\gamma = \frac{1}{2}[Cu^+] \qquad (4.5)$$

Substitution of Eq. (4.3) into Eq. (4.5) yields:

$$\gamma = \frac{1}{2}\rho - [Cu_2O_2^{2+}] \qquad (4.6)$$

Assuming constant temperature and NO and NH_3 partial pressures, the following equations describe the rates of the lumped reduction and oxidation steps, assuming the simplest case in which rates of these lumped steps are proportional to the concentrations of their respective reactive intermediates:

$$r_{red} = k_{red}[Cu_2O_2^{2+}] \qquad (4.7)$$

$$r_{ox} = k_{ox}[O_2]\gamma \qquad (4.8)$$

Substitution of Eq. (4.6) into Eq. (4.8) yields:

$$r_o = k_{ox}[O_2]\left(\frac{1}{2}\rho - [Cu_2O_2^{2+}]\right) \qquad (4.9)$$

At steady-state, rates of the lumped oxidation and reduction processes are equal, and Eqs. (4.7) and (4.9) can be combined to write:

$$k_{red}[Cu_2O_2^{2+}] = k_{ox}[O_2]\left(\frac{1}{2}\rho - [Cu_2O_2^{2+}]\right) \qquad (4.10)$$

Eq. (4.10) can be rearranged to obtain an expression for the steady-state concentration of binuclear $Cu_2O_2^{2+}$ intermediates:

$$[Cu_2O_2^{2+}] = \frac{\rho k_{ox}[O_2]}{2(k_{red}+k_{ox}[O_2])} \qquad (4.11)$$

In the lumped reduction step (Scheme 4.1), 4 molecules of NO are consumed per cycle, so the steady-state rate of NO consumption (per volume) can be written as:

$$-r_{NO} = 4r_r = \frac{2\rho k_{red}k_{ox}[O_2]}{k_{red}+k_{ox}[O_2]} \qquad (4.12)$$

This rate equation (Eq. (4.12)) in a rate normalized by total Cu content by dividing both sides of the equation by $[Cu_{tot}]$ to yield:

$$\frac{-r_{NO}}{[Cu_{tot}]} = \frac{2\rho' k_{red}k_{ox}[O_2]}{k_{red}+k_{ox}[O_2]} \qquad (4.13)$$

where ρ' represents the fraction of total Cu that is contained within the active pool of Cu sites (i.e., those able to form binuclear intermediates):

$$\rho' = \frac{\rho}{[Cu_{tot}]} \tag{4.14}$$

Comparing Eq. (4.14) to the Langmuirian rate equation (Eq. (4.1)) that empirically describes experimentally measured NO consumption rates (473 K, per mol Cu) with varying O_2 pressure (0-70 kPa) yields the following expressions for the apparent first-order and zero-order rate constants:

$$k_1 = 2\rho'k_{ox} \tag{4.15}$$

$$k_0 = 2\rho'k_{red} \tag{4.16}$$

From this simplified kinetic model, the apparent first-order (Eq. (4.15)) and zero-order (Eq. (4.16)) rate constants measured on a given Cu-CHA sample should depend on the fraction of total Cu sites that are contained within its active pool of Cu sites (ρ'), which are those able to participate in SCR turnovers under the reaction conditions studied, and on its respective (reactivity ensemble-averaged) rate constants for Cu^I oxidation and Cu^{II} reduction.

4.4.4 Dependence of apparent first-order and zero-order rate constants on Cu spatial density

Values of the apparent first-order (k_1) and zero-order (k_0) rate constants, determined by regressing the data in Figure 4.2b to Eq. (4.1), are listed for each sample in Table 4.3. The dependence of k_0 on Cu spatial density in Cu-CHA is shown in Figure 4.3a. At low ρ_{Cu} values (<0.2 Cu per 1000 A^3), k_0 increases linearly with Cu density, while at high ρ_{Cu} values (>0.3 Cu per 1000 A^3), k_0 becomes independent of Cu density. The intrinsic rate constant for reduction (k_{red}) of NH_3-solvated Cu^{II} complexes in flowing NO and NH_3 (473 K) was estimated from a series of transient XAS experiments performed on Cu-CHA samples of varying Cu spatial density (details in chapter 6).

Table 4.3 Apparent first-order (k_1) and zero-order (k_0) rate constants (obtained from steady state kinetics), along with and intrinsic oxidation (k_{ox}) and reduction (k_{red}) rate constants (obtained from transient kinetics under XAS) on a series of Cu-CHA-15-Y samples used in this study.

Cu-CHA-X-Y	$Cu^I \rightarrow Cu^{II}$ oxidation-limited regime			$Cu^{II} \rightarrow Cu^I$ reduction-limited regime	
	Apparent first-order rate constant (k_1) (10^{-3} mol NO mol Cu^{-1} s^{-1})	Expected first-order rate (10^{-3} mol NO mol Cu^{-1} s^{-1})	Intrinsic oxidation rate constant (k_{ox}) (10^{-3} s^{-1})	Apparent zero-order rate constant (k_0) (10^{-3} mol NO mol Cu^{-1} s^{-1})	Intrinsic reduction rate constant (k_{red}) (10^{-3} s^{-1})
Cu-CHA-15-0.07	0.47	4.70	13.00	4.77	--
Cu-CHA-15-0.09	0.78	7.80	10.00	6.23	19.00
Cu-CHA-15-0.11	--	--	--	--	--
Cu-CHA-15-0.16	0.95	9.50	25.00	10.58	--
Cu-CHA-15-0.18	--	--	--	--	--
Cu-CHA-15-0.23	1.88	18.80	30.00	13.29	21.00
Cu-CHA-15-0.30	2.45	24.50	47.00	13.30	--
Cu-CHA-15-0.34	2.52	25.20	45.00	13.12	--
Cu-CHA-15-0.42	3.04	30.40	43.00	13.29	20.50

--: not measured

For all Cu-CHA samples, the transient Cu^{II} reduction rate showed a first-order dependence on Cu concentration (Figure 4.3b), and the first-order rate constant for this reduction (0.019, 0.021 and 0.020 mol NO mol Cu^{-1} s^{-1}) were independent of Cu spatial density, consistent with the single-site mechanism of NO and NH$_3$-assisted co-reduction of mononuclear NH$_3$-solvated Cu^{II} sites [13]. Values of k_{red} are plotted on the secondary ordinate of Figure 4.3a and are independent of Cu spatial density, with a horizontal dashed line shown at the average value of k_{red} measured for all of the samples. Given that k_{red} is independent of Cu spatial density, the dependence of k_0 on Cu spatial density reflects the number of Cu sites that are turning over during steady-state SCR catalysis, as the term k_0 contains the fraction of total Cu that is contained within the active pool of Cu sites (ρ') (i.e., equation 4.16). Thus, analysis of apparent and intrinsic reduction rate constants enables more accurately quantifying the influence of Cu ion spatial density in Cu-CHA on the kinetics of reduction processes in the SCR redox cycle, and can be extended to quantitatively determine how changes to catalyst properties, including zeolite topology and framework Al density and arrangement, influence the fraction of active Cu ion sites and the rate constants of reduction steps in the SCR cycle.
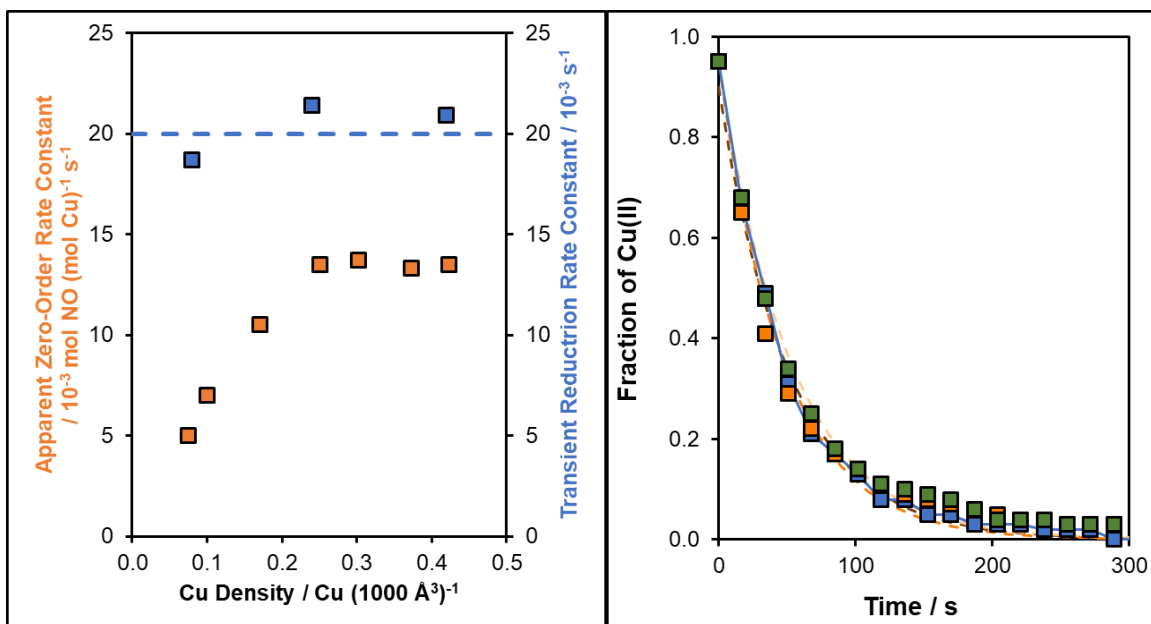
Figure 4.3 Left (a): Apparent zero-order rate constants (k_0) and intrinsic reduction rate constants (k_{red}) obtained from transient XAS experiments on varying Cu spatial density Cu-CHA samples. Right (b): Temporal evolution of the XANES-measured Cu^{II} fraction during transient reduction of NH_3-solvated Cu^{II} complexes in flowing NO and NH_3 (473 K) on Cu-CHA-15-0.09 (blue), Cu-CHA-15-0.23 (green) and Cu-CHA-15-0.42 (orange), along with the best least-squares first-order fit (w.r.t. Cu^{II}).

The dependence of first-order SCR rate estimated as the product of first-order rate constant (k_1) and [O_2], on Cu spatial density in Cu-CHA is shown in Figure 4.4a. In the full range of ρ_{Cu} values studied (0.08-0.44 Cu per 1000 A^3), k_1 increases linearly with Cu density, consistent with the second-order dependence on Cu concentration of O_2-assisted oxidation of NH_3-solvated Cu^I sites [13]. The intrinsic rate constant for oxidation (k_{ox}) of NH_3-solvated Cu^I complexes in flowing O_2 (473 K) was estimated from a series of transient XAS experiments performed on Cu-CHA samples of varying Cu spatial density (details in chapter 6). For all Cu-CHA samples, the transient Cu^I oxidation rate showed a pseudo-second-order dependence on Cu concentration, as reported previously [13], and the pseudo-second-order rate constant (k_{ox}) for this oxidation process (estimated as initial rate from $Cu^I(NH_3)_2$ oxidation transient with O_2) increased systematically with increasing Cu spatial density (Table 4.3). Values of k_{ox} are plotted on the secondary ordinate of Figure 4.4b and show a similar dependence as k_1 values (estimated at 10 kPa O_2), reinforcing that the SCR kinetics is exclusively limited by dual site $Cu^I \rightarrow Cu^{II}$ oxidation. Similar dependence of both the k_1 and k_{ox} on Cu spatial density suggests that number of Cu sites that are oxidizable and turning over during the steady-state SCR catalysis is constant

and invariable of Cu spatial density. Thus, analysis of apparent and intrinsic oxidation rate constants enables more accurately quantifying the influence of Cu ion spatial density in Cu-CHA on the kinetics of oxidation processes in the SCR redox cycle, and can be extended to quantitatively determine how changes to catalyst properties, including zeolite topology and framework Al density and arrangement, influence the fraction of active Cu ion sites and the rate constants of oxidation steps in the SCR cycle.
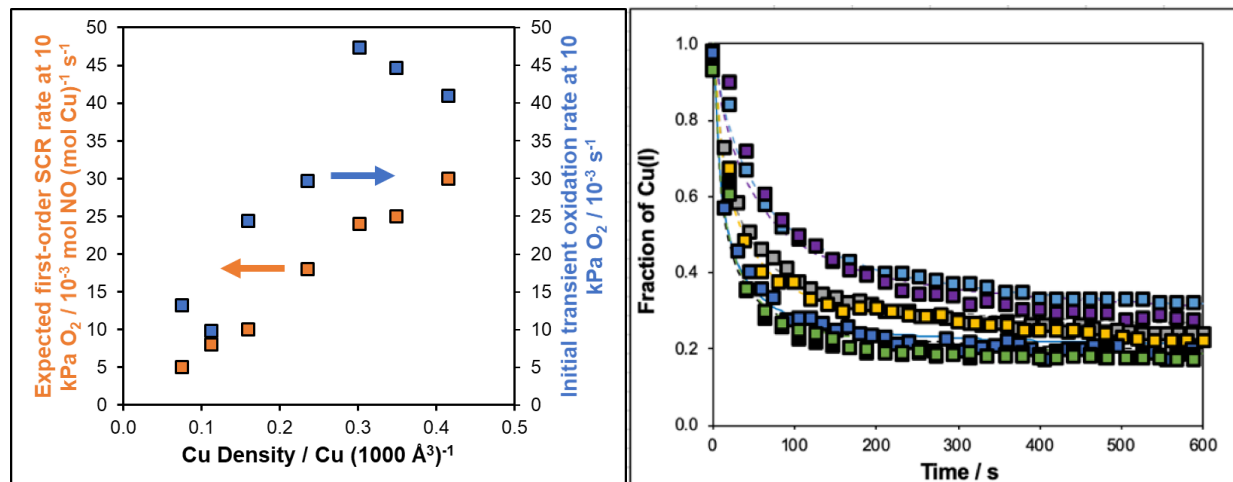
Figure 4.4 Left (a): Apparent first-order SCR rate (estimated from first-order rate constants: k_1) and transient Cu^I oxidation rate (estimated from intrinsic oxidation rate constants: k_{ox}) obtained from transient XAS experiments on varying Cu density Cu-CHA samples. Right (b): Temporal evolution of the XANES-measured Cu^I fraction during transient oxidation of NH_3-solvated Cu^I complexes with O_2 (473 K) on Cu-CHA-15-0.09 (light blue), Cu-CHA-15-0.11 (purple), Cu-CHA-15-0.16 (grey), Cu-CHA-15-0.23 (yellow), Cu-CHA-15-0.30 (dark blue), Cu-CHA-15-0.34 (green) and Cu-CHA-15-0.42 (black), along with the best least-squares second-order fit (w.r.t. Cu^I).

4.5   Conclusions

SCR reaction kinetics measured on a series of varying Cu spatial density Cu-CHA samples under typical gas conditions is representative of mixed kinetic regime, viz. $Cu^I \rightarrow Cu^{II}$ oxidation- and $Cu^{II} \rightarrow Cu^I$ reduction-limited regime, with increase in Cu spatial density resulting in increased kinetic relevance of $Cu^{II} \rightarrow Cu^I$ reduction. In order to measure the reaction kinetics exclusively in either $Cu^I \rightarrow Cu^{II}$ oxidation or $Cu^{II} \rightarrow Cu^I$ reduction-limited regime, Cu^{II} - Cu^I SCR redox cycle was perturbed by varying reactant dioxygen pressure. SCR rate (per mol Cu) vs. reactant dioxygen pressure follows a Langmuiran type behavior, where the SCR rate shows asymptotic behavior at low O_2 (O_2 order ~ 0.0, along with NO order ~ 1.0, NH_3 order ~ 0.0) and high O_2 (O_2 order ~ 1.0, along with NO order ~ 0.0, NH_3 order ~ -0.5). Low O_2 limit was found to be representative of $Cu^I \rightarrow Cu^{II}$ oxidation being the rate-limiting step, while high O_2 limit was found to be representative of $Cu^{II} \rightarrow Cu^I$ reduction being the rate-limiting step.

Apparent first-order and zero-order rate constants were from regression of rate data to an empirical model that describes the observed Langmuirian dependence on O_2 pressure, and are compared to a kinetic rate equation derived from a simplified mechanistic model for the SCR reaction., which are representative of Cu^I oxidation and Cu^{II} reduction-limited regime respectively. Furthermore, the intrinsic oxidation and reduction rate constants were obtained by measuring transient oxidation and reduction kinetics using XAS experiments. Analysis of apparent and intrinsic oxidation rate constants enables more accurately quantifying the influence of Cu ion spatial density in Cu-CHA on the kinetics of oxidation and reduction processes in the SCR redox cycle, and can be extended to quantitatively determine how changes to catalyst properties, including zeolite topology and framework Al density and arrangement, influence the fraction of active Cu ion sites and the rate constants of different elementary steps in the SCR cycle.

4.6   Methods

4.6.1   Synthesis and Characterization

4.6.1.1   Synthesis of H-CHA zeolites

Synthesis of H-SSZ-13 zeolites with Si/Al 15 was done as previously reported in the above chapters 2 and 3.

4.6.1.2   X-Ray diffraction of CHA zeolites

The CHA crystal framework was determined from powder X-ray diffraction (XRD) patterns collected as previously reported in the above chapters 2 and 3.

4.6.1.3   Adsorption isotherms to measure micropore volumes of CHA zeolites

Micropore volumes of CHA zeolites were determined from Ar adsorption isotherms measured as previously reported in the above chapters 2 and 3.

4.6.1.4   Aqueous-phase Copper Ion-Exchange of H-SSZ-13

Cu-SSZ-13 zeolites were prepared by aqueous-phase Cu ion-exchange as previously reported in the above chapters 2 and 3.

4.6.1.5   Elemental Analysis using Atomic Absorption Spectroscopy

Bulk elemental composition (Si, Al and Cu in H-CHA and Cu-CHA) was determined using atomic absorption spectroscopy (AAS) as previously reported in the above chapter 3.

4.6.1.6   Cu site characterization and quantification

Cu sites were characterized using Cu K-edge X-ray absorption near edge spectroscopy (XANES) and o UV-Visible spectroscopy as previously reported in the above chapters 2 and 3. Further enumeration of isolated Cu^{II} and $Cu^{II}OH$ sites on each Cu-CHA zeolite was determined after oxidative treatment (20% O_2, 773 K) by quantifying the number of residual protons that remained after Cu exchange, as previously reported in the above chapter 3.

4.6.2   X-ray Absorption Spectroscopy (XAS)

More generic details about *operando* and transient X-ray absorption spectroscopy have been illustrated in above chapter 3.

4.6.3   Differential Standard SCR Kinetics

Selective catalytic reduction (SCR) kinetics were measured using a bench-top tubular quartz reactor system described elsewhere [24]. All samples were sieved to a obtain particle sizes between 125-250 μm and a bed height of approximately 2.5 cm was obtained by dilution with

silica gel. NO conversions were kept below 20% for all steady-state kinetic measurements to ensure that the entire bed was exposed to approximately the same gas concentrations, using a reactant gas mixture of 300 ppm NO (3.5% NO/Ar, Praxair), 300 ppm NH_3 (3.0% NH_3/Ar, Praxair), 7% CO_2 (liquid, Indiana Oxygen), 1-70% O_2 (99.5%, Indiana Oxygen), 2.5% H_2O (deionized, 18.2 MΩ, introduced through saturator), and balance N_2 (99.999% UHP, Indiana Oxygen) at 473K and 1 atm. The total gas flow rate was maintained at 1.5 L min^{-1}. Outlet NO, NO_2, NH_3, CO_2, and H_2O concentrations were measured every 0.95s using on-board gas calibrations on an MKS MultigasTM 2030 gas-phase Fourier Transform Infrared (FTIR) spectrometer.

In the differential NO conversion limit, the gas concentrations and catalyst bed temperature can be assumed constant, allowing the differential rate of NO consumption to be calculated using Equation (1):

$$-r_{NO} = \frac{(y_{NO,in} - y_{NO,out})}{1000000} \frac{P\dot{V}_{total}}{RT} \qquad (4.17)$$

where y is the volume fraction of NO in ppm before and after the catalyst bedin ppm before and after the catalyst bed, $\dot{V}_{total}$ is the total flow rate, P is 1 atm, T is ambient temperature, and R is the gas constant. The experimental data are fitted to a power law rate expression (Equation (2)) where k_{app} (Equation (3)) is the apparent rate constant and $\alpha, \beta, \gamma, \delta$, and ϵ are the apparent reaction orders with respect to concentrations of NO, NH_3, O_2, H_2O, and CO_2, respectively.

$$-r_{NO} = k_{app} C_{NO}^{\alpha} C_{NH_3}^{\beta} C_{O_2}^{\gamma} C_{H_2O}^{\delta} C_{CO_2}^{\epsilon} \qquad (4.18)$$

$$k_{app} = A_0 \exp\left(-\frac{E_{a,app}}{RT}\right) \qquad (4.19)$$

All reported rates are free of external diffusion limitations (invariant of space velocity) and internal diffusion limitations, as seen from turnover rates being independent of crystallite sizes ranging from 0.5 to 2.5 microns [6,24,25]. The low values for δ and ε shown our previous work [26], show that product inhibition is negligible, validating the use of equation (1).

4.7 References

[1]   C. Paolucci, J.R. Di Iorio, F.. Ribeiro, R. Gounder, W.F. Schneider, Catalysis Science of NOx Selective Catalytic Reduction with Ammonia over Cu-SSZ-13 and Cu-SAPO-34, Adv. Catal. 59 (2016). doi:10.1016/bs.acat.2016.10.002.

[2]   F. Gao, D. Mei, Y. Wang, J. Szanyi, C.H.F. Peden, F. Gao, et al., Selective Catalytic Reduction over Cu / SSZ-13 : Linking Homo- and Heterogeneous Catalysis Selective

Catalytic Reduction over Cu / SSZ-13 : Linking Homo- and Heterogeneous Catalysis, (2017). doi:10.1021/jacs.7b01128.

[3]   K. Kamasamudram, N. Currier, T. Szailer, A. Yezerets, Why Cu- and Fe-zeolite SCR catalysts behave differently at low temperatures, SAE Int. J. Fuels Lubr. (2010). doi:10.4271/2010-01-1182.

[4]   K.A. Lomachenko, E. Borfecchia, C. Negri, G. Berlier, C. Lamberti, P. Beato, et al., The Cu-CHA deNO$_x$ catalyst in action: temperature-dependent NH$_3$-SCR monitored by *operando* X-ray absorption and emission spectroscopies, J. Am. Chem. Soc. (2016) jacs.6b06809. doi:10.1021/jacs.6b06809.

[5]   A.R. Fahami, T. Günter, D.E. Doronkin, M. Casapu, D. Zengel, T.H. Vuong, et al., The dynamic nature of Cu sites in Cu-SSZ-13 and the origin of the seagull NOx conversion profile during NH3-SCR, React. Chem. Eng. (2019). doi:10.1039/C8RE00290H.

[6]   C. Paolucci, A.A. Parekh, I. Khurana, J.R. Di Iorio, J. Albarracin, A. Shih, et al., Catalysis in a Cage : Condition-Dependent Speciation and Dynamics of Exchanged Cu Cations in SSZ-13 Zeolites, J. Am. Chem. Soc. (2016) 1–63. doi:10.1021/jacs.6b02651.

[7]   E. Borfecchia, K. a. Lomachenko, F. Giordanino, H. Falsig, P. Beato, a. V. Soldatov, et al., Revisiting the nature of Cu sites in the activated Cu-SSZ-13 catalyst for SCR reaction, Chem. Sci. 6 (2015) 548–563. doi:10.1039/C4SC02907K.

[8]   F. Giordanino, P.N.R. Vennestrøm, L.F. Lundegaard, F.N. Stappen, S. Mossin, P. Beato, et al., Characterization of Cu-exchanged SSZ-13: a comparative FTIR, UV-Vis, and EPR study with Cu-ZSM-5 and Cu-β with similar Si/Al and Cu/Al ratios., Dalt. Trans. 42 (2013) 12741–61. doi:10.1039/c3dt50732g.

[9]   T. Günter, D.E. Doronkin, A. Boubnov, H.W.P. Carvalho, M. Casapu, J.D. Grunwaldt, The SCR of NOx with NH3 Examined by Novel X-ray Emission and X-ray Absorption Methods, Top. Catal. (2016). doi:10.1007/s11244-016-0561-7.

[10]   T.V.W. Janssens, H. Falsig, L.F. Lundegaard, P.N.R. Vennestrøm, S. Rasmussen, P.G. Moses, et al., A consistent reaction scheme for the selective catalytic reduction of nitrogen oxides with ammonia, ACS Catal. (2015) 150319102200004. doi:10.1021/cs501673g.

[11]   J. Hun Kwak, H. Zhu, J.H. Lee, C.H.F. Peden, J. Szanyi, Two different cationic positions in Cu-SSZ-13, Chem. Commun. 48 (2012) 4758. doi:10.1039/c2cc31184d.

[12]   C. Paolucci, A.A. Verma, S.A. Bates, V.F. Kispersky, J.T. Miller, R. Gounder, et al., Isolation of the Copper Redox Steps in the Standard Selective Catalytic Reduction on Cu-SSZ-13 **, (2014) 12022–12027. doi:10.1002/ange.201407030.

[13]   C. Paolucci, I. Khurana, A.A. Parekh, S. Li, A.J. Shih, H. Li, et al., Dynamic multinuclear sites formed by mobilized copper ions NO$_x$ selective catalytic reduction, Science 357 (2017) 898-903.

[14]   J.C. Holtz, M.A. Elliott, The Significance of Diesel-Exhaust-Gas Analysis, Trans. ASME. 63 (1941).

[15]   M. Schwidder, S. Heikens, A. De Toni, S. Geisler, M. Berndt, A. Brückner, et al., The role of NO2 in the selective catalytic reduction of nitrogen oxides over Fe-ZSM-5 catalysts: Active sites for the conversion of NO and of NO/NO2 mixtures, J. Catal. 259 (2008) 96–103. doi:10.1016/j.jcat.2008.07.014.

[16]   M. Koebel, M. Elsener, M. Kleemann, Urea-SCR: a promising technique to reduce NOx emissions from automotive diesel engines, Catal. Today. (2000). doi:10.1016/S0920-5861(00)00299-6.

[17]   G. Tuenter, W.F. van Leeuwen, L.J.M. Snepvangers, Kinetics and Mechanism of the NOx

Reduction with NH3 on V2O5-WO3-TiO2 Catalyst, Ind. Eng. Chem. Prod. Res. Dev. (1986). doi:10.1021/i300024a607.

[18] M. Devadas, O. Kröcher, M. Elsener, A. Wokaun, N. Söger, M. Pfeifer, et al., Influence of NO2 on the selective catalytic reduction of NO with ammonia over Fe-ZSM5, Appl. Catal. B Environ. (2006). doi:10.1016/j.apcatb.2006.04.015.

[19] A. Grossale, I. Nova, E. Tronconi, D. Chatterjee, M. Weibel, The chemistry of the NO/NO2-NH3 "fast" SCR reaction over Fe-ZSM5 investigated by transient reaction analysis, J. Catal. 256 (2008) 312–322. doi:10.1016/j.jcat.2008.03.027.

[20] F. Gao, E.D. Walter, M. Kollar, Y. Wang, J. Szanyi, C.H.F. Peden, Understanding ammonia selective catalytic reduction kinetics over Cu/SSZ-13 from motion of the Cu ions, J. Catal. 319 (2014) 1–14. doi:10.1016/j.jcat.2014.08.010.

[21] F. Gao, N.M. Washton, Y. Wang, M. Kollár, J. Szanyi, C.H.F. Peden, Effects of Si/Al ratio on Cu/SSZ-13 NH3-SCR catalysts: Implications for the active Cu species and the roles of Brønsted acidity, J. Catal. 331 (2015) 25–38. doi:10.1016/j.jcat.2015.08.004.

[22] V.F. Kispersky, a. J. Kropf, F.H. Ribeiro, J.T. Miller, Low absorption vitreous carbon reactors for operando XAS: a case study on Cu/Zeolites for selective catalytic reduction of NOx by NH3, Phys. Chem. Chem. Phys. 14 (2012) 2229. doi:10.1039/c1cp22992c.

[23] J.R. Di Iorio, S. a. Bates, A. a. Verma, W.N. Delgass, F.H. Ribeiro, J.T. Miller, et al., The Dynamic Nature of Brønsted Acid Sites in Cu–Zeolites During NOx Selective Catalytic Reduction: Quantification by Gas-Phase Ammonia Titration, Top. Catal. (2015) 424–434. doi:10.1007/s11244-015-0387-8.

[24] S. A. Bates, A. a. Verma, C. Paolucci, A. a. Parekh, T. Anggara, A. Yezerets, et al., Identification of the active Cu site in standard selective catalytic reduction with ammonia on Cu-SSZ-13, J. Catal. 312 (2014) 87–97. doi:10.1016/j.jcat.2014.01.004.

[25] R.M. Koros, E.J. Nowak, A diagnostic test of the kinetic regime in a packed bed reactor, Chem. Eng. Sci. 22 (1967) 470. doi:10.1016/0009-2509(67)80134-9.

[26] A.J. Shih, I. Khurana, H. Li, J. González, A. Kumar, C. Paolucci, et al., Spectroscopic and kinetic responses of Cu-SSZ-13 to SO 2 exposure and implications for NO x selective catalytic reduction, Appl. Catal. A Gen. (2019). doi:10.1016/j.apcata.2019.01.024.

5. EXPLORING THE EFFECTS OF NH₃ INHIBITION ON STANDARD SCR KINETICS OVER CU-SSZ-13

5.1 Abstract

Herein, we suggest that NH$_3$ inhibition is related to the Cu^I → Cu^{II} oxidation step of the low temperature (473 K) standard SCR reaction mechanism and inhibits rates above a certain partial pressure or NH$_3$/NO ratio. Understanding the effects of changing gas composition on SCR rate is crucial to maximize the NO$_x$ conversion, as the catalyst is transiently exposed to fluctuations in gas concentrations during vehicle application. We use kinetic and spectroscopic characterization to study the range of NH$_3$ concentration and Cu spatial density in which NH$_3$ inhibition is observed. Furthermore, we employ transient spectroscopic measurements to gain insight into the origin of NH$_3$ inhibition effect.

5.2 Introduction

Overall SCR of NO$_x$ with ammonia post-diesel engine exhaust is usually assumed as stoichiometric consumption of NO and NH$_3$ in presence of oxygen to product nitrogen and water (standard SCR as shown below), as diesel exhaust NO$_x$ usually comprises of 90% NO[1,2].

$$4NO + 4NH_3 + O_2 \rightarrow 4N_2 + 6H_2O \tag{5.1}$$

In presence of NO₂, equimolar consumption of NO and NO₂ in presence of NH$_3$ also becomes important, as this has been suggested to occur much faster than standard SCR (fast SCR as shown below)[3–6].

$$NO + NO_2 + 2NH_3 \rightarrow 2N_2 + 3H_2O \tag{5.2}$$

Also, there could be other side reactions, like NH$_3$ oxidation at high temperatures as follows[2,3]:

$$4NH_3 + 3O_2 \rightarrow 2N_2 + 6H_2O \tag{5.3}$$

$$4NH_3 + 5O_2 \rightarrow 4NO + 6H_2O \tag{5.4}$$

Relative relevance of aforementioned reactions would depend on gas composition as well as temperature. Additionally, transient conditions during vehicle applications further results in more fluctuations in gas compositions and temperatures[7]. This necessitates investigation of standard SCR rate at varying gas compositions of NO, NH_3 and O_2 in order achieve highest NO_x conversions and avoid NH_3 slip[8]. Effect of changing NO and O_2 concertation on standard SCR rate has been reported in our previous study as apparent reaction orders with respect to NO (200-600 ppm) and O_2 (5-20%) respectively[9–11]. It was seen that apparent reaction order with respect to O_2 changes from 0.3 (with NO order ~ 0.9) to 0.8 (with NO order ~ 0.2) with decrease in Cu spatial density, representative of increase in kinetic relevance of $Cu^I \rightarrow Cu^{II}$ oxidation (involves O_2) relative to $Cu^{II} \rightarrow Cu^I$ reduction (involves NO)[11]. However, variations in NH_3 reaction order and the origin of observed NH_3 inhibition (negative reaction order) was not well understood.

Moreover, NH_3 is one of the reactants in the SCR gas mixture which binds most favorably on Cu sites in Cu-SSZ-13 resulting in Cu sites to be predominantly covered with NH_3 during steady state catalysis[10,12,13]. Therefore, optimum inlet NH_3 concentration would be the key to potentially help minimize excess NH_3 inhibiting SCR reaction rate and avoid NH_3 slip. It has previously indicated that NH_3 inhibits the rate-limiting $Cu^I \rightarrow Cu^{II}$ oxidation step, as the transient monitoring of Cu oxidation state (XAS) and NO consumption showed that upon NH_3 cut-off from steady state SCR gas mixture, there was complete $Cu^I \rightarrow Cu^{II}$ oxidation (with $NO+O_2$) and short-lived increase of NO conversion[14]. However, as shown previously that low temperature $Cu^I \rightarrow Cu^{II}$ oxidation requires only O_2 activation and not $NO+O_2$[11], above results showing $NO+O_2$ oxidation of $Cu^I \rightarrow Cu^{II}$ cannot be directly translated into actual O_2 oxidation of $Cu^I \rightarrow Cu^{II}$ during SCR. Therefore, detailed understanding of the cause/origin and effect of observed NH_3 inhibition could help in optimization of NH_3 concentration to maximize NO_x conversion

In order to investigate various causes behind NH_3 inhibition, range of reactant NH_3 pressure and Cu loadings in Cu-SSZ-13 samples have been studied. To further probe the origin of this NH_3 inhibition in low temperature reaction mechanism, effects of presence of reactant NH_3 on kinetics of Cu^I oxidation (with O_2) step while monitoring the changes in Cu oxidation state (with XAS) have been monitored.

5.3   Results and Discussion

In order to study the causes and effects of NH_3 inhibition over a wide range of Cu spatial density, we use model Cu-SSZ-13 samples with varying spatial density of isolated Cu sites (present either as Cu^{II} at paired framework Al sites or as $[Cu^{II}OH]^+$ at isolated Al sites) reported in our previous study[11]. These samples are denoted Cu-CHA-X-Y, where X refers to Si/Al and Y refers to the mean Cu-Cu distance in Å, as estimated assuming a homogeneous distribution of Cu throughout the zeolite crystallite volume as done in Paolucci et al.[11]. Relevant structural and Cu site characterization of these model samples are provided in Table 5.1, including bulk elemental analysis, the number of isolated Cu^{II} and $[Cu^{II}OH]^+$ sites (per Al), the concentration of Cu ions per crystallite volume, and the mean Cu-Cu distance. Additional details, including bulk structural characterization (XRD patterns, micropore volume, SEM images) and Cu site characterization (*ex situ* X-ray absorption, UV-Visible spectroscopy) can be found in our previous study[11].

Table 5.1 Elemental analysis, number of isolated Cu^{II} and $[Cu^{II}OH]^+$ sites (per Al), concentration of Cu ions per crystallite volume, and the mean Cu-Cu distance in oxidized Cu^{II} forms of model Cu-CHA-X-Y samples (X=Si/Al, Y = mean Cu-Cu distance).

Si/Al	Cu/Al	Cu^{II}/Al^*	$Cu^{II}OH/Al^*$	Cu / $1000Å^3$	Mean Cu-Cu distance (Å)	Sample Cu-CHA-X-Y
15	0.03	0.03	0.00	0.03	40.7	Cu-CHA-15-41
15	0.08	0.08	0.00	0.07	29.4	Cu-CHA-15-29
15	0.10	0.09	0.35	0.09	27.2	Cu-CHA-15-27
15	0.12	0.09	0.03	0.11	25.6	Cu-CHA-15-26
15	0.17	0.09	0.08	0.16	22.8	Cu-CHA-15-23
15	0.19	0.09	0.10	0.18	22.0	Cu-CHA-15-22
15	0.25	0.09	0.16	0.23	20.1	Cu-CHA-15-20
15	0.37	0.09	0.28	0.35	17.6	Cu-CHA-15-18
15	0.44	0.09	0.35	0.41	16.6	Cu-CHA-15-17

*Determined from titration of residual H^+ sites by NH_3 and thermodynamic preferences for Cu^{II} and $[Cu^{II}OH]^+$ siting in the SI[11].

5.3.1 Observed NH₃ inhibition effect

Observed negative reaction order w.r.t NH₃ (150-400 ppm NH₃) in the low temperature (473 K) regime is referred to as NH₃ inhibition. Typical NH₃ reaction order plots shown in Figure 5.1. This NH₃ inhibition effect or negative reaction order is generally observed for low Cu loading samples (< 0.35 Cu /1000Å), as will be discussed in more details in the next section.
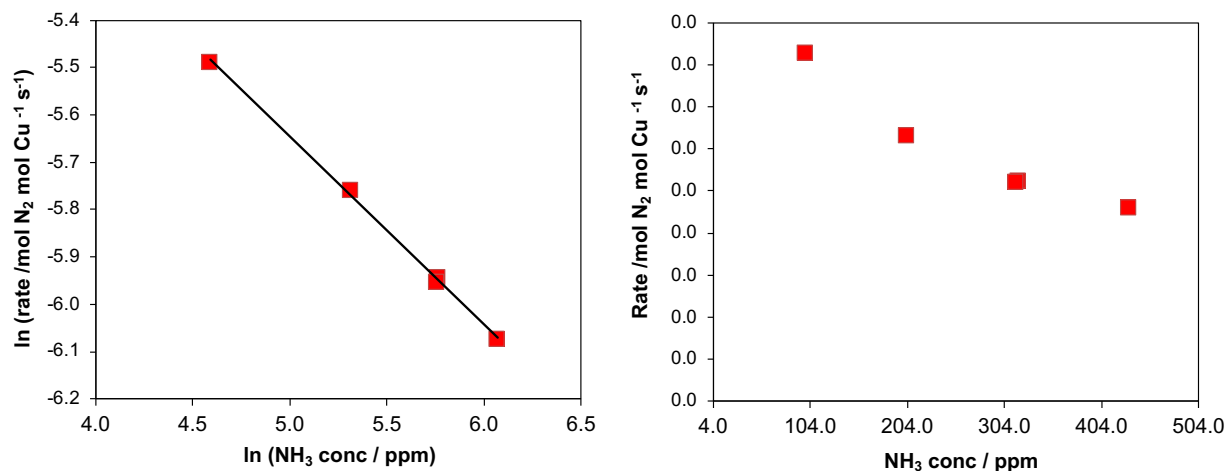
Figure 5.1 SCR rate plotted as a function of NH₃ pressure on model Cu-CHA-15-27 sample. Left: log-log plot, Right: normal plot. (300 ppm NO, 200-400 ppm NH₃, 10% O_2, 3% H_2O, 7% CO_2 in balance He at 473 K)

5.3.2 Effects of Cu spatial density on NH₃ inhibition

NH₃ inhibition was found to increase with decrease in Cu spatial density, as seen from more negative NH₃ reaction order with decrease in Cu spatial density in Table 5.2. We have shown previously that decrease in Cu spatial density also increases the kinetic relevance of Cu^I → Cu^{II} oxidation-half making it more rate-limiting. Therefore, it can be concluded that NH₃ inhibition likely originates from Cu^I → Cu^{II} oxidation-half of SCR Cu^{II} - Cu^I redox mechanism.

Table 5.2 Apparent reaction order w.r.t NH$_3$ on a series of model Cu-CHA-X-Y samples with Cu/Al varying from 0.03-0.44; arranged by increasing Cu/Al. (X=Si/Al, Y = Mean Cu-Cu distance in Å, rounded down)

Cu-CHA-X-Y	Cu /1000Å	SCR Rate (/10^{-3} mol NO/mol Cu/s)*	SCR Rate (/10^{-3} NO/1000Å^3/s) *	NH$_3$ order†
Cu-CHA-15-41	0.03	1.8	0.05	-0.5
Cu-CHA-15-29	0.07	2.3	0.17	-0.5
Cu-CHA-15-27	0.09	3.3	0.31	-0.5
Cu-CHA-15-26	0.11	4.4	0.51	-0.4
Cu-CHA-15-23	0.16	4.6	0.74	-0.3
Cu-CHA-15-20	0.24	7.1	1.67	-0.2
Cu-CHA-15-19	0.30	7.2	2.16	-0.1
Cu-CHA-15-18	0.35	7.3	2.54	0.0
Cu-CHA-15-17	0.40	7.8	3.08	0.0

*Conditions: 300 ppm NO, 300 ppm NH$_3$, 10% O$_2$, 7% CO$_2$, 3% H$_2$O and balance He at 473 K
†Errors in the apparent rate order are ± 0.1
‡Errors in the apparent activation energy (E$_{app}$) are ± 7 kJ/mol.

5.3.3   Origin of NH$_3$ inhibition effect: Cu^I → Cu^{II} oxidation

Two model Cu-CHA samples (Cu-CHA-15-17 and Cu-CHA-15-27) have been chosen to further probe the effect of NH$_3$ on Cu^I → Cu^{II} oxidation on different Cu spatial density samples. Two model Cu-CHA samples were first reduced in NO and NH$_3$ (300 ppm each, 473 K) to their monomeric Cu^I state (Cu^I(NH$_3$)$_2$) followed by sequential stoichiometric oxidation with O$_2$. Time-resolved XANES spectra were measured during Cu^I oxidation with O$_2$ on two model Cu-CHA samples, and the transient decay in Cu^I fraction with increasing time after O$_2$ exposure is shown in Figure 5.2. Each sample showed only partial oxidation of Cu^I from the NH$_3$-solvated state (Cu^I(NH$_3$)$_2$) to give NH$_3$-solvated Cu^{II}-dimer complexes ((NH$_3$)$_2$Cu^{II}(O$_2$)Cu^{II}(NH$_3$)$_2$), as shown in our previous study[11].

Oxidizable Cu^I during Cu^I → Cu^{II} oxidation in presence of NH$_3$ (O$_2$+NH$_3$ transient) is relatively lower as compared to oxidizable Cu^I fraction during Cu^I → Cu^{II} oxidation in absence of NH$_3$ (O$_2$ only transient). Such observed decrease in oxidizable Cu^I(NH$_3$)$_2$ during Cu^I → Cu^{II} oxidation (difference between oxidizable Cu^I during Cu^I → Cu^{II} oxidation in O$_2$ and O$_2$+NH$_3$), can be referred to as NH$_3$ inhibiting Cu^I(NH$_3$)$_2$ oxidation. Upon comparison of extent of NH$_3$

inhibiting $Cu^I \rightarrow Cu^{II}$ oxidation on Cu-CHA-15-17 and Cu-CHA-15-27 samples (Figure 5.2), it can be seen that NH_3 inhibits $Cu^I(NH_3)_2$ oxidation to almost the same extent (~20%) irrespective of Cu spatial density. Therefore, NH_3 inhibition mechanism likely involves excess physisorbed NH_3 hindering the mobility and oxidation of $Cu^I(NH_3)_2$, which could either be direct binding on $Cu^I(NH_3)_2$ inhibiting Cu^I mobility or inhibiting O_2 adsorption[17], or binding to neighboring NH_4^+ site which are shown to facilitate $Cu^I(NH_3)_2$ mobility[15,16]. Comparison of binding energies of NH_3 and O_2 on $Cu^I(NH_3)_2$ sites could further corroborate one of the above hypotheses. This observed NH_3 inhibition of $Cu^I(NH_3)_2$ oxidation can rationalize the observed NH_3 inhibition during steady state SCR (negative NH_3 orders), wherein more negative reaction order with respect to NH_3 for low Cu spatial density samples represents NH_3 inhibited $Cu^I \rightarrow Cu^{II}$ oxidation being more rate-limiting. Therefore, the origin of observed negative reaction order (NH_3 inhibition) during steady state SCR lies in NH_3 inhibiting $Cu^I \rightarrow Cu^{II}$ oxidation step.
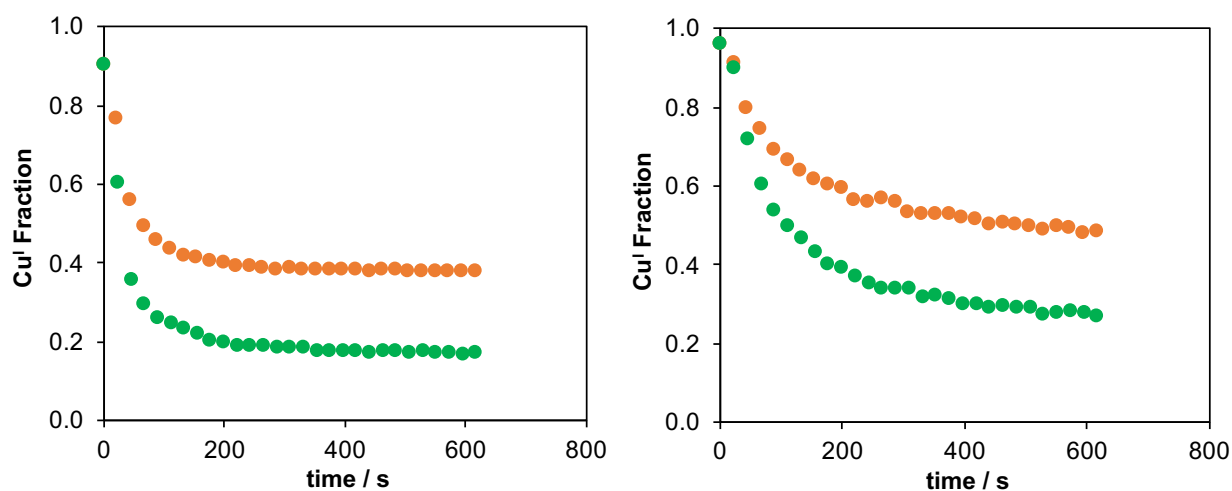
Figure 5.2 Transient oxidation of $Cu^I(NH_3)_2$ with O_2 (green) (10% O_2 in balance He at 473 K) and O_2+NH_3 (orange) (10% O_2 and 300 ppm NH_3 in balance He at 473 K) on model Cu-CHA-15-17 (left) and Cu-CHA-15-27 (right) samples

5.3.4   Effects of varying NH₃ pressure on NH₃ inhibition

Increase in NH_3 pressure initially increases the overall reaction rate (0-150 ppm NH_3; Cu-CHA-15-17), followed by decrease in overall reaction rate (150-800 ppm NH_3; Cu-CHA-15-17) (Figure 5.3), consistent with commonly reported negative reaction order with respect to NH_3 (NH_3 inhibition effect). Since the observed negative reaction order with respect to NH_3 stems

from $Cu^I \rightarrow Cu^{II}$ oxidation step (when SCR is limited by $Cu^I \rightarrow Cu^{II}$ oxidation), positive reaction order with respect to NH_3 likely arises from $Cu^{II} \rightarrow Cu^I$ reduction step (when SCR is limited by $Cu^{II} \rightarrow Cu^I$ reduction). Further details of such transition of NH_3 reaction order from negative to positive as a function of Cu spatial density will need to be investigated separately.
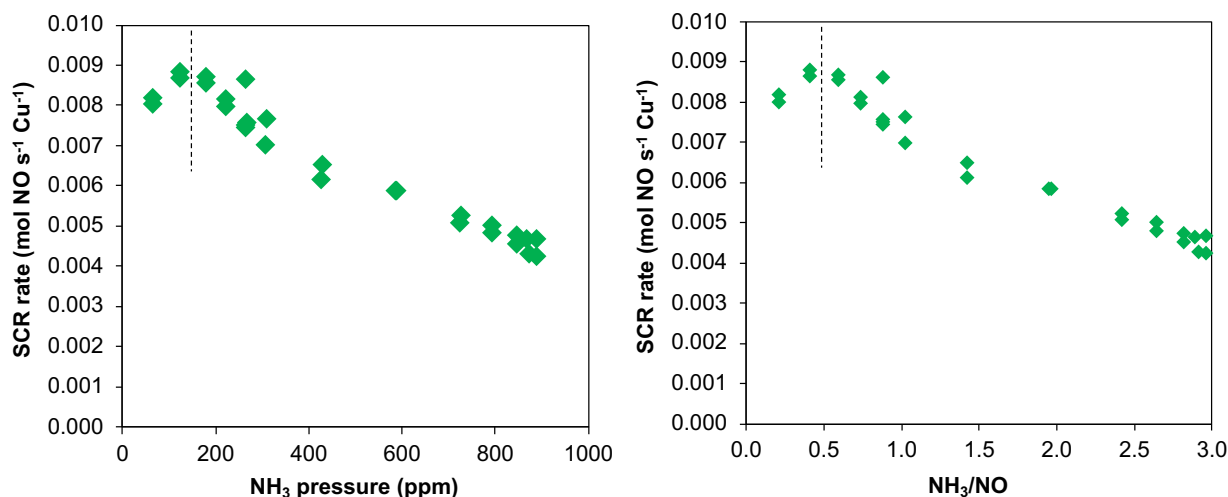
Figure 5.3 SCR rate plotted as a function of NH_3 pressure (0-800 ppm NH_3) and NH_3/NO ratio (0-3) on model Cu-CHA-15-17 sample (300 ppm NO, 0-800 ppm NH_3, 10% O_2, 3% H_2O, 7% CO_2 in balance He at 473 K)

5.3.5   Effects of varying O_2 pressure on NH_3 inhibition

As discussed in chapter 5, increasing reactant O_2 pressure increases the rate of $Cu^I \rightarrow Cu^{II}$ oxidation relative to $Cu^{II} \rightarrow Cu^I$ reduction, and thereby making $Cu^I \rightarrow Cu^{II}$ oxidation under high O_2 limit (~70%). On the other hand, decreasing O_2 pressure (~0.5%) increases the kinetic relevancy of $Cu^I \rightarrow Cu^{II}$ oxidation relative to $Cu^{II} \rightarrow Cu^I$ reduction. Herein we measure apparent reaction order with respect to NH_3 under high (60% O_2) and low O_2 (2% O_2) limits and compare that to the reaction order under conventional O_2 range (10% O_2). As can be seen from Figure 5.4, NH_3 order becomes more negative with decrease in O_2 pressure (-0.4 at 2% O_2, -0.3 at 10% O_2 and -0.2 at 60% O_2), as $Cu^I \rightarrow Cu^{II}$ oxidation becomes more rate-limiting. This corroborates NH_3 inhibition stemming from $Cu^I \rightarrow Cu^{II}$ oxidation step of reaction mechanism.
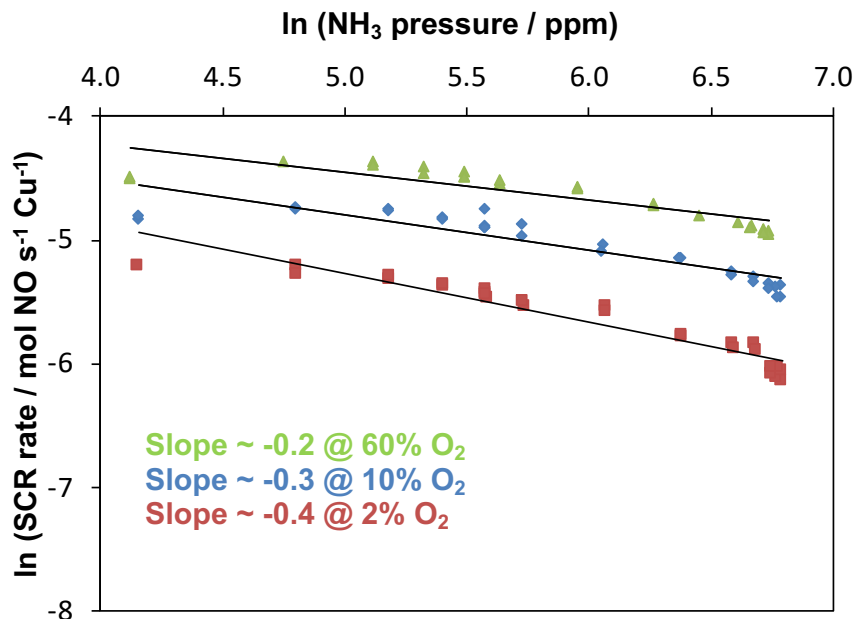
Figure 5.4 NH$_3$ reaction order plots at 2,10 and 60 % O$_2$ on model Cu-CHA-23 sample (300 ppm NO, 150-400 ppm NH$_3$, 2/10/60% O$_2$, 3% H$_2$O, 7% CO$_2$ in balance He at 473 K)

5.4   Methods

Procedures for catalyst synthesis, structural and Cu site characterization, differential reaction kinetics and XAS can be found in previous chapters 3 and 4.

5.5   Conclusions

This work elaborates on observed NH$_3$ inhibition effect on standard SCR kinetics in the low temperature (473 K) regime, wherein negative reaction order with respect to NH$_3$ is observed in the low NH$_3$ pressure range (150-800 ppm). Effects of varying Cu spatial density and reactant O$_2$ pressure on the extent of NH$_3$ inhibition have been studied. Using a series of model Cu-SSZ-13 samples containing isolated Cu^{II} sites of varying Cu spatial density, it has been found that NH$_3$ inhibition increases with decrease in Cu spatial density, indicating that NH$_3$ inhibition likely originates from Cu^{I} → Cu^{II} oxidation-half of SCR Cu^{II} - Cu^{I} redox mechanism. We further confirm that NH$_3$ inhibition effect indeed originates from Cu^{I} → Cu^{II} oxidation-half of SCR Cu^{II} - Cu^{I} redox cycle by showing that oxidizable Cu^{I} fraction during O$_2$ oxidation transient decreases in presence of NH$_3$ (O$_2$+NH$_3$ vs. O$_2$), hypothesized to be either because of direct binding of

excess NH_3 on $Cu^I(NH_3)_2$ inhibiting Cu^I mobility or inhibiting O_2 adsorption, or binding to neighboring NH_4^+ site which are shown to facilitate $Cu^I(NH_3)_2$ mobility. NH_3 inhibition originating from $Cu^I \rightarrow Cu^{II}$ oxidation-half results in increase in NH_3 inhibition with decrease in O_2 pressure, as decreasing O_2 pressure makes $Cu^I \rightarrow Cu^{II}$ oxidation more rate-limiting.

5.6 References

1 T. Johnson and A. Joshi, in *SAE Technical Paper Series*, 2018.
2 S. Brandenberger, O. Kröcher, A. Tissler and R. Althoff, *The State of the Art in Selective Catalytic Reduction of NOx by Ammonia Using Metal-Exchanged Zeolite Catalysts*, 2008, **50**, 492-531.
3 M. Schwidder, S. Heikens, A. De Toni, S. Geisler, M. Berndt, A. Brückner and W. Grünert, *J. Catal.*, 2008, **259**, 96–103.
4 M. Koebel, G. Madia and M. Elsener, *Catal. Today*, 2002, **73**, 239–247.
5 M. Koebel, M. Elsener and G. Madia, in *SAE Technical Paper Series*, 2010.
6 M. Colombo, I. Nova and E. Tronconi, *Catal. Today*, 2012, **197**, 243–255.
7 K. Kamasamudram, N. W. Currier and X. Chen, *Catal. Today*, 2010, **151**, 212–222.
8 L. Olsson, H. Sjövall and R. J. Blint, *Appl. Catal. B Environ.*, 2008, **81**, 203–217.
9 S. A. Bates, A. a. Verma, C. Paolucci, A. a. Parekh, T. Anggara, A. Yezerets, W. F. Schneider, J. T. Miller, W. N. Delgass and F. H. Ribeiro, *J. Catal.*, 2014, **312**, 87–97.
10 C. Paolucci, A. A. Parekh, I. Khurana, J. R. Di Iorio, H. Li, J. D. Albarracin Caballero, A. Shih, T. Anggara, W. Nicholas Delgass, J. T. Miller, F. H. Ribeiro, R. Gounder and W. F. Schneider, 2016, **138** (18), 6028-6048.
11 C. Paolucci, I. Khurana, A. A. Parekh, S. Li, A. J. Shih, H. Li, J. R. Di Iorio, J. D. Albarracin-Caballero, A. Yezerets, J. T. Miller, W. N. Delgass, F. H. Ribeiro, W. F. Schneider and R. Gounder, *Science*, 2017, **357**, 898 – 903.
12 F. Giordanino, E. Borfecchia, K. a. Lomachenko, A. Lazzarini, G. Agostini, E. Gallo, A. V. Soldatov, P. Beato, S. Bordiga and C. Lamberti, *J. Phys. Chem. Lett.*, 2014, **5**, 1552–1559.
13 K. A. Lomachenko, E. Borfecchia, C. Negri, G. Berlier, C. Lamberti, P. Beato, H. Falsig and S. Bordiga, *J. Am. Chem. Soc.*, 2016, **138** (37), 12025-12028.
14 A. Marberger, A. W. Petrov, P. Steiger, M. Elsener, O. Kröcher, M. Nachtegaal and D. Ferri, *Nat. Catal.*, 2018, **1**, 221–227.
15 V. Rizzotto, P. Chen and U. Simon, *Catalysts*, 2018, **8**, 162.
16 P. Chen and U. Simon, *Catalysts*, 2016, **6**, 204.
17 Y. Takamitsu, Y. Ito, H. Ogawa and T. Sano, *J. Japan Pet. Inst.*, 2012, **55**, 57–66.

6.   MECHANISTIC PATHWAYS OF MONONUCLEAR AND BINUCLEAR COPPER COMPLEXES IN CU-SSZ-13 DURING LOW TEMPERATURE STANDARD SCR

6.1   Preface

Chapter 6 contains the most recent draft of a manuscript in preparation. Building upon the mechanistic work from chapter 3, this chapter aims to fill in remaining unresolved pieces in the low temperature standard SCR reaction pathway to put forth a plausible and consistent low temperature standard SCR reaction mechanism. This chapter majorly contains experimental work viz. synthetic, titrimetric, spectroscopic and kinetic characterization during steady state catalysis as well as during transient non-steady state sequential reaction steps (kinetically relevant), with minimal computational work from our collaborators.

6.2   Abstract

In this work, we investigate plausible reaction pathways of dimeric Cu^{II} intermediates (formed via reaction of $Cu^{I}(NH_3)_2$ with O_2) to complete the SCR redox cycle on Cu-SSZ-13, which are mechanistic steps that currently are unknown. On a series of model Cu-SSZ-13 samples of different Cu ion spatial density, we first confirm that, monomeric Cu^{II} reduction with $NO+NH_3$ occurs via single-site kinetics that are independent of Cu ion spatial density, monomeric Cu^{I} oxidation with O_2 occurs via dual-site kinetics that depend on Cu ion spatial density, and dimeric Cu^{II}-oxo reactions with $NO/NO+NH_3$ are also dependent on Cu ion spatial density. From these observations, the most plausible mechanism for reactions of dimeric Cu^{II} intermediates in standard SCR is reductive disproportionation to form a NH_3-solvated Cu^{I} complex and a NH_3-solvated Cu^{II}-nitrate species, which can establish Cu^{II}-nitrite/nitrate equilibrium with gaseous NO and NO_2, and close the SCR pathway via reaction of nitrite species and reaction of gaseous NO_2 via "fast" SCR pathways. Building upon prior work, this study fills in unresolved aspects of the reaction mechanism for low T SCR, and the kinetic and mechanistic dependences of the cycle on Cu ion density. It identifies new reaction pathways that consume binuclear Cu^{II}-oxo species in zeolites. Detailed mechanism enables better interpretation of measured reaction kinetics, and guidance for improved catalyst design and modeling efforts for

SCR. A suite of model Cu-CHA catalysts containing isolated Cu ions at varying spatial density, coupled with kinetic measurements under various kinetic regimes (to cause different parts of the SCR cycle to become rate-limiting) and monitoring the distribution of Cu^{II} and Cu^{I} intermediates during steady-state and transients XAS. Thermodynamic feasibility and reaction stoichiometry of relevant catalytic reaction steps using DFT-computed energetics are used to probe candidate reaction steps. Further, steady state and transient reaction steps using in situ FTIR to identify plausible reaction intermediates.

6.3 Introduction

It has been widely accepted that low temperature standard SCR proceeds via. Cu^{II}-Cu^{I} redox cycle, as seen from prevalence of a mixture of Cu^{I} and Cu^{II} with *operando* x-ray absorption spectroscopy (XAS) experiments under steady-state SCR catalysis and no observed correlation of standard SCR rate with either Cu^{I} or Cu^{II} fraction[1-4]. This Cu^{II}-Cu^{I} redox cycle begins with reduction of isolated Cu^{II} cations with $NO+NH_3$ to give $Cu^{I}(NH_3)_2$, which was shown to occur via NO assisted dissociation of N-H bond of a Cu-bound NH_3 ligand[2,5]. DFT-computed energetics ascertains the thermodynamic feasibility (reaction energy ~ (-) 68-267 kJ mol^{-1}) and kinetic relevance (activation energy ~ 71-74 kJ mol^{-1}) of such NO-assisted reduction of NH_3 solvated Cu^{II} sites [2,5]. This reduction half is followed by pairing and oxidation of two mobile $Cu^{I}(NH_3)_2$ sites to yield Cu dimer intermediate, with the extent and rate of such dual-site oxidation being directly proportional to Cu spatial density[6-7]. Computations further corroborate the thermodynamically feasibility (reaction energy ~ (-) 59 kJ mol^{-1}) and kinetic relevancy (activation energy~ 35 kJ mol^{-1}) of such Cu^{I} diffusion and pairing in oxidation half [6]. Such dual-site and Cu spatial density (Cu/Al) dependent nature of Cu^{I} oxidation step (oxidation half) consequently results in steady state kinetics being dependent on Cu spatial density (Cu/Al) and vary with Cu^2 in oxidation-limited regime (low Cu loadings)[6-7].

There still remain some unresolved pieces in SCR Cu^{II}-Cu^{I} redox cycle, including, (1) unknown reactivity of monomeric Cu and dimeric Cu intermediates to close the catalytic redox cycle, (2) reaction intermediates and elementary steps, and (3) unrecognized role of Bronsted acid sites (H^+). Nature of various possible reactions of Cu^{II}-dimer intermediate (with $NO/NO+NH_3$), specifically Cu site requirements and relevant reaction intermediates, has not been explored previously. Given that the dimeric Cu intermediate reacts with $NO/NO+NH_3$,

there is also a need to calculate and compare relative energy barriers of this step with other subsequent reaction steps to probe the kinetic relevancy.

In this work, we performed steady state *operando* measurement of Cu intermediates under reduction-limited regime along with monitoring the chemical nature of Cu during various non-steady state transient reaction steps using spectroscopic (XAS and FTIR) and titration techniques. Previously unrecognized nature of isolated Cu^{II} reduction with $NO+NH_3$ has been revealed here to be single-site, and independent of Cu spatial density, while corroborating the dual-site and Cu spatial density dependence of Cu^I oxidation with O_2. Nature of Cu^{II}-dimer reaction with $NO+NH_3$, which was also previously undiscovered, has been probed by first considering and comparing the DFT-computed energetics of various thermodynamically feasible pathways. Selection of most plausible dimeric Cu intermediate reaction pathway is enabled by measurement of most abundant surface intermediate coverages, viz. steady state Cu^{II} and Cu^I intermediates coverages, under the regime exclusively limited by reduction half. To further reveal the reactivity and fate of dimeric Cu intermediate, we also monitor the non-steady state temporal changes to chemical nature of Cu (oxidation state and coordination number) during sequential reactions of dimeric Cu intermediate with $NO+NH_3$ on varying Cu spatial density samples. Stoichiometric NO titration experiments were also used to: (1) show that NO consumption stoichiometry during such proposed sequential reaction is consistent with overall SCR reaction stoichiometry, and (2) speculate the direct participation of NH_3 storage NH_4^+ sites. Further attempts are made to identify reaction intermediates during reaction of dimeric Cu intermediate using FTIR experiments. Even though the results are inconclusive likely due to short-lived nature of formed surface intermediates, a speculation could be made on Cu-nitrates and Cu-nitrites being the relevant reaction intermediates.

6.4 Results and Discussion

Here, we study the effects of Cu ion spatial density in Cu-SSZ-13, under reaction conditions wherein different elementary steps of the SCR catalytic cycle become kinetically-relevant. First, six model Cu-SSZ-13 samples with varying spatial density of isolated Cu sites (present either as Cu^{II} at paired framework Al sites or as $[Cu^{II}OH]^+$ at isolated Al sites), were chosen as representatives from a broader Cu-SSZ-13 sample set reported in our previous study[6]. These samples are denoted Cu-CHA-X-Y, where X=Si/Al and Y refers to the mean Cu-Cu

distance in Å, as estimated assuming a homogeneous distribution of Cu throughout the zeolite crystallite volume as done in Paolucci et al.[6]. Relevant structural and site characterization of these model samples are provided in Table 6.1, including bulk elemental analysis, the number of isolated Cu^{II} and $[Cu^{II}OH]^+$ sites (per Al), the concentration of Cu ions per crystallite volume, and the mean Cu-Cu distance. Additional details, including bulk structural characterization (XRD patterns, micropore volume, SEM images) and Cu site characterization (*ex situ* X-ray absorption, UV-Visible spectroscopy) can be found in the appendix D.

Table 6.1 Bulk elemental analysis, number of isolated Cu^{II} and $[Cu^{II}OH]^+$ sites (per Al), concentration of Cu ions per crystallite volume, and the mean Cu-Cu distance in oxidized Cu^{II} forms of model Cu-CHA samples (X = Si/Al, Y = mean Cu-Cu distance).

Sample Name Cu-CHA-X-Y	Si/Al	Cu/Al	Cu^{II}/Al^*	$Cu^{II}OH/Al^*$	Cu / 1000Å^3	Mean Cu-Cu distance (Å)
Cu-CHA-5-15	4.5	0.21	0.21	0.00	0.57	15
Cu-CHA-5-20	4.5	0.08	0.08	0.00	0.18	20
Cu-CHA-15-17	15	0.44	0.09	0.35	0.41	17
Cu-CHA-15-20	15	0.25	0.09	0.16	0.18	20
Cu-CHA-15-29	15	0.08	0.08	0.00	0.07	29
Cu-CHA-25-20	25	0.40	0.05	0.35	0.18	20

*Determined from titration of residual H^+ sites by NH_3 and thermodynamic preferences for Cu^{II} and $[Cu^{II}OH]^+$

6.4.1   Kinetics and mechanisms of $Cu^{II} \rightarrow Cu^{I}$ reduction with NO+NH$_3$

Time-resolved XANES spectra were measured during Cu^{II} reduction with NO+NH$_3$ on each of the three out of six model Cu-CHA samples (Table 6.1), and the transient decay in Cu^{II} fraction with increasing time after NO+NH$_3$ exposure is shown in Figure 6.1. Each Cu-CHA sample showed complete reduction of Cu^{II} from the NH$_3$-solvated monomeric Cu^{II} state ($Cu^{II}(NH_3)_4$, $Cu^{II}(NH_3)_3(OH)$) to the monomeric Cu^I state ($Cu^I(NH_3)_2$) (appendix D), consistent with previous studies[2,4,5,8,9], and the fraction of reducible Cu^{II} is listed in Table 6.2.

Table 6.2 Fraction of Cu^{II} reducible in $NO+NH_3$, Cu^{I} oxidizable in O_2 and NO_2, and Cu^{II} in Cu^{II}-dimer state reducible in $NO+NH_3$ on model Cu-CHA-X-Y samples (X=Si/Al, Y = mean Cu-Cu distance).

Cu-CHA-X-Y	Fraction of Cu^{II} reducible in $NO+NH_3$ (Cu_red/ Cu_total)[a]	Fraction of Cu^{I} oxidizable in O_2 (Cu_ox_O_2/ Cu_total)[b]	Fraction of Cu^{I} oxidizable in NO_2 (Cu_ox_NO_2/ Cu_total)[c]	Fraction of Cu^{II} in Cu^{II}-dimer state reducible in $NO+NH_3$ (Cu_dim_red/ Cu_total)[d]
Cu-CHA-25-15	0.98	0.95	1.00	0.05
Cu-CHA-15-29	0.98	0.70	1.00	0.10
Cu-CHA-15-17	1.00	0.85	1.00	0.07

[a]obtained from section 1, [b]obtained from section 2, [c]obtained from appendix D, [d]obtained from section 3. Cu^{II} and Cu^{I} fractions reported contain an absolute 5% error from fitting.

Figure 6.1 also shows least-squares regression of the data to a rate expression for Cu^{II} reduction that is first-order in Cu concentration, which is the power law expression that best described these data (Equation 6.1) (detail kinetic model derivation in appendix D):

$$Cu^{II} \text{ Fraction} = \frac{[Cu^{II}(t)]}{[Cu^{II}(0)]} = e^{-k_r' t} \qquad (6.1)$$

Values of the apparent first-order reduction rate constants (Table 6.3) were identical on all three Cu-CHA samples and independent of Cu spatial density as expected from a single-site $NO+NH_3$ reduction mechanism. Additionally, the identical apparent reduction rate constants on these samples, which contain either isolated Cu^{II} sites or mixture of isolated Cu^{II} and $[Cu^{II}OH]^+$ sites (Table 6.1), indicates that the kinetics of single-site Cu^{II} reduction with $NO+NH_3$ are identical on both types of monomeric Cu^{II} sites. The indistinguishable reduction kinetics of monomeric Cu^{II} and $[Cu^{II}OH]^+$ site motifs is consistent with their full solvation by NH_3 (from *operando* XAS and DFT-computed phase diagram) as reported previously, which resulted in experimentally measured SCR rates (per Cu) in reduction-limited regimes and computed activation barriers (71-74 kJ mol^{-1}) that were similar on both site type[5]. The time constants estimated for $NO+NH_3$ reduction of isolated Cu^{II} sites (0.021 s^{-1} at 473 K, Figure 6.1) were the same order of magnitude as the steady-state standard SCR turnover frequencies (per Cu) measured on Cu-CHA samples (0.023-0.078 s^{-1} at 473 K, Table 6.1), suggesting that the $NO+NH_3$-mediated single-site Cu^{II} reduction pathways measured here are relevant to the reactions that occur during steady-state catalytic SCR turnovers.
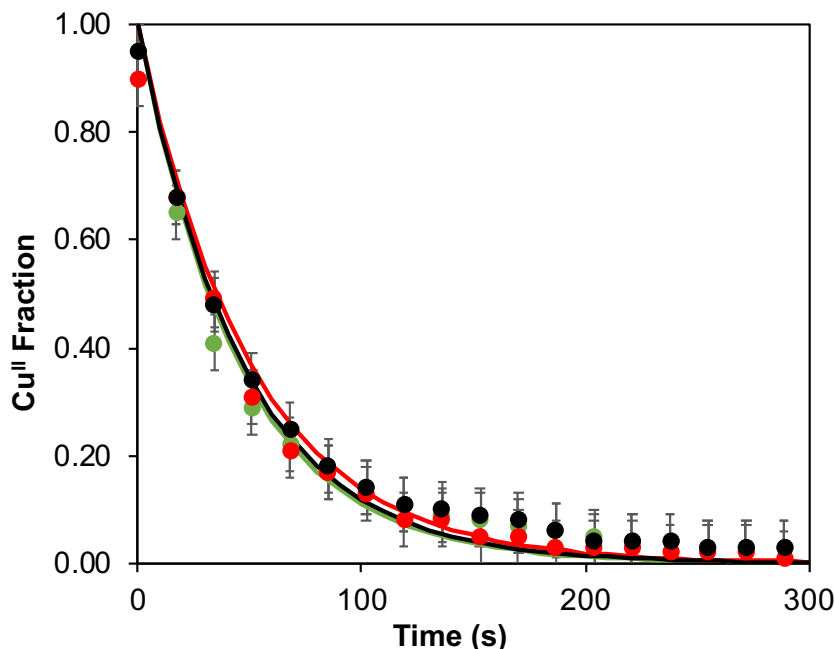
Figure 6.1 Temporal evolution of the XANES-measured Cu^{II} fraction for the Cu-CHA-15-29 (green), Cu-CHA-15-17 (red), and Cu-CHA-5-15 (black) during reduction in 300 ppm NO and NH_3 each at 473 K. Least-squares fit to Eq. 6.1 is shown by solid lines. The Cu^{II} fractions reported contain an absolute 5% error from fitting.

Table 6.3 Cu^{II}-reduction (with $NO+NH_3$) rate constants, NO consumption stoichiometry per reducible Cu^{II} ion, and Cu^{II}-reduction rates during steady state turnover on Cu-CHA-15-29, Cu-CHA-15-17 and Cu-CHA-5-15 samples

Sample	Cu^{II} reduction rate constant from 1st order transient (k_r') (s^{-1})	NO consumed per reducible Cu^{II} (mol NO/mol Cu_red)	Cu^{II} reduction rate during steady state (s^{-1})[a]
Cu-CHA-5-15	0.019	0.98	0.0061
Cu-CHA-15-17	0.022	0.97	0.0063
Cu-CHA-15-29	0.019	0.97	0.0021

[a]Measured at reaction conditions: 300 ppm NO, 300 ppm NH_3, 70% O_2, 3% H_2O and 7% CO_2 in balance He at 200°C.

The reduction of Cu^{II} to Cu^I occurred concomitantly with the consumption of one mole of NO equivalent on each Cu-CHA sample (Figure 6.1), consistent with previously proposed Cu^{II} reduction pathways that occur via NO-assisted NH_3 dissociation (Equation 6.1) [2,4,5]. Specifically, these $Cu^{II} \rightarrow Cu^I$ reduction pathways involve NO attack of an NH_3-solvated Cu^{II} ion to form an N-N bond, with a single-electron transfer to Cu^{II} and a transfer from the H^+ on NH_3 to an acceptor, which is either an anionic lattice oxygen at one Al in a paired Al configuration to form a surface H^+, or an anionic OH^- ligand on $Cu^{II}OH$ in an isolated Al configuration to form H_2O[5]:

$$(NH_3)_4Cu(II) + NO \rightarrow Cu(I)(NH_3)_2|NH_4^+ + N_2 + H_2O \qquad (6.2)$$

$$(NH_3)_3Cu(II)(OH) + NO \rightarrow Cu(I)(NH_3)_2 + N_2 + 2H_2O \qquad (6.3)$$
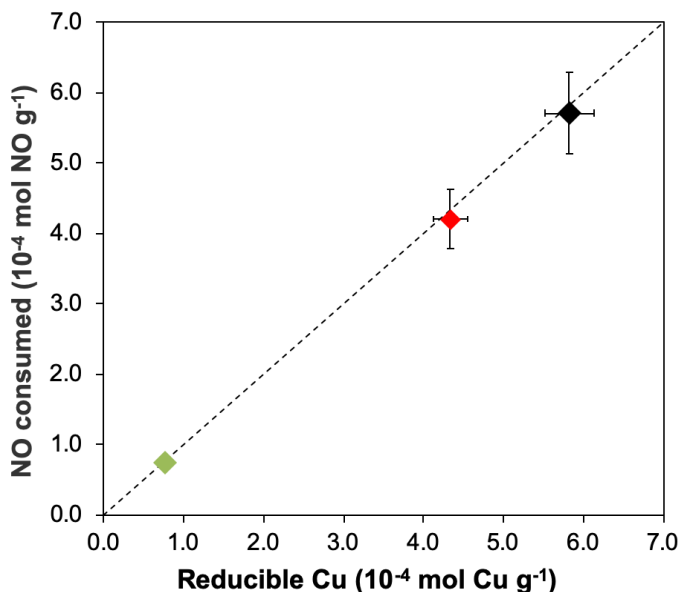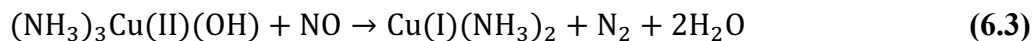
Figure 6.2 NO consumption (per g) during reduction of Cu-CHA samples in their monomeric Cu^{II} state with $NO+NH_3$, plotted against reducible Cu (per g) (Table 6.2) on Cu-CHA-15-29 (green), Cu-CHA-15-17 (red) and Cu-CHA-5-15 (black). Dotted line represents a parity line.

6.4.2   Nature of $Cu^{I} \rightarrow Cu^{II}$ oxidation with O_2

The three model Cu-CHA samples were first reduced in NO and NH_3 (300 ppm each, 473 K) to their monomeric Cu^{I} state ($Cu^{I}(NH_3)_2$) followed by sequential stoichiometric oxidation with O_2. Time-resolved XANES spectra were measured during Cu^{I} oxidation with O_2 on all three model Cu-CHA samples, and the transient decay in Cu^{I} fraction with increasing time after O_2 exposure is shown in Figure 6.3. Each sample showed only partial oxidation of Cu^{I} from the NH_3-solvated state ($Cu^{I}(NH_3)_2$) to give NH_3-solvated Cu^{II}-dimer complexes $((NH_3)_2Cu^{II}(O_2)Cu^{II}(NH_3)_2)$ (XANES and EXAFS in appendix D), consistent with our previous study[6].

Figure 6.3 also shows least-squares regression of the data to a rate expression for Cu^{I} oxidation that is second-order in Cu concentration, which is the power law expression that best described these data (Equation 6.2) (detail kinetic model derivation in appendix D):

$$2Cu^I(NH_3)_2 + O_2 \rightarrow (NH_3)_2Cu^{II}(O_2)Cu^{II}(NH_3)_2 \qquad (6.4)$$
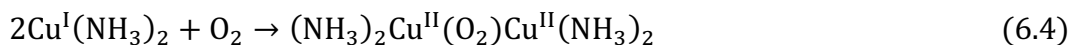
$$Cu^I \text{ Fraction} = \frac{[Cu^I(t)]}{[Cu^I(0)]} = \frac{1-[Cu^I(\infty)]/[Cu^I(0)]}{1 + 2k_o'([Cu^I(0)]-[Cu^I(\infty)])t} + \frac{[Cu^I(\infty)]}{[Cu^I(0)]} \qquad (6.5)$$
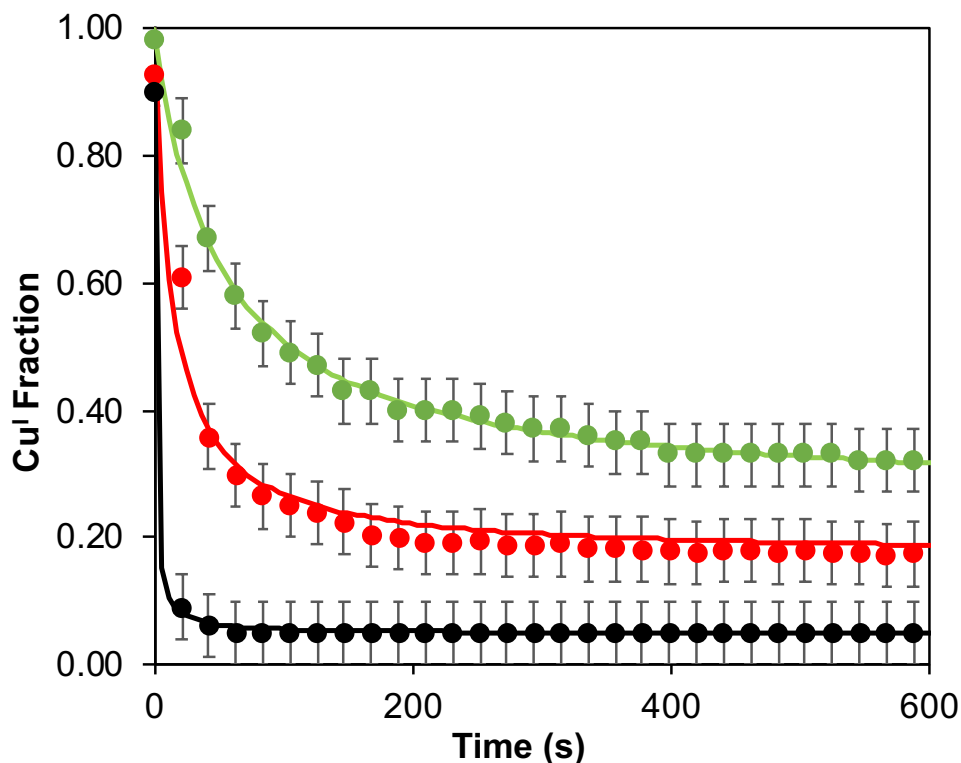
Figure 6.3 Temporal evolution of the XANES-measured Cu^I fraction is plotted for the Cu-CHA-15-29 (green) Cu-CHA-15-17 (red) and Cu-CHA-5-15 (black) samples during transient oxidation in 10% O_2 at 473 K. Least-squares fit to Eq. 5.2 is shown by solid lines. The Cu^I fractions reported contain an absolute 5% error from fitting.

Values of the apparent second-order reduction rate constants, the initial oxidation rate (at t=0) and fraction of Cu^I that is oxidizable in O_2 are tabulated in Table 6.2. Initial oxidation rates increase with Cu spatial density, and the fraction of oxidizable Cu^I also increases with Cu spatial density. The pseudo-second-order kinetics of Cu^I oxidation with O_2 (Figure 6.3), together with the effects of $Cu^I(NH_3)_2$ spatial density on initial oxidation rates and on the total fraction of Cu^I that can be oxidized with O_2, indicate that two $Cu^I(NH_3)_2$ complexes are required in this dual-site oxidation pathway, in agreement with our previous study[6]. As seen from Table 6.4, O_2 oxidation of $Cu^I(NH_3)_2$ state results in proximal $Cu^I(NH_3)_2$ sites (within the diffusion distance from each other[6]) forming an NH_3-solvated Cu^{II}-dimer, while isolated $Cu^I(NH_3)_2$ sites (outside the diffusion

distance from each other[6]) remain unoxidized. This results in preparing the sample in a state containing a mixture of NH_3-solvated Cu^{II}-dimer (dimerizable Cu^I from Table 6.4) and isolated Cu^I (isolated Cu^I from Table 6.4).

Table 6.4 Initial and final states of Cu (average coordination number from EXAFS) during Cu^I oxidation with O_2 on Cu-CHA-15-29, Cu-CHA-15-17 and Cu-CHA-5-15 samples

Sample	2nd order rate constant (m^3 mol $Cu^{-1}s^{-1}$)	Initial rate of Cu^I oxidation[a]		Average CN before Cu^I oxidation (EXAFS)	Average CN after Cu^I oxidation (EXAFS)
		(mol $m^{-3}s^{-1}$)	(s^{-1})		
Cu-CHA-15-29	0.00011	1.1	0.009	2.1	3.5
Cu-CHA-15-17	0.00005	21.1	0.032	2.0	3.8
Cu-CHA-5-15	0.00082	134.9	0.141	2.0	3.9

Initial rate is defined as rate of change of Cu oxidation state at t=0 from transient XAS
[a]computed from decrease in Cu^I from transient XANES during $Cu^I(NH_3)_2$ oxidation with O_2
CN=Coordination Number. Error from LC fitting XANES Cu^I fraction and EXAFS fitted CN are 0.05 and 0.1.

6.4.3   Nature of Cu^{II}-dimer reduction

6.4.3.1 Cu^{II}-dimer reduction mediated by NO+NH_3

The three model Cu-CHA samples were first treated in NO and NH_3 (300 ppm each, 473 K) to reduce to their monomeric Cu^I state, followed by stoichiometric oxidation with O_2 (section 3) to obtain the dimeric Cu^{II} state, which is comprised of a mixture of NH_3-solvated dimeric Cu^{II} (Cu_ox_O_2) and NH_3-solvated monomeric Cu^I sites. Subsequent reactions of these samples in their dimeric Cu^{II} states with either NO or a mixture of NO+NH_3 were studied while monitoring changes in Cu oxidation state by XANES and coordination number by EXAFS. Linear combination fitting of XANES spectra is non-trivial and subject to significant uncertainty given the large number of candidate Cu^{II} and Cu^I structures that may form upon reaction of this dimeric Cu^{II} complex and given the limited number of experimental Cu^{II} and Cu^I standards used for this fitting; as a result, the distribution of Cu^{II} and Cu^I states was determined from average first-shell Cu-O/N coordination numbers in EXAFS, assuming that Cu^{II} prefers four-fold coordination [5,10,11] and Cu^I prefers two-fold coordination[5,10,11].
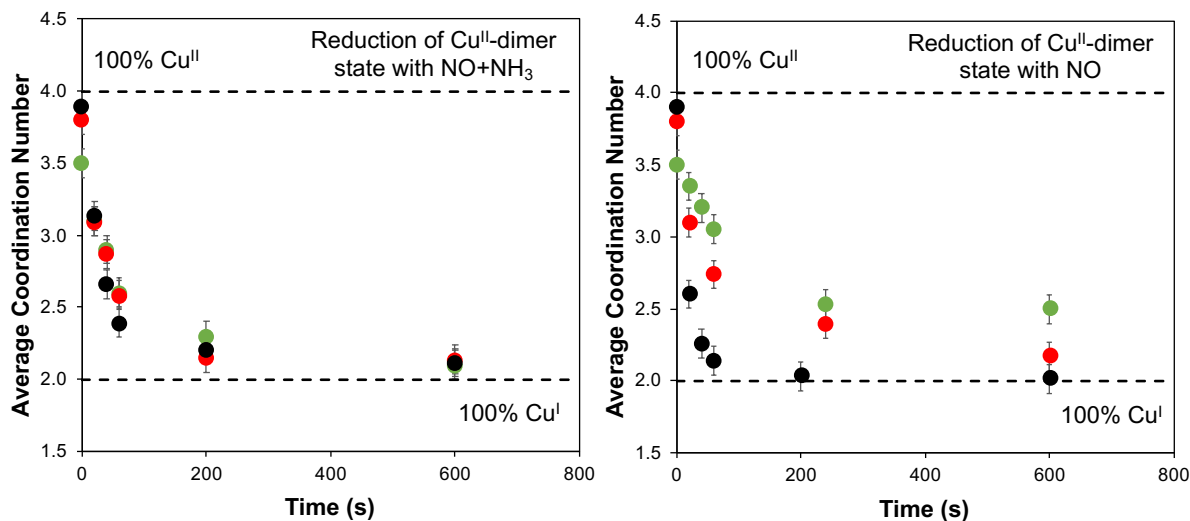
Figure 6.4 Temporal evolution of EXAFS-measured average Cu coordination number plotted for Cu-CHA-15-29 (green) Cu-CHA-15-17 (red) and Cu-CHA-5-15 (black) samples during transient reduction in 300 ppm NO+NH$_3$ (left) and 300 ppm NO (right) at 473 K.

Prior to introducing either NO or a mixture of NO+NH$_3$, the average first shell Cu-O/N coordination number is ~4.0 on the Cu-CHA sample with the highest Cu spatial density (Cu-CHA-5-15) and decreases to a value of 3.5 with decreasing Cu spatial density (Table 6.4, Figure 6.4). Time-resolved EXAFS spectra on the three model Cu-CHA samples showed a decrease in the average first shell Cu-O/N coordination number (appendix D) when reacting with NO+NH$_3$ or with NO alone (Figure 6.4). On all samples, irrespective of Cu spatial density, reaction from the dimeric Cu^{II} state with NO+NH$_3$ results in a decrease of the average first shell Cu-O/N coordination number to 2.0, consistent with full reduction to the monomeric Cu^{I} state (Cu^{I}(NH$_3$)$_2$). In contrast, reaction of the dimeric Cu^{II} state with NO alone caused a decrease in the first-shell coordination number to different values (2.0, 2.2, and 2.5 in order of samples with decreasing Cu spatial density), suggesting that the extent of reduction increased with increasing Cu spatial density, and only reached a state consistent with full reduction to Cu^{I} on Cu-CHA-15. These observations indicate that reactions of NO with dimeric Cu^{II} complexes are sensitive to the Cu spatial density, and that complete reduction of dimeric Cu^{II} complex requires NO+NH$_3$.

The reduction of the model Cu-CHA samples in their dimeric Cu^{II} states to their monomeric Cu^{I} state occurred concomitantly with the consumption of NO (Figure 5.5). In the case of reaction with NO alone, fewer than 2 molecules of NO (~1.5) were consumed per Cu contained within dimeric Cu^{II} complexes (~1.5 mol NO per Cu_dimer). In the case of reaction

with both NO+NH$_3$, 2 molecules of NO were consumed per Cu within dimeric Cu^{II} complexes (4 NO molecules consumed per dimeric Cu^{II} complex), consistent with standard SCR reaction stoichiometry, as shown below:

$$4NO + 4NH_3 + O_2 \rightarrow 4N_2 + 6H_2O \qquad (6.6)$$
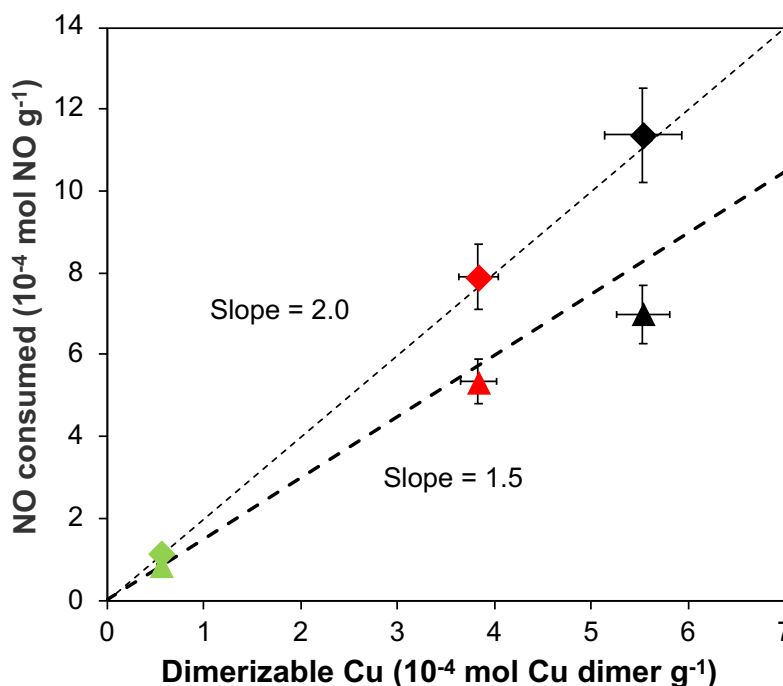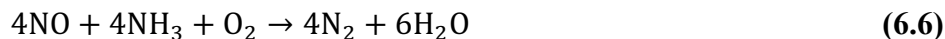
Figure 6.5 NO consumption (per g) during reduction of dimeric Cu^{II} states to Cu^{I} states in NO+NH$_3$ (diamonds) and NO (triangles) plotted against the amount of dimeric Cu^{II} (per g) as solid symbols on Cu-CHA-15-29 (green), Cu-CHA-15-17 (red) and Cu-CHA-5-15 (black). Dashed line with slope of 2 represents the consumption of 2 NO molecules per dimeric Cu^{II} complex.

The NO consumption stoichiometries of 2.0 (NO/Cu_dimer = 4/2) during reduction with NO+NH and of about 1.5 (NO/Cu_dimer ~ 3/2) during reduction with NO may also reflect NO consumption with other non-Cu-coordinated NH$_3$ on the sample. For example, NO can form NO$_2$ via nitrate-nitrite equilibrium, and this NO$_2$ can react with NH$_3$/NH$_4^+$ in a "fast" SCR reaction (equation 6.7) as previously proposed on H$^+$ sites[14,26]. NO$_2$ is not observed in the reactor effluent, suggesting that any NO$_2$ formed *in situ* would react via NH$_3$ species in an SCR reaction such as in [27,28]:

$$NO_2 + NO + 2NH_3 \text{ (sufficient reactive } NH_3 \text{ on } NH_4^+) \leftrightarrow 4N_2 + 3H_2O \qquad (6.7)$$
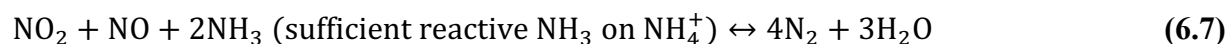
In order to study the effect of NH_4^+ sites, model Cu-CHA samples were prepared with fixed Cu ion spatial density but with varying amounts of residual NH_4^+ sites by varying the framework Si/Al ratio: Cu-CHA-5-20, Cu-CHA-15-20, and Cu-CHA-25-20 (Table 6.5). On these Cu-CHA-X-20 samples, the residual NH_4^+/Al was calculated by titration of residual H^+/Al sites by NH_3 (procedure in chapter 2), and listed in Table 6.5. To probe the role of NH_4^+ sites exclusively during $Cu^{II} \rightarrow Cu^I$ reduction half of Cu^{II}-Cu^I redox cycle, apparent $Cu^{II} \rightarrow Cu^I$ reduction rate constants were measured on these Cu-CHA-X-20 samples during steady-state under the "high O_2-pressure kinetic limit" of SCR (apparent reaction orders of zero in dioxygen: 300 ppm NO, 300 ppm NH_3, 70% O_2, 3% H_2O and 7% CO_2 in balance He at 200°C) (Table 6.5) (additional discussion in chapter 4). These apparent $Cu^{II} \rightarrow Cu^I$ reduction rate constants were further normalized by total pairable Cu (Table 6.5) (obtained from Cu^I oxidation transients in chapter 4) (k_r: mol NO mol pairable $Cu^{-1}s^{-1}$), and plotted as a function of NH_4^+/Al sites in Figure 6.6. Positive correlation between the amount of NH_4^+ ion and apparent $Cu^{II} \rightarrow Cu^I$ reduction rate constant (Figure 6.6) is suggestive of direct involvement of NH_4^+ ions during some $Cu^{II} \rightarrow Cu^I$ reduction step, likely with *in-situ* NO_2 (formed via. nitrate-nitrite equilibrium) in a "fast SCR" reaction on NH_4^+ sites (equation 6.7), as discussed in the previous paragraph.
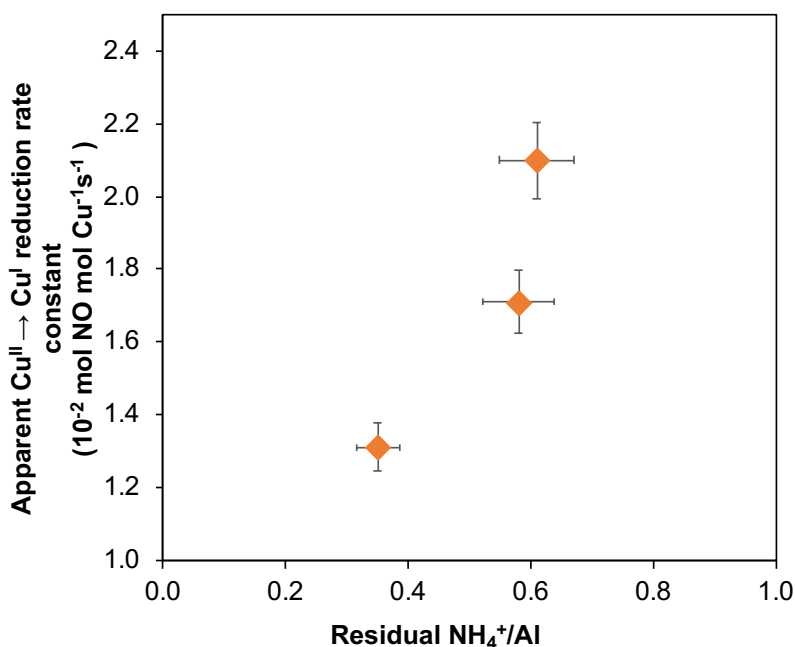
Figure 6.6 Apparent $Cu^{II} \rightarrow Cu^I$ reduction rate constants (NO consumption rate constants) plotted as a function of amount of NH_4^+ ions on a series of Cu-CHA samples with similar Cu spatial density and varying NH_4^+/Al (Si/Al) (Cu-CHA-5-20, Cu-CHA-15-20 and Cu-CHA-25-20)

Table 6.5 Comparison of apparent $Cu^{II} \rightarrow Cu^{I}$ reduction rate constants a series of model Cu-CHA-X-20 samples with similar Cu spatial density and varying NH_4^+/Al (Si/Al)

Sample	Residual NH_4^+/Al	Apparent reduction rate constant (10^{-2} mol NO mol $Cu^{-1}s^{-1}$)	Fraction of Cu^{I} oxidizable/pairable in O_2 (Cu_ox_O2/ Cu_total)	Apparent reduction rate constant (10^{-2} mol NO mol pairable $Cu^{-1}s^{-1}$)
Cu-CHA-5-20	0.35	1.24	0.95	1.31
Cu-CHA-15-20	0.58	1.33	0.78	1.71
Cu-CHA-25-20	0.61	1.52	0.73	2.08

6.4.3.2   Evaluation of reaction pathways of Cu^{II}-dimer reduction with NO+NH$_3$

Four possible reaction pathways of the dimeric Cu^{II} complex with NO were considered, to compare with the experimental observations in Section 6.4.3.1 and to perform DFT calculations to assess their thermodynamic feasibility (Figure 6.6). Pathway 1 involves reaction of two NH_3 ligands in the dimeric Cu^{II} complex with two equivalents of NO, via the Cu^{II}-nitrosamine (H_2NNO) intermediates identified previously in single-site Cu^{II} reduction pathways[5], followed by dissociation to give NH_3-solvated $Cu^{II}OH$, N_2 and H_2O. Pathway 1 involves direct formation of an N-N bond (denoted N-route), and is conceptually different from the other pathways (2a, 2b, 2c) involving NO reaction at bridging O atoms in the dimeric Cu^{II} complex (denoted O-routes) to form nitrate or nitrite intermediates. Pathway 2a involves two equivalents of NO reacting with two bridging O atoms in the dimeric Cu^{II} complex to yield two NH_3-solvated Cu^{II}-nitrite species[12], wherein NH_3 bound to the Cu^{II}-nitrite could react with the nitrite ligand to give NH_3-solvated $Cu^{II}OH$, N_2 and H_2O[4]. Pathway 2b involves two equivalents of NO reacting with two bridging O atoms in the dimeric Cu^{II} complex to yield two NH_3-solvated Cu^{II}-nitrite species (as in Pathway 2a), followed by subsequent decomposition to form a NH_3-solvated Cu^{I} complex and gaseous NO_2[13], which can subsequently close the SCR cycle via "fast" SCR pathways [4,7,14]. Pathway 2c involves disproportionation of the dimeric Cu^{II} complex to form a NH_3-solvated Cu^{I} complex and a NH_3-solvated Cu^{II}-nitrate species[12], which can establish Cu^{II}-nitrite/nitrate equilibrium with gaseous NO and NO_2, and close the SCR pathway via reaction of nitrite species as in Pathway 2a or via reaction of gaseous NO_2 via "fast" SCR pathways [4,7,14].
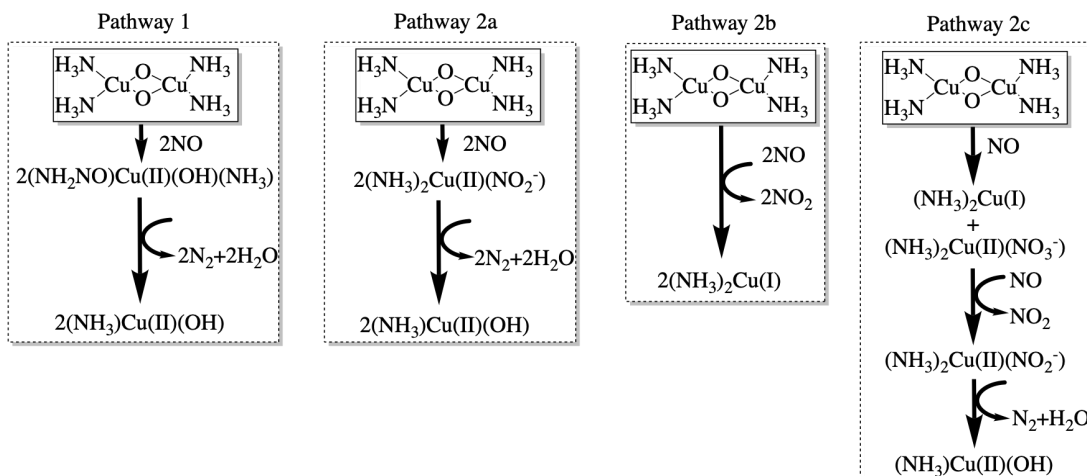
Figure 6.7 Different possible pathways for Cu^{II}-dimer reaction with NO (Pathways 1, 2a, 2b and 2c) (Note: Complete elementary steps and formed products are not shown for the sake of simplicity)

The energetics of the considered non-elementary lumped pathways 1, 2a, 2b and 2c have been depicted in Figure 6.8 (details of energetics calculations in appendix D). All pathways have favorable reaction energies that are very exothermic, and so are thermodynamically feasible. Therefore, further experimental evidence is needed to discriminate and identify the most plausible pathway.
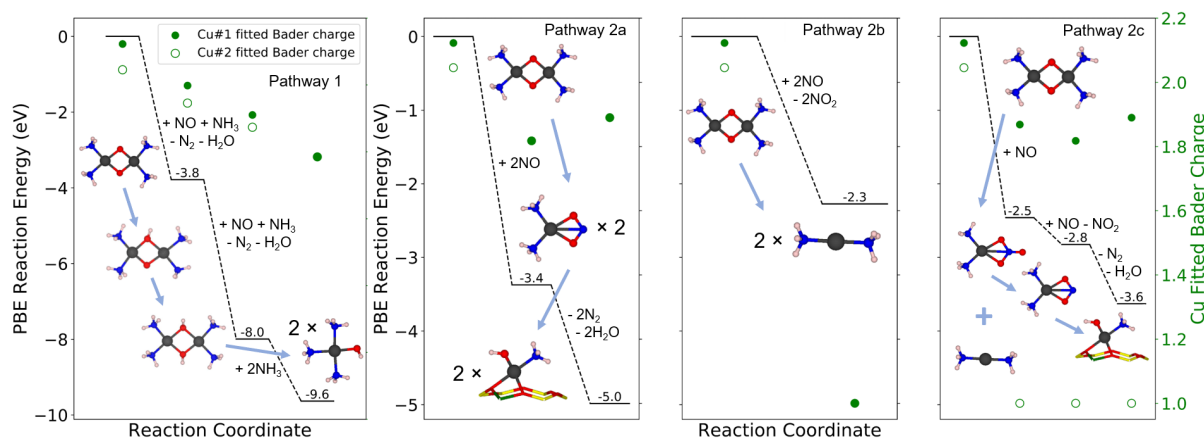
Figure 6.8 DFT-computed energetics for considered pathways 1, 2a, 2b and 2c

6.4.3.3   Cu^{II}/Cu^{I} distribution under standard SCR and high O$_2$-pressure limits

In order to differentiate between the pathways depicted in Figure 6.7, the steady state distribution of Cu oxidation states by XANES and average coordination number by EXAFS under standard SCR reaction conditions (300 ppm NO, 300 ppm NH$_3$, 10% O$_2$, 3% H$_2$O and 7% CO$_2$ in balance He at 200°C) and under the "high O$_2$-pressure kinetic limit" of SCR (apparent reaction orders of zero in dioxygen: 300 ppm NO, 300 ppm NH$_3$, 70% O$_2$, 3% H$_2$O and 7% CO$_2$ in balance He at 200°C) were measured on model Cu-CHA samples. Herein we focus only on the distribution of Cu^{II}/Cu^{I} oxidation states obtained reliably from linear combination fitting of XANES spectra, as Cu^{II} and Cu^{I} states are NH$_3$-solvated during steady state concurrent with the used Cu^{II} and Cu^{I} standards during linear combination fitting (Table 6.6). Under standard SCR conditions (blue, Figure 6.9), the fraction of Cu present at Cu^{I} decreases with increasing Cu spatial density and the acceleration of oxidation SCR half-cycles, as reported in our prior work[6]. In the high O$_2$-pressure limiting regime, wherein Cu^{II} →Cu^{I} reduction was shown to be the sole kinetically relevant step in chapter 4, both Cu^{II} and Cu^{I} oxidation states are still observed (green, Figure 6.9, Table 6.6), although the steady-state distribution of Cu^{I} on each sample is smaller than present during steady-state standard SCR, consistent with the acceleration of oxidation SCR half-cycles at higher O$_2$ pressure (Table 6.6).

Table 6.6 Comparison of *operando* steady-state Cu^{I} fraction, apparent O$_2$ reaction order and unoxidizable Cu^{I} fraction under standard SCR conditions and high O$_2$-pressure limit on a series of model Cu-CHA-5-15, Cu-CHA-15-17 and Cu-CHA-15-29 samples

Sample	O$_2$ order (standard SCR conditions)	O$_2$ order (high O$_2$-pressure kinetic limit)	Fraction of unoxidizable Cu^{I} in O$_2$	Steady state Cu^{I} fraction (standard SCR conditions)	Steady state Cu^{I} fraction (high O$_2$-pressure kinetic limit)
Cu-CHA-5-15	0.2	0.0	0.06	0.10	0.05
Cu-CHA-15-17	0.3	0.0	0.17	0.42	0.21
Cu-CHA-15-29	0.7	0.1	0.30	0.95	0.81

standard SCR conditions: 300 ppm NO, 300 ppm NH$_3$, 10% O$_2$, 3% H$_2$O and 7% CO$_2$ in balance He at 200°C
high O$_2$-pressure limit:300 ppm NO, 300 ppm NH$_3$, 70% O$_2$, 3% H$_2$O and 7% CO$_2$ in balance He at 200°C
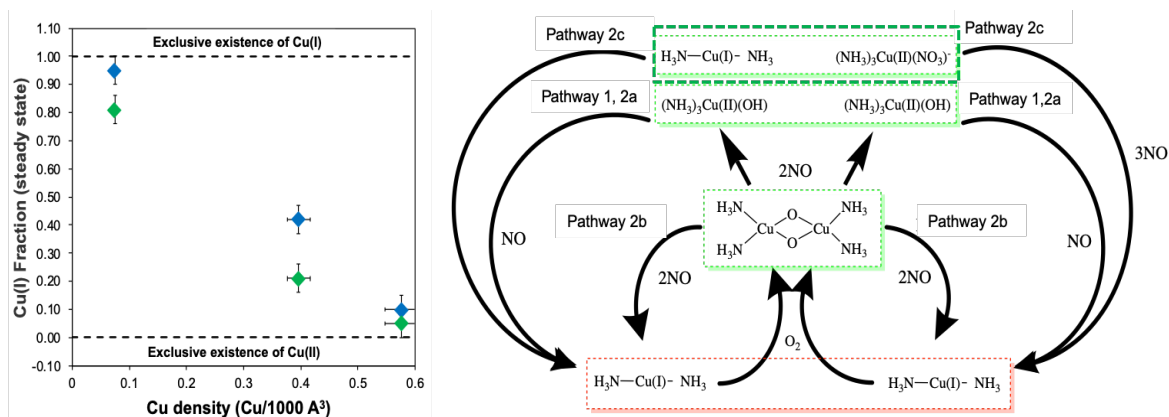
Figure 6.9 Steady state Cu^{II} fraction plotted as a function of Cu density on Cu-CHA-29, Cu-CHA-17 and Cu-CHA-15 under conventional SCR conditions (blue) as well as "reduction-limited" conditions (green) (Left). Pathways 1, 2a, 2b and 2c incorporated into Cu^{II}-Cu^{I} redox cycle (Right). Note: Complete elementary steps and formed products are not shown for simplicity

Amongst the proposed pathways 1, 2a, 2b and 2c, only pathway 2c would reconcile the coexistence of Cu^{II} and Cu^{I} as the most abundant reaction intermediates, when limited by Cu^{II} reduction with NO in the "high O$_2$-pressure kinetic limit" (Figure 6.9, right). Therefore, this is suggestive of Cu^{II}-dimer disproportionately reducing to yield a mixture of Cu^{II} and Cu^{I} intermediates during standard SCR cycle, making the proposed pathway 2c more plausible. It is worthwhile to note that some of the Cu^{I} intermediates (upon Cu^{II}-dimer disproportionation) would temporarily remain as spectator species till they find remaining Cu^{I} species (upon Cu^{II} reduction to Cu^{I}) within the diffusion distance for pairing and oxidation. This would result in appearance of some remnant Cu^{I} intermediates, despite the cycle limited by Cu^{II} reduction.
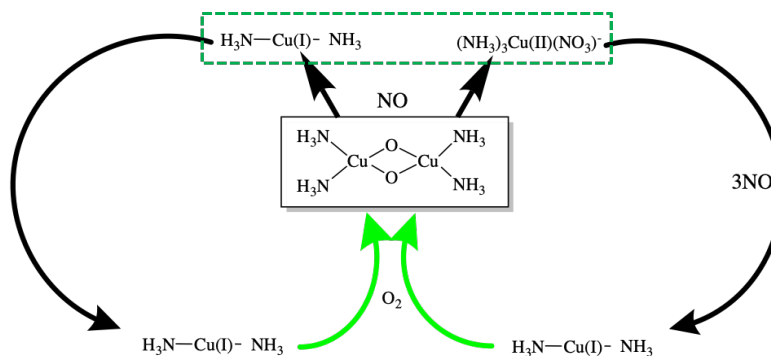
Figure 6.10 Most plausible Cu^{II}-dimer disproportionation and reduction pathway incorporated into Cu^{II}-Cu^{I} redox cycle. Note: Complete elementary steps and formed products are not shown for simplicity

6.4.3.4 Kinetics of reduction of Cu^{II}-dimer with NO+NH$_3$ to Cu^{I}(NH$_3$)$_2$

The transient reaction of the dimeric Cu^{II} state with NO + NH$_3$ resulted in the complete reduction to the Cu^{I}(NH$_3$)$_2$ state, consistent with standard SCR stoichiometry and the proposed most plausible pathway in Figure 6.10 and equation 6.8.

$$(NH_3)_2Cu(II)(O_2)Cu(II)(NH_3)_2 + 4NO + 4NH_3 \rightarrow 2Cu(I)(NH_3)_2 + 4N_2 + 6H_2O \qquad \textbf{(6.8)}$$

The transient evolution from the Cu^{II} to the Cu^{I} state is shown for each sample in Figure 6.11, after converting the average EXAFS first-shell coordination number converted to Cu^{II} fraction, assuming that Cu^{II} prefers four-fold coordination and Cu^{I} prefers two-fold coordination.
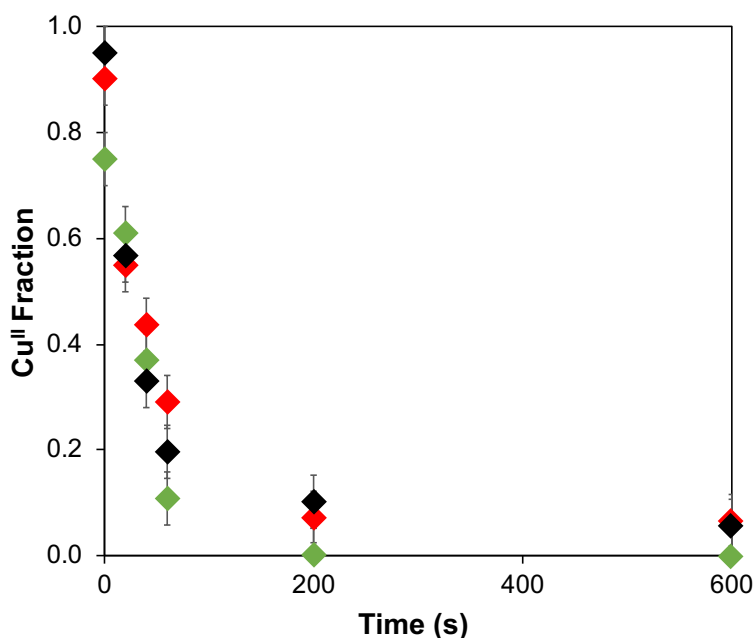
Figure 6.11 Temporal evolution of Cu^{II} fraction (obtained from EXAFS-measured Cu coordination number in Figure 6.4) is plotted for the Cu-CHA-29 (green) Cu-CHA-17 (red) and Cu-CHA-15 (black) samples (left), and converted to Cu^{II} fraction (right) during transient reduction of NH$_3$-solvated Cu^{II}-dimer in 300 ppm NO and NH$_3$ each at 473 K.

The transient decay in Cu^{II} fraction with increasing time after NO+NH$_3$ exposure to Cu^{II}-dimer state is rapid (<15 sec) on all three Cu-CHA samples (Figure 6.11), consistent with proposed pathway (2c) of Cu^{II}-dimer reductively disproportionating to form Cu^{II}-nitrate and Cu^{I} in Figure 6.10. In order to further compare the kinetic relevances of Cu^{II}-dimer reduction step (with NO+NH$_3$) with other reaction steps like Cu^{II} reduction (with NO+NH$_3$) and Cu^{I} oxidation

(with O_2), initial rates of change of Cu oxidation state (or coordination number) are extracted from time-resolved transient reactions. It is worthwhile to note here that Cu^{II}-dimer reduction probed here is a non-elementary lumped reaction step, and therefore, only the initial rate of Cu^{II}-dimer reduction is compared as opposed to a rate constant. As can be seen from Table 6.7, initial rates of Cu^{II}-dimer reduction are directly proportional to Cu spatial density, and are equal to or less than initial rates of isolated Cu^{II} reduction and Cu^{I} oxidation steps. While Cu^{II}-dimer reduction is more rate-limiting than isolated Cu^{II} reduction step in the low Cu density regime (Cu-CHA-15-29), both Cu^{II}-dimer and isolated Cu^{II} reduction steps are rate-limiting in high Cu spatial density regime (Cu-CHA-15-17 and Cu-CHA-5-15) (Table 6.7).

Table 6.7 Comparison of initial rates of Cu^{II}-dimer reduction (with NO+NH$_3$), Cu^{II} reduction (with NO+NH$_3$) and Cu^{I} oxidation (with O_2) transient sequential steps with steady state turnover rates on Cu-CHA-29, Cu-CHA-17 and Cu-CHA-15 samples

Sample	Initial rate of Cu^{II}-dimer reduction[a]		Initial rate of Cu^{I} oxidation[b]		Initial rate of Cu^{II} reduction[c]	
	(mol m^{-3} s^{-1})	(s^{-1})	(mol m^{-3} s^{-1})	(s^{-1})	(mol m^{-3} s^{-1})	(s^{-1})
Cu-CHA-15-29	1.2	0.009	1.1	0.009	2.4	0.019
Cu-CHA-15-17	12.8	0.019	21.1	0.032	13.8	0.022
Cu-CHA-5-15	19.2	0.020	134.9	0.141	17.2	0.019

Initial rate is defined as rate of change of Cu oxidation state at t=0 from transient XAS
[a]computed from decrease in Cu^{II} (from conversion of Cu coordination number in EXAFS) during Cu^{II}-dimer reduction with NO+NH$_3$; initial rates have been corrected for different initial state prior to Cu^{II}-dimer reduction
[b]computed from decrease in Cu^{I} from transient XANES during Cu^{I}(NH$_3$)$_2$ oxidation with O_2
[c]computed from decrease in Cu^{II} from transient XANES during Cu^{II} reduction with NO+NH$_3$

6.4.3.5 Attempts to directly identify nitrates and other reaction intermediates

This section describes transient reactions monitored using *in situ* IR spectroscopy to characterize various possible surface intermediates under different gas conditions. This approach forces the catalyst to operate under conditions away from steady-state NO$_x$ SCR in order to isolate potential reactive intermediates that may otherwise be short-lived and undetectable during steady-state SCR catalysis. In the NH$_3$-solvated Cu^{II}-dimer state, IR spectra (1300 - 1800 cm^{-1}) shows signatures for NH$_3$ adsorbed on Cu sites (NH$_3$ on Cu^{II}: 1620 cm^{-1}; NH$_3$ on Cu^{I}: 1613 cm^{-1}; [10,15-17]) and NH$_3$ adsorbed on H$^+$ sites (NH$_4^+$: 1400 and 1450 cm^{-1} and (NH$_4^+$)(NH$_3$)$_n$: 1460 cm$^-$

[1;10]) (Figure 6.12). Another possible assignment of 1620 cm^{-1} may reflect presence of H_2O [16,18,19]; thus, this peak may reflect a combination of species due to NH_3 and H_2O.

The first set of experiments monitored the reaction intermediates during transient reaction of the dimeric Cu^{II} state with NO+NH$_3$ to form N$_2$ and H$_2$O. This resulted in changes to NH$_3$ on Cu (Cu^{II}/Cu^{I}) and NH$_3$ adsorbed on H$^+$ sites, which are difficult to deconvolute and interpret (Figure 6.12). However, no NO$_x$ intermediates (bridging nitrates: 1627, 1607 cm^{-1} and bidentate nitrates: 1570 cm^{-1} [15,20,21]) were observed during this reduction. In order to eliminate the possible overlapping contributions from co-adsorbed H$_2$O and NH$_3$, labelled NH$_3$ (i.e. ND$_3$) was also used, but NO$_x$ intermediates could still not be detected (appendix D).
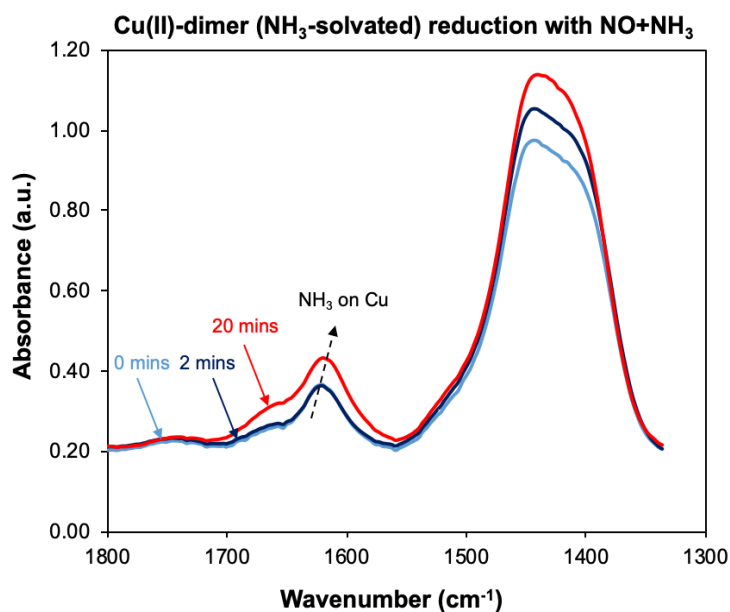
Figure 6.12 FTIR spectra collected on Cu-CHA-15-17 sample before and after NO+NH$_3$ exposure (300 ppm NO and NH$_3$ in He; 473 K) of Cu^{II}-dimer (NH$_3$-solvated)

The second set of experiments monitored the reaction intermediates during transient reaction of the dimeric Cu^{II} state with NO to form N$_2$ and H$_2$O. This resulted in nearly complete consumption of NH$_3$ on Cu (Cu^{II}/Cu^{I}), along with some changes to NH$_3$ adsorbed on H$^+$ sites, which are difficult to deconvolute and interpret (Figure 6.13). However, no NO$_x$ intermediates (bridging nitrates: 1627, 1607 cm^{-1} and bidentate nitrates: 1570 cm^{-1} [15,20,21]) were observed for both the cases of unlabelled NH$_3$ and labelled ND$_3$ (appendix D). This could be indicative of the short-lived nature of nitrate intermediates generated in presence of NH$_3$ due to fast reactions with NH$_3$, consistent with reports in the literature[22].
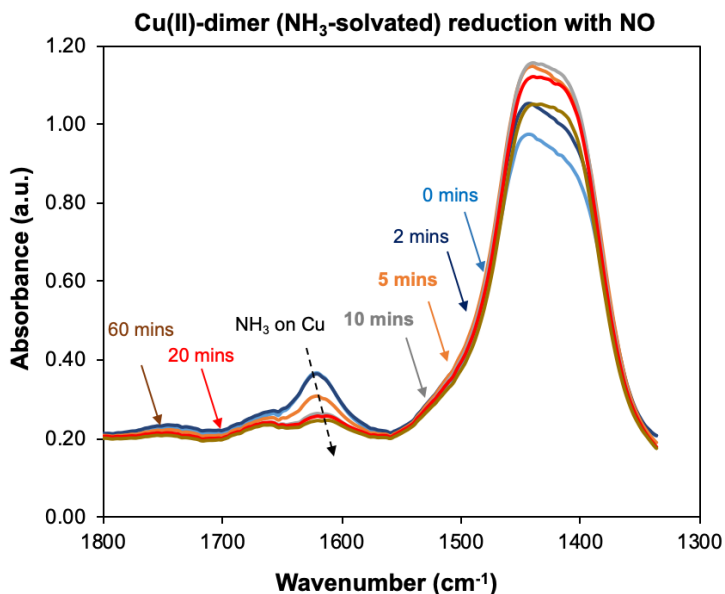
Figure 6.13 FTIR spectra collected on Cu-CHA-15-17 sample during NO exposure (300 ppm NO in He; 473 K) of Cu^{II}-dimer (NH_3-solvated)

In the NH_3-solvated Cu^{I} state, IR spectra (1300 - 1800 cm^{-1}) shows signatures for NH_3 adsorbed on Cu sites (NH_3 on Cu^{II}: 1620 cm^{-1}; NH_3 on Cu^{I}: 1613 cm^{-1}; [10,15-17]) and NH_3 adsorbed on H^+ sites (NH_4^+: 1400 and 1450 cm^{-1} and $(NH_4^+)(NH_3)_n$: 1460 cm^{-1};[10]) (Figure 6.14). For the next set of experiments, reaction intermediates are monitored during transient reaction of the NH_3-solvated Cu^{I} with $NO+O_2$ to form N_2 and H_2O. This resulted in consumption of surface NH_3 on Cu (Cu^{II}/Cu^{I}), along with relatively slower consumption of NH_3 adsorbed on H^+ sites (Figure 6.14). It is only upon complete consumption of NH_3 on Cu (Cu^{II}/Cu^{I}) that the surface nitrates (bridging nitrates: 1627, 1607 cm^{-1} and bidentate nitrates: 1570 cm^{-1};[15,20,21]) start accumulating on Cu sites. This likely indicates the short-lived nature of possibly generated Cu^{II}-nitrate intermediates (in $NO+O_2$) in presence of NH_3[22,23]. because Cu^{II}-nitrate intermediates (in $NO+O_2$) have been shown to react readily with NO/NH_3 to form mixed-ligand NH_3-solvated Cu^{II}-nitrate complexes at much lower temperature of 323 K as identified spectroscopically using IR, XAS and DRUV-Vis[24]. So, these mixed-ligand NH_3-solvated Cu^{II}-nitrate complexes could be the plausible reaction intermediates as also suggested to form during the most plausible Cu^{II}-dimer reductive disproportionation pathway (Figure 6.9), but they are just too reactive to detect in such analogous IR experiments at reaction temperature (473 K).
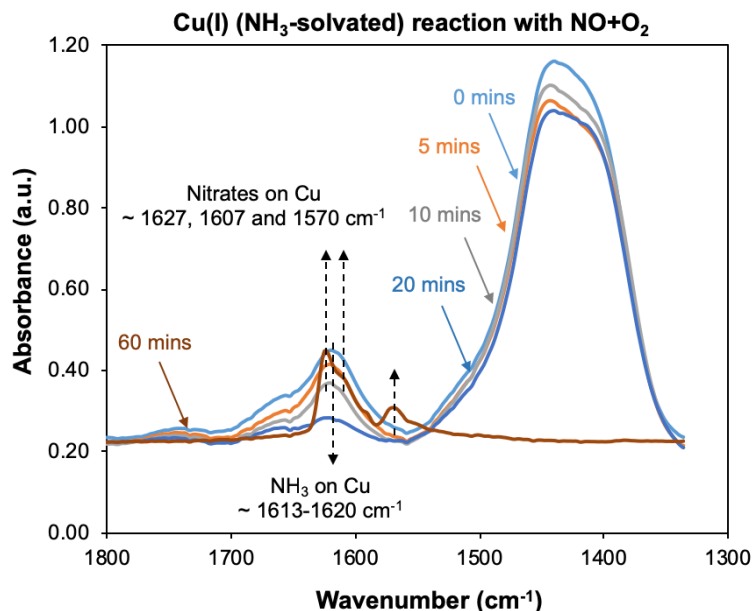
Figure 6.14 FTIR spectra collected on Cu-CHA-17 sample during NO+O$_2$ exposure (300 ppm NO and 10% O$_2$ in He; 473 K) of Cu^I (NH$_3$-solvated)

6.4.3.6 Confirming the short-lived nature of Cu-nitrates in presence of NH$_3$

In order to probe the reactivity of nitrates, the catalyst was exposed to certain conditions (300 ppm NO, 10% O$_2$ in balance He at 473 K) to isolate the formation of NO$_x$ intermediates (nitrate/nitrite). Observed NO$_x$ intermediates on Cu sites (bridging nitrates: 1627, 1607 cm^{-1} and bidentate nitrates: 1570 cm^{-1}; [15,20,21]) under these conditions suggests existence of commonly observed nitrate-nitrite equilibrium (equation 6.9) [4,25], wherein NO can reversibly reduce nitrate to nitrite and NO$_2$ (Figure 6.15)

$$Cu(II)NO_3^{2-} + NO \leftrightarrow Cu(II)NO_2^{-} + NO_2 \qquad\qquad (6.9)$$

Upon introduction of NH$_3$, these Cu-nitrates (Cu^{II}-NO$_3^{2-}$) are reacted off rapidly (< 60 sec) at 473 K (Figure 6.15), as opposed to the formation of relatively less reactive NH$_3$-solvated Cu^{II}-nitrate complexes upon reaction of NH$_3$ with Cu-nitrates at lower temperature of 323 K[24]. Such rapid disappearance of Cu-nitrates upon introduction of NH$_3$ likely indicates shifting of nitrate-nitrite equilibrium (equation 6.9) to the right[4,23]. Timescale for this Cu-nitrate$^-$ disappearance in presence of NH$_3$ is way shorter (20 sec) than SCR turnover (100 sec) corroborating the

hypothesized short-lived nature of plausible Cu-nitrate intermediates during the relevant transient reduction of Cu^{II}-dimer (NH_3-solvated) with $NO+NH_3$ (Figure 6.12). Such short-lived nature of Cu-nitrates in presence of NH_3 could be attributed to fast reaction of nitrite (from equation 6.9) with NH_3 to form $Cu^{II}(OH)$, N_2 and H_2O (equation 6.10), and accelerating the reduction of nitrates to nitrites i.e. shifting the equilibrium (equation 6.9) to the nitrite side during relevant steady state SCR catalysis.

$$Cu(II)NO_2^- + 2NH_3 \leftrightarrow (NH_3)_2Cu(II)NO_2^- \rightarrow (NH_3)Cu(II)(OH) + N_2 + 2H_2O \qquad \textbf{(6.10)}$$
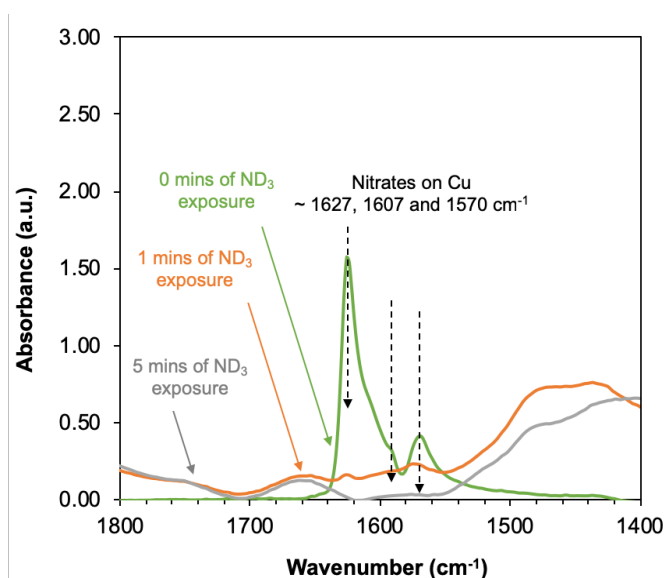
Figure 6.15 FTIR spectra collected on Cu-CHA-15-17 sample during ND_3 exposure (300 ppm ND_3 in He; 473 K) of catalyst surface covered with nitrates (300 ppm NO, 10% O_2 in balance He; 473 K)

6.4.3.7 Thermodynamic feasibility of proposed Cu^{II}-dimer reduction steps

Aforementioned reaction steps including the plausible reaction intermediates of Cu-nitrate (NH_3-solvated) and Cu-nitrite (NH_3-solvated) during complete Cu^{II}-dimer reduction with $NO+NH_3$ could be reconciled as follows:

1. Cu^{II}-dimer reductive disproportionation to yield a mixture of $Cu^{II}(NO_3)^-$ (NH_3-solvated) and Cu^I (NH_3-solvated)

2. Reduction of Cu^{II}-nitrate with NO to yield $Cu^{II}(NO_2)^-$ (NH_3-solvated) and NO_2

3. Reduction of Cu^{II}-nitrite (NH_3-solvated) to $Cu^{II}(OH)$ (NH_3-solvated)

4. Reduction of $Cu^{II}(OH)$ (NH_3-solvated) to $Cu(I)$ (NH_3-solvated)

Energetics have been calculated using DFT computations (details of energetics calculations in appendix D) to probe the thermodynamic feasibility of the above sequential reaction steps, as shown below:
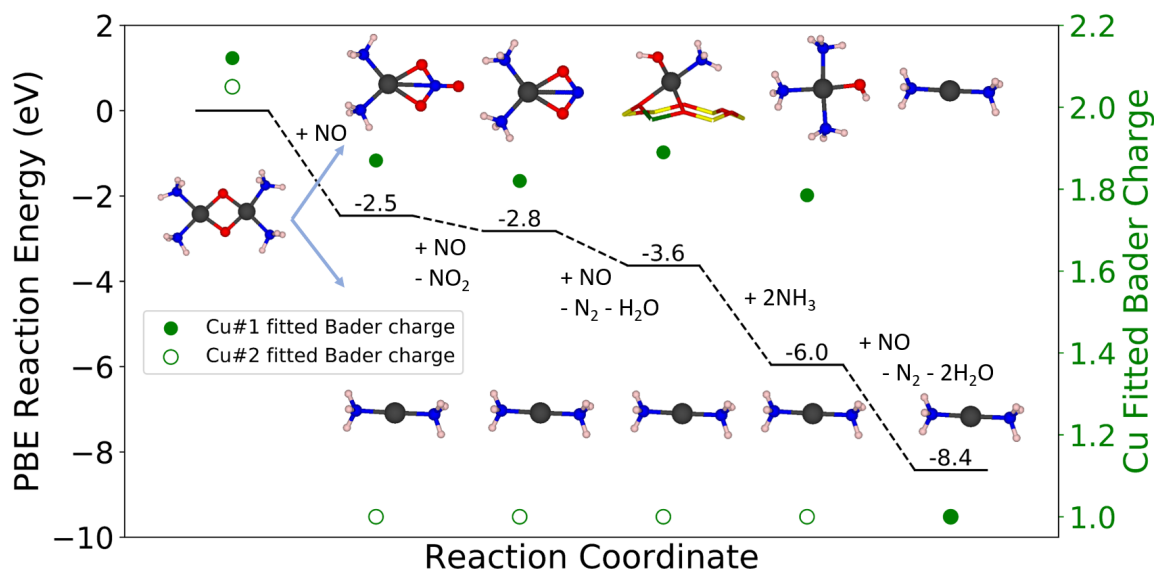
Figure 6.16 DFT-computed energetics for the most plausible pathway 2c

6.4.4 Proposed SCR mechanism

It was previously proposed that $Cu^{II} \rightarrow Cu^{I}$ reduction occurs via. NO-assisted NH_3 dissociation[2,5]. This step starts from NH_3-saturated Cu^{II} identified experimentally (XAS) and computationally (DFT), followed by attack of NO on a Cu-bound NH_3 to form an N−N bond[5]. This process proceeds via. proton transfer to an acceptor and an electron to Cu, leaving an H_2NNO intermediate that can decompose to form N_2 and H_2O as follows[5]:

$$Cu(II) + 4NH_3 \leftrightarrow (NH_3)_4Cu(II) \tag{6.11}$$

$$(NH_3)_4Cu(II) + NO \rightarrow Cu(I)(NH_3)_3(H_2NNO) + H^+ \tag{6.12}$$

$$Cu(I)(NH_3)_3(H_2NNO) \rightarrow Cu(I)(NH_3)_2|NH_4^+ + N_2 + H_2O \tag{6.13}$$
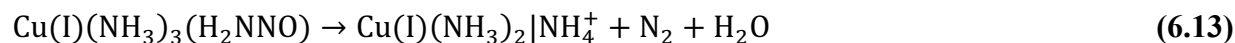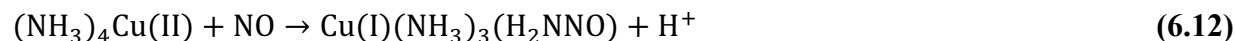
In the case of isolated $[Cu^{II}OH]^+$ site, the Cu−OH ligand acts as the proton acceptor, to form an extra H_2O molecule as follows[5]:

$$Cu(II)(OH) + 3NH_3 \leftrightarrow (NH_3)_3Cu(II)(OH) \tag{6.14}$$

$$(NH_3)_3Cu(II)(OH) + NO \rightarrow Cu(I)(NH_3)_2(H_2NNO) + H_2O \tag{6.15}$$

$$Cu(I)(NH_3)_2(H_2NNO) \rightarrow Cu(I)(NH_3)_2 + N_2 + H_2O \tag{6.16}$$
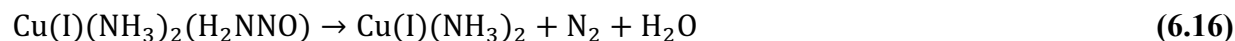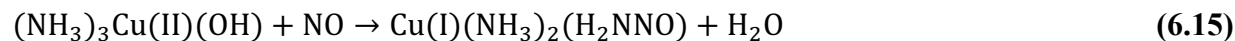
It has been shown that re-oxidation of Cu^I occurs via. diffusion and pairing of two mobile $Cu^I(NH_3)_2$ species with O_2 to form dimeric Cu intermediate as follows[6]:

$$2Cu(I)(NH_3)_2 + O_2 \rightarrow (NH_3)_2Cu(II)(O_2)Cu(II)(NH_3)_2 \tag{6.17}$$
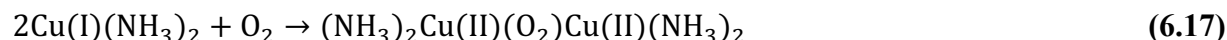
Herein, we propose that dimeric Cu intermediate reductively disproportionates with $NO+NH_3$ to yield a mixture of $Cu^{II}(NO_3)^-$ (NH_3-solvated) and Cu^I (NH_3-solvated) as follows:

$$(NH_3)_2Cu(II)(O_2)Cu(II)(NH_3)_2 + NO \rightarrow (NH_3)_2Cu(II)NO_3^- + Cu(I)(NH_3)_2 \tag{6.18}$$
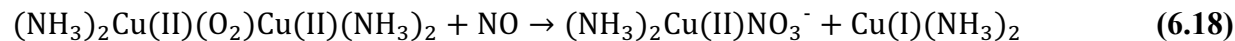
We speculate that $Cu^{II}(NO_3)$ (NH_3-solvated) can be reduced by NO to yield $Cu^{II}(NO_2)^-$ (NH_3-solvated) and NO_2. Such reduction of $Cu^{II}(NO_3)^-$ (NH_3-solvated) by NO has been well documented previously in the literature[25].

$$(NH_3)_2Cu(II)NO_3^- + NO \leftrightarrow (NH_3)_2Cu(II)NO_2^- + NO_2 \tag{6.19}$$
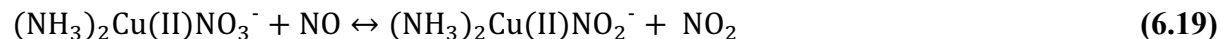
We recall the observed potential involvement of NH_4^+ ions in the mechanism and NO overconsumption in presence of excess NH_3 (Figure 6.5), we propose that formed NO_2 (+NO) can react on NH_4^+ ions via. fast SCR, which has been previously proposed on H-SSZ-13[14]. Also, the reported fast SCR rates (on H-SSZ-13; 473 K) are comparable (same order of magnitude) to standard SCR rates (on Cu-SSZ-13; 473 K) [14]

$$NO_2 + NO + 2NH_3(NH_4^+) \leftrightarrow 4N_2 + 3H_2O \tag{6.20}$$

Further reduction of $Cu^{II}(NO_2)^-$ (NH_3-solvated) to $Cu^{II}(OH)$ can occur via. numerous pathways including gas phase NH_3 reacting with $Cu^{II}(NO_2)^-$ (bimolecular reaction), or adsorbed NH_3 reacting with $(NO_2)^-$ on $Cu^{II}(NO_2)^-$ (unimolecular reaction).

$$(NH_3)_2Cu(II)NO_2^- \leftrightarrow (NH_3)_1Cu(II)(OH) + N_2 + H_2O \qquad \textbf{(6.21)}$$
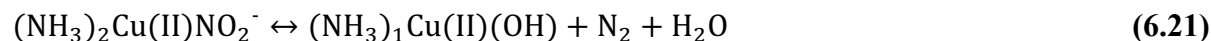
Coupling all the proposed elementary/lumped reaction steps together
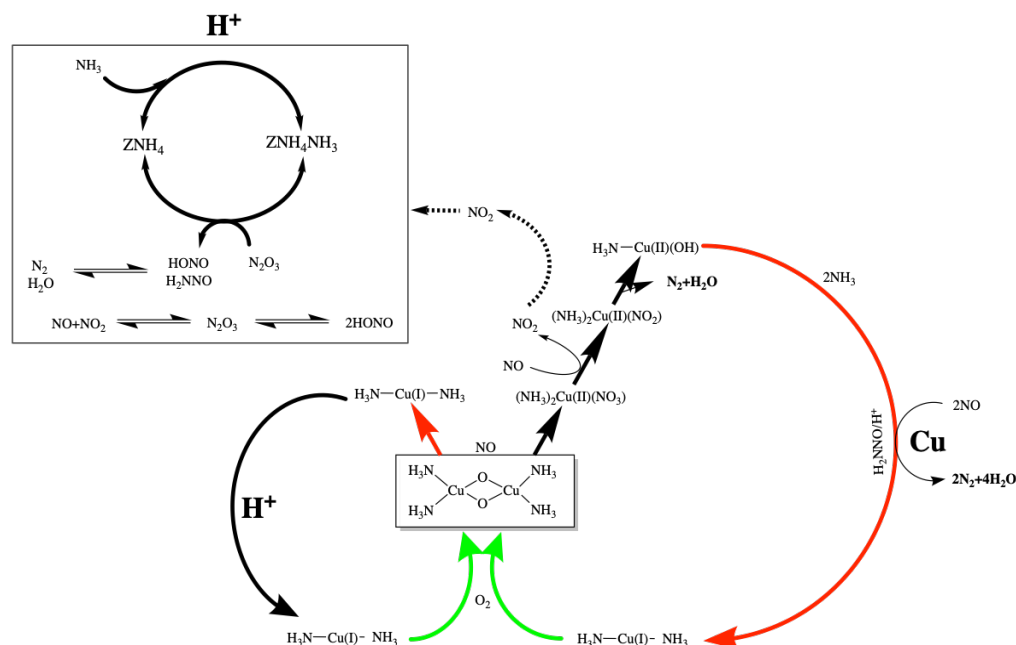
Figure 6.17 Proposed low temperature standard SCR reaction mechanism

6.5 Conclusions

Previously unrecognized kinetic behavior and Cu site requirements for Cu^{II} and Cu^{II}-dimer reaction with $NO+NH_3$ have been revealed with the aid of monitoring Cu chemical nature during steady state and transient sequential reaction. While it was shown that isolated Cu^{II} undergoes single-site reduction to give $Cu^{I}(NH_3)_2$, dimeric Cu intermediate was found to undergo reductive disproportionation with $NO+NH_3$ to yield a mixture of Cu^{II} and Cu^{I} intermediates, which eventually reduces completely to give $Cu^{I}(NH_3)_2$. The rate of this Cu^{II}-dimer reductive disproportionation is comparable (same order of magnitude) to rates of subsequent Cu^{II} reduction and Cu^{I} oxidation steps, establishing the relevance of this step during steady state SCR. NO consumption stoichiometry during proposed Cu^{II}-dimer reductive

disproportionation was shown to be consistent with overall reaction stoichiometry. Further with the aid of FTIR spectroscopy, speculations have been made on involvement of Cu-nitrate/nitrite intermediates and NH_3 storage $NH_4^+(H^+)$ sites during Cu^{II}-dimer disproportionation. Coupling these new findings of Cu^{II}-dimer reductive disproportionation (via. formation and reaction of nitrate/nitrite) and speculated role of NH_3 storage NH_4^+ sites (via. parallel fast SCR pathway) along with previously established reaction steps, complete reaction mechanism scheme is laid out. Few important implications of this newly proposed complete mechanism scheme as follows:

○ Bifunctional nature, i.e. direct involvement of Cu as well as NH_4^+/H^+ sites, opens the avenue to optimize the Cu loading to maximize the SCR reactivity

○ Detailed molecular level reaction network (mechanism) leads the way to potential microkinetic and global kinetic modeling

○ Helps with better understanding/interpretation of experimentally measured reaction kinetics

6.6 Methods

6.6.1 Synthesis and Characterization

6.6.1.1 Synthesis of H-CHA zeolites

Synthesis of H-SSZ-13 zeolites with Si/Al 4.5 and 15 was done as previously reported in the above chapters 2 and 3.

6.6.1.2 X-Ray diffraction of CHA zeolites

The CHA crystal framework was determined from powder X-ray diffraction (XRD) patterns collected as previously reported in the above chapters 2 and 3.

6.6.1.3 Adsorption isotherms to measure micropore volumes of CHA zeolites

Micropore volumes of CHA zeolites were determined from Ar adsorption isotherms measured as previously reported in the above chapters 2 and 3.

6.6.1.4 Aqueous-phase Copper Ion-Exchange of H-SSZ-13

Cu-SSZ-13 zeolites were prepared by aqueous-phase Cu ion-exchange as previously reported in the above chapters 2 and 3.

6.6.1.5 Elemental Analysis using Atomic Absorption Spectroscopy

Bulk elemental composition (Si, Al and Cu in H-CHA and Cu-CHA) was determined using atomic absorption spectroscopy (AAS) as previously reported in the above chapter 3.

6.6.1.6 Cu site characterization and quantification

Cu sites were characterized using Cu K-edge X-ray absorption near edge spectroscopy (XANES) and o UV-Visible spectroscopy as previously reported in the above chapters 2 and 3. Further enumeration of isolated Cu^{II} and $Cu^{II}OH$ sites on each Cu-CHA zeolite was determined after oxidative treatment (20% O_2, 773 K) by quantifying the number of residual protons that remained after Cu exchange, as previously reported in the above chapter 3.

6.6.2 X-ray Absorption Spectroscopy (XAS)

More generic details about X-ray absorption spectroscopy have been illustrated in above chapters 2 and 3.

6.6.2.1 *Operando* XAS experiments

Operando experiments were performed in a special glassy carbon tube reactor, and the details of the custom *operando* XAS reactor setup were described in above chapters 2 and 3.

6.6.2.2 Transient XAS experiments

Reduction of mononuclear NH_3-solvated Cu^{II} sites with $NO+NH_3$

First, Cu-CHA samples in their mononuclear Cu^{II} states were obtained by high temperature oxidation treatment (10% O_2, balance He, 500 ml min^{-1}, 773 K, 30 mins). Samples were then cooled to 473 K, followed by removal of O_2 from the gas stream, while the reductant mixture (300 ppm NO, 300 ppm NH_3, balance He, 500 ml min^{-1}) was flowed in a bypass line. The reductant mixture was then switched from the bypass to the reactor in order to reduce Cu^{II} sites to $Cu^{I}(NH_3)_2$ at 473 K. The fraction of Cu^{I} and Cu^{II} sites during transient reduction experiments were monitored by collecting XAS spectra in quick scan mode from 8700 to 9700 eV. Each spectrum took 1 min 48 s to collect, with a step size of 0.5 eV and a dwell time of 0.05 s.

Oxidation of mononuclear NH$_3$-solvated Cu^I sites with O$_2$

After the reduction treatments at 473 K, Cu-CHA samples contained predominantly Cu^I(NH$_3$)$_2$. Next, NO was removed from the gas stream, followed by removal of NH$_3$ from the gas stream, while the oxidant stream (10% O$_2$, balance He) was flowed in a bypass line. Once the concentration of NO and NH$_3$ reductants were each less than 5 ppm, the oxidant gas stream was switched from the bypass line to the reactor, in order to oxidize the Cu^I(NH$_3$)$_2$ species present, a larger fraction of which are reported to oxidize with increasing Cu ion spatial density. The fractions of Cu^I and Cu^{II} sites during transient oxidation experiments were monitored by collecting XAS spectra in quick scan mode from 8700 to 9700 eV. Each spectrum took 1 min 48 s to complete, with a step size of 0.5 eV and a dwell time of 0.05 s.

Reactions of binuclear NH$_3$-solvated Cu^I intermediates with NO+NH$_3$

After the oxidation treatments at 473 K, Cu-CHA samples contained a mixture of NH$_3$-solvated mononuclear Cu(I) species and NH$_3$-solvated binuclear O$_2$-bridged Cu^{II} species. Next, O$_2$ was removed from the gas stream, while the reductant mixture (300 ppm NO, 300 ppm NH$_3$, balance He, 500 ml min^{-1}) was flowed in a bypass line. The reductant mixture was then switched from the bypass line to the reactor, in order to allow NH$_3$-solvated binuclear O$_2$-bridged Cu^{II} species to react in the presence of NO and NH$_3$. The fractions of Cu^I and Cu^{II} fractions during these transient experiments were monitored by collecting XAS spectra in quick scan mode from 8700 to 9700 eV. Each spectrum took 1 min 48 s to complete, with a step size of 0.5 eV and a dwell time of 0.05 s.

6.6.3 NO titration experiments to probe reaction stoichiometry

The consumption of NO (per Cu) in sequential SCR reaction steps on Cu-CHA samples was measured and used to corroborate the reaction stoichiometry depicted in Figure 6.10. Typically, 10 to 20 mg of sample was loaded into the reactor system used to measure steady-state SCR kinetics. The total gas flow rate used in the following procedure was 600 mL min^{-1}. The Cu-CHA samples in Figure 6.10 were first oxidized and dehydrated to their Cu^{II} form by treatment to 823 K (0.167 K s^{-1}) in flowing 20% O$_2$ (99.5%, Indiana Oxygen) in balance He (99.999%, Indiana Oxygen), and then cooling to 473 K. The sample was then held flowing He for 30 minutes, and then fully reduced in a mixture of 300 ppm NO (3.5% NO in Ar, Praxair)

and 300 ppm NH_3 (3.0% NH_3 in Ar, Praxair) in balance He. Following reduction of Cu sites to their $Cu^I(NH_3)_2$ states (corresponding to 6 o'clock positions in Figure 6.10), the samples were exposed to flowing 10% O_2 in balance He until steady-state was achieved (corresponding to the central position in Figure X). The O_2 oxidized sample was then held in a flowing stream of 300 ppm of NO in balance He, until steady-state was achieved. The O_2 oxidized sample was also held in a flowing stream of mixture of 300 ppm NO and 300 ppm NH_3 in balance He in a separate experiment, to completely reduce the sample back to $Cu^I(NH_3)_2$ (corresponding to 6 o'clock positions in Figure 6.10).

Each of these sequential treatments was also performed in a blank reactor to measure a baseline signal in the FTIR spectrometer (MKS Multigas TM 2030) used to account for gas holdup and residence time in the reactor setup (NO conversion was not detected in the blank reactor), in order to calculate the NO consumption from the Cu-CHA catalyst during each treatment step.

6.6.4   Transient FTIR experiments to probe reaction intermediates

FTIR data were collected on zeolite samples using a Nicolet 6700 FTIR spectrometer equipped with a liquid nitrogen-cooled HgCdTe (MCT) detector. Catalyst samples (ca. 40-50 mg) were pressed into a self-supporting wafer (ca. 2 cm in diameter) and placed in a custom-built FTIR cell that has been described elsewhere [REF]. Wafers were treated in flowing oxygen (10% O_2, balance He) to 673 K for 30 min and then cooled to 473 K, prior to the exposure to SCR gases. Spectra were collected with a resolution of 4 cm^{-1} and averaged over 36 scans and baseline corrected.

Sample was then reduced with 300 ppm of NO+NH_3 at 473 K till the point when there is no further change in the spectra collected. This was followed by NO and NH_3 cut-off. Different reactants (including 300 ppm NO or 300 ppm NO + 10% O_2 or 300 ppm NO after 10% O_2 in balance He, total flow of 50 mL min^{-1}) were flowed at 473 K and a series of time resolved IR spectra was collected during each gas flows.

<u>Reaction of $Cu^I(NH_3)_2$ sites with NO+O_2</u>

Following the complete reduction of Cu^{II} sites with NO+NH_3 to $Cu^I(NH_3)_2$ at 473 K, NO was first cut-off followed by NH_3 from the gas stream, while oxidizing reaction mixture (300 ppm

NO, 10% O_2, balance He) was being prepared through the bypass. After approximately 2 mins to flush out gas phase NO and NH_3, oxidizing gas stream (300 ppm NO, 10% O_2, balance He, 50 ml min^{-1}) was switched from bypass to reactor in order to react $Cu^I(NH_3)_2$ with NO+O_2, while monitoring temporal changes to FTIR spectra.

Reaction of Cu^{II}-dimer intermediate with NO+NH_3

Following the O_2 oxidation of $Cu^I(NH_3)_2$ to Cu^{II}-dimer (NH_3-solvated) at 473 K, O_2 was cut-off from the gas stream, while reaction mixture (300 ppm NO, 300 ppm NH_3, balance He,500 ml min^{-1}) was being prepared through the bypass. Reaction mixture was then switched from bypass to reactor in order to react Cu^{II}-dimer (NH_3-solvated) with NO+NH_3, while monitoring temporal changes to FTIR spectra.

Reaction of Cu^{II}-dimer intermediate with NO

Following the O_2 oxidation of $Cu^I(NH_3)_2$ to Cu^{II}-dimer (NH_3-solvated) at 473 K, $O_2$was cut-off from the gas stream, while reaction mixture (300 ppm NO, balance He, 500 ml min^{-1}) was being prepared through the bypass. Reaction mixture was then switched from bypass to reactor in order to react Cu^{II}-dimer (NH_3-solvated) with NO, while monitoring temporal changes to FTIR spectra.

6.7   References

[1]   V.F. Kispersky, A.J. Kropf, F.H. Ribeiro, J.T. Miller, Low absorption vitreous carbon reactors for operando XAS: a case study on Cu/Zeolites for selective catalytic reduction of NO x by NH 3 w, Phys. Chem. Chem. Phys. Phys. Chem. Chem. Phys. 14 (2012) 2229–2238. doi:10.1039/c1cp22992c.

[2]   C. Paolucci, A.A. Verma, S.A. Bates, V.F. Kispersky, J.T. Miller, R. Gounder, et al., Isolation of the Copper Redox Steps in the Standard Selective Catalytic Reduction on Cu-SSZ-13 **, (2014) 12022–12027. doi:10.1002/ange.201407030.

[3]   J.S. McEwen, T. Anggara, W.F. Schneider, V.F. Kispersky, J.T. Miller, W.N. Delgass, et al., Integrated operando X-ray absorption and DFT characterization of Cu-SSZ-13 exchange sites during the selective catalytic reduction of NO x with NH 3, Catal. Today. 184 (2012) 129–144. doi:10.1016/j.cattod.2011.11.037.

[4]   T.V.W. Janssens, H. Falsig, L.F. Lundegaard, P.N.R. Vennestrøm, S. Rasmussen, P.G. Moses, et al., A consistent reaction scheme for the selective catalytic reduction of nitrogen oxides with ammonia, ACS Catal. (2015) 150319102200004. doi:10.1021/cs501673g.

[5]   C. Paolucci, A.A. Parekh, I. Khurana, J.R. Di Iorio, J. Albarracin, A. Shih, et al., Catalysis in a Cage : Condition-Dependent Speciation and Dynamics of Exchanged Cu Cations in SSZ-13 Zeolites, J. Am. Chem. Soc. (2016) 1–63. doi:10.1021/jacs.6b02651.

[6]   C. Paolucci, I. Khurana, A.A. Parekh, S. Li, A.J. Shih, H. Li, et al., Dynamic multinuclear sites formed by mobilized copper ions in NOx selective catalytic reduction, 903 (2017) 898–903.

[7]   F. Gao, D. Mei, Y. Wang, J. Szanyi, C.H.F. Peden, F. Gao, et al., Selective Catalytic Reduction over Cu / SSZ-13 : Linking Homo- and Heterogeneous Catalysis Selective Catalytic Reduction over Cu / SSZ-13 : Linking Homo- and Heterogeneous Catalysis, (2017). doi:10.1021/jacs.7b01128.

[8]   S. Kieger, G. Delahay, B. Coq, B. Neveu, Selective catalytic reduction of nitric oxide by ammonia over Cu-FAU catalysts in oxygen-rich atmosphere, J. Catal. 183 (1999) 267–280. doi:DOI: 10.1006/jcat.1999.2398.

[9]   A. Marberger, A.W. Petrov, P. Steiger, M. Elsener, O. Kröcher, M. Nachtegaal, et al., Time-resolved copper speciation during selective catalytic reduction of NO on Cu-SSZ-13, Nat. Catal. 1 (2018) 221–227. doi:10.1038/s41929-018-0032-6.

[10]   F. Giordanino, E. Borfecchia, K. a. Lomachenko, A. Lazzarini, G. Agostini, E. Gallo, et al., Interaction of NH3 with Cu-SSZ-13 catalyst: A complementary FTIR, XANES, and XES study, J. Phys. Chem. Lett. 5 (2014) 1552–1559. doi:10.1021/jz500241m.

[11]   K.A. Lomachenko, E. Borfecchia, C. Negri, G. Berlier, C. Lamberti, P. Beato, et al., The Cu-CHA deNO $_x$ catalyst in action: temperature-dependent NH $_3$ -SCR monitored by *operando* X-ray absorption and emission spectroscopies, J. Am. Chem. Soc. (2016) jacs.6b06809. doi:10.1021/jacs.6b06809.

[12]   L. Chen, H. Falsig, T.V.W. Janssens, H. Grönbeck, Activation of oxygen on (NH 3 ACuANH 3) + in NH 3 -SCR over Cu-CHA, 358 (2018) 179–186. doi:10.1016/j.jcat.2017.12.009.

[13]   H. Falsig, P.N.R. Vennestrøm, P.G. Moses, T.V.W. Janssens, Activation of Oxygen and NO in NH3-SCR over Cu-CHA Catalysts Evaluated by Density Functional Theory, Top. Catal. DOI 10.100 (2016). doi:10.1007/s11244-016-0560-8.

[14]   S. Li, Y. Zheng, F. Gao, J. Szanyi, W.F. Schneider, Experimental and Computational Interrogation of Fast SCR Mechanism and Active Sites on H-Form SSZ-13, ACS Catal. 7 (2017) 5087–5096. doi:10.1021/acscatal.7b01319.

[15]   K. Hadjiivanov, Use of overtones and combination modes for the identification of surface NOx anionic species by IR spectroscopy, Catal. Letters. (2000).

[16]   K. Hadjiivanov, D. Klissurski, G. Ramis, G. Busca, Fourier transform IR study of NOx adsorption on a CuZSM-5 DeNOx catalyst, Appl. Catal. B Environ. (1996). doi:10.1016/0926-3373(95)00034-8.

[17]   F. Yin, A.L. Blumenfeld, V. Gruver, J.J. Fripiat, NH 3 as a Probe Molecule for NMR and IR Study of Zeolite Catalyst Acidity , J. Phys. Chem. B. (2002). doi:10.1021/jp9618542.

[18]   A. Jentys, G. Warecka, J.A. Lercher, Surface chemistry of H-ZSM5 studied by time-resolved IR spectroscopy, J. Mol. Catal. (1989). doi:10.1016/0304-5102(89)80010-0.

[19]   A. Jentys, G. Warecka, M. Derewinski, J.A. Lercher, Adsorption of water on ZSM 5 zeolites, J. Phys. Chem. (2005). doi:10.1021/j100349a032.

[20] F. Poignant, J.L. Freysz, M. Daturi, J. Saussey, Mechanism of the selective catalytic reduction of NO in oxygen excess by propane on H-Cu-ZSM-5 - Formation of isocyanide species via acrylonitrile intermediate, Catal. Today. (2001). doi:10.1016/S0920-5861(01)00418-7.

[21] K.I. HADJIIVANOV, Identification of Neutral and Charged $N_x O_y$ Surface Species by IR Spectroscopy, Catal. Rev. 42 (2000) 71–144. doi:10.1081/CR-100100260.

[22] M.P. Ruggeri, T. Selleri, M. Colombo, I. Nova, E. Tronconi, Investigation of NO2 and NO interaction with an Fe-ZSM-5 catalyst by transient response methods and chemical trapping techniques, J. Catal. 328 (2015) 258–269. doi:10.1016/j.jcat.2015.02.003.

[23] T. Selleri, M.P. Ruggeri, I. Nova, E. Tronconi, The Low Temperature Interaction of NO + O2 with a Commercial Cu-CHA Catalyst: A Chemical Trapping Study, Top. Catal. 59 (2016) 678–685. doi:10.1007/s11244-016-0543-9.

[24] C. Negri, E. Borfecchia, M. Cutini, K.A. Lomachenko, T.V.W. Janssens, G. Berlier, et al., Evidence of mixed-ligand complexes in Cu-CHA by reaction of Cu nitrates with NO/NH3 at low temperature, ChemCatChem. (2019) cctc.201900590. doi:10.1002/cctc.201900590.

[25] C. Tyrsted, E. Borfecchia, G. Berlier, K.A. Lomachenko, C. Lamberti, S. Bordiga, et al., Nitrate–nitrite equilibrium in the reaction of NO with a Cu-CHA catalyst for NH_3-SCR, Catal. Sci. Technol. 6 (2016) 8314–8324. doi:10.1039/C6CY01820C.

[26] F. Gao, N.M. Washton, Y. Wang, M. Kollár, J. Szanyi, C.H.F. Peden, Effects of Si/Al ratio on Cu/SSZ-13 NH3-SCR catalysts: Implications for the active Cu species and the roles of Brønsted acidity, J. Catal. 331 (2015) 25–38. doi:10.1016/j.jcat.2015.08.004.

[27] M. Colombo, I. Nova, E. Tronconi, Detailed kinetic modeling of the NH 3-NO/NO 2 SCR reactions over a commercial Cu-zeolite catalyst for Diesel exhausts after treatment, Catal. Today. 197 (2012) 243–255. doi:10.1016/j.cattod.2012.09.002.

[28] K. Rahkamaa-Tolonen, T. Maunula, M. Lomma, M. Huuhtanen, R.L. Keiski, The effect of NO2 on the activity of fresh and aged zeolite catalysts in the NH3-SCR reaction, Catal. Today. 100 (2005) 217–222. doi:10.1016/j.cattod.2004.09.056.

[29] S. Shwan, J. Jansson, L. Olsson, M. Skoglundh, Chemical deactivation of H-BEA and Fe-BEA as NH3-SCR catalysts-effect of potassium, Appl. Catal. B Environ. 166–167 (2015) 1–10. doi:10.1016/j.apcatb.2014.11.042.

7.   CATALYTIC CONSEQUENCES OF FRAMEWORK AL SPATIAL DENSITY IN CU-SSZ-13 ZEOLITE ON STANDARD SCR KINETICS

7.1   Preface

Chapter 7 contains the most recent draft of a manuscript in preparation. This chapter studies different types of effects of zeolite framework Al spatial density (Si/Al) on observed standard SCR kinetics. It also decouples the contribution from different Al spatial density effects on measured overall SCR kinetics, thereby enhancing our understanding of role of zeolite support parameters in affecting standard SCR.

7.2   Abstract

In this work, we report that increasing zeolite framework Al spatial density has an overall promotional effect on steady state SCR kinetics. Residual NH_4^+ ions (anchored to framework Al sites) may facilitate the $Cu^I \rightarrow Cu^{II}$ oxidation step in Cu^{II} - Cu^I redox SCR mechanism, and may serve as storage sites for reactive NH_3 used in $Cu^{II} \rightarrow Cu^I$ reduction steps. We further studied these effects by perturbing the catalyst to operate in either $Cu^{II} \rightarrow Cu^I$ reduction-limited or $Cu^I \rightarrow Cu^{II}$ oxidation-limited regime. Understanding the origin of effects of zeolite framework Al spatial density would enable improved interpretation of observed SCR kinetic differences, and open avenues to further optimize catalyst structural parameters to improve SCR performance. Framework Al spatial density in Cu-SSZ-13 was altered by varying Si/Al ratio. Synthetic, spectroscopic and kinetic techniques have been employed to study the promotional effect of zeolite framework Al spatial density in Cu-SSZ-13 on kinetics of selective catalytic reduction (SCR) of NO_x with ammonia.

7.3   Introduction

Isolated Cu cationic sites, viz. Cu^{II} charge compensated by two framework Al sites and $[Cu^{II}(OH)]^+$ charge compensated by one framework Al site, have been shown to be precursors to the active sites for low temperature SCR.[1] These isolated Cu sites were found to be mobile due to NH_3 solvation during low temperature SCR, with Cu^{II} existing as $Cu^{II}(NH_3)_4$ and $[Cu^{II}(OH)]^+$ existing as $Cu^{II}(OH)(NH_3)_3$. Additionally, Cu^{II} and Cu^I intermediates were found to exist under

steady state reaction conditions in NH_3-solvated state, provided Cu^{II} - Cu^{I} redox nature of reaction mechanism. Mobility of $Cu^{I}(NH_3)_2$ was discovered to be a key parameter, as Cu^{I} re-oxidation occurs via. $Cu^{I}(NH_3)_2$ diffusion and pairing.[2,3]

Due to dynamic nature of Cu sites, catalyst composition parameters affecting the Cu site mobility need to be considered to enhance the SCR reactivity. As indicated in our previous work[2], catalyst design parameters to regulate Cu site mobility, other than Cu spatial density, would be the support structure (type of zeolite support – pore size and channel interconnectivity), electronic conductivity, composition (framework Al spatial density and distribution), and the molecules that solvate such sites. Among all these design parameters, varying framework Al spatial density of the zeolite support seems to be the most simple and convenient one.

There are only a few reports discussing the effect of framework Al density on Cu mobility, and in turn affecting SCR kinetics. In line with how framework Al can play a role in facilitating Cu mobility and pairing, a specific framework Al distribution in Cu-SSZ-13 (with an intermediate Al-Al distance about 7.5 Å) was shown to be most favorable for Cu-pair formation due to balance of electrostatic Coulomb interactions[4], solely with the aid of DFT and *ab-initio* molecular dynamics simulations. Furthermore, with the help of in situ electrical impedance spectroscopy (IS) to measure conductivity of zeolite catalysts, framework Al anchored NH_4^+ and $NH_4^+(NH_3)_n$ complexes were found to provide additional paths or carriers for proton transport, which consequently increase the proton conductivity, further facilitating the diffusion/mobility of NH_3-solvated Cu sites[5–7]. However, experimental evidence is needed for the effects of framework Al spatial density on Cu mobility, and in turn affecting SCR kinetics. Additionally, it was suggested that framework Al density (acid site density) can directly affect SCR kinetics by NH_4^+ sites acting as a reservoir for weakly bound NH_3 (needed for NO consumption) based on observed linear correlation between framework Al density (acid site density) and SCR rate[8]. However, such proposed effects of framework Al density (acid site density) on SCR kinetics could be convoluted with effects of framework Al anchored NH_4^+ ions promoting Cu^{I} mobility/diffusion. This could also be masked by kinetics measured under different kinetic regimes (Cu^{I} oxidation- and Cu^{II} reduction-limited regimes). Therefore, there is a need to isolate and elucidate different types of effects of framework Al density on SCR kinetics.

Herein, different types of effects of framework Al spatial density in Cu-SSZ-13 zeolite on SCR kinetics have been investigated experimentally. Promotional effects of framework Al spatial density on steady state SCR kinetics were decoupled into contributions from residual NH_4^+/H^+ ions anchored to framework Al sites facilitating Cu mobility by comparison of $Cu^I \rightarrow Cu^{II}$ oxidation kinetics, and residual NH_4^+/H^+ ions anchored to framework Al sites participating in NO consumption step of SCR mechanism as isolated by by operating the catalyst in $Cu^{II} \rightarrow Cu^I$ reduction-limited regime.

7.4   Results and Discussion

Here, we study the effects of zeolite framework Al spatial density in Cu-SSZ-13 on SCR kinetics. First, three model Cu-SSZ-13 samples with same spatial density of isolated Cu sites (present either as Cu^{II} at paired framework Al sites or as $[Cu^{II}OH]^+$ at isolated Al sites), but varying spatial density of framework Al sites (Si/Al 5, 15 and 25), were chosen (Table 7.1), as representatives from a broader Cu-SSZ-13 sample set reported in our previous study[2]. These samples are denoted Cu-CHA-X-Y, where X refers to the Si/Al ratio and Y refers to the mean Cu-Cu distance in Å, as estimated assuming a homogeneous distribution of Cu throughout the zeolite crystallite volume as done in Paolucci et al.[2]. Relevant structural and site characterization of these model samples are provided in Table 7.2, including bulk elemental analysis, the number of isolated Cu^{II} and $[Cu^{II}OH]^+$ sites (per Al), the concentration of Cu ions per crystallite volume, concentration of Al per crystallite volume and residual NH_4^+/Al.

Table 7.1 Standard SCR kinetics parameters on Cu-exchanged SSZ-13 samples with Si/Al = 5, 15 and 25 and Cu/Al varying from 0.03-0.44. (Y = Mean Cu-Cu distance in Å, X = Si/Al)

Cu-CHA-X-Y	Cu /1000Å^3	SCR Rate (/10^{-3} mol NO/mol Cu/s)	SCR Rate (/10^{-3} NO/1000Å^3/s)	O_2 order[†]	NO order[†]	NH_3 order[†]
Cu-CHA-5-20	0.23	8.1	4.85	0.2	0.8	0.0
Cu-CHA-5-15	0.58	8.4	1.78	0.2	0.9	0.0
Cu-CHA-15-40	0.03	1.8	0.05	0.8	0.4	-0.5
Cu-CHA-15-29	0.07	2.3	0.16	0.7	0.4	-0.5
Cu-CHA-15-27	0.09	3.3	0.30	0.7	0.4	-0.5
Cu-CHA-15-25	0.11	4.5	0.50	0.7	0.4	-0.4
Cu-CHA-15-22	0.18	6.5	1.17	0.5	0.7	-0.3
Cu-CHA-15-20	0.23	7.8	1.79	0.4	0.6	-0.2
Cu-CHA-15-17	0.35	7.4	2.59	0.4	0.7	0.0
Cu-CHA-15-16	0.41	7.8	3.20	0.3	0.8	0.0
Cu-CHA-25-38	0.03	0.5	0.02	0.9	0.4	-0.5
Cu-CHA-25-25	0.12	1.6	0.18	0.8	0.5	-0.6
Cu-CHA-25-22	0.17	2.6	0.46	0.7	0.5	-0.4
Cu-CHA-25-20	0.23	3.8	0.88	0.5	0.6	-0.3
Cu-CHA-25-18	0.34	7.7	2.63	0.3	0.7	-0.2

[†]Errors in the apparent reaction rate orders are ± 0.1.

Table 7.2 Bulk elemental analysis, number of isolated Cu^{II} and $[Cu^{II}OH]^+$ sites (per Al), concentration of Cu ions and Al per crystallite volume, and residual NH_4^+/Al in oxidized Cu^{II} forms of model Cu-CHA-X-Y samples (Y = mean Cu-Cu distance, X = Si/Al).

Cu-CHA-X -Y	Si/Al	Cu/Al	Cu^{II}/Al*	$Cu^{II}OH$/Al*	Cu /1000Å^3	Al /1000Å^3	Residual NH_4^+/Al*
Cu-CHA-5-20	4.5	0.08	0.08	0.00	0.23	0.96	0.31
Cu-CHA-15-20	15	0.25	0.09	0.16	0.23	0.61	0.58
Cu-CHA-25-20	25	0.40	0.05	0.35	0.23	0.37	0.61

*Determined from titration of residual H$^+$ sites by NH_3 and thermodynamic preferences for Cu^{II} and $[Cu^{II}OH]^+$ siting[1]

7.4.1 Overall promotional effect of framework Al density on SCR kinetics

As discussed in our previous study, standard SCR rates vary quadratically with Cu density below 0.25 Cu/1000Å on a series of model Cu-CHA samples with Si/Al 15 (Cu-CHA-15-Y) due to dual-site oxidation being the rate-limiting step[2]. Measurement of reaction kinetics

on a series of Cu-CHA samples with varying Cu and Al density (Si/Al 5, 15 and 25) samples exhibit different quadratic dependences of standard SCR rates (Figure 7.1). The quadratic dependence of SCR rates (per Cu) on Cu spatial density extends up to higher critical Cu density (~0.35 Cu/1000Å) for lower framework Al density samples (Si/Al 25), as opposed to lower critical Cu density (~0.25 Cu/1000Å) for higher framework Al density samples (Si/Al 15). This wider regime of quadratic dependence coupled with reaction O_2 orders representative of O_2 oxidation of Cu^I reaction step (O_2 order ~ 1.0), is indicative of increased kinetic relevance of Cu^I oxidation with O_2 step for lower framework Al density samples (Si/Al 25) relative to higher framework Al density samples (Si/Al 15).
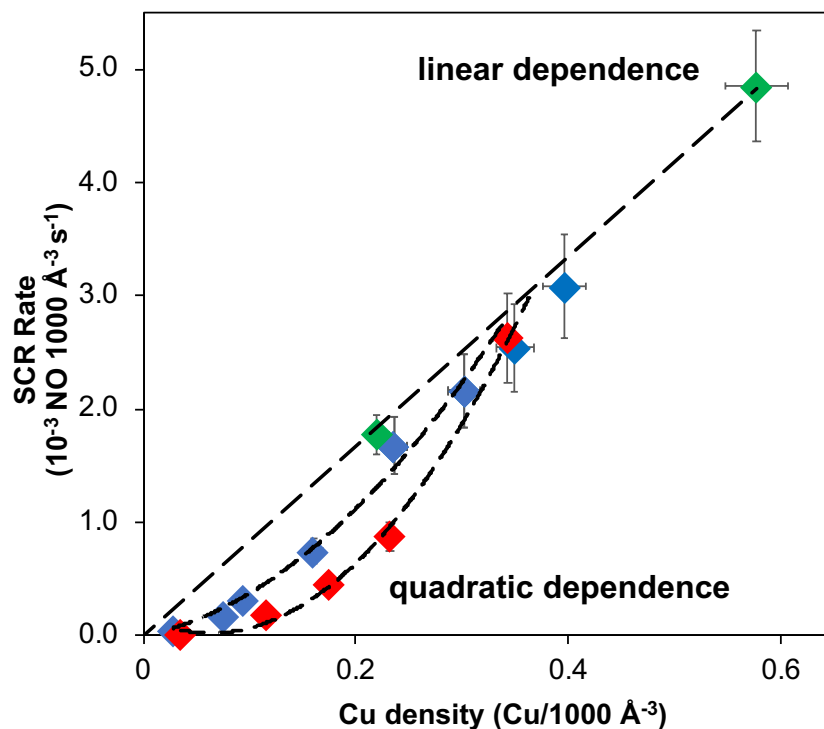
Figure 7.1 Standard NO_x SCR rates (per volume catalyst, 473 K) measured on Cu-CHA-X-Y samples (Y = Mean Cu-Cu distance in Å, X=Si/Al), with green: Cu-CHA-5-Y, blue: Cu-CHA-15-Y and red: Cu-CHA-25-Y (Conditions: 300 ppm NO, 300 ppm NH_3, 10% O_2, 7% CO_2, 3% H_2O and balance He at 473 K)

This is indicative of a promotional effect of framework Al spatial density on steady state SCR kinetics, wherein increase in Al density (decrease in Si/Al) seems to increase the rate of Cu^I $\rightarrow$ Cu^{II} oxidation (decreasing the kinetic relevance of Cu^I oxidation). This agrees with the theoretical proposal that framework Al anchored extraframework NH_4^+ ions can assist the

migration of $Cu^I(NH_3)_2$ [5], which is a prerequisite to $Cu^I \rightarrow Cu^{II}$ oxidation with O_2. Here it is important to note that changing framework Al density (Si/Al) results in both the change of Bronsted acid site density as well as active Cu cationic site speciation. As it was shown that structurally different Cu sites behave similarly under SCR reaction conditions due to NH_3 solvation[1], effect of framework Al density can be treated primarily as an effect of acid site density. In addition, the amount of framework Al anchored residual NH_4^+ ions could also directly affect SCR kinetics by weakly binding reactive NH_3 species as indicated previously[8]. In summary, framework Al density can affect overall SCR kinetics through involvement of its electrostatically anchored extraframework co-cation like H^+, NH_4^+, Cu, etc., in the following two ways: 1) Residual $NH_4^+/H^+/Cu$ ions facilitate Cu^I diffusion/mobility/pairing during $Cu^I \rightarrow Cu^{II}$ oxidation, and 2) Residual NH_4^+ ions bind NH_3 that participate in SCR mechanism in NO reduction/consumption during $Cu^{II} \rightarrow Cu^I$ reduction.

7.4.2   Promotional effect on Cu mobility

Increasing Cu density increases the amount of oxidizable Cu^I as well as rate of $Cu^I \rightarrow Cu^{II}$ oxidation, consistent with previously proposed dual-site nature of Cu^I oxidation, however, the effect of framework Al density on Cu diffusion is not considered here[2]. It has been found that increasing framework Al anchored NH_4^+ site density also increases the amount of oxidizable Cu^I (from Cu^I oxidation transients reported in chapter 4) as well as initial rate of $Cu^I \rightarrow Cu^{II}$ oxidation (obtained from rate of Cu^I oxidation at t=0 in Cu^I oxidation transients from chapter 4), as seen in Figure 7.2. This is indicative of a promotional effect of framework Al density on Cu mobility, and in turn on SCR kinetics. Such effect can be reconciled based on previously reported additional Cu diffusion pathway assisted by NH_4^+/H^+ ions transport/hopping/exchange mechanism[4].
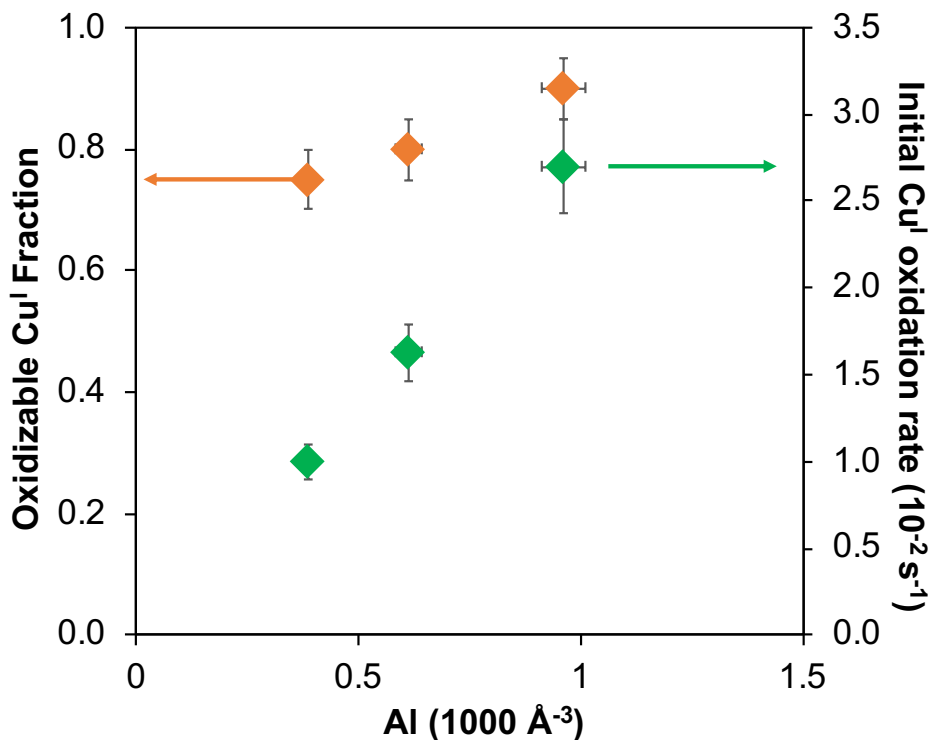
Figure 7.2 Oxidizable Cu^I fraction and initial Cu^I oxidation rate (normalized by total Cu spatial density) (from O_2 transients at t = 0 s) on model Cu-CHA-5-20, Cu-CHA-15-20 and Cu-CHA-25-20 samples with varying Al density at a fixed Cu density

7.4.3 Isolating this promotional effect of Al density on Cu mobility

The effects on Cu ion mobility are first isolated by operating in $Cu^I \rightarrow Cu^{II}$ oxidation kinetic regime, where Cu ion mobility is kinetically relevant, and then extracting apparent first-order (k_1) or oxidation rate constants (k_{ox}), as discussed in chapter 4. Observed increase in oxidation rate constant with increase in framework Al density (Table 7.3 and Figure 7.3) can be rationalized by framework Al (residual NH_4^+) promoting SCR reactivity via. facilitating $Cu^I \rightarrow Cu^{II}$ oxidation during SCR.

Table 7.3 Apparent $Cu^I \rightarrow Cu^{II}$ oxidation rate constants on model Cu-CHA-5-20, Cu-CHA-15-20 and Cu-CHA-25-20 samples with varying Al density and fixed Cu spatial density

Cu-CHA-X-Y	Cu / 1000Å³	Al / 1000Å³	k_1 (apparent oxidation rate constant) (10^{-3} mol NO kPa O_2 mol $Cu^{-1}s^{-1}$)
Cu-CHA-5-20	0.23	0.96	3.10
Cu-CHA-15-20	0.23	0.61	1.90
Cu-CHA-25-20	0.23	0.37	0.37
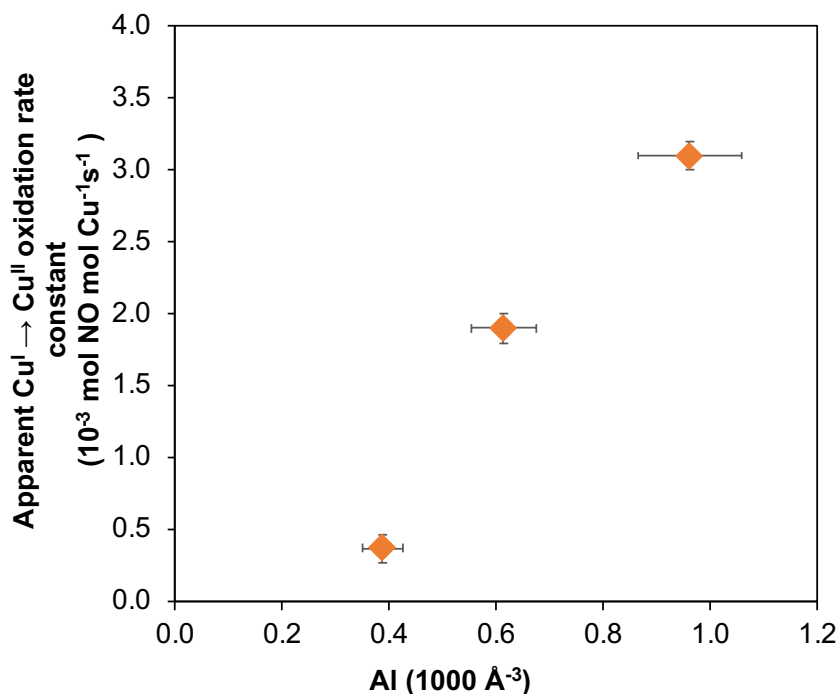
Figure 7.3 Apparent $Cu^I \rightarrow Cu^{II}$ oxidation rate constants on model Cu-CHA-5-20, Cu-CHA-15-20 and Cu-CHA-25-20 samples with varying Al density and fixed Cu spatial density

7.4.4 Promotional effect involving NH_4^+ ions in reaction mechanism

It has been recently proposed that residual NH_4^+ ions act as NH_3-storage sites providing reactive NH_3 for NO consumption during $Cu^{II} \rightarrow Cu^I$ reduction step SCR mechanism (in chapter 4). This involvement of NH_3-storage residual NH_4^+ sites differs from aforementioned participation of NH_4^+ ions via. facilitation of Cu^I diffusion and pairing during $Cu^I \rightarrow Cu^{II}$ oxidation.

7.4.5 Isolating the promotional effect of Al density on reactive NH₃

In order to isolate this promotional effect, we first attenuate the effects of Cu ion mobility by operating in the kinetic regime where Cu ion mobility is not kinetically relevant. Operating in such $Cu^{II} \rightarrow Cu^{I}$ reduction-limited kinetic regime enables extraction of apparent zero-order/ reduction rate constants (k_0), as discussed in chapter 4 on model Cu-CHA-X-20 sample with fixed Cu spatial density, varying amounts of residual NH_4^+ ions (per Al). These apparent $Cu^{II} \rightarrow Cu^{I}$ reduction rate constants (k_0) are reported in Table 7.4.

Table 7.4 Apparent $Cu^{II} \rightarrow Cu^{I}$ reduction rate constants (k_r: per pairable Cu) on model Cu-CHA-5-20, Cu-CHA-15-20 and Cu-CHA-25-20 samples with fixed Cu spatial density, varying amounts of residual NH_4^+ ions (per Al).

Cu-CHA-X-Y	Cu / 1000Å³	Al / 1000Å³	Residual NH_4^+/Al	k_0 (apparent reduction rate constant) (10^{-2} mol NO mol pairable Cu^{-1}s^{-1})
Cu-CHA-5-20	0.23	0.96	0.35	1.31
Cu-CHA-15-20	0.23	0.61	0.58	1.71
Cu-CHA-25-20	0.23	0.37	0.61	2.08
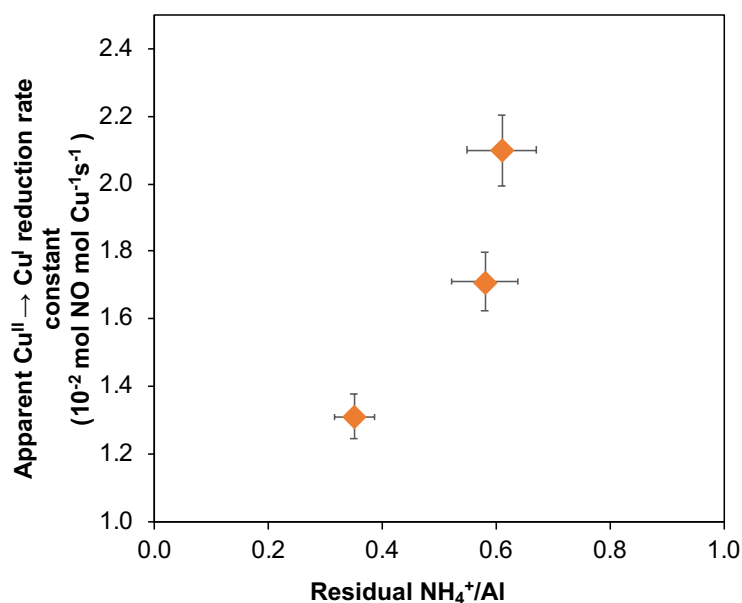
Figure 7.4 Apparent $Cu^{II} \rightarrow Cu^{I}$ reduction rate constants on model Cu-CHA-4.5-20, Cu-CHA-15-20 and Cu-CHA-25-20 samples with fixed Cu spatial density and varying Al amounts of residual NH_4^+ ions (per Al)

Apparent reduction rate constant positively correlates with amount of residual NH_4^+ ions (Figure 7.4) suggesting the direct involvement of NH_4^+ ions during $Cu^{II} \rightarrow Cu^I$ reduction with NO step. The amount of residual NH_4^+ ions appears to matter more than Al density for direct involvement in $Cu^{II} \rightarrow Cu^I$ reduction with NO step.

7.5 Conclusions

Framework Al spatial density in Cu-SSZ-13 was shown to promote steady state SCR kinetics. This overall promotional effect of framework Al spatial density comprises of framework Al sites anchored NH_4^+/H^+ ions aiding Cu mobility during $Cu^I \rightarrow Cu^{II}$ oxidation, and framework Al sites anchored NH_4^+/H^+ ions acting as reactive NH_3 storage sites during $Cu^{II} \rightarrow Cu^I$ reduction. These effects influence the $Cu^I \rightarrow Cu^{II}$ oxidation half of SCR redox cycle, and the $Cu^{II} \rightarrow Cu^I$ reduction half of SCR redox cycle, respectively. Understanding the origins of promotional effects of framework Al density would enable better interpretation of observed kinetic differences with changes in catalyst composition, and also opens avenues to further refine catalyst structural parameters to improve SCR reactivity.

7.6 Methods

7.6.1 Synthesis and Characterization

7.6.1.1 Synthesis of H-CHA zeolites

Synthesis of H-SSZ-13 zeolites with Si/Al 4.5, 15 and 25 was done as previously reported in the above chapters 2 and 3.

7.6.1.2 X-Ray diffraction of CHA zeolites

The CHA crystal framework was determined from powder X-ray diffraction (XRD) patterns collected as previously reported in the above chapters 2 and 3.

7.6.1.3 Adsorption isotherms to measure micropore volumes of CHA zeolites

Micropore volumes of CHA zeolites were determined from Ar adsorption isotherms measured as previously reported in the above chapters 2 and 3.

7.6.1.4 Aqueous-phase Copper Ion-Exchange of H-SSZ-13

Cu-SSZ-13 zeolites were prepared by aqueous-phase Cu ion-exchange as previously reported in the above chapters 2 and 3.

7.6.1.5 Elemental Analysis using Atomic Absorption Spectroscopy

Bulk elemental composition (Si, Al and Cu in H-CHA and Cu-CHA) was determined using atomic absorption spectroscopy (AAS) as previously reported in the above chapter 3.

7.6.1.6 Cu site characterization and quantification

Cu sites were characterized using Cu K-edge X-ray absorption near edge spectroscopy (XANES) and o UV-Visible spectroscopy as previously reported in the above chapters 2 and 3. Further enumeration of isolated Cu^{II} and $Cu^{II}OH$ sites on each Cu-CHA zeolite was determined after oxidative treatment (20% O_2, 773 K) by quantifying the number of residual protons that remained after Cu exchange, as previously reported in the above chapter 3.

7.6.2 X-ray Absorption Spectroscopy (XAS)

More generic details about X-ray absorption spectroscopy have been illustrated in above chapters 2 and 3.

7.6.2.1 *Operando* XAS experiments

Operando experiments were performed in a special glassy carbon tube reactor, and the details of the custom *operando* XAS reactor setup were described in above chapters 2 and 3.

7.6.2.2 Transient XAS experiments

Oxidation of $Cu^{I}(NH_3)_2$ sites with O_2

Following the reduction of Cu^{II} to $Cu^{I}(NH_3)_2$ with $NO+NH_3$ at 473 K, NO was first cut-off followed by NH_3 from the gas stream, while oxidizing mixture (10% O_2, balance He) was being prepared through the bypass. As soon as the outlet concentration of reductants NO and NH_3 were less than 5 ppm, oxidizing gas stream (10% O_2, balance He, 500 ml min^{-1}) was switched from bypass to reactor in order to oxidize $Cu^{I}(NH_3)_2$ to Cu^{II}-dimer (NH_3-solvated). The Cu^{I}-Cu^{II} fractions during these transient oxidation experiments were followed by collecting XAS spectra

in quick scan mode from 8700 to 9700 eV. Each spectrum took 1 min 48 s to complete with a step size of 0.5 eV and a dwell time of 0.05 s.

7.6.3   Kinetics

Differential SCR kinetics under $Cu^{II} \rightarrow Cu^I$ reduction-limited high O_2 limit (70 kPa) and $Cu^I \rightarrow Cu^{II}$ oxidation-limited low O_2 limit (0.5 kPa) were measured on a bench-top tubular glass reactor described in the appendix B of chapter 3 and above chapter 5.

7.7   References

1   C. Paolucci, A. A. Parekh, I. Khurana, J. R. Di Iorio, J. Albarracin, A. Shih, T. Anggara, W. Nicholas, J. T. Miller, F. H. Ribeiro and R. Gounder, *J. Am. Chem. Soc.*, 2016, **138**, 6028–6048.
2   C. Paolucci, I. Khurana, A. A. Parekh, S. Li, A. J. Shih, H. Li, J. R. Di Iorio, J. D. Albarracin-Caballero, A. Yezerets, J. T. Miller, W. N. Delgass, F. H. Ribeiro, W. F. Schneider and R. Gounder, *Science*, 2017, **357**, 898 – 903.
3   F. Gao, D. Mei, Y. Wang, J. Szanyi and C. H. F. Peden, *J. Am. Chem. Soc.*, 2017, **139**, 4935–4942.
4   L. Chen, H. Falsig, T. V. W. Janssens and H. Grönbeck, 2018, **358**, 179–186.
5   V. Rizzotto, P. Chen and U. Simon, *Catalysts*, 2018, **8**, 162.
6   P. Chen, D. Rauch, P. Weide, S. Schönebaum, T. Simons, M. Muhler, R. Moos and U. Simon, *Catal. Sci. Technol.*, 2016, **6**, 3362–3366.
7   P. Chen, M. Jab, P. Weide, T. Caumanns, E. Weirich, M. Muhler, R. Moos, R. Palkovits, U. Simon, M. Muhler, R. Moos, R. Palkovits and U. Simon, 2016.
8   F. Gao, N. M. Washton, Y. Wang, M. Kollar, J. Szanyi and C. H. F. Peden, *J. Catal.*, 2015, **331**, 25–38.

8. CATALYTIC CONSEQUENCES OF STABILITY OF SMALL PORE CU-ZEOLITES AGAINST HYDROTHERMAL DEACTIVATION ON STANDARD SCR KINETICS

8.1 Preface

Chapter 8 reflects the reproduction of my equal contribution coauthored article published in Reaction Chemistry and Engineering, 2 (2), 168-179, 2017, titled "Structural and kinetic changes to small-pore Cu-zeolites after hydrothermal aging treatments and selective catalytic reduction of NO$_x$ with ammonia". This chapter use a detailed step-wise approach on model Cu-zeolite catalysts (three small-pore zeolite frameworks- CHA, AEI and RTH) to study atomic level hydrothermal deactivation mechanism, which would further aid in development of more hydrothermal stable catalysts. This work employs bulk characterization techniques, direct Cu site and kinetic characterization.

8.2 Abstract

Three small-pore, eight-membered ring (8-MR) zeolites of different cage-based topology (CHA, AEI, RTH), in their proton- and copper-exchanged forms, were first exposed to high temperature hydrothermal aging treatments (1073 K, 16 h, 10% (v/v) H$_2$O) and then to reaction conditions for low temperature (473 K) standard selective catalytic reduction (SCR) of NOx with ammonia, in order to study the effect of zeolite topology on the structural and kinetic changes that occur to Cu-zeolites used in NOx abatement. UV-Visible spectra were collected to monitor changes to Cu structure and showed that band intensities for isolated, hydrated Cu^{2+} cations (~12,500 cm^{-1}) remain constant after hydrothermal aging but decrease in intensity upon subsequent exposure to low temperature SCR reaction conditions. Standard SCR rates (per Cu, 473 K), activation energies, and reaction orders are similar between Cu-AEI and Cu-CHA

zeolites before and after hydrothermal aging, although rates are lower after hydrothermal aging as expected from the decreases in intensity of UV-Visible bands for Cu^{2+} active sites. For Cu-RTH, rates are lower (by 2-3x) and apparent activation energies are lower (by ~2x) than for Cu-AEI or Cu-CHA. These findings suggest that the RTH framework imposes internal transport restrictions, effectively functioning as a one-dimensional framework during SCR catalysis. Hydrothermal aging of Cu-RTH results in complete deactivation and undetectable SCR rates, despite X-ray diffraction patterns and Ar micropore volumes (87 K) that remain unchanged after hydrothermal aging treatments and subsequent SCR exposure. These findings highlight some of the differences in low temperature SCR behavior among small-pore Cu-zeolites of different topology, and the beneficial properties conferred by double six-membered ring (D6R) composite building units. They demonstrate that deleterious structural changes to Cu sites occur after exposure to hydrothermal aging conditions and SCR reactants at low temperatures, likely reflecting the formation of inactive copper-aluminate domains. Therefore, the viability of Cu-zeolites for practical low temperature NO_x SCR catalysis cannot be inferred solely from assessments of framework structural integrity after hydrothermal aging treatments, but also require Cu active site and kinetic characterization after hydrothermally aged zeolites are exposed to low temperature SCR reaction conditions.
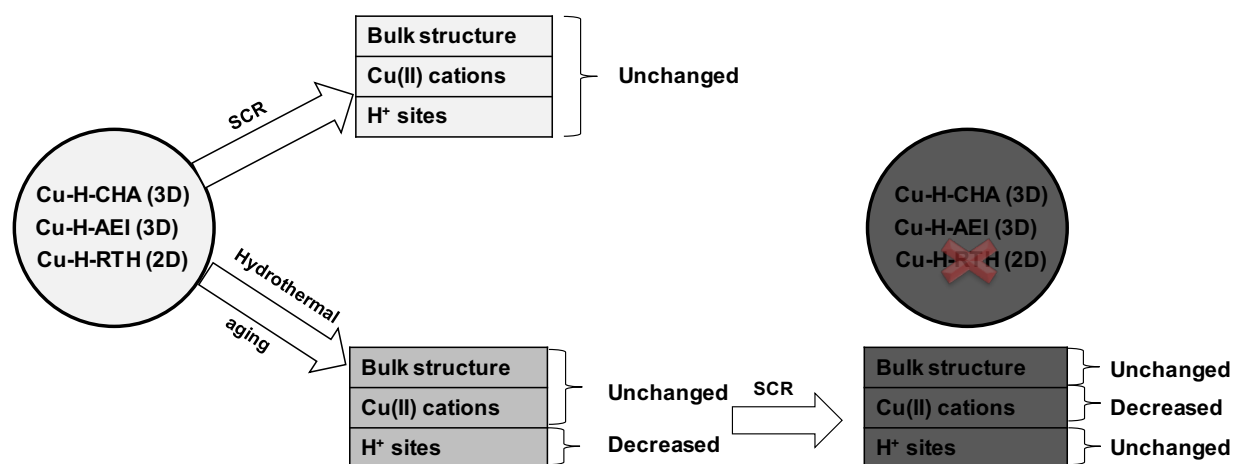
8.3 Introduction

Leading emissions control strategies for the abatement of hazardous nitrogen oxide pollutants (NOx, x = 1, 2) in lean-burn and diesel engine exhaust involve their selective catalytic reduction (SCR) with ammonia, which is generated from the decomposition of urea stored in an on-board tank. Cu- and Fe-exchanged molecular sieves used to practice automotive SCR aftertreatment[1–6] are required to retain sufficient SCR performance after excursions to high temperatures (>923 K) in the presence of steam (~7% H_2O (v/v)),[7–10] conditions experienced during regeneration of particulate filters. The structural integrity of molecular sieve frameworks with medium pores (e.g., MFI,[11–16] FER;[11] ~0.5 nm diam.) and large pores (e.g., BEA,[13,14,17,18] FAU;[14] >0.6 nm diam.) becomes compromised during hydrothermal aging;[11–18] moreover, active sites within such frameworks can be poisoned chemically by residual hydrocarbons in exhaust streams. These deactivation issues are mitigated within small-pore, eight-membered ring (8-MR; <0.4 nm diam.) frameworks, which led to the advent of the aluminosilicate (SSZ-13) and silicoaluminophosphate (SAPO-34) compositions of the chabazite (CHA) topology[8,19,20] as commercially used NOx SCR catalysts. Other small-pore molecular sieves with three-dimensional (e.g., AFX,[13] AEI,[21] KFI,[13] SAV,[22] SFW[23,24]) and two-dimensional (e.g., LEV,[13] DDR,[13] RTH[25]) pore connectivity have been considered as alternatives to CHA molecular sieves, based on observations that small-pore frameworks retain their structural integrity after exposure to hydrothermal aging conditions.

Hydrothermal aging of zeolites leads to the removal of aluminum atoms from framework locations,[13,26–28] which stabilize redox-active, extraframework Cu cations and ammonium species during SCR catalysis. Framework dealumination generally leads to sintering of extraframework alumina and mixed oxide domains with concomitant losses in microporous structure[29–31] that may restrict molecular traffic to active sites. The effects of hydrothermal aging treatments on dealumination have been assessed by changes in Al coordination using solid-state ^{27}Al magic angle spinning nuclear magnetic resonance (MAS NMR), and in long-range crystalline structure using X-ray diffraction (XRD) and micropore volume measurements.[14,32–35] Structural changes upon dealumination are more severe in Cu-exchanged medium-pore and large-pore zeolites (e.g., Cu-MFI, Cu-BEA) than in small-pore zeolites (e.g., Cu-CHA, Cu-AEI),[14,17,36] which are more recalcitrant to hydrothermal deactivation. Aluminum hydroxide species (Al(OH)$_3$; ~0.5 nm in diam.) formed upon dealumination at high temperatures are thought to be unable to diffuse

through 8-MR windows in CHA[13] and AEI[36] (~0.38 nm in diam.), which prevents the formation of larger extraframework alumina aggregates and allows for reincorporation of monomeric Al species within framework vacancy positions at low temperatures. Dealumination upon hydrothermal aging is also suppressed by the presence of extraframework cations (e.g., Cu, Na, Li, Mg),[36–38] which remove Brønsted acid sites that are vulnerable locations for hydrolysis of framework bonds.[39–41] Consequently, the ability of a zeolite framework to resist dealumination and retain its structural integrity upon hydrothermal aging has been used to identify promising candidates for practical NO_x SCR catalysis.

Deactivation caused by hydrothermal aging of molecular sieves may also reflect changes to the structure and location of extraframework Cu cations, such as their aggregation into larger Cu oxide species (Cu_xO_y), because the former isolated cations have been implicated as active sites for low temperature (473 K) SCR catalysis[42–44] while the latter oxide clusters are unreactive.[45] The disappearance of isolated Cu^{2+} cations upon hydrothermal aging of Cu-SSZ-13 has been inferred from the attenuation of absorption features characteristic of framework (T-O-T) vibrations (900 and 940 cm^{-1}) perturbed by ion-exchanged Cu species in diffuse-reflectance infrared (DRIFTS) spectra, from decreases in the amount of NH_3 desorbed from Lewis acidic Cu cations (~553 K) in TPD experiments,[32] and from decreases in electron paramagnetic resonance (EPR) signals for isolated Cu^{2+} cations.[33] The aggregation of isolated Cu^{2+} cations into larger Cu_xO_y domains upon hydrothermal aging has been detected by electron microscopy (TEM, SEM) and energy dispersive X-ray spectroscopy (EDX).[32–34] Isolated Cu^{2+} cations have also been proposed to interact with extraframework Al species, formed via dealumination, to generate inactive copper-aluminate domains in hydrothermally aged Cu-SSZ-13, evident in extended X-ray absorption fine structure (EXAFS) spectra that show decreased Cu-Cu scattering distances and increased Cu-Al scattering distances, and in H_2 temperature programmed reduction (TPR) profiles that show decreased intensities of lower temperature (500-670 K) reduction features for isolated Cu cations with the concomitant appearance of higher temperature (790-880 K) reduction features attributed to copper-aluminates.[35] Additionally, ^{27}Al MAS NMR spectra show decreased intensities for tetrahedral Al lines ($\delta \sim 60$ ppm) without concomitant increases in intensities for octahedral Al lines ($\delta \sim 0$ ppm), suggesting that interactions of Al with paramagnetic Cu render them invisible to NMR detection.[14] These results provide evidence for one possible deactivation mechanism of Cu-SSZ-13 through loss of isolated Cu^{2+} active sites

during hydrothermal aging, but do not account for structural changes to active sites that may result from subsequent exposure to standard SCR reactants. Thus, identifying new zeolite topologies that retain SCR reactivity after hydrothermal aging treatments requires knowledge of how such treatments, and subsequent exposure to SCR reaction conditions, affect the structures of both Cu active sites and the zeolite framework.

Here, we investigate the effects of hydrothermal aging and subsequent exposure to standard SCR reactants at low temperatures (473 K) on the structural and active site changes experienced by three different small-pore Cu-exchanged zeolites (Cu-CHA, Cu-AEI, Cu-RTH). Bulk characterization techniques, including XRD patterns and micropore volumes, reveal only subtle differences between Cu-zeolites before and after hydrothermal aging, and after subsequent exposure to low temperature SCR reaction conditions, and are unable to provide direct insight into the decreases in SCR reactivity measured on hydrothermally aged, small-pore Cu-zeolites. We provide evidence that exposure of hydrothermally aged catalysts to SCR reaction conditions at low temperatures causes further structural changes to active Cu sites that are detectable by UV-Visible spectroscopy, consistent with the formation of mixed copper-aluminate domains via reaction with extraframework Al species formed upon dealumination during hydrothermal aging. These findings demonstrate that active site and structural characterization of hydrothermally aged Cu-zeolites after exposure to SCR reactants at low temperatures provide more accurate inferences about their catalytic behavior.

8.4   Results and Discussions
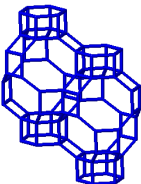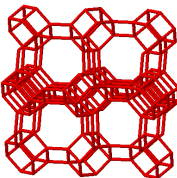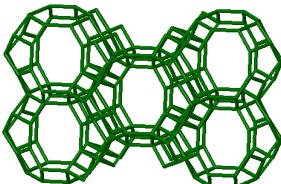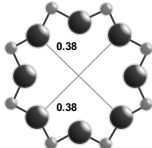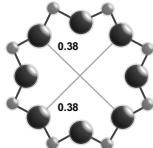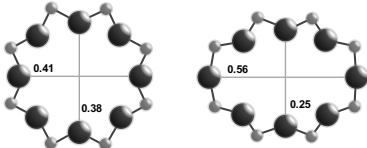
8.4.1   Structural features of CHA, AEI and RTH topologies

The salient structural features of the three molecular sieve framework topologies studied here are summarized in Table 8.1. The CHA framework[46] has three-dimensional micropore interconnectivity and is formed by the repetitive stacking of a hexagonal array of planar 6-membered rings (6-MR) connected in an AABBCC-type stacking scheme that form hexagonal prisms (double 6-MR). These double 6-MR (D6R) units are ordered to form large chabazite cages that are ~0.73 nm in diameter, which are limited by symmetric 8-MR windows that are ~0.38 nm in diameter. The CHA framework contains only one crystallographically unique T-site

and its unit cell contains 36 tetrahedrally-coordinated atoms (T-atoms) connected by 4-MR, 6-MR, and 8-MR units that are shared between adjacent cages.

The AEI framework[54] also has three-dimensional micropore interconnectivity and is constructed from a hexagonal array of 6-MR units similar to CHA, but neighboring D6R units are rotated 180° with respect to each other (Table 8.1). The D6R units are ordered to form AEI cavities that are ~0.73 nm in diameter and are contained within 4-MR, 6-MR, and 8-MR units, with access into AEI cavities limited by symmetric 8-MR windows that are ~0.38 nm in diameter, as in the case of CHA. In contrast to the CHA unit cell, the AEI unit cell contains 48 T-atoms and three crystallographically-distinct T-sites.

Table 8.1 Structural properties of the 8-MR molecular sieve frameworks in this study (CHA, AEI, RTH)

Framework	CHA	AEI	RTH
Crystal Topology			
Zeolite Trade Name	SSZ-13 [46]	SSZ-39 [54]	SSZ-50 [55]
Space Group	R-3m	Cmcm	C2/m
Ring sizes (X-MR)[a]	8, 6, 4	8, 6, 4	8, 6, 5, 4
Number of unique T-sites[a]	1	3	4
Connectivity[a]	3-D	3-D	2-D
Window diameter (nm)[b]	0.38 x 0.38	0.38 x 0.38	0.54 x 0.25 0.41 x 0.38
Cage diameter (nm)[c]	0.73	0.73	0.81

[a]Structural information from the International Zeolite Association structural database [51].
[b]Window diameter taken as the maximum diameter of a sphere that can diffuse through the framework [68].
[c]Cage size taken as the maximum diameter of a sphere that be occluded within the framework [68].

The RTH framework[55] is unique among the three small-pore zeolites studied here because it does not contain D6R building units, but instead is formed by two sets of three 4-MR that are connected via 5-MR linkages. These chained 4-MR and 5-MR periodic building units are repeated with simple translations to form RTH cavities that are 0.81 nm in diameter, and are contained within 4-MR, 5-MR, 6-MR, and 8-MR units. Consequently, the RTH unit cell (32 T-atoms) contains both symmetric (0.38 nm x 0.41 nm) and asymmetric (0.25 nm x 0.56 nm) 8-MR windows that result in only two-dimensional pore interconnectivity. RTH contains four crystallographically-distinct T-sites, three of which occupy positions accessible through either of the two 8-MR windows, and one that resides within the interconnected 4-MR chain and is inaccessible from the RTH cavity.

8.4.2 Characterization of H- and Cu-form zeolites before hydrothermal aging

Powder XRD patterns of H-form AEI, CHA, and RTH zeolites (Figure E1, Appendix E.) were consistent with reported diffraction patterns for these topologies [51] and did not show diffraction peaks for phase impurities. Ar adsorption isotherms (87 K) on H-form zeolites (Figure E2, Appendix E) gave micropore volumes (Table 8.2) consistent with the AEI,[54] CHA,[46] and RTH[55] topologies. ^{27}Al MAS NMR spectra of H-form zeolites (Figures E3-S5, Appendix E.) show predominantly Al incorporated into tetrahedral framework positions (Al$_f$, $\delta \sim 60$ ppm), with Al$_f$/Al$_{tot}$ values quantified to be 0.85 for H-CHA, 0.85 for H-AEI and 0.98 for H-RTH (Table 8.2). The number of protons per framework Al atom (H$^+$/Al$_f$, Table 8.2) measured by NH$_3$ TPD (Figure 8.2) on H-form zeolites was 0.95 and 0.85 for H-CHA and H-AEI, respectively, indicating that nearly every framework Al generated a proton. In contrast, the H$^+$/Al$_f$ value was much lower on H-RTH (0.60, Table 8.2), suggesting either that some framework Al atoms generate H$^+$ sites that are inaccessible to NH$_3$, or that not all Al atoms are associated with a corresponding proton site. In the RTH framework, it is plausible that some H$^+$ sites are inaccessible to NH$_3$, which has a kinetic diameter ($\sim$0.26 nm)[56] that is larger than one of the dimensions of the distorted RTH window (0.56 nm x 0.25 nm), and because one of the four T-sites in RTH is in a location that is inaccessible from the RTH cage. Infrared spectra collected after H-RTH was exposed to NH$_3$ (433 K), however, showed complete disappearance of Brønsted acidic OH stretches (Figure E6, Appendix E) indicating that all H$^+$ sites are accessible to NH$_3$. Therefore, the H$^+$/Al$_f$ value of 0.60 on H-RTH reflects the presence of distorted Al

structures that do not generate H^+ sites, but are otherwise detected as Al_f species in NMR spectra, as noted previously.[45,57,58]

Table 8.2 Site and structural properties of H-form and Cu-form zeolites prior to hydrothermal aging

Sample	Si/Al Ratio[a]	Cu wt%[a]	Cu/Al Ratio[a]	$V_{ads, micro}$ $(cm^3\ g^{-1})$[b]	$V_{ads, meso}$ $(cm^3\ g^{-1})$[b]	H^+/Al Ratio[c]	Al_f/Al_{tot}[d]	H^+/Al_f
H-CHA	15	-	-	0.18	0.04	0.95	0.85	1.10
Cu-CHA	15	0.7	0.12	0.17	0.05	0.72	0.90	-
H-AEI	9.5	-	-	0.20	0.01	0.85	0.85	1.00
Cu-AEI	9.5	1.7	0.17	0.19	0.01	0.54	0.91	-
H-RTH	15	-	-	0.20	0.05	0.60	0.98[e]	0.61
Cu-RTH	15	0.7	0.11	0.17	0.04	0.38	0.98	-

[a]Elemental composition determined by atomic absorption spectroscopy (AAS).
[b]Micropore and mesopore volumes determined from Ar adsorption isotherms (87 K). (Figure S.2, Supp. Info.).
[c]Number of H^+ sites quantified by selective NH_3 titration and temperature-programmed desorption.
[d]Fraction of tetrahedrally coordinated Al determined from ^{27}Al MAS NMR (Figure S.3.1-3.3, Supp. Info).
[e]Value on Cu-RTH.

Powder XRD patterns of AEI, CHA, and RTH zeolites after Cu exchange do not show significant changes in structure compared to their respective H-form zeolites or the presence of bulk Cu_xO_y (Figure E1, Appendix E). The micropore volume of each Cu-exchanged zeolite decreased slightly (Table 8.2; Figure E2, Appendix E) due to the presence of extraframework Cu cations, which occupy a small, but detectable, fraction of the void volume. Gaseous NH_3 titration[53,59] of residual H^+ sites on Cu-CHA (Cu/Al = 0.12) shows that H^+ sites are replaced with an exchange stoichiometry of two protons per Cu, reflecting the presence of only divalent Cu^{2+} cations (Table 8.2, Figure 8.2). This result is consistent (within experimental error) with the sequential exchange of isolated Cu^{2+} at paired Al sites until saturation followed by subsequent exchange of monovalent $[CuOH]^+$ at isolated Al sites.[42,60,61] Cu-RTH (Cu/Al = 0.11) shows an H^+/Cu exchange stoichiometry of two that suggests only Cu^{2+} sites are present, while Cu-AEI (Cu/Al = 0.17) shows an H^+/Cu exchange stoichiometry between 1 and 2 that suggests a mixture of Cu^{2+} and $[CuOH]^+$ sites are present. UV-Visible spectra of hydrated Cu-AEI, Cu-CHA, and Cu-RTH zeolites (Figure 8.3) show absorption bands characteristic of d-d transitions for hydrated Cu^{2+} complexes (~12,500 cm^{-1}) and broad bands for metal-ligand charge transfer (35,000-47,000 cm^{-1}), which are convoluted by zeolitic framework metal-oxygen charge transfer (36,750 and 43,500 cm^{-1}) and Cu-O charge transfer (~42,000 cm^{-1}).[62–64] An additional feature is present at ~25,000 cm^{-1} in the UV-Vis spectrum of Cu-RTH, but not in spectra of either Cu-AEI

or Cu-CHA, and appears in a region attributed to Cu-O charge transfer in small Cu oxide clusters.[63]

8.4.3   Standard SCR kinetics of Cu-zeolites before hydrothermal aging

Rates of NO consumption (473 K, per Cu) during standard SCR (equimolar NO and NH_3, with O_2 as the oxidant) are shown in Table 8.3 and plotted in Figure 8.4. The measured NO consumption rate (per Cu) was similar on Cu-AEI and Cu-CHA (within 1.3x), although direct quantitative comparison of these turnover rates is not rigorously justified since they appear to be measured in different kinetic regimes, reflected in the different apparent NH_3 reaction orders of -0.5 and -0.1 on Cu-CHA and Cu-AEI (Table 8.3), respectively. The measured NO consumption rate was lower (by 2.2-2.9x) on Cu-RTH than on either Cu-AEI or Cu-CHA (Table 8.3). At first glance, the similar turnover rates (per Cu) on Cu-CHA, Cu-AEI and Cu-RTH (within 3x, 473 K) seem reminiscent of standard SCR turnover rates (473 K) that have been reported to be insensitive to the zeolite topology (CHA, BEA, MFI), as a consequence of the solvation of Cu cations by NH_3 during low temperature SCR conditions.[42]

Apparent activation energies (Table 3) estimated from rate data collected between 444-476 K (Figure 8.4) were similar on Cu-AEI (46 ± 5 kJ mol^{-1}) and Cu-CHA (56 ± 5 kJ mol^{-1}), and in a range previously reported for standard SCR activation energies on Cu-CHA (Si/Al = 35, Cu/Al = 0-0.31).[44,45] Apparent activation energies were much lower on Cu-RTH (28 ± 5 kJ mol^{-1}), however, and approximately half of the value measured on Cu-CHA, characteristic of severe intrazeolite mass transfer limitations. Both the CHA and AEI frameworks contain three-dimensional pore systems interconnected by symmetric 8-MR windows (0.38 nm diameter), but the RTH framework is a two-dimensional pore system with a limiting asymmetric 8-MR ring of size (0.25 nm) similar to the kinetic diameter of the SCR reactants (~0.3 nm). In effect, the RTH framework appears to behave as a one-dimensional pore system for this reaction, in which reactants preferentially diffuse through the symmetric 8-MR window. Internal diffusion limitations have been proposed to account for the lower NOx conversions (423-573 K) in two-dimensional, small-pore LEV and DDR zeolites, when compared to three-dimensional small-pore CHA zeolites.[13] Thus, while small-pore zeolites show improved hydrothermal stability over medium and large-pore zeolites,[14,17] considerations of pore connectivity and limiting aperture sizes are also critical in determining the reactivity of Cu sites located within them.
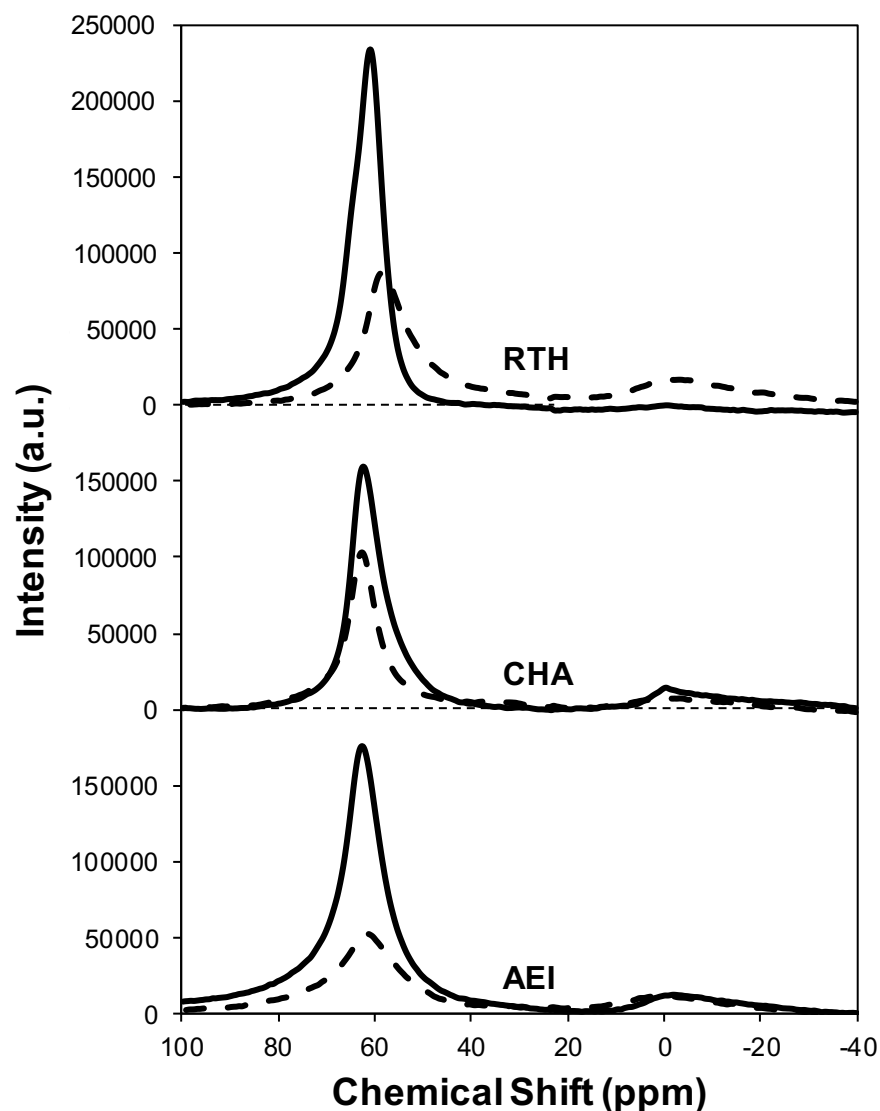
Figure 8.1 ^{27}Al MAS NMR spectra of hydrated fresh (solid) and aged (dashed) Cu-form of RTH, CHA and AEI zeolites.

The number of residual H^+ sites (per Al_{tot}) on Cu-CHA before and after exposure to SCR gases was 0.72 and 0.70 ± 0.05, respectively. Similarly, the residual H^+/Al_f value on Cu-AEI and Cu-RTH changed only from 0.54 to 0.50 ± 0.05 and from 0.38 to 0.39 ± 0.05, respectively (Table 8.3). Therefore, exposure to SCR gases did not significantly change the number of residual H^+ sites on Cu-AEI, Cu-CHA and Cu-RTH, indicating that framework Al remained largely intact on Cu-zeolites after NO_x SCR catalysis. Ar micropore and mesopore volume measurements (87 K) on Cu-AEI, Cu-CHA and Cu-RTH before and after exposure to SCR gases

were unchanged (Table 8.3 and Figure 8.6), with micropore volumes for both Cu-CHA and Cu-RTH of 0.17 cm^3 g^{-1} and for Cu-AEI of 0.18-0.19 cm^3 g^{-1} before and after exposure to SCR gases, respectively. Similarly, the mesopore volume for Cu-AEI, Cu-CHA and Cu-RTH zeolites before and after exposure to SCR gases were the same, within experimental error, between 0.03-0.05 cm^3 g^{-1} (Table 8.3). Taken together, these characterization data of Cu-zeolites that have not been exposed to hydrothermal aging treatments indicate that minimal changes to H$^+$ or Cu sites, or the zeolite framework, occur after exposure to low temperature standard SCR reaction conditions (473 K).

8.4.4   Characterization of Cu-form zeolites before and after hydrothermal aging

Hydrothermal aging treatments of each Cu-exchanged zeolite, performed to reproduce the effects experienced during a 135,000 mile lifetime (1073 K, 10% (v/v) H$_2$O, 16 h),[34] did not result in detectable loss of long-range structure as inferred from powder XRD patterns (Figure 8.5). After hydrothermal aging treatments, the Ar micropore volumes decreased by only ~10% on Cu-AEI and Cu-CHA but remained constant on Cu-RTH (Table 8.3, Figure 8.6). ^{27}Al MAS NMR spectra of Cu-zeolites after hydrothermal aging (Figure 8.1) show decreased intensities for tetrahedrally-coordinated Al lines (Al$_f$, $\delta \sim$ 60 ppm; Table 8.3) and increased intensities in octahedrally-coordinated Al lines (Al$_{ex}$, $\delta \sim$ 0 ppm; Figure 8.1), indicating the formation of some extraframework Al species from framework dealumination. Framework dealumination occurred to greater extents on Cu-RTH (~25% loss in Al$_f$) than on either Cu-AEI or Cu-CHA (~7% loss in Al$_f$), although we note that Al quantification from NMR spectra of Cu-zeolites will be affected by species that are not detected because of interactions with paramagnetic Cu. Moreover, hydrothermal aging of Cu-RTH results in the appearance of a broad shoulder at ~40-50 ppm reflecting penta-coordinated or distorted tetrahedral Al,[65] which did not occur in either Cu-AEI or Cu-CHA. After hydrothermal aging, each Cu-zeolite sample showed a ~70-80% decrease in the number of H$^+$ sites measured by NH$_3$ TPD (Table 8.3; Figure E7, Appendix E), in spite of the only minor decreases in Al$_f$ intensity observed in the ^{27}Al MAS NMR spectra, which may reflect structural changes to extraframework Al species caused by the hydration treatments used prior to recording NMR spectra. These findings demonstrate that characterization of the bulk structure (e.g. XRD patterns, micropore volumes) or Al atoms (^{27}Al MAS NMR) are insufficient to describe the local site and structural changes caused by hydrothermal aging treatments,[36] and

serve as a reminder for the need to use techniques that probe and quantify active sites directly (e.g. base titration of proton sites) to accurately detect such structural changes.[59,66,67]

In contrast to the dramatic changes observed for H^+ sites on each Cu-zeolite after hydrothermal aging, the identity and coordination of Cu species appear to remain unchanged as inferred from UV-Vis spectra (Figure 8.3). UV-Vis absorption bands for Cu^{2+} d-d transitions ($\sim$12,500 cm^{-1}) appear identical for hydrated Cu-zeolites before and after hydrothermal aging, without any new features observed in the region for Cu oxide clusters ($\sim$25,000 cm^{-1}). Slight changes in the intensities of absorbance bands characteristic of metal-ligand charge transfer (35,000-47,000 cm^{-1}) are observed for each Cu-zeolite after hydrothermal aging, which may reflect changes in the zeolite structure caused by removal of framework aluminum atoms. Taken together, these results indicate that hydrothermal aging treatments of Cu-exchanged CHA, AEI and RTH zeolites cause framework dealumination and a decrease in the numbers of corresponding H^+ sites, but do not result in detectable changes to the exchanged Cu cations or to the long-range structural order in the zeolite framework.

Table 8.3 Site and structural properties of H-form zeolites, and of Cu-exchanged zeolites before and after hydrothermal aging, and before and after exposure to standard SCR gases. Standard SCR rates (473 K), apparent activation energies, and apparent reaction orders for Cu-form zeolites before and after hydrothermal aging treatments.

Sample	Exposure to SCR gases	$V_{ads, micro}$ $(cm^3\ g^{-1})^a$	$V_{ads, meso}$ $(cm^3\ g^{-1})^a$	H^+/Al_{tot} Ratio[b]	Al_f/Al_{tot}	Standard SCR Rate (per total Cu, 473 K)[c]	E_{app}^d (kJ/mol)	NO Order[e]	O_2 Order[e]	NH_3 Order[e]
CHA										
H-form		3	0.04	0.95	0.85					
Cu-form	*before*	0.17	0.05	0.72	0.90					
	after	0.17	0.03	0.70		3.1	56 ± 5	0.4	0.6	-0.5
Cu-form aged	*before*	0.15	0.01	0.16	0.84					
	after	0.15	0.07	0.14		2.2	51 ± 5	0.5	0.4	-0.1
AEI										
H-form		0.20	0.01	0.85	0.85					
Cu-form	*before*	0.19	0.01	0.54	0.91					
	after	0.18	0.00	0.50		4.1	46 ± 5	0.5	0.4	-0.1
Cu-form aged	*before*	0.17	0.06	0.16	0.78					
	after	0.16	0.02	0.15		1.9	49 ± 5	0.5	0.4	0.0
RTH										
H-form		0.20	0.05	0.60	0.98[f]					
Cu-form	*before*	0.17	0.04	0.38	0.98					
	after	0.17	0.03	0.39		1.4	28 ± 5	0.4	0.4	-0.1
Cu-form aged	*before*	0.17	0.10	0.07	0.72					
	after	0.17	0.08	0.00		n.d.*	-	-	-	-

[a]Micropore and mesopore volumes determined from Ar adsorption isotherms (87 K) (Figure 6).
[b]Number of H^+ sites quantified by selective NH_3 titration and temperature-programmed desorption.
[c]Units of 10^{-3} mol NO (mol Cu)$^{-1}$ s^{-1}.
[d]Errors ± 7 kJ/mol, [e]Errors are ± 0.1, [f]Value on Cu-RTH,. *n.d., not detectable (<0.3 x 10^{-3} mol NO (mol Cu)$^{-1}$ s^{-1}

8.4.5 Standard SCR kinetics of Cu-form zeolites before and after hydrothermal aging

The standard SCR rate (per Cu, 473 K) measured on hydrothermally aged Cu-AEI decreased by ~50% compared to the rate measured on Cu-AEI prior to aging (Table 8.3, Figure 8.4). The standard SCR rate measured on hydrothermally aged Cu-CHA decreased by ~25% compared to the rate measured on Cu-CHA prior to aging (Table 8.3, Figure 8.4). The standard SCR rate on Cu-RTH, however, was not measureable ($<0.3 \times 10^{-3}$ mol NO (mol Cu)$^{-1}$ s^{-1}) after hydrothermal aging despite the presence of isolated, hydrated Cu^{2+} species detected in its UV-Vis spectrum (Figure 8.3). As a result, apparent activation energies and reaction orders could not be measured on Cu-RTH subjected to hydrothermal aging treatments. Although hydrothermally aged Cu-RTH shows undetectable SCR rates, XRD patterns and Ar micropore volumes indicate virtually no changes to Cu-RTH before and after aging. As a result, assessments of long-range structural features by XRD and micropore volume after Cu-zeolites have been hydrothermally aged cannot be used as accurate predictors of SCR catalytic behavior.

Hydrothermal aging treatments did not affect the apparent activation energies on either Cu-AEI (46-49 kJ mol^{-1}) or Cu-CHA (51-56 kJ mol^{-1}), nor the apparent NO (0.5), O$_2$ (0.4) and NH$_3$ (~0) orders on Cu-AEI and the apparent NO (0.4-0.5) and O$_2$ (0.4-0.6) orders on Cu-CHA (Table 8.3). The apparent NH$_3$ order measured on Cu-CHA (-0.5) became less negative after hydrothermal aging (-0.1, Table 8.3); we surmise that structural changes caused by hydrothermal aging and exposure to SCR gases led to a change in operation to a new kinetic regime characterized by weaker NH$_3$ inhibition. Turnover rates were similar between the hydrothermally-aged Cu-CHA and Cu-AEI samples ($1.9-2.2 \times 10^{-3}$ mol NO (mol Cu)$^{-1}$ s^{-1}) and the apparent reaction orders and activation energies were identical for both samples (Table 8.3), providing evidence that these rate data were measured in equivalent kinetic regimes. These data indicate that the Cu species that remain active on both CHA and AEI after hydrothermal aging behave catalytically similar, which may be linked to the nature of the Cu^{2+} exchange sites at the 6-MR windows of D6R composite building units that are found in both CHA and AEI.
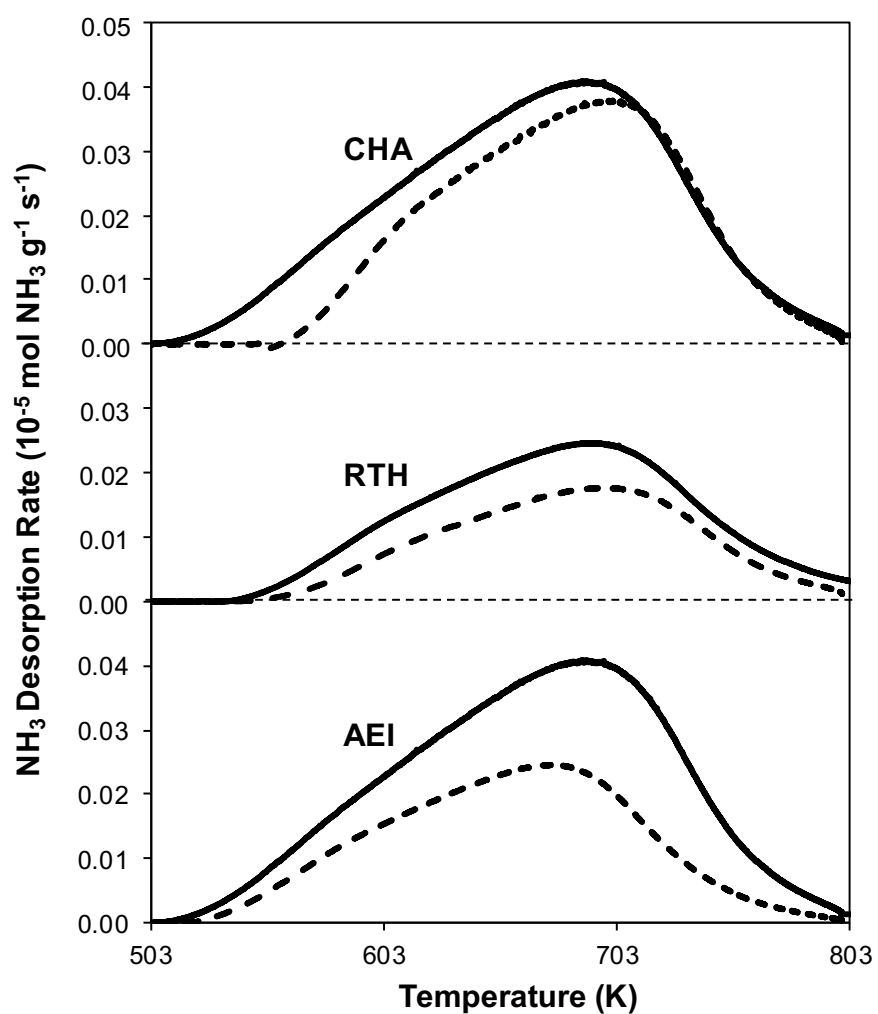
Figure 8.2 NH₃ desorption rates as a function of temperature on H-form (solid) and fresh Cu-form (dashed) on AEI, CHA, and RTH zeolites.

8.4.6 Characterization of Cu-zeolites before and after hydrothermal aging, and after exposure to NO_x SCR
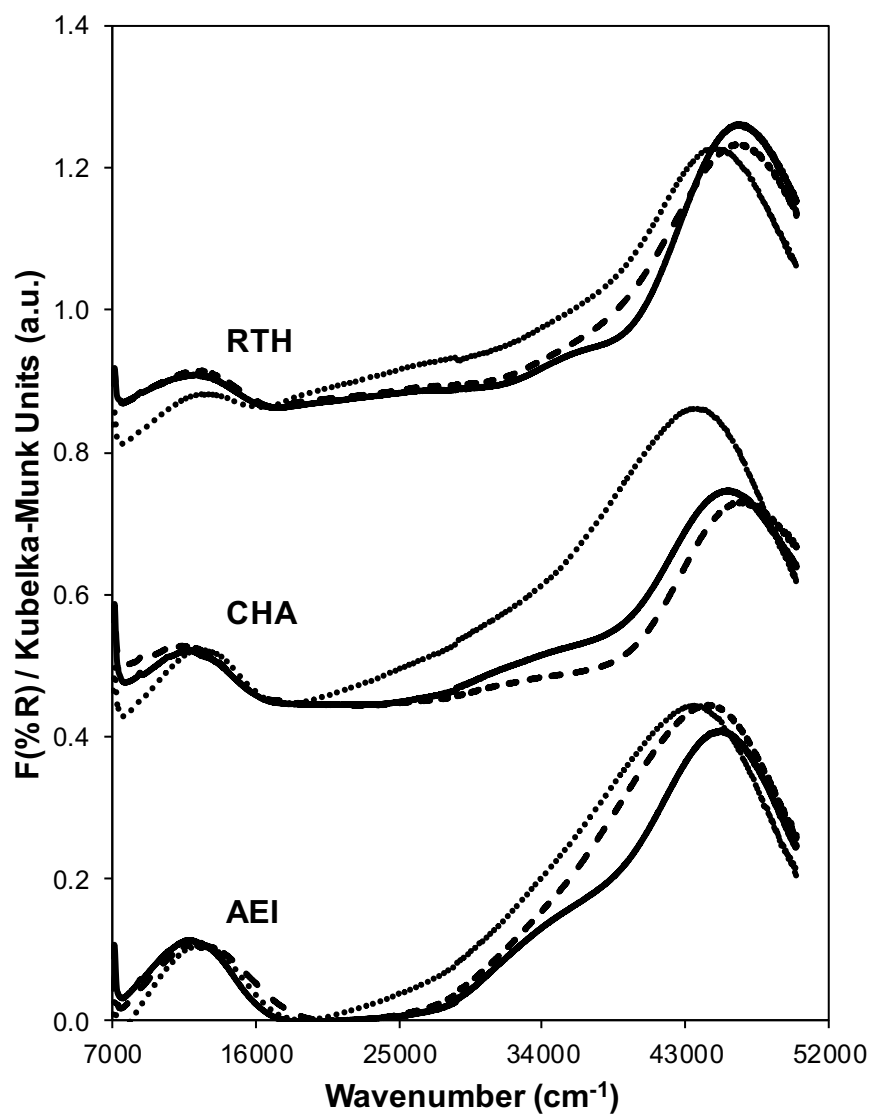
Figure 8.3 UV-Vis spectra on hydrated fresh Cu-form before SCR (solid), aged Cu-form before SCR (dashed), and aged after SCR (dotted) on RTH, CHA and AEI zeolites. Spectra are offset for clarity (CHA: by 0.42 a.u., RTH: by 0.82 a.u.).

Ar adsorption isotherms (87 K) and micropore volumes (Figure 8.6, Table 8.3) of Cu-zeolites after hydrothermal aging were indistinguishable before and after exposure to low temperature standard SCR reaction conditions (473 K). XRD patterns were also similar for hydrothermally-aged Cu-zeolites before and after exposure to standard SCR gases (Figure 8.5). These characterization data indicate that further structural changes to the zeolite framework did not occur when aged Cu-zeolites were exposed to standard SCR gas mixtures. The number of H^+ sites on hydrothermally-aged Cu-AEI and Cu-CHA zeolites were also similar before and after exposure to standard SCR gas mixtures (Table 8.3), but H^+ sites were no longer detectable (<0.03 H^+/Al, Table 8.3) on hydrothermally-aged Cu-RTH exposed to SCR gases. UV-Vis spectra of hydrothermally-aged Cu-CHA and Cu-RTH zeolites after exposure to standard SCR reactants (Figure 8.3) showed a reduction in Cu^{2+} d-d transition intensity (~12,500 cm^{-1}) and concomitant increases in intensity for broad absorption bands between 20,000-40,000 cm^{-1}. The spectra of Cu-AEI, however, retained similar d-d transition intensity after aging and exposure to SCR reactants, with an increase in intensity in the metal-ligand charge transfer region (35,000-47,000 cm^{-1}) that is also observed for Cu-CHA, but not for Cu-RTH.

The Cu structure in Cu-CHA, Cu-AEI and Cu-RTH, characterized by UV-Vis spectra, showed hardly any changes after hydrothermal aging treatments, but showed noticeable decreases in Cu^{2+} intensity upon subsequent exposure to low temperature SCR reaction conditions. These findings provide evidence that hydrothermal aging causes removal of Al from framework to extraframework positions, and that further structural changes continue to occur in the presence of SCR reactants at low temperatures (473 K) because NH_3 facilitates the solvation and mobility of Cu cations.[42] We speculate that an inactive copper aluminate phase ($CuAl_xO_y$) forms as a result of interactions of active Cu sites with extraframework $Al(OH)_3$ species, as proposed previously.[14,17,35] UV-Vis spectra of hydrothermally-aged Cu-RTH reveal decreased intensities for hydrated Cu^{2+} d-d transitions along with increases in new charge transfer bands between 20,000-40,000 cm^{-1} that may reflect $CuAl_xO_y$ species and account for decreases in SCR rate. Interestingly, any remaining H^+ sites in Cu-RTH upon hydrothermal aging and subsequent exposure to standard SCR reactants become inaccessible to NH_3, suggesting that Cu active sites in RTH, which appear to catalyze SCR in a diffusion-limited regime before hydrothermal aging, also become inaccessible to SCR reactants after hydrothermal aging.
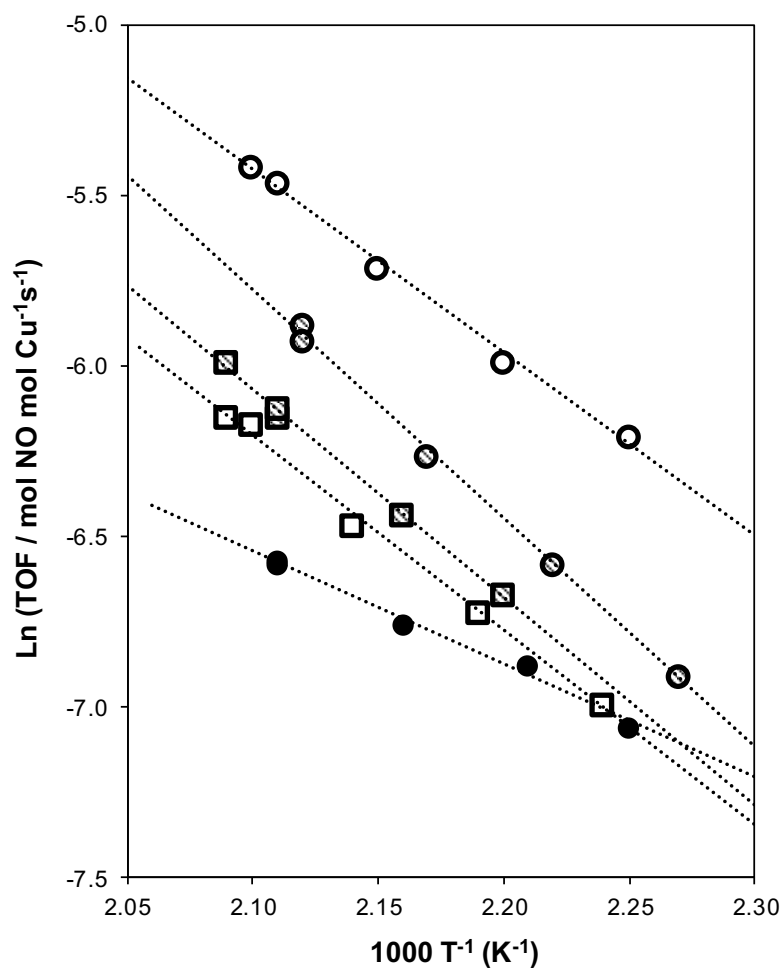
Figure 8.4 Dependence of standard SCR turnover rates (per Cu) on temperature for fresh (circles) and aged (squares) Cu-form AEI (hollow), CHA (cross hatched), and RTH (filled) zeolites.
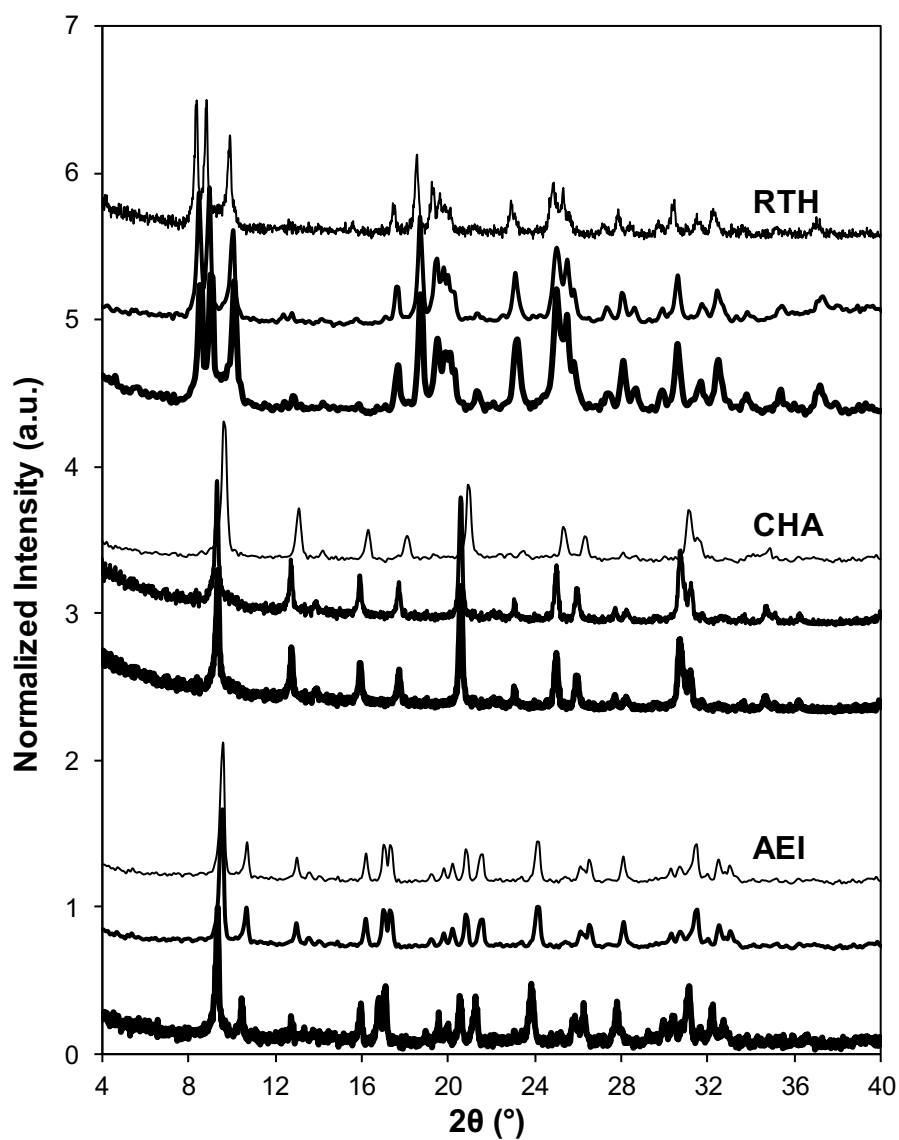
Figure 8.5 Powder XRD patterns of fresh Cu-form before SCR (dark), aged Cu-form before SCR (medium), and aged Cu-form after SCR (light) on AEI, CHA, and RTH zeolites. Diffraction patterns are normalized so that the maximum peak intensity in each pattern is unity, and offset for clarity.
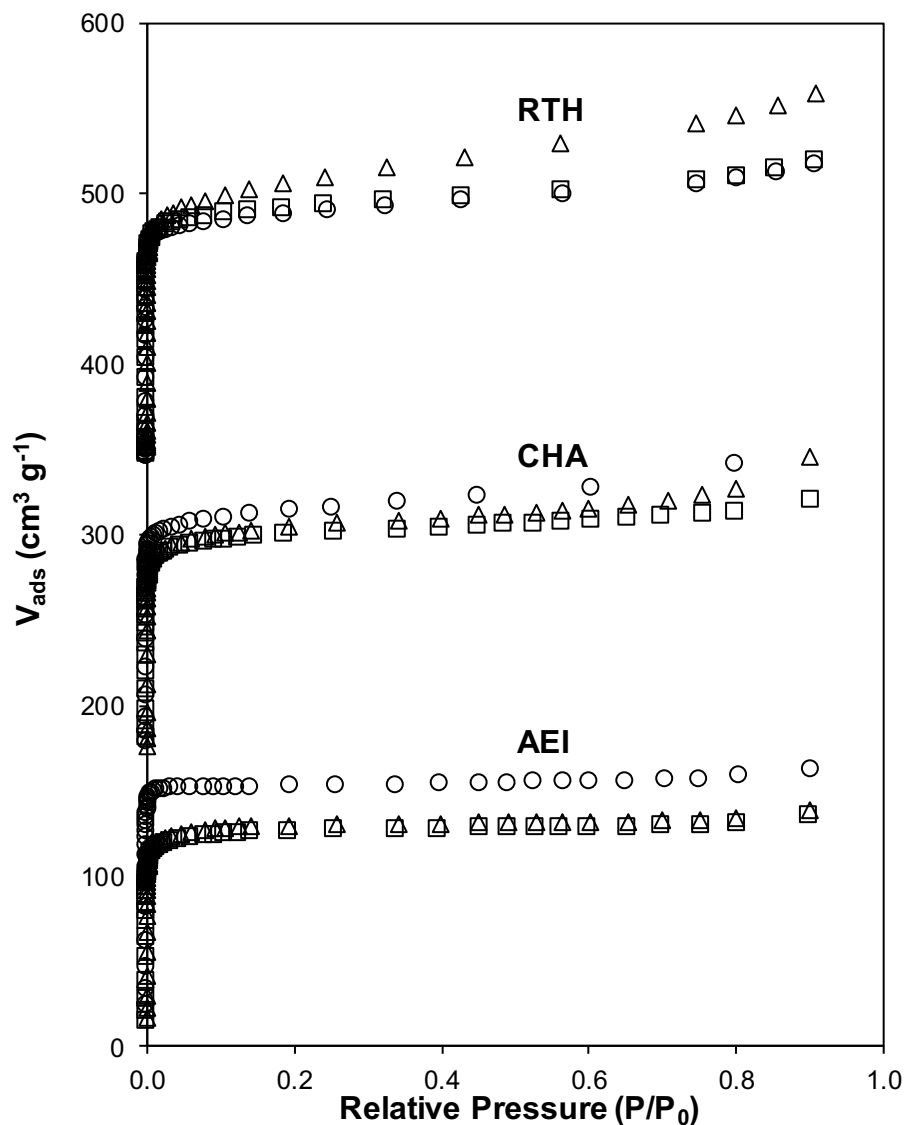
Figure 8.6 Ar adsorption isotherms (87 K) on fresh Cu-form before SCR (circles), aged Cu-form before SCR (triangles), aged Cu-form after SCR (squares) on AEI (red), CHA (blue), and RTH (green) zeolites. Isotherms are vertically offset for clarity (CHA: 160 cm^3 g^{-1}, RTH: by 320 cm^3 g^{-1})

8.5   Conclusions

CHA and AEI zeolites are similar in structure, with three-dimensional micropore systems connected by symmetric 8-MR windows (0.38 nm diameter), while the RTH framework is a two-dimensional pore system with constrained, asymmetric 8-MR windows (0.56 nm x 0.25 nm) that limit access in one dimension and effectively causes the RTH framework to behave as a one-dimensional pore system for NO_x SCR with NH_3. As a result, standard SCR turnover rates (per

Cu, 473 K) and apparent activation energies are similar between Cu-CHA and Cu-AEI, but turnover rates are lower (by ~2-3x) and apparent activation energies are lower (by ~2x) on Cu-RTH. Hydrothermal aging causes dealumination of Cu-CHA, Cu-AEI and Cu-RTH, evident in a decrease in the fraction of Al_f determined from ^{27}Al MAS NMR spectra and corresponding decreases in the number of H^+ sites quantified by NH_3 TPD, but does not cause noticeable changes in the bulk framework structure assessed by XRD and micropore volume or in the Cu structure by UV-Vis spectroscopy. The number of active Cu sites, however, decreased after hydrothermally aged samples were subsequently exposed to low temperature standard SCR reactants, evident in changes to UV-Vis spectra and concomitant decreases in standard SCR turnover rates. Hydrothermal aging causes removal of Al from framework to extraframework positions, and further structural changes continue to occur in the presence of ammonia at low temperatures (473 K), which solvate and mobilize extraframework cations to facilitate the formation of inactive copper-aluminate phases ($CuAl_xO_y$). These structural changes appear to occur more readily in Cu-RTH than either Cu-AEI or Cu-CHA, providing further evidence linking the presence of double six-membered rings (D6R) in small-pore molecular sieve frameworks to increased resistance to active site and framework structural changes upon hydrothermal aging.

Bulk structural characterization of small-pore zeolites after hydrothermal aging treatments cannot be used to accurately infer catalytic behavior for low temperature NO_x SCR with NH_3. This is evident in the case of hydrothermally-aged Cu-RTH, which deactivates completely upon exposure to standard SCR reactants but is characterized by similar bulk properties (XRD, micropore volume) before and after hydrothermal aging. Probes of Al structure (e.g., ^{27}Al MAS NMR) reveal that octahedrally-coordinated Al species are formed after hydrothermal aging of Cu-zeolites, but in amounts that are unable to account for the much larger disappearance in Brønsted acid sites titrated by NH_3, providing another reminder that methods to directly probe active sites are needed to assess their structural changes. We conclude that more accurate assessments of molecular sieve framework topologies that are viable for practical NO_x SCR catalysis require quantification and characterization of Al and Cu site structures after hydrothermally aged samples are exposed to low temperature SCR reaction conditions. We expect that holistic approaches to active site characterization, especially of Al and Cu sites, in Cu-zeolites after hydrothermal aging and subsequent exposure to low temperature SCR reaction

conditions will be able to provide more accurate guidance about molecular sieve topologies that are viable candidates for practical SCR technologies.

8.6 Methods

8.6.1 Catalyst synthesis and treatment

A sample of CHA (SSZ-13) zeolite with a Si/Al ratio of 15 was made as reported elsewhere.[46] Briefly, 28.4 g of N,N,N-trimethyl-1-adamantylammonium hydroxide (TMAdaOH, Sachem, 25 wt%) were mixed with 71.4 g of deionized water (18.2 MΩ), 0.87 g of aluminum hydroxide (SPI Pharma, 99.9 wt%, 0325 grade), and 34.6 g of 0.1 M sodium hydroxide (NaOH; Alfa Aesar), then stirred for 15 minutes at ambient conditions. 10 g of fumed silica (Cab-o-Sil M-5) were added to the mixture and stirred for 2 hours at ambient conditions. The final molar composition of the synthesis solution was 1 SiO_2/ 0.033 Al_2O_3/ 0.20 TMAdaOH/ 0.02 NaOH/ 23.8 H_2O. All reagents were used without further purification. The resulting solution was transferred to eight Teflon-lined Parr autoclaves (45 mL each) and held at 433 K for 10 days under rotation.

A sample of AEI (SSZ-39) zeolite with a Si/Al ratio of 9.5 was synthesized in a rotating oven at 413 K for 4 days as reported elsewhere,[47] using *cis*-2,6-dimethylpiperidinium hydroxide as the organic structure directing agent (OSDA). The molar composition of the synthesis mixture was 1 SiO_2/ 0.017 Al_2O_3/ 0.07 OSDA/ 0.65 OH^-/ 0.58 Na^+/ 12.3 H_2O, obtained by mixing (aqueous) OSDA, NaOH (1M, RT Baker), double distilled water, sodium silicate (N° type, PQ Corporation) and CBV500 (NH₄-USY, Si/Al = 2.6, Zeolyst). A sample of RTH (SSZ-50) zeolite with a Si/Al ratio of 15 was made using the CBV720 synthesis protocol reported elsewhere.[48–50]

As-synthesized zeolites were washed alternately with deionized water and acetone, recovered via centrifugation, and dried at 323 K for 24 hours. The dried samples were then treated to 873 K (0.0083 K s^{-1}) in air (Commercial grade, Indiana Oxygen) for 6 hours before ion-exchanging in an aqueous 0.1M NH_4NO_3 solution (Sigma Aldrich; 1000 mL per g zeolite) at 353 K for 10 hours. NH₄-exchanged zeolites were washed with deionized H_2O, recovered via centrifugation, dried at 323 K for 24 hours, then treated at 823 K (0.0083 K s^{-1}) in air for 6 hours to obtain H-form zeolites. Cu-exchanged CHA, AEI, and RTH zeolites were prepared via liquid phase ion-exchange of H-form zeolites using an aqueous 0.2M $Cu(NO_3)_2$ solution (99.999 %

trace metals basis, Sigma-Aldrich; 150 mL per g zeolite) at ambient temperature for 4 hours. The pH during the exchange was not controlled and the final pH of the solution was ~3.6.

Hydrothermal aging experiments were performed on Cu-zeolites in a three-zone horizontal tube furnace (Applied Test Systems Series 3210), in which each zone was equipped with independent temperature control (Watlow EZ-Zone PM Express). Once the furnace temperature reached 373 K, water was introduced via syringe pump (KD Scientific Legato 100) into a stream of flowing air (100 mL min^{-1}, 99.999%, Indiana Oxygen), which was transferred to the furnace through stainless steel lines held at >373 K. Approximately 1 gram of catalyst was loaded into quartz boats held within the tube furnace and treated to 1073 K (0.033 K s^{-1}) for 16 hours in flowing air (100 mL min^{-1}, 99.999%, Indiana Oxygen) containing 10% (v/v) water. After treatment for 16 hours at 1073 K, water was removed from the flowing air stream while the sample was cooled to ambient.

8.6.2   Catalyst structural characterization

Powder diffraction patterns were collected using a Rigaku SmartLab diffractometer with a Cu Kα radiation source (1.76kW), from 4 to 40° with a scan rate of 0.05° s^{-1} and a step size of 0.01°. Diffraction patterns are normalized so that the maximum peak intensity in each pattern is unity. The diffraction patterns were compared to reference patterns to confirm the RTH, CHA and AEI topologies.[51]

Ar adsorption isotherms were used to determine micropore volumes on zeolite samples (87 K) using a Micromeritics ASAP 2020 Surface Area and Porosity Analyzer. Micropore volumes were obtained by converting adsorbed gas volumes (cm^3 g$_{cat}^{-1}$ at STP) to liquid volumes assuming the liquid density of Ar at 87 K. Samples were pelleted and sieved to retain particles between 125-250 μm in diameter. Samples (0.03-0.05 g) were degassed by heating to 393 K (0.167 K s^{-1}) under high vacuum (~5 μmHg) for 2 h, and then heating to 623 K (0.167 K s^{-1}) under high vacuum (~5 μmHg) and holding for 9 h. Micropore volumes (cm^3 g$_{cat}^{-1}$ at STP) were estimated from extrapolation of the linear volumetric uptake during the beginning of mesopore filling (~0.08–0.30 P/P$_0$) to zero relative pressure, which agreed with micropore volumes estimated from analyzing the semi-log derivative plot of the adsorption isotherm ($\partial(V_{ads})/\partial(\ln(P/P_0))$ vs. $\ln(P/P_0)$).

In order to quantify the fractions of framework and extraframework Al, ^{27}Al magic angle spinning nuclear magnetic resonance (MAS NMR) spectra were recorded on H-form and Cu-form CHA, AEI and RTH zeolite samples. NMR spectra were collected using a Chemagnetics CMX-Infinity 400 spectrometer in a wide-bore 9.4 Tesla magnet (Purdue Interdepartmental NMR Facility) and were acquired at ambient conditions using a 2.3 μs pulse (equivalent to ca. 30 degrees), an acquisition time of 12.8ms and a relaxation delay of 1s, and were measured at 104.24 MHz and a MAS rate of 5 kHz. ^{1}H decoupling was used during acquisition, employing two-pulse phase modulation (TPPM) scheme. Prior to packing in a 4mm ZrO_2 rotor, zeolite samples were hydrated by holding for >48 h in a desiccator containing a saturated potassium chloride (KCl) solution. All ^{27}Al MAS NMR spectra are referenced to a static sample of $AlCl_3$ dissolved in D_2O (0 ppm ^{27}Al line).

Diffuse reflectance UV-Visible spectra were recorded under ambient conditions using a Varian UV-VIS-NIR spectrophotometer (Cary 5000) with a diffuse reflectance accessory consisting of two ellipsoidal mirrors (Harrick Scientific Praying Mantis). Barium sulfate ($BaSO_4$, 99.9%, Sigma-Aldrich) was used as the 100% reflectance standard. An *ex-situ* sample holder was loaded with 0.1 g of sample, which was pelleted and sieved to retain particles between 125-250 μm in diameter. Spectra were collected from 7000 to 50000 cm^{-1} with a scan speed of 2000 cm^{-1} min^{-1}, and spectra of the H-form zeolite was subtracted from those for corresponding Cu-zeolites to correct for contributions of absorption from the framework.

8.6.3 Brønsted acid site quantification using NH$_3$ titration methods

The total number of Brønsted acid sites (H$^+$) on H-form and Cu-exchanged zeolites was quantified by temperature programmed desorption (TPD) of NH$_3$ on a gas-phase plug flow reactor, as described by Bates et al.,[52] using a procedure described elsewhere.[53] For H-form zeolites, NH$_3$ saturation was performed via aqueous-phase exchange with NH$_4^+$ cations, as reported elsewhere.[52] For Cu-exchanged zeolites, samples were saturated with 500 ppm NH$_3$ diluted with He (99.999%, UHP, Indiana Oxygen) at 433 K for 2 h with a total flow rate of 350 mL min^{-1}. Following this NH$_3$ saturation step, the sample was flushed with 2.5-3.0% water in UHP He (wet purge) at 433 K for 8 h while maintaining the same total flow rate to desorb NH$_3$ bound to non-protonic sites. Following the wet purge step, samples were heated to 820 K (0.167 K s^{-1}) under flowing He (UHP, 350 mL min^{-1}). The total moles of NH$_3$ desorbed during the TPD

experiment was measured using on-board calibrations in an MKS Multigas 2030 gas-phase FT-IR spectrometer.[52]

8.6.4 Kinetic measurements of standard SCR turnover rates

Standard selective catalytic reduction (SCR) kinetics were measured on a bench-top tubular glass reactor described elsewhere.[52] All samples were sieved to a nominal size of 125-250 μm and diluted with silica gel to obtain a bed height of ~2.5 cm. Steady-state kinetic data were collected at NO conversions below 20% (differential); thus, the entire catalyst bed was exposed to approximately the same gas concentrations. The reactant gas mixture comprised 300 ppm NO (3.6% NO/Ar, Praxair), 300 ppm NH_3 (3.0% NH_3/Ar, Praxair), 7% CO_2 (liquid, Indiana Oxygen), 10% O_2 (99.5%, Indiana Oxygen), 2.5% H_2O (deionized, 18.2 MΩ, introduced through saturator), and balance N_2 (99.999% UHP, Indiana Oxygen) at 473 K and 1 atm. The total gas flow rate was maintained at 1.5 L min^{-1}. Outlet gas concentrations were analyzed using on-board gas calibrations on an MKS Multigas™ 2030 gas-phase Fourier Transform Infrared (FTIR) spectrometer and NO, NO_2, NH_3, CO_2, and H_2O concentration data was recorded every 0.95 s.

8.7 Acknowledgements

8.8 References

1   S. Brandenberger, O. Kröcher, A. Tissler and R. Althoff, *Catalysis Reviews*, 2008, **50**, 492-531.

2   T. Komatsu, M. Nunokawa, I. S. Moon, T. Takahara, S. Namba and T. Yashima, *J. Catal.*, 1994, **148**, 427–437.

3   G. Delahay, S. Kieger, N. Tanchoux, P. Trens and B. Coq, *Appl. Catal. B.*, 2004, **52**, 251–257.

4   G. Delahay, E. A. Villagomez, J.-M. Ducere, D. Berthomieu, A. Goursot and B. Coq, *ChemPhysChem*, 2002, **3**, 686–692.

5   J. H. Baik, S. D. Yim, I.-S. Nam, Y. S. Mok, J.-H. Lee, B. K. Cho and S. H. Oh, *Top. Catal.*, 2004, **30**, 37–41.

6   J.-H. Park, H. J. Park, J. H. Baik, I.-S. Nam, C.-H. Shin, J.-H. Lee, B. K. Cho and S. H. Oh, *J. Catal.*, 2006, **240**, 47–57.

7   K. Kamasamudram, N. W. Currier and X. Chen, *Catal. Today*, 2010, **151**, 212–222.

8   J. H. Kwak, R. G. Tonkyn, D. H. Kim, J. Szanyi and C. H. F. Peden, *J. Catal.*, 2010, **275**, 187-190.

9   S. T. Korhonen, D. W. Fickel, R. F. Lobo, B. M. Weckhuysen and A. M. Beale, *Chem. Commun.*, 2011, **47**, 800–802.

10   A. M. Beale, F. Gao, I. Lezcano-Gonzalez, C. H. F. Peden and J. Szanyi, *Chem. Soc. Rev.*, 2015, **44**, 7371–7405.

11   K. Rahkamaa-Tolonen, T. Maunula, M. Lomma, M. Huuhtanen and R. L. Keiski, *Catal. Today*, 2005, **100**, 217–222.

12   Q. Ye, L. Wang and R. T. Yang, *Appl. Catal. A* , 2012, **427**, 24–34.

13   D. W. Fickel, E. D'Addio, J. A. Lauterbach and R. F. Lobo, *Appl. Catal. B.*, 2011, **102**, 441–448.

14   J. H. Kwak, D. Tran, S. D. Burton, J. Szanyi, J. H. Lee and C. H. F. Peden, *J. Catal.*, 2012, **287**, 203–209.

15   K. C. C. Kharas, H. J. Robota and D. J. Liu, *Appl. Catal. B*, 1993, **2**, 225–237.

16   S. A. Gómez, A. Campero, A. Martínez-Hernández and G. A. Fuentes, *Appl. Catal. A*, 2000, **197**, 157–164.

17   P. G. Blakeman, E. M. Burkholder, H. Y. Chen, J. E. Collier, J. M. Fedeyko, H. Jobson and R. R. Rajaram, *Catal. Today*, 2014, **231**, 56–63.

18   S. Shwan, R. Nedyalkova, J. Jansson, J. Korsgren, L. Olsson and M. Skoglundh, *Ind. Eng. Chem. Res.*, 2012, **51**, 12762–12772.

19   P.J. Andersen, J. E. Bailie, J. L. Casci, H. Y. Chen, J. M. Fedeyko, R. K. Shin Foo and R. R. Rajaram, US Pat., 0290963, 2010.

20   D. W. Fickel, E. D'Addio, J. A. Lauterbach and R. F. Lobo, US Pat., 0226545, 2008.

21   M. Moliner, C. Franch, E. Palomares, M. Grill and A. Corma, *Chem. Commun.*, 2012, **48**, 8264-8266.

22   A. Lorena Picone, S. J. Warrender, A. M. Z. Slawin, D. M. Dawson, S. E. Ashbrook, P. A. Wright, S. P. Thompson, L. Gaberova, P. L. Llewellyn, B. Moulin, A. Vimont, M. Daturi, M. B. Park, S. K. Sung, I.-S. Nam and S. B. Hong, *Microporous Mesoporous Mater.*, 2011, **146**, 36–47.

23   D. Xie, L. B. McCusker, C. Baerlocher, S. I. Zones, W. Wan and X. Zou, *J. Am. Chem. Soc.*, 2013, **135**, 10519–10524.

24   T. M. Davis, A. T. Liu, C. M. Lew, D. Xie, A. I. Benin, S. Elomari, S. I. Zones and M. W. Deem, *Chem. Mater.*, 2016, **28**, 708–711.

25   D. Jo, J. Bin Lim, T. Ryu, I.-S. Nam, M. A. Camblor and S. B. Hong, *J. Mater. Chem. A*, 2015, **3**, 19322–19329.

26   S. Altwasser, J. Jiao, S. Steuernagel, J. Weitkamp and M. Hunger, *Stud. Surf. Sci. Catal.*, 2004, **154B**, 1212–1213.

27   M. Nielsen, R. Y. Brogaard, H. Falsig, P. Beato, O. Swang and S. Svelle, *ACS Catal.*, 2015, **5**, 7131–7139.

28   K. Ehrhardt, M. Suckow and W. Lutz, *Stud. Surf. Sci. Catal.*, 1995, **94**, 179–186.

29   L. Ma, Y. Cheng, G. Cavataio, R. W. McCabe, L. Fu and J. Li, *Appl. Catal. B*, 2014, **156–157**, 428–437.

30   M. V. L. Pereira, A. Nicolle and D. Berthout, *Catal. Today*, 2015, **258**, 424–431.

31   L. R. Aramburo, L. Karwacki, P. Cubillas, S. Asahina, D. A. M. de Winter, M. R. Drury, I. L. C. Buurmans, E. Stavitski, D. Mores, M. Daturi, P. Bazin, P. Dumas, F. Thibault-Starzyk, J. A. Post, M. W. Anderson, O. Terasaki and B. M. Weckhuysen, *Chem. Eur. J.*, 2011, **17**, 13773–13781.

32   D. Wang, Y. Jangjou, Y. Liu, M. K. Sharma, J. Luo, J. Li, K. Kamasamudram and W. S. Epling, *Appl. Catal. B.*, 2015, **165**, 438–445.

33   J. Wang, Z. Peng, H. Qiao, L. Han, W. Bao, L. Chang, G. Feng and W. Liu, *RSC Adv.*, 2014, **4**, 42403–42411.

34   S. J. Schmieg, S. H. Oh, C. H. Kim, D. B. Brown, J. H. Lee, C. H. F. Peden and D. H. Kim, *Catal. Today*, 2012, **184**, 252–261.

35   W. Su, Z. Li, Y. Peng and J. Li, *Phys. Chem. Chem. Phys.*, 2015, **17**, 29142–29149.

36   M. Dusselier, M. A. Deimund, J. E. Schmidt and M. E. Davis, *ACS Catal.*, 2015, **5**, 6078–6085.

37   F. Gao, Y. Wang, N. M. Washton, M. Kollar, J. Szanyi and C. H. F. Peden, *ACS Catal.*, 2015, **5**, 6780-6791.

38   A. V. Kucherov and A. A. Slinkin, *Zeolites*, 1986, **6**, 175–180.

39   G. T. Kerr, *J. Phys. Chem.*, 1967, **71**, 4155–4156.

40   G. T. Kerr, *J. Catal.*, 1969, **15**, 200–204.

41   M.-C. Silaghi, C. Chizallet, E. Petracovschi, T. Kerber, J. Sauer and P. Raybaud, *ACS Catal.*, 2015, **5**, 11–15.

42   C. Paolucci, A. A. Parekh, I. Khurana, J. R. Di Iorio, H. Li, J. D. Albarracin Caballero, A. Shih, T. Anggara, W. Nicholas Delgass, J. T. Miller, F. H. Ribeiro, R. Gounder and W. F. Schneider, *J. Am. Chem. Soc.*, 2016, **138**, 6028–6048.

43   T. V. W. Janssens, H. Falsig, L. F. Lundegaard, P. N. R. Vennestrøm, S. Rasmussen, P. G. Moses, F. Giordanino, E. Borfecchia, K. A. Lomachenko, C. Lamberti, S. Bordiga, A. Godiksen, S. Mossin and P. Beato, *ACS Catal.*, 2015, **5**, 2832-2845.

44   F. Gao, N. M. Washton, Y. Wang, M. Kollár, J. Szanyi and C. H. F. Peden, *J. Catal.*, 2015, **331**, 25–38.

45   S. A. Bates, A. a. Verma, C. Paolucci, A. a. Parekh, T. Anggara, A. Yezerets, W. F. Schneider, J. T. Miller, W. N. Delgass and F. H. Ribeiro, *J. Catal.*, 2014, **312**, 87–97.

46   S.I. Zones, US Pat., 4544538 A, 1985.

47   M. Dusselier, J. E. Schmidt, R. Moulton, B. Haymore, M. Hellums and M. E. Davis, *Chem. Mater.*, 2015, **27**, 2695–2702.

48   J. E. Schmidt, M. A. Deimund, D. Xie and M. E. Davis, *Chem. Mater.*, 2015, **27**, 3756–3762.

49   J. E. Schmidt, M. W. Deem and M. E. Davis, *Angew. Chemie Int. Ed.*, 2014, **53**, 8372–8374.

50   J. E. Schmidt, M. A. Deimund and M. E. Davis, *Chem. Mater.*, 2014, **34**, 7774-7779.

51   C. Baerlocher, W. H. Baur, J. M. Bennett, H. Gies, J. B. Higgins, R. Kirchner and D.H. Olson, *Zeolites*, 1996, **17**, 1-230.

52   S. A. Bates, A. A. Verma, C. Paolucci, A. A. Parekh, T. Anggara, A. Yezerets, W. F. Schneider, J. T. Miller, W. N. Delgass and F. H. Ribeiro, *J. Catal.*, 2014, **312**, 87–97.

53   J. R. Di Iorio, S. A. Bates, A. A. Verma, W. N. Delgass, F. H. Ribeiro, J. T. Miller and R. Gounder, *Top. Catal.*, 2015, **58**, 424–434.

54   S. I. Zones, Y. Nakagawa, S. T. Evans and G. S. Lee, US Pat., 5958370 A, 1999.

55   G. S. Lee and S. I. Zones, US Pat., 6605267 B1, 2003.

56   G. Centi and S. Perathoner, *Appl. Catal. A, Gen.*, 1995, **132**, 179–259.

57   R. Gounder, A. J. Jones, R. T. Carr and E. Iglesia, *J. Catal.*, 2012, **286**, 214–223.

58   A. I. Biaglow, D. J. Parrillo, G. T. Kokotailo and R. J. Gorte, *J. Catal.*, 1994, **148**, 213–223.

59   S. A. Bates, W. N. Delgass, F. H. Ribeiro, J. T. Miller and R. Gounder, *J. Catal.*, 2014, **312**, 26–36.

60   J. R. Di Iorio and R. Gounder, *Chem. Mater.*, 2016, **28**, 2236–2247.

61   C. Paolucci, J. R. Di Iorio, F. H. Ribeiro, R. Gounder and W. F. Schneider, *Adv. Catal.*, 2016, **59**, DOI: 10.1016/bs.acat.2016.10.002

62   J. Texter, D. H. Strome, R. G. Herman and K. Klier, *J. Phys. Chem.*, 1977, **81**, 333–338.

63   F. Giordanino, P. N. R. Vennestrøm, L. F. Lundegaard, F. N. Stappen, S. Mossin, P. Beato, S. Bordiga and C. Lamberti, *Dalt. Trans.*, 2013, **42**, 12741–61.

64   K. L. Fujdala, I. J. Drake, A. T. Bell and T. D. Tilley, *J. Am. Chem. Soc.*, 2004, **126**, 10864–10866.

65   J. A. van Bokhoven, A. L. Roest, D. C. Koningsberger, J. T. Miller, G. H. Nachtegaal and A. P. M. Kentgens, *J. Phys. Chem. B*, 2000, **104**, 6743–6754.

66   A. I. Biaglow, D. J. Parrillo, G. T. Kokotailo and R. J. Gorte, *J. Catal.*, 1994, **148**, 213–223.

67   R. Gounder and E. Iglesia, *J. Catal.*, 2011, **277**, 36–45.

68   M. D. Foster, I. Rivin, M. M. J. Treacy and O. D. Friedrichs, *Microporous Mesoporous Mater.*, 2006, **90**, 32–38.

9. CATALYTIC CONSEQUENCES OF STABILITY OF CU-SSZ-13 AGAINST SULFUR POISONING ON STANDARD SCR KINETICS

9.1 Preface

Chapter 9 reflects the reproduction of my coauthored article published in Applied Catalysis A: General, 574, 122-131, 2019, titled "Spectroscopic and kinetic responses of Cu-SSZ-13 to SO_2 exposure and implications for NO_x selective catalytic reduction". This chapter aims to build upon the previous literature work to investigate the stability of different Cu sites towards sulfur poisoning deactivation. This work decouples the effects of SO_2 poisoning on ZCuOH and Z_2Cu sites in Cu-SSZ-13 zeolites. We use a combination of detailed kinetic (reaction rate, orders and activation energies), spectroscopic (XAS, UV-Visible, FTIR), Brønsted acid site titration (NH_3) methods, and density functional theory (DFT) calculations measurements to show that sulfur transforms both ZCuOH and Z_2Cu sites to inactive states, resulting in a constant SCR turnover rate when normalized by the number of residual Cu sites that are not poisoned by sulfur. Effect of exposure conditions on poisoning intermediates further highlights chemical differences between the two Cu site types, including differences in the number of titratable Brønsted acid sites.

9.2 Abstract

The effects of sulfur poisoning on Cu-SSZ-13 zeolites, used commercially for the selective catalytic reduction (SCR) of nitrogen oxides (NO_x) with ammonia, were studied by exposing model Cu-zeolite powder samples to dry SO_2 and O_2 streams at 473 and 673 K, and then analyzing the surface intermediates formed using spectroscopic and kinetic assessments. Model Cu-SSZ-13 zeolites were synthesized to contain distinct Cu active site types, predominantly

either divalent Cu^{II} ions exchanged at proximal framework Al (Z_2Cu), or monovalent $[Cu^{II}OH]^+$ complexes exchanged at isolated framework Al (ZCuOH). SCR turnover rates (473 K, per Cu) decreased linearly with increasing S content to undetectable values at equimolar S:Cu ratios, consistent with poisoning of each Cu site with one SO_2-derived intermediate. Cu and S K-edge X-ray absorption spectroscopy and density functional theory calculations were used to identify the structures and binding energies of different SO_2-derived intermediates at Z_2Cu and ZCuOH sites, revealing that bisulfates are particularly low in energy, and residual Brønsted protons are liberated at Z_2Cu sites as bisulfates are formed. Molecular dynamics simulations also show that Cu sites bound to one HSO_4^- are immobile but become liberated from the framework and more mobile when bound to two HSO_4^-. These findings indicate that Z_2Cu sites are more resistant to SO_2 poisoning than ZCuOH sites and are easier to regenerate once poisoned.

9.3 Introduction

Sulfur levels in diesel fuel were regulated by the Environmental Protection Agency (EPA) in 1993 to "low-sulfur" contents (500 ppm), and further in 2006 to "ultra-low sulfur" diesel fuel (15 ppm)[1]. Sulfur oxides (SO_x, x = 2, 3) formed during the combustion of diesel fuel deactivate Cu-SSZ-13 zeolite catalysts, which are used for the selective catalytic reduction (SCR) of nitrogen oxides (NO_x, x = 1, 2) with ammonia (NH_3-SCR). The "standard" SCR reaction stoichiometry is:

$$4NO + 4NH_3 + O_2 \rightarrow 4N_2 + 6H_2O \tag{9.1}$$

High temperature (673-1073 K) regeneration is a typical strategy used to reverse the deactivation of SO_x-poisoned Cu-SSZ-13 zeolites. A molecular understanding of how different Cu site types in Cu-SSZ-13 zeolites respond to sulfur exposure would aid in improving strategies to regenerate sulfur-poisoned materials and in developing catalysts that are more sulfur-tolerant[2-4].

Both physical and chemical processes have been invoked to explain sulfur deactivation of Cu-zeolites for NO_x SCR. In Figure 9.1, we summarize the reported decreases in Cu-zeolite micropore volume as a function of sulfur content following various sulfur exposure conditions as collected from the literature. Ham et al. [5-7] reported a decrease in NO_x conversion during NH_3-SCR, and a concurrent decrease in the BET-derived surface area as measured by N_2 adsorption, with increasing sulfur content on Cu-MOR catalysts. Wijayanti et al.[8] (Cu-SAPO-34) and

Brookshear et al.[9] (Cu-SSZ-13) reported similar observations on Cu-CHA exposed concurrently to SO_2 and NH_3, and this evidence has been used to support the proposal that pore-blocking by sulfur-derived species is the dominant mechanism of sulfur poisoning. In contrast, the BET-derived surface areas of Cu-SAPO-34 exposed only to SO_2 (in the absence of NH_3) is not observed to decrease with increasing sulfur content, leading Shen et al. to propose that sulfur-derived species adsorbed at Cu sites cause inhibition or deactivatio[10]. Temperature programmed desorption (TPD) experiments reveal that Cu-zeolites store significantly more SO_2 than do H-form zeolites[10-12].
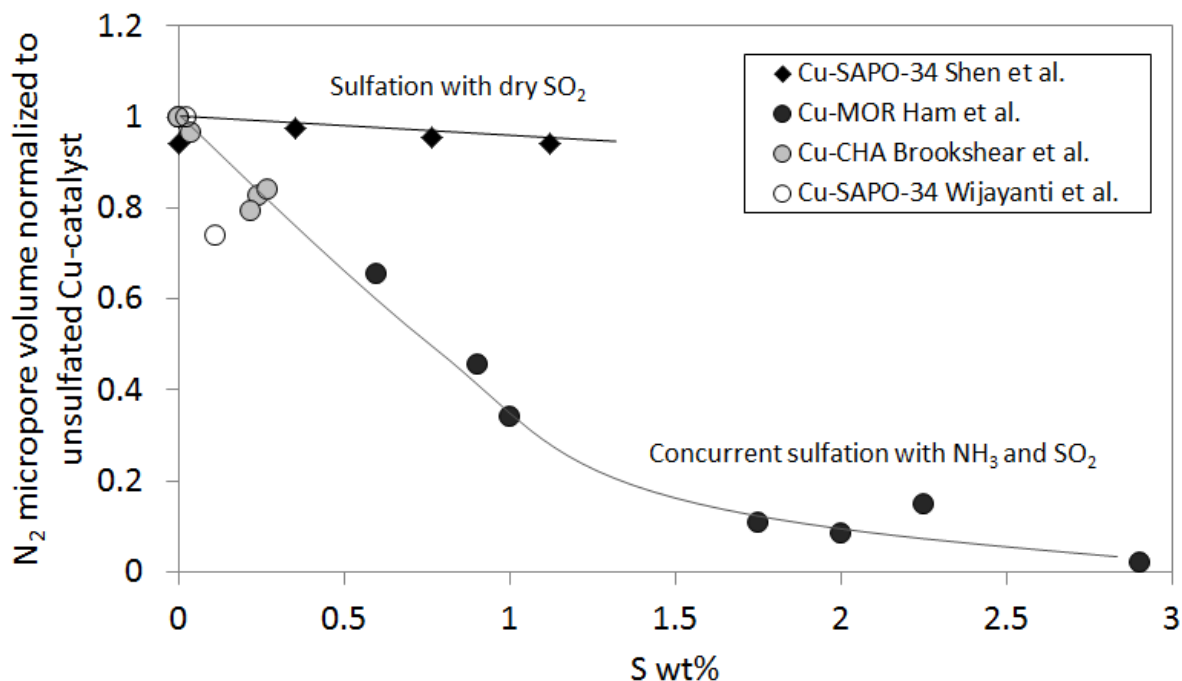
Figure 9.1 Normalized micropore volume (BET-surface areas derived from N_2 adsorption) with increasing S content reported by Ham et al.[5], Brookshear et al.[9], Wijayanti et al.[8], and Shen et al.[10] when Cu-zeolites are poisoned with SO_2, or with SO_2 and NH_3 concurrently.

SO_2 and other molecules relevant to NH_3-SCR catalysis, such as O_2 or NH_3, may have a concurrent effect on the poisoning of Cu-zeolite catalysts. Oxidation catalysts upstream of the SCR catalyst in diesel exhaust aftertreatment systems oxidize SO_2 to SO_3, with the fraction of SO_3 reported to increase with temperature until thermodynamic equilibrium between SO_2, O_2, and SO_3 is reached[13-15]. Cheng et al.[16] reported that the SO_3 deactivates a Cu-zeolite catalyst (framework not specified) to a greater extent than does SO_2 alone. X-ray photoelectron spectroscopy (XPS) shows that the surface sulfur species are in the 6+ oxidation state after

sulfation, regardless of whether SO_3 was present or not during poisoning treatments[16]. Hammershøi et al.[17] and Wijayanti et al.[18] demonstrated that total sulfur storage on Cu-CHA materials during SO_2 dosing increases in the presence of H_2O, NH_3, and NO_x. Observed S:Cu ratios are greater on Cu-SAPO-34 materials exposed to SO_2 and NH_3-SCR gases at low temperature (<573 K) than when exposed to SO_2, O_2 and H_2O at higher temperatures (>573 K)[19].

Cu-CHA catalysts often only partially recover NH_3-SCR reactivity after desulfation[11,12,14,20,21]. Hammershøi et al. report that SCR rates (per mass, 2-30% NO_x conversion) on Cu-SSZ-13 catalysts recover to only ~80% following repeated desulfation treatments under NH_3-SCR conditions (823 K)[17]. Desulfation under these NH_3-SCR conditions occurs only at temperatures greater than 573 K, consistent with sulfur desorption temperatures from TPD experiments [11,16,17,21,22]. Kumar et al. [23] and Ando et al.[24] demonstrated that desulfation occurs more readily in reducing environments (NO + NH_3, NH_3, C_3H_6, n-$C_{12}H_{16}$) than in oxidizing environments, enabling catalyst regeneration at more moderate temperatures. These authors proposed that redox cycling of Cu from the 2+ to 1+ oxidation state promotes regeneration of sulfur-poisoned Cu sites. In contrast, temperatures up to 823 K are required to regenerate Cu under the more oxidizing conditions of standard NH_3-SCR.

Three major conclusions have emerged regarding the NH_3-SCR reaction mechanism on sulfur-free Cu-SSZ-13 catalysts: (1) NH_3-SCR involves a Cu^{II}/Cu^{I} redox process, (2) at low temperatures (<573 K), the SCR active sites are derived from isolated Cu cations that are exchanged at anionic Al sites in the zeolite framework, and (3) the pool of isolated Cu cation sites includes those present as $CuOH^+$ (ZCuOH) and Cu^{II} (Z_2Cu) that are respectively charge compensated by one and two framework Al centers[25-30]. Cu^{II}/Cu^{I} redox cycling is supported using in operando X-ray absorption spectroscopy (XAS) to observe both Cu^{I} and Cu^{II} during standard NH_3-SCR[29,31]. The redox cycle involves binuclear Cu-oxo complexes formed from mononuclear NH_3-solvated Cu^{I} sites during low temperature (<573 K) NH_3-SCR[31,32]. The evidence for two distinct mononuclear Cu^{II} site types in Cu-SSZ-13 includes infrared spectroscopy (DRIFTS, FTIR) observation and quantification of the ν(O-H) stretching vibration at 3660 cm^{-1} of $[Cu^{II}OH]^+$ sites, H_2-temperature programmed reduction (H_2-TPR), Rietveld refinement of X-ray diffraction patterns[33-35], and Cu:H^+ site exchange stoichiometries. From these characterization studies, Cu ions preferentially exchange in SSZ-13 as Z_2Cu to saturation, and then as ZCuOH[30].

Luo et al.[35] and Jangjou et al. [21,35,36] compared the effects of sulfur exposure on Z_2Cu and ZCuOH sites. Luo et al. reported that the framework vibrational mode associated with ZCuOH (950 cm^{-1}) is completely suppressed following sulfur exposure, while the Z_2Cu mode (900 cm^{-1}) decreases to a lesser extent, implying that the former are more susceptible to sulfur poisoning than are the latter[35]. Jangjou et al. used in situ DRIFTS of Cu-SAPO-34 and NO as a probe molecule to conclude that ZCuOH sites deactivate through chemical poisoning and Z_2Cu sites via pore blocking[20]. They further develop kinetic models that incorporate different poisoning species on the two site types[36].

Here, we build on this prior work to isolate the effects of SO_2 exposure alone on ZCuOH and Z_2Cu sites in Cu-SSZ-13 zeolites, by combining an approach that interprets changes in NH_3-SCR kinetic parameters with varying sulfur content, structural characterization of surface species using spectroscopy (XAS, UV-Visible, FTIR), Brønsted acid site titration (NH_3) methods, and density functional theory (DFT) calculations. Kinetic measurements (reaction rate, reaction orders, and apparent activation energies) provide insights on the effects of sulfur poisoning and regeneration on ZCuOH and Z_2Cu sites. We find that the sulfur transforms both ZCuOH and Z_2Cu sites to inactive states, resulting in a constant SCR turnover rate when normalized by the number of residual Cu sites that are not poisoned by sulfur. We use DFT calculations and first-principles thermodynamics to compare poisoning intermediates as a function of exposure conditions that highlight chemical differences between the two Cu site types, including differences in the number of titratable Brønsted acid sites that can be detected in experiments.

9.4   Results and Discussions

9.4.1   Characterization of SO_2-exposed Z_2Cu and ZCuOH samples

Elemental analysis (AAS, ICP, EDS) of the model Cu-SSZ-13 catalysts before and after various SO_2 dosing treatments (600 mL min^{-1} of 100 ppm SO_2 in balance N_2 at 473 K or 673 K to reach a cumulative sulfur exposure of S:Cu = 5) are reported in Figure 9.2. For a given exposure, the ZCuOH model catalyst stored more sulfur (per Cu) than the Z_2Cu model catalyst. The sulfur uptake increases with increasing sulfur exposure temperatures (Figure 9.2), as also observed following SO_2, O_2 and H_2O dosing to Cu-SAPO-34 and Cu-SSZ-13[19,53].
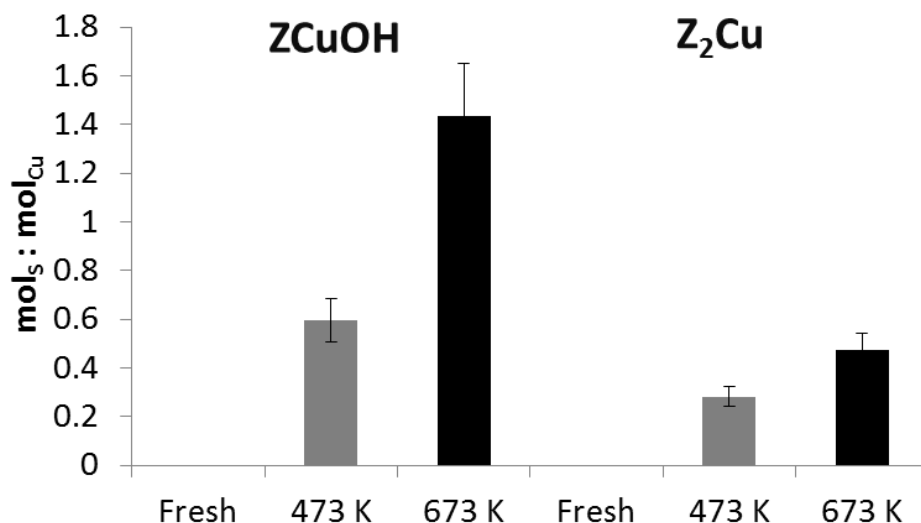
Figure 9.2 Molar S:Cu ratios on model Cu-SSZ-13 samples following various SO_2 exposures.

NH_3-SCR kinetic parameters (apparent activation energies, apparent reaction orders) measured on the two model Cu-SSZ-13 samples at standard (10%) and excess (60%) O_2 feed compositions are reported in Table 9.1 (activation energy and reaction order plots for all samples can be found in Figures S6-S27 and Table S1-S6, supplementary information in Shih et al.[57]). Kinetic parameters (apparent activation energies, apparent reaction orders) collected at 10% O_2 (Table 9.1) suggest the ZCuOH and Z_2Cu samples to be operating in different rate-limiting regimes, complicating comparisons of their kinetic response to sulfur. In contrast, the apparent activation energy ($\sim$50 kJ mol^{-1}) and apparent NO orders ($\sim$1) are similar in 60% O_2 (Table 8.1), suggesting that O_2 is in kinetic excess and rates are limited by an NO + NH_3 reduction step in both samples[29,31,39]. Measurements made at these conditions provide more direct comparisons between the two samples. Figure 9.3 shows the dependence of SCR rates (per Cu) and the apparent activation energy on S content for both model Cu-SSZ-13 samples. With increasing S content, the SCR rate (per Cu) decreases linearly to undetectable values at a S:Cu ratio of 1, while apparent activation energies appear constant (40-55 kJ mol^{-1}), suggesting equimolar poisoning of each Cu active site by an SO_2-derived intermediate.

Table 9.1 Apparent activation energies and reactant orders on unsulfated ZCuOH and Z_2Cu model catalysts collected under "10% O_2 SCR" conditions (300 ppm NO, 300 ppm NH_3, 10% O_2, 2.5% H_2O, 8% CO_2, balance N_2 at 473 K) and "60% O_2 SCR" conditions (300 ppm NO, 300 ppm NH_3, 60% O_2, 2.5% H_2O, 8% CO_2, balance N_2 at 473 K).

	E_{app} 10% O_2 SCR	E_{app} 60% O_2 SCR	NO order 10% O_2 SCR	NO order 60% O_2 SCR	O_2 order 10% O_2 SCR	O_2 order 60% O_2 SCR	NH_3 order 10% O_2 SCR	NH_3 order 60% O_2 SCR
ZCuOH	52	46	0.60	0.90	0.65	0.37	-0.40	-0.63
Z_2Cu	69	54	0.90	0.94	0.30	0.02	0.00	-0.04
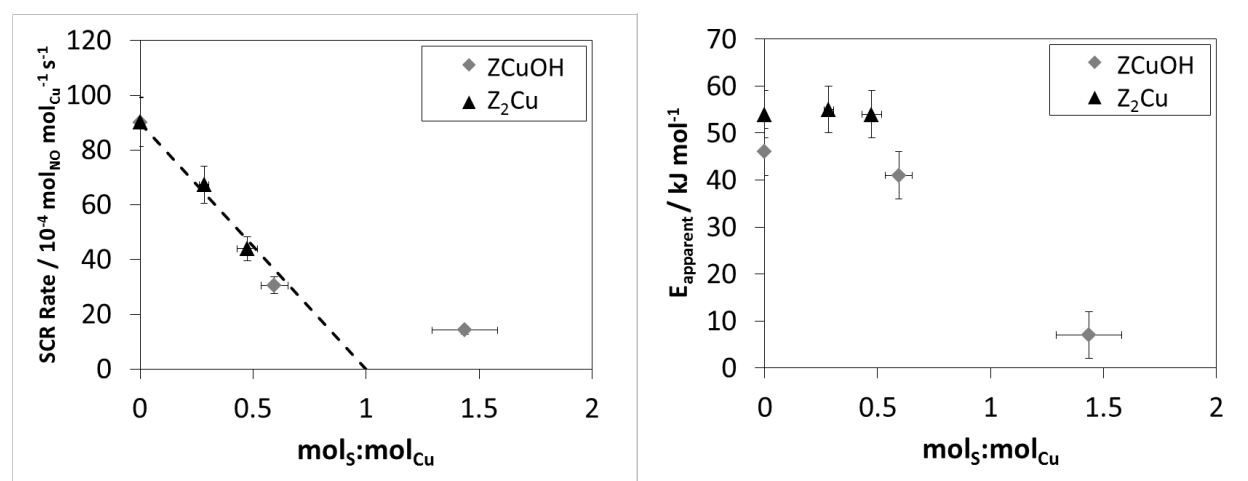
Figure 9.3 Reaction rates and apparent activation energies for ZCuOH (red) and Z_2Cu (blue) model materials after sulfation. SCR conditions are 300 ppm NO, 300 ppm NH_3, 60% O_2, 2.5% H_2O, 8% CO_2, balance N_2 at 473 K.

One ZCuOH sample adsorbed sulfur to an excess molar value of S:Cu of 1.4, and does not follow the equimolar poisoning behavior indicated by the dashed line in Figure 9.4. This observation suggests sulfur to be present both as associated with Cu sites and adsorbed elsewhere on the sample. The E_{app} value of 14 kJ mol^{-1} on this sample is also much lower than on the other samples. The apparent activation energy and reaction orders on this sulfated sample are similar to those measured on a Cu-SSZ-13 sample that is volumetrically dilute in Cu (Cu wt% = 0.1 and Si:Al = 100, Table S7 and Figures S28-S30 from supplementary information in Shih et al.[57]), suggesting that sulfur may be effectively diminishing the ability of isolated Cu ions to form dimeric Cu intermediates during the SCR cycle. Thermograviometric analysis (TGA) indicates that the ZCuOH sample poisoned to a S:Cu ratio of 1.4 contains a larger fraction of species that

desorb at 1000 K than do other sulfated samples (Figure S31 from supplementary information in Shih et al.[57]). Under SCR conditions at 473 K, this sample is less than 100% selective to N_2 and is 20% selective towards NO oxidation to NO_2 (Figure S32 from supplementary information in Shih et al.[57]). This NO_2 generation and its subsequent consumption, for instance via fast SCR (Equation 9.2) on acid or Cu sites, makes it impossible to directly compare SCR kinetic parameters obtained on these materials with those on the other SO_2-poisoned samples[54].

$$2NO_2 + 2NO + 4NH_3 \rightarrow 4N_2 + 6H_2O \tag{9.2}$$

SCR rates (per Cu) decrease with S content on the two model Cu-SSZ-13 catalysts studied here, consistent with each S atom poisoning one ZCuOH or Z_2Cu site. Diffuse reflectance UV-Visible spectra were collected on the model ZCuOH and Z_2Cu samples before and after sulfation treatments to identify electronic signatures correlated with sulfur uptake (Figure 9.4). Spectra collected at ambient conditions (Figure S33, supplementary information in Shih et al.[57]) are consistent with water-solvated Cu ions on both samples. Upon partial dehydration (523 K in dry air, to retain sulfur), however, qualitative differences in the d-d transition and charge transfer regions become apparent[28,30]. With increasing sulfur content, three of the four features in the d-d transition region disappear on the sample prepared to contain nominally ZCuOH sites, while the corresponding features in the sample prepared to contain nominally Z_2Cu sites are unchanged. Similarly, a new lower-energy feature in the charge transfer region (38,000 cm^{-1}) is more pronounced on the ZCuOH sample than the Z_2Cu sample. While the stoichiometric response to sulfur is similar on the two samples, the changes in UV-Vis spectral features are not.
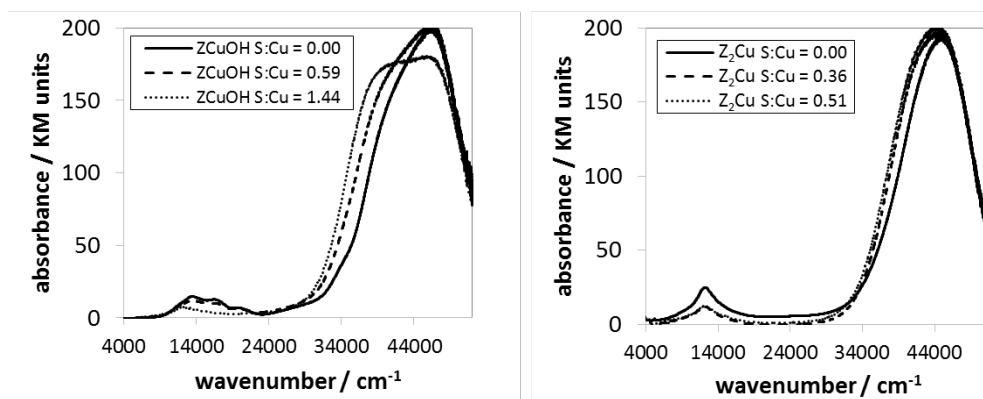
Figure 9.4 Diffuse reflectance UV-Visible spectra on ZCuOH (left) and Z_2Cu (right) after partial dehydration at 523 K under dry air.

In situ and in operando XAS was used to probe qualitative changes in the Cu oxidation state following sulfation, because accurate quantification of Cu oxidation state in the presence of sulfur was not possible (details in supplementary information in Shih et al.[57], Section S4). The fraction of Cu^{II} that is reducible by exposure to NO and NH_3 decreases from 100% on the unsulfated samples to ~70% on all four sulfated samples (Table S9, supplementary information in Shih et al.[57]) under reaction conditions from in operando XAS measurements, the Cu^{II}/Cu^I fraction is higher on sulfur-exposed ZCuOH samples than on sulfur-free ones. The Cu^{II}/Cu^I fraction is 0.9 on Z_2Cu samples even before sulfur exposure, so changes in response to sulfur could not be resolved (Table S8, supplementary information in Shih et al.[57]). From analysis of the EXAFS region, average Cu coordination numbers increased on ZCuOH materials and were unchanged on Z_2Cu materials following sulfation (Table S10, supplementary information in Shih et al.[57]). This observation corroborates the qualitative changes observed in UV-Visible features of the ZCuOH sample, but not of the Z_2Cu sample, with increasing sulfur poisoning.

S K-edge XAS was used to probe the state of the sulfur species bound to the Cu sites. Ex situ XANES spectra were collected on the Z_2Cu and ZCuOH samples sulfated at either 473 K or 673 K, each of these samples exposed to 300 ppm NH_3 at 473 K for 1 hour, and each of these samples exposed to standard SCR gas mix for 30 min. Figure 6 plots all the normalized XANES spectra for the Z_2Cu samples (Figure 9.5a) and the ZCuOH samples (Figure 9.5b). All 12 spectra show a single prominent peak at 2480 eV, indicating the presence of S^{6+} species, regardless of sulfation and any subsequent gas treatment conditions. There is no other feature in between 2470 eV and 2477 eV, which rules out the presence of sulfur in other oxidation states (e.g. S^{2-} and S^{4+}).
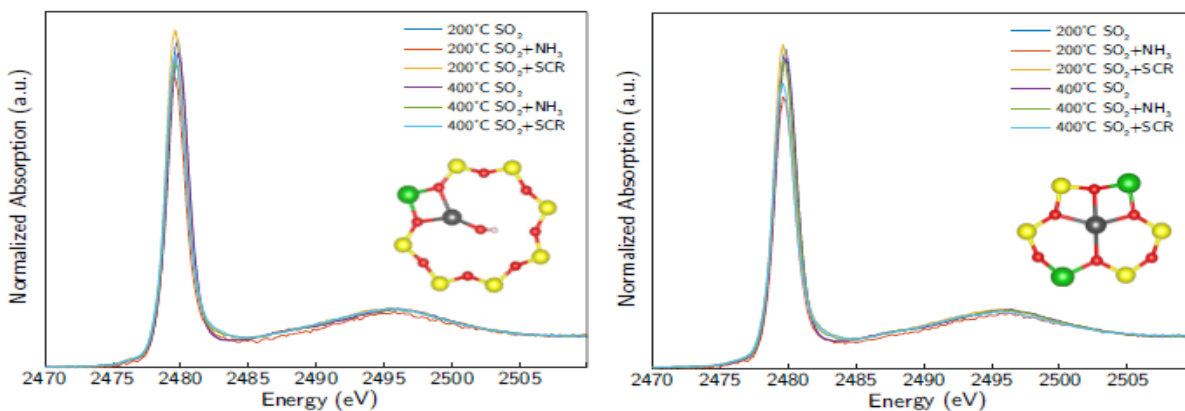
Figure 9.5 Sulfur K-edge XANES measured ex situ at ambient conditions of ZCuOH (left) and Z_2Cu (right) samples treated with SO_2 and O_2 at either 200°C or 400 °C.

9.4.2   Characterization of desulfated Z_2Cu and ZCuOH samples

The four sulfated catalysts were desulfated in a NO + NH$_3$ feed stream (300 ppm NO, 300 ppm NH$_3$, balance N$_2$, 673 K) until a cumulative molar exposure of NO:S of 100 was obtained[23]. Elemental analysis results in Figure 9.6 show that the sulfur content decreases by different proportions on each sample. Successive desulfation treatments were not performed due to experimental limitations on the amount of sample studied.
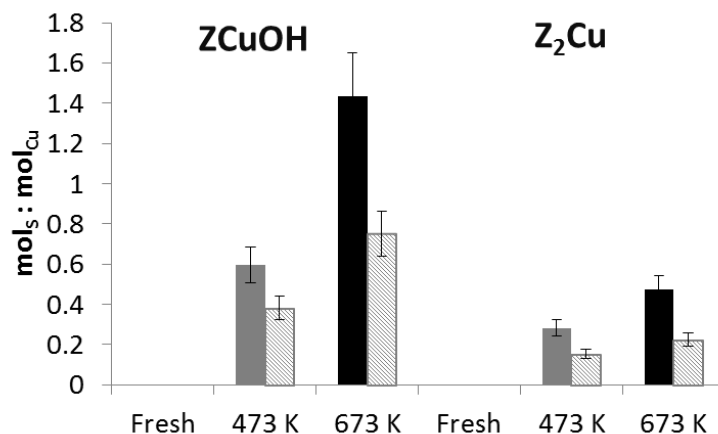
Figure 9.6 S:Cu ratios before (solid bars) and after desulfation (hatched bars) on ZCuOH and Z_2Cu model materials.
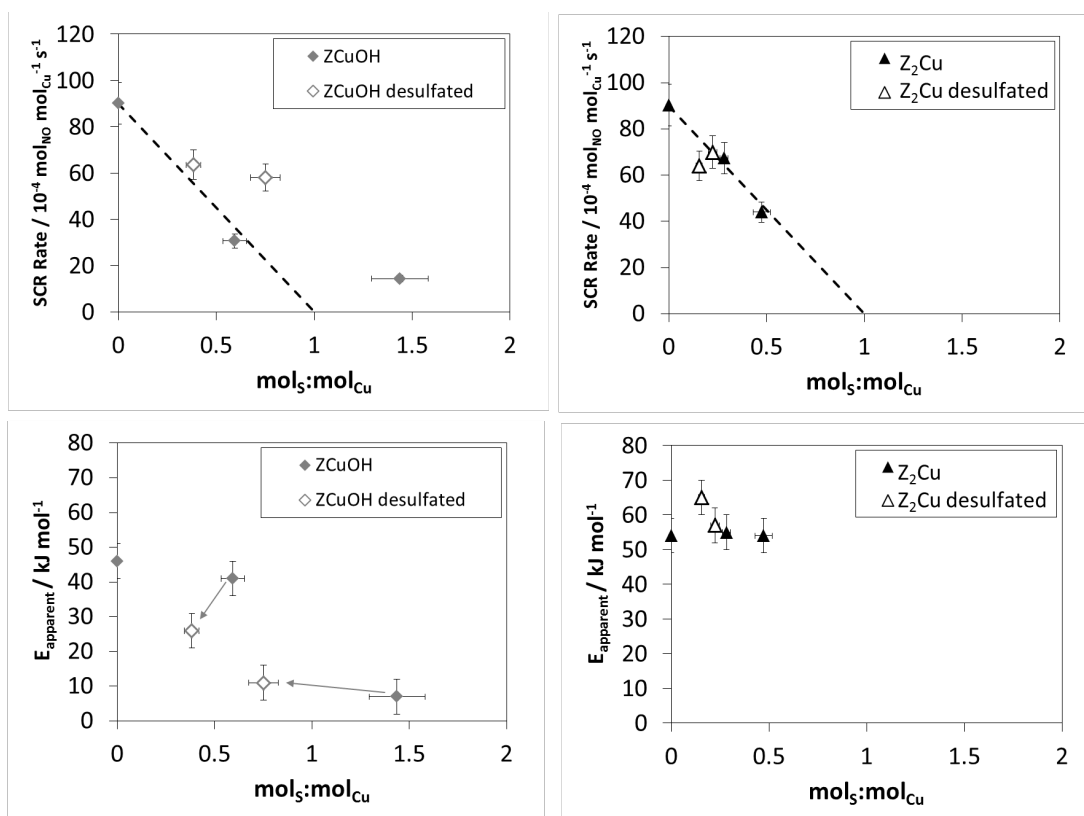
Figure 9.7 Reaction rates and apparent activation energies for ZCuOH and Z_2Cu model materials after sulfation (filled) and desulfation (hollow). SCR conditions are 300 ppm NO, 300 ppm NH_3, 60% O_2, 2% H_2O, 8% CO_2, balance N_2 at 473 K. Arrows indicate the starting and ending samples after desulfation, and thus how the apparent activation energy changes after desulfation.

SCR reaction rates (per Cu) and activation energies measured on desulfated samples are shown in Figure 9.7. Rates on Z_2Cu samples increase in direct proportion to the number of sulfur species removed, while the apparent activation energy and reaction orders are unchanged within error (Figure 9.7, Figure S50 in supplementary information in Shih et al.[57]). Sulfation thus appears to result in the loss of Z_2Cu active sites and to be reversible. In contrast, rates measured on desulfated ZCuOH samples do not recover to the original values after S content is accounted for, and apparent activation energies are also different before and after desulfation treatments, suggesting that some sites are irreversibly deactivated by sulfur. Reaction rates at a given S:Cu ratio on desulfated samples are higher on the ZCuOH catalyst that was initially poisoned to S:Cu > 1, than on the other catalysts, suggesting that desulfation may preferentially remove sulfur bound to the Cu over other types of sulfur species stored on the sample (Figure S50, supplementary information in Shih et al.[57]).

We present quantitative evidence that, taken together, shows that sulfur poisons and deactivates both ZCuOH and Z_2Cu sites in an equimolar ratio at S:Cu < 1, but via mechanisms that reveal themselves differently in spectroscopic and pore volume measurements (N_2 and Ar micropore volume measurements and XRD data in section S5 of supplementary information in Shih et al.[57]). Apparent activation energy and reaction orders are constant during the sulfation and desulfation processes. Turnover rates are constant when reaction rate is normalized to the number of initial Cu sites less the number of S species on each sample (mol_{Cu} – mol_S) (Figure 9.8).
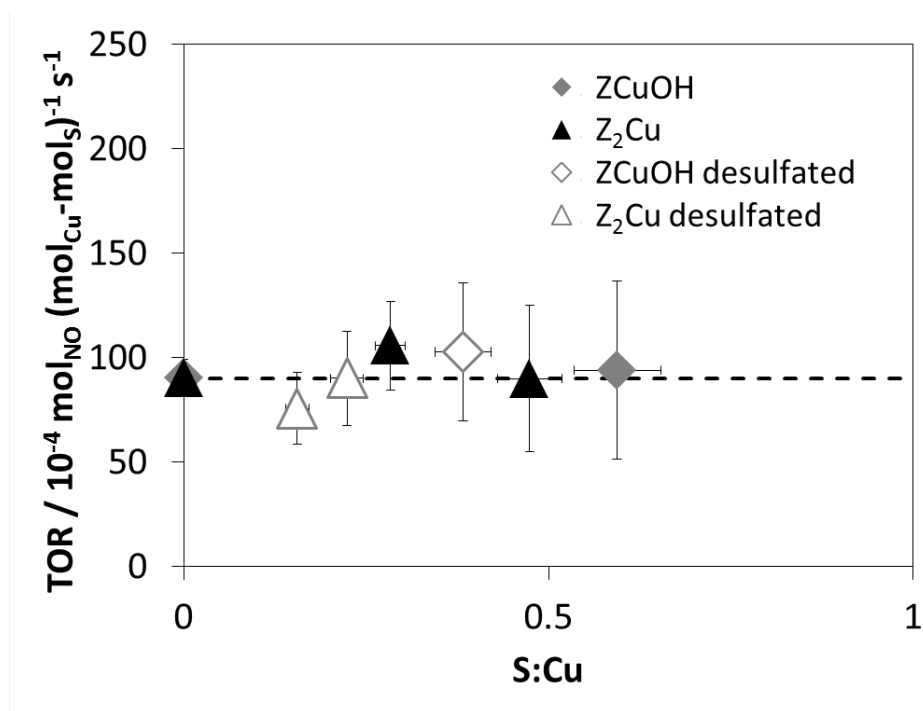
Figure 9.8 Fresh, sulfated, and desulfated samples that exhibit the same apparent activation energy collapse to the same turnover rate when normalized to (mol_{Cu} – mol_S).

9.4.3 Structures and energies of sulfur species bound to Cu sites

We used DFT calculations and first principles thermodynamics[30] to explore the differences in response of Z_2Cu and ZCuOH sites to exposure to SO_2, H_2O, O_2, and NH_3 as a function of temperature and exposure conditions. We drew on literature results[21,55,56] and chemical intuition to construct a variety of candidate structures containing up to two SO_x combined with NH_3 and H_2O, and then considered chemically relevant S/O/H compounds (SO_2, SO_3, sulfide, (bi)sulfite, (bi)sulfate) as ligands with and without OH, H_2O, NH_4^+ and NH_3

ligands. We annealed using AIMD at 473 K and relaxed to obtain final DFT formation energies. All structures are provided as VASP CONTCAR files, and HSE06-D2 energies and normalized Bader charges are presented in the supporting information (section S5, Tables S14 and S15 in supplementary information in Shih et al.[57]).
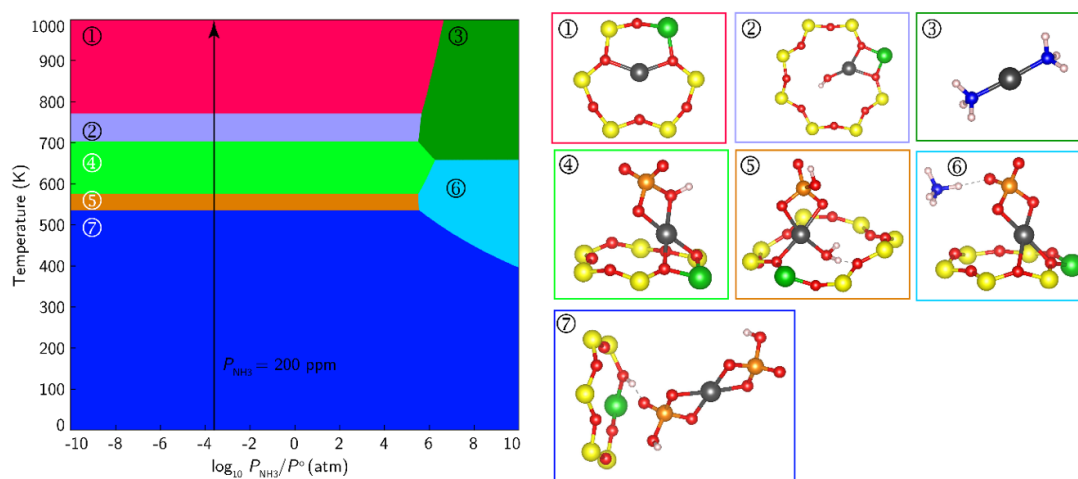
Figure 9.9 First-principles phase diagram for $S_wO_xH_yN_z$ species on a ZCuOH site vs temperature and NH_3 partial pressure at 1 atm total pressure and 20 ppm SO_2, 10% O_2, and 5% H_2O. Molecular structures corresponding to each region indicated by numbers. Gray, red, yellow, green, blue, orange, and white spheres correspond to Cu, O, Si, Al, N, S, and H atoms, respectively. Zeolite framework included only when directly hosting Cu or H.
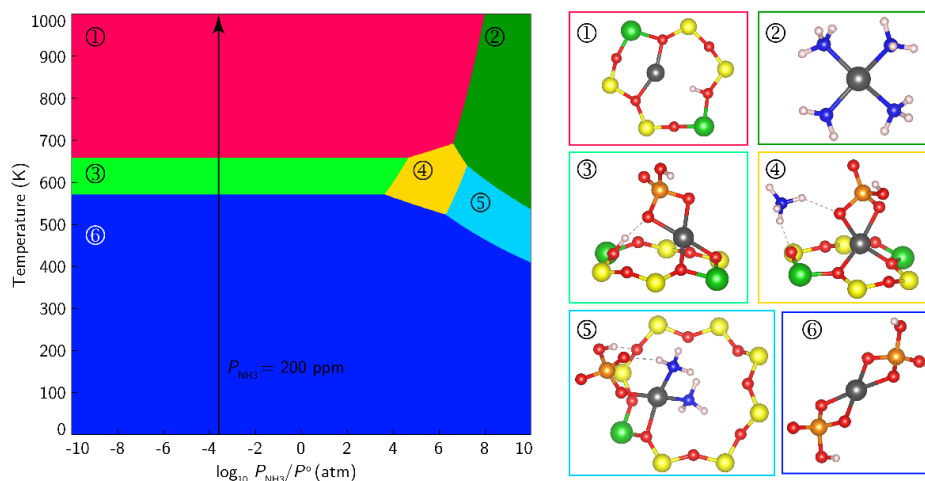
Figure 9.10 First-principles phase diagram for $S_wO_xH_yN_z$ species on a Z_2Cu site vs temperature and NH_3 partial pressure at 1 atm total pressure and 20 ppm SO_2, 10% O_2, and 5% H_2O. Molecular structures corresponding to each region indicated by numbers. Gray, red, yellow, green, blue, orange, and white spheres correspond to Cu, O, Si, Al, N, S, and H atoms, respectively. Zeolite framework included only when directly hosting Cu or H.

Figure 9.9 and 9.10 show the equilibrium phase diagrams for ZCuOH and Z_2Cu sites, respectively, as a function of NH_3 pressure and temperature at 20 ppm SO_2, 10% O_2, and 5% H_2O, 1 atm total pressure, chosen as variables to simplify presentation and to emphasize any differences between non-SCR and SCR conditions as a function of temperature. These diagrams report the thermodynamic equilibrium species without consideration of formation kinetics, and thus must be interpreted appropriately. Across the entire composition space, save for the highest temperature region of the ZCuOH diagram, Cu is present in the 2+ oxidation state, and all S species are present as bisulfate (HSO_4^-), consistent with the Cu and S oxidation states observed in the XAS above. Further, Cu^{2+} is always present in four-fold coordination consistent with EXAFS analysis (section S4 and Table S10 from supplementary information in Shih et al.[57]). The left sides of the diagrams correspond to SO_2 exposure in the absence of NH_3. In this limit, the most stable species on both Cu sites contain two bisulfate ligands at low temperature, transitioning to a single bisulfate at temperatures closer to those relevant to experimental dosing and consistent with the uptake stoichiometry of 1 S: 1 Cu. The temperature to fully desorb sulfur is predicted to be upwards of 100˚C higher on ZCuOH than Z_2Cu. A key difference between the two sites is the predicted creation of a new Brønsted acid site upon sulfation for Z_2Cu but not ZCuOH.

To test this prediction, we employed methods we have developed previously to selectively quantify NH_3 adsorbed on Brønsted acid and Cu sites, while excluding physisorbed NH_3[38,40]. Table 2 reports the number of excess NH_3 (per S), relative to the unsulfated Cu-SSZ-13 samples:

$$NH_3:S = \frac{(\text{mol } NH_3 \text{ on sulfated sample}) - (\text{mol } NH_3 \text{ on unsulfated sample})}{(\text{mol S on sulfated sample})} \tag{9.3}$$

Sulfation does not change the total number of NH_3 stored on the model ZCuOH catalyst, but does increase the amount of NH_3 stored in a ratio of 1 NH_3:S for the model Z_2Cu catalyst (Table 9.2). The excess 1:1 NH_3:S molar ratio on sulfated-Z_2Cu sites may reflect storage at excess Brønsted acid sites after sulfation, consistent with DFT predictions (Figure 9.11) that the sulfation of Z_2Cu sites results in the generation of new Brønsted acid sites.

Table 9.2 Molar NH_3:S values calculated from excess NH_3 storage on Cu-SSZ-13 catalysts after dry SO_2 poisoning. Corresponding S:Cu loadings on the four samples and the total NH_3:Cu molar ratios are also included for comparison.

Sample	NH_3:S	S:Cu	NH_3:Cu
ZCuOH	-0.2 ± 0.2	0.59	2.7
ZCuOH	0.0 ± 0.2	1.44	2.8
Z_2Cu	1.2 ± 0.2	0.36	3.0
Z_2Cu	0.9 ± 0.2	0.51	3.0

Moving to the right in Figures 9.9 and 9.10, corresponding to increasing exposure to NH_3, Z_2Cu sites eventually transition to an ammonium bisulfate and ZCuOH to an ammonium sulfate (regions 4 and 6, respectively). While absolute NH_3 pressures along this axis should be viewed cautiously due to the approximations used to capture the entropy of the products and uncertainties in the DFT energies themselves, it is clear that the ammonium species forms more readily on the Z_2Cu site than the ZCuOH. Further, it is clear that either in the absence or presence of NH_3, sulfur species persist to higher temperature on ZCuOH than Z_2Cu sites, consistent with the experimentally observed trend in thermal desulfurization.

These results are consistent with an equivalent sulfur deactivation stoichiometry on the two sites and hint at differences in the deactivating species, but do not directly inform observed differences in deactivation mechanism. To test the effect of sulfur uptake on Cu mobility, we turned to AIMD calculations. We considered one and two bisulfate species on both Z_2Cu and ZCuOH sites, including species predicted to be stable near to the experimental conditions in the presence of NH3: $[ZCu^{II}(HSO_4)][ZH]$ and $[Cu^{II}(HSO_4)_2][Z_2H_2]$ on Z_2Cu and $[ZCu^{II}(HSO_4)]$ and $[Cu^{II}(HSO_4)_2][ZH]$ on ZCuOH. We ran an extended period of AIMD and extracted the last 90 ps of the AIMD trajectory for further structural analysis. We estimated effective first shell coordination number (CN) from the computed radial distribution function (RDF) between Cu and all other heavy atoms integrated to 2.3 Å [30]. As shown in Table 9.3, the CN is 4 regardless of site or state of sulfation.

Figure 9.11 displays the Cu positions visited during the 90 ps of AIMD, superimposed onto a fixed zeolite framework. The relative Cu mobility was quantified by a spatial discretization method described previously[30] and quantified and compared to previous results in Table 9.3. The mobility of Cu ions bound to a single bisulfate are roughly unchanged from the parent Z_2Cu and ZCuOH sites and slightly increased when two bisulfates are bound to a Cu. The

mobilities of all sulfated species are much lower than the mobilities of the NH$_3$-solvated Z$_2$Cu and ZCuOH sites that would be present in the absence of sulfur (Table 9.3).
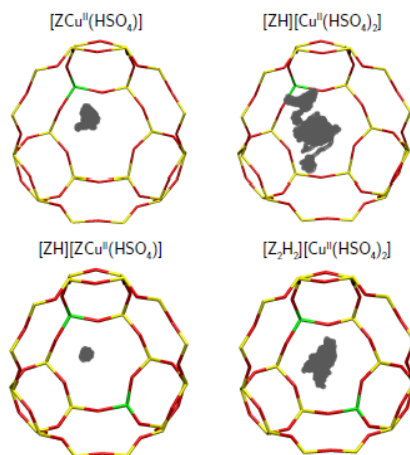
Figure 9.11 Cu positions visited during 90 ps of AIMD at 473 K, represented by gray balls superimposed on a fixed zeolite framework. Framework was not constrained during the actual AIMD run.

Table 9.3 Comparison of AIMD characterization of the 1Al/2Al samples, including composition of stable species, Cu-X (X = O,N) first shell coordination number (CN), average Cu-X bond distances (Å), and Cu mobility.

Condition	Sample	Chemical composition	CN	Avg. bond. Dist. / Å	Cu mobility
Model sites (300 K)[a]	1Al	[ZCu^{II}OH]	3.0	1.96	1.1
	2Al	[Z$_2$Cu^{II}]	4.0	1.96	1.0
NH$_3$-solvated (473 K)[a]	1Al	Z[Cu^{I}(NH$_3$)$_2$]	2.0	1.89	27.7
		Z[Cu^{II}(OH)(NH$_3$)$_3$]	4.0	2.05	18.2
	2Al	Z[Cu^{I}(NH$_3$)$_2$][ZNH$_4$]	2.0	1.89	13.4
		Z$_2$[Cu^{II}(NH$_3$)$_4$]	4.0	2.07	8.3
Sulfated (473 K)[b]	1Al	[ZCu^{II}(HSO$_4$)]	4.0	1.96	1.1
		[ZH] [Cu^{II}(HSO$_4$)$_2$]	4.0	1.96	4.6
	2Al	[ZH] [ZCu^{II}(HSO$_4$)]	4.0	1.98	1.7
		[Z$_2$H$_2$][Cu^{II}(HSO$_4$)$_2$]	4.0	1.96	2.6

[a]data from C. Paolucci, et al., J. Am. Chem. Soc., 138 (2016), 6028-6048[30]
[b]data from this work.

9.5   Conclusions

The effects of dry SO$_2$ poisoning at 473 and 673 K were determined on model Cu-SSZ-13 catalysts synthesized to contain nominally Cu^{II} exchanged at proximal Al centers (Z$_2$Cu sites)

or [Cu^{II}OH]$^+$ exchanged at isolated Al centers (ZCuOH sites). ZCuOH sites are more prone to SO$_2$-poisoning than Z$_2$Cu sites, reflected in the larger amounts of SO$_2$-derived intermediates that were stored on the model ZCuOH sample than on the model Z$_2$Cu sample, upon exposure to the same sulfation treatment. NH$_3$-SCR rates (473 K, per Cu) decrease proportionally with the S:Cu ratio on the Z$_2$Cu and ZCuOH samples, while apparent activation energies are essentially unaffected, consistent with equimolar Cu site poisoning by each SO$_2$-derived intermediate. Additional SO$_2$ storage is also observed on non-Cu sites in the ZCuOH sample, and evidence is provided for partial micropore occlusion by SO$_2$-derived species. Computation shows that bisulfates are particularly low in energy, that Z$_2$Cu and ZCuOH can take up one or two bisulfates, and that residual Brønsted acid sites are liberated as bisulfates are formed at Z$_2$Cu sites. Molecular dynamics simulations also show that Cu sites bound to one HSO$_4$ are immobile, but those bound to two are liberated from the framework and become more mobile. Taken together, experimental and theoretical characterizations support the hypothesis that Z$_2$Cu sites are more resistant to SO$_2$ poisoning than ZCuOH sites, and can be regenerated more easily once poisoned.

9.6   Methods

9.6.1   Synthesis, sulfation, and de-sulfation of Cu-zeolites

H-SSZ-13 zeolites were synthesized following a procedure reported by Fickel et al[33], which is based on a patent by Zone[37]. The procedure was reported in our earlier publication[30]. SSZ-13 with Si:Al molar ratios of 4.5 and 25 were synthesized. The sodium form (Na-SSZ-13) was synthesized hydrothermally in a rotating oven at 433 K for 10 days, washed with water and acetone, then calcined at 823 K in dry air (AirZero, Indiana Oxygen) for 10 h to remove the template[29,38,39]. The resulting Na-SSZ-13 zeolite was converted to the NH$_4$-form by ion exchange with 0.1 M NH$_4$NO$_3$ (>99%, Aldrich) (100 g solution per gram of catalyst) at 353 K for 10 h. The H-SSZ-13 zeolite was obtained by calcining the NH$_4$-SSZ-13 at 823 K in dry air (AirZero, Indiana Oxygen) for 10 h.

Copper was exchanged onto H-SSZ-13 samples via aqueous-phase ion exchange with between 0 and 0.02 M solutions of Cu(NO$_3$)$_2$ (99.9% Aldrich). During this process, NH$_4$NO$_3$ (>99% Aldrich) 0.1 M was added drop-wise to control the pH at a value of 5. The Cu-SSZ-13

samples were dried at 373 K, cooled to room temperature under ambient air, then pelleted and sieved to retain 125 to 250 μm particles (W.S. TYLER No. 60 and No. 120 all-stainless-steel).

In this paper, two model catalysts were synthesized, one with a Si:Al of 4.5 with a Cu wt% of 3.8 (100% Z_2Cu, 0% ZCuOH) and one with a Si:Al of 25 with a Cu wt% of 1.5 (80% ZCuOH, 20% Z_2Cu). The relative fraction of Z_2Cu and ZCuOH active sites were confirmed using Cu elemental analysis and selective titration of Brønsted acid sites using NH_3, as outlined in our previous publication[30]. Sulfation treatments were performed by saturating 0.5 g of sieved catalyst in a flowing stream of N_2 (600 mL min^{-1}) containing 100 ppm SO_2 at 473 K or 673 K for a pre-determined time, such that the cumulative molar exposure was S:Cu = 5. In this paper, sulfated sample names are preceded by 473 K SO_2 or 673 K SO_2 to denote sulfation treatments at 473 K and 673 K, respectively.

Desulfation treatments of sulfated samples were performed in a reductive environment in flowing N_2 (800 mL min^{-1}) containing of 500 ppm NH_3 and 500 ppm NO at 673 K. Typically, 0.02 to 0.05 g of each sulfated catalyst was heated to 673 K in dry nitrogen (liquid nitrogen boil-off, Linde) with a ramp rate of 283 K per minute, then exposed to flowing NH_3 and NO stream for a pre-determined time, such that the cumulative molar exposure of NO:S was 100. The de-sulfated catalysts were then cooled to ambient temperature in N_2 flow.

9.6.2   Catalyst Characterization

Bulk Si, Al and Cu contents in all Cu-SSZ-13 samples were determined by atomic absorption spectroscopy (AAS) on a PerkinElmer AAnalyst® 300 atomic absorption spectrometer. For AAS sample preparation, 20 to 50 mg of sample was dissolved in 2 mL of hydrofluoric acid (HF, 48 wt%, Sigma Aldrich) for 24 hours. The dissolved sample was then diluted with 50 to 140 g of deionized H_2O (Millipore, 18.2 mΩ).

Si, Al, Cu, and S were also measured using inductively coupled plasma – optical emission spectroscopy (ICP-OES) on an iCAP 7400 ICP-OES analyzer. Samples were prepared by acid microwave digestion. For ICP-OES sample preparation, about 30 mg of sample is transferred to a Teflon liner with 9 mL of HNO_3, 3 mL HF, and a magnetic stir bar, then heated while stirring to 503 K (temperature reached in 5 minutes) and holding at 503 K for 20 minutes. Next, the sample was allowed to cool to ambient temperature for 1 hour, after which point 10 mL

of 4% boric acid was added. The sample was heated while stirring to 453 K in 4 minutes and held for 15 minutes. Once cooled, the resulting liquid was diluted to 100 mL.

Scanning electron microscopy images were collected using a FEI Quanta 3D FEG® scanning electron microscope. Electron dispersive X-ray analysis was used to determine the elemental content for Si, Al, Cu, and S. X-ray powder diffraction patterns between 4 and 40° 2θ were obtained using a Rigaku Smart Lab® X-ray diffractometer with a Cu K(α) radiation source operated at 1.76 kW.

Selective NH_3 titration of Brønsted acid sites was used to quantify the number of Brønsted acid sites, as described in our previous publications[38,40]. Briefly, 500 ppm of NH_3 in balance N_2 is flown through the catalyst at 433 K until saturation, then a stream of 2% H_2O in balance N_2 is used to flush out NH_3 bound to Lewis acidic Cu sites until steady state. At this point, temperature-programmed desorption (TPD) in performed and the NH_3:Al is determined from integrating and quantifying the TPD profile.

UV-Vis-NIR spectroscopy was used to identify changes in the coordination of copper active sites in sulfated Cu-SSZ-13, as evidence of SO_2 binding to Cu species. Also, the formation of intermediate NH_4-SOx-like species was studied by collecting spectra after saturating the samples with 500 ppm NH_3 at 298 K and 473 K. UV-Vis-NIR spectra from 4000 to 50000 cm^{-1} and scan speed of 2000 cm^{-1} min^{-1} were collected on a Cary 5000® UV-VIS-NIR spectrophotometer equipped with a Harrick-Scientific Praying-Mantis® diffuse reflectance optics and cell. $BaSO_4$ (99%, Sigma-Aldrich) was used as a 100% reflectance standard. All samples were dehydrated with 100 mL min^{-1} air (AirZero, Indiana Oxygen) at 523 K for 6 h before analysis. The low dehydration temperature of 523 K was selected to avoid desorption of sulfur species [11,16,17,21,22].

Argon (87 K) and nitrogen (77 K) micropore measurements were collected on a Micromeritics Accelerated Surface Area and Porosimetry (ASAP) 2020 system and were used to probe changes in accessible catalyst volumes after sulfation treatments. Prior to analysis, 15 to 30 mg of unsulfated Cu-SSZ-13 samples were degassed at 673 K under vacuum (<5 μtorr) for 12 h and were compared to the same samples degassed at 423 K under vacuum (<5 μtorr) for 4 h. Both degas treatments resulted in measurement of the same micropore volume within error, thus the lower temperature degas treatment was performed on the sulfated samples before collecting micropore volumes. Subjecting a sulfated sample to the 423 K degas treatment did not result in a

significant decrease in sulfur content, as measured by ICP (Figure S1 from supplementary information in Shih et al.[57]).

Fluorescence sulfur K-edge X-ray absorption spectroscopy (XAS) was performed at Sector 9-BM of the Advanced Photon Source at Argonne National Laboratory. Samples were pressed into circular wafers (8 mm x 0.5 mm) and adhered to carbon tape, then transferred to a He-purged chamber to minimize losses in fluorescence signal. Energies were calibrated using a sodium thiosulfate pre-edge feature at 2469.20 eV. XAS spectra were collected in an energy range between 2420 and 2550 eV. Since sulfur content on all samples were low (<1 wt%), dilution was not performed to minimize self-absorption. The sulfur content was not constant enough for quantitative analysis. XANES spectra are plotted as the ratio of the intensity of the total fluorescence signal to the intensity of the excitation radiation as a function of the photon energy. Pre-edge and post-edge spectra were normalized to 0 and 1, respectively.

Copper-edge X-ray absorption spectroscopy (XAS) was performed at Sector 10-ID of the Advanced Photon Source at Argonne National Laboratory [41,42]. A Cu metal foil spectrum was simultaneously collected while measuring sample spectra to calibrate the Cu K-edge to 8979 eV. Operando and in situ experiments were performed in a glassy carbon reactor with catalyst diluted with spherical carbon beads to minimize beam absorption[25]. For operando XAS experiments, a standard SCR gas mixture was introduced to the reactor. H_2O was introduced into a N_2 (UHP, Airgas) and CO_2 (HP, Airgas) through a PermaPure MH® humidifier. Then, NO (3000 ppm in N_2, Matheson Tri-Gas), O_2 (20% in He, Airgas) were added to the stream. NH_3 (3000 ppm in He, Matheson Tri-gas) was added last to minimize the formation of NH_4NO_3. The reaction mixture was preheated to 473 K using preheater coil upstream of the reactor. For in situ XAS measurements under reducing conditions, 500 mL min^{-1} of a 300 ppm NO (3000 ppm in N_2, Matheson Tri-Gas) and 300 ppm NH_3 (3000 ppm in He, Matheson Tri-gas) in balance N_2 was used. Again, the inlet flow was preheated to 473 K via heat tracing and a preheater coil. Sulfated catalysts were not calcined prior to exposure to gases and were not exposed to temperatures greater than 523 K to prevent desorption of sulfur species. For both operando and in situ experiments, concentrations were stabilized through a bypass before exposure to the catalyst bed. XAS spectra were collected in an energy range between 8700 and 9890 eV for samples held under different gas conditions, and between 8700 and 9780 eV for operando experiments. Once the catalyst was exposed to the gases, XAS spectra were taken approximately every 2 min until

stabilization. NO_x, NH_3, H_2O, CO_2 concentrations were measured using a Multi-Gas 2030® FTIR gas analyzer during operando and in situ experiments.

A method that quantifies only NH_3 adsorbed on Brønsted acid sites and Lewis acidic Cu sites, and not physisorbed on the zeolite structure, was developed. The procedure involves saturation of the catalyst in a packed bed reactor with 500 ppm NH_3 in balance N_2 at 433 K (Figure S2 from supplementary information in Shih et al.[57]). On unsulfated samples, the NH_3:Al quantified from NH_3 consumption during the saturation step, and from NH_3 formation during the TPD step, were identical within error (Figure S3 from supplementary information in Shih et al.[57]). The parity in NH_3:Al measured during saturation and during TPD allow quantifying the ammonia stored on sulfated Cu-SSZ-13 materials without desorbing sulfur, which can damage downstream equipment.

9.6.3   SCR kinetic measurements

Kinetic measurements of NH_3-SCR were collected in a down-flow 3/8'' ID tubular quartz reactor. Typically, 2 to 50 mg of sieved Cu-SSZ-13 catalyst were mixed with enough inert silica gel (Fisher Chemical Silica Gel (Davisil) Sorbent, Grade 923) to obtain a bed height of ~0.5 cm. Aluminum foil was wrapped around the quartz reactor to an outer diameter of ~1 inch to enhance heat conduction and minimize radial and axial temperature gradients that may be present within the bed. The reactor was then placed within a clamshell furnace and pressure-tested with nitrogen (liquid nitrogen boil-off, Linde) at 5 psig for 20 minutes.

Steady state kinetic data were collected under differential NO conversions (below 20%)[43] and with products (H_2O and N_2) co-fed to ensure the entire bed was exposed to approximately the same gas concentrations and temperatures using a gas mixture of 300 ppm NO (3.5% NO/Ar, Praxair), 300 ppm NH_3 (3.0% NH_3/Ar, Praxair), 8% CO_2 (liquid, Indiana Oxygen), 10% O_2 (99.5%, Indiana Oxygen), 2.5% H_2O (deionized, introduced through 24'' PermaPure MH Humidifier), and balance N_2 (boil-off liquid N_2, Linde) at 473 K and 1 atm. All concentrations are stabilized through the bypass prior to exposure to the catalyst bed. The gas hourly space velocity (GHSV) was varied between 600,000 to 4,000,000 h^{-1} for all kinetic experiments while maintaining differential conversion. The fresh and sulfated catalysts were not calcined in dry air at elevated temperatures (~773 K) prior to collecting reaction kinetics due to sulfur desorption at temperature higher than 573 K. Dehydrating the catalyst with dry air at 523 K does not affect the

SCR reaction rate (Figure S4 from supplementary information in Shih et al.[57]). In addition, continuous exposure to SCR gases between 423 and 523 K for 24 consecutive days did not affect the SCR reaction rate (Figure S5 from supplementary information in Shih et al.[57]). NO, NO_2, NH_3, CO_2, N_2O, and H_2O concentration data were recorded every 0.95 seconds using a MKS MultiGas 2030 gas-phase Fourier transform infrared (FTIR) spectrometer with on-board calibrations. Reaction temperatures were collected using two Omega® K-type 1/16'' OD thermocouples with one placed in contact with the quartz wool above the top of the bed and the second placed in contact with the quartz frit below the bottom of the bed. The temperature difference was always within 3 K during steady state SCR catalysis. Total gas flow rates were measured using a soap bubble gas flow meter.

In the limit of differential NO conversion, the gas concentrations and catalyst bed temperature can be assumed constant, allowing the differential NO conversion rate to be calculated using Equation (9.4):

$$-r_{NO} = \frac{(C_{NO,in}-C_{NO,out})}{1000000} \frac{P\dot{V}_{total}}{RT} \tag{9.4}$$

where C is the concentrations of NO in ppm before and after the catalyst bed, $\dot{V}_{total}$ is the total flow rate, P is 1 atm, T is ambient temperature, and R is the gas constant. The experimental data are fitted to a power law rate expression (Equation 9.5) where k_{app} (Equation 9.6) is the apparent rate constant and $\alpha, \beta, \gamma, \delta$, and ϵ are the apparent reaction orders with respect to concentrations of NO, NH_3, O_2, H_2O, and CO_2, respectively.

$$-r_{NO} = k_{app} C_{NO}^{\alpha} C_{NH_3}^{\beta} C_{O_2}^{\gamma} C_{H_2O}^{\delta} C_{CO_2}^{\epsilon} \tag{9.5}$$

$$k_{app} = A_0 \exp\left(-\frac{E_{a,app}}{RT}\right) \tag{9.6}$$

All reported rates are free of external diffusion limitations (independent of space velocity) and internal diffusion limitations, evident in turnover rates that are similar for crystallite sizes ranging from 0.5 to 2.5 microns[30,39,44]. The low values for δ and ε shown in Tables S5 and S6 from supplementary information in Shih et al.[57], show that product inhibition is negligible, validating the use of equation 9.2.

9.6.4 DFT simulation details

Calculations were performed within periodic triclinic SSZ-13 supercell that contains 12 T-sites[30], consistent with our previous studies[30,31,39]. Figure 9.12 a show the structure of one chabazite (CHA) cage with some atoms presented as spheres to highlight the ring structures. Figure 9.12(b) shows the Z_2Cu site where 2 Al ("Z") atoms were substituted in the 6-membered ring (6MR). Figure 9.12(c) shows the ZCuOH site were 1 Al atom was substituted.
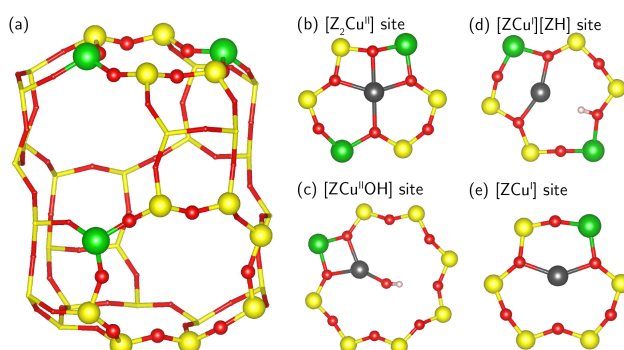
Figure 9.12 Molecular structure of a SSZ-13 (CHA) cage, with the 1Al (ZCuOH) and 2Al (Z_2Cu) Cu sites on the right. Red, yellow, green, gray, and pink spheres correspond to O, Si, Al, Cu, and H atoms, respectively.

To locate the minimum energy structures reported here, we first performed ab initio molecular dynamics (AIMD) simulations at 473 K for 30 ps on candidate structures using the Car-Parrinello molecular dynamics software (CPMD)[45]. Calculations were performed within the Perdew-Becke-Erzenhof (PBE) generalized gradient approximation (GGA)[46-48], ions described with Vanderbilt ultrasoft pseudopotentials[49] and plane waves cut off at 30 Ry. Simulations were run in the canonical (NVT) ensemble with 0.6 fs timesteps. A Nose-Hoover thermostat was used to control temperature to 473 K. Low energy geometry snapshots were extracted from the trajectories and optimized to obtain the local minima energy and structure at 0 K. At least two low energy configurations were extracted from the trajectories and relaxed to ensure consistency. Subsequent geometry optimizations were performed within the Vienna Ab initio Simulation Package (VASP) software[50]. Plane wave cutoff was 400 eV and the Brillouin zone sampled at the Γ-point, as appropriate for a solid insulator. Electronic energies were converged to 10^{-6} eV and geometries relaxed until atomic forces were less than 0.01 eV Å^{-1} using the hybrid screened-exchange method of Heyd-Scuseria-Erzenhof (HSE06) and D2 for dispersion

corrections. Charge analysis was performed by the method of Bader, and reported normalized to Cu^{II} and Cu^I references (Z_2Cu and ZCu). We report Bader charges as a superscript to Cu (i.e. Cu^I and Cu^{II}).

The relative mobility of the Cu centers was quantified by running 150 ps of AIMD within CPMD and following the method described in a previous publication[30]. In order to sample possible configurations efficiently, we performed five independent 30 ps AIMD simulations starting from geometries slightly perturbed (maximum perturbation = 0.1Å) from the equilibrium geometry. From each of the five simulations, 12 ps was used for equilibration and 18 ps was used for data collection.

We report the free energies of formation of various combinations of $S_wO_xH_yN_z$ on Cu sites with respect to SO_2, O_2, H_2O, and NH_3:

$$\Delta G_{w,x,y,z}^{form}\left(T, \Delta\mu_{SO_2}, \Delta\mu_{O_2}, \Delta\mu_{H_2O}, \Delta\mu_{NH_3}\right) = \Delta E_{w,x,y,z}^{form} - w\Delta\mu_{SO_2} - \frac{x}{2}\Delta\mu_{O_2} - \frac{y}{2}\left(\Delta\mu_{H_2O} - \right.$$

$$\left. \frac{1}{2}\Delta\mu_{O_2}\right) - z\left(\Delta\mu_{NH_3} - \frac{3}{2}\Delta\mu_{H_2O} + \frac{3}{4}\Delta\mu_{O_2}\right) - T\Delta S(T) \tag{9.7}$$

$$\Delta E_{w,x,y,z}^{form} = E_{Z_*CuS_wO_xH_yN_z} - E_{Z_*Cu} - wE_{SO_2} - \frac{x}{2}E_{O_2} - \frac{y}{2}\left(E_{H_2O} - \frac{1}{2}E_{O_2}\right) - z\left(E_{NH_3} - \frac{3}{2}E_{H_2O} + \right.$$

$$\left. \frac{3}{4}E_{O_2}\right) \tag{9.8}$$

where Z_*Cu (*= 1,2) represents either a Cu bound near one Al or or two Al placed as third nearest neighbors (3NN) position in the 6MR. $\Delta E_{w,x,y,z}^{form}$ is the formation energy of reaction:

$$Z^*Cu + wSO_2 + \frac{x}{2}O_2 + \frac{y}{2}\left(H_2O - \frac{1}{2}O_2\right) + z\left(NH_3 - \frac{3}{2}H_2O + \frac{3}{4}O_2\right) \rightarrow Z^*CuS_wO_xH_yN_z \tag{9.9}$$
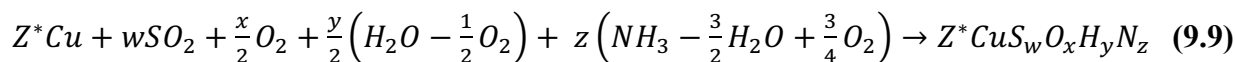
computed using the HSE06-D2 optimized energies of all species. To compute free energies, we neglect PV and heat capacity differences between the adsorbate-free and adsorbate-covered Cu sites and compute their entropy difference using a previously reported correlation derived from ab initio potential of mean force (PMF) free energy simulations[32], $\Delta_{ads}S^o = -0.35S^{o,\,i.g.}_{total}$ for the ZCuOH site and $\Delta_{ads}S^o = -0.51S^{o,\,i.g.}_{total}$ for the Z_2Cu site[30,51]. $\Delta\mu_{SO2}$, $\Delta\mu_{O2}$, $\Delta\mu_{H2O}$, $\Delta\mu_{NH3}$ are difference in ideal gas chemical potential (μ) between 0 K and the desired temperature (T) and pressure (P). We used the ΔH^o and ΔS^o values from the JANAF table[52] to calculate the $\Delta\mu$ at each discrete temperature (0 K, 100 K, etc, up to 1000 K), and linearly interpolated any other temperatures in between those discrete points.

9.7 Acknowledgements

9.8 References

[1]   United States Environmental Protection Agency, Diesel Fuel Stand. (2017).
[2]   I. Bull, W. Xue, P. Burk, R.S. Boorse, W.M. Jaglowski, G.S. Koermer, A. Moini, J.A. Patchett, J.C. Dettling, M.T. Claude, U. S. Patent No. 7,601,662 B2 (2009).
[3]   J. Luo, K. Kamasamudram, N. Currier, A. Yezerets, Chem. Eng. Sci. 190 (2018) 60–67.
[4]   S. Dahlin, C. Lantto, J. Englund, B. Westerberg, F. Regali, M. Skoglundh, L.J. Pettersson, Catal. Today 320 (2019) 72–83.
[5]   S.W. Ham, H. Choi, I.S. Nam, Y.G. Kim, Ind. Eng. Chem. Res. 34 (1995) 1616–1623.
[6]   S.-W. Ham, I.-S. Nam, Y.G. Kim, Korean J. Chem. Eng. 17 (2000) 318–324.
[7]   M.H. Kim, I.S. Nam, Y.G. Kim, J. Catal. 179 (1998) 350–360.
[8]   K. Wijayanti, S. Andonova, A. Kumar, J. Li, K. Kamasamudram, N.W. Currier, A. Yezerets, L. Olsson, Appl. Catal. B 166–167 (2015) 568–579.

[9] D.W. Brookshear, J.G. Nam, K. Nguyen, T.J. Toops, A. Binder, Catal. Today 258 (2015) 359–366.

[10] M. Shen, H. Wen, T. Hao, T. Yu, D. Fan, J. Wang, W. Li, J. Wang, Catal. Sci. Technol. 5 (2015) 1741–1749.

[11] A. Kumar, K. Kamasamudram, N. Currier, A. Yezerets, SAE Int. J. Engines 10 (2017) 9.

[12] L. Zhang, D. Wang, Y. Liu, K. Kamasamudram, J. Li, W. Epling, Appl. Catal. B 156–157 (2014) 371–377.

[13] A. Kumar, J. Li, J. Luo, S. Joshi, A. Yezerets, K. Kamasamudram, N. Schmidt, K. Pandya, P. Kale, T. Mathuraiveeran, in: Symp. Int. Automot. Technol., 2017.

[14] A. Kumar, M.A. Smith, K. Kamasamudram, N.W. Currier, H. An, A. Yezerets, Catal. Today 231 (2014) 75–82.

[15] T. Hamzehlouyan, C. Sampara, J. Li, A. Kumar, W. Epling, Top. Catal. 59 (2016) 1028–1032.

[16] Y. Cheng, C. Lambert, D. Heui, J. Hun, S. June, C.H.F. Peden, Catal. Today 151 (2010) 266–270.

[17] P.S. Hammershøi, Y. Jangjou, W.S. Epling, A.D. Jensen, T.V.W. Janssens, Appl. Catal. B Environ. 226 (2018) 38–45.

[18] K. Wijayanti, K. Xie, A. Kumar, K. Kamasamudram, L. Olsson, Appl. Catal. B 219 (2017) 142–154.

[19] P.S. Hammershøi, P.N.R. Vennestrøm, H. Falsig, A.D. Jensen, T.V.W. Janssens, Appl. Catal. B 236 (2018) 377–383.

[20] Y. Jangjou, D. Wang, A. Kumar, J. Li, W.S. Epling, ACS Catal. 6 (2016) 6612–6622.

[21] Y. Jangjou, Q. Do, Y. Gu, L.G. Lim, H. Sun, D. Wang, A. Kumar, J. Li, L.C. Grabow, W.S. Epling, ACS Catal. 8 (2018) 1325–1337.

[22] Z. Zhang, J.D. Atkinson, B. Jiang, M.J. Rood, Z. Yan, Appl. Catal. B 164 (2015) 573–583.

[23] A. Kumar, M.A. Smith, K. Kamasamudram, N.W. Currier, A. Yezerets, Catal. Today 267 (2016) 10–16.

[24] R. Ando, T. Hihara, Y. Banno, M. Nagata, in: WCX™ 17 SAE World Congr. Exp., 2017.

[25] V.F. Kispersky, A.J. Kropf, F.H. Ribeiro, J.T. Miller, Phys. Chem. Chem. Phys. 14 (2012) 2229–2238.

[26] T.V.W. Janssens, H. Falsig, L.F. Lundegaard, P.N.R. Vennestrøm, S.B. Rasmussen, P.G. Moses, F. Giordanino, E. Borfecchia, K.A. Lomachenko, C. Lamberti, S. Bordiga, A. Godiksen, S. Mossin, P. Beato, ACS Catal. 5 (2015) 2832–2845.

[27] T. Günter, H.W.P. Carvalho, D.E. Doronkin, T. Sheppard, P. Glatzel, A.J. Atkins, J. Rudolph, C.R. Jacob, M. Casapu, J.-D. Grunwaldt, Chem. Commun. 51 (2015) 9227–9230.

[28] F. Giordanino, P.N.R. Vennestrøm, L.F. Lundegaard, F.N. Stappen, S. Mossin, P. Beato, S. Bordiga, C. Lamberti, Dalton Trans. 42 (2013) 12741–12761.

[29] C. Paolucci, A.A. Verma, S.A. Bates, V.F. Kispersky, J.T. Miller, R. Gounder, W.N. Delgass, F.H. Ribeiro, W.F. Schneider, Angew. Chemie Int. Ed. 53 (2014) 11828–11833.

[30] C. Paolucci, A.A. Parekh, I. Khurana, J.R. Di Iorio, H. Li, J.D. Albarracin Caballero, A.J. Shih, T. Anggara, W.N. Delgass, J.T. Miller, F.H. Ribeiro, R. Gounder, W.F. Schneider, J. Am. Chem. Soc. 138 (2016) 6028–6048.

[31] C. Paolucci, I. Khurana, A.A. Parekh, S. Li, A.J. Shih, H. Li, J.R. Di Iorio, J.D. Albarracin-Caballero, A. Yezerets, J.T. Miller, W.N. Delgass, F.H. Ribeiro, W.F. Schneider, R. Gounder, Science 357 (2017) 898–903.

[32] F. Gao, D. Mei, Y. Wang, J. Szanyi, C.H.F. Peden, J. Am. Chem. Soc. 139 (2017) 4935–4942.

[33] D.W. Fickel, R.F. Lobo, J. Phys. Chem. C 114 (2010) 1633–1640.

[34] J. H. Kwak, H. Zhu, J.H. Lee, C.H.F. Peden, J. Szanyi, Chem. Commun. 48 (2012) 4758–60.

[35] J. Luo, D. Wang, A. Kumar, K. Kamasamudram, N. Currier, A. Yezerets, Catal. Today 267 (2016) 3-9.

[36] Y. Jangjou, C. S. Sampara, Y. Gu, D. Wang, A. Kumar, J. Li, W. S. Epling, React. Chem. Eng. (2019), DOI: 10.1039/C8RE00210J

[37] S.I. Zones, U. S. Patent No. 4,544,538 A (1985).

[38] S.A. Bates, W.N. Delgass, F.H. Ribeiro, J.T. Miller, R. Gounder, J. Catal. 312 (2014) 26–36.

[39] S.A. Bates, A.A. Verma, C. Paolucci, A.A. Parekh, T. Anggara, A. Yezerets, W.F. Schneider, J.T. Miller, W.N. Delgass, F.H. Ribeiro, J. Catal. 312 (2014) 87–97.

[40] J.R. Di Iorio, S.A. Bates, A.A. Verma, W.N. Delgass, F.H. Ribeiro, J.T. Miller, R. Gounder, Top. Catal. 58 (2015) 424–434.

[41] C.U. Segre, N.E. Leyarovska, L.D. Chapman, W.M. Lavender, P.W. Plag, A.S. King, A.J. Kropf, B.A. Bunker, K.M. Kemner, P. Dutta, R.S. Duran, J. Kaduk, AIP Conf. Proc. 521 (2000) 419–422.

[42] A.J. Kropf, J. Katsoudas, S. Chattopadhyay, T. Shibata, E.A. Lang, V.N. Zyryanov, B. Ravel, K. McIvor, K.M. Kemner, K.G. Scheckel, S.R. Bare, J. Terry, S.D. Kelly, B.A. Bunker, C.U. Segre, AIP Conf. Proc. 1234 (2010) 299–302.

[43] H.A. Massaldi, J.A. Maymo, J. Catal. 14 (1969) 61–68.

[44] R.M. Koros, E.J. Nowak, Chem. Eng. Sci. 22 (1967) 470.

[45] CPMD, http://www.cpmd.org/, Copyright IBM Corp 1990−2016, Copyright MPI für Festkörperforschung Stuttgart 1997−2001.

[46] J.P. Perdew, Y. Wang, Phys. Rev. 45 (1992) 244.

[47] J.P. Perdew, K.A. Jackson, M.R. Pederson, D.J. Singh, C. Fiolhais, Phys. Rev. B 46 (1992) 6671.

[48] J.P. Perdew, K. Burke, M. Ernzerhof, Phys. Rev. Lett. 77 (1996) 3865–3868.

[49] K. Laasonen, A. Pasquarello, R. Car, C. Lee, D. Vanderbilt, Phys. Rev. B 47 (1993) 10142–10153.

[50] G. Kresse, J. Furthmüller, Phys. Rev. B: Condens. Matter Mater. Phys. 54 (1996) 11169−11186.

[51] H. Li, C. Paolucci, W.F. Schneider, J. Chem. Theory Comput. 14 (2018) 929–938.

[52] NIST-JANAF, https://kinetics.nist.gov/janaf, Last Accessed: December 2, 2018.

[53] P.S. Hammershøi, A.D. Jensen, T.V.W. Janssens, Appl. Catal. B 238 (2018) 104–110.

[54] S. Li, Y. Zheng, F. Gao, J. Szanyi, W.F. Schneider, ACS Catal. 7 (2017) 5087–5096.

[55] G. Yang, X. Du, J. Ran, X. Wang, Y. Chen, J. Phys. Chem. C 122 (2018) 21468–21477.

[56] P.S. Hammershøi, Y. Jangjou, W.S. Epling, A.D. Jensen, T.V.W. Janssens, Appl. Catal. B 226 (2018) 38–45.

[57]   A.J. Shih, I. Khurana, H. Li, J. González, A. Kumar, C. Paolucci, T. M. Lardinois, C.B. Jones, J.D. Albarracin Caballero, K. Kamasamudram, A. Yezerets, W.N. Delgass, J.T. Miller, A.L. Villa, W.F. Schneider, R. Gounder, F.H. Ribeiro, Appl. Catal. B 574 (2019) 122–131.

10.   CONSEQUENCES OF EXCHANGE-SITE HETEROGENEITY AND DYNAMICS ON THE UV-VISIBLE SPECTRUM OF CU-EXCHANGED SSZ-13

10.1 Preface

Chapter 10 reflects the reproduction of my coauthored article published in Chemical Science, 10, 2373-2384, 2019, titled "Consequences of exchange-site heterogeneity and dynamics on the UV-visible spectrum of Cu-exchanged SSZ-13", and the current draft of another manuscript in preparation. With the combination of these two separate manuscripts, this chapter deals with identification and quantification of multinuclear Cu-oxo complexes evolved from mononuclear Cu cations, and their relevancy for standard SCR and NO oxidation reaction.

10.2 Abstract

The speciation and structure of Cu ions and complexes in chabazite (SSZ-13) zeolites, which are relevant catalysts for nitrogen oxide reduction and partial methane oxidation, depend on material composition and reaction environment. Ultraviolet-visible (UV-Vis) spectra of Cu-SSZ-13 zeolites synthesized to contain specific Cu site motifs, together with ab initio molecular dynamics and time-dependent density functional theory calculations, were used to test the ability to relate specific spectroscopic signatures to specific site motifs. Geometrically distinct arrangements of two framework Al atoms in six-membered rings are found to exchange Cu^{II} ions that become spectroscopically indistinguishable after accounting for the finite-temperature fluctuations of the Cu coordination environment. Nominally homogeneous single Al exchange sites are found to exchange a heterogeneous mixture of $[Cu^{II}OH]^+$ monomers, O- and OH-bridged Cu dimers, and larger polynuclear complexes. The UV-Vis spectra of the latter are sensitive to framework Al proximity, to precise ligand environment, and to finite-temperature structural fluctuations, precluding the precise assignment of spectroscopic features to specific Cu

structures. In all Cu-SSZ-13 samples, these dimers and larger complexes are reduced by CO to Cu^I sites at 523K, leaving behind isolated $[Cu^{II}OH]^+$ sites with a characteristic spectroscopic identity. The various mononuclear and polynuclear Cu^{II} species are distinguishable by their different responses to reducing environments, with implications for their relevance to catalytic redox reactions.

10.3 Introduction

Copper ions exchanged onto zeolites are implicated as active sites for the selective catalytic reduction of nitrogen oxides,[1-10] oxidation of NO to NO_2,[11,12] decomposition of NO and N_2O,[13-16] and partial methane oxidation to methanol.[17-33] These Cu ions are associated with charge-compensating AlO_4 tetrahedral sites that are distributed throughout the zeolite lattice. Because these Al substitutions are not ordered under typical zeolite synthesis conditions, a given framework and macroscopic Si/Al ratio will present a heterogeneous distribution of microscopic Al site ensembles, each of which provides a distinct exchange environment for a Cu ion. The precise Cu species and their relative densities in a given material are thus functions of framework topology,[34-37] of the density and underlying distribution of framework Al (Si/Al), of the Cu loading (Cu/Al), and even of the protocols used to introduce Cu onto the zeolite supports.[38-44] Further, multiple Cu ion site motifs may be of similar free energy at a given Al site or ensemble, and at finite temperatures these motifs may interchange at timescales relevant to observation or to catalytic turnover.[45-47] Given these many sources of structural diversity, assignment of spectroscopic features to specific Cu motifs in a heterogeneous solid is a non-trivial endeavor, but a critical one to make connections between local structure and catalytic function.

One strategy to reduce this complexity is to intentionally synthesize zeolites with framework Al distributions that present one or a few distinct Al site ensembles. This strategy is particularly promising for zeolites of relatively high symmetry, such as the chabazite (SSZ-13) framework that is composed of a single symmetry-distinct tetrahedral site. SSZ-13 samples synthesized using only organic N,N,N-trimethyl-1-adamantylammonium ($TMAda^+$) structure-directing cations nominally contain only isolated framework Al sites,[39] and are found to contain predominantly $[Cu^{II}OH]^+$ ions after aqueous Cu ion exchange and high temperature (>473 K) oxidation, based on titrimetric analysis and vibrational and X-ray spectroscopies.[38] In contrast, SSZ-13 samples synthesized in the presence of $TMAda^+$ and Na^+ as co-structure-directing

cations[39] contain detectable fractions of paired Al sites in 6- membered rings (6MR). After Cu ion exchange and high temperature oxidative treatment, these paired Al sites are observed to preferentially host Cu^{II} ions (Z_2Cu) before isolated Al sites are occupied by $[Cu^{II}OH]+$ ions (ZCuOH).[38] Z_2Cu and ZCuOH are expected to contribute differently to ultraviolet-visible (UV-Vis) absorption spectra based on ligand-field arguments and density functional theory (DFT) calculations, consistent with d-d transition and ligand-to-metal charge transfer (LMCT) features in experimentally-measured UV-Vis spectra that are observed to change with Cu content in Cu-SSZ-13 samples.6,48{50

These single Cu species may coexist with dimeric or higher nuclearity Cu clusters. Oxygen-bridged Cu dimers are well established to be present and quantifiable with CO temperature programmed reduction,[15] to be plausible active sites for NO and N_2O decomposition[14,15,51-53] and partial CH_4 oxidation in Cu-exchanged zeolites,[17,30,33,54-62] including Raman[63,64] and UV-Vis[14,55] spectroscopic observations and CO temperature programmed reduction to quantify such sites. In Cu-SSZ-13 samples of certain composition (Si/Al=5, Cu/Al=0.3-1.6), oxygen-bridged Cu dimers and larger Cu oxide aggregates are detected by X-ray spectroscopy and are the dominant active sites for NO oxidation to NO_2 under dry conditions.[11] UV-Vis spectra of certain Cu-SSZ-13 samples (Si/Al=13, Cu/Al=0.45) following high temperature O_2 treatment show features consistent with those for oxygen-bridged Cu dimers,[48] and these features disappear upon reduction with CH_4,[18,50] implicating them as active sites for partial methane oxidation. The precise relationship between sample composition and treatment history, and the numbers and structures of Cu dimers or larger aggregates formed, however, remains less well resolved than such relationships for monomeric Cu sites in Cu-SSZ-13.

Here, we report UV-Vis spectra of model Cu-SSZ-13 zeolites prepared to contain predominantly Z_2Cu or ZuOH sites, by virtue of their different framework Al arrangements and elemental compositions. We use supercell time-dependent DFT (TD-DFT) calculations to correlate observed UV-Vis spectral features with specific Cu motifs. We find that spectra computed for single, static, minimum energy structures are in poor agreement with experimental observation, because Cu ion dynamics have a significant impact on computed spectral features even at ambient temperature. We construct synthetic spectra by averaging over configurations visited during finite-temperature ab initio molecular dynamics (AIMD) simulations and show that these dynamically averaged spectra correspond closely with experimental observation.

Further, experimental and simulated spectra are compared to identify features associated with a confounding subset of Cu dimers or larger aggregates in samples prepared to contain predominantly $[Cu^{II}OH]^+$ species. These results resolve several inconsistencies in spectral and site assignments reported in Cu-exchanged zeolites.

10.4 Results

10.4.1 Z_2Cu

First, UV-Vis spectra were collected on a Cu-SSZ-13 sample that contains only Z_2Cu sites. [38,65] This sample was prepared by starting from an SSZ-13 sample (Si/Al = 5) crystallized using a mixture of TMAda$^+$ and Na$^+$ cations to contain a finite and detectable fraction of paired Al sites,[39] followed by aqueous ion exchange with a cupric nitrate solution to achieve a compo- sition (Cu/Al = 0.21) demonstrated previously to contain only isolated Z_2Cu sites through X-ray absorption spectroscopy, Brønsted acid site exchange stoichiometries with Cu^{II} and Co^{II} (2 H$^+$ replaced per Cu^{II} or Co^{II}), and IR spectroscopy[38] (sample preparation details in section S2.1 and elemental analysis in Table S4 from supplementary information in Li et al.[89]). This Cu-SSZ-13 sample was treated in flowing dry air to 673 K for 2 h, cooled to 300 K, and UV-Vis spectra were collected from 7000 to 50 000 cm^{-1}. Spectra are reported in quasi-absorption (K.M.) units in Figure 1a, and show a broad d-d transition feature from about 8000 to 16 000 cm^{-1} characteristic of a d^9 Cu^{2+} ion and a broad ligand-to-metal charge transfer (LMCT) feature from about 30000 to 50 000 cm^{-1}. The spectrum is consistent with that previously reported for a Cu-SSZ-13 sample after high temperature oxidative treatment.[6]
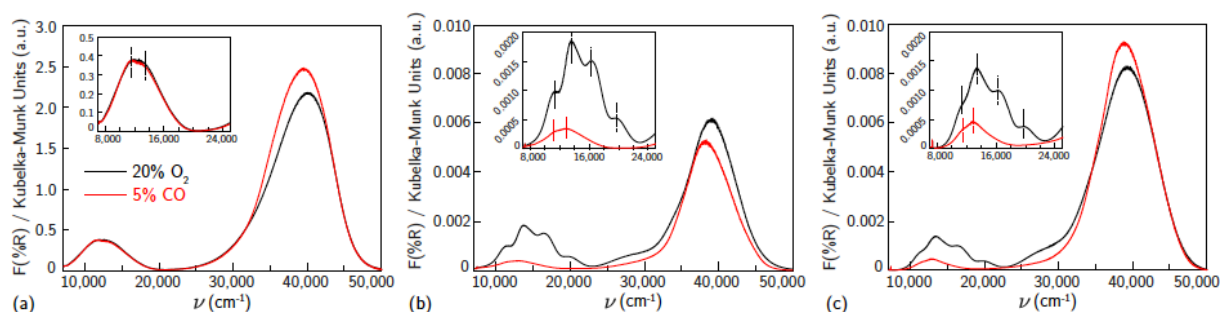
Figure 10.1 UV-visible spectra collected at 300 K of samples containing predominantly (a) Z_2Cu (Si/Al=5, Cu/Al=0.21), (b) ZCuOH (Si/Al=15, Cu/Al=0.24) and (c) ZCuOH (Si/Al=15, Cu/Al=0.15), after 20% O_2 treatment at 673 K (black), and 5% CO treatment at 523 K (red). Insets show magnification of the d-d transition region.

The Cu^{II} ions in this zeolite sample are associated with ensembles of two Al centers separated by two or one intervening Si tetrahedral (T-) sites in the same six-membered ring (6MR), which we term "para" and "meta" respectively. We used a triclinic 12 T-site SSZ-13 supercell described elsewhere[11,66] to represent each ensemble (Figure 10.2). In each case, a single Cu ion was placed within the 6MR and the structure annealed at 673K for 150 ps using thermostated AIMD (computational details in section S1 from supplementary information in Li et al.[89]). 400 equally spaced configurations were extracted from the trajectories and relaxed. In each Al ensemble, all configurations relaxed to one of three energy minima shown in Figures 10.2a and 10.2e. These three minima differ in the combination of Al-adjacent and non-Al-adjacent framework oxygen (O_f) that comprise the first Cu coordination sphere. The framework distorts to accommodate these different Cu-containing minima, behavior consistent with structural distortions reported previously in calculations of metal-exchanged MFI,[67,68] MOR,[67,69] and FER,[70] and inferred from the appearance of two T-O-T deformation bands (900, 950 cm^{-1}) in DRIFTS spectra after Cu exchange into SSZ-13.[71] Despite these structural differences, the three para configurations differ in energy by less than 5 and meta by less than 20 kJ mol^{-1} (Figure 10.2a, 10.2e, and also Table S1 from supplementary information in Li et al.[89]). The lowest-energy para and meta configurations differ in absolute energy by 21 kJ mol^{-1} (Table S1 from supplementary information in Li et al.[89]).

We performed additional AIMD at 300K to gain insight into variations in Cu coordination environment at finite temperature[38,72] that might influence the observed spectra. Figure 10.2b reports histograms of distances between Cu and each of the six 6MR O_f, collected at 0.6 fs intervals over the 150 ps simulation of para Z_2Cu. Distances segregate into two groups centered at 2.1 and 3.3 A, corresponding to Cu-coordinated and free O_f, each group having widths >0.5 A (Table S2 from supplementary information in Li et al.[89]) that arise from finite temperature fluctuations of the lattice and Cu. The unimodal O1, O2 and O3 and bimodal O4, O5, and O6 distributions are due to transitions between the three different minimum energy configurations of Figure 10.2a. Inspection of the trajectory shows that transitions occur by extension of the four Cu-O_f bonds, distortion of the lattice, and relaxation into an adjacent minimum. We used these observations to categorize each AIMD frame into one of the three minima or into an intermediate state (example structure in Figure S2 from supplementary information in Li et al.[89]), based on the identity and number of O_f within 2.6 A of Cu, chosen to

represent the upper bound of a Cu-O coordination and shown in the pie chart inset to Figure 10.2b.

Figure 10.2 (a) DFT-computed local Cu environment in three Z_2Cu para minima. (b) Individual and aggregate para Z_2Cu Cu-Of distance histograms collected over 150 ps 300 K AIMD. Inset indicates percent time spent in each minimum. (c) TD-DFT-computed UV-Vis spectra of three Z_2Cu para minima, color-coded by (a). (d) UV-Vis spectra averaged over 1 (green), 10 (yellow), 25 (orange), 100 (blue), 200 (red), and 400 (black) para Z_2Cu snapshots equally spaced in time along the 150 ps trajectory. (e)-(h) Corresponding results for Z_2Cu meta configuration.

All three minima are visited, and the fractions of time spent in each is generally consistent with the relative energies of the corresponding minima. A non-negligible fraction of time is also spent outside any minimum.

Analogous results for meta Z_2Cu are shown in Figure 10.2f. Again, $Cu-O_f$ distances segregate into the same two groups, and the aggregate histogram of all $Cu-O_f$ distances have identical means and standard deviations in the para and meta cases. The individual $Cu-O_f$ histograms are all unimodal. The large energy difference between minima guarantees that meta Z_2Cu remains in the lowest energy configuration throughout the simulation.

We used TD-DFT to compute frequency-dependent dielectric tensors and corresponding optical absorption spectra of the six minima. The computational details and codes for the VASP inputs and subsequent analysis are provided in section S1.2 (from supplementary information in Li et al.[89]) and also on the external Zenodo repository (https://doi.org/10.5281/zenodo.1473128). Computed spectra are shown in Figure 10.2c and 10.2g, reported in arbitrary K.M. units. All six spectra exhibit features in the d-d and LMCT regions not evident in the experimental spectrum in Figure 10.1a. Coordinatively similar (as measured from Cu-O distances and O-Cu-O angles) para minima 1 and 3 and meta minimum 2 exhibit equivalent spectra. Absolute intensities are greatest for lowest symmetry and least for highest symmetry minima.[73] Neither any individual spectrum nor a Boltzmann weighting of all spectra at 300K (shown in Figure S3 from supplementary information in Li et al.[89]) recovers the experimental spectrum in Figure 10.1a. To simulate the effects of these geometric variations on observed spectra, we computed the absorption spectra of 400 equally spaced snapshots from the 300 K AIMD trajectories (Figure S4a (para), Figure S4b (meta) from supplementary information in Li et al.[89]). Individual spectra are sensitive to local structure. The d-d transitions shift generally to higher frequency with decreasing mean $Cu-O_f$ distance (Figure S5 from supplementary information in Li et al.[89]), consistent with behavior expected from ligand field arguments. The LMCT features do not simply correlate with the $Cu-O_f$ distances. Figure 10.2d and 10.2h show the results of averaging increasing numbers of spectra computed from configurations extracted with equal spacing along the AIMD trajectories. Sharp features in both the d-d and LMCT regions become broadened upon averaging an increasing number of spectra from 1 to 200 structures and converge at approximately 200 structures, as evidenced by the small changes resulting from further averaging up to 400 structures. In contrast

to spectra computed from the minimum energy structures, final averaged meta and para UV-Vis spectra are indistinguishable and consistent with experimental observations in Figure 10.1a.

10.4.2 ZCuOH

For comparison to the sample containing predominantly Z_2Cu sites, we synthesized different Cu-SSZ-13 samples that contain predominantly the ZCuOH site motif that results when Cu^{II} ions are exchanged near isolated framework Al sites. We previously reported that crystallization of SSZ-13 zeolites in the presence of only $TMAda^+$ cations produces a material with predominantly isolated framework Al, reflected in the inability to exchange divalent Co^{II} cations.[39,40] A sample of SSZ-13 (Si/Al = 15) was synthesized using this method and exchanged with differents amounts of Cu^{II} (Cu/Al = 0.15, 0.24) to generate two Cu-SSZ-13 samples of different ZCuOH density (sample preparation details and elemental analysis in section S2.1 and Table S4 from supplementary information in Li et al.[89]).

After Cu^{II} ion exchange, each model ZCuOH sample was treated in flowing oxygen at 673K (20% O2, balance He) for 120 mins (details in section S2.2 from supplementary information in Li et al.[89]). UV-Vis spectra of these Cu-SSZ-13 samples collected at 300K are shown in Figure 10.1b and 10.1c. Spectra of both samples show absorbance features in the 8000 to 22000 cm^{-1} region that are centered around 11059, 13593, 16379, and 20 077 cm^{-1}, and a shoulder in the 24000 to 30000 cm^{-1} range, and these features are higher in intensity for the sample with higher Cu content. These spectra are similar to those reported following similar pretreatments of Cu-SSZ-13 materials that are expected to contain predominantly ZCuOH species,[18,48,50] by virtue of the Na^+-free synthesis methods used to prepare the parent SSZ-13 sample. In contrast, these spectra are markedly different from those reported on materials expected to only contain Z_2Cu species (Korhonen et al.[6] and Figure 10.1a). The four d-d transitions have different relative intensities in the two Cu-SSZ-13 samples shown in Figures 10.1b and 10.1c. Literature Cu-SSZ-13 samples prepared to contain ZCuOH sites and exposed to the same O_2 pre-treatment also share the same four d-d transitions but again with different relative intensities.[18,48,50] We conclude that a mononuclear ZCuOH species cannot be solely responsible for the quadruplet feature. The sample-dependent variation suggests the presence of

additional multinuclear ZCuOH derived species with structures and populations that depend on synthesis, treatment and composition.

Da Costa et al.[15] reported that CO reduces multinuclear Cu-oxo species in Cu-ZSM-5 to isolated Cu^+ (d^{10}) ions that do not exhibit d-d transitions. Similarly, we hypothesize that multinuclear Cu-oxo species present in Cu-SSZ-13 samples after treatment in O_2 at 673K will be reduced by CO at 523 K, leaving behind only isolated ZCuOH species and any residual Z2Cu sites. Model Z_2Cu and ZCuOH samples were held in a owing stream of 5% CO at 523K until no further changes in UV-Vis spectra were observed (details in section S2.4 from supplementary information in Li et al.[89]), prior to sealing the UV-Vis cell and cooling to 300K to record the spectra shown in Figure 10.1, an approach similar to that applied by Ipek et al. to Cu-SSZ-13 samples containing mixtures of Z_2Cu and ZCuOH sites.[18] As expected, no changes were observed to the d-d transition region in the spectrum of the Z_2Cu sample upon CO exposure (Figure 10.1a). In sharp contrast, the d-d features at 16379 and 20077 cm^{-1} and LMCT transition at 27000 cm^{-1} in the spectra of both ZCuOH samples (Figures 10.1b and 10.1c) disappeared after exposure to CO, and features at 11059 and 13593 cm^{-1} were shifted to 11350 and 13000 cm^{-1} and decrease markedly in absorbance. Despite differences in the d-d quadruplet feature intensity that are detectable after high temperature O_2 treatment, the d-d transition features of both ZCuOH samples become similar after CO treatment. These findings indicate that not all Cu^{II} sites in Cu-SSZ-13 are reducible to Cu^I in the presence of CO, that the Cu^{II} sites remaining after CO reduction are similar for both samples (Figure 10.1b and 10.1c, red), and that these signatures are of isolated ZCuOH sites.

We used the same triclinic supercell to describe a $[Cu^{II}OH]^+$ ion-exchanged near an isolated Al. Each T-site in the chabazite lattice is common to two 8MR, one 6MR, and three 4MR. We used 473K AIMD and geometry optimizations to compare the energies of the $[Cu^{II}OH]^+$ ion in each of these orientations. The two 8MR orientations are isoenergetic and the Cu-X (X=Si, Al, O) radial distribution function (RDF) computed from their AIMD trajectories are identical (SI Figure S6). From a nudged elastic band calculation, the two 8MR minima are separated by a 63 kJ mol^{-1} barrier (SI Figure S7). Similar calculations with the $[Cu^{II}OH]^+$ ion directed into a 6MR and 4MR result in configurations 15 and 45 kJ mol^{-1} higher in energy. We thus expect a $[Cu^{II}OH]^+$ ion to adopt and remain in one of the 8MR orientations at typical conditions of observation here.

Again, to explore the consequence of ion dynamics on spectroscopy, we performed additional AIMD simulations at 300K for 150 ps on a $[Cu^{II}OH]^+$ ion in one of the 8MR orientations. During the course of the simulation the Cu ion remained coordinated to the same two O_f, bond distances fluctuated, and the OH ligand rotated between Cu-OH rotational conformers twice. Figure 10.3b reports histograms of the two Cu-O_f and Cu-OH distances. The Cu-OH bond is shorter and has a narrower distribution than the Cu-O_f bond. The Cu-O_f mean distance are slightly shorter than those from the Z_2Cu simulations while the standard deviations are the same as the Z_2Cu trajectories (Table S2 from supplementary information in Li et al.[89]). Thus, the coordination environment around ZCuOH varies less than Z_2Cu. The inset to Figure 10.3b reports the fraction of the trajectory spent in each of the two rotational conformations.

The 8MR $[Cu^{II}OH]^+$ ion can exist in one of two rotational conformers that differ in energy by 6 kJ mol^{-1} and are distinguished by whether the OH ligand points into or out of the 8MR (Figure 10.3a). Figure 10.3c reports the computed UV-Vis spectra of a relaxed 8MR $[Cu^{II}OH]^+$ ion; each conformer yields a spectrum with two equivalent sharp features in the d-d transition region and a single sharp LMCT band. Predicted ZCuOH absorption intensities are less than either the Z_2Cu para and meta spectra in Figure 10.2c and 10.2g, consistent with the higher symmetry of ZCuOH and prior predictions that ZCuOH may have small or unobservable d-d transition.[49,74] However the two spectra in Figure 10.3c for the two ZCuOH isomers are only in rough correspondence with the observed spectrum of the ZCuOH samples.

We computed the absorption spectra of 400 equally spaced structures chosen from the 300K AIMD simulation; all computed spectra are overlaid in Figure S4c (from supplementary information in Li et al.[89]). Significant variations are present in the d-d (7000 to 14000 cm^{-1}) and LMCT (30000 to 50000 cm^{-1}) regions (Figure S6c from supplementary information in Li et al.[89]), with shorter mean Cu-O distances again correlating with shifts to higher frequency d-d transitions (Figure S5 from supplementary information in Li et al.[89]). Figure 3d reports spectra averaged over 1, 10, 25, 100, 200, and 400 structures. The two-sharp d-d features at 8000 and 13000 cm^{-1} broaden and begin to merge, while
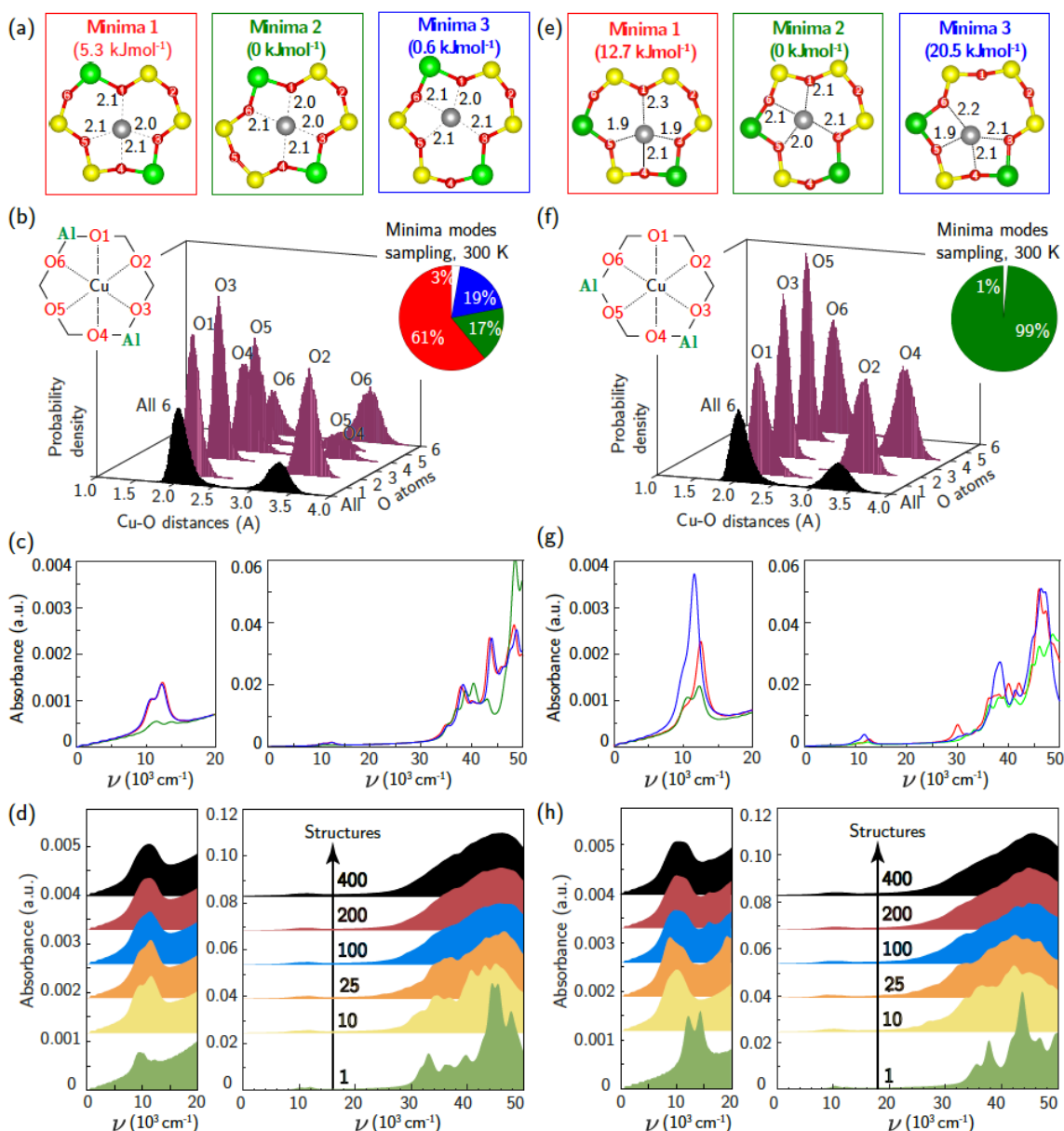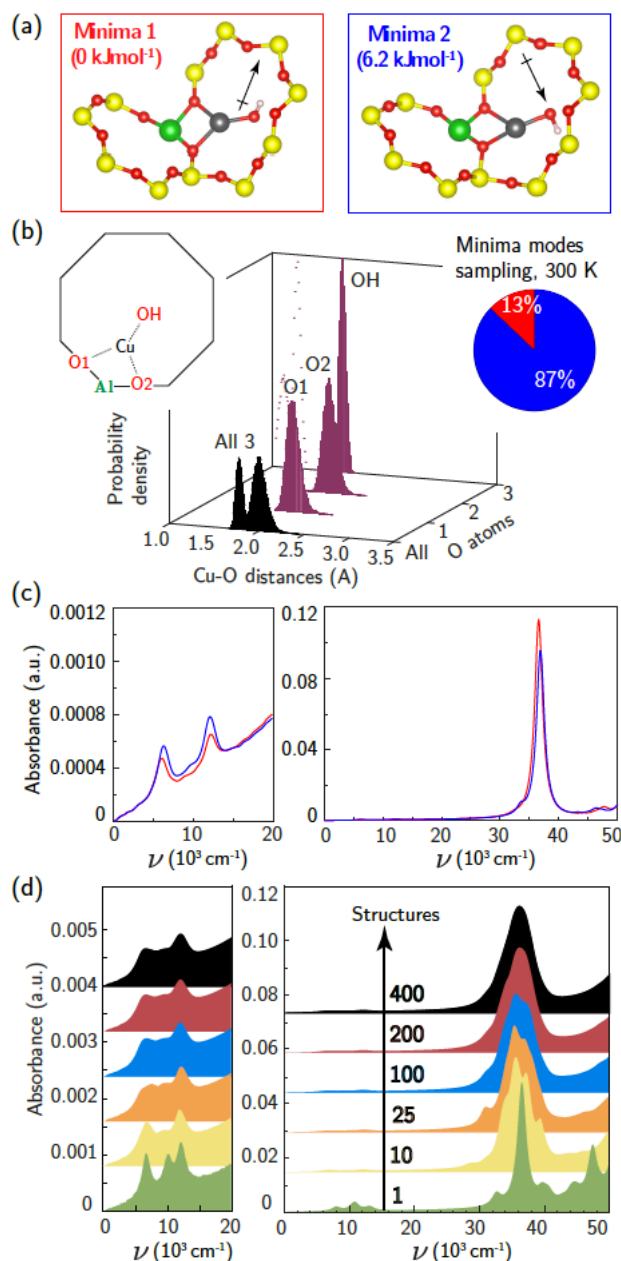
Figure 10.3 (a) DFT-computed local Cu environment in two 8MR ZCuOH minima. (b) Individual and aggregate Cu-O distance histograms collected over 150 ps of 300K AIMD. Inset indicates percent time spent in each minimum. (c) TD-DFT-computed UV-Vis spectra of two ZCuOH minima, color-coded by (a). (d) UV-Vis spectra averaged over 1 (green), 10 (yellow), 25 (orange), 100 (blue), 200 (red), and 400 (black) snapshots equally spaced in time along the 150 ps trajectory.

the LMCT region converges to a peak spanning 30000 to 45000 cm^{-1}. The averaged d-d and LMCT regions ~1000 cm^{-1} are red-shifted but similar in shape to those observed after CO

reduction of the ZCuOH samples (Figure 10.1b, 10.1c). Further, the decrease in computed intensity of the d-d relative to LMCT bands in ZCuOH compared to Z_2Cu models corresponds with experimental observation. These observations support both the assignment of the Figure 10.1b and 10.1c spectra following CO treatment (red) to isolated ZCuOH and the conclusion that the quadruplet features after O_2 treatment (black) cannot be solely assigned to ZCuOH but rather have contributions from multinuclear Cu complexes.

10.4.3 Cu Dimers

The additional features in Figure 10.1b and 10.1c following 673 K 20% O_2 treatment are from CO reducible Cu species. A discrete, exchanged $[CuO]^+$ ion is an unlikely candidate because it has a unfavorable computed formation free energy and its computed spectrum (Figure S8 from supplementary information in Li et al.[89]) is inconsistent with experimental observation. More likely are dimeric or larger Cu clusters. To test the potential for isolated ZCuOH to condense into dimers, we considered two $[Cu^{II}OH]^+$ ions located at Al separated by four T-sites in the same 8-MR using a 36-T-site supercell. Figure 10.4a, structures C and E show the ZCu(OH)$_2$CuZ condensation product and of its ZCuOCuZ dehydration product, respectively (details in section S1.12 and Figure S9 from supplementary information in Li et al.[89]). Within the generalized gradient and harmonic approximations, the free energies to form ZCu(OH)$_2$CuZ and dehydrate to ZCuOCuZ are computed to be -108 and -116 kJ mol^{-1}, respectively (details in section S1.12 from supplementary information in Li et al.[89]). This energetics is consistent with the formation of dimers from $[Cu^{II}OH]^+$ ions of suitable proximity.

We performed 150 ps AIMD at 300K on these two dimer structures in the 12-T-site supercell. In both trajectories the dimers remain roughly in the plane of the 8MR and retain coordination to the same bridging and framework O, unlike the more dynamic Z_2Cu behavior described above. Both dimers vibrate internally and against the framework. Histograms of the Cu-O and Cu-Cu distances are shown in Figure 10.4b and 10.4c. In ZCuOCuZ, Cu-O$_b$ (bridging O) distances are systematically shorter and fluctuate less than Cu-O$_f$. The Cu-Cu separation oscillates around 2.7 A, and Cu-O-Cu angle varies from 90 to 115^0. The Cu(OH)$_2$Cu core of ZCu(OH)$_2$CuZ remains essentially planar and tilted at an angle of ~35^0 with respect to the 8MR plane during the AIMD (structure in Figure S12 from supplementary information in Li et al.[89]).

The $Cu-O_b(H)$ and $Cu-O_f$ distances cover a similar range, and the Cu-Cu separation oscillates around 3 A.

We used TD-DFT and spectral averaging methods identical to those above to simulate UV-Vis spectra of both dimers at 300 K. We observed computed spectra to be sensitive to the geometries of the dimers, similar to the monomer Z_2Cu and ZCuOH. Figure S10 (from supplementary information in Li et al.[89]) shows spectra averaged over various numbers of snapshots; spectral averaging converges after ~ 200 structures. Figure 10.4d shows the spectra averaged over 400 snapshots. The spectrum of $ZCu(OH)_2CuZ$ structure (C) exhibits a broad and low intensity d-d feature around 12400 cm^{-1} and a LMCT band blue-shifted to beyond 50000 cm^{-1}. In contrast, the spectrum of ZCuOCuZ structure (E) has two distinct d-d features around 8500 and 12400 cm^{-1} and an LMCT band edge that begins near 30000 cm^{-1}. These two are clearly distinct from one another and from the computed spectrum of ZCuOH.

The spectroscopy of Cu dimers may be sensitive to Al proximity, through its influence on geometric and electronic structures. To test this effect, we constructed two additional ZCuOCuZ models with two Al placed third- and second- nearest-neighbor in an 8MR and introduced a Cu-O-Cu dimer so as to maintain Cu-O distances and a Cu-O-Cu angle similar to previous reports.[11,18] Figure 10.4a shows the optimized structures F and G used to initiate subsequent dynamics. At 3NN, the ZCuOCuZ dimer is symmetrically coordinated to O_f associated with Al; at 2NN, this symmetry is broken, although both Cu remain bound to two O_f. During subsequent 300K AIMD simulations the Cu ions retain their coordination; as shown in the histograms, Cu-O distances vary across the same ranges at all Al placements while Cu-Cu distances and Cu-O-Cu angles vary considerably with Al separation. While the computed spectra of the optimized structures are different, these differences largely disappear during averaging. As shown in Figure 10.4d, averaged spectra have similar d-d features and differ only in the LMCT band edge position.

The Cu dimer spectroscopy could also be sensitive to geometric isomerism. To test this effect, we considered several examples of Cu dimers bridged by two O, a well-known motif that exhibits several geometric isomers that are sensitive to Al separation.[34,74-76] Figure 10.4a structures

A, B, and D correspond to three different Al placements and three different isomers, all of which were obtained by geometry relaxations beginning from literature structures.[11,18] A and B have

triplet and D has a singlet ground states, consistent with earlier results.[34,75] Computed spectra at the optimized geometries (Figure S10 from supplementary information in Li et al.[89]) exhibit sharp and distinct peaks in both the d-d and LMCT regions. We performed AIMD on all three isomers; distance histograms collected during the simulations are shown in Figure 10.4b and Figure 10.4c. The dioxo dimer D is the least variable across the trajectory; dimers A and B sample much larger $Cu-O_f$ and Cu-Cu distances, respectively. During the infinite temperature simulation, dimer A moves from a cis to a trans μ-peroxo orientation whereas the optimized geometry has a slightly twisted O-O linkage, resulting in smaller Cu-OpO angles (geometry comparison in Figure S13 from supplementary information in Li et al.[89]). Figure 10.4d reports computed spectra averaged over 400 snapshots. Spectra differ significantly in band location and intensity both in the d-d and LMCT regions.
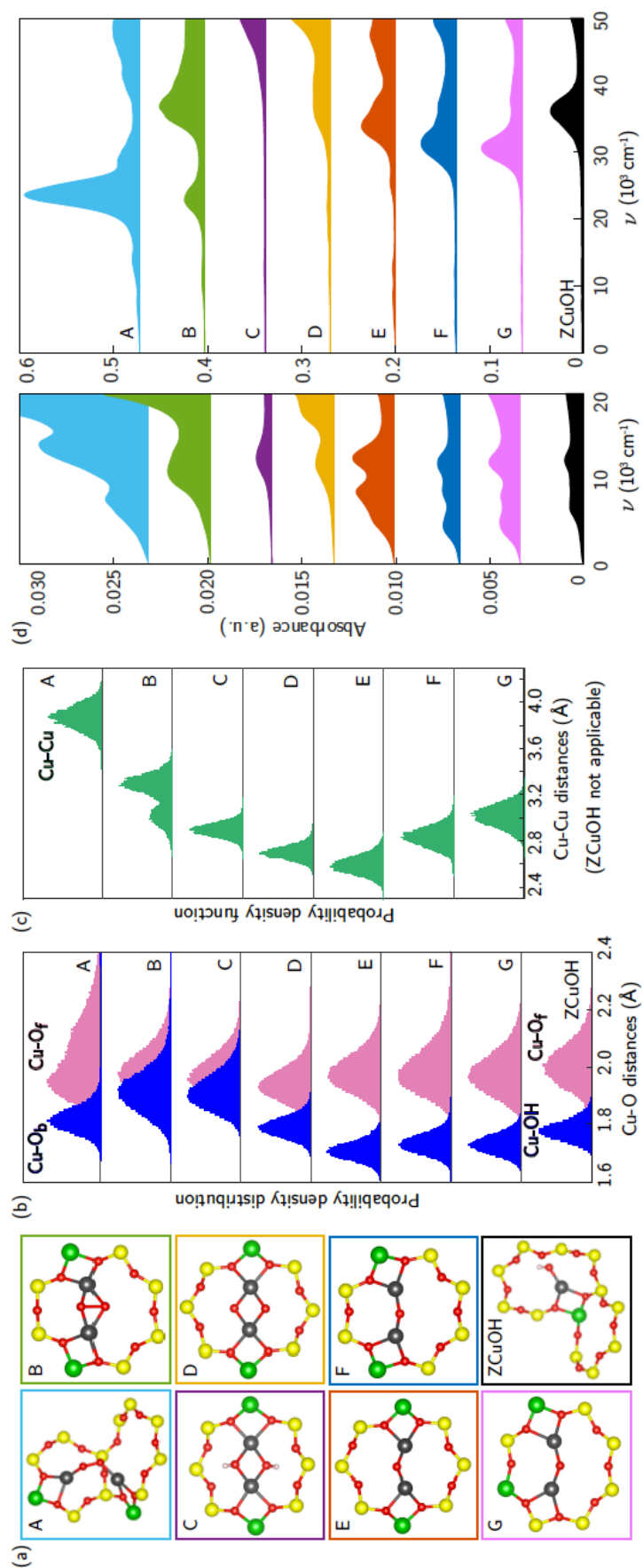
Figure 10.4 (a) Optimized geometries of Cu dimers A-G, and ZCuOH for reference. (b)/(c) Aggregate Cu-O distance (b) and Cu-Cu distance (c) histograms for dimers A-G and ZCuOH collected over 150 ps 300 K AIMD. Bridging O_b and OH distances are presented in blue, O_f distances are in pink, Cu-Cu distances are in green. (d) Averaged spectra of Cu dimers A-G (left panel is from 0-20000 cm^{-1}, right panel is from 0 to 50000 cm^{-1}, each spectrum is off set on the y-axis. Colors of spectra are consistent with those in (a) Averaged ZCuOH spectrum is plotted at the bottom in black for reference.

UV-Vis spectra are thus sensitive to Cu dimer composition and structure and dynamics. Comparisons with the experimental spectra collected after 20% O_2 treatment at 673K in Figure 10.1b and c are complicated by the ill-defined number and nuclearity of Cu species present in the samples. Nevertheless, we can make some useful connections. The relative intensities of the d-d transitions for some dimeric Cu species (in particular A, B, and E) are computed to be greater than that of monomeric ZCuOH, consistent with the observation of decreases in d-d peak intensity following CO reduction. Structures B, E, and F have features that roughly correspond with those observed at 11059, 13593, 16379, and 20077 cm^{-1} (Figure 10.1b and 10.1c), but red-shifted by an amount similar to that found in the comparison of computed and observed ZCuOH spectra. Structures C and D contain features that are plausible candidates for the features observed at 16000 and 19 000 cm^{-1}. Structures A and B contain features that could account for the broad low energy LMCT shoulder from ~ 22000 to 27000 cm^{-1} that disappears after the CO reduction treatment. All these results imply that the variations in the quadruplet feature in the d-d region of nominally ZCuOH samples shown in Figures 10.3b and 10.3c are associated at least in part with the contributions of different numbers and/or types of dimers from sample to sample.

10.5 Discussion

Cu-SSZ-13 samples used here and reported in the literature are now well understood to be intrinsically heterogeneous at the microscopic scale, as a result of variations in composition and location of Al[77] and charge-compensating Cu ions, among other factors. Some of these differences are readily observed spectroscopically; for instance, ZCuOH sites are clearly indicated by their distinctive O-H stretch vibration at 3660 cm^{-1},[38,78,79] while others are more subtle to infer. The UV-vis results reported here provide some guidance for distinguishing three types of Cu species. Z_2Cu species are distinguished by relatively intense d-d transitions with maxima near 12000 and 14000 cm^{-1} (Figure 10.1a), and these features persist upon exposure to CO. Isolated ZCuOH species are indicated by lower intensity d-d features near 11000 and 13000 cm^{-1}, which also persist during exposure to CO. We fund that samples intentionally prepared to contain exclusively ZCuOH always contain a confounding set of species that have relatively intense but irregular d-d features, which we assign to a mixture of higher nuclearity Cu oxo and hydroxo species. These species contribute four relatively prominent features in the d-d region, but they do not persist following CO reduction treatments.

Discrimination within these sets is more challenging. Samples prepared to contain only Z2Cu species potentially contain two geometrically distinct sites distinguished by the location of the charge-compensating Al,[80] and such sites are predicted here to have distinct UV-Vis spectra if computed at one minimum energy structure. Accounting for the finite temperature fluctuations in Cu location between local minima and associated fluctuations in Cu coordination environment, however, attenuates these differences, such that the two sites become spectroscopically indistinguishable. Similar factors affect the interpretation of XAS[79,81-84], EPR[49,83,85] spectroscopies, and X-ray diffraction[5,82,85,86] patterns, and caution should be applied in inferring Z_2Cu geometric information by comparison of observations to predictions from single, minimum energy structures.

In samples in which Cu exchange is predominantly associated with isolated Al T-sites and contain a majority of ZCuOH sites, observed UV-Vis spectra contain features in the d-d and LMCT regions that cannot be accounted for by the spectrum computed of these sites.[18,48,49,87] Strategies to directly prepare and characterize Cu-SSZ-13 samples that contain exclusively ZCuOH sites, either by exchanging dilute amounts of Cu or using higher silica content SSZ-13 supports, are unlikely to be successful because of the difficulties of observing dilute ZCuOH and the presence of a confounding set of framework Al sites that can stabilize dimeric forms of Cu even at low Al density. Therefore, a strategy that combines synthetic efforts to bias formation of predominantly one Cu site type with treatments that selectively remove minority Cu species, is more likely to allow access to individual Cu site types.

The exact shapes and positions of the features depend on the zeolite composition and the precise pretreatment conditions, including temperature, pressure and duration of O_2 exposure, all suggestive of additional Cu sites produced dynamically. Calculations here show that $[Cu^{II}OH]^+$ ions can move between adjacent 8MRs with an activation barrier of 63 kJ mol^{-1} (Figure S7 from supplementary information in Li et al.[89]) and that suitably proximal ions can condense into dimers. This proposal is consistent with experimental observations of a decrease in the approximately 3660 cm^{-1} vibrational feature associated with the ZCuO-H stretch with increasing temperature,[41] corresponding Raman shifts for multiple Cu_2O_x motifs.[18,19,55] It is also consistent with the observation of dry NO oxidation to NO_2 on nominally ZCuOH-containing samples, ascribed to dimeric Cu sites.[11,88] Because computed UV-Vis spectra of Cu dimers (Figure 10.4) are sensitive to Al proximity, extra-lattice ligands, and to finite temperature structural

fluctuations, assignment of specific spectroscopic features to individual types of dimeric Cu species is not possible based on results reported here.

The samples prepared to contain Z_2Cu sites have spectral features that are invariant to reduction in CO. Literature results on similar samples find that they are insensitive to exposure to He, O_2, or CH_4.[6,19] The four features observed in the d-d region of the ZCuOH samples following oxidizing treatment are similar to those reported previously in similar samples,[18,48,50] but these bands do respond differently to subsequent reducing treatments. We find that 5% CO exposure at 523K reproducibly preserves a portion of the d-d and LMCT features, which we assign to isolated ZCuOH sites. In contrast, exposure to CH_4 at 473K results only in a decrease in the lower energy portion (25000 to 38000 cm^{-1}) of the LMCT band and disappearance of the 29000 cm^{-1} band.[18,50,87] These results suggest that at the same temperature CH_4 reduces a different population of $Cu_xO_yH_z$ moieties to Cu^I than exposure to inert (He), and exposure to CO reduces all of the $Cu_xO_yH_z$ observed to reduce in either CH_4 or He.[18] Spectral features we assign here to isolated ZCuOH moieties are observed in similar materials to persist after CH_4 exposure.[18,50] Precise identification of the Cu dimer sites responsible for CH_4 activation under different conditions remains an important challenge for experiment and computation.

10.6 Conclusions

Cu-exchanged zeolites remain a topic of great scientific interest because of their intriguing performance in catalyzing difficult transformations involving the nitrogen oxides and methane. Identification of active sites is complicated by the sensitivity of Cu exchange to zeolite framework types, the number and distribution of framework Al atoms, Cu content, and pretreatment conditions. The SSZ-13 zeolite framework is constructed of a single symmetry distinct type of T site, in principle reducing the number of possible distinct ion exchange sites and thus simplifying spectroscopic interrogation of those sites. Here we use directed synthetic approaches to emphasize different types of exchange sites, and DFT evaluations of site structure and spectral signatures to test this principle. We find that in SSZ-13 samples prepared to contain only isolated Al T-sites, and thus in principle a homogeneous array of $[Cu^{II}OH]^+$ ion exchange sites, always contain a confounding subset of O- or OH-bridged Cu dimers and/or larger aggregates in the Cu/Al exchange regime explored here. These latter species are intrinsically heterogeneous due to heterogeneity in bridging ligands and/or in arrangements of framework Al

substituents, which likely involve more than one Al T-site. The underlying $[Cu^{II}OH]^+$ UV-Vis spectrum can be revealed by selective CO reduction of the polynuclear Cu species. The UV-Vis spectrum, even of isolated $[Cu^{II}OH]^+$ ions, is found to be influenced by the intrinsic, finite-temperature dynamics of the site, as revealed through AIMD and TD-DFT calculations. In SSZ-13 samples prepared to contain 2NN (meta) and 3NN (para) Al pairs in the 6MR, the same dynamical factors serve to obscure spectroscopic differences between these two distinct types of Z_2Cu sites. While calculations performed at the optimized geometries predict that the meta and para Cu-exchange sites are spectroscopically distinct, those differences are indistinguishable after accounting for the finite-temperature fluctuations in Cu ion coordination environment. [20] These results highlight the potential and the practical challenges of developing correlations between observed spectroscopy and the contributions of various Cu ion exchange sites and motifs to observed chemical reactivity. They highlight that precise characterization of active sites in this and similar systems demands a careful integration of chemical and spectroscopic interrogation with computational models that account for the structural and dynamical complexities of the materials.

10.7 Acknowledgements

10.8 References

(1) Paolucci, C.; Di Iorio, J.; Ribeiro, F.; Gounder, R.; Schneider, W. Adv. Catal.; Elsevier, 2016; Vol. 59; pp 1-107.

(2) Beale, A. M.; Gao, F.; Lezcano-Gonzalez, I.; Peden, C. H.; Szanyi, J. Recent advances in automotive catalysis for NOx emission control by small-pore microporous materials. Chem. Soc. Rev. 2015, 44, 7371-7405.

(3) Gao, F.; Kwak, J. H.; Szanyi, J.; Peden, C. H. Current understanding of Cu-exchanged chabazite molecular sieves for use as commercial diesel engine DeNOx catalysts. Top. Catal. 2013, 56, 1441-1459.

(4) Nova, I.; Tronconi, E. Urea-SCR technology for deNOx after treatment of diesel exhausts; Springer, 2014.

(5) Fickel, D. W.; Lobo, R. F. Copper coordination in Cu-SSZ-13 and Cu-SSZ-16 investigated by variable-temperature XRD. J. Phys. Chem. C 2010, 114, 1633-1640.

(6) Korhonen, S. T.; Fickel, D. W.; Lobo, R. F.; Weckhuysen, B. M.; Beale, A. M. Isolated Cu^{2+} ions: active sites for selective catalytic reduction of NO. Chem. Commun. 2011, 47, 800-802.

(7) Marberger, A.; Petrov, A. W.; Steiger, P.; Elsener, M.; Kröcher, O.; Nachtegaal, M.; Ferri, D. Time-resolved copper speciation during selective catalytic reduction of NO on Cu-SSZ-13. Nat. Catal. 2018, 1, 221-227.

(8) Janssens, T. V.; Falsig, H.; Lundegaard, L. F.; Vennestr_m, P. N.; Rasmussen, S. B.; Moses, P. G.; Giordanino, F.; Borfecchia, E.; Lomachenko, K. A.; Lamberti, C. A consistent reaction scheme for the selective catalytic reduction of nitrogen oxides with ammonia. ACS Catalysis 2015, 5, 2832-2845.

(9) Lomachenko, K. A.; Borfecchia, E.; Negri, C.; Berlier, G.; Lamberti, C.; Beato, P.; Falsig, H.; Bordiga, S. The Cu-CHA deNOx Catalyst in Action: Temperature-Dependent NH_3 Assisted Selective Catalytic Reduction Monitored by Operando XAS and XES. Journal of the American Chemical Society 2016, 138, 12025-12028.

(10) Kwak, J. H.; Tonkyn, R. G.; Kim, D. H.; Szanyi, J.; Peden, C. H. Excellent activity and selectivity of Cu-SSZ-13 in the selective catalytic reduction of NO_x with NH_3. Journal of Catalysis 2010, 275, 187-190.

(11) Verma, A. A.; Bates, S. A.; Anggara, T.; Paolucci, C.; Parekh, A. A.; Kamasamudram, K.; Yezerets, A.; Miller, J. T.; Delgass, W. N.; Schneider, W. F.; Ribeiro, F. H. NO oxidation: A probe reaction on Cu-SSZ-13. J. Catal. 2014, 312, 179-190.

(12) Ruggeri, M. P.; Nova, I.; Tronconi, E.; Pihl, J. A.; Toops, T. J.; Partridge, W. P. In-situ DRIFTS measurements for the mechanistic study of NO oxidation over a commercial Cu-CHA catalyst. Appl. Catal. B: Environ. 2015, 166, 181-192.

(13) Centi, G.; Perathoner, S. Nature of active species in copper-based catalysts and their chemistry of transformation of nitrogen oxides. Appl. Catal. A, General 1995, 132, 179-259.

(14) Groothaert, M. H.; Van Bokhoven, J. A.; Battiston, A. A.; Weckhuysen, B. M.; Schoonheydt, R. A. Bis(μ-oxo)dicopper in Cu-ZSM-5 and its role in the decomposition of NO: A combined in situ XAFS, UV-vis-near-IR, and kinetic study. J. Am. Chem. Soc. 2003, 125, 7629-7640.

(15) Da Costa, P.; Moden, B.; Meitzner, G. D.; Lee, D. K.; Iglesia, E. Spectroscopic and chemical characterization of active and inactive Cu species in NO decomposition catalysts based on Cu-ZSM-5. Phys. Chem. Chem. Phys. 2002, 4, 4590-4601.

(16) Vanelderen, P.; Vancauwenbergh, J.; Sels, B. F.; Schoonheydt, R. A. Coordination chemistry and reactivity of copper in zeolites. Coord. Chem. Rev. 2013, 257, 483-494.

(17) Wulfers, M. J.; Lobo, R. F.; Ipek, B.; Teketel, S. Conversion of Methane to Methanol on Copper-Containing Small-Pore Zeolites and Zeotypes. Chem. Commun. 2015, 51, 4447-4450.

(18) Ipek, B.; Wulfers, M. J.; Kim, H.; Goltl, F.; Hermans, I.; Smith, J. P.; Booksh, K. S.; Brown, C. M.; Lobo, R. F. Formation of $[Cu_2O_2]^{2+}$ and $[Cu_2O]^{2+}$ toward C-H Bond Activation in Cu-SSZ 13 and Cu-SSZ-39. ACS Catal. 2017, 7, 4291-4303.

(19) Pappas, D. K. et al. Methane to Methanol: Structure-Activity Relationships for Cu- CHA. J. Am. Chem. Soc. 2017, 139, 14961-14975.

(20) Kulkarni, A. R.; Zhao, Z.; Siahrostami, S.; N_rskov, J. K.; Studt, F. Cation-Exchanged Zeolites for the Selective Oxidation of Methane to Methanol. Catal. Sci. Technol. 2017, 8, 114-123.

(21) Tomkins, P.; Mansouri, A.; Bozbag, S. E.; Krumeich, F.; Park, M. B.; Alayon, E. M. C.; Ranocchiari, M.; van Bokhoven, J. A. Isothermal Cyclic Conversion of Methane into Methanol over Copper-Exchanged Zeolite at Low Temperature. Angew. Chem. Int. Ed. 2016, 55, 5467-5471.

(22) Woertink, J. S.; Smeets, P. J.; Groothaert, M. H.; Vance, M. A.; Sels, B. F.; Schoonheydt, R. A.; Solomon, E. I. A [Cu2O]2+ core in Cu-ZSM-5, the active site in the oxidation of methane to methanol. Proc. Natl. Acad. Sci. 2009, 106, 18908-18913.

(23) Grundner, S.; Markovits, M. A. C.; Li, G.; Tromp, M.; Pidko, E. A.; Hensen, E. J. M.; Jentys, A.; Sanchez-Sanchez, M.; Lercher, J. A. Single-site trinuclear copper oxygen clusters in mordenite for selective conversion of methane to methanol. Nat. Commun. 2015, 6, 7546.

(24) Borfecchia, E.; Beato, P.; Svelle, S.; Olsbye, U.; Lamberti, C.; Bordiga, S. Cu-CHA: a model system for applied selective redox catalysis. Chem. Soc. Rev. 2018, in press.

(25) Dusselier, M.; Davis, M. E. Small-Pore Zeolites: Synthesis and Catalysis. Chem. Rev. 2018, 118, 5265-5329.

(26) Snyder, B. E.; Bols, M. L.; Schoonheydt, R. A.; Sels, B. F.; Solomon, E. I. Iron and Copper Active Sites in Zeolites and Their Correlation to Metalloenzymes. Chem. Rev. 2017, 118, 2718-2768.

(27) Dinh, K. T.; Sullivan, M. M.; Serna, P.; Meyer, R. J.; Dinc_a, M.; Rom_an-Leshkov, Y. Viewpoint on the Partial Oxidation of Methane to Methanol Using Cu-and Fe- Exchanged Zeolites. ACS Catal. 2018, 8, 8306-8313.

(28) Latimer, A. A.; Kulkarni, A. R.; Aljama, H.; Montoya, J. H.; Yoo, J. S.; Tsai, C.; Abild-Pedersen, F.; Studt, F.; N_rskov, J. K. Understanding trends in C{H bond activation in heterogeneous catalysis. Nature materials 2017, 16, 225.

(29) Kulkarni, A. R.; Zhao, Z.-J.; Siahrostami, S.; N_rskov, J. K.; Studt, F. Monocopper active site for partial methane oxidation in Cu-exchanged 8MR zeolites. ACS Catalysis 2016, 6, 6531-6536.

(30) Pappas, D. K. et al. The nuclearity of the active site for methane to methanol conversion in Cu-mordenite: a quantitative assessment. J. Am. Chem. Soc. 2018, Just Accepted Manuscript.

(31) Sushkevich, V. L.; Palagin, D.; Ranocchiari, M.; van Bokhoven, J. A. Selective anaerobic oxidation of methane enables direct synthesis of methanol. Science 2017, 356, 523-527.

(32) Li, G.; Vassilev, P.; Sanchez-Sanchez, M.; Lercher, J. A.; Hensen, E. J.; Pidko, E. A. Stability and reactivity of copper oxo-clusters in ZSM-5 zeolite for selective methane oxidation to methanol. Journal of Catalysis 2016, 338, 305-312.

(33) Lan, Z.; Sharada, S. M. Computational strategies to probe CH activation in dioxodicopper complexes. Phys. Chem. Chem. Phys 2018, 20, 25602-25614.

(34) Goodman, B. R.; Schneider, W. F.; Hass, K. C.; Adams, J. B. Theoretical analysis of oxygen bridged Cu pairs in Cu-exchanged zeolites. Catal. Lett. 1998, 56, 183-188.

(35) Trout, B. L.; Chakraborty, A. K.; Bell, A. T. Local spin density functional theory study of copper ion-exchanged ZSM-5. J. Phys. Chem. 1996, 100, 4173-4179.

(36) Deka, U.; Lezcano-Gonzalez, I.; Weckhuysen, B. M.; Beale, A. M. Local environment and nature of Cu active sites in zeolite-based catalysts for the selective catalytic reduction of NO_x. ACS Catal. 2013, 3, 413-427.

(37) Dedecek, J.; Sobalik, Z.; Wichterlova, B. Siting and distribution of framework aluminium atoms in silicon-rich zeolites and impact on catalysis. Catal. Rev. 2012, 54, 135-223.

(38) Paolucci, C.; Parekh, A. A.; Khurana, I.; Di Iorio, J. R.; Li, H.; Albarracin Caballero, J. D.; Shih, A. J.; Anggara, T.; Delgass, W. N.; Miller, J. T.; Ribeiro, F. H.; Gounder, R.; Schneider, W. F. Catalysis in a cage: Condition-Dependent Speciation and Dynamics of Exchanged Cu Cations in SSZ-13 Zeolites. J. Am. Chem. Soc. 2016, 138, 6028-6048.

(39) Di Iorio, J. R.; Gounder, R. Controlling the Isolation and Pairing of Aluminum in Chabazite Zeolites Using Mixtures of Organic and Inorganic Structure-Directing Agents. Chem. Mater. 2016, 28, 2236-2247.

(40) Di Iorio, J. R.; Nimlos, C. T.; Gounder, R. Introducing catalytic diversity into single-site chabazite zeolites of fixed composition via synthetic control of active site proximity. ACS Catal. 2017, 7, 6663-6674.

(41) Borfecchia, E.; Lomachenko, K. A.; Giordanino, F.; Falsig, H.; Beato, P.; Soldatov, A. V.; Bordiga, S.; Lamberti, C. Revisiting the nature of Cu sites in the activated Cu-SSZ-13 catalyst for SCR reaction. Chem. Sci. 2014, 8, 548-563.

(42) Albarracin-Caballero, J. D.; Khurana, I.; Di Iorio, J. R.; Shih, A. J.; Schmidt, J. E.; Dusselier, M.; Davis, M. E.; Yezerets, A.; Miller, J. T.; Ribeiro, F. H.; Gounder, R. Structural and kinetic changes to small-pore Cu-zeolites after hydrothermal aging treatments and selective catalytic reduction of NOx with ammonia. React. Chem. Eng. 2017, 2, 168-179.

(43) Schmidt, J. E.; Oord, R.; Guo, W.; Poplawsky, J. D.; Weckhuysen, B. M. Nanoscale tomography reveals the deactivation of automotive copper-exchanged zeolite catalysts. Nat. Commun. 2017, 8, 1666.

(44) Goltl, F.; Sautet, P.; Hermans, I. The impact of _nite temperature on the coordination of Cu cations in the zeolite SSZ-13. Catal. Today 2016, 267, 41-46.

(45) Chen, P.; Khetan, A.; Jablonska, M.; Simbock, J.; Muhler, M.; Palkovits, R.; Pitsch, H.; Simon, U. Local dynamics of copper active sites in zeolite catalysts for selective catalytic reduction of NO_x with NH_3. Appl. Catal. B: Environmental 2018, 237, 263-272.

(46) Li, H.; Paolucci, C.; Schneider, W. F. Zeolite Adsorption Free Energies from ab Initio Potentials of Mean Force. J. Chem. Theory Comput. 2018, 14, 929-938.

(47) Chen, L.; Falsig, H.; Janssens, T. V.; Jansson, J.; Skoglundh, M.; Gr onbeck, H. Effect of Al-distribution on oxygen activation over Cu-CHA. Catal. Sci. Technol. 2018, 8, 2131-2136.

(48) Giordanino, F.; Vennestr_m, P. N. R.; Lundegaard, L. F.; Stappen, F. N.; Mossin, S.; Beato, P.; Bordiga, S.; Lamberti, C. Characterization of Cu-exchanged SSZ-13: a comparative FTIR, UV Vis, and EPR study with Cu-ZSM-5 and Cu-Beta with similar Si/Al and Cu/Al ratios. Dalton Trans. 2013, 42, 12741-61.

(49) Godiksen, A.; Stappen, F. N.; R Vennestr_m, P. N.; Giordanino, F.; Birk Rasmussen, S.; Lundegaard, L. F.; Mossin, S. Coordination Environment of Copper Sites in Cu-CHA Zeolite Investigated by Electron Paramagnetic Resonance. J. Phys. Chem. C 2014, 118, 23126-23138.

(50) Oord, R.; Schmidt, J. E.; Weckhuysen, B. M. Methane-to-methanol conversion over zeolite Cu-SSZ-13, and its comparison with the selective catalytic reduction of NO$_x$ with NH$_3$. Catal. Sci. Technol. 2018, 8, 1028-1038.

(51) Lei, G. D.; Adelman, B. J.; Sarkany, J.; Sachtler, W. M. H. Identification of copper(II) and copper(I) and their interconversion in Cu/ZSM-5 De-NOx catalysts. Appl. Catal. B, Environ. 1995, 5, 245-256.

(52) Moden, B.; Da Costa, P.; Fonf_e, B.; Lee, D. K.; Iglesia, E. Kinetics and Mechanism of Steady-State Catalytic NO Decomposition Reactions on Cu-ZSM5. J. Catal. 2002, 209, 75-86.

(53) Moden, B.; Da Costa, P.; Lee, D. K.; Iglesia, E. Transient studies of oxygen removal pathways and catalytic redox cycles during NO decomposition on Cu-ZSM5. J. Phys. Chem. B 2002, 106, 9633-9641.

(54) Smeets, P. J.; Hadt, R. G.; Woertink, J. S.; Vanelderen, P.; Schoonheydt, R. A.; Sels, B. F.; Solomon, E. I. Oxygen precursor to the reactive intermediate in methanol synthesis by Cu-ZSM-5. J. Am. Chem. Soc. 2010, 132, 14736-14738.

(55) Woertink, J. S.; Smeets, P. J.; Groothaert, M. H.; Vance, M. A.; Sels, B. F.; Schoonheydt, R. A.; Solomon, E. I. A [Cu2O]2+ Core in Cu-ZSM-5, the Active Site in the Oxidation of Methane to Methanol. Proc. Natl. Acad. Sci. 2009, 106, 18908-18913.

(56) Groothaert, M. H.; Smeets, P. J.; Sels, B. F.; Jacobs, P. A.; Schoonheydt, R. A. Selective oxidation of methane by the bis(μ-oxo)dicopper core stabilized on ZSM-5 and mordenite zeolites. J. Am. Chem. Soc. 2005, 127, 1394-1395.

(57) Grundner, S.; Markovits, M. A.; Li, G.; Tromp, M.; Pidko, E. A.; Hensen, E. J.; Jentys, A.; Sanchez-Sanchez, M.; Lercher, J. A. Single-site trinuclear copper oxygen clusters in mordenite for selective conversion of methane to methanol. Nat. Commun. 2015, 6, 7546.

(58) Sushkevich, V. L.; Palagin, D.; van Bokhoven, J. A. E_ect of Active Sites Structure on Activity of Copper Mordenite in Aerobic and Anaerobic Conversion of Methane to Methanol. Angew. Chem. Int. Ed. 2018, 57, 8906-8910.

(59) van Bokhoven, J. A.; Lamberti, C. In XAFS Techniques for Catalysts, Nanomaterials, and Surfaces; Iwasawa, Y., Asakura, K., Tada, M., Eds.; Springer International Publishing: Cham, 2017; pp 299-316.

(60) Kosinov, N.; Liu, C.; Hensen, E. J.; Pidko, E. A. Engineering of transition metal catalysts confined in zeolites. Chem. Mater. 2018, 30, 3177-3198.

(61) Palagin, D.; Knorpp, A. J.; Pinar, A. B.; Ranocchiari, M.; van Bokhoven, J. A. Assessing the relative stability of copper oxide clusters as active sites of a CuMOR zeolite for methane to methanol conversion: size matters? Nanoscale 2017, 9, 1144-1153.

(62) Borfecchia, E.; Pappas, D. K.; Dyballa, M.; Lomachenko, K. A.; Negri, C.; Signorile, M.; Berlier, G. Evolution of active sites during selective oxidation of methane to methanol over Cu CHA and Cu-MOR zeolites as monitored by operando XAS. Catal. Today 2018, in press.

(63) Henson, M. J.; Vance, M. a.; Zhang, C. X.; Liang, H.-C.; Karlin, K. D.; Solomon, E. I. Resonance raman investigation of equatorial ligand donor effects on the Cu$_2$O$_2^{2+}$ core in

end-on and side-on μ-peroxo-dicopper(II) and bis-μ-oxo-dicopper(III) complexes. J. Am. Chem. Soc. 2003, 125, 5186-5192.

(64) Vanelderen, P.; Hadt, R. G.; Smeets, P. J.; Solomon, E. I.; Schoonheydt, R. A.; Sels, B. F. Cu-ZSM-5: A biomimetic inorganic model for methane oxidation. J. Catal. 2011, 284, 157-164.

(65) Paolucci, C.; Khurana, I.; Parekh, A. A.; Li, S.; Shih, A. J.; Li, H.; Iorio, J. R. D.; Albarracin-caballero, J. D.; Yezerets, A.; Miller, J. T.; Delgass, W. N.; Ribeiro, F. H.; Schneider, W. F.; Gounder, R. Dynamic multinuclear sites formed by mobilized copper ions in NO_x selective catalytic reduction. Science 2017, 357, 898-903.

(66) McEwen, J. S.; Anggara, T.; Schneider, W. F.; Kispersky, V. F.; Miller, J. T.; Delgass, W. N.; Ribeiro, F. H. Integrated operando X-ray absorption and DFT characterization of Cu-SSZ-13 exchange sites during the selective catalytic reduction of NO_x with NH_3. Catal. Today 2012, 184, 129-144.

(67) Smeets, P. J.; Woertink, J. S.; Sels, B. F.; Solomon, E. I.; Schoonheydt, R. A. Transition-metal ions in zeolites: Coordination and activation of oxygen. Inorg. Chem. 2010, 49, 3573-3583.

(68) Godiksen, A.; Vennestrom, P. N. R.; Rasmussen, S. B.; Mossin, S. Identification and quantification of copper sites in zeolites by electron paramagnetic resonance spectroscopy. Top. Catal. 2017, 60, 13-29.

(69) Snyder, B. E. R.; Bols, M. L.; Schoonheydt, R. A.; Sels, B. F.; Solomon, E. I. Iron and Copper Active Sites in Zeolites and Their Correlation to Metalloenzymes. Chem. Rev. 2018, 118, 2718-2768.

(70) Sklenak, S.; Andrikopoulos, P. C.; Whittleton, S. R.; Jirglova, H.; Sazama, P.; Benco, L.; Bucko, T.; Hafner, J.; Sobalik, Z. Effect of the Al siting on the structure of Co(II) and Cu(II) cationic sites in ferrierite. A periodic DFT molecular dynamics and FTIR study. J. Phys. Chem. C 2013, 117, 3958-3968.

(71) Luo, J.; Wang, D.; Kumar, A.; Li, J.; Kamasamudram, K.; Currier, N.; Yezerets, A. Identification of two types of Cu sites in Cu/SSZ-13 and their unique responses to hydrothermal aging and sulfur poisoning. Catal. Today 2016, 267, 3-9.

(72) Goeltl, F.; Muller, P.; Uchupalanun, P.; Sautet, P.; Hermans, I. Developing a Descriptor-Based Approach for CO and NO Adsorption Strength to Transition Metal Sites in Zeolites. Chemistry of Materials 2017, 29, 6434-6444.

(73) Harris, D.; Bertolucci, M. Symmetry and Spectroscopy: An Introduction to Vibrational and Electronic Spectroscopy; Dover Books on Chemistry Series; Dover Publications, 1989.

(74) Solomon, E. I.; Heppner, D. E.; Johnston, E. M.; Ginsbach, J. W.; Cirera, J.; Qayyum, M.; Kieber-Emmons, M. T.; Kjaergaard, C. H.; Hadt, R. G.; Tian, L. Copper active sites in biology. Chem. Rev. 2014, 114, 3659-3853.

(75) Goodman, B. R.; Hass, K. C.; Schneider, W. F.; Adams, J. B. Cluster Model Studies of Oxygen-Bridged Cu Pairs in Cu-ZSM-5 Catalysts. J. Phys. Chem. B 1999, 103, 10452-10460.

(76) Mahyuddin, M. H.; Tanaka, T.; Shiota, Y.; Staykov, A.; Yoshizawa, K. Methane Partial Oxidation over $[Cu_2(μ-O)]^{2+}$ and $[Cu_3(μ-O)3]^{2+}$ Active Species in Large-Pore Zeolites. ACS Catal. 2018, 8, 1500-1509.

(77) Knott, B. C.; Nimlos, C. T.; Robichaud, D. J.; Nimlos, M. R.; Kim, S.; Gounder, R. Consideration of the Aluminum Distribution in Zeolites in Theoretical and Experimental Catalysis Research. ACS Catal. 2018, 8, 770-784.

(78) Lezcano-Gonzalez, I.; Deka, U.; Arstad, B.; Van Yperen-De Deyne, A.; Hemelsoet, K.; Waroquier, M.; Van Speybroeck, V.; Weckhuysen, B. M.; Beale, A. M. Determining the storage, availability and reactivity of NH_3 within Cu-Chabazite-based Ammonia Selective Catalytic Reduction systems. Phys. Chem. Chem. Phys. 2014, 16, 1639-1650.

(79) Giordanino, F.; Borfecchia, E.; Lomachenko, K. A.; Lazzarini, A.; Agostini, G.; Gallo, E.; Soldatov, A. V.; Beato, P.; Bordiga, S.; Lamberti, C. Interaction of NH3 with Cu-SSZ-13 catalyst: A complementary FTIR, XANES, and XES study. J. Phys. Chem. Lett. 2014, 5, 1552-1559.

(80) Li, S.; Li, H.; Gounder, R.; Debellis, A.; Muller, I. B.; Prasad, S.; Moini, A.; Schneider, W. F. First-Principles Comparison of Proton and Divalent Copper Cation Exchange Energy Landscapes in SSZ-13 Zeolite. J. Phys. Chem. C 2018, 122, 23564-23573.

(81) Martini, A.; Borfecchia, E.; Lomachenko, K. A.; Pankin, I.; Negri, C.; Berlier, G.; Beato, P.; Falsig, H.; Bordiga, S.; Lamberti, C.; Pankin, I. A. Composition-driven Cuspeciation and reducibility in Cu-CHA zeolite catalysts: a multivariate XAS/FTIR approach to complexity. Chem. Sci. 2017, 8, 6836-6851.

(82) Andersen, C. W.; Borfecchia, E.; Bremholm, M.; J_rgensen, M. R. V.; Vennestrom, P. N. R.; Lamberti, C.; Lundegaard, L. F.; Iversen, B. B. Redox-Driven Migration of Copper Ions in the Cu-CHA Zeolite as Shown by the In Situ PXRD/XANES Technique. Angew. Chem. Int. Ed. 2017, 56, 10367-10372.

(83) Berlier, G.; Crocell_a, V.; Signorile, M.; Borfecchia, E.; Bonino, F.; Bordiga, S. In Struct. Bond.; Mingos, M. P. F., Ed.; Springer, Berlin, Heidelberg, 2018; Chapter 1, pp 1-64.

(84) Martini, A.; Alladio, E.; Borfecchia, E. Determining Cu Speciation in the Cu-CHA Zeolite Catalyst: The Potential of Multivariate Curve Resolution Analysis of In Situ XAS Data. Top. Catal. 2018, 61, 1396-1407.

(85) Godiksen, A.; Isaksen, O. L.; Rasmussen, S. B.; Vennestrom, P. N.; Mossin, S. Site-Specific Reactivity of Copper Chabazite Zeolites with Nitric Oxide, Ammonia, and Oxygen. ChemCatChem 2018, 10, 366-370.

(86) Andersen, C. W.; Bremholm, M.; Vennestrom, P. N. R.; Blichfeld, A. B.; Lundegaard, L. F.; Iversen, B. B. Location of Cu^{2+} in CHA zeolite investigated by X-ray diffraction using the Rietveld/maximum entropy method. IUCrJ 2014, 1, 382-386.

(87) Oord, R. Spectroscopic Insights into Copper-Based Microporous Zeolites for NH_3-SCR of NO_x and Methane-to-Methanol Activation. Ph.D. thesis, Utrecht University, 2017.

(88) Gao, F.; Washton, N. M.; Wang, Y.; Koll_ar, M.; Szanyi, J.; Peden, C. H. Effects of Si/Al ratio on Cu/SSZ-13 NH_3-SCR catalysts: Implications for the active Cu species and the roles of Bronsted acidity. Journal of Catalysis 2015, 331, 25-38.

(89) Li, H; Paolucci, C; Khurana, I; Wilcox, L.N; Göltl, F; Albarracin-Caballero, J.D;, Shih, A.J; Ribeiro, F.H; Gounder, R; Schneider, W.F. Consequences of exchange-site heterogeneity and dynamics on the UV-visible spectrum of Cu-exchanged SSZ-13. Chemcial Science 2019, 10, 2373-2384.

11. MULTINUCLEAR CU-OXO SITES FROM MONONUCLEAR CU SITES IN CU-SSZ-13: CHARACTERIZATION BY SELECTIVE TITRATION AND NO OXIDATION PROBE REACTION

11.1 Preface

Chapter 11 reflects the reproduction of current draft of another manuscript in preparation. This chapter deals with identification and quantification of multinuclear Cu-oxo complexes evolved from mononuclear Cu cations, and their relevance for standard SCR and NO oxidation reaction.

11.2 Abstract

Herein, we have indicated that proximal monomeric $[Cu^{II}OH]^+$ cations anchored to zeolite framework Al sites can evolve into multinuclear Cu-oxo species under certain conditions, which are different from directly incorporated Cu as Cu_xO_y clusters. Such Cu-oxo species have been identified, selectively titrated and correlated with NO oxidation rates. Furthermore, detailed NO oxidation kinetic measurement and analysis enabled proposing plausible NO oxidation reaction mechanism, consistent with experimentally measured kinetic parameters, suggesting multinuclear Cu-oxo species as the active sites for NO oxidation reaction. This would allow NO oxidation to be used as a probe reaction to enumerate Cu site speciation, specifically multinuclear Cu-oxo cations in Cu-zeolites. Such understanding of NO oxidation active site requirements and reaction mechanism aids in resolving the outstanding question of whether NO oxidation to gas phase NO_2 is an elementary step during the selective catalytic reduction (SCR) of NO_x with ammonia reaction on zeolite supported transition metal or not. Model Cu-SSZ-13 samples have been synthesized to contain varying amounts of homogeneously dispersed monomeric Cu cations. CO-temperature programmed reduction has been used to selectively titrate multinuclear Cu-oxo species in model Cu-SSZ-13 samples, along with UV-visible spectroscopy to further corroborates the presence of multinuclear Cu-oxo cations.

11.3 Introduction

Selective catalytic reduction of NO_x using NH_3 as a reductant (NH_3-SCR) is one of the most efficient emission control strategies for abatement of NO_x in lean-burn and diesel exhaust. NO oxidation to gas phase NO_2 was proposed to be one of the key elementary steps during the SCR reaction on zeolite supported transition metal catalysts by many groups, as the presence of NO_2 in the feed promotes the SCR rate until NO_2:NO ratio of 1:1[1–4]. However, evidence suggests that gas phase NO_2 is not necessarily involved or at least not directly involved in the standard SCR reaction, as NO to NO_2 oxidation rate is orders of magnitude lower than standard SCR reaction rate under identical conditions[5]. Firstly, NO_2 has promotional effect on standard NH_3-SCR reaction rate, while NO_2 has been shown to inhibit NO to NO_2 oxidation reaction. Secondly, NO to NO_2 oxidation reaction is inhibited by H_2O, which, on the contrary, has negligible impact on standard NH_3-SCR reaction [6–9]. Attempts have been made by few groups to reconcile these disparities by proposing that reaction rates measured during NO oxidation cannot be representative of the NO to NO_2 oxidation rate under SCR reaction conditions [10–12]. It was suggested that desorption of NO_2 could be the rate-limiting step under NO oxidation reaction conditions due to dominant surface coverage of nitrates and nitrite groups. While NH_3 would react with the surface nitrate and nitrite groups under standard SCR reaction conditions and thus, accelerating the desorption or consumption of NO_2. Even though a few explanations exist in the literature to explain the inconsistencies, hardly any efforts have been dedicated in understanding the differences in active site requirements between NO oxidation reaction and NO to NO_2 oxidation reaction under SCR conditions. Detailed understanding of the mechanistic pathway as well as active site requirements with the ways to quantify the active sites is essential in unravelling the causes behind kinetic discrepancies and differences between the nature of Cu sites active for NO oxidation and for standard NH_3-SCR.

Copper-exchanged zeolites are a class of catalysts for reduction of NO_x in presence of excess O_2 using NH_3 as a reductant via selective catalytic reduction (SCR)[1]. Cu-SSZ-13 is commercially attractive because of its ability to meet emission regulations than its predecessors (Cu-ZSM-5 and Cu-Beta), primarily due to its hydrothermal stability[13][14]. Advancements have been made in understanding the Cu cation speciation in SSZ-13 as well as the mechanistic pathway of standard SCR reaction on Cu-SSZ-13 over the last decade. Many groups have proposed monomeric Cu^{II} cations present near the six-membered ring of SSZ-13 as the dominant

active site for the standard SCR [15–18]. Further characterization studies on Cu-SSZ-13 showed two different cationic positions for monomeric Cu viz. divalent Cu^{II} cations charge balanced by two framework Al atoms in the double six membered rings (D6R) of the CHA structure and monovalent $[Cu^{II}OH]^+$ complexes charge balanced by one framework Al atom[19–22]. In accordance with these results, our recent study[23] also found Cu cation speciation into two distinct type of Cu sites, the relative population of which depend on zeolite composition. Regardless of structural differences between these two types of Cu sites, both divalent Cu^{II} and monovalent $[Cu^{II}OH]^+$ complexes exchanged at paired Al and isolated Al sites, respectively, catalyze NO_x SCR reactions[24–26] at similar turnover rates (per Cu^{2+}; 473 K). More importantly, different active Cu sites were enumerated and tracked as they evolved under different gas exposure conditions, from ambient conditions (existing as monomeric hydrated mobile Cu^{II} and $Cu^{II}OH$ species), to dry and inert high temperature treatment (dehydrated Cu^{II} and Cu^I species), to *operando* conditions (monomeric Cu species solvated by NH_3). Thus, this study highlighted the significance of exposing gas conditions in evolution of monomeric Cu active sites.

Recent efforts have been directed towards identifying Cu_3O_y [27] and Cu_2O_y [27][28][29] species in Cu-SSZ-13 formed upon high temperature oxidative treatment (673 K in 20% O_2), which have shown to be reactive for selective oxidation of methane to methanol. Using UV-vis and Raman spectroscopy, various reactive Cu_2O_y species $\{Cu^{II}–O_2–Cu^{II}\}^{2+}$ (trans-µ-1,2-peroxo dicopper(II)) and $\{Cu^{II}–O–Cu^{II}\}^{2+}$ (mono–(µ–oxo) dicopper(II)) species have been proposed[29]. Such species have been proposed to evolve from $[Cu^{II}OH]^+$ precursors, under high temperature oxidative treatment (10% O_2 at 773 K), either from direct reaction of self-reduced Cu^I with O_2, giving $\{Cu^{II})–O_2–Cu^{II}\}^{2+}$, or from the condensation of proximal $[Cu^{II}OH]^+$ species, resulting e.g. in mono-(µ-oxo) dicopper cores ($\{Cu^{II}–O–Cu^{II}\}^{2+}$)[28,29]. It is important to note that these Cu_2O_y species arising from nominally monomeric $[Cu^{II}OH]^+$ species are different from Cu_xO_y species (clustered Cu^{2+} ions with $x \geq 2$, $y \geq 1$), which result from over-exchange of Cu. Though these studies provide evidence toward the identity of active Cu_2O_y species, no quantitative correlation between the number of these species to the reaction rate was reported.

Very few studies have focused on identification and quantification of NO oxidation active Cu sites in SSZ-13 along with their correlation with NO oxidation rate. Moreover, there has not been any fully consistent NO oxidation reaction mechanism on Cu-SSZ-13 previously proposed in the literature. Verma et al. demonstrated that under ''dry'' reaction conditions (300

ppm NO, 150 ppm NO_2, 10% O_2 in balance He, 543 K), NO oxidation is catalyzed by clustered Cu_xO_y species (formed because of over-exchanged Cu in Si/Al 6) while monomeric Cu^{2+} are completely inert at a reaction temperature of 543 K [9]. Additionally, Cu ion dimers like {Cu(II)–O–Cu(II)}$^{2+}$, formed at higher Cu loadings (Si/Al 6, Cu/Al > 0.3) after high temperature oxidative treatment (10% O_2 at 773 K), were proposed to be the active site for NO oxidation reaction [30231]. However, these studies did not unambiguously identify, quantify and correlate them with their respective NO oxidation reactivity on Cu-SSZ-13. Additionally, detailed kinetic analysis, with reaction orders and energy of activation, along with fully consistent NO oxidation reaction mechanism on such dimeric Cu sites in Cu-SSZ-13 was not reported.

In this work, we synthesized a series of Cu-SSZ-13 catalysts with varying Cu cation density such that they only contain monomeric Cu cation species and no clustered Cu_xO_y species. NO oxidation kinetics were collected and the number of reactive Cu-oxo cations were titrated using CO-TPR. A correlation is established between NO oxidation reactivity and active Cu-oxo cations, which are proposed to be the active site evolving from proximal $[Cu^{II}OH]^+$ sites. The influence of proximity of Cu cations on NO oxidation rate was explored. These Cu-oxo active sites are proposed to be dimeric Cu (Cu_2O_2 and Cu_2O), inferred from *ex-situ* and *in-situ* UV-vis specroscopy. Finally, with the aid of FTIR spectroscopy to probe the reaction intermediate, a NO oxidation reaction mechanism consistent with our measured reaction orders is proposed.

11.4 Results and Discussion

11.4.1 Preparation of Cu-SSZ-13 Zeolites of Varying Cu Cation Density

Cu-SSZ-13 zeolites at different Si/Al and Cu/Al ratios were prepared in order to study the effects of Cu site speciation and density on kinetic and mechanistic details of NO oxidation reaction. Structural integrity of SSZ-13 zeolites was confirmed by measuring micropore volumes (Table 11.1). The numbers of monomeric Cu^{II} and $[Cu^{II}OH]^+$ sites on each Cu-SSZ-13 zeolite after oxidative treatment (20% O_2, 773 K) were quantified (Table 11.1) by quantifying the number of residual protons using methods that selectively titrate H^+ sites before and after Cu-exchange in small-pore, metal-exchanged zeolites[32]. Therefore, Cu-SSZ-13 samples studied here contain only monomeric Cu^{II} cations, present either as Cu^{II} at paired framework Al sites or as $[Cu^{II}OH]^+$ at isolated Al sites. These Cu-SSZ-13 samples comprise a set of model catalysts with

monomeric Cu cations at varying density, which we use to investigate the consequences of Cu site proximity for NO oxidation reaction.

Table 11.1 Bulk elemental analysis and fraction of monomeric Cu^{II} and $[Cu^{II}OH]$ sites on a series of Cu-exchanged SSZ-13 samples with varying Si/Al (4.5-25) and Cu/Al (0.03-0.44)

Si/Al[a]	Cu wt %[a]	Cu/Al[a]	H⁺/Al[b]	Excess H⁺/Al[b]	Co/Al[c]	Micropore Volume[d]	$Cu^{II}OH/Al$[e]	Cu^{II}/Al[e]
4.5	0.0	0.00	0.65	-	0.19	0.26	0.00	0.00
	1.7	0.08	0.42	0.05	-	-	0.00	0.08
15	0.0	0.00	0.98	-	0.10	0.18	0.00	0.00
	0.2	0.03	0.93	0.03	-	-	0.00	0.03
	0.8	0.12	0.73	0.09	-	-	0.03	0.09
	1.6	0.24[f]	0.80	0.00	-	-	0.24	0.00
	1.7	0.25	0.64	0.10	-	-	0.16	0.09
	2.4	0.37	0.58	0.08	-	-	0.28	0.09
	2.8	0.42	0.50	0.08	-	-	0.33	0.09
	2.9	0.44	0.51	0.09	-	-	0.35	0.09
25	0.0	0.00	0.98	-	0.05	0.20	0.00	0.00
	1.1	0.30	0.67	0.04	-	-	0.26	0.04
	1.6	0.42	0.58	0.04	-	-	0.38	0.04

[a]Atomic composition determined using Atomic Absorption Spectroscopy
Errors are Si/Al = ± 1 and Cu/Al = ± 0.03
[b]Residual Brønsted acid sites counted in oxidized and reduced form using NH_3 titration method describe in [33]
[c]Paired Al sites counted using amount of Co titrated following the procedure described in [34].
[d]Micropore volume from Ar adsorption isotherms.
Error is ± 0.01 cm³ g⁻¹
[e]Determined from titration of residual H⁺ sites by NH_3 and thermodynamic preferences for Cu^{II} and $Cu^{II}OH$ siting [33] and [32]. [f]Sample synthesized with all framework Al as isolated Al and 100% of the Cu is exchanged as [Cu-OH]

11.4.2 NO oxidation kinetics

NO oxidation kinetics previously measured on Cu-SSZ-13 samples with Si/Al 5 by Verma et al. are also reported in Table 11.2 for the purpose of comparison [9]. Samples with Si/Al 5 and Cu/Al above 0.20, which were found to contain Cu_xO_y species (clustered Cu^{II} ions $x \geq 2$, $y \geq 1$) as detected from XANES under ambient conditions, show substantial NO oxidation rate. CuO_2Cu type of dimeric Cu species was assumed to be representative of active Cu-oxo species and proposed mechanism involved non-elementary step of sequential abstraction of O atoms by NO to form NO_2 molecules[9]. Cu-SSZ-13 with exclusively contain monomeric isolated Cu^{II} cations (Cu/Al =< 0.20), exhibited non-detectable NO oxidation rates under reaction conditions, leading to the conclusion that monomeric Cu^{II} sites do not contribute measurably to NO oxidation rates. Our data on a few additional Cu-SSZ-13 samples (Si/Al 5, Cu/Al 0.08 and 0.20) (Table 11.2) exclusively containing monomeric isolated Cu^{II} cations also show non-detectable NO oxidation reactivity.

On the other hand, Cu-SSZ-13 samples with monomeric $[Cu^{II}OH]^+$ cations present above a certain value (Si/Al 15 and 25, $[Cu^{II}OH]^+/Al > 0.03$) showed significant NO oxidation reactivity, implying that $[Cu^{II}OH]^+$ species need to be close enough to each other to be active for NO oxidation. This indicates two possibilities: 1) Monomeric $[Cu^{II}OH]^+$ sites containing extra-framework oxygen act as the active site for NO oxidation, 2) Monomeric $[Cu^{II}OH]^+$ act as the precursor to some polymeric Cu-oxo species with more reactive active extra-framework oxygen active for NO oxidation. Non-linear dependence of NO oxidation rate on $Cu^{II}OH$ density (Figure 11.1) eliminates the possibility of monomeric $[Cu^{II}OH]^+$ being the only active site. Similar reaction kinetics parameters including reaction orders (w.r.t NO, O_2 and NO_2) and energy of activation suggests similar NO oxidation reaction mechanism as previously proposed on CuO_2Cu type Cu-oxo species by Verma et al.[9].

Table 11.2 Summary of NO oxidation kinetic data on a series of Cu-exchanged SSZ-13 samples with varying Si/Al (4.5-25) and Cu/Al (0.03-0.44)

Cu/Al	$Cu^{II}OH$/Al	$Cu^{II}OH$ /1000$Å^3$	E_{app}[a] (kJ mol^{-1})	Rate[b] (10^{-4} mol NO mol Cu^{-1} s^{-1})	NO order[a]	NO_2 order[a]	O_2 order[a]
				SSZ-13 Si/Al = 4.5			
0.08	0.00	0.00	n.m.	0.0	n.m.	n.m.	n.m.
0.20	0.00	0.00	n.m.	0.0	n.m.	n.m.	n.m.
0.31*	0.00	0.00	45	0.6	1.5	-0.8	0.9
0.35*	0.00	0.00	51	1.4	1.4	-0.7	0.8
0.39*	0.00	0.00	53	1.5	1.5	-0.8	0.8
1.60*	0.00	0.00	55	1.7	1.6	-0.9	0.9
				SSZ-13 Si/Al = 15			
0.03	0.00	0	n.m.	0.0	n.m.	n.m.	n.m.
0.12	0.03	0.02	n.m.	0.0	n.m.	n.m.	n.m.
0.24[c]	0.24	0.23	48	0.5	0.9	-0.9	0.7
0.25	0.16	0.15	46	0.7	1.4	-0.6	0.7
0.37	0.28	0.26	56	0.9	1.4	-0.6	0.7
0.42	0.33	0.32	65	1.2	1.4	-0.8	0.7
0.44	0.35	0.33	55	1.3	1.3	-0.6	0.7
				SSZ-13 Si/Al =25			
0.30	0.25	0.19	61	0.8	1.5	-0.8	0.9
0.42	0.37	0.30	67	1.0	1.3	-1.0	0.8

[a] Measured at 573 K. Error in activation energy $\pm$ 7 kJ mol^{-1} and orders $\pm$ 0.1 (NO_2 and O_2) and $\pm$ 0.2 (NO)

[b] Measured under NO oxidation conditions of 300 ppm NO, 150 ppm NO_2, 10% O_2 and 550 K

[c] Sample synthesized with isolated Al on the SSZ-13 framework 100% of the Cu is exchanged as [Cu-OH]$^+$

*From [9]

n.m. did not display measurable NO oxidation rate ($< 0.3 \times 10^{-4}$ mol NO (mol Cu)$^{-1}$ s^{-1}).
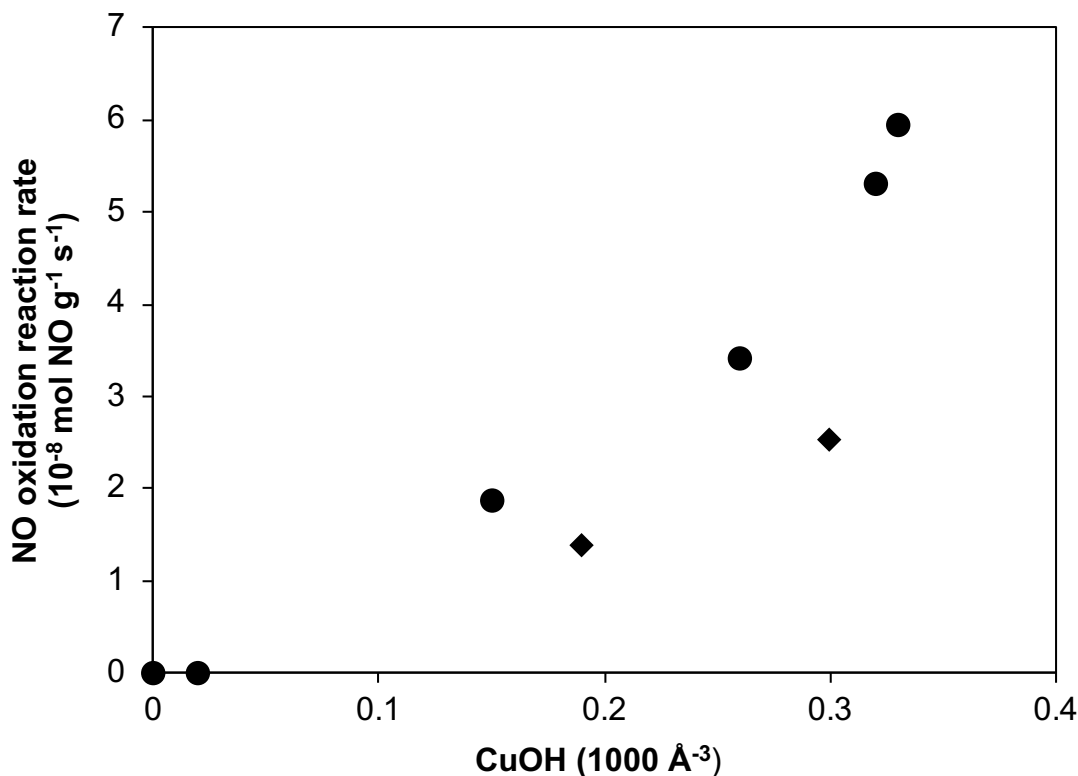
Figure 11.1 NO oxidation rates measured under NO oxidation conditions of 300 ppm NO, 150 ppm NO_2, 10% O_2 and 550 K as function of concentration of [$Cu^{II}OH$] ions per crystallite volume (diamonds: Si/Al 25 and circles: Si/Al 15)

11.4.3 Quantification of Cu-oxo sites

Fraction of Cu species with reactive oxygen atoms (e.g. CuO and CuO_xCu) were previously quantified from evolution of CO_2 during temperature-programmed reduction with CO (CO-TPR) in Cu-ZSM-5[35][36]. To quantify Cu-oxo species with reactive oxygen atoms in our Cu-CHA samples pretreated under high temperature oxidative conditions (10% O_2 at 673 K), we employ the same CO-TPR technique and quantify the evolved CO_2. Cu-SSZ-13 catalysts with only monomeric Cu^{II} cations exhibit no measurable CO_2 evolution during CO-TPR (Figure 11.2), likely due to the absence of a proton required for charge balance. In addition, catalysts with $Cu^{II}OH/Al \leq 0.03$ showed no detectable CO_2 evolution, which is consistent with incomplete reaction stoichiometry during reduction of monomeric [$Cu^{II}OH$]$^+$ sites with CO. However, we can envisage CO reduction of some polymeric Cu-oxo species to evolve CO_2 as follows:

$$[Cu(II)OCu(II)]^{2+} + CO \rightarrow 2Cu(I) + CO_2$$

$$[Cu(II)O_2Cu(II)]^{2+} + 2CO \rightarrow 2Cu(I) + 2CO_2$$
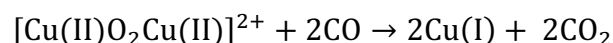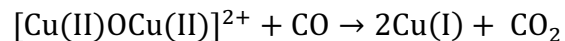
CO-TPR profiles for all the samples show four different peaks between 350 K and 823 K. While the peaks at 443 K, 523 K and 773 K are unresolved, the peak at 400 K was previously assigned to $\{Cu^{II}–O_2–Cu^{II}\}^{2+}$ in Cu-ZSM-5[37]. The formation of CO_2 requires adsorption of CO followed by the reaction with removable oxygen atoms in Cu-oxo cations. The broad CO_2 evolution profile may suggest the presence of Cu-oxo species with different removable oxygen to Cu ratio ($\{Cu^{II}–O_2–Cu^{II}\}^{2+}$, $\{Cu^{II}–O–Cu^{II}\}^{2+}$, etc.) and/or different reactivity towards CO, either because of their local coordination to two exchange sites of varying structure or because of their non-uniform distances from CO adsorption sites.
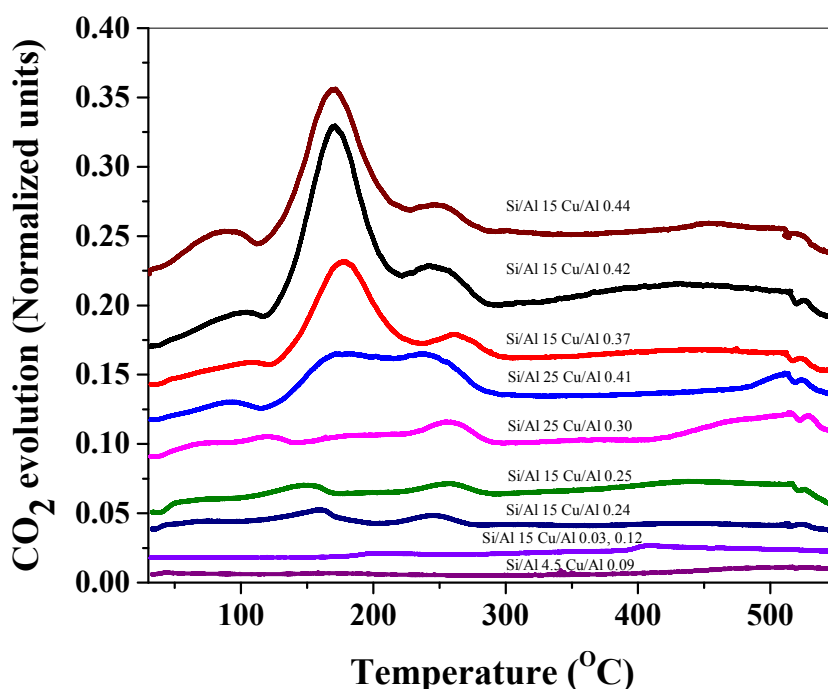
Figure 11.2 CO-Temperature Programmed Reduction (CO-TPR) profiles for a series of Cu-SSZ-13 samples with Si/Al 5-25 and Cu/Al 0.09-0.44

Total moles of CO_2 evolved is quantified by integrating the entire profile up to 823 K. Moles of CO_2 formed normalized per mole of total Cu in addition to per mole of $[Cu^{II}OH]^+$ are shown in Table 11.3. Since monomeric Cu^{II} cation showed no CO_2 evolution, moles of CO_2 evolved were normalized per mole of $[Cu^{II}OH]^+$ and $\{CO_2/[Cu^{II}OH]^+\}$ on various samples are compared. $\{CO_2/[Cu^{II}OH]^+\}$ is less than unity and increases monotonically with increase in

{[Cu^{II}OH]$^+$/Al} implying that CO does not reduce all [Cu^{II}OH]$^+$ sites but selectively reduces only proximal [Cu^{II}OH]$^+$ sites. Thus, CO$_2$ evolution from CO-TPR is indicative of polymeric Cu-oxo species with removable oxygen (s) likely produced during high temperature oxidative treatment (10% O$_2$ at 673 K) from proximal [Cu^{II}OH]$^+$ sites.

Table 11.3 CO TPR (Temperature Programmed Reduction) results yielding CO$_2$ produced and fraction of Cu titrated by CO

Si/Al	Cu/ wt %	Cu/Al	Cu^{II}OH/Al	CO$_2$/Cu$_{total}$	CO$_2$/[Cu-OH]$^+$
4.5	1.7	0.08	0.00	0	0
15	0.2	0.03	0.00	0.03	0.00
	0.8	0.12	0.03	0.04	0.00
	1.6	0.24	0.24	0.24	0.24
	1.7	0.25	0.16	0.24	0.35
	2.4	0.37	0.28	0.34	0.42
	2.8	0.42	0.33	0.41	0.52
	2.9	0.44	0.35	0.40	0.50
25	1.1	0.30	0.26	0.29	0.34
	1.6	0.41	0.38	0.38	0.42

11.4.4 Correlating CO reducible Cu-oxo sites with NO oxidation rates

NO oxidation rate increases linearly with {CO$_2$/[Cu^{II}OH]$^+$}, as shown in Figure 11.3. This indicates that polymeric Cu-oxo species with removable/reactive oxygen are the active site for NO oxidation. Therefore, CO-TPR can be used a probe for NO oxidation reactivity.
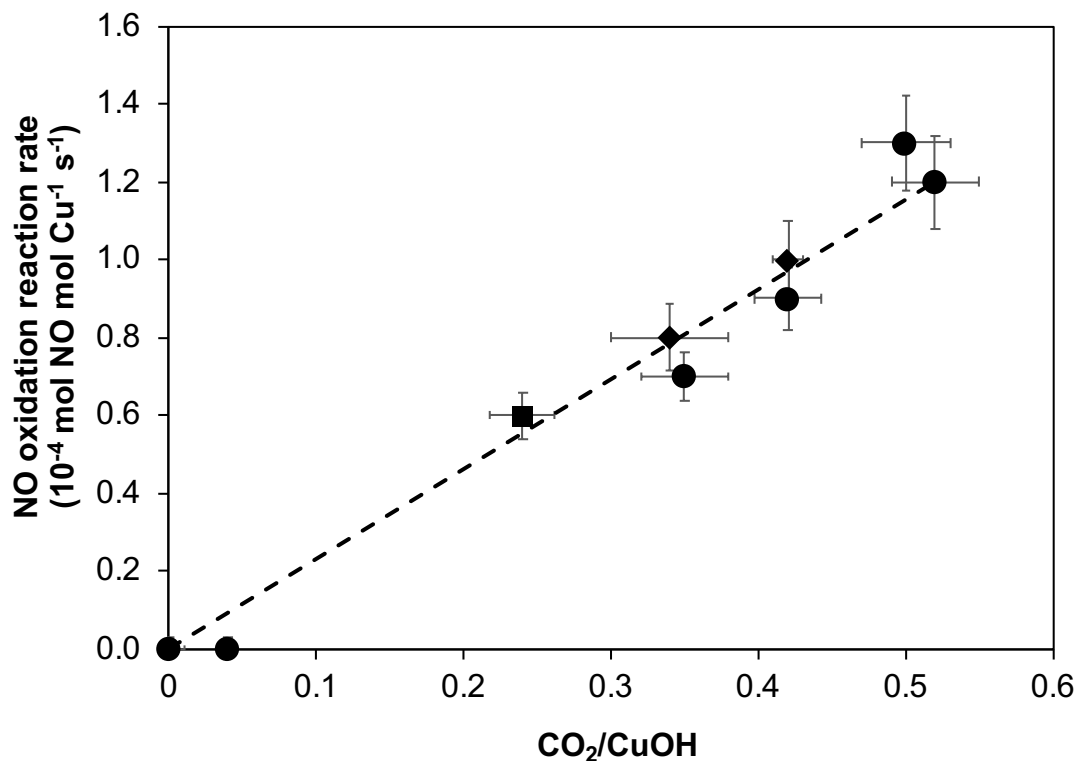
Figure 11.3 NO oxidation rates per mol of Cu as a function of moles of CO_2 evolved normalized per mole of $[Cu^{II}OH]^+$ sites (diamonds: Si/Al 25, circles: Si/Al 15, squares: Si/Al 15 isolated Al)

11.4.5 Effects of $[CuOH]^+$ concentration and zeolite composition on Cu-oxo formation

From Figure 11.4, it is observed that the fraction of NO oxidation active Cu-oxo sites ($\{CO_2/[Cu^{II}OH]^+\}$) is proportional to concentration of $[Cu^{II}OH]^+$ ions per crystallite volume. However, concentration of these Cu-oxo sites has a very weak dependence on Si/Al, as nearly the same $[Cu^{II}OH]^+$ concentration for Si/Al 15 and 25 yields the same amount of CO_2 during CO-TPR.
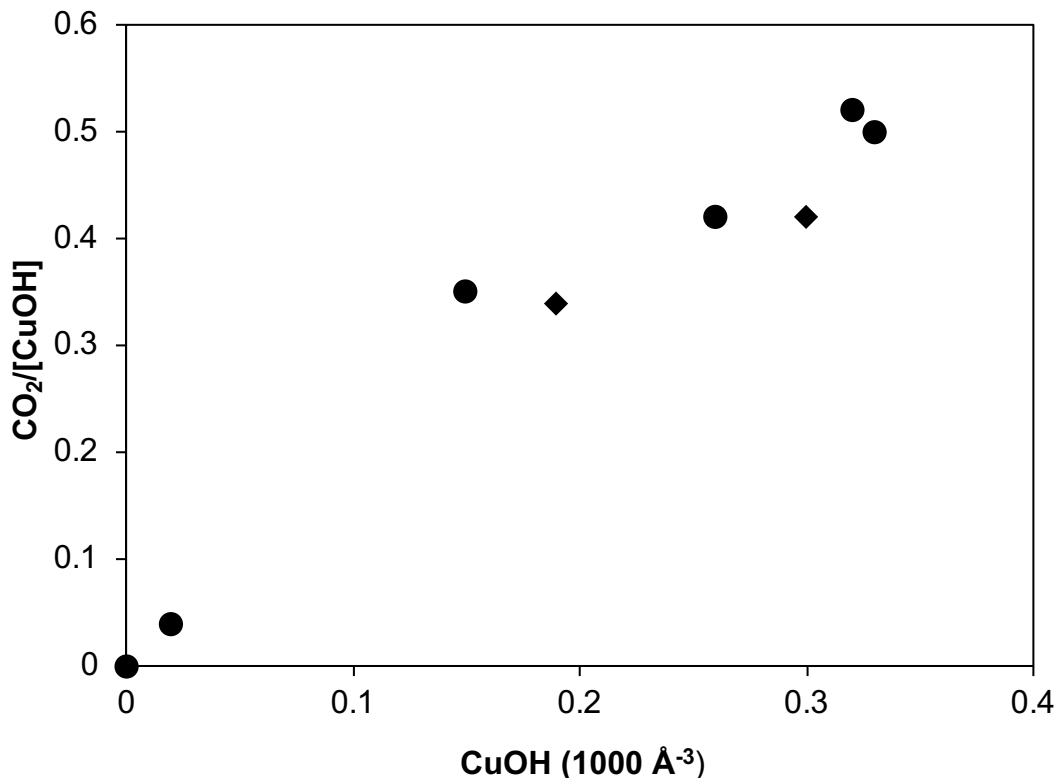
Figure 11.4 CO$_2$ evolution from CO-TPR plotted as a function of concentration of [Cu^{II}OH] ions per crystallite volume (diamonds: Si/Al 25 and circles: Si/Al 15)

11.4.6 Cu dimers as the candidate for NO oxidation active Cu-oxo species

As discussed before, proximal [CuOH]$^+$ sites lead to formation of polymeric Cu-oxo species during high temperature oxidative treatment. Existence of Cu$_2$O$_y$ species in Cu-SSZ-13 has been proposed by several groups [2,9,28,29,38] on samples with high Cu densities, but not on samples with low Cu densities. Formation of {Cu^{II}–O$_2$–Cu^{II}}$^{2+}$ (trans-μ-1,2-peroxo dicopper(II)) and {Cu^{II}–O–Cu^{I}}$^{2+}$ (mono–(μ–oxo) dicopper(II)) from proximal [CuOH]$^+$ sites after O$_2$ treatment at 723 K has been proposed based on evidence from Raman and UV-vis spectroscopy[29] along with their formation pathways. Similarly, various Cu$_2$O$_y$ ({Cu^{II}–O$_2$–Cu^{II}}$^{2+}$ and {Cu^{II}–O–Cu^{II}}$^{2+}$) formation pathways starting from [Cu^{II}OH]$^+$ as the precursor sites were proposed by Pappas et al.[28]. We propose Cu dimers ({Cu^{II}–O$_2$–Cu^{II}}$^{2+}$ and/or {Cu^{II}–O–Cu^{II}}$^{2+}$) as candidate Cu-oxo species active for NO oxidation. Spectroscopic characterization of these dimeric Cu species is discussed in the next section.

11.4.7 Spectroscopic identification of NO oxidation active Cu dimers

Diffusive Reflectance UV-vis spectra of Cu-SSZ-13 samples at 473 K (after high temperature oxidative treatment in 10% O_2 at 673 K) showed multiple absorption bands at 10900 cm^{-1}, 13600 cm^{-1}, 16500 cm^{-1} and 19700 cm^{-1} corresponding to d-d transitions of d^9 Cu^{II} state[39] as well as shoulders at 28200 cm^{-1} and 34800 cm^{-1} representative of Ligand to Metal Charge Transfer (LMCT) electronic transitions[39] (Figure 11.5). The absorptions between 16000 cm^{-1} and 20000 cm^{-1} that contribute to absorption features at 16500 cm^{-1} and 19700 cm^{-1} have been previously assigned to $\{Cu^{II}–O_2–Cu^{II}\}^{2+}$ (trans-μ-1,2-peroxo dicopper(II))[29]. The broad band with maximum intensity at 28200 cm^{-1} in Figure 11.5 was interpreted as a peroxo to Cu^{II} charge transfer band for $\{Cu^{II}–O_2–Cu^{II}\}^{2+}$ (trans-μ-1,2-peroxo dicopper(II))[29,39]. On the other hand, the absorption shoulder at 34800 cm^{-1} was ascribed to $\{Cu^{II}–O–Cu^{II}\}^{2+}$ (mono–(μ–oxo) dicopper(II))[29,39].
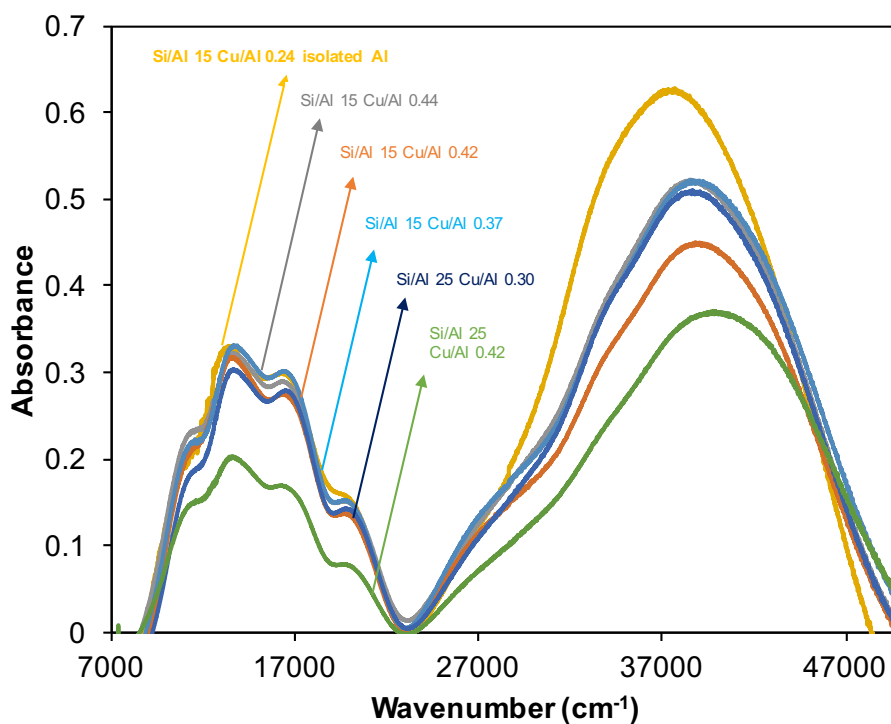
Figure 11.5 DRUV-vis spectra at 473 K of Cu-SSZ-13 samples (Si/Al 15 Cu/Al 0.12-0.44) after high temperature oxidative treatment (10% O_2 at 673 K)

Samples with measurable NO oxidation reactivity exhibited features at 16500 cm^{-1} and 19700 cm^{-1} (d-d transitions), and 28200 cm^{-1} (peroxo to Cu^{II} charge transfer band) corresponding to $\{Cu^{II}–O_2–Cu^{II}\}^{2+}$ (trans-μ-1,2-peroxo dicopper(II)) as well as absorption shoulder at 34800

cm^{-1} representatives of {Cu^{II}–O–Cu^{II}}$^{2+}$ (mono–(μ–oxo) dicopper(II)). However, there were no signature peaks of these Cu dimers for Cu-CHA samples which did not have detectable NO oxidation reactivity. This alludes to the fact that {Cu^{II}–O$_2$–Cu^{II}}$^{2+}$ and/or {Cu^{II}–O–Cu^{II}}$^{2+}$ are possibly the active Cu-oxo sites for NO oxidation.

In-situ UV-vis spectra were collected under NO oxidation reaction conditions to corroborate these dimeric Cu sites as the active site for NO oxidation (Figure 11.6). Upon admission of NO and O$_2$, decrease of absorption peak intensities at 16500 cm^{-1} and 19700 cm^{-1}, ascribed to {Cu^{II}–O$_2$–Cu^{II}}$^{2+}$ (trans-μ-1,2-peroxo dicopper(II)), indicate that the NO oxidation reactive species is Cu^{II}–O$_2$–Cu^{II}}$^{2+}$ and/or Cu^{II}–O–Cu^{II}}$^{2+}$.
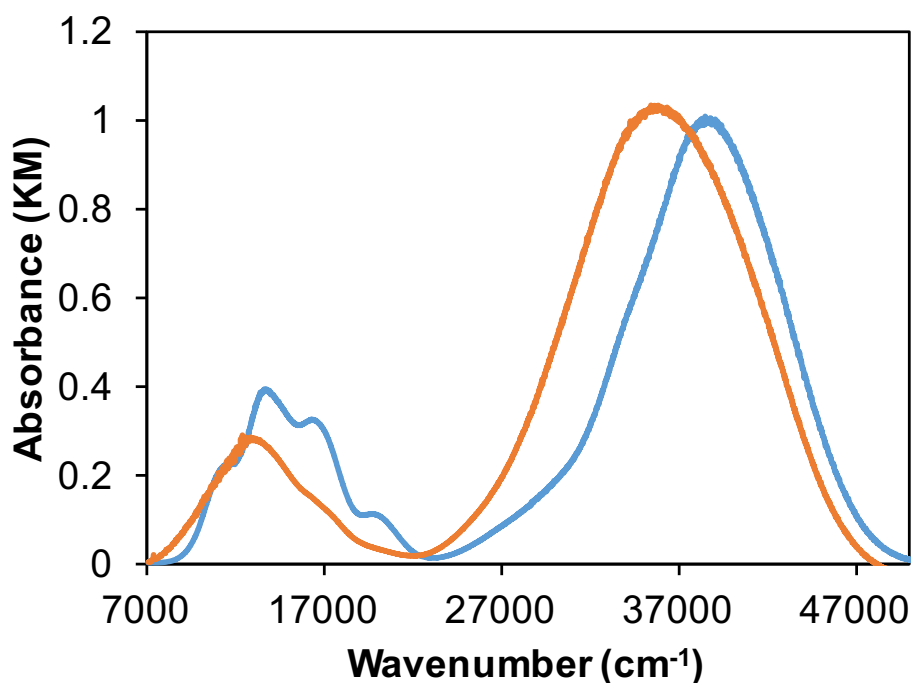
Figure 11.6 DRUV-vis spectra at 250^{0}C of Cu-SSZ-13 Si/Al 15 Cu/Al 0.44 after high temperature oxidative treatment (10% O$_2$ at 673 K) (blue) and under NO oxidation reaction conditions (300 ppm NO, 150 ppm NO$_2$ and 10% O$_2$ in balance He) (orange)

11.4.8 NO oxidation reaction mechanism

FTIR spectroscopy was used to detect reaction intermediates on Cu-SSZ-13 under NO oxidation reaction conditions. Figure 11.7 compares FTIR spectra of samples showing measurable and non-measurable NO oxidation reactivity in presence of 300 ppm NO, 150 ppm NO_2, and 10% O_2 in balance He at 523 K. There is an appearance of three distinct peaks at 1570, 1607 and 1627 cm^{-1} only for samples which show detectable NO oxidation reactivity (Figure 11.7). Feature at 1570 cm^{-1} was previously assigned to N-O stretch in bidentate nitrates, while the peaks at 1607 and 1627 cm^{-1} were ascribed to bridged nitrates[40,41]. Even though more investigation will be needed to identify which of these nitrates correspond to spectator and reactive species, exclusive presence of nitrates only for NO oxidation active samples implies that nitrates are the most abundant reaction intermediate. Hence, they need to be incorporated in the reaction mechanism scheme.
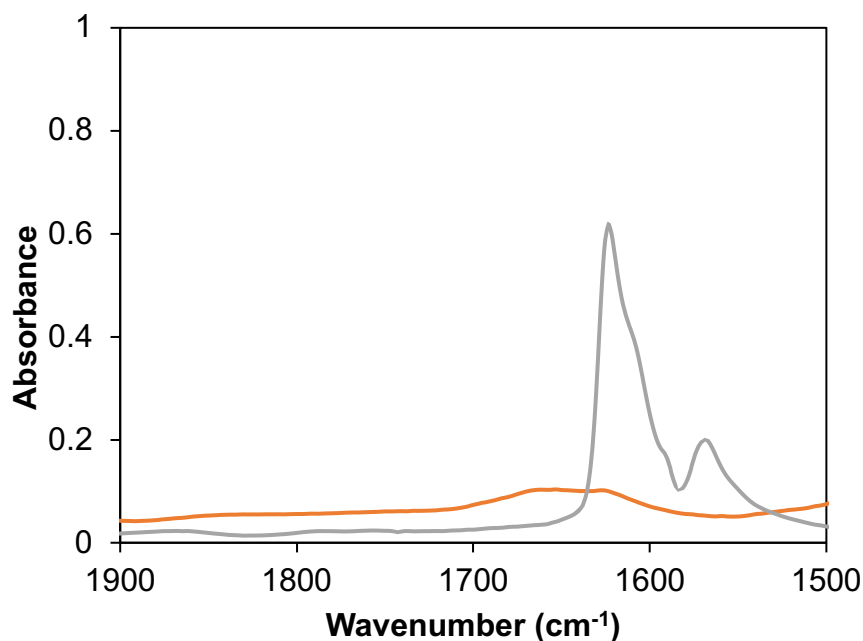
Figure 11.7 FTIR spectra on Si/Al 15 Cu/Al 0.44 (showed measurable NO oxidation reactivity, grey) and Si/Al 15 Cu/Al 0.12 (showed no detectable NO oxidation activity, orange) collected at 200^0C under NO oxidation reaction conditions (300 ppm NO, 150 ppm NO_2, and 10% O_2 in balance He at 250^0C)

Based on aforementioned results, the following elementary steps for NO oxidation on Cu-SSZ-13 are proposed, along with the pictorial representation of various reactive Cu intermediates:

$$O_2 + * \; \underset{\longleftarrow}{\overset{K_1}{\longrightarrow}} \; O_2*$$

$$NO + O_2* \; \underset{\longleftarrow}{\overset{K_2}{\longrightarrow}} \; NO_3*$$

$$NO_3* \; \overset{k_3}{\longrightarrow} \; NO_2 + O*$$

$$NO + O* \; \underset{\longleftarrow}{\overset{K_4}{\longrightarrow}} \; NO_2*$$

$$NO_2* \; \underset{\longleftarrow}{\overset{K_5}{\longrightarrow}} \; NO_2 + *$$
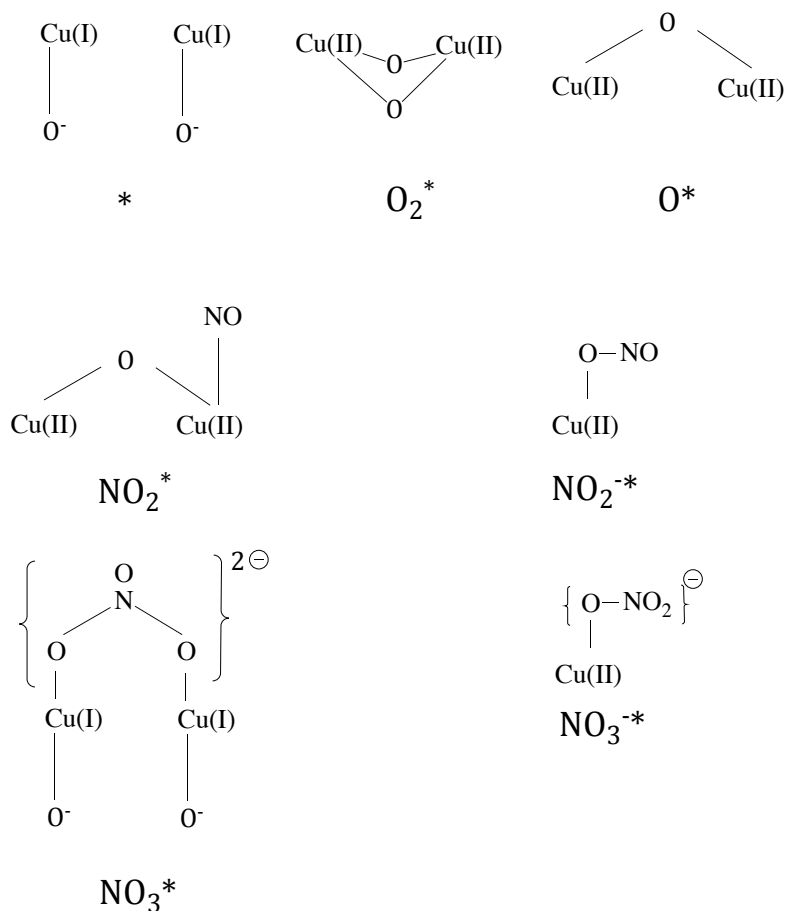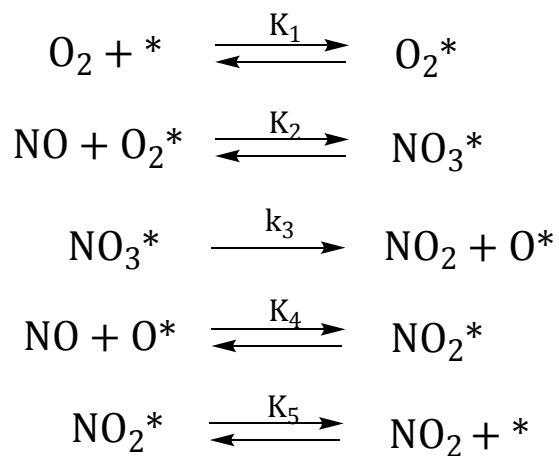
The first step in the above scheme represents quasi-equilibrated binding of O_2 on * (Cu sites) to form O_2* (Cu-oxo) active sites (step 1). This is followed by quasi-equilibrium reaction of NO with O_2* to yield NO_3* (step 2). NO_3* irreversibly decomposes to form NO_2 and O* (step 3). The next step involves quasi-equilibrium reaction of NO with O* to yield NO_2* (step 4), followed by quasi-equilibrated desorption of NO_2 (step 5). K_1, K_2, K_4 and K_5 represent the equilibrium constants of quasi-equilibrated steps 1, 2, 4 and 5 respectively, while k_2 is the rate constant for irreversible and rate-limiting step 3. These proposed elementary steps exhibit some similarity to those suggested by DFT treatments for NO oxidation reaction on Cu_xO_y species (clustered Cu^{2+} ions with x≥2, y≥1), which result from over exchange of Cu in Cu-SSZ-13[9]. However, the proposed mechanism has additional steps of nitrate formation and decomposition. All the steps in the above scheme, taken together with the customary pseudo-steady-state and with the reversibility assumptions discussed above, give the rate equation 11.1. Decomposition of nitrates is assumed to be the slowest step, with all other steps being quasi-equilibrated.

$$-r_{NO} = \frac{k_3 K_1 K_2 [NO][O_2][L]}{1 + K_1[O_2] + K_1 K_2 [NO][O_2] + K_5^{-1}[NO_2] + \dfrac{K_4^{-1}K_5^{-1}[NO_2]}{[NO]}} \qquad \text{(11.1)}$$

$$(*) \quad (O_2^*) \quad (NO_3^*) \quad (NO_2^*) \quad (O^*)$$

The coverages of each indicated intermediate, relative to those for vacant sites, are given by each term in the denominator of equation 11.1. The values of rate and equilibrium constants (and their 95% confidence intervals), obtained by the regression of all rate data to the functional form of equation 1, are shown in Table 11.5.

Table 11.4 Fitted rate constant and equilibrium constants from the rate model in equation 11.1

Temperature (K)	K_1 (unitless)	K_2 (unitless)	k_3 (mol NO g^{-1} s^{-1})	K_4 (unitless)	K_5 (unitless)
575	1.20×10^{-2}	2.00×10^{-2}	1.26×10^{-4}	2.71×10^{-1}	1.33×10^{-1}
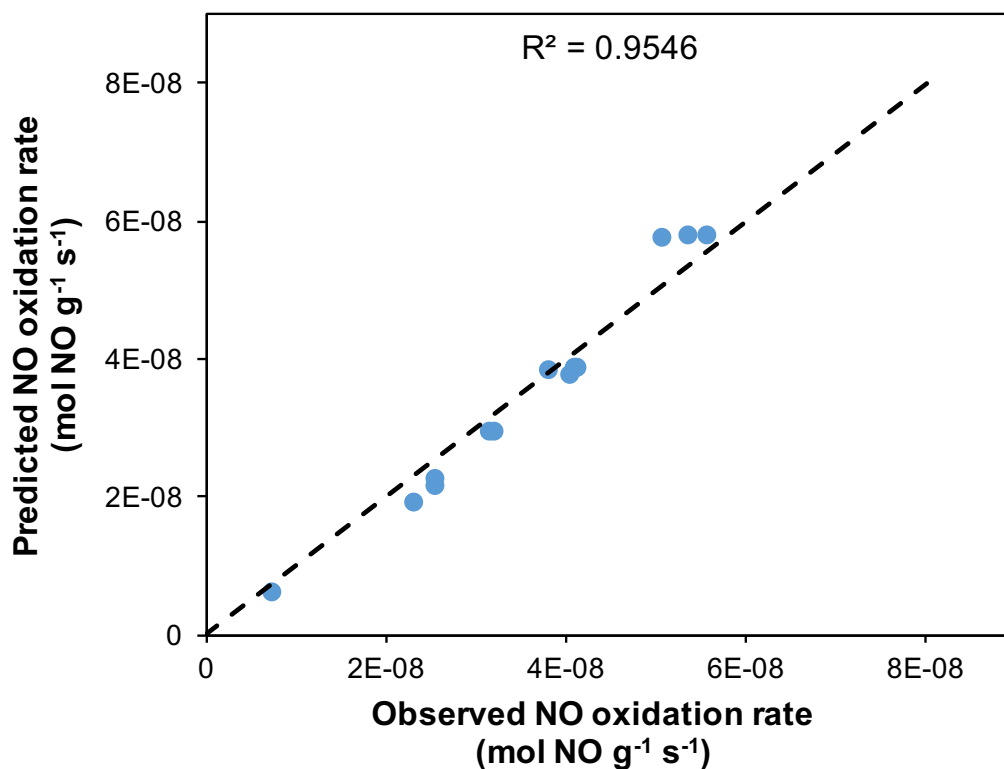
Figure 11.8 Parity plot of measured and predicted (from equation 11.1) forward NO oxidation rates on Cu-SSZ-13 at 575 K (Si/Al 15 and 25) at 523 K (using kinetic and thermodynamic parameters in Table 11.4)

Equation 11.1 accurately describes all rate data, as evident from the parity plot of predicted and measured rates in Figure 11.8. All other sequences considered with all permutations of irreversible and quasi-equilibrium steps did not account for the measured effects of reactant and product concentrations with comparable accuracy (appendix H). There could other side pathways of formation of stable nitrates from NO_2 that could add to NO_2 inhibition effect and are not illustrated here.

The calculated (fractional) coverages $(\theta(*), \theta(O^*), \theta(O_2^*), \theta(NO_2^*), \theta(NO_3^*))$ can be calculated from the parameters in Table X; their ranges are 0.02-0.06 (at 575 K), 0.45-0.61 (at 575 K), 0.002-0.007 (at 575 K), 0.21-0.50 (at 575 K) and 0.00005-0.0005 for $*$, O^*, O_2^*, NO_2^*, and NO_3^* respectively, suggesting that all species must be considered in the kinetic description of measured rates, with O^* and NO_2^* being the most abundant reactive intermediate.

11.4.9 Relationship between standard SCR and NO oxidation

As can be seen from comparison of SCR and NO oxidation rates in Figure 11.8, there is orders of magnitude difference in the reaction rates. No observed direct correlation between SCR and NO oxidation reactivity could be reconciled by differences in active site requirements and their formation pathways. While formation of NO oxidation active dimeric Cu requires proximal $[Cu^{II}OH]^+$ sites, presence or proximity of these $[Cu^{II}OH]^+$ sites is not the necessary requirement for the proposed SCR active Cu sites. Secondly, Cu dimer formation occurs during SCR is through pairing of NH$_3$-solvated mobile Cu^I species formed from reduction of Cu^{II} and/or $[Cu^{II}OH]^+$ species[38]. However, Cu dimer formation during high temperature oxidative treatment has been proposed via. autoreduction of $[Cu^{II}OH]^+$ to Cu^I followed by O_2 oxidation of Cu^I to form Cu_2O_2[29].

This fundamental understanding of site requirement and mechanism of NO oxidation will aid in devising strategies for more efficient catalyst. NO oxidation can also be employed as a probe reaction in identification of Cu dimeric sites and other types of Cu_xO_y species in different zeolite frameworks, further extending our understanding of Cu cation speciation in zeolites. The dimeric Cu sites identified and quantified here can also provide insights into other fundamental and applied chemistries like CO oxidation[42], NO decomposition[43], and selective oxidation of methane [44,45] and benzene[46] to methanol and phenol respectively, which involve similar Cu-oxo cations as the active centers. Additionally, such Cu-oxo sites are also known to promote undesirable side reactions like NH$_3$ oxidation, which can lead to formation of undesirable N_2O[47,48]. Tailoring the Cu-zeolite synthesis to minimize the formation of such Cu-oxo cations could possibly aid in abatement of undesirable side reactions.
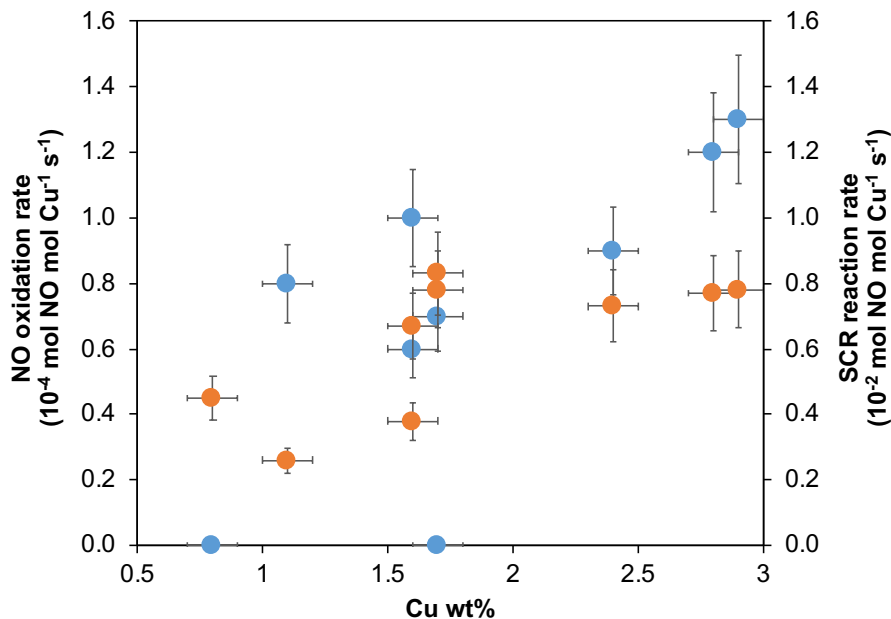
Figure 11.9 Forward NO oxidation rates (blue) and SCR reaction rates (orange) on Cu-SSZ-13 Si/Al 15 and 25 samples in Table 11.2. NO oxidation conditions: 300 ppm NO, 150 ppm NO_2, and 10% O_2 in balance He at 523 K. SCR conditions: 300 ppm NO, 300 pm NH_3, 10% O_2, 7% CO_2, 3% H_2O in balance He at 473 K

11.5 Conclusions

Rigorous kinetic measurements of NO oxidation on Cu-SSZ-13 allowed derivation of rate equations which are consistent with the proposed NO oxidation mechanism. Mechanism proceeds with quasi-equilibrated reversible chemisorption of O_2, followed by subsequent quasi-equilibrated reaction with NO to form nitrates, and kinetically-relevant irreversible decomposition of nitrates, which have been identified as one of the reaction intermediates using *in-situ* FTIR spectroscopy. Cu-oxo cation is proposed to be the active site, as NO oxidation rates were correlated with amount of reactive Cu-oxo cations, titrated using CO-TPR. As all the synthesized model samples, obtained using careful and controlled synthesis, had nominally monomeric Cu sites (Cu^{II} and $[Cu^{II}OH]^+$) and monomeric Cu^{II} sites were shown previously to be inactive for NO oxidation, reactive Cu-oxo cations seem to have evolved from proximal monomeric $[Cu^{II}OH]^+$ sites duing high temperature oxidative treatment. In order to gain more structural information about Cu-oxo cations, *ex-situ* and *in-situ* UV-vis specroscopy is employed, and dimeric Cu (Cu_2O_2 and Cu_2O) are found to be the potential Cu-oxo active site candidates. Based on the acquired understanding about NO oxidation reaction mechanim and active site,

commonly observed no direct correlation between standard SCR and dry NO oxidation can be justified, as the nature of active Cu dimers during the two different reaction environments is different.

Since it is shown that the concentration of NO oxidation active Cu-oxo cations is directly proportional to proximity of $[Cu^{II}OH]^+$ sites and such Cu-oxo sites act as the active sites for many other important oxidation reactions, maximization of $[Cu^{II}OH]^+$ population density is desired. Various controlled synthesis strategies, like changing framework Al distribution (via. varying inorganics/SDA ratio) and Al density (via. varying Si/Al ratio), can be adapted to maximize the population density of $[Cu^{II}OH]^+$ sites.

11.6 Methods

11.6.1 Synthesis and Characterization

11.6.1.1 Synthesis of H-SSZ-13 zeolites

Synthesis of H-SSZ-13 zeolites with Si/Al 4.5, 15 and 25 was done as previously reported in the above chapters 2 and 3.

11.6.1.2 X-Ray diffraction of SSZ-13 (CHA) zeolites

The CHA crystal framework of SSZ-13 zeolites was determined from powder X-ray diffraction (XRD) patterns collected as previously reported in the above chapters 2 and 3.

11.6.1.3 Adsorption isotherms to measure micropore volumes of CHA zeolites

Micropore volumes of SSZ-13 zeolites were determined from Ar adsorption isotherms measured as previously reported in the above chapters 2 and 3.

11.6.1.4 Aqueous-phase Copper Ion-Exchange of H-SSZ-13

Cu-SSZ-13 zeolites were prepared by aqueous-phase Cu ion-exchange as previously reported in the above chapters 2 and 3.

11.6.1.5 Elemental Analysis using Atomic Absorption Spectroscopy

Bulk elemental composition (Si, Al and Cu in H-and Cu-SSZ-13) was determined using atomic absorption spectroscopy (AAS) as previously reported in the above chapter 3.

11.6.1.6 Cu site characterization and quantification

Cu sites were characterized using Cu K-edge X-ray absorption near edge spectroscopy (XANES) and o UV-Visible spectroscopy as previously reported in the above chapters 2 and 3. Further enumeration of isolated Cu^{II} and $Cu^{II}OH$ sites on each Cu-CHA zeolite was determined after oxidative treatment (20% O_2, 773 K) by quantifying the number of residual protons that remained after Cu exchange, as previously reported in the above chapter 3.

11.6.2 NO oxidation kinetic measurements

NO oxidation kinetics were measured on a down-flow tubular quartz reactor with an inner diameter of 13 mm and an overall length of 400 mm. The reactor setup used was similar to the one used by Verma et al.[9]. A porous glass frit was installed at the midpoint of the reactor, over which a layer of quartz wool was placed in a flattened position. All samples were pelletized (Specac 13mm Diameter Stainless Steel Evaluable Pellet Die) under 10,000 psi pressure (Carver Laboratory Press), ground using a mortar and pestle, then sieved to retain 125 to 250 μm particles (W.S. TYLER No. 60 and No. 120 all-stainless-steel) to minimize the pressure drop of the flow of gas across the powder catalyst bed. Typically, 0.015-0.050 g of sieved Cu/SSZ-13 catalyst was mixed with enough inert silica gel (Fisher Chemical Silica Gel (Davisil) Sorbent, Grade 923) to obtain a bed height of ~5 mm. Another layer of quartz wool was pressed slightly over the top of the catalyst bed to ensure uniformity of the bed. The temperature across the catalyst bed was measured by placing two K-type thermocouples, one at ~2 mm above the catalyst bed and the other at ~2 mm below the glass frit. Aluminum foil was wrapped around the quartz reactor to an outer diameter of ~2.54 cm, in order to enhance heat conduction and minimize any radial temperature gradients that may be present within the bed. The reactor was then placed within a clamshell furnace (Applied Test Systems) and pressure-tested with helium (99.999%, Indiana Oxygen) at 5 psig for 20 minutes. Moreover, the feed gases from the gas manifold were first fed to a gas preheater (maintained at 300 °C) and then into the main reactor. The gas-phase concentrations of NO, NO_2, CO_2, H_2O, and N_2O were measured by a Fourier transform infrared (FTIR) analyzer (MKS Multigas™ 2030 gas-phase FTIR spectrometer). The FTIR analyzer had a spectral resolution of 0.5 cm^{-1}, and factory supplied calibrations were used to quantify the various gas concentrations.

The conversion of NO was measured according to the following equation:

$$NO\ conversion = \frac{NO_{in} - NO_{out}}{NO_{in}} \times 100 \tag{11.2}$$

In the limit of differential NO conversion (<10%), the gas concentrations and catalyst bed temperature can be assumed constant, allowing the NO consumption rate to be calculated using the following equation:

$$-r_{overall}(mol\ NO\ mol\ Cu^{-1}s^{-1}) = \frac{NO\ conversion}{1000000 * mol\ Cu} \times NO_{in} \times \dot{V}_{total} \times \frac{P}{RT} \tag{11.3}$$

where C values are the concentrations of NO before and after the catalyst bed in ppm, $\dot{V}_{total}$ is the total volumetric flow rate, P is 1 atm, T is ambient temperature, and R is the gas constant. Based on overall NO oxidation rate ($r_{overall}$), the normalized forward rates (r_{fwd}) were reported in the form of power rate law model. The approach to equilibrium (β) was included because the NO oxidation rates were possibly limited by equilibrium under the relevant reaction temperature.

$$r_{fwd} = r_{overall}\ (1 - \beta) \tag{11.4}$$

$$r_{fwd} = Ae^{\frac{-E_A}{RT}}[NO]^a[O_2]^b[NO_2]^c \tag{11.5}$$

$$\beta = \frac{[NO_2]}{K[NO]^2[O_2]} \tag{11.6}$$

K is the equilibrium constant for the NO oxidation reaction Value of β for all the measurements was between 0.02 and 0.18 meaning that equilibrium was not attained under the used temperature range. A is the pre-exponential factor (A/s^{-1}) and activation energy (E$_a$/kJ mol^{-1}). a, b, and c represent forward reaction orders w.r.t NO, O$_2$ and NO$_2$ respectively. In order to complete the mass balance, balance NOx was calculated as (NO + NO$_2$) in - (NO + NO$_2$) out and it was less than 5% for all kinetic measurements. This indicated that no side reactions were pertinent. Also, N$_2$O formation was ruled out as its concentration was measured in negligible quantities (< 2 ppm).

11.6.3 CO-Temperature Programmed Reduction (CO-TPR)

Sample was heated to 773 K at 9 K min^{-1} under the flow of 50 mL min^{-1} dry air (Commercial grade, Indiana Oxygen) and held for 2 hours, before it was cooled down to room temperature. Sample was then flushed with UHP He at room temperature for 2 hours. Temperature programmed reduction was then performed under 18 mL min^{-1} flow of 5% CO/He up to the temperature of 833 K at 10 K min^{-1}.

11.6.4 Diffuse reflectance UV-visible spectroscopy

Diffuse reflectance UV-Visible spectra were recorded under various gas conditions using a Varian UV-VIS-NIR spectrophotometer (Cary 5000) with a diffuse reflectance accessory consisting of two ellipsoidal mirrors (Harrick Scientific Praying Mantis). Barium sulfate (BaSO$_4$, 99.9%, Sigma-Aldrich) was used as the 100% reflectance standard. An *in-situ* sample holder was loaded with approximately 0.1 g of sample, which was pelleted and sieved to retain particles between 125-250 µm in diameter. Spectra were collected from 7000 to 50000 cm^{-1} with a scan speed of 2000 cm^{-1} min^{-1}.

Condition 1:

Sample was dehydrated at 673 K in oxidizing atmosphere of dry air (Commercial grade, Indiana Oxygen) (total flow of 50 ml min^{-1}) and held for 2 hrs. Sample was then cooled down to 473 K under the same oxidizing atmosphere. Sample spectra was then collected at 473 K.

Condition 2:

Sample was exposed to NO oxidation reaction conditions i.e. 150 ppm NO, 150 ppm NO$_2$ and 10% O$_2$ at 575 K (total flow of 50 ml min^{-1}) and held for 2 hrs. Sample was then cooled down to 473 K under the same gas condition. Sample spectra was then collected at 473 K.

11.6.5 Fourier-Transform Infrared Spectroscopy (FTIR)

FTIR data were collected on zeolite samples using a Nicolet 6700 FTIR spectrometer equipped with a liquid nitrogen-cooled mercury cadmiumtelluride (MCT) detector. Catalyst samples (≈40-50 mg) were pressed into a self-supporting wafer (≈2 cm in diameter) and placed in a custom-

built FTIR cell that has been described elsewhere (Wang et al.). Wafers were treated in flowing oxygen (10% O_2, balance He) to 673 K for 30 min and then cooled to 575 K, prior to the exposure to NO oxidation reaction conditions. Spectra were collected with a resolution of 4 cm^{-1} and averaged over 36 scans and baseline corrected.

11.7 References

1   S. Brandenberger, O. Kröcher, A. Tissler and R. Althoff, *The state of the art in selective catalytic reduction of NOx by ammonia using metal-exchanged zeolite catalysts*, 2008, **50**, 492-531.

2   F. Gao, E. D. Walter, E. M. Karp, J. Luo, R. G. Tonkyn, J. H. Kwak, J. Szanyi and C. H. F. Peden, *J. Catal.*, 2013, **300**, 20–29.

3   K. Rahkamaa-Tolonen, T. Maunula, M. Lomma, M. Huuhtanen and R. L. Keiski, *Catal. Today*, 2005, **100**, 217–222.

4   A. M. Beale, F. Gao, I. Lezcano-Gonzalez, C. H. F. Peden and J. Szanyi, *Chem. Soc. Rev.*, 2015, **44**, 7371–7405.

5   M. Schwidder, S. Heikens, A. De Toni, S. Geisler, M. Berndt, A. Brückner and W. Grünert, *J. Catal.*, 2008, **259**, 96–103.

6   P. S. Metkar, V. Balakotaiah and M. P. Harold, *Catal. Today*, 2012, **184**, 115–128.

7   M. Colombo, I. Nova and E. Tronconi, *Catal. Today*, 2012, **197**, 243–255.

8   M. P. Ruggeri, I. Nova and E. Tronconi, *Top. Catal.*, 2013, **56**, 109–113.

9   A. A. Verma, S. a. Bates, T. Anggara, C. Paolucci, A. a. Parekh, K. Kamasamudram, A. Yezerets, J. T. Miller, W. N. Delgass, W. F. Schneider and F. H. Ribeiro, *J. Catal.*, 2014, **312**, 179–190.

10   M. Iwasaki, in *Urea-SCR Technology for deNOx After Treatment of Diesel Exhausts*, eds. I. Nova and E. Tronconi, Springer New York, New York, NY, 2014, pp. 221–246.

11   L. Olsson, H. Sjövall and R. J. Blint, *Appl. Catal. B Environ.*, 2009, **87**, 200–210.

12   T. Selleri, F. Gramigni, I. Nova and E. Tronconi, *Appl. Catal. B Environ.*, 2017, **225**, 324-331.

13   J. H. Kwak, D. Tran, S. D. Burton, J. Szanyi, J. H. Lee and C. H. F. Peden, *J. Catal.*, 2012, **287**, 203–209.

14   J. D. Albarracin-Caballero, I. Khurana, J. R. Di Iorio, A. J. Shih, J. E. Schmidt, M. Dusselier, M. E. Davis, A. Yezerets, J. T. Miller, F. H. Ribeiro and R. Gounder, *React. Chem. Eng.*, 2017, **2**, 168-179..

15   U. Deka, A. Juhin, E. a. Eilertsen, H. Emerich, M. a. Green, S. T. Korhonen, B. M. Weckhuysen and A. M. Beale, *J. Phys. Chem. C*, 2012, **116**, 4809–4818.

16   S. T. Korhonen, D. W. Fickel, R. F. Lobo, B. M. Weckhuysen and A. M. Beale, *Chem. Commun. (Camb).*, 2011, **47**, 800–2.

17   S. A. Bates, A. a. Verma, C. Paolucci, A. A. Parekh, T. Anggara, A. Yezerets, W. F. Schneider, J. T. Miller, W. N. Delgass and F. H. Ribeiro, *J. Catal.*, 2014, **312**, 87–97.

18   J. S. McEwen, T. Anggara, W. F. Schneider, V. F. Kispersky, J. T. Miller, W. N. Delgass and F. H. Ribeiro, *Catal. Today*, 2012, **184**, 129–144.

19   J. Hun Kwak, H. Zhu, J. H. Lee, C. H. F. Peden and J. Szanyi, *Chem. Commun.*, 2012, **48**,

4758.

20   E. Borfecchia, K. a. Lomachenko, F. Giordanino, H. Falsig, P. Beato, a. V. Soldatov, S. Bordiga and C. Lamberti, *Chem. Sci.*, 2015, **6**, 548–563.

21   F. Giordanino, P. N. R. Vennestrøm, L. F. Lundegaard, F. N. Stappen, S. Mossin, P. Beato, S. Bordiga and C. Lamberti, *Dalt. Trans.*, 2013, **42**, 12741–61.

22   F. Gao, N. M. Washton, Y. Wang, M. Kollár, J. Szanyi and C. H. F. Peden, *J. Catal.*, 2015, **331**, 25–38.

23   C. Paolucci, A. A. Parekh, I. Khurana, J. R. Di Iorio, H. Li, J. D. Albarracin Caballero, A. Shih, T. Anggara, W. Nicholas Delgass, J. T. Miller, F. H. Ribeiro, R. Gounder and W. F. Schneider, 2016, **138**, 6028-6048.

24   F. Gao, E. D. Walter, M. Kollar, Y. Wang, J. Szanyi and C. H. F. Peden, *J. Catal.*, 2014, **319**, 1–14.

25   T. V. W. Janssens, H. Falsig, L. F. Lundegaard, P. N. R. Vennestrøm, S. Rasmussen, P. G. Moses, F. Giordanino, E. Borfecchia, K. a. Lomachenko, C. Lamberti, S. Bordiga, A. Godiksen, S. Mossin and P. Beato, *ACS Catal.*, 2015, **5**, 2832-2845.

26   Y. J. Kim, J. K. Lee, K. M. Min, S. B. Hong, I.-S. Nam and B. K. Cho, *J. Catal.*, 2014, **311**, 447–457.

27   S. Grundner, W. Luo and J. A. Lercher, *Chem. Commun.*, 2016, **52**, 2553–2556.

28   D. K. Pappas, E. Borfecchia, M. Dyballa, I. Pankin, K. A. Lomachenko, A. Martini, M. Signorile, S. Teketel, B. Arstad, G. Berlier, S. Bordiga, U. Olsbye, K. P. Lillerud, S. Svelle, P. Beato, D. K. Pappas, E. Borfecchia, M. Dyballa, I. A. Pankin and K. A. Lomachenko, 2017, **139**, 14961-14975.

29   B. Ipek, M. J. Wulfers, H. Kim, F. Göltl, I. Hermans, J. P. Smith, K. S. Booksh, C. M. Brown, R. F. Lobo, B. Ipek, M. J. Wulfers, H. Kim, F. Goeltl, I. Hermans and P. Joseph, 2017, **7**, 4291-4303.

30   Y. Iwase, K. Motokura, T. Koyama, A. Miyaji and T. Baba, *Phys. Chem. Chem. Phys.*, 2009, **11**, 9268–9277.

31   F. Gao, N. M. Washton, Y. Wang, M. Kollar, J. Szanyi and C. H. F. Peden, *J. Catal.*, 2015, **331**, 25–38.

32   J. R. Di Iorio, S. a. Bates, A. a. Verma, W. N. Delgass, F. H. Ribeiro, J. T. Miller and R. Gounder, *Top. Catal.*, 2015, **58**, 424–434.

33   S. A. Bates, W. N. Delgass, F. H. Ribeiro, J. T. Miller and R. Gounder, *J. Catal.*, 2014, **312**, 26–36.

34   J. R. Di Iorio and R. Gounder, *Chem. Mater.*, 2016, **28**, 2236–2247.

35   T. Beutel, J. Sarkany, G.-D. Lei, J. Y. Yan, W. M. H. Sachtler and J. Sa, *J. Phys. Chem.*, 1996, **100**, 845–851.

36   P. Da Costa, B. Moden, G. D. Meitzner, D. K. Lee and E. Iglesia, *Phys. Chem. Chem. Phys.*, 2002, **4**, 4590–4601.

37   J. Sárkány, J. L. d'Itri and W. M. H. Sachtler, *Catal. Letters*, 1992, **16**, 241–249.

38   C. Paolucci, I. Khurana, A. A. Parekh, S. Li, A. J. Shih, H. Li, J. R. Di Iorio, J. D. Albarracin-Caballero, A. Yezerets, J. T. Miller, W. N. Delgass, F. H. Ribeiro, W. F. Schneider and R. Gounder, *Science (80-.).*, 2017, **357**, 898-903.

39   H. Li, C. Paolucci, I. Khurana, L. N. Wilcox, F. Göltl, J. D. Albarracin-Caballero, A. J. Shih, F. H. Ribeiro, R. Gounder and W. F. Schneider, *Chem. Sci.*, 2019, **10**, 2373-2384.

40   F. Poignant, J. L. Freysz, M. Daturi and J. Saussey, *Catal. Today*, 2001.

41   K. Hadjiivanov, *Catal. Letters*, 2000.

42   T. J. Huang and D. H. Tsai, *Catal. Letters*, 2003, **87**, 173-178.

43   H. Yahiro and M. Iwamoto, *Appl. Catal. A Gen.*, 2001, **222**, 163-181.

44   P. Vanelderen, J. Vancauwenbergh, B. F. Sels and R. a. Schoonheydt, *Coord. Chem. Rev.*, 2013, **257**, 483–494.

45   C. Kalamaras, D. Palomas, R. Bos, A. Horton, M. Crimmin and K. Hellgardt, *Catal. Letters*, 2016, **146**, 483-492.

46   K. Yoshizawa, Y. Shiota, T. Yumura and T. Yamabe, *J. Phys. Chem. B*, 2000, **104**, 734-740.

47   M. Devadas, O. Kröcher, M. Elsener, A. Wokaun, N. Söger, M. Pfeifer, Y. Demel and L. Mussmann, *Appl. Catal. B Environ.*, 2006, **67**, 187-196.

48   S. Yang, S. Xiong, Y. Liao, X. Xiao, F. Qi, Y. Peng, Y. Fu, W. Shan and J. Li, *Env. Sci Technol*, 2014, **48**, 10354–10362.

12.   RECOMMENDATIONS

12.1 Further identification and manipulation of relevant catalyst design parameters

Rational catalyst design approach requires identification of various catalyst design parameters (macroscopic and microscopic) that have a positive influence (direct and indirect) on catalyst performance, including catalytic reactivity (herein low temperature standard SCR reaction rate) as well as stability (against hydrothermal deactivation and sulfur poisoning). For Cu-zeolite catalyst, design parameters could be divided into zeolite support characteristics (framework topology, T-atoms spatial density, dimensionality, pore size, pore and channel interconnectivity) and exchanged Cu properties (Cu speciation, spatial distribution, exchange levels, mobility and stability). The aim would be to first identify all the different design parameters associated with zeolite support as well as exchanged Cu, and then manipulating the relevant catalyst design parameters to optimize catalyst performance.

12.1.1 Design parameters related to zeolite support of Cu-zeolite catalyst

This work discusses the effects of a only a few zeolite support properties, including zeolite framework topology and dimensionality, on catalyst stability (against hydrothermal deactivation) using a holistic step-wise approach to demonstrate how small-pore size coupled with dimensionality and double six-membered ring structure confers excellent hydrothermal stability to a given zeolite support. This study also describes how zeolite framework T-atoms spatial density positively influences catalyst reactivity via. promoting Cu mobility and NO activation. Firstly, there is a need to consider the effects of such support properties (zeolite framework topology, dimensionality and T-atoms spatial density) on both catalyst reactivity and catalyst stability in conjunction. Secondly, the effects of some additional zeolite support properties such as electronic conductivity, pore size, pore and channel interconnectivity, etc. on catalyst performance could be explored, as these properties could enhance catalyst reactivity via. regulating Cu active site mobility. Hence, identification of support properties which optimizes catalyst performance (reactivity and stability) followed by their favorable manipulation is recommended to design next generation catalyst formulations.

The first step of identifying such zeolite support properties could be to perform a kinetic and stability study on Cu exchanged on various different zeolite supports like Cu-FER, Cu-AEI, Cu-MFI, Cu-BEA, etc. to investigate how zeolite framework dimensionality, T-atoms (framework Al) spatial density, pore size, and channel interconnectivity influences overall catalyst performance. And the next step could to optimize various identified zeolite properties to optimize catalyst performance.

12.1.2 Design parameters related to exchanged Cu site of Cu-zeolite catalyst

1. Cu speciation

Chapter 2 describes how structurally and chemically different Cu sites (Z_2Cu and ZCuOH) behave similarly during low temperature standard SCR conditions, due to NH_3 solvation nullifying the differences between Cu sites. Chapter 7 describes how Z_2Cu sites are more stable against sulfur poisoning than ZCuOH sites. However, the effect of Cu speciation on catalyst stability against hydrothermal deactivation needs to be studied systematically. This will enable us to tune Cu speciation to optimize catalyst performance (catalyst reactivity, catalyst stability against sulfur poisoning and hydrothermal deactivation).

2. Cu spatial distribution

Chapter 3 illustrates how higher Cu spatial density enhances Cu active site mobility, and therefore, increases catalyst reactivity. However, the effect of Cu spatial density on catalyst stability needs to be studied systematically to optimize catalyst performance (catalyst reactivity, catalyst stability against sulfur poisoning and hydrothermal deactivation).

3. Cu exchange levels (relative to residual H^+ sites)

Expanding on commonly accepted proposition of Cu cation being the active site for low temperature standard SCR, this work seems to suggest that cationic Cu sites work in conjunction with residual Bronsted acid sites (H^+) to carry out low temperature standard SCR reaction. Firstly, this proposed bifunctional nature (involvement of Cu and H^+) of Cu-zeolite catalyst under low temperature needs to be corroborated by performing kinetics study on Cu-zeolite samples containing a wide range of $Cu/(Cu+H^+)$ ratios (0.0-1.0). Secondly, if this could be verified, then there would be a need to optimize $Cu/(Cu+H^+)$ ratio for optimum catalyst

performance. (catalyst reactivity, catalyst stability against sulfur poisoning and hydrothermal deactivation).

12.2 Understanding low temperature N_2O formation

Cu-zeolite catalyst has been shown to be more selective to N_2O formation at low temperatures (<573 K) (undesirable potent greenhouse gas) as compared to other proven SCR catalysts such as Fe-zeolite and Vanadia based catalysts[3]. However, the underlying mechanism for the higher selectivity to N_2O on Cu-zeolite catalysts is not well understood. Given the knowledge acquired from this work about Cu site speciation, preference along with synthetic and characterization handle, we could design and characterize model Cu-zeolite catalysts with different distribution of Cu sites viz. Z_2Cu and ZCuOH sites, and investigate which of the two Cu sites (Z_2Cu and ZCuOH) is more selective to N_2O formation. This would enable the design of new Cu-zeolite catalysts with maximum NO_x conversion and minimal N_2O formation.

Furthermore, *in-situ* and *operando* characterization of identified Cu-zeolite catalyst exhibiting significant N_2O formation coupled with detailed understanding of elementary steps and reaction intermediates could enable to track down the origin of N_2O formation, as to which Cu-zeolite properties and reaction intermediate leads to of N_2O formation.

12.3 Extension of understanding of low temperature to high temperature

With this work, we established how NH_3 solvation plays a crucial role in mobilizing Cu^I sites at low temperatures (<250⁰C), enabling them to pair and oxidize during $Cu^I \rightarrow Cu^{II}$ re-oxidation to close catalytic cycle. This work involved integration of experimental and computational approach to unravel the nature of active Cu sites as a function of sample composition and operating conditions, and complete reaction pathway in low temperature regime (<250⁰C). The experimental approach comprised of titrimetric, spectroscopic and kinetic characterization during non-steady state transient sequential reaction steps and steady state catalysis. This experimental approach and acquired knowledge could be effectively extrapolated to investigate the reaction pathways in the high temperature regime (>250⁰C).

One of the atypical phenomena observed at high temperatures ($>200^0$C) is the seagull shape profile of NO conversion vs. temperature, which is characterized by decrease in standard SCR NO_x conversion followed by increase in conversion between 250-350^{0}C[1]. It was found that seagull profile is more pronounced at low O_2 content, high space velocity and low Cu loadings[2–4]. One of the leading explanations for decrease in NO conversion in seagull profile was competitive NH_3 oxidation at high temperatures until the recent suggestion of decline in NH_3 coverage causing overall decline of the standard SCR NO conversion or reaction rate[5]. There was also a proposition of presence of different Cu sites at low and high temperatures, wherein NH_3-solvated mobile Cu^{II} and Cu^I species were proposed to be the active sites upto 200^{0}C and zeolite framework-coordinated Cu^{II} to be the dominant active sites above 250^{0}C[6]. In the recent paper by Fahami et al[1], it was shown that even though monomeric Cu sites undergo NH_3 desorption to lose NH_3-conferred mobility at high temperatures, these Cu sites become more thermally mobile at such higher temperatures to regain their ability to form dimeric Cu sites during Cu^I re-oxidation, resulting in increase in NO conversion above 350^{0}C. It was then suggested that these Cu dimeric structures will be more localized due to NH_3 and H_2O-desolvation, resulting in the drop of NO conversion at about 350^{0}C before further increase in NO conversion above 350^{0}C[1]. The observation that seagull profile becomes more pronounced at low Cu loadings seems to suggest that Cu proximity is still critical till temperatures of about 350^{0}C, and that loss of Cu site mobility due to NH_3-desorption is likely the cause for decrease in NO conversion in seagull profile. However, more careful and rigorous study needs to be performed to convincingly illustrate the origin of seagull profile in the temperature range of 250-350^{0}C and unravel reaction pathways (as a function of Cu spatial density) at temperatures above 350^{0}C.

12.4 References

(1) Fahami, A. R.; Günter, T.; Doronkin, D. E.; Casapu, M.; Zengel, D.; Vuong, T. H.; Simon, M.; Breher, F.; Kucherov, A. V; Brückner, A.; Grunwaldt, J.-D. *React. Chem. Eng.* **2019**.

(2) Olsson, L.; Wijayanti, K.; Leistner, K.; Kumar, A.; Joshi, S. Y.; Kamasamudram, K.; Currier, N. W.; Yezerets, A. *Appl. Catal. B Environ.* **2015**, *174-175*, 212-224.

(3) Kwak, J. H.; Varga, T.; Peden, C. H. F.; Gao, F.; Hanson, J. C.; Szanyi, J. *J. Catal.* **2014**, *314*, 83–93.

(4) Ma, L.; Cheng, Y.; Cavataio, G.; McCabe, R. W.; Fu, L.; Li, J. *Chem. Eng. J.* **2013**, *225*, 323-330.

(5)   Joshi, S. Y.; Kumar, A.; Luo, J.; Kamasamudram, K.; Currier, N. W.; Yezerets, A. *Appl. Catal. B Environ.* **2018**, *226*, 565-574.

(6)   Lomachenko, K. A.; Borfecchia, E.; Negri, C.; Berlier, G.; Lamberti, C.; Beato, P.; Falsig, H.; Bordiga, S. *J. Am. Chem. Soc.* **2016**, *138*, 37, 12025-12028.

APPENDIX A. SUPPLEMENTARY MATERIALS TO CHAPTER 2

For the sake of brevity, supplementary material is not inserted here. Refer to supplementary information of my original coauthored article published in The Journal of the American Chemical Society, 138 (18), 6028-6048, 2016, titled "Catalysis in a Cage: Condition-Dependent Speciation and Dynamics of Exchanged Cu Cations in SSZ-13 Zeolites".

APPENDIX B. SUPPLEMENTARY MATERIALS TO CHAPTER 3

B1. Synthesis Methods and Characterization

Synthesis of SSZ-13 zeolites

Here, SSZ-13 is used to refer to materials of aluminosilicate composition and the chabazite (CHA) framework. High-aluminum SSZ-13 zeolites (Si/Al = 4.5) were synthesized as previously reported[10]. A molar ratio of 1 SiO_2/ 0.031 Al_2O_3/ 0.017 TMAdaOH/ 0.770 Na_2O/ 12.1 H_2O was used in the synthesis solution. Briefly, a 1M NaOH solution (3.3 wt% NaOH, Alfa Aesar) was added to deionized water (18.2 MΩ) in a perfluoroalkoxy alkane (PFA) jar and stirred for 15 minutes at ambient conditions. Next, sodium silicate (10.6 wt % Na_2O, 25.6 wt% SiO_2; Sigma Aldrich) was added to the NaOH solution and stirred for 15 minutes under ambient conditions. Then, NH_4-Y zeolite (Zeolyst CBV300, Si/Al = 2.6) was added and the mixture was stirred for 30 minutes under ambient conditions. Finally, an aqueous TMAdaOH solution (25 wt%, Sachem) was added to the mixture and stirred for 30 minutes under ambient conditions. The synthesis mixture was then transferred to 45 mL Teflon-lined stainless steel autoclaves (Parr Instruments) and placed in a forced convection oven (Yamato DKN-402C) at 413 K and rotated at 60 RPM for 6 days.

Low aluminum SSZ-13 zeolites (Si/Al = 15-25) were synthesized in hydroxide media using a previously reported procedure[10]. A molar ratio of 1 SiO_2/ 0.0167-0.033 Al_2O_3/ 0.25 TMAdaOH/ 0.125 Na_2O/ 44 H_2O was used to obtain Na^+/$TMAda^+$ = 1 and Si/Al = 15 or 25 in the synthesis solution. A typical synthesis involved adding an aqueous TMAdaOH solution to deionized H_2O in a PFA jar and stirring the solution under ambient conditions for 15 minutes. Next, aluminum hydroxide was added to the aqueous TMAdaOH solution. Then, a 5M NaOH solution (16.7 wt% NaOH in deionized water; NaOH pellets 98 wt%, Alfa Aesar) was added dropwise to the solution and stirred under ambient conditions for 15 minutes. Finally, colloidal silica was added and the mixture was stirred for 2 h under ambient conditions. All synthesis reagents were used without further purification. The synthesis solution was then transferred to a 45 mL Teflon-lined stainless steel autoclave and placed in a forced convection oven at 433 K and rotated at 40 RPM for 6 days.

X-Ray diffraction of CHA zeolites

The CHA crystal framework was determined from powder X-ray diffraction (XRD) patterns measured on a Rigaku SmartLab X-ray diffractometer with a Cu Kα radiation source (λ=0.154 nm) operated at 1.76 kW. 0.01 g of zeolite powder were loaded onto a low-volume sample holder (Rigaku) and the diffraction pattern was recorded from 4-40° 2θ at a scan rate of 0.04° s^{-1}. Powder XRD patterns for all synthesized materials were compared to diffraction patterns for CHA reported in the International Zeolite Association (IZA) structure database[19]. All XRD patterns reported here are normalized such that the maximum peak intensity in each pattern is unity. Diffraction patterns of CHA zeolites are shown in Figure B1.

Adsorption isotherms to measure micropore volumes of CHA zeolites

Micropore volumes of CHA zeolites were determined from Ar adsorption isotherms measured at 87 K on a Micromeritics ASAP 2020 Surface Area and Porosity Analyzer. Typically, 0.03–0.05 g of pelleted and sieved sample (nominal diameter between 180-250 μm) were degassed by heating to 393 K (0.167 K s^{-1}) under vacuum (<5 μmHg) for 2 h, and then further heating to 623 K (0.167 K s^{-1}) under vacuum (<5 μmHg) and holding for 9 h. Volumetric gas adsorption within micropores (cm^3 g^{-1} at STP) was estimated from analysis of semi-log derivative plots of the adsorption isotherm ($\partial(V_{ads})/\partial(\ln(P/P_0))$ vs. $\ln(P/P_0)$) to identify the micropore filling transition (first maximum) and then the end of micropore filling (subsequent minimum). Micropore volumes (cm^3 g^{-1}) were obtained on SSZ-13 zeolites by converting standard gas adsorption volumes (cm^3 g$_{cat}^{-1}$ at STP) to liquid volumes using a density conversion factor assuming the liquid density of Ar at 87 K. Micropore volumes of CHA zeolites are shown in Figure B2. In each figure, adsorption isotherms are offset in increments of 200 cm^{-3} g for clarity.

Aqueous-phase Copper Ion-Exchange of H-SSZ-13

Cu-SSZ-13 zeolites were prepared by aqueous-phase Cu ion-exchange using $Cu(NO_3)_2$ as the precursor. A pH meter (Mettler Toledo SevenEasy™ pH Meter S20) calibrated at pH values of 1.0 (Sigma Aldrich FLUKA 31044 Buffer solution pH 1.0 at 20°C), 4.0 (Hach Buffer Solution

pH 4.0±0.02 at 25°C), and 7.0 (Hach Buffer Solution pH 7.00±0.02 at 25°C) was used to monitor the pH throughout the Cu ion-exchange process.

Typically, 1 to 2 g of H-SSZ-13 were added to 40 mL of deionized water (Millipore, Synergy UV Water Purification System, 18.2 MΩ cm^{-1} resistivity at 298 K) in a 250 mL borosilicate Erlenmeyer flask and stirred at 300 rpm using a magnetic stir bar for 30 minutes at 313 K. Depending on the Cu exchange level targeted, 20 to 100 mL of 0.001 M to 0.1M $Cu(NO_3)_2$ solution (Sigma Aldrich, Copper^{II} nitrate hydrate, 99.999% trace metals basis) was added to the slurry. The pH was controlled to 4.9±0.1 by dropwise addition (~2 drops per second) of 1.0 M NH_4OH (Sigma Aldrich, 28.0% Ammonium hydroxide solution, ACS reagent grade) immediately after addition of $Cu(NO_3)_2$ and was maintained at 4.9±0.1 for 4 hours. Cu-exchanged SSZ-13 was recovered via centrifugation, and then washed with deionized water six times (70 mL H_2O $g_{catalyst}^{-1}$ per wash). Cu-SSZ-13 catalysts were dried at 373 K in ambient air in a free convention oven for 12 hours, crushed with a mortar and pestle, then treated in flowing dry air (100 mL $g_{catalyst}^{-1}$, Indiana Oxygen, Zero grade air, < 1ppm THC) to 773 K at a rate of 1 K min^{-1}.

Elemental Analysis using Atomic Absorption Spectroscopy

Typically, 0.02-0.050 g of dry sample (H-SSZ-13 or Cu-SSZ-13) were dissolved in approximately 2 mL of hydrofluoric acid (HF) (Mallinckrodt Baker, 48% HF, Baker Analyzed® A.C.S. Reagent) in a 60 mL high density polyethylene (HDPE) bottle (2 oz., 60 mL Nalgene™ Wide-Mouth Amber HDPE bottles). A polyethylene pipet was used to transfer the HF. The sample was capped and left to dissolve for 12 hours then diluted with approximately 50 mL of deionized water (Millipore, Synergy UV Water Purification System, 18.2 MΩ cm^{-1} resistivity at 298 K).

Bulk elemental composition was determined using atomic absorption spectroscopy (AAS) on a Perkin Elmer AAnalyst 300. Silicon AAS standards were created by diluting a 1000 ppm silicon AAS standard solution (Sigma Aldrich, TraceCERT®, 1000 mg/L Si in NaOH) to 15, 75, and 150 ppm. A linear calibration curve (ppm_{Si} versus Si absorbance at 251.6 nm) was determined by plotting the absorbance of each silicon standard at 251.6 nm. Similar procedures were used for aluminum, copper and sodium on all reported SSZ-13 catalysts.

Cu site characterization and quantification

Cu K-edge X-ray absorption near edge spectroscopy (XANES) of samples under ambient conditions were indistinguishable from that of an aqueous Cu^{II} nitrate solution (Cu-CHA-20 and Cu-CHA-29 shown in Figure B3) and did not show absorption characteristic of Cu^{I} (edge at ~8983 eV[37,38]) or of Cu^{II} within Cu_xO_y clusters[39,40]. Diffuse reflectance UV-Visible spectra collected on these samples under ambient, hydrated conditions are shown in Figure B4. The peak at 12500 cm^{-1} is representative of hydrated isolated Cu^{II} ions. Peaks at ~22500 cm^{-1}, reported to be due to Cu-dimers in ZSM-5[41], are not observed, indicating that predominantly isolated Cu^{II} species are present. The broad absorption features between 30000 cm^{-1} and 50000 cm^{-1} are due to contributions from the zeolite framework.

The enumeration of isolated Cu^{II} and $Cu^{II}OH$ sites on each Cu-CHA zeolite was determined after oxidative treatment (20% O_2, 773 K) by quantifying the number of residual protons that remained after Cu exchange, given that Cu^{II} sites exchange two protons and $Cu^{II}OH$ sites exchange one proton. The quantification was performed using methods that selectively titrate residual H^+ sites in small-pore, metal-exchanged zeolites[42], in which NH_3-saturated samples are purged in flowing wet helium (3% H_2O in He, 433 K) to desorb Lewis acid-bound NH_3, prior to temperature programmed desorption (Table S1). The Cu^{II} and $Cu^{II}OH$ site quantities in the samples studied here are consistent with the thermodynamic preference for Cu^{II} exchange at paired Al sites until saturation[10], followed by further exchange of $Cu^{II}(OH)$ sites at isolated Al. Taken together, the ex situ characterization of Cu sites by X-ray absorption, UV-Visible and quantification of residual H^+ sites by NH_3 titration, confirm that the Cu-CHA samples studied here contain only isolated Cu^{II} cations, present either as Cu^{II} at paired framework Al sites or as $[CuOH]^+$ at isolated Al sites[10].

B2. SCR Kinetics

Standard selective catalytic reduction (SCR) kinetic data were measured on a down-flow 3/8'' ID tubular quartz reactor. All samples were pelletized (Specac 13mm Diameter Stainless Steel Evaluable Pellet Die) under 10,000 psi pressure (Carver Laboratory Press), ground using a mortar and pestle, then sieved to retain 125 to 250 μm particles (W.S. TYLER No. 60 and No. 120 all-stainless-steel). Typically, 0.015-0.050 g of sieved Cu/SSZ-13 catalyst were mixed with enough inert silica gel (Fisher Chemical Silica Gel (Davisil) Sorbent, Grade 923) to obtain a bed height of ~0.5 cm. Aluminum foil was wrapped around the quartz reactor to an outer diameter of ~2.54 cm, in order to enhance heat conduction and minimize any radial temperature gradients that may be present within the bed. The reactor was then placed within a clamshell furnace (Applied Test Systems) and pressure-tested with helium (99.999%, Indiana Oxygen) at 5 psig for 20 minutes.

Steady state kinetic data were collected according to methods we have reported previously[17]. Briefly, rate data were measured at differential NO conversion below 20% (total gas flow rate was varied between 0.8 to 1.5 L min^{-1}), to ensure the entire bed was exposed to approximately the same gas concentrations and temperatures using a gas mixture of 300 ppm NO (3.5% NO in Ar, Praxair), 300 ppm NH_3 (3.0% NH_3 in Ar, Praxair), 5% CO_2 (liquid, Indiana Oxygen), 10% O_2 (99.5%, Indiana Oxygen), 2.5% H_2O (deionized, introduced through 24'' PermaPure MH Humidifier), and balance N_2 (boiloff liquid N_2, Linde) at 473 K and 1 atm. The gas hourly space velocity (GHSV) was varied between 600,000 to 4,000,000 h^{-1} for all kinetic experiments. NO, NO_2, NH_3, CO_2, N_2O, and H_2O concentration data were recorded every 0.95 seconds using a MKS MultiGas 2030 gas-phase Fourier transform infrared (FTIR) spectrometer with on-board calibrations. Reaction temperatures were collected using two Omega® K-type 1/16'' OD thermocouples with one placed in contact with the top of the bed and the second placed in contact with the bottom of the bed. The temperature difference was always within 3 K during steady state SCR catalysis. Total gas flow rates were measured using a soap bubble flow meter.

In the limit of differential NO conversion, the gas concentrations and catalyst bed temperature can be assumed constant, allowing the NO consumption rate to be calculated using equation (B1):

$$-r_{NO}(\text{mol NO mol Cu}^{-1}\text{s}^{-1}) = \frac{(C_{NO,in}-C_{NO,out})}{1000000 * \text{mol Cu}} * \dot{V}_{total} * \frac{P}{RT} \tag{B1}$$

where C values are the concentrations of NO before and after the catalyst bed in ppm, $\dot{V}_{total}$ is the total volumetric flow rate, P is 1 atm, T is ambient temperature, and R is the gas constant. The rate of NO consumption can further be converted from rate per Cu (mol NO mol Cu^{-1} s^{-1} or NO Cu^{-1} s^{-1}) to rate per volume (molecules of NO consumed per 1000 Å^{-3} s^{-1}) using a multiplier for the number of Cu atoms per 1000 Å^3.

The experimental data are fitted to a power law rate expression where k_{app} is the apparent rate constant and α, _ =, and _ = are the apparent reaction orders with respect to concentrations of NO, NH$_3$, and O$_2$, respectively.

$$-r_{NO} = k_{app}C_{NO}^{\alpha}C_{NH_3}^{\beta}C_{O_2}^{\gamma} \tag{B2}$$

$$k_{app} = A\exp\left(-\frac{E_{a,app}}{RT}\right) \tag{B3}$$

SCR rates measured as a function of Cu density (Cu-CHA catalysts depicted in Figure B1 and table B3) were fit to two different models, as shown below. The four lowest Cu density samples were fit to rate = $a \times \rho_{Cu}^2$ (best fit $a = 39.3$, $R^2=0.99$) and the four highest Cu density samples to rate = $a \times \rho_{Cu}$ (best fit $a = 7.56$, $R^2=0.99$).

Low Cu Density (Fit to $a \times \rho_{Cu}^2$)　　　High Cu Density (Fit to $a \times \rho_{Cu}$)
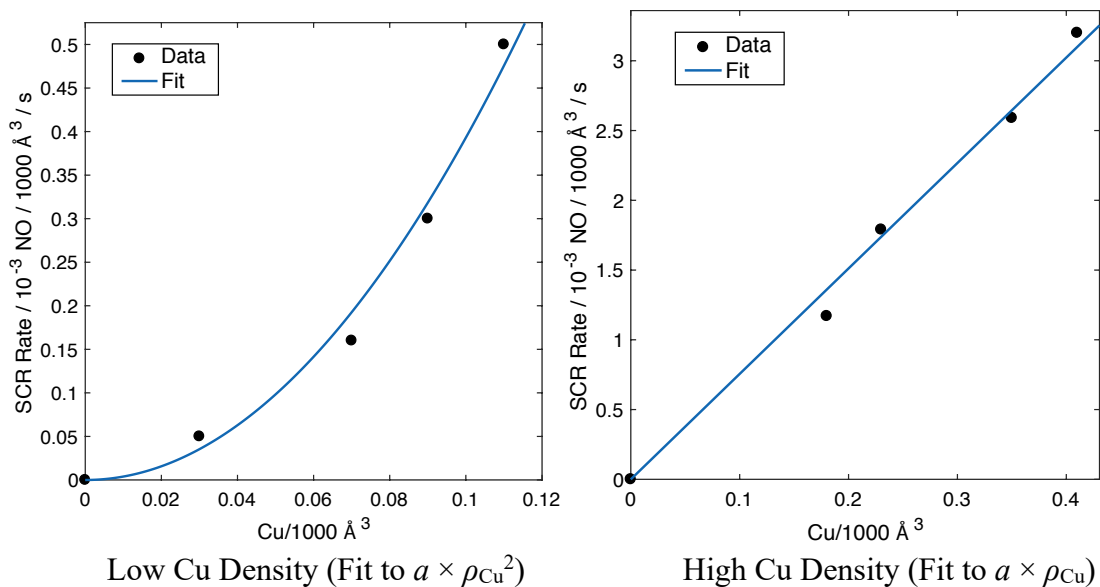
B3. X-ray Absorption Spectroscopy

X-ray absorption spectroscopy (XAS) experiments were performed at sector 10 MR-CAT (Materials Research Collaborative Access Team) of the Advanced Photon Source, Argonne National Laboratory. The insertion device beamline at sector 10 (10-ID) was used for the *operando* and *in situ* oxidation experiments due to the high photon flux available at that beamline. Incident and transmitted X-ray intensities were measured in ion chambers filled with 20% He in N_2 and 20% Ar in N_2, respectively, to obtain approximately 10% and 70% absorption of the beam before and after the sample, respectively. A Cu metal foil reference spectrum (edge energy of 8979 eV) was measured simultaneously with each sample spectrum to calibrate the X-ray beam for spectral measurements at the Cu-K edge. All sample spectra were normalized using 1st and 3rd order polynomials for background subtraction of the pre- and post-edges, respectively.

The Cu K-edge XANES spectra consists of several distinct features indicative of the various electronic transitions for the Cu^I and Cu^{II} oxidation states[43,44]. The peaks at 8977 eV and 8987 eV are representative of Cu^{II}. The peak centered at 8977 eV is due to the symmetry forbidden 1s → 3d transition, which becomes allowed due to mixing of the 3d and 4p orbitals and has been reported in several studies as a low intensity, pre-edge feature[45-48]. The shoulder at 8987 eV is due to the 1s → 4p electronic transition[49,50]. The presence of the sharp peak centered around 8983 eV is characteristic of the 1s → 4p transition for a two-coordinate Cu^I complex. This peak has previously been reported in the literature under a variety of environments including hydrocarbon SCR [51] and NO decomposition on Cu-ZSM-5[52], thermal reduction of Cu-mordenite[53], Cu-Y[54], and two-coordinate Cu^I model compounds including copper(I) diamine complexes[37,55,56].

XAS is a bulk technique and each sample spectrum represents a mixture of oxidation states. Therefore, a linear combination XANES fitting of the Cu^I and Cu^{II} references was used to obtain the relative amounts of Cu in each oxidation state in a given spectrum. Information about how the Cu^I and Cu^{II} references were generated is provided in our previous publication[10]. An absolute error of 5% was used as a conservative estimate for the uncertainty in the linear combination XANES fitting. The largest source of uncertainty is the Cu^I reference used in the fitting, as there is no specific Cu^I reference spectrum, and the choice of reference may not exactly reproduce the Cu^I amine structure present in the sample. If the Cu^I reference used in the

fitting is assumed to be an accurate representation of the Cu^I structure present, the uncertainty in the linear combination XANES fitting would decrease to 2-3%.

The Debye-Waller factor (DWF) was determined to be 0.005 $Å^2$ for gas conditions that included NH_3 and was 0.003 $Å^2$ for all other gas conditions. All extended X-ray absorption fine structure (EXAFS) fitting was performed with the DWF fixed at the appropriate value, and EXAFS fitting was only performed on the first coordination shell of Cu-O. The k^2-weighted data in R-space was fit by least-squares optimization to provide coordination numbers (CN) and interatomic bond distances. The EXAFS data was fit over k = 2.7 to ~8.5 $Å^{-1}$, incorporating as much data at high k values as possible.

Operando XAS

Operando experiments were performed in a special glassy carbon tube reactor, and the details of the custom *operando* XAS reactor setup were described by Kispersky et al.[39]. During these experiments, XAS spectra were simultaneously collected while measuring the reaction rates for each sample to ensure that the standard SCR rate per mole Cu measured at APS were quantitatively the same, within error, to that measured in laboratory differential plug-flow reactors (PFR). Figure B20 shows standard SCR reaction rates measured on a representative sample (Cu-CHA-19) in the laboratory PFR and *operando* XAS reactor over a temperature range (450-480 K), indicating that rates are reproduced in the two reactor setups to within 10%. Table B5 shows that standard SCR reaction rates for catalyst samples in the *operando* reactor described above are within 10% of those measured in a separate plug flow reactor, thus establishing kinetic equivalence of the two reactors.

In *operando* experiments, 7-13 mg of Cu-CHA-15, 30 mg of Cu-CHA-20, or 25 mg of Cu-CHA samples (sieved to 125-250 μm) were loaded in the *operando* reactor to maintain differential conditions (< 20% conversion). Gases were mixed and introduced into the reactor in a precise manner to avoid any side reactions. De-ionized H_2O was introduced into the feed stream by flowing He carrier gas through a heated shell type humidifier (Perma Pure MH-Series). All gas lines downstream of the humidifier were heated to above 373 K to prevent H_2O condensation. After introducing H_2O, NO (300 ppm in N_2, Matheson Tri-Gas) was introduced into the gas stream, followed by the introduction of O_2 (20% in He, Airgas, Inc.). The reaction mixture was then preheated to 473 K. Ammonia (300 ppm in He, Airgas, Inc.) was introduced

through a 1/16" stainless steel line that was located immediately upstream of the catalyst bed to minimize the possibility of gas-phase side reactions. Gas concentrations were measured using a MKS Multi-Gas 2030 gas analyzer FTIR with a cell temperature of 464 K and based on factory provided calibration files. Standard SCR conditions of 300 ppm NO, 300 ppm NH_3, 10% O_2, 2% H_2O, 5% CO_2, a total flow rate of 1000-1200 mL min^{-1} and a temperature of 463-473 K was used for all steady state experiments. Steady state spectra were collected in the quick scan mode with an edge step of 0.5 eV, a dwell time of 0.05 s at each step and an energy range between 8700 and 9700 eV, with each spectrum taking 2-3 min to acquire. Steady state data were averaged over 3-5 scans depending on the data quality obtained under different experimental conditions. Linear combination XANES fits to determine the Cu^I and Cu^{II} fractions under *operando* conditions were carried out using the appropriate references, as explained in our previous publications[15,17,39].

Transient XAS

Transient O_2 and NO_2 oxidation experiments were carried out in the same flow reactor setup as used for *operando* experiments. Reduction with 300 ppm NO and 300 ppm NH_3 under a total flow of 1200 mL min^{-1} at approximately 447 K gave 90±5, 90±5 and 98±5 % Cu^I, for Cu-CHA-15, Cu-CHA-20, and Cu-CHA-29 samples, respectively. Following the reduction to Cu^I, samples were exposed to either 10% O_2 or 100 ppm NO_2 at the same temperature in separate experiments. The Cu^I and Cu^{II} fractions during these transient experiments were followed by collecting XANES spectra (Figures B6, B7, B8) in quick scan mode from 8800 to 9400 eV. Each spectrum took 21 s to acquire with a step size of 0.5 eV and a dwell time of 0.03 s. Higher quality spectra were collected at the end of these transients by increasing the dwell time from 0.03 s to 0.05 s. Linear combination XANES fits to determine the Cu^I and Cu^{II} fractions from spectra collected during transient experiments were performed using the same procedure to fit spectra collected during *operando* XAS experiments. The fitted Cu^I fraction before and at the end of O_2 and NO_2 oxidation transients are tabulated in Tables B6, B7, B8.

B4. Kinetic models for the transient oxidation experiments

O$_2$ oxidation of Cu^I(NH$_3$)$_2$

      The transient O$_2$ data in Figure B.3A were fit to a modified pseudo-second-order rate law described below. The approximate second-order behavior can be rationalized by postulating that the following termolecular reaction describes the oxidation of two Cu^I diamine complexes with O$_2$:

$$2\left[\text{Cu}^{\text{I}}(\text{NH}_3)_2\right] + \text{O}_2 \longrightarrow \left[(\text{NH}_3)_2\,\text{Cu}^{\text{II}}-\text{O}_2-\text{Cu}^{\text{II}}(\text{NH}_3)_2\right] \qquad \textbf{(B4)}$$
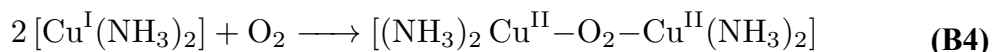
If this step were elementary and all sites behaved identically, the following rate law would describe the rate of consumption of Cu^I species:

$$\frac{d[\text{Cu}^{\text{I}}(t)]}{dt} = -2k_{\text{a}}[\text{Cu}^{\text{I}}(t)]^2[\text{O}_2] \qquad \textbf{(B5)}$$

Because O$_2$ is in stoichiometric excess during these transient experiments, its concentration can be subsumed into k_a and the above expression can be rewritten as:

$$\frac{d[\text{Cu}^{\text{I}}(t)]}{dt} = -2k[\text{Cu}^{\text{I}}(t)]^2 \qquad \textbf{(B6)}$$

where k is a pseudo-second-order rate constant. To correct for the unoxidizable, recalcitrant fraction of Cu^I (defined as $[\text{Cu}^{\text{I}}]_\infty$) in the transient O$_2$ experiments (Figure 3A),,we introduce the transformation:

$$[\text{Cu}^{\text{I}}(t)]_{\text{corr}} = [\text{Cu}^{\text{I}}(t)] - [\text{Cu}^{\text{I}}]_\infty$$
$$\frac{d[\text{Cu}^{\text{I}}(t)]_{\text{corr}}}{dt} = -2k[\text{Cu}^{\text{I}}(t)]^2_{\text{corr}} \qquad \textbf{(B7)}$$

$[\text{Cu}^{\text{I}}(t)]_{\text{corr}}$ is defined as the concentration of oxidizable Cu^I (by O$_2$) as a function of time during the transient O$_2$ experiment. Integrating from 0 to t and rearranging:

$$\text{Cu}^{\text{I}}\ \text{Fraction} = \frac{[\text{Cu}^{\text{I}}](t)}{[\text{Cu}^{\text{I}}]_0} = \frac{1 - [\text{Cu}^{\text{I}}]_\infty/[\text{Cu}^{\text{I}}]_0}{1 + 2k\left([\text{Cu}^{\text{I}}]_0 - [\text{Cu}^{\text{I}}]_\infty\right)t} + \frac{[\text{Cu}^{\text{I}}]_\infty}{[\text{Cu}^{\text{I}}]_0} \qquad \textbf{(B8)}$$

where Cu^I Fraction is the time-dependent Cu^I concentration divided by the initial Cu^I concentration ($[CuI]_0$). The parameters in Eqn. B8 are k and $[CuI]_\infty$. For each data series, we set $[Cu^I]_\infty$ to the last (longest time) Cu^I Fraction data point, and used nonlinear least-squares regression to obtain the best-fit parameter of k. Results are summarized below:

	Cu-CHA-29	Cu-CHA-20	Cu-CHA-15
k(m^3 mol Cu^{-1}s^{-1})	0.00011	0.00017	0.00082
$[CuI]_\infty$/ $[CuI]_0$	0.26	0.10	0.05
R^2	0.99	0.98	0.99

NO$_2$ oxidation of $Cu^I(NH_3)_2$

The transient NO$_2$ data in Figure B13 were fit to a pseudo-first-order rate law described below. The first-order behavior can be rationalized if we postulate that the observed oxidation kinetics are governed by the bimolecular reaction of a single Cu^I diamine with NO$_2$:

$$[Cu^I(NH_3)_2] + NO_2 \longrightarrow [(NH_3)_2 - Cu^{II} - NO_2] \qquad \textbf{(B9)}$$
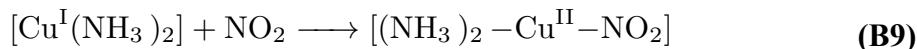
If this reaction is elementary, then the rate law that describes the rate of consumption of Cu^I species is:

$$\frac{d[Cu^I(t)]}{dt} = -k_a[Cu^I(t)][NO_2] \qquad \textbf{(B10)}$$

Because NO$_2$ is in stoichiometric excess during these transient experiments, its concentration can be subsumed into k_a and the above expression rewritten as:

$$\frac{d[Cu^I(t)]}{dt} = -k[Cu^I(t)] \qquad \textbf{(B11)}$$

Upon integration and rearranging, the above expression becomes:

$$Cu(I)\ Fraction = \frac{[Cu^I(t)]}{[Cu^I]_0} = e^{-kt} \qquad \textbf{(B12)}$$

where Cu^I Fraction and $[Cu^I(t)]$ and $[Cu^I]_0$ are defined in the same way as reported in the previous subsection. The only unknown parameter in Eqn. B11 is k. Nonlinear least-squares regression was used to obtain the best-fit k value from the data in Figure B13. The results are summarized below:

	Cu-CHA-29	Cu-CHA-20	Cu-CHA-15
k (s^{-1})	0.026	0.028	0.030
R^2	0.98	0.98	0.89

B5. DFT Methods

To construct the energy landscape for Cu diffusion through an 8-MR and reaction with O_2 we calculated the energies of structures for A through E in Figure 3.4 using the following protocol. All structures are attached to the supplementary information in CONTCAR format in the file CONTCARs.zip.

Due to the dynamic and mobile nature of solvated Cu species in the zeolite cage, we used AIMD on all structures to seek low energy configurations. A 12 T-site supercell containing two Al atoms was used for Figure 3.4 structures C and D, such that each Cu charge compensates 1Al. For Figure 3.4 structure A, the 12 T-site supercell was doubled to create a 24 T-site supercell, so that each $Cu^I(NH_3)_2$ can occupy one CHA cage. Multiple initial structures were guessed, and each geometry was sampled by Born-Oppenheimer molecular dynamics in the canonical ensemble (NVT) using the Car-Parrinello Molecular Dynamics (CPMD) software version 3.17.1[57]. We used the Perdew-Becke-Erzenhof (PBE)[58] flavor of the generalized gradient approximation (GGA) exchange-correlation functionals and Vanderbilt ultrasoft pseudopotentials[59], and a plane wave cutoff of 30 Ry. The first Brillouin zone was sampled at the Γ point only for this insulator, and a Nose-Hoover thermostat was used to achieve the target temperature of 473 K. A 0.6 fs time step was used for a total sampling time of 150 ps, for each of structures A, C and D in Figure 3.4. Structures B and E came from guessing product structures for the Climbing Image Nudged Elastic Band (CI-NEB) calculations described below and were not sampled by AIMD.

Next, for structures A, C, and D, we selected several (3 to 4) low energy structures from the 150 ps of AIMD trajectories and performed electronic energy optimizations using the Vienna Ab initio Simulation Package (VASP) version 5.4.1 [60] and the same supercell. Periodic DFT calculations were performed using the projector augmented wave (PAW) method with the PBE functional [58] and a 400 eV plane wave cutoff, and DFT-D2 [61] to calculate van der Waals dispersion energies. Electronic energies were converged self-consistently to less than 10^{-8} eV, and forces to less than 0.01 eV/Å, on each atom. For the above calculations, PBE POTCARs for each atom were used. We performed spin-polarized calculations for Cu dimers to sample both the singlet and triplet state of the dimers. The lower energy structure was chosen and plotted on Figure 3.4 and reported in Table B10. Structures A, B, D and E are in singlet states and structure C is in triplet state. All structures in Figure 3.4 are attached to the SI in CONTCAR format.

Transition states (A to B, and D to E) were computed using the Climbing Image Nudged Elastic Band (CI-NEB) method [62] and the same functional and plane wave cutoff described above. Convergence criteria were tightened to less than 10^{-8} eV for electronic energy and less than 0.01 eV/Å for force on each atom. The transition state from C to D is spin forbidden and was not computed here; we estimated the effective barrier from the literature as reported in Figure 3.4.

We followed a similar protocol for reactions of one $Cu^I(NH_3)_2$ with O_2 and NO_2. We first performed 150 ps of AIMD for O_2 and NO_2 adsorption on $Cu^I(NH_3)_2$, using a 12 T-site supercell with 1 Al, and with the CPMD software. Low energy structures were then selected and optimized (spin polarized) with both PBE/DFT-D2 and the hybrid screened-exchange Heyd-Scuseria-Ernzerhof (HSE06) functionals [63] with the Tkatchenko Scheffier method (TSvdW)[64] to correct for dispersion interactions. We performed these additional HSE06-TSvdw calculations because hybrid functionals have been shown to predict NO_x adsorption energies more accurately than GGA functionals[12]. Figure B14 and Table B10 reports the structures and adsorption energies.

B6. NO titrations to probe reaction stoichiometry

The consumption of NO (per Cu) in sequential SCR reaction steps on Cu-CHA zeolites was measured and used to corroborate the reaction stoichiometry depicted in Figure 3.6. Typically, 10 to 20 mg of sample was loaded into the reactor system used to measure steady-state SCR kinetics. The total gas flow rate used in the following procedure was 600 mL min^{-1}. The samples in Figure 3.3A were first oxidized and dehydrated to their Cu^{II} form[10] by treatment to 823 K (0.167 K s^{-1}) in flowing 20% O_2 (99.5%, Indiana Oxygen) in balance He (99.999%, Indiana Oxygen), and then cooling to 473 K. The sample was then held flowing He for 30 minutes, and then fully reduced in a mixture of 300 ppm NO (3.5% NO in Ar, Praxair) and 300 ppm NH_3 (3.0% NH_3 in Ar, Praxair) in balance He. Following reduction of Cu sites to their Cu^{I}(NH_3)$_2$ states (corresponding to 6 o'clock positions in Figure 3.6), the samples were exposed to flowing 10% O_2 in balance He until steady-state was achieved (corresponding to the central position in Figure 3.6). The O_2 oxidized sample was then held in a flowing stream of 300 ppm of NO in balance He, until steady-state was achieved. Finally, 300 ppm NH_3 was introduced to the flow of NO in balance He, to reduce the sample back to Cu^{I}(NH_3)$_2$ (corresponding to 6 o'clock positions in Figure 3.6). Each of these sequential treatments was also performed in a blank reactor to measure a baseline signal in the FTIR spectrometer (MKS Multigas TM 2030) used to account for gas holdup and residence time in the reactor setup (NO conversion was not detected in the blank reactor), in order to calculate the NO consumption from the Cu-CHA catalyst during each treatment step (Figure B12).

Summarizing, after O_2 oxidation of Cu^{I}(NH_3)$_2$ to form a NH_3-solvated Cu^{II} dimer (central position in Figure 3.6), the two-step procedure described above exposes the catalyst to NO alone, and then to NO and NH_3 together. Exposure of NO in the step immediately following O_2-assisted oxidation results in the consumption of one NO equivalent (NO:Cu = 0.98 ± 0.10) per Cu site. Once steady-state is achieved, the sequential addition of NH_3 to the flowing stream (already containing NO) consumes another equivalent of NO per Cu site (NO:Cu = 1.07 ± 0.11) and fully reduces the sample to Cu^{I}(NH_3)$_2$ (6 o'clock positions in Figure 3.6), which closes the catalytic cycle. The 2:1 NO:Cu consumption ratio is consistent with Figure 3.6. Starting from the Cu-oxo dimer in the center of the Figure 6, two NO molecules per Cu are required to return to the 6 o'clock position in each cycle corresponding to the formation of Cu^{I}(NH_3)$_2$ species.

B7. Random Distribution of Cu per Cage

To eliminate the possibility that the oxidizable fraction of Cu^I corresponds to Cu pairs or larger aggregates that, by random chance, are present in the same cage and not from pairs formed from mobile Cu^I ions, we estimated the fraction of persistent pairs that would be present assuming that Cu are randomly distributed among cages. Results are compared with the observed fraction of oxidizable Cu^I in Figure B15. For Cu densities corresponding to the zeolites studied in Figure 3.3, this "immobile Cu dimer" model predicts values that are much smaller than the $[Cu^I]_\infty$ values observed experimentally and predicted from the non-mean-field model described in B10:

Cu-CHA-15: Oxidizable Cu Fraction = 0.072, $[Cu^I]_\infty / [Cu^I]_0 = 0.928$

Cu-CHA-20: Oxidizable Cu Fraction = 0.012, $[Cu^I]_\infty / [Cu^I]_0 = 0.988$

Cu-CHA-29: Oxidizable Cu Fraction = 0.002, $[Cu^I]_\infty / [Cu^I]_0 = 0.998$

B8. Metadynamics

We used metadynamics to compute the free energy landscape for a $Cu^I(NH_3)_2$ to diffuse away from a charge-compensating Al center into an adjacent cage. To avoid interaction between periodic cells, a CHA supercell with 72 T-sites was adopted. The 72-T-site supercell (pictured below) was generated by propagating the 36 T-site CHA-silica supercell obtained from the database of zeolite structures[19] along one direction. A T-site silicon is replaced by aluminum and a $Cu^I(NH_3)_2$ complex was inserted into a cage near the Al to create the initial $Cu^I(NH_3)_2$ structure.
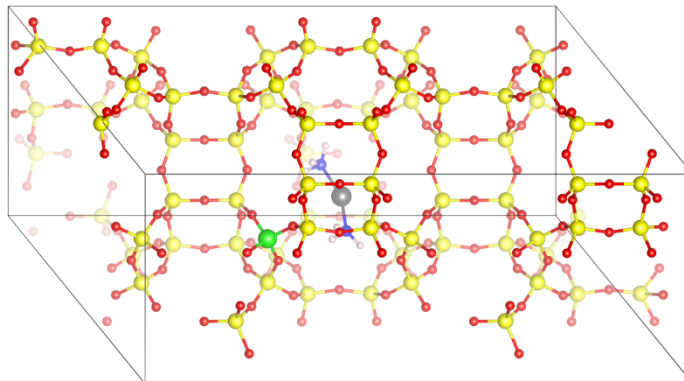
72-T site supercell for metadynamics simulation. Color code for different elements in superimposed figure: gray=Cu, green=Al, yellow=Si, red=O, blue=N and white=H.

All calculations were performed in the CPMD program[57]. 6 ps of *NVT* molecular dynamics were run to pre-equilibrate the system. The NVT MD simulation was initiated by quenching the system to the non-spin-polarized Born−Oppenheimer potential surface with the Perdew−Becke−Erzenhof generalized gradient approximation (GGA) exchange-correlation functional[58] and ultrasoft pseudopotentials[59]. Plane waves were included up to 30 Rydberg and the Brillouin zone sampled at the Γ point. Self-consistent-field (SCF) electronic energies were converged to 1×10^{-7} Ha. The converged wavefunction was subsequently used to perform Car–Parrinello molecular dynamics [57] (CPMD) at 473 K with a time step of 0.12 fs. A Nose-Hoover thermostat was used for both ions and electrons. The electronic temperature was set to 0.02 K with frequency 10000 cm^{-1}. The fictitious electron mass was set to 400 atomic unit.

The pre-equilibrated structure, wavefunction, atomic velocities and thermostat were used for the subsequent metadynamics [65,66] simulation with a total simulation time of 12.5 ps. The time step and thermostat setting were the same as those in the MD simulation. The collective variable was chosen to be the Cu-Al coordination number (CN), defined as

$$CN = \frac{1 - \left(\frac{d_{ij}}{d_0}\right)^p}{1 - \left(\frac{d_{ij}}{d_0}\right)^{p+q}}$$

(B13)

where d_{ij} is defined as distance between Al and Cu and p and q are arbitrary scaling constants. Values of other parameters are summarized in Table B11. d_0 was chosen as largest Cu-Al separation distance observed in the regular *NVT* MD simulation at 473 K. The k and μ were

chosen such that the Lagrangian collective variable s and the physical collective variable S stay close, and that S fluctuates frequently at each position in the configuration space.

B9. Electrostatics

We estimated the electrostatic interaction between a Cu^I ion and its charge-compensating Al center using Coulomb's Law. We assumed Cu and Al to be elementary positive and negative point charges, respectively, carrying the same electric charge as a proton, 1.6×10^{-19} C, and we used the computed dielectric constant of CHA-zeolite (ε_r), 2.7, reported by Rybicki and Sauer[67]. The equilibrium Cu-Al distance of 4.6 Å taken from the DFT-optimized $Cu^I(NH_3)_2$ structure was used as the initial Cu-Al distance in the calculation. The energy of ionic separation of Cu^I and framework Al from 4.6 Å to r was calculated following Coulomb's law:

$$F = \frac{k_e}{\varepsilon_r} \frac{q_{Cu} q_{Al}}{r^2}$$

(B14)

$$\Delta E = N_a \int_{4.6\text{Å}}^{r} F dr^*$$

(B15)

where k_e is the electric force constant in vacuum, N_a is the Avogadro constant, ε_r is dielectric constant of CHA-zeolite, q_{Cu} and q_{Al} are Cu and Al charges, and r is the Cu-Al distance.

The computed Coulombic potential as a function of Cu-Al distance was plotted and compared with the metadynamics-computed free energy profile in Figure 3.5. The Coulombic potential and the computed free energy are similar up to 7 Å, consistent with electrostatics dominating the interaction. The computed free energy is slightly more positive than the Coulombic potential for Cu-Al distance between 7 Å and 8 Å, highlighting the activation barrier for $Cu^I(NH_3)_2$ to travel through an 8-member-ring window to a neighboring CHA cage, which is not captured by the Coulombic model. The computed free energy falls after $Cu^I(NH_3)_2$ reaches the new cage and stays relatively invariant thereafter. The Coulombic potential continues to increase rapidly and surpasses the computed free energy above 8 Å. Such difference can be rationalized by many-body long range Coulombic interaction between $Cu^I(NH_3)_2$ and framework Al in periodic images in the metadynamics simulation, which intrinsically lower the computed free energy compared to a two-point-charge Couloumbic model.

B10. Stochastic Simulation

Here, we estimate the fraction of Cu^I able to form an oxo-bridged dimer (Figure 3.4), given a density of Cu and Al atoms in a CHA zeolite and a maximum distance that each Cu can diffuse from its charge compensating Al. Cu number densities between 7×10^{-4} and 0.99 Cu/1000 $Å^3$ and Cu-Al diffusion distances (represented by the green spheres in Figure B.3B) from 5-12.5 Å were modeled (Figure B16); procedural details are described below.

We use a 1536 T-site CHA periodic supercell[19] with a total volume of 1.0172×10^5 $Å^3$. The large cell size was used to avoid bias due to an even or odd number of exchanged Cu present at smaller cell sizes and long Cu diffusion distances. We performed stochastic simulations as a function of Si/Al (spanning 2 to 511), Cu/Al (0.0059 to 1), and a maximum Cu diffusion distance of 12.5 Å from the compensating framework Al atom.

A 2D schematic representation of the simulation scheme is shown below; the actual simulation was carried out on the 3D CHA lattice described above. In step [1], CHA T-sites were randomly populated with Al avoiding any Al-Al first-nearest-neighbors (Loewenstein's rule)[34]. In step [2], we associated Cu ions with these Al, obeying the previously validated rule[10] that 2Al 6MR sites first exchange Cu^{II} before remaining 1Al sites exchange $Cu^{II}OH$. Three types of Al exist at this point: those that are not associated with a Cu ion, those that compensate a $Cu^{II}OH$, and 2Al 6MR sites that share a Cu^{II}. In step [3], we delete from the lattice the Cu-free Al sites and one member of every Al pair that compensate a Cu^{II} ion. In step [4], we created an Al-Al neighbor list, including only neighbors that are within twice the prescribed Cu diffusion radius. In step [5], we then deleted overlapping pairs at random from the neighbor list, stopping when the number of available pairs vanishes. We recorded the number of remaining entries divided by the initial number of Cu as the Cu^I fraction. The simulation was then repeated until the average Cu^I fraction converged.

As we explored different Si/Al and Cu/Al ratios, we discovered that results were sensitive to total initial Cu^I density and insensitive to the underlying Si/Al and Cu/Al ratios. Results are shown in Figure B16, plotted as final Cu^I fraction vs initial Cu^I density, for a range of diffusion distances. Simulation results are of course discrete; for visual convenience we present the data using cubic spline interpolation. A diffusion distance of 9 Å, consistent with predictions from the metadynamics simulation (Figure 3.5), predicts final Cu^I fractions in close agreement with experimental observation (Figure B.3A).
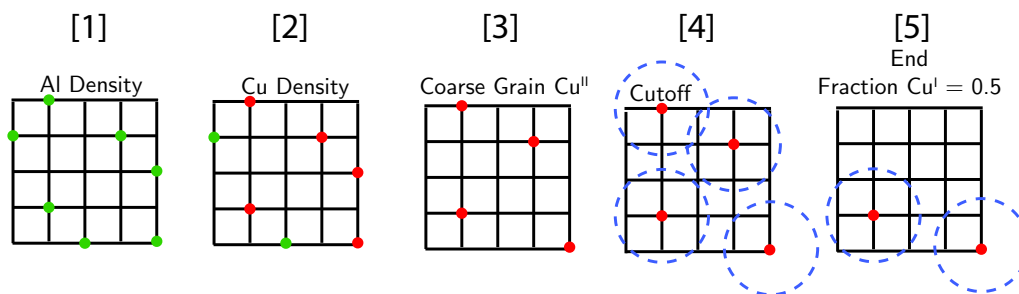
To provide a visual representation of the simulation results, we took a snapshot of steps [3] and [5] for one simulation iteration at the initial Cu densities for the Cu-CHA zeolites represented in Figure B.3A. Cartesian coordinates of Al charge compensated by Cu were extracted from the stochastic simulations and green spheres 9 Å in radius were plotted, representing the maximum diffusion length of each $Cu^I(NH_3)_2$ (Figure B.3B, t=0). Spheres are translucent so that overlapping spheres are easily visualized and periodic boundary conditions used to show the diffusion range of Cu across the supercell boundaries. Intersecting spheres around Cu coordinates were plotted both before step [3] and after step [5] pairing to show the geometrically isolated Cu (Iso) and statistically isolated "musical chairs" Cu (MC).
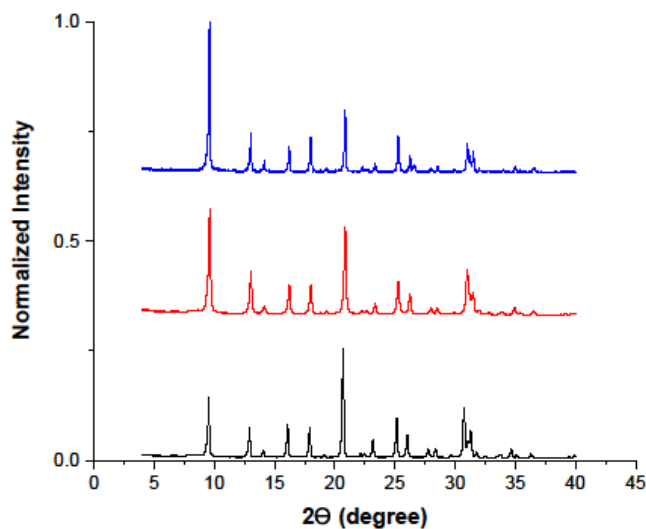
Figure B1. X-Ray diffraction patterns of H-SSZ-13 zeolites with Si/Al = 4.5 (blue), Si/Al = 15 (red), and Si/Al = 25 (black), measured using a Cu K-alpha source (λ = 0.154 nm). Diffraction patterns are vertically offset for clarity. Cu-exchanged forms of these materials show equivalent XRD patterns[68].
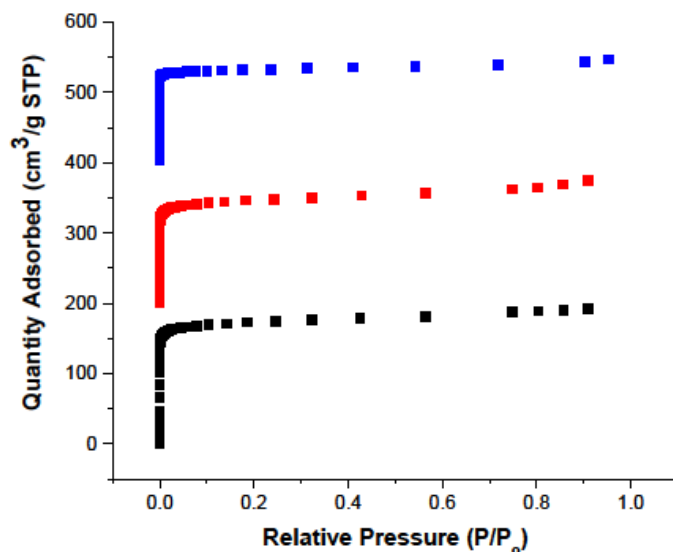
Figure B2. Ar adsorption isotherms on H-SSZ-13 with Si/Al = 4.5 (blue), Si/Al = 15 (red), and Si/Al = 25 (black). Isotherms are vertically offset for clarity (Si/Al=15: by 200 cm^3 g^{-1}, Si/Al=25: by 400 cm^3 g^{-1}). Cu-exchanged forms of these materials show similar adsorption isotherms, with slight decreases in micropore volumes caused by the presence of Cu[68].
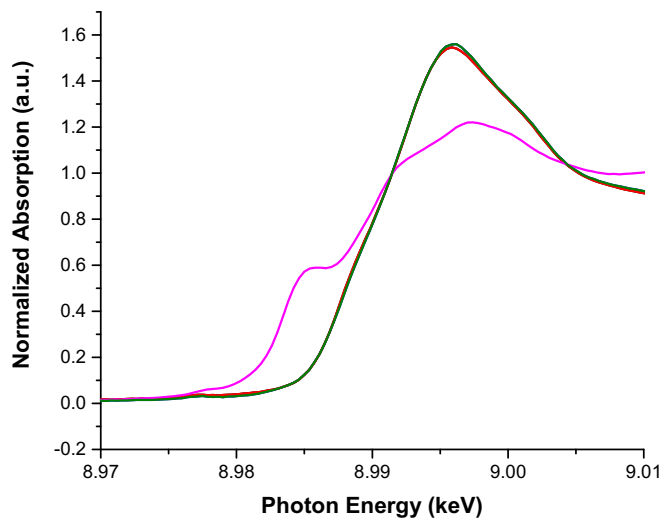
Figure B3. XANES spectra for Cu-CHA-20 (red) and Cu-CHA-29 (green) at ambient conditions, and for bulk Cu^{II}O (pink).
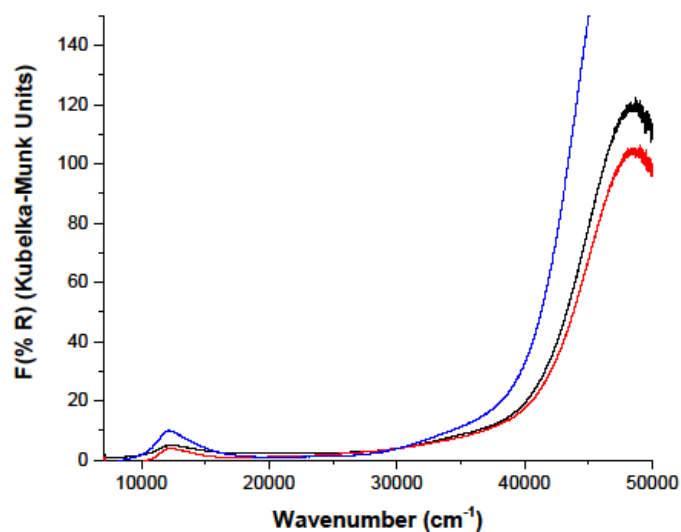
Figure B4. UV-Vis spectra for Cu-CHA-15 (blue), Cu-CHA-20 (black), and Cu-CHA-29 samples (red) recorded at ambient conditions.
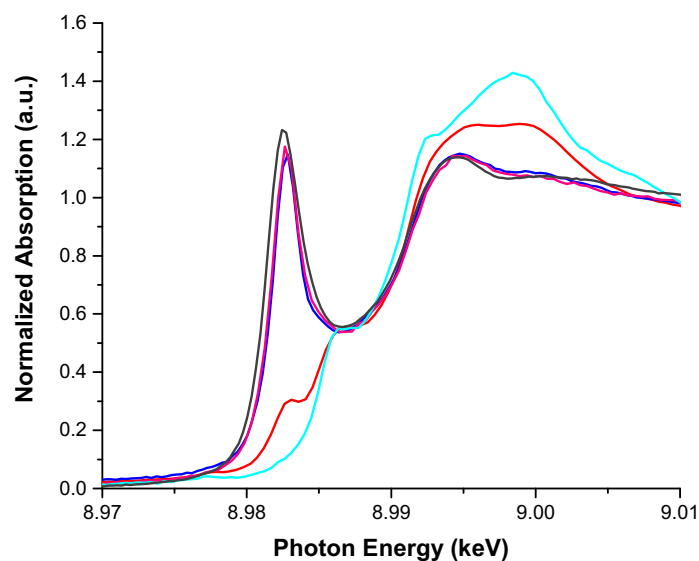
Figure B5. *Operando* XANES spectra of Cu-CHA-15 (red) and Cu-CHA-29 (dark blue) during steady-state standard SCR (300 ppm NO, 300 ppm NH_3, 10% O_2, 2% H_2O, 5% CO_2, 463-473 K). Reference spectra for aqueous $Cu^I(NH_3)_2$ (grey), isolated Cu^I (*10*) (pink) and isolated Cu^{II} (light blue) sites[10].
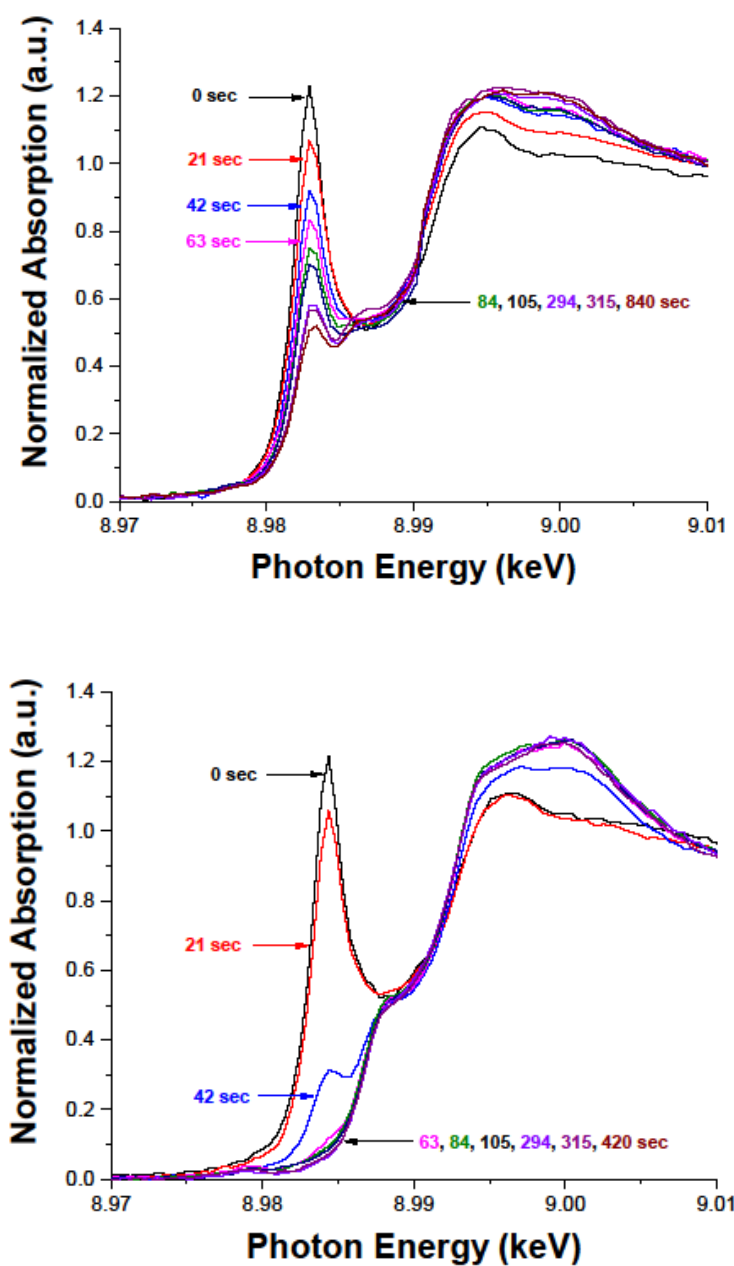
Figure B6. XANES spectra collected during transient oxidation of the reduced forms of Cu-CHA-29 sample with 10% O_2 (top) and 100 ppm NO_2 (bottom), as a function of time (labeled in figure).
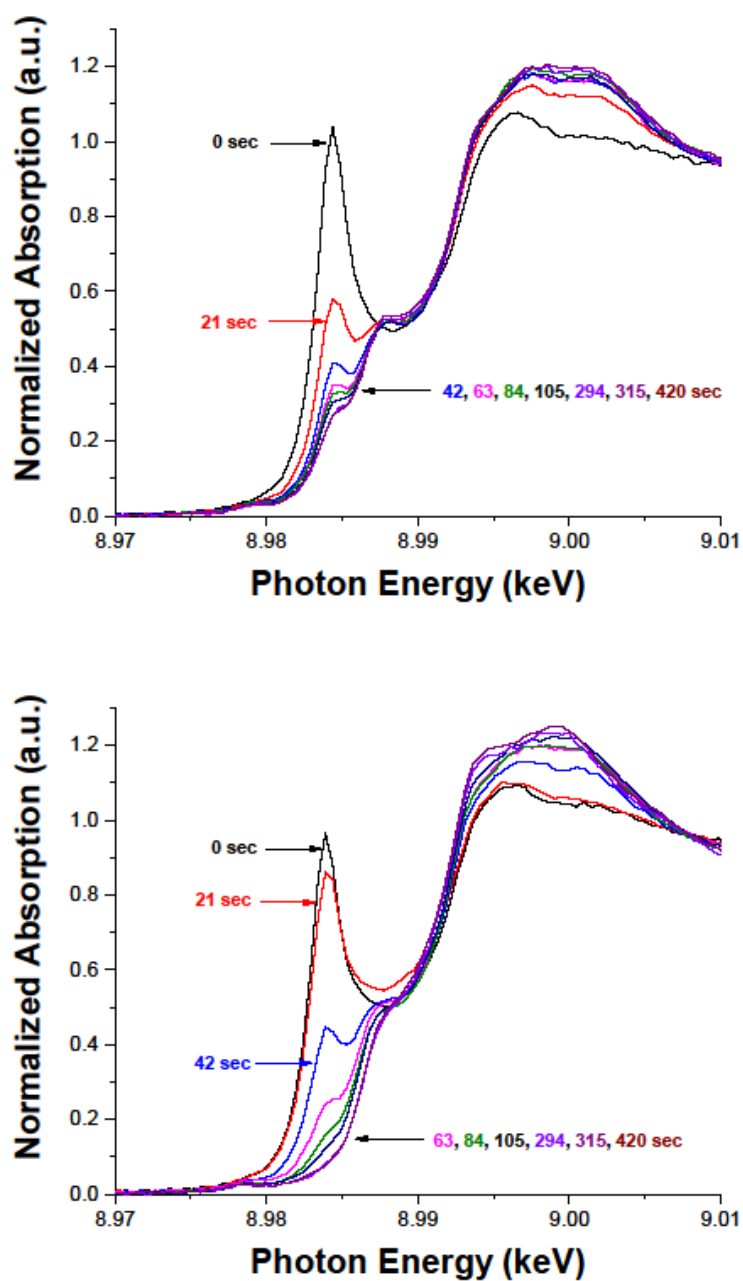
Figure B7. XANES spectra during transient oxidation of the reduced forms of Cu-CHA-20 sample with 10% O_2 (top) and 100 ppm NO_2 (bottom), as a function of time (labeled in figure).
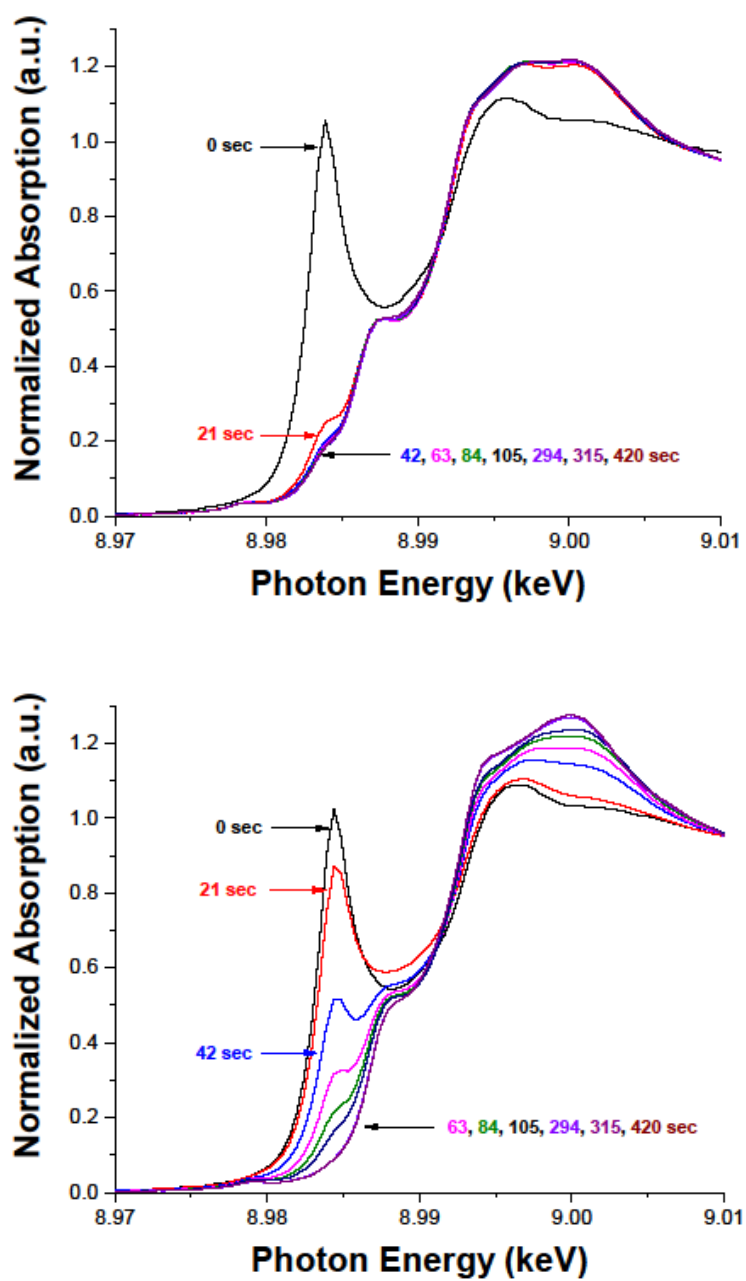
Figure B8. XANES spectra during transient oxidation of the reduced forms of Cu-CHA-15 sample with 10% O_2 (top) and 100 ppm NO_2 (bottom), as a function of time (labeled in figure).
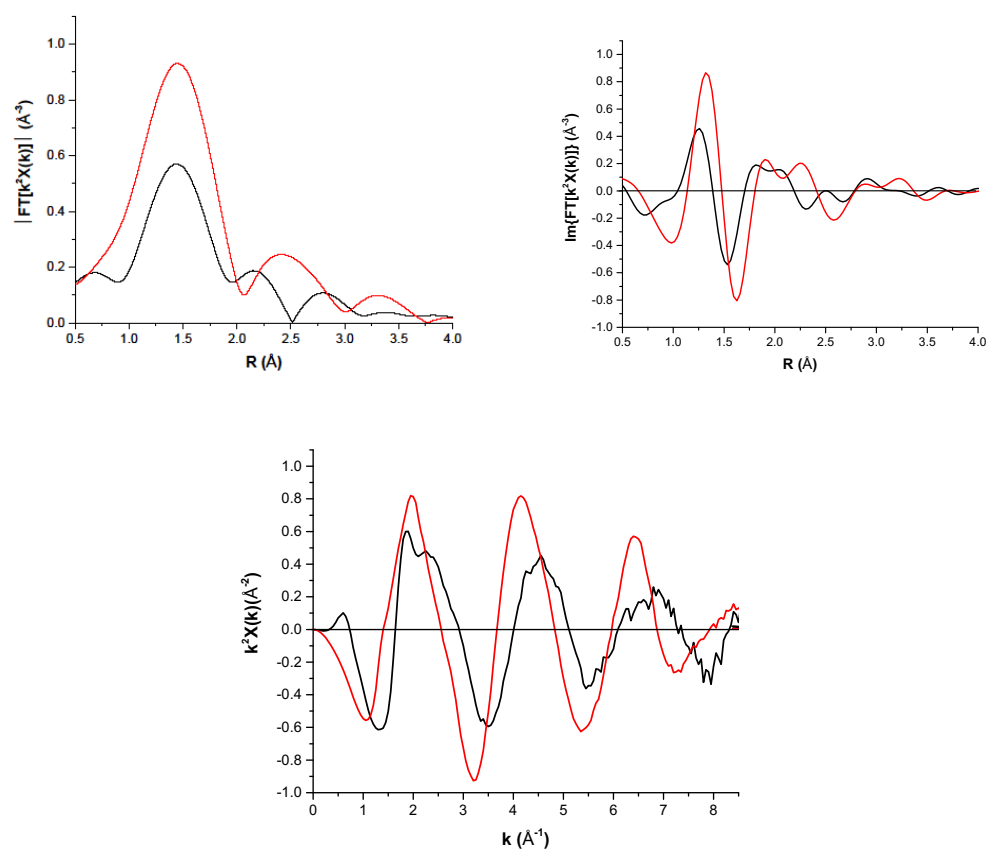
Figure B9. The k^2 weighted Fourier transform (moduli and imaginary parts of FT on top left and top right, respectively) and raw EXAFS spectra (bottom) collected before (black) and after (red) oxidation with 10% O_2 at 473 K, starting from the reduced $Cu(I)(NH_3)_2$ state of Cu-CHA-29.
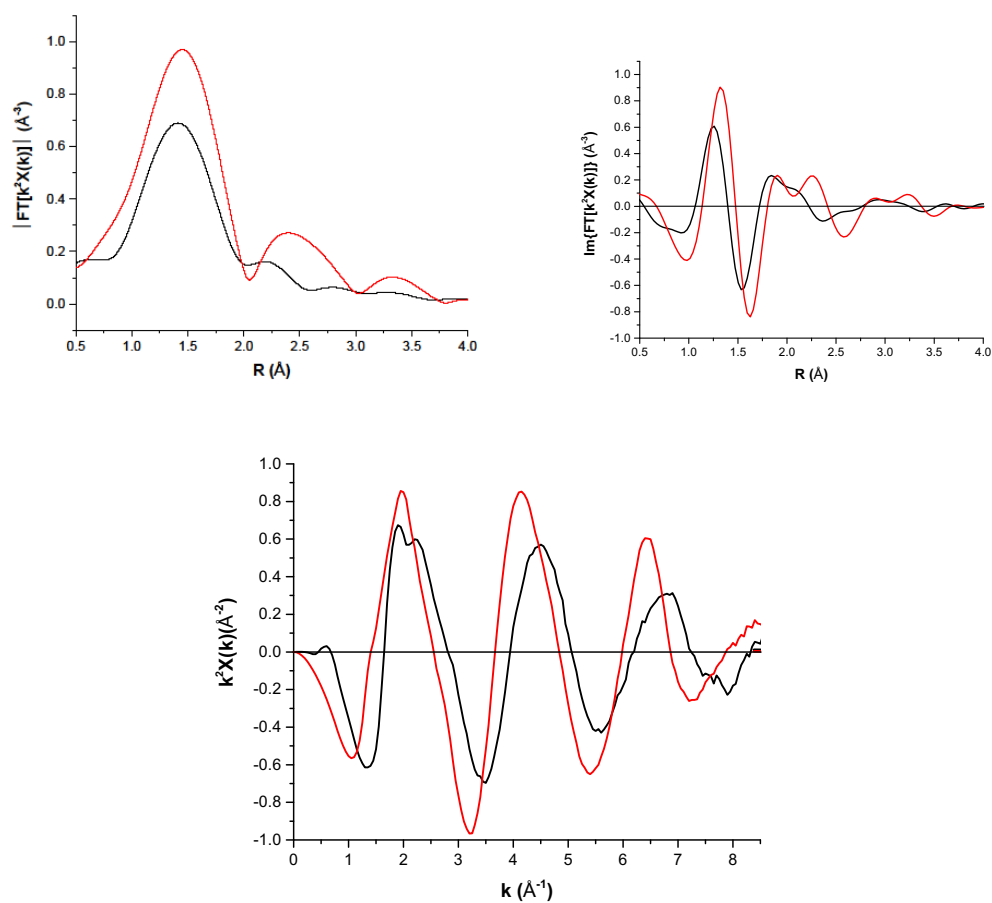
Figure B10. The k^2 weighted Fourier transform (moduli and imaginary parts of FT on top left and top right, respectively) and raw EXAFS spectra (bottom) collected before (black) and after (red) oxidation with 10% O_2 at 473 K, starting from the reduced $Cu(I)(NH_3)_2$ state of Cu-CHA-20.
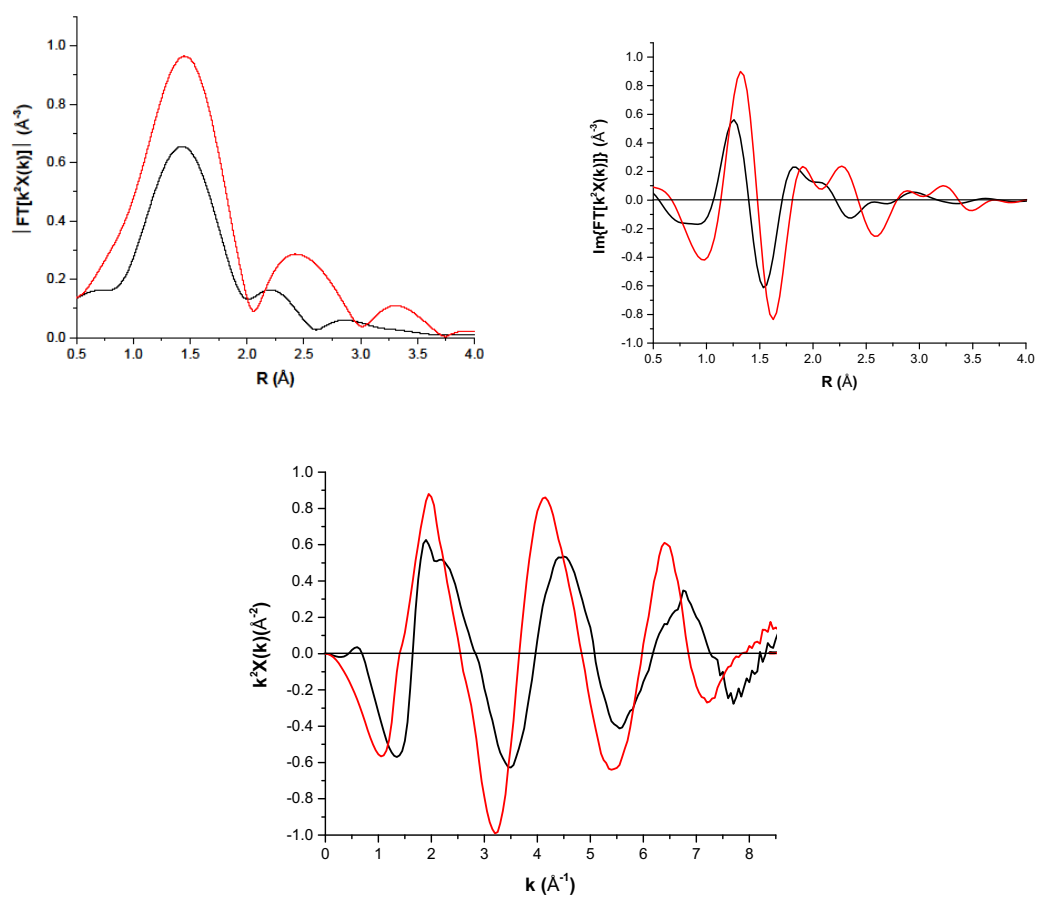
Figure B11. The k^2 weighted Fourier transform (moduli and imaginary parts of FT on top left and top right, respectively) and raw EXAFS spectra (bottom) collected before (black) and after (red) oxidation with 10% O_2 at 473 K, starting from the reduced $Cu(I)(NH_3)_2$ state of Cu-CHA-15.
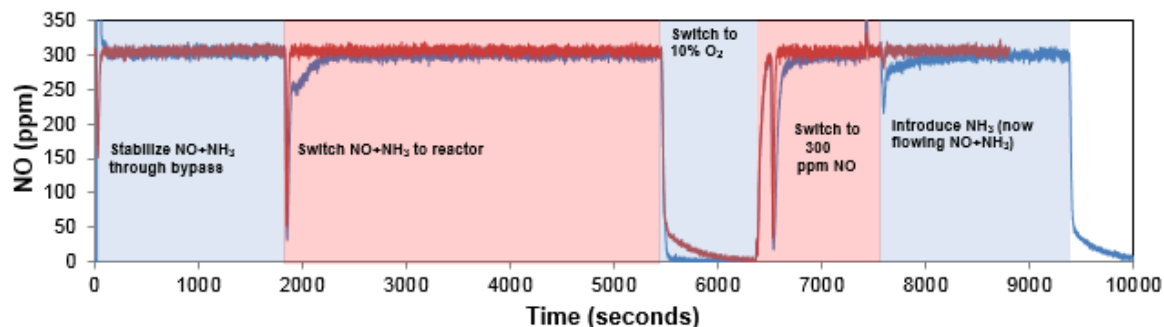
Figure B12. NO concentrations measured in the reactor effluent during five step-wise treatments of Cu-CHA-15, in order to quantify NO consumption (per Cu) in treatment steps 2, 4, and 5 above, which correspond to different steps in the proposed standard SCR cycle (Figure 6). Red and blue traces indicate experiments with the blank reactor and catalyst-loaded reactor, respectively.
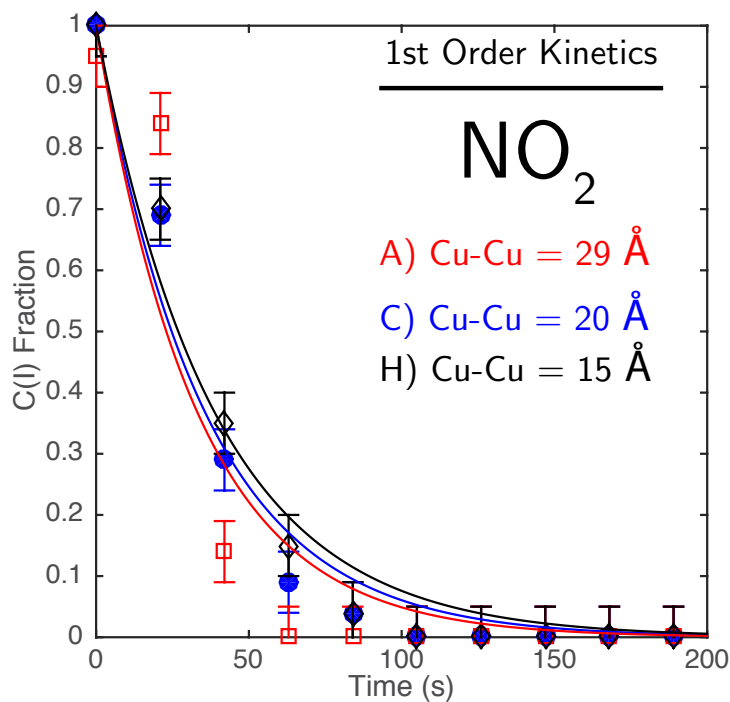
Figure B13. Temporal evolution of the XANES-measured Cu^I fraction in Cu-CHA-29 (A, red), Cu-CHA-20 (C, blue), and Cu-CHA-15 (H, black) during transient oxidation in 100 ppm NO_2 at 473 K. Least-squares fit to Eq. B11 is shown by solid lines.
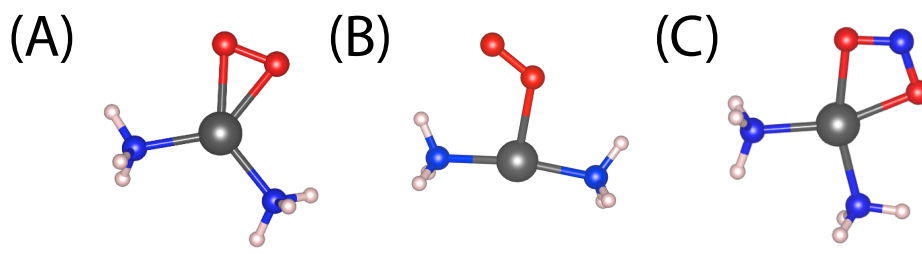
Figure B14. Structures for O_2 configuration (A), O_2 configuration (B) and NO_2 (C) adsorbed on a single $Cu^I(NH_3)_2$. Calculations were performed in the CHA supercell described in B5, and the framework removed from this figure for clarity.
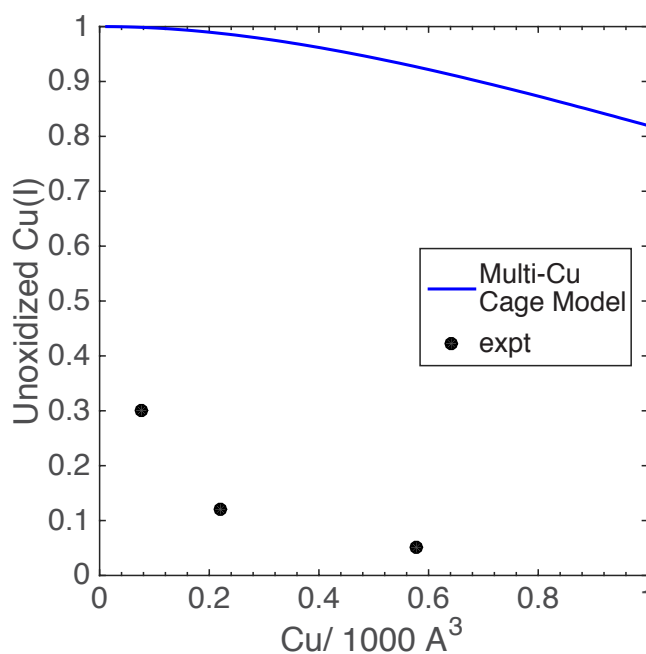
Figure B15. The fraction of lone Cu within zeolite cages randomly dispersed on the zeolite framework unable to oxidize compared with experimental measurements.
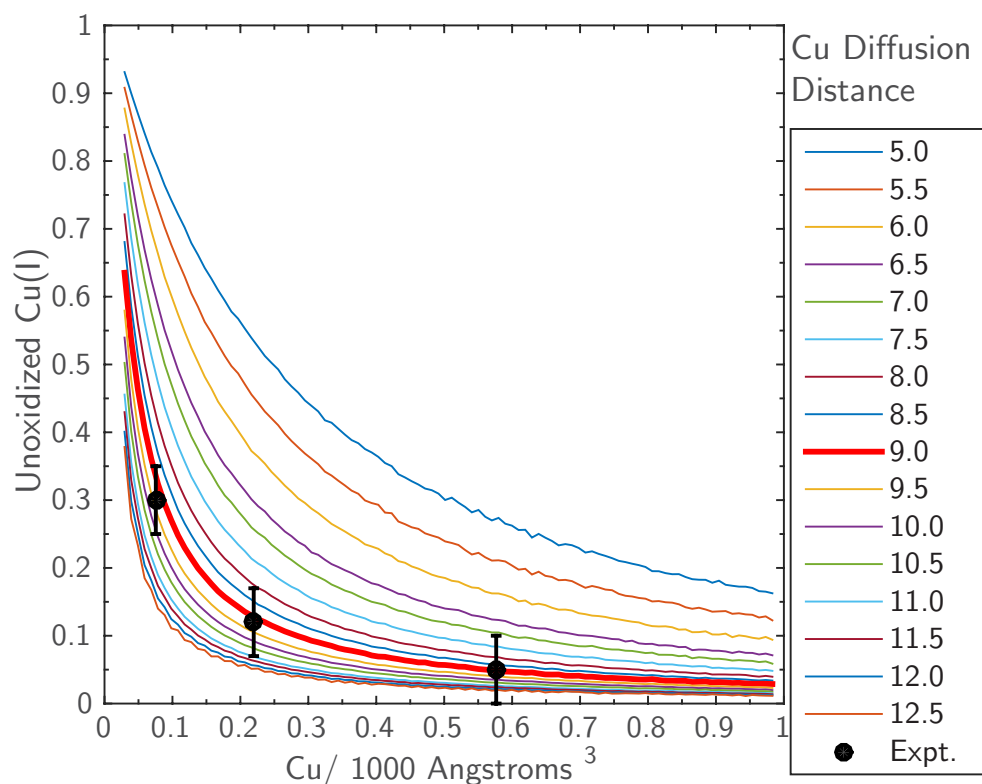
Figure B16. Fraction of unoxidizable Cu^I as a function of Cu density from simulation. Splines were drawn through the discrete simulations at each density to yield continuous curves in the figure. 9 Å (bold red line) represents the metadynamics-predicted maximum Cu diffusion distance. Black data points are experimental observations from Figure 3.3A.
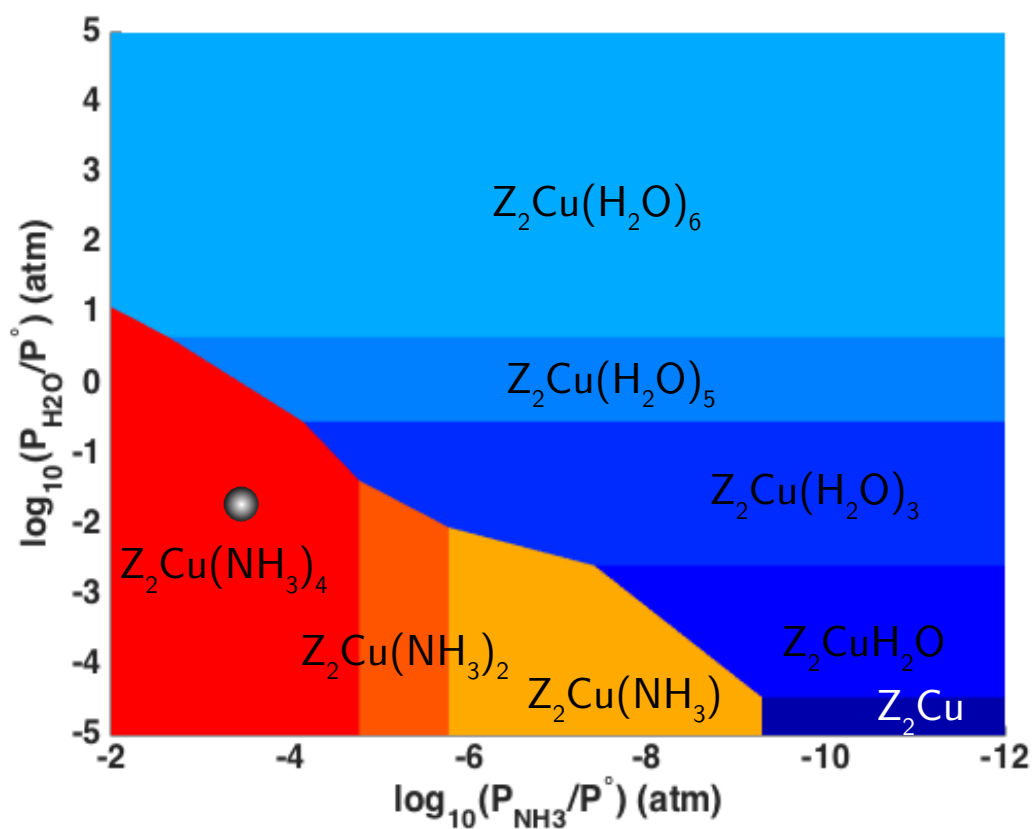
Figure B17. Phase diagrams for 2Al ("Z_2") exchanged Cu sites with varying P_{NH3} and P_{H2O} at 473 K and 10% O_2. The chrome sphere demarcates NH_3 and H_2O pressures equivalent to those used in the kinetic experiments reported in figure 3.1B and figure 3.2. All DFT-computed structures, energies, and methods used to generate this diagram can be found in Paolucci et al.[10].
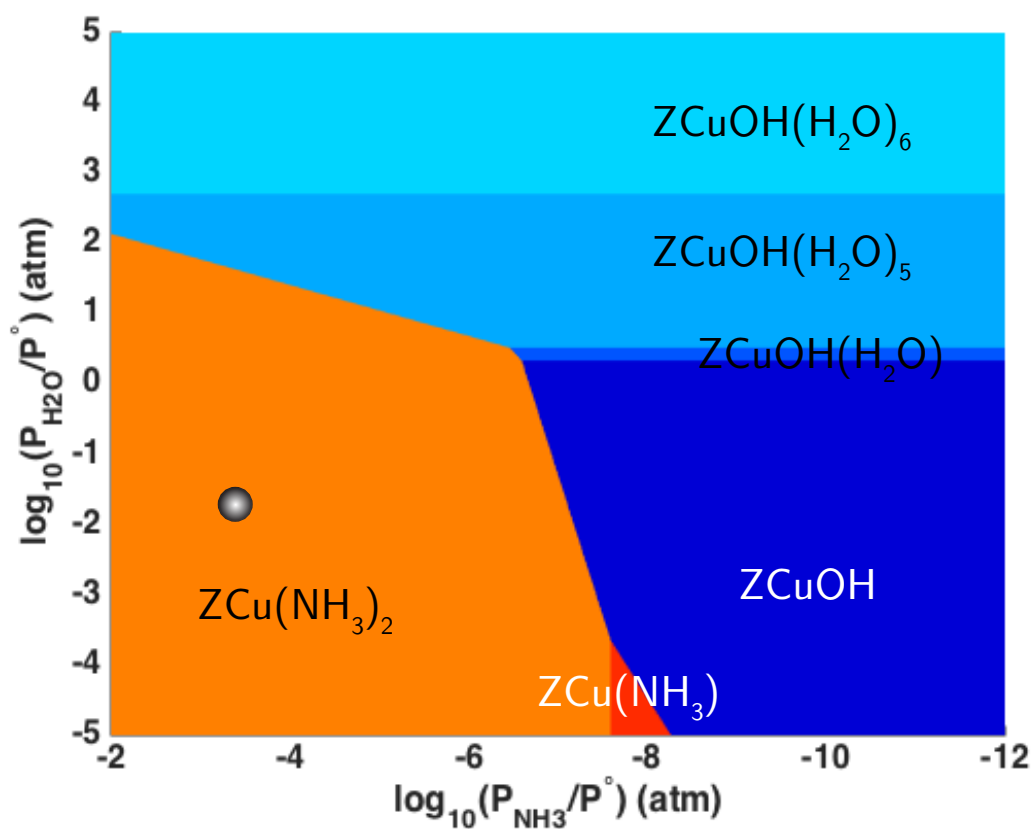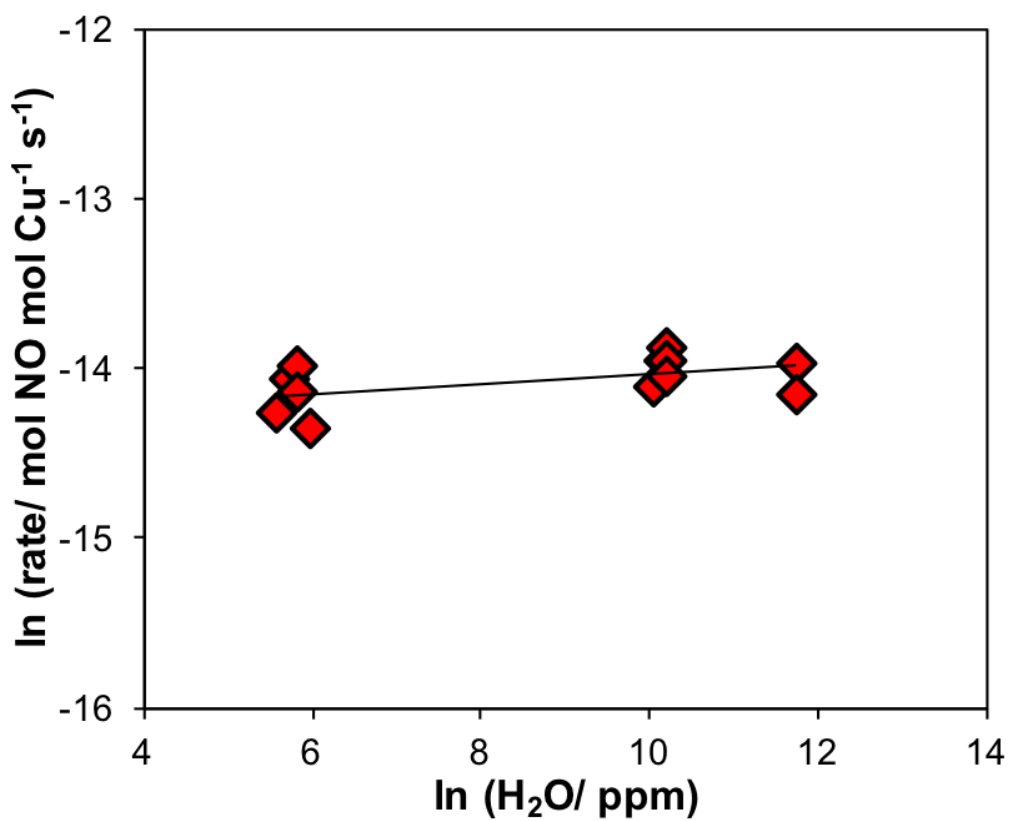
Figure B18. Phase diagrams for 1Al ("Z") exchanged Cu sites with varying P_{NH3} and P_{H2O} at 473 K and 10% O_2. The chrome sphere demarcates NH_3 and H_2O pressures equivalent to those used in the kinetic experiments reported in figure 3.1B and figure 3.2. All DFT-computed structures, energies, and methods used to generate this diagram can be found in Paolucci et al.[10].

Figure B19. Dependence of SCR turnover rates (300 ppm NO, 300 ppm NH$_3$, 10% O$_2$, 7% CO$_2$, 200-120000 ppm H$_2$O and balance N$_2$ at 473 K) on H$_2$O pressure on Cu-CHA-19. Line denotes regression of power rate law to measured rate data, with a best-fit slope of 0.03, corresponding to the apparent H$_2$O reaction order.
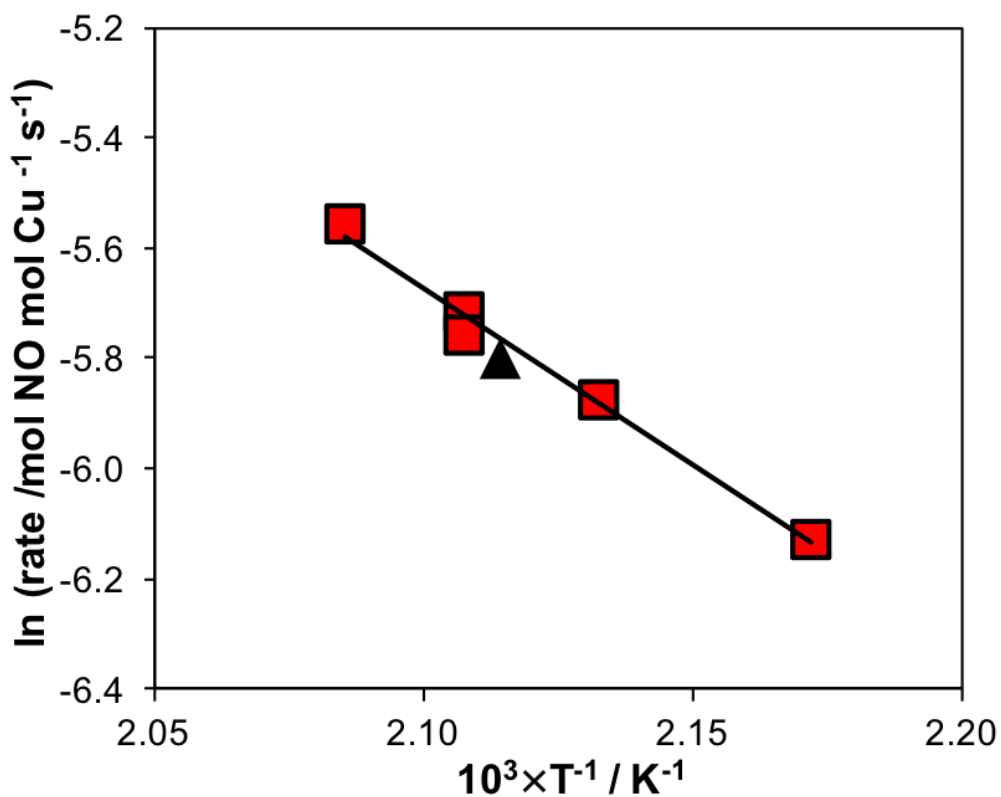
Figure B20. Standard SCR rates (300 ppm NO, 300 ppm NH$_3$, 10% O$_2$, 7% CO$_2$, 3% H$_2$O and balance N$_2$) measured in the temperature range of 450-480 K on Cu-CHA-19 in the laboratory differential PFR (red squares) and in the *operando* XAS reactor (black triangle). Line denotes regression of an Arrhenius rate equation to the lab PFR rate data.

Table B1. Bulk elemental analysis and fraction of isolated Cu^{II} and $Cu^{II}(OH)$ sites on a series of Cu-exchanged SSZ-13 samples with varying Si/Al (4.5-25) and Cu/Al (0.03-0.59); arranged by increasing Cu/Al for a fixed Si/Al ratio.

Si/Al	Cu/Al	Cu wt%	H^+/Al (H-form)	H^+/Al (Cu-form)	$Cu^{II}OH$/Al*	Cu^{II}/Al*
4.5	0.08	1.4	0.46	0.31	0	0.08
4.5	0.21	3.7	0.87	0.42	0	0.21
15	0.03	0.3	0.98	0.93	0	0.03
15	0.08	0.5	0.98	0.81	0	0.08
15	0.10	0.7	0.98	0.80	0.01	0.09
15	0.12	0.8	0.98	0.73	0.03	0.09
15	0.19	1.3	0.98	0.68	0.10	0.09
15	0.25	1.7	1.00	0.64	0.16	0.09
15	0.37	2.4	0.98	0.58	0.28	0.09
15	0.44	2.9	0.98	0.51	0.35	0.09
25	0.21	0.8	0.98	0.74	0.17	0.04
25	0.42	1.6	0.98	0.58	0.37	0.04
25	0.59	2.4	0.98	0.47	0.55	0.04

*Determined from titration of residual H^+ sites by NH_3 and thermodynamic preferences for Cu^{II} and $Cu^{II}OH$ siting.

Table B2. A series of Cu-exchanged SSZ-13 samples with varying Si/Al (4.5-25) and Cu/Al (0.03-0.44) (X = Mean Cu-Cu distance in Å, rounded down, labels (a-h) correspond to those in Figure 3.2); arranged by increasing Cu/Al for a fixed Si/Al ratio.

Si/Al	Cu/Al	Cu cation density (mol Cu/m³)	Cu /1000Å³	Cu per CHA cage	Mean Cu-Cu distance (Å)	Cu-CHA-X
4.5	0.08	365	0.22	0.17	20.6	Cu-CHA-20 (c)
4.5	0.21	958	0.57	0.44	15.0	Cu-CHA-15 (h)
15	0.03	47	0.03	0.02	40.7	Cu-CHA-40
15	0.08	125	0.07	0.05	29.4	Cu-CHA-29 (a)
15	0.10	157	0.09	0.07	27.2	Cu-CHA-27
15	0.12	188	0.11	0.08	25.6	Cu-CHA-25
15	0.19	298	0.18	0.14	22.0	Cu-CHA-22
15	0.25	395	0.23	0.18	20.1	Cu-CHA-20*
15	0.37	580	0.35	0.27	17.6	Cu-CHA-17 (f)
15	0.44	689	0.41	0.31	16.6	Cu-CHA-16 (g)
25	0.21	193	0.11	0.08	25.4	Cu-CHA-25 (b)
25	0.42	395	0.24	0.18	19.8	Cu-CHA-19 (d)
25	0.59	569	0.34	0.26	17.7	Cu-CHA-17*(e)

*Identifies the higher Si/Al density sample of two samples that share the same mean (rounded down) Cu-Cu distance.

Table B3. Standard SCR kinetic parameters measured on a series of Cu-exchanged SSZ-13 samples with Si/Al = 15 and Cu/Al varying from 0.03-0.44; arranged by increasing Cu/Al. (X = Mean Cu-Cu distance in Å, rounded down, labels (a, f, and g) correspond to those in Figure 3.2)

Cu-CHA-X	Cu /1000Å^3	SCR Rate (/10^{-3} mol NO/mol Cu/s)	SCR Rate (/10^{-3} NO/1000Å^3/s)	O$_2$ order[†]	E$_{app}$[‡] (kJ mol^{-1})
Cu-CHA-40 (a)	0.03	1.8	0.05	0.8	47
Cu-CHA-29	0.07	2.3	0.16	0.7	50
Cu-CHA-27	0.09	3.3	0.30	0.7	56
Cu-CHA-25	0.11	4.5	0.50	0.7	56
Cu-CHA-22	0.18	6.5	1.17	0.5	60
Cu-CHA-20*	0.23	7.8	1.79	0.4	63
Cu-CHA-17 (f)	0.35	7.4	2.59	0.4	66
Cu-CHA-16 (g)	0.41	7.8	3.20	0.3	74

*Identifies the higher Si/Al density sample of two samples that share the same mean (rounded down) Cu-Cu distance.

†Errors in the apparent O$_2$ rate order are ± 0.1.

‡Errors in the apparent activation energy (E$_{app}$) are ± 7 kJ/mol. Consistent with prior reports (17, 18) E$_{app}$ increases systematically with increasing Cu density, reflecting the gradual transition from a kinetic regime in which O$_2$ activation is rate-determining (low Cu density) to one in which it is not (high Cu density).

Table B4. *Operando* steady state Cu^I fraction for a series of Cu-SSZ-13 samples with varying Cu density from 0.07-0.57 atom/1000Å^3. Feed conditions: 300 ppm NO, 300 ppm NH$_3$, 10% O$_2$, 5% CO$_2$, 2% H$_2$O, 473 K.

Si/Al	Cu/Al	Cu-CHA-X	Cu cation density (Cu/1000Å^3)	*Operando* steady state Cu^I fraction[†]	EXAFS first shell coordination number
4.5	0.08	Cu-CHA-20 (c)	0.22	0.50	3.4
4.5	0.21	Cu-CHA-15 (h)	0.57	0.10	3.9
15	0.08	Cu-CHA-29 (a)	0.07	0.96	2.1
15	0.37	Cu-CHA-17 (f)	0.35	0.53	3.2
15	0.44	Cu-CHA-16 (g)	0.41	0.47	3.3
25	0.21	Cu-CHA-25 (b)	0.11	0.85	2.4
25	0.42	Cu-CHA-19 (d)	0.24	0.63	2.8
25	0.59	Cu-CHA-17*(e)	0.34	0.51	3.1
16 (20)	0.20	-	0.18	0.60	-
4.5 (17)	0.16	-	0.44	0.26	-

*Identifies the higher Si/Al density sample of two samples that share the same mean (rounded down) Cu-Cu distance.

†Errors are ± 0.05.

Table B5. Comparison of standard SCR reaction rates measured in the PFR and the *operando* reactor for different Cu-CHA samples. Feed conditions: 300 ppm NO, 300 ppm NH_3, 10% O_2, 5% CO_2, 2% H_2O, 473 K.

Si/Al	Cu/Al	Cu-CHA-X	PFR Rate (/10^{-3} mol NO/mol Cu/s)	*Operando* Reactor Rate (/10^{-3} mol NO/mol Cu/s)
4.5	0.08	Cu-CHA-20	8.3	8.0
4.5	0.21	Cu-CHA-15	7.4	7.5
15	0.08	Cu-CHA-29	2.3	2.0
15	0.37	Cu-CHA-17	7.4	7.4
15	0.44	Cu-CHA-16	7.8	7.7
25	0.21	Cu-CHA-25	1.6	1.5
25	0.42	Cu-CHA-19	3.8	3.1
25	0.59	Cu-CHA-17*	7.7	7.0

*Identifies the higher Si/Al density sample of two samples that share the same mean (rounded down) Cu-Cu distance.

Table B6. Fitted Cu^I fraction before and after oxidation with 10% O_2 at 473 K starting from $Cu^I(NH_3)_2$ for Cu-CHA-20, Cu-CHA-15 and Cu-CHA-29.

Cu-CHA-X	Cu^I fraction before O_2 transients*	Cu^I fraction after O_2 transients*
Cu-CHA-20	0.90	0.12
Cu-CHA-15	0.90	0.05
Cu-CHA-29	0.98	0.30

*Fitting error ± 0.05.

Table B7. Fitted Cu^I fraction before and after repeated subsequent oxidation with 10% O_2 at 473 K starting from $Cu^I(NH_3)_2$ in each cycle for Cu-CHA-29.

Cu^I fraction before O_2 transients	Cu^I fraction after O_2 transients
Cycle 1	
0.98	0.30
Cycle 2	
0.95	0.32
Cycle 3	
0.98	0.31

Table B8. Fitted Cu^I fraction before and after oxidation with 100 ppm NO_2 at 473 K starting from $Cu^I(NH_3)_2$ for Cu-CHA-20, Cu-CHA-15 and Cu-CHA-29.

Cu-CHA-X	Cu^I fraction before NO_2 transients	Cu^I fraction after NO_2 transients
Cu-CHA-20	0.90	0.00
Cu-CHA-15	0.90	0.00
Cu-CHA-29	0.98	0.00

Table B9. PBE+D2 DFT computed reaction energies (column 2), total energy differences along the reaction coordinate (column 3), and normalized Bader charge[10] derived Cu oxidation states for the product in each step (column 4) for all results reported in Figure 3.4.

Reaction	Reaction Energy (kJ mol^{-1})	Energy (kJ mol^{-1})	Cu Oxidation State
A	-	0	1.00
A → TS1	35	35	
TS1 → B	23	23	1.00
B → C	-59	-36	1.39
C → TS2	20, Ref (25)	-16	
TS2 → D	-26	-42	1.80
D → TS3	19	-23	
TS3 → E	-36	-60	2.10

Table B10. Computed PBE+D2 and HSE06+TSvdw reaction energies for O_2 and NO_2 adsorption on a $Cu^I(NH_3)_2$ monomer. Rows 1 and 2 reference the two different (A, B) O_2 adsorption configurations in Figure B14. Columns 3 and 5 report the normalized Bader charge[10] derived Cu oxidation state.

	PBE+D2 (kJ mol^{-1})	Cu Oxidation State	HSE06+TSvdw (kJ mol^{-1})	Cu Oxidation State
$Cu^I(NH_3)_2+O_2$ (A)	2	1.65	1	1.47
$Cu^I(NH_3)_2+O_2$ (B)	-26	1.32	-11	1.15
$Cu^I(NH_3)_2+NO_2$ (C)	-46	1.92	-71	2.27

Table B11. Metadynamics parameters.

Parameter	CV
Harmonic spring constant, k (hartree)	5
Mass of the fictitious particle, μ (hartree (a.u.)^2)	100
Gaussian height, W (hartree)	0.0005
Gaussian width, s'	0.02
Minimum Metadyanmics time step, Δt_{min} (a.u.)	100
p	6
q	6
d_0 (Å)	6.2

B11. References

1.   J. M. Thomas, The societal significance of catalysis and the growing practical importance of single-site heterogeneous catalysts. *Proc. R. Soc. A* **468**, 1884-1903 (2012).
2.   M. Boudart, Turnover Rates in Heterogeneous Catalysis. *Chemical Reviews* **95**, 661-666 (1995).
3.   K. Ding *et al.*, Identification of active sites in CO oxidation and water-gas shift over supported Pt catalysts. *Science* **350**, 189-192 (2015).
4.   J. Jones *et al.*, Thermally stable single-atom platinum-on-ceria catalysts via atom trapping. *Science* **353**, 150-154 (2016).
5.   E. J. Peterson *et al.*, Low-temperature carbon monoxide oxidation catalysed by regenerable atomically dispersed palladium on alumina. *Nature Communications* **5**, 4885 (2014).
6.   G. Kyriakou *et al.*, Isolated Metal Atom Geometries as a Strategy for Selective Heterogeneous Hydrogenations. *Science* **335**, 1209-1212 (2012).
7.   H. Wei *et al.*, FeOx-supported platinum single-atom and pseudo-single-atom catalysts for chemoselective hydrogenation of functionalized nitroarenes. *Nature Communications* **5**, 5634 (2014).
8.   M. Yang *et al.*, Catalytically active Au-O(OH)x- species stabilized by alkali ions on zeolites and mesoporous oxides. *Science* **346**, 1498-1501 (2014).
9.   M. Yang *et al.*, A Common Single-Site Pt(II)–O(OH) x – Species Stabilized by Sodium on "Active" and "Inert" Supports Catalyzes the Water-Gas Shift Reaction. *Journal of the American Chemical Society* **137**, 3470-3473 (2015).
10.   C. Paolucci *et al.*, Catalysis in a Cage: Condition-Dependent Speciation and Dynamics of Exchanged Cu Cations in SSZ-13 Zeolites. *Journal of the American Chemical Society* **138**, 6028-6048 (2016).
11.   J. M. Thomas, R. Raja, D. W. Lewis, Single-Site Heterogeneous Catalysts. *Angewandte Chemie International Edition* **44**, 6456-6482 (2005).
12.   C. Paolucci, J. Di Iorio, F. Ribeiro, R. Gounder, W. Schneider, Chapter One-Catalysis Science of NOx Selective Catalytic Reduction With Ammonia Over Cu-SSZ-13 and Cu-SAPO-34. *Advances in Catalysis* **59**, 1-107 (2016).
13.   S. T. Korhonen, D. W. Fickel, R. F. Lobo, B. M. Weckhuysen, A. M. Beale, Isolated Cu^{2+} ions: active sites for selective catalytic reduction of NO. *Chemical Communications* **47**, 800-802 (2011).
14.   E. Borfecchia *et al.*, Revisiting the nature of Cu sites in the activated Cu-SSZ-13 catalyst for SCR reaction. *Chemical Science* **6**, 548-563 (2015).
15.   C. Paolucci *et al.*, Isolation of the Copper Redox Steps in the Standard Selective Catalytic Reduction on Cu-SSZ-13. *Angewandte Chemie International Edition* **53**, 11828-11833 (2014).
16.   T. V. W. Janssens *et al.*, A Consistent Reaction Scheme for the Selective Catalytic Reduction of Nitrogen Oxides with Ammonia. *ACS Catalysis* **5**, 2832-2845 (2015).
17.   S. A. Bates *et al.*, Identification of the active Cu site in standard selective catalytic reduction with ammonia on Cu-SSZ-13. *Journal of Catalysis* **312**, 87-97 (2014).
18.   F. Gao *et al.*, Understanding ammonia selective catalytic reduction kinetics over Cu/SSZ-13 from motion of the Cu ions. *Journal of Catalysis* **319**, 1-14 (2014).
19.   C. Baerlocher, L. B. McCusker, Database of Zeolite Structures. (2017).

20. T. Günter *et al.*, Structural snapshots of the SCR reaction mechanism on Cu-SSZ-13. *Chemical Communications* **51**, 9227-9230 (2015).

21. K. A. Lomachenko *et al.*, The Cu-CHA deNO x Catalyst in Action: Temperature-Dependent NH₃ -Assisted Selective Catalytic Reduction Monitored by Operando XAS and XES. *Journal of the American Chemical Society* **138**, 12025-12028 (2016).

22. P. J. Smeets *et al.*, Oxygen Precursor to the Reactive Intermediate in Methanol Synthesis by Cu-ZSM-5. *Journal of the American Chemical Society* **132**, 14736-14738 (2010).

23. P. Vanelderen *et al.*, Spectroscopic Definition of the Copper Active Sites in Mordenite: Selective Methane Oxidation. *Journal of the American Chemical Society* **137**, 6383-6392 (2015).

24. J. S. Woertink *et al.*, A [Cu2O]2+ core in Cu-ZSM-5, the active site in the oxidation of methane to methanol. *Proceedings of the National Academy of Sciences of the United States of America* **106**, 18908-18913 (2009).

25. M. Metz, E. I. Solomon, Dioxygen Binding to Deoxyhemocyanin: Electronic Structure and Mechanism of the Spin-Forbidden Two-Electron Reduction of O₂. *Journal of the American Chemical Society* **123**, 4938-4950 (2001).

26. L. M. Mirica, X. Ottenwaelder, T. D. P. Stack, Structure and Spectroscopy of Copper−Dioxygen Complexes. *Chemical Reviews* **104**, 1013-1046 (2004).

27. L. M. Mirica *et al.*, Tyrosinase reactivity in a model complex: an alternative hydroxylation mechanism. *Science* **308**, 1890-1892 (2005).

28. P. Chen, E. I. Solomon, O2 activation by binuclear Cu sites: noncoupled versus exchange coupled reaction mechanisms. *Proceedings of the National Academy of Sciences of the United States of America* **101**, 13105-13110 (2004).

29. S. D. McCann, S. S. Stahl, Copper-Catalyzed Aerobic Oxidations of Organic Molecules: Pathways for Two-Electron Oxidation with a Four-Electron Oxidant and a One-Electron Redox-Active Catalyst. *Accounts of Chemical Research* **48**, 1756-1766 (2015).

30. B. R. Goodman, K. C. Hass, W. F. Schneider, J. B. Adams, Cluster Model Studies of Oxygen-Bridged Cu Pairs in Cu−ZSM-5 Catalysts. *The Journal of Physical Chemistry B* **103**, 10452-10460 (1999).

31. E. I. Solomon *et al.*, Copper active sites in biology. *Chemical Reviews* **114**, 3659-3853 (2014).

32. L. Chen, J. Jansson, M. Skoglundh, H. Grönbeck, Mechanism for Solid-State Ion Exchange of Cu+ into Zeolites. *The Journal of Physical Chemistry C* **120**, 29182-29189 (2016).

33. H. Falsig, P. N. R. Vennestrøm, P. G. Moses, T. V. W. Janssens, Activation of Oxygen and NO in NH3-SCR over Cu-CHA Catalysts Evaluated by Density Functional Theory. *Topics in Catalysis* **59**, 861-865 (2016).

34. W. Lowenstein, The distribution of aluminium in the tetrahedra of silicates and aluminates. *American Mineralogist* **39**, 92-96 (1954).

35. F. Gao, D. Mei, Y. Wang, J. Szanyi, C. H. F. Peden, Selective Catalytic Reduction over Cu/SSZ-13: Linking Homo- and Heterogeneous Catalysis. *Journal of the American Chemical Society* **139**, 4935-4942 (2017).

36. J. H. Kwak, R. G. Tonkyn, D. H. Kim, J. Szanyi, C. H. F. Peden, Excellent activity and selectivity of Cu-SSZ-13 in the selective catalytic reduction of NOx with NH3. *Journal of Catalysis* **275**, 187-190 (2010).

37. G. Lamble, A. Moen, D. G. Nicholson, Structure of the diamminecopper (I) ion in solution. An X-ray absorption spectroscopic study. *Journal of the Chemical Society, Faraday Transactions* **90**, 2211-2213 (1994).

38. L.-S. Kau, D. J. Spira-Solomon, J. E. Penner-Hahn, K. O. Hodgson, E. I. Solomon, X-ray absorption edge determination of the oxidation state and coordination number of copper: application to the type 3 site in Rhus vernicifera laccase and its reaction with oxygen. *Journal of the American Chemical Society* **109**, 6433-6442 (1987).

39. V. F. Kispersky, A. J. Kropf, F. H. Ribeiro, J. T. Miller, Low absorption vitreous carbon reactors for operandoXAS: a case study on Cu/Zeolites for selective catalytic reduction of NOx by NH3. *Physical Chemistry Chemical Physics.* **14**, 2229-2238 (2012).

40. A. a. Verma *et al.*, NO oxidation: A probe reaction on Cu-SSZ-13. *Journal of Catalysis* **312**, 179-190 (2014).

41. M. H. Groothaert *et al.*, Bis (μ-oxo) dicopper as Key Intermediate in the Catalytic Decomposition of Nitric Oxide. *ChemPhysChem* **4**, 626-630 (2003).

42. J. R. Di Iorio *et al.*, The Dynamic Nature of Brønsted Acid Sites in Cu–Zeolites During NOx Selective Catalytic Reduction: Quantification by Gas-Phase Ammonia Titration. *Topics in Catalysis* **58**, 424-434 (2015).

43. S. Bordiga, E. Groppo, G. Agostini, J. A. van Bokhoven, C. Lamberti, Reactivity of surface species in heterogeneous catalysts probed by in situ X-ray absorption techniques. *Chemical reviews* **113**, 1736-1850 (2013).

44. J. A. Van Bokhoven, C. Lamberti, *X-ray absorption and X-ray emission spectroscopy: theory and applications.* (Wiley, 2016), vol. 1.

45. C. Lamberti *et al.*, Determination of the oxidation and coordination state of copper on different Cu-based catalysts by XANES spectroscopy in situ or in operando conditions. *Physical Chemistry Chemical Physics* **5**, 4502-4509 (2003).

46. F. Giordanino *et al.*, Characterization of Cu-exchanged SSZ-13: a comparative FTIR, UV-Vis, and EPR study with Cu-ZSM-5 and Cu-BETA with similar Si/Al and Cu/Al ratios. *Dalton Transactions* **42**, 12741-12761 (2013).

47. G. Shulman, Y. Yafet, P. Eisenberger, W. Blumberg, Observations and interpretation of X-ray absorption edges in iron compounds and proteins. *Proceedings of the National Academy of Sciences* **73**, 1384-1388 (1976).

48. J. E. Hahn *et al.*, Observation of an electric quadrupole transition in the X-ray absorption spectrum of a Cu (II) complex. *Chemical Physics Letters* **88**, 595-598 (1982).

49. F. Giordanino *et al.*, Interaction of NH 3 with Cu-SSZ-13 Catalyst: A Complementary FTIR, XANES, and XES Study. *The Journal of Physical Chemistry Letters* **5**, 1552-1559 (2014).

50. P. N. Vennestrøm *et al.*, Influence of lattice stability on hydrothermal deactivation of Cu-ZSM-5 and Cu-IM-5 zeolites for selective catalytic reduction of NOx by NH3. *Journal of Catalysis* **309**, 477-490 (2014).

51. D.-J. Liu, H. J. Robota, On the mechanism of NO selective catalytic reduction by hydrocarbons over Cu-ZSM-5 via X-ray absorption spectroscopic study. *The Journal of Physical Chemistry B* **103**, 2755-2765 (1999).

52. D.-J. Liu, H. J. Robota, In situ XANES characterization of the Cu oxidation state in Cu-ZSM-5 during NO decomposition catalysis. *Catalysis letters* **21**, 291-301 (1993).

53. Y. Kuroda *et al.*, Specific feature of copper ion-exchanged mordenite for dinitrogen adsorption at room-temperature. *Journal of Physical Chemistry* **99**, 10621-10628 (1995).

54.   C. Lamberti *et al.*, Cu I-Y and Cu II-Y zeolites: a XANES, EXAFS and visible-NIR study. *Chemical Physics Letters* **269**, 500-508 (1997).

55.   K. Mathisen, M. Stockenhuber, D. G. Nicholson, In situ XAS and IR studies on Cu: SAPO-5 and Cu: SAPO-11: the contributory role of monomeric linear copper (i) species in the selective catalytic reduction of NO x by propene. *Physical Chemistry Chemical Physics* **11**, 5476-5488 (2009).

56.   A. Moen, D. G. Nicholson, M. Rønning, Studies on the pre-edge region of the X-ray absorption spectra of copper (I) oxide and the diamminecopper (I) ion. *Journal of the Chemical Society, Faraday Transactions* **91**, 3189-3194 (1995).

57.   R. Car, M. Parrinello, Unified approach for molecular dynamics and density-functional theory. *Physical Review Letters* **55**, 2471 (1985).

58.   J. P. Perdew, K. Burke, M. Ernzerhof, Generalized gradient approximation made simple. *Physical Review Letters* **77**, 3865 (1996).

59.   D. Vanderbilt, Soft self-consistent pseudopotentials in a generalized eigenvalue formalism. *Physical Review B* **41**, 7892-7895 (1990).

60.   G. Kresse, J. Furthmüller, Efficient iterative schemes for ab initio total-energy calculations using a plane-wave basis set. *J. Phys. Rev. B: Condens. Matter Mater. Phys.*, **54**, 11169−11186 (1996)..

61.   S. Grimme, Semiempirical GGA-type density functional constructed with a long-range dispersion correction. *Journal of Computational Chemistry* **27**, 1787-1799 (2006).

62.   G. Henkelman, B. P. Uberuaga, H. Jónsson, A climbing image nudged elastic band method for finding saddle points and minimum energy paths. *The Journal of Chemical Physics* **113**, 9901-9904 (2000).

63.   J. Heyd, G. E. Scuseria, M. Ernzerhof, Erratum: "Hybrid functionals based on a screened Coulomb potential" [J. Chem. Phys. 118, 8207 (2003)]. *The Journal of Chemical Physics* **124**, 219906 (2006).

64.   A. Tkatchenko, M. Scheffler, Accurate Molecular Van Der Waals Interactions from Ground-State Electron Density and Free-Atom Reference Data. *Phys. Rev. Lett.* **102**, 73005 (2009).

65.   M. Iannuzzi, A. Laio, M. Parrinello, Efficient Exploration of Reactive Potential Energy Surfaces Using Car-Parrinello Molecular Dynamics. *Physical Review Letters* **90**, 238302 (2003).

66.   A. Barducci, M. Bonomi, M. Parrinello, Metadynamics. *Wiley Interdisciplinary Reviews: Computational Molecular Science* **1**, 826-843 (2011).

67.   M. Rybicki, J. Sauer, Acidity of two-dimensional zeolites. *Physical Chemistry Chemical Physics* **17**, 27873-27882 (2015).

68.   J. D. Albarracin-Caballero *et al.*, Structural and kinetic changes to small-pore Cu-zeolites after hydrothermal aging treatments and selective catalytic reduction of NO x with ammonia. *Reaction Chemistry & Engineering* **2**, 168-179 (2017).

APPENDIX C. SUPPLEMENTARY MATERIALS TO CHAPTER 4C1. CU SITE CHARACTERIZATION ON MODEL CU-CHA SAMPLES WITH VARYING CU DENSITY

Table C1. Bulk characterization data including residual H^+/Al on H- and Cu-SSZ-13 samples (Si/Al 15) to determine fraction of isolated Cu^{II} and $[Cu^{II}(OH)]^+$ sites on the oxidized Cu^{II} forms of Cu-CHA samples

Sample Cu-CHA-X-Y	H^+/Al (H-form)	H^+/Al (Cu-form)	$Cu^{II}OH/Al^*$	Cu^{II}/Al^*
Cu-CHA-15-40	0.98	0.93	0.00	0.03
Cu-CHA-15-29	0.98	0.81	0.00	0.08
Cu-CHA-15-27	0.98	0.80	0.35	0.09
Cu-CHA-15-25	0.98	0.73	0.03	0.09
Cu-CHA-15-23	0.98	0.70	0.08	0.09
Cu-CHA-15-22	0.98	0.68	0.10	0.09
Cu-CHA-15-20	1.00	0.64	0.16	0.09
Cu-CHA-15-17	0.98	0.58	0.28	0.09
Cu-CHA-15-16	0.98	0.51	0.35	0.09

*Determined from titration of residual H^+ sites by NH_3 and thermodynamic preferences for Cu^{II} and $Cu^{II}OH$ siting.

C2. Cu^I oxidation with O$_2$

Observed second-order transient could be reconciled based on our previous proposition of the following dual-site oxidation of two Cu(I)(NH$_3$)$_2$ with O$_2$:

$$2Cu^I(NH_3)_2 + O_2 \rightarrow (NH_3)_2Cu^{II}(O_2)Cu^{II}(NH_3)_2$$

Transient decay of Cu^I would be described by the following rate law, assuming this step was elementary and identical behaviour of all sites:

$$\frac{d[Cu^I(t)]}{dt} = -2k_o[O_2][Cu^I(t)]^2$$

As the concentration of O$_2$ is in stoichiometric excess, O$_2$ concentration term can be lumped into k_o to give k_o' as pseudo-second-order-rate constant, as follows:

$$\frac{d[Cu^I(t)]}{dt} = -2k_o'[Cu^I(t)]^2$$

In order to correct for unoxidizable Cu^I fraction (referred to as $[Cu^I(\infty)]$) in the transient O$_2$ oxidation experiments (Figure 12), we define the corrected Cu^I as follows:

$$[Cu^I(t)]_{corr} = [Cu^I(t)] - [Cu^I(\infty)]$$

$$\frac{d[Cu^I(t)]_{corr}}{dt} = -2k_o'[Cu^I(t)]_{corr}^2$$

As $[Cu^I(t)]_{corr}$ is the concentration of oxidizable Cu^I (by O$_2$) as a function of time, we could integrate from 0 to t and rearranging to get the following:

$$Cu^I \text{ Fraction} = \frac{[Cu^I(t)]}{[Cu^I(0)]} = \frac{1 - [Cu^I(\infty)]/[Cu^I(0)]}{1 + 2k_o'([Cu^I(0)] - [Cu^I(\infty)])t} + \frac{[Cu^I(\infty)]}{[Cu^I(0)]}$$

where Cu^I Fraction is defined as the ratio of Cu^I concentration at any time t to the initial Cu^I concentration ($[Cu^I(0)]$), and k and $[Cu^I(\infty)]$ are the parameters.

For each data series, we set $[Cu^I(\infty)]$ to the last Cu^I Fraction data point, and used nonlinear least-squares regression to obtain the best-fit parameter of k.

APPENDIX D. SUPPLEMENTARY MATERIALS TO CHAPTER 5

D1. Bulk structural characterization data on H-CHA samples with varying Si/Al
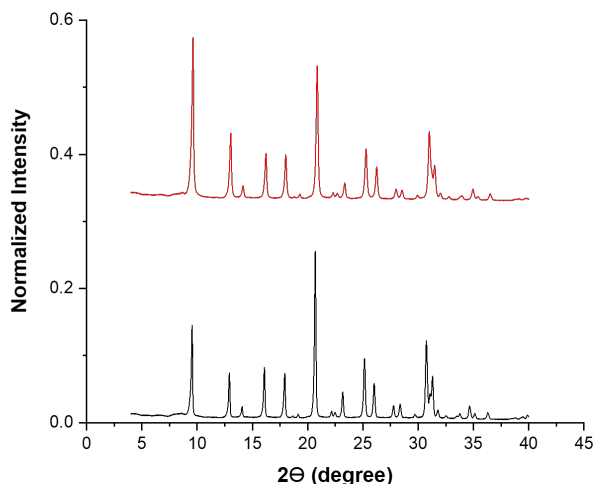
Figure D1. X-Ray diffraction patterns of H-CHA (H-SSZ-13) zeolites with Si/Al = 4.5 (black) and Si/Al = 15 (red), measured using a Cu K-alpha source (l= 0.154 nm). Diffraction patterns are vertically offset for clarity. Cu-CHA forms of these materials show equivalent XRD patterns.
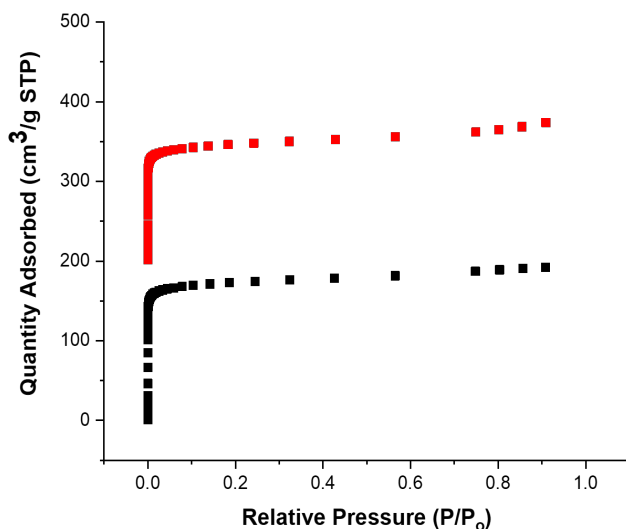
Figure D2. Ar adsorption isotherms on H-CHA (H-SSZ-13) with Si/Al = 4.5 (black) and Si/Al = 15 (red). Isotherms are vertically offset for clarity (Si/Al=15: by 200 $cm^3 g^{-1}$). Cu-CHA forms of these materials show similar adsorption isotherms, with slight decreases in micropore volumes caused by the presence of Cu.

D2. Cu site characterization on model Cu-CHA samples with varying Cu density

Table D1. Bulk characterization data including micropore volume (Ar, 87 K), and residual H^+/Al on H- and Cu-SSZ-13 samples to determine fraction of isolated Cu^{II} and $[Cu^{II}(OH)]^+$ sites on the oxidized Cu^{II} forms of Cu-CHA samples

Sample	V_{ads} (cm^3g^{-1}) (H-form)	H^+/Al (H-form)	H^+/Al (Cu-form)	$Cu^{II}OH/Al^*$	Cu^{II}/Al^*
Cu-CHA-5-15	0.18	0.87	0.42	0	0.21
Cu-CHA-5-20	n.m.	0.46	0.31	0.00	0.08
Cu-CHA-15-17	0.19	0.98	0.51	0.35	0.09
Cu-CHA-15-20	n.m.	1.00	0.58	0.16	0.09
Cu-CHA-15-29	0.19	0.98	0.81	0	0.08
Cu-CHA-25-20	n.m.	1.00	0.61	0.35	0.05

*Determined from titration of residual H^+ sites by NH_3 and thermodynamic preferences for Cu^{II} and $Cu^{II}OH$ siting.
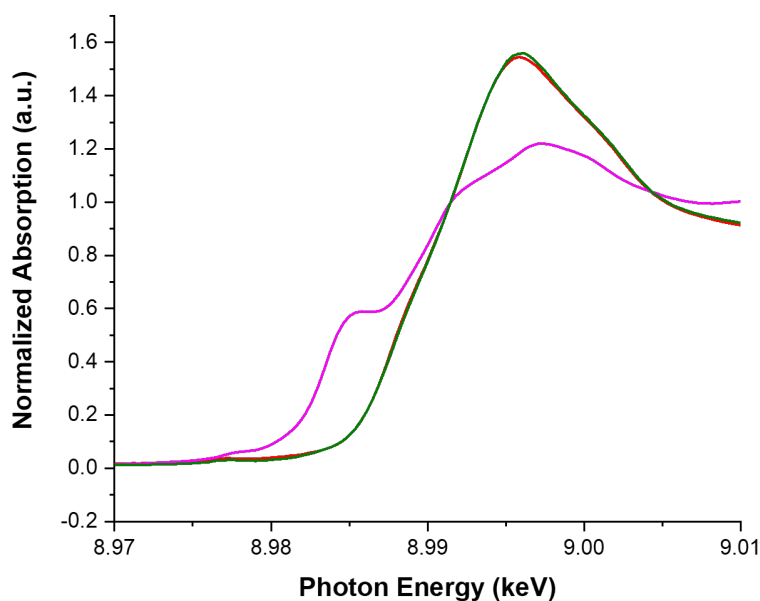
Figure D3. XANES spectra for Cu-CHA-5-15 (black), Cu-CHA-15-17 (red) and Cu-CHA-15-29 (green) at ambient conditions, and for bulk $Cu^{II}O$ (pink).
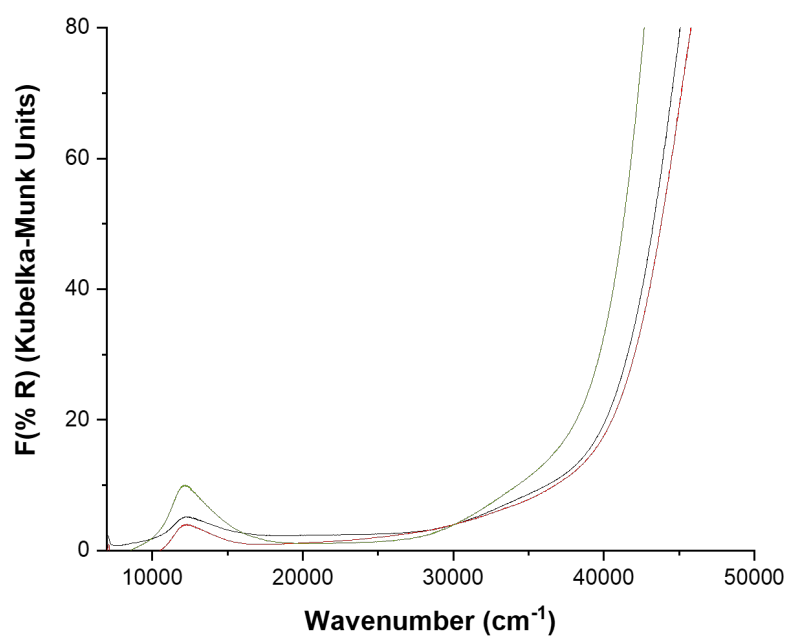
Figure D4.UV-Vis spectra for Cu-CHA-5-15 (black), Cu-CHA-15-17 (red), and Cu-CHA-15-29 (green) recorded at ambient conditions.

D3. Nature of Cu^{II} reduction with NO+NH$_3$
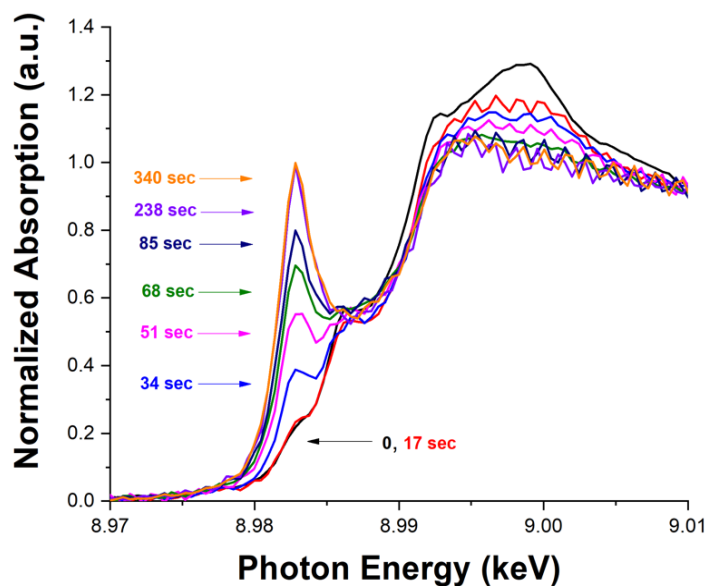
Figure D5. XANES spectra collected during transient reduction of the oxidized forms of Cu-CHA-5-15 sample with 300 ppm NO+NH$_3$, as a function of time (labelled in figure).
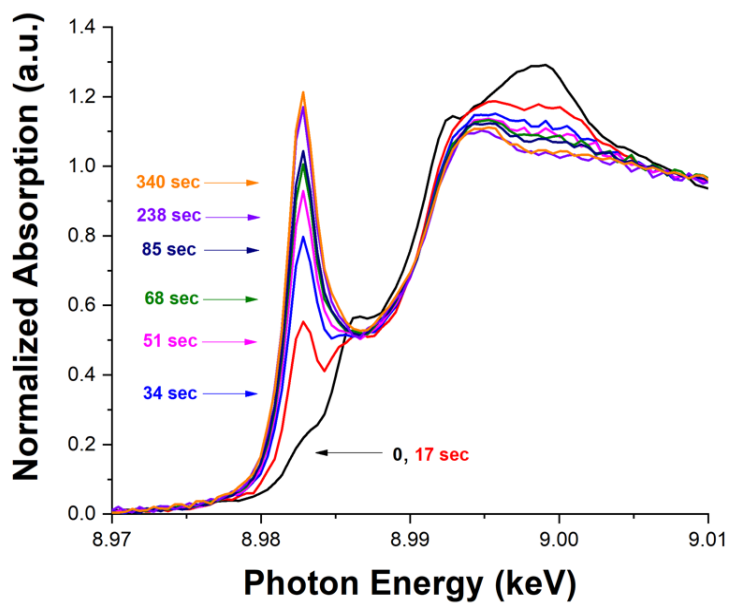
Figure D6. XANES spectra collected during transient reduction of the oxidized forms of Cu-CHA-15-17 sample with 300 ppm NO+NH$_3$, as a function of time (labelled in figure).
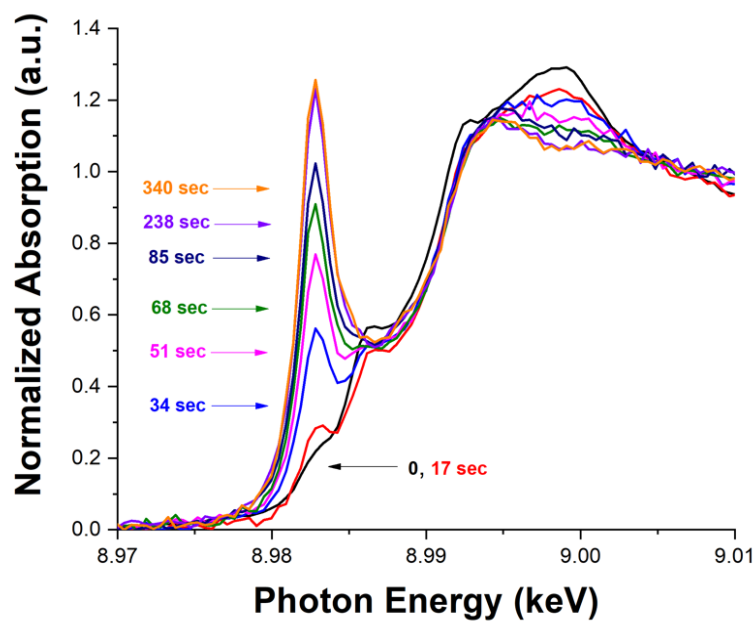
Figure D7. XANES spectra collected during transient reduction of the oxidized forms of Cu-CHA-15-29 sample with 300 ppm $NO+NH_3$, as a function of time (labelled in figure).

D4. Nature of Cu^I(NH$_3$)$_2$ oxidation with NO$_2$
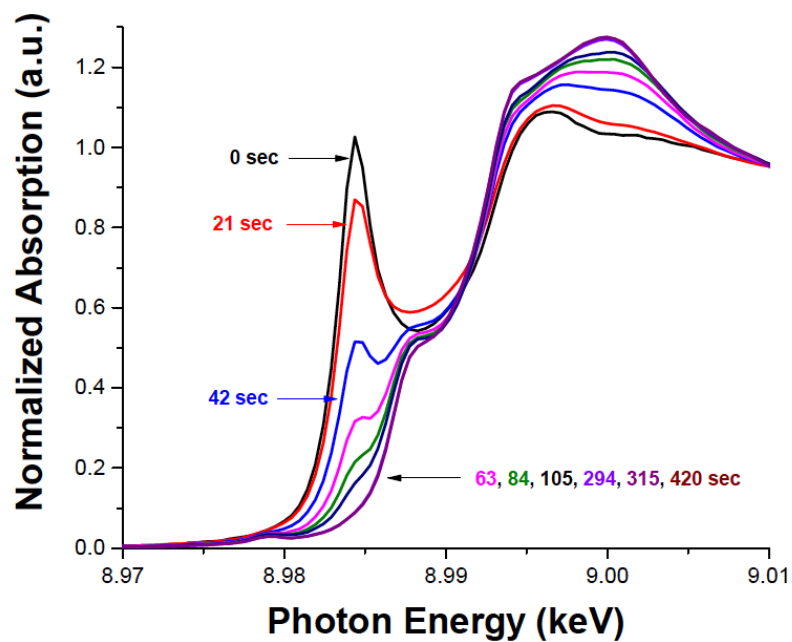
Figure D8. XANES spectra collected during transient oxidation of the Cu^I(NH$_3$)$_2$ with 150 ppm NO$_2$ on Cu-CHA-5-15 sample, as a function of time (labeled in figure).
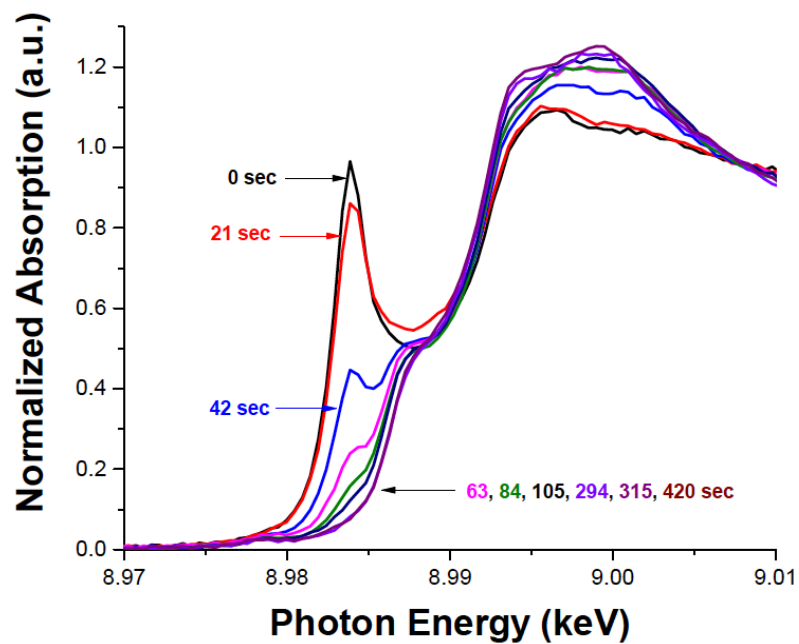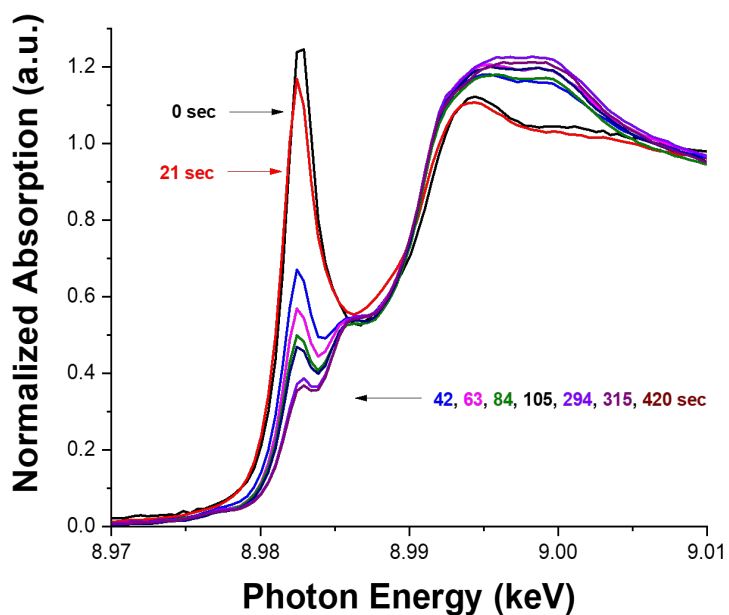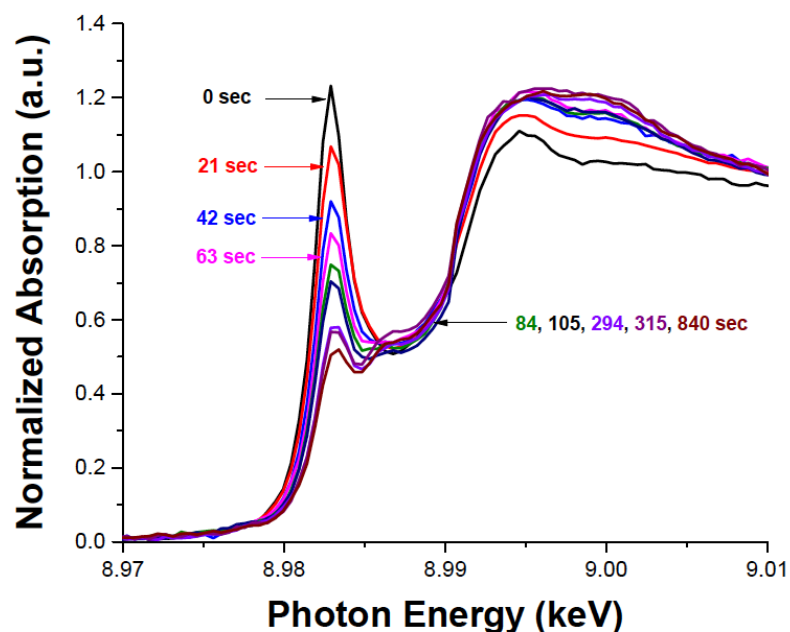

Figure S10. XANES spectra collected during transient oxidation of the Cu^I(NH$_3$)$_2$ with 150 ppm NO$_2$ on Cu-CHA-15-17 sample, as a function of time (labeled in figure).
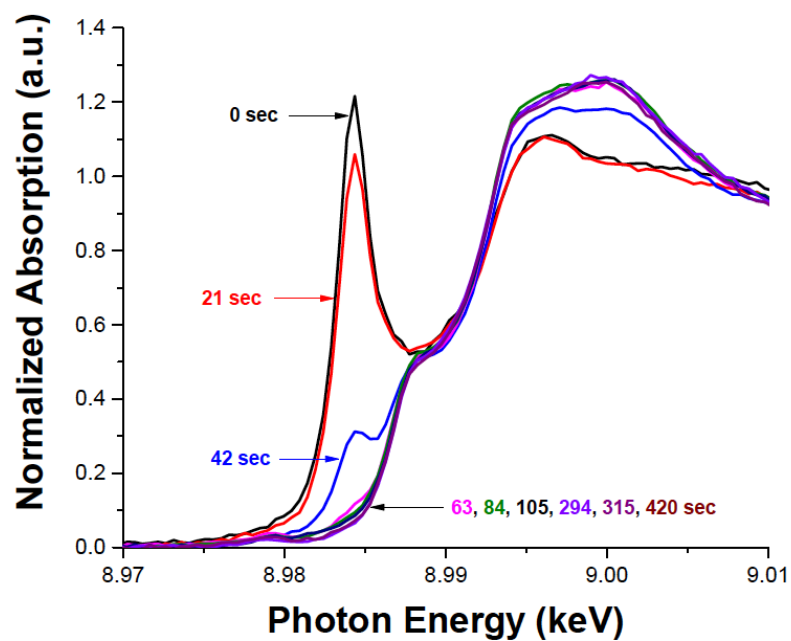
Figure D9. XANES spectra collected during transient oxidation of the $Cu^I(NH_3)_2$ with 150 ppm NO_2 on Cu-CHA-15-29 sample, as a function of time (labeled in figure).

D5. Nature of Cu^I(NH$_3$)$_2$ oxidation with O$_2$
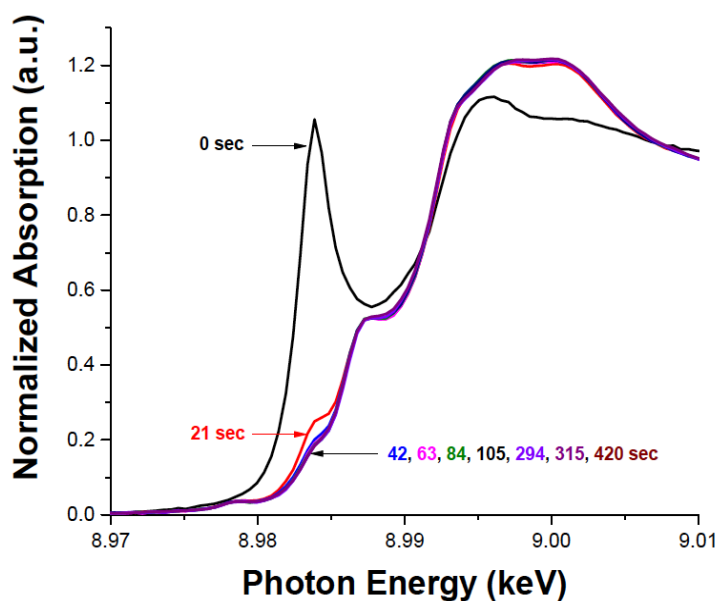
Figure D10. XANES spectra collected during transient oxidation of the Cu^I(NH$_3$)$_2$ with 10% O$_2$ on Cu-CHA-5-15 sample, as a function of time (labelled in figure).

Figure D11. XANES spectra collected during transient oxidation of the Cu^I(NH$_3$)$_2$ with 10% O$_2$ on Cu-CHA-15-17 sample, as a function of time (labelled in figure).

Figure D12. XANES spectra collected during transient oxidation of the $Cu^I(NH_3)_2$ with 10% O_2 on Cu-CHA-15-29 sample, as a function of time (labelled in figure).
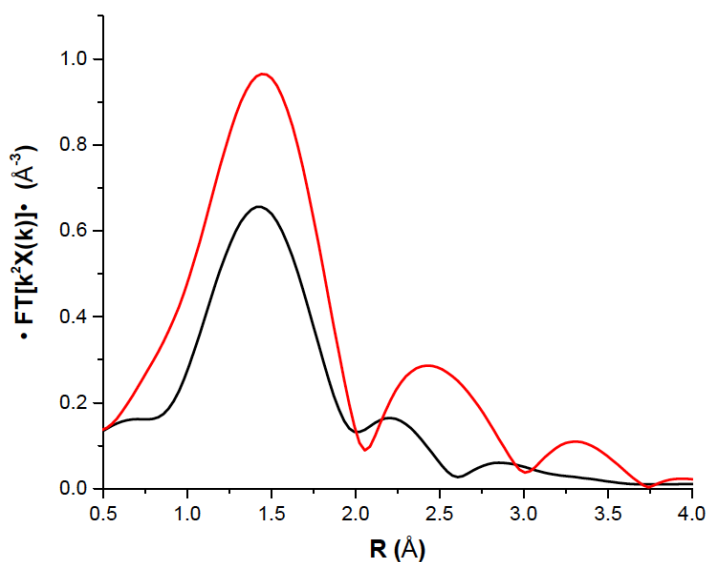
Figure D13. The k^2 weighted Fourier transform (moduli) EXAFS spectra collected before (black) and after (red) oxidation with 10% O_2 at 473 K, starting from the reduced $Cu^I(NH_3)_2$ state of Cu-CHA-5-15 sample.
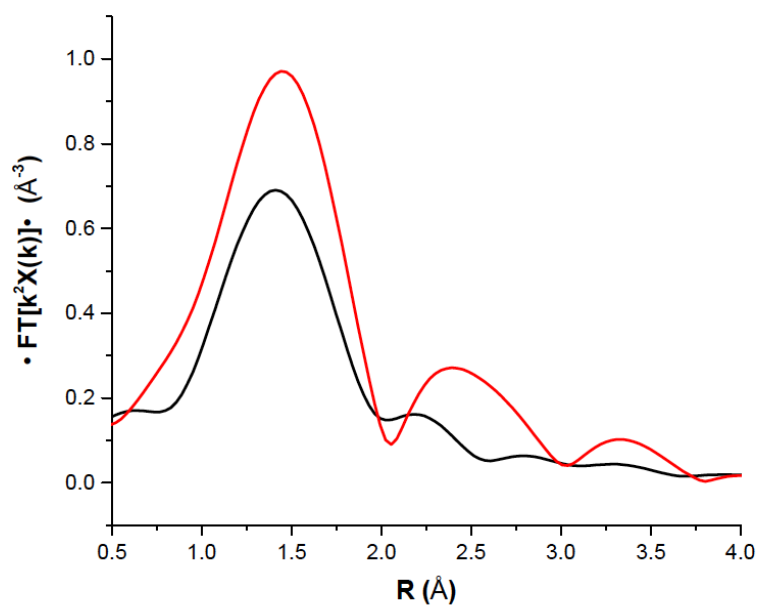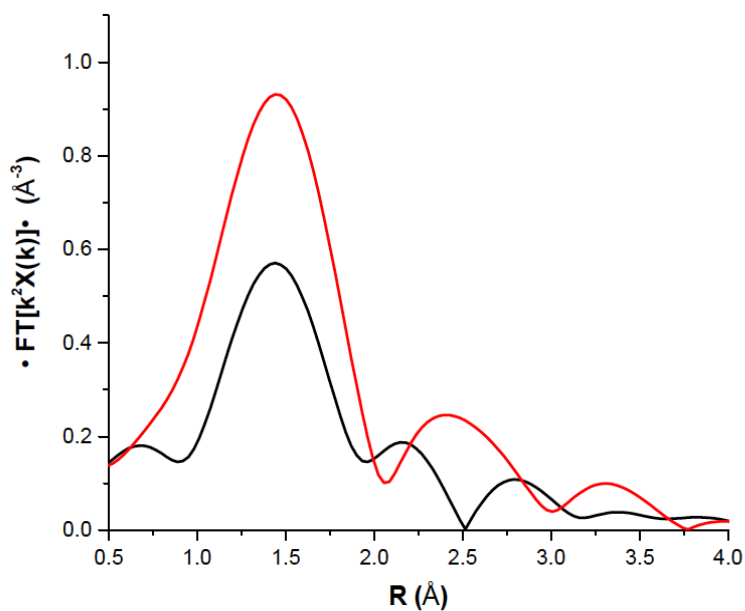
Figure D14. The k^2 weighted Fourier transform (moduli) EXAFS spectra collected before (black) and after (red) oxidation with 10% O_2 at 473 K, starting from the reduced $Cu^I(NH_3)_2$ state of Cu-CHA-15-17 sample

Figure D15. The k^2 weighted Fourier transform (moduli) EXAFS spectra collected before (black) and after (red) oxidation with 10% O_2 at 473 K, starting from the reduced $Cu^I(NH_3)_2$ state of Cu-CHA-15-29 sample.
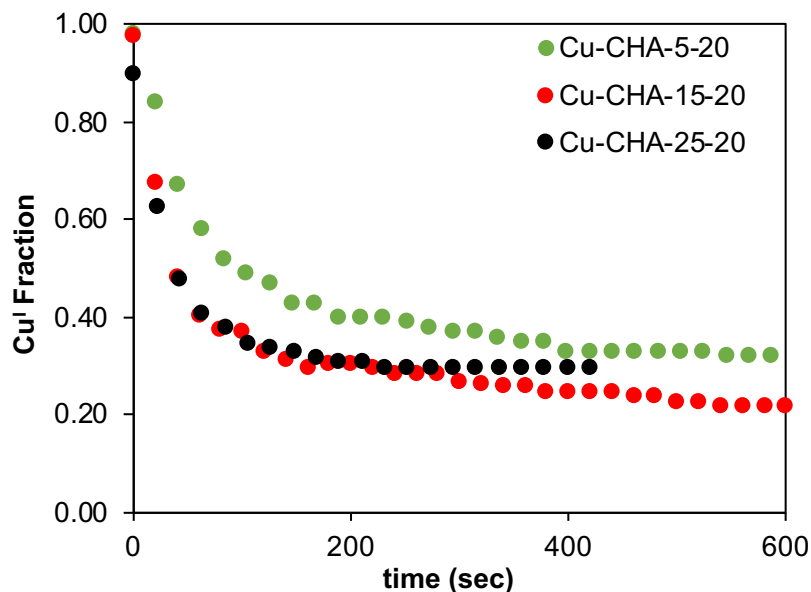
Figure D16. Temporal evolution of the XANES-measured Cu^I fraction is plotted for the Cu-CHA-5-20 (green) Cu-CHA-15-20 (red) and Cu-CHA-25-20 (black) samples during transient oxidation in 10% O_2 at 473 K. The Cu^I fractions reported contain an absolute 5% error from fitting.
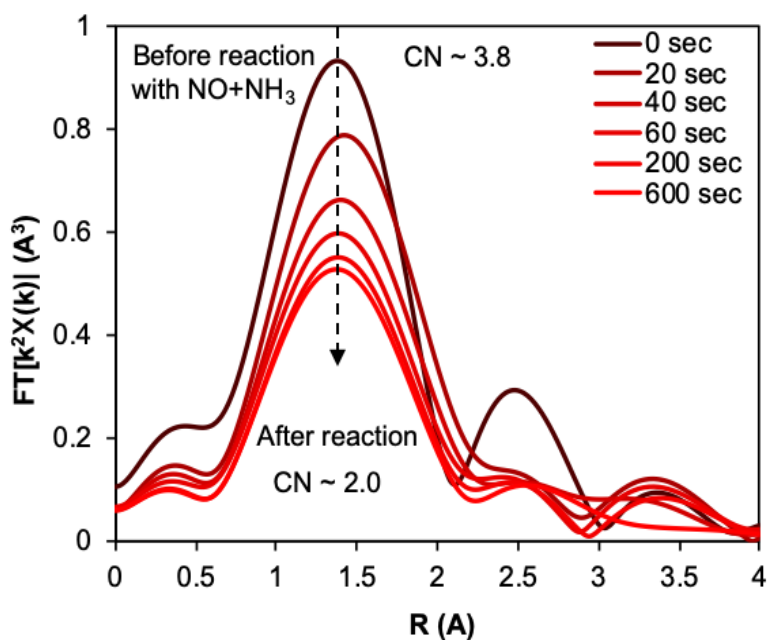
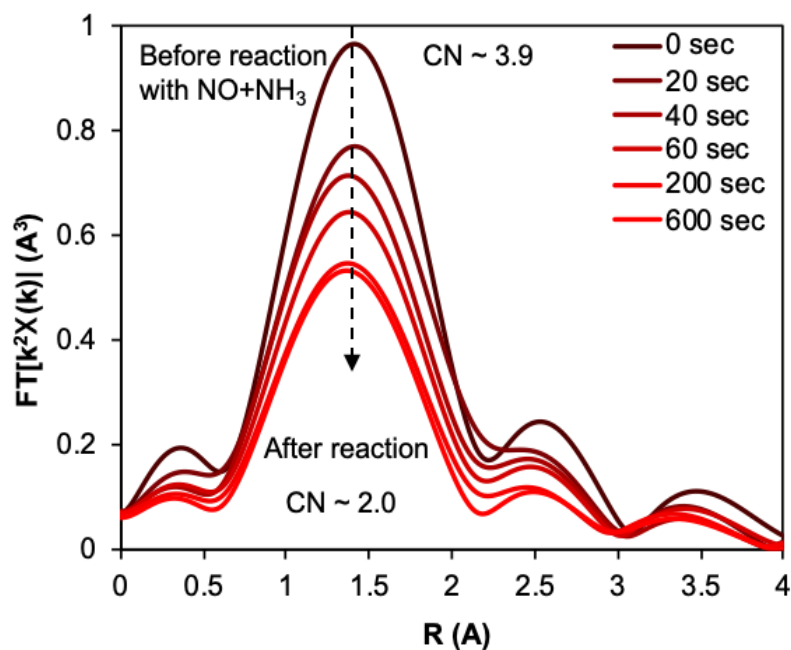## D6. Nature of Cu^{II}-dimer reduction with NO+NH₃

Figure D17. The k^2 weighted Fourier transform EXAFS spectra (moduli) collected during transient reduction of NH₃-solvated Cu^{II}-dimer with 300 ppm NO+NH₃ on Cu-CHA-5-15 sample, as a function of time (labeled in figure). (CN= Cu-O/N coordination Number)
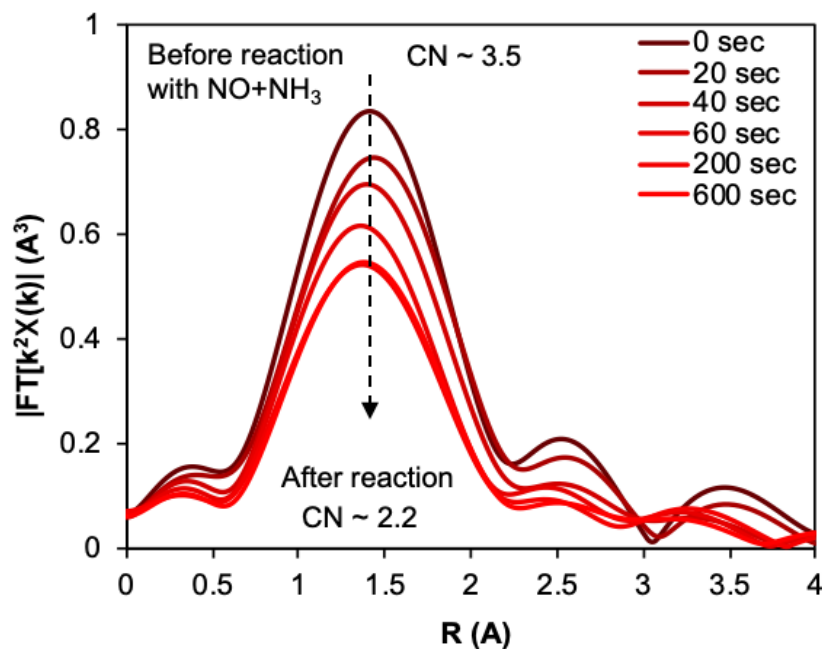
Figure D18. The k^2 weighted Fourier transform EXAFS spectra (moduli) collected during transient reduction of NH$_3$-solvated Cu^{II}-dimer with 300 ppm NO+NH$_3$ on Cu-CHA-15-17 sample, as a function of time (labeled in figure). (CN= Cu-O/N coordination Number)

Figure D19. The k^2 weighted Fourier transform EXAFS spectra (moduli) collected during transient reduction of NH$_3$-solvated Cu^{II}-dimer with 300 ppm NO+NH$_3$ on Cu-CHA-15-29 sample, as a function of time (labeled in figure). (CN= Cu-O/N coordination Number)
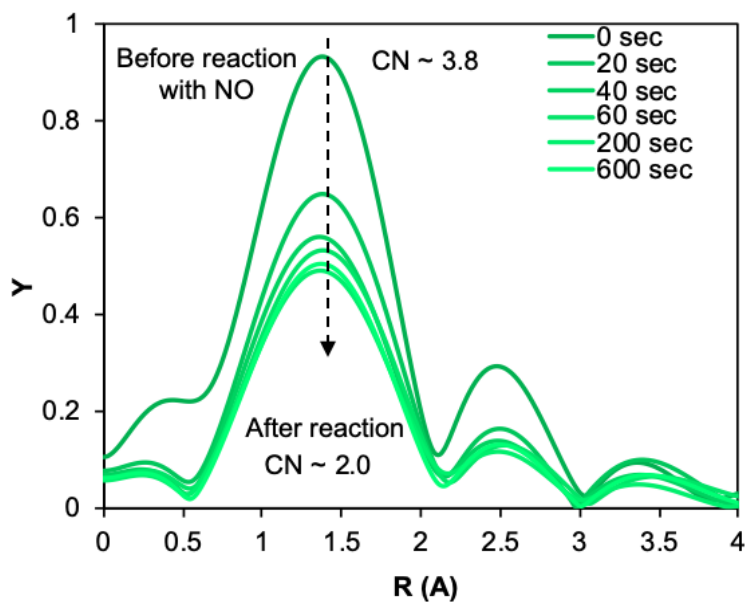
D7. Nature of Cu^{II}-dimer reduction with NO

Figure D20. The k^2 weighted Fourier transform EXAFS spectra (moduli) collected during transient reduction of NH$_3$-solvated Cu^{II}-dimer with 300 ppm NO on Cu-CHA-5-15 sample, as a function of time (labeled in figure). (CN= Cu-O/N coordination Number)
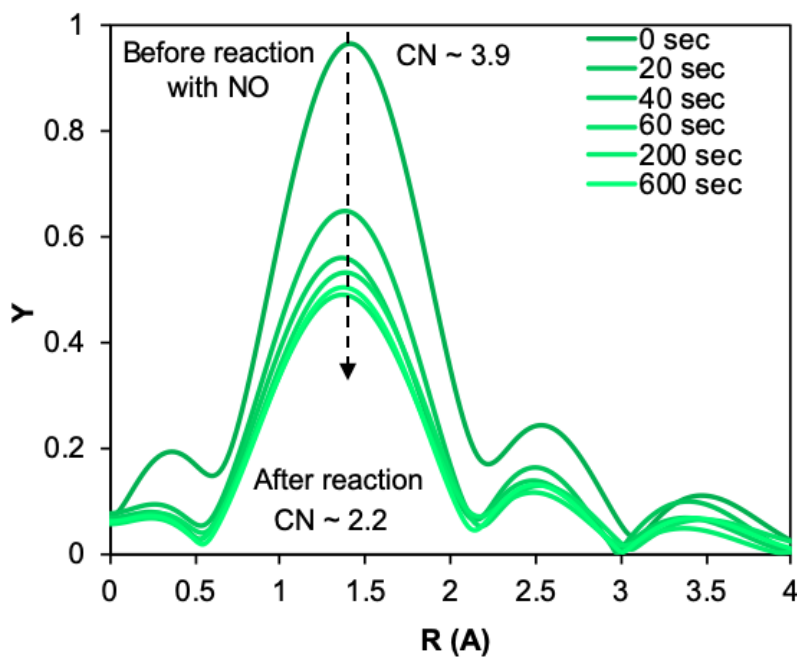

Figure D21. The k^2 weighted Fourier transform EXAFS spectra (moduli) collected during transient reduction of NH$_3$-solvated Cu^{II}-dimer with 300 ppm NO on Cu-CHA-15-17 sample, as a function of time (labeled in figure). (CN= Cu-O/N coordination Number)
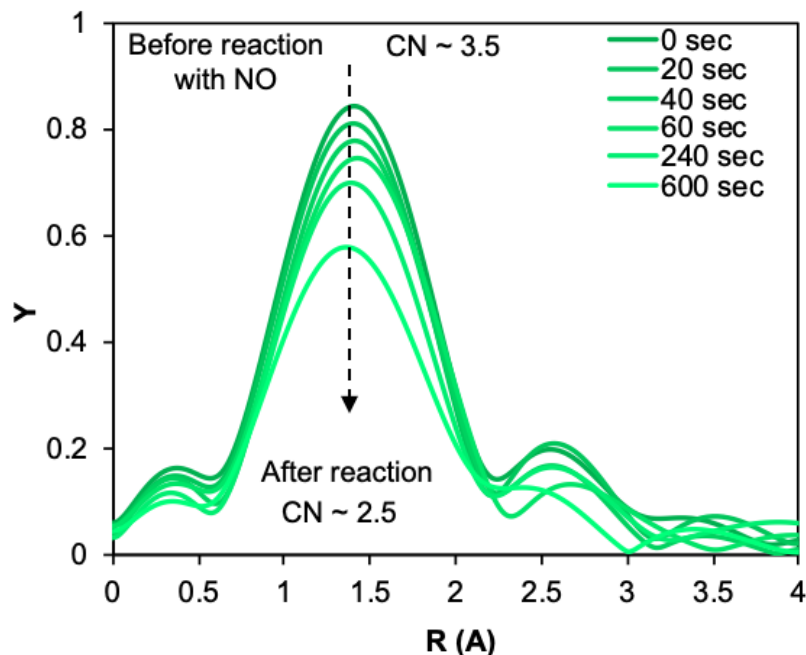
Figure D22. The k^2 weighted Fourier transform EXAFS spectra (moduli) collected during transient reduction of NH_3-solvated Cu^{II}-dimer with 300 ppm NO on Cu-CHA-15-29 sample, as a function of time (labeled in figure). (CN= Cu-O/N coordination Number)

D8. Cu^{II} reduction with NO+NH$_3$

Observed transient Cu^{II}-reduction with NO+NH$_3$ was fit to a pseudo-first order rate law, wherein the first-order transient behavior could be reconciled by postulating bimolecular reaction of single NH_3-solvated Cu^{II} with NO as follows:

$$(NH_3)_3Cu^{II}OH + NO \rightarrow Cu^I(NH_3)_2 + N_2 + 2H_2O$$
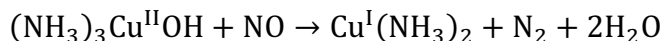
Transient decay of Cu^{II} would be described by the following rate law, assuming this step was elementary and identical behavior of all sites:

$$\frac{d[Cu^{II}(t)]}{dt} = -k_r[NO][Cu^{II}(t)]$$

As the concentration of NO is in stoichiometric excess, NO concentration term can be lumped into k_r to give k_r' as pseudo-first-order-rate constant, as follows:

$$\frac{d[Cu^{II}(t)]}{dt} = -k_r'[Cu^{II}(t)]$$

After integration from 0 to t and rearranging, we get the following expression:

$$\text{Cu}^{II} \text{ Fraction} = \frac{[\text{Cu}^{II}(t)]}{[\text{Cu}^{II}(0)]} = e^{-k_r't}$$

where Cu^{II} Fraction is defined as the ratio of Cu^{II} concentration at any time t to the initial Cu^{II} concentration ($[\text{Cu}^I(0)]$), and k is the only unknown parameter. Nonlinear least-squares regression was used to obtain the best-fit k value from the data.

D9. Cu^I oxidation with O$_2$

Observed second-order transient could be reconciled based on our previous proposition of the following dual-site oxidation of two Cu(I)(NH$_3$)$_2$ with O$_2$:

$$2\text{Cu}^I(\text{NH}_3)_2 + \text{O}_2 \rightarrow (\text{NH}_3)_2\text{Cu}^{II}(\text{O}_2)\text{Cu}^{II}(\text{NH}_3)_2$$

Transient decay of Cu^I would be described by the following rate law, assuming this step was elementary and identical behavior of all sites:

$$\frac{d[\text{Cu}^I(t)]}{dt} = -2k_o[\text{O}_2][\text{Cu}^I(t)]^2$$

As the concentration of O$_2$ is in stoichiometric excess, O$_2$ concentration term can be lumped into k_o to give k_o' as pseudo-second-order-rate constant, as follows:

$$\frac{d[\text{Cu}^I(t)]}{dt} = -2k_o'[\text{Cu}^I(t)]^2$$

In order to correct for unoxidizable Cu^I fraction (referred to as $[\text{Cu}^I(\infty)]$) in the transient O$_2$ oxidation experiments (Figure X), we define the corrected Cu^I as follows:

$$[\text{Cu}^I(t)]_{corr} = [\text{Cu}^I(t)] - [\text{Cu}^I(\infty)]$$

$$\frac{d[\text{Cu}^I(t)]_{corr}}{dt} = -2k_o'[\text{Cu}^I(t)]_{corr}^2$$

As $[\text{Cu}^I(t)]_{corr}$ is the concentration of oxidizable Cu^I (by O$_2$) as a function of time, we could integrate from 0 to t and rearranging to get the following:

$$\text{Cu}^I \text{ Fraction} = \frac{[\text{Cu}^I(t)]}{[\text{Cu}^I(0)]} = \frac{1 - [\text{Cu}^I(\infty)]/[\text{Cu}^I(0)]}{1 + 2k_o'([\text{Cu}^I(0)] - [\text{Cu}^I(\infty)])t} + \frac{[\text{Cu}^I(\infty)]}{[\text{Cu}^I(0)]}$$

where Cu^I Fraction is defined as the ratio of Cu^I concentration at any time t to the initial Cu^I concentration ($[\text{Cu}^I(0)]$), and k and $[\text{Cu}^I(\infty)]$ are the parameters.

For each data series, we set $[\text{Cu}^I(\infty)]$ to the last Cu^I Fraction data point, and used nonlinear least-squares regression to obtain the best-fit parameter of k.
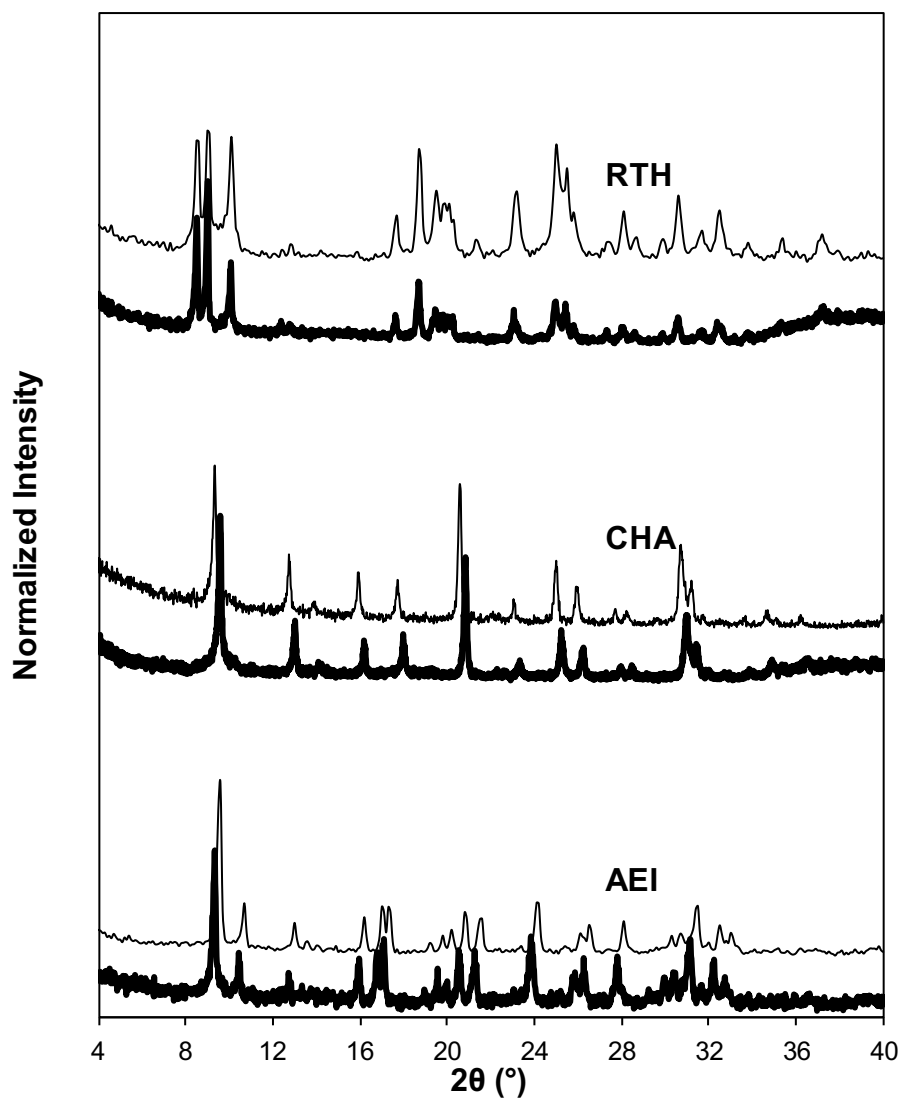
APPENDIX E. SUPPLEMENTARY MATERIALS TO CHAPTER 8

E1. Powder X-ray diffraction patterns on H- and Cu-zeolites

Figure E1. XRD patterns of H-form (dark) and Cu-form (light) AEI, CHA, and RTH zeolites. Diffraction patterns are normalized so that the maximum peak intensity in each pattern is unity.

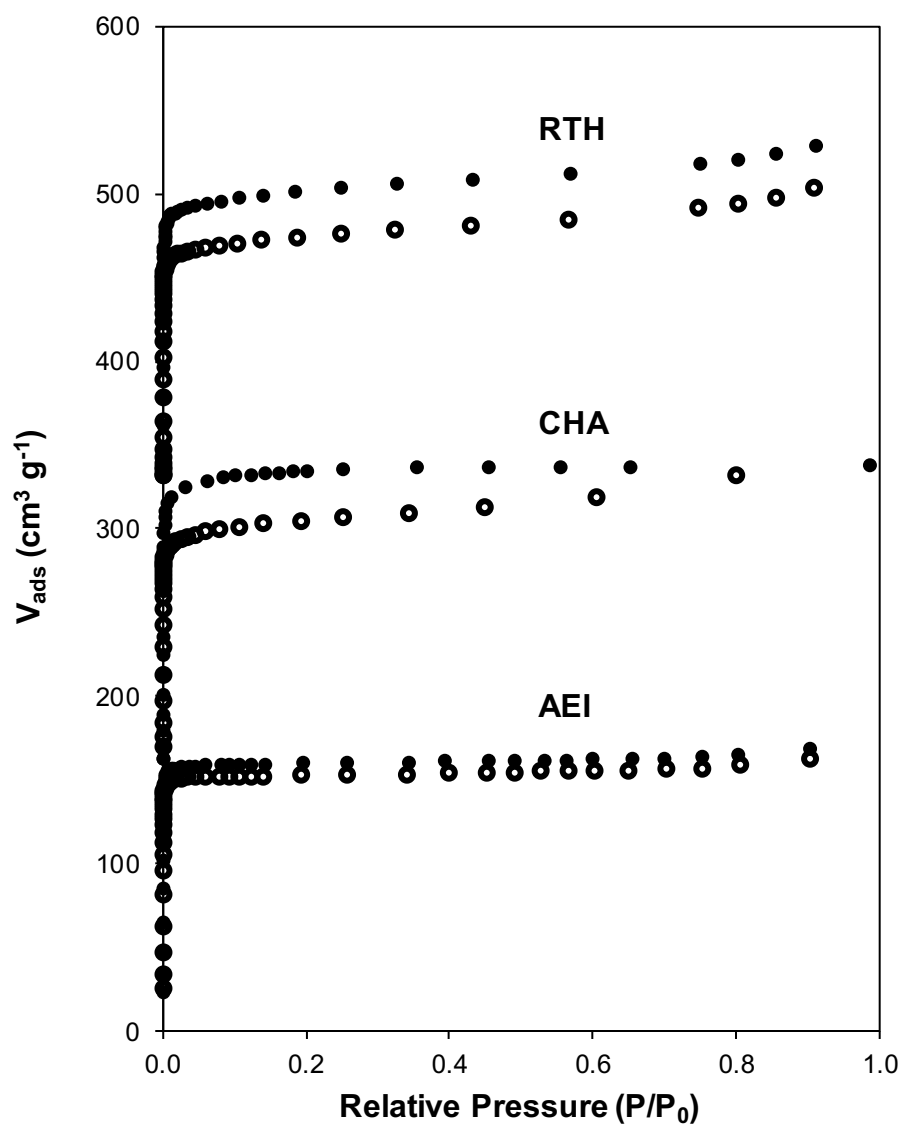**E2. Argon adsorption isotherms on H- and Cu-zeolites**

Figure E2. Ar adsorption isotherms (87 K) on H-form (filled) and Cu-form (open) RTH, CHA and AEI zeolites. Adsorption isotherms are vertically offset (CHA: 160 cm^3 g^{-1}, RTH: 320 cm^3 g^{-1}) for clarity.

E3. ^{27}Al MAS NMR spectra on H- and Cu-zeolites

^{27}Al MAS NMR spectra were measured on the H- and Cu-forms of the three zeolites in this study, AEI (Figure E.3), CHA (Figure E4) and RTH (Figure E5), in order to estimate the distribution of framework (Al_f) and extra-framework (Al_{ex}) Al species. NMR lines centered at 60 ppm were present for tetrahedral Al for RTH, and a small shoulder for penta-coordinated Al[1,2] was present for CHA and AEI. The tetrahedral along with distorted tetrahedral and penta-coordinated Al NMR lines were integrated together to estimate the total number of Al_f species, although we recognize difficulties in quantifying Al_f content from NMR spectra, because some species can reversibly change between tetrahedral and octahedral coordination depending on the conditions of the measurement[3–5], and some extraframework alumina may also contain tetrahedrally-coordinated Al.[1,6] The Al NMR lines centered at 0 ppm for octahedral Al were taken to reflect Al_{ex} species. Spectra of H- and Cu- form zeolites show Al incorporated predominantly into tetrahedral framework positions, with Al_f/Al_{tot} values given in Table 7.2 of the main text.
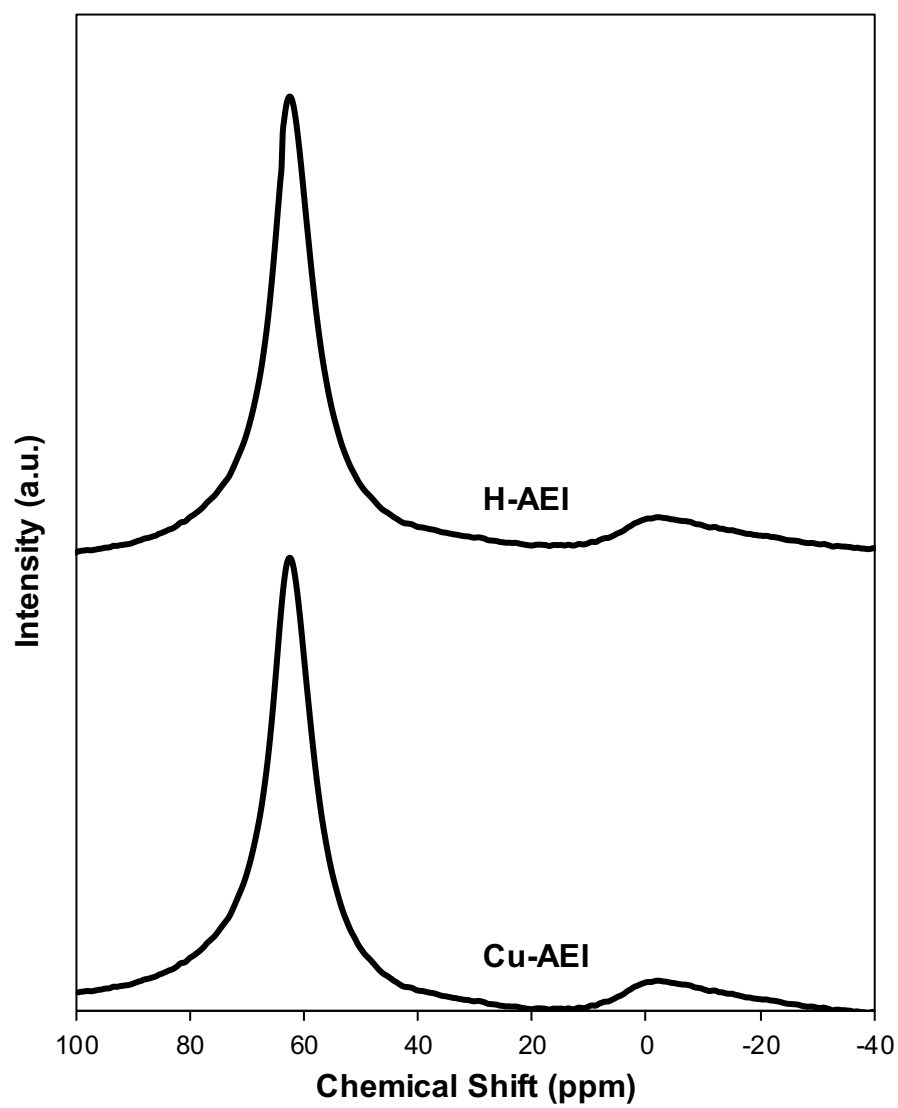
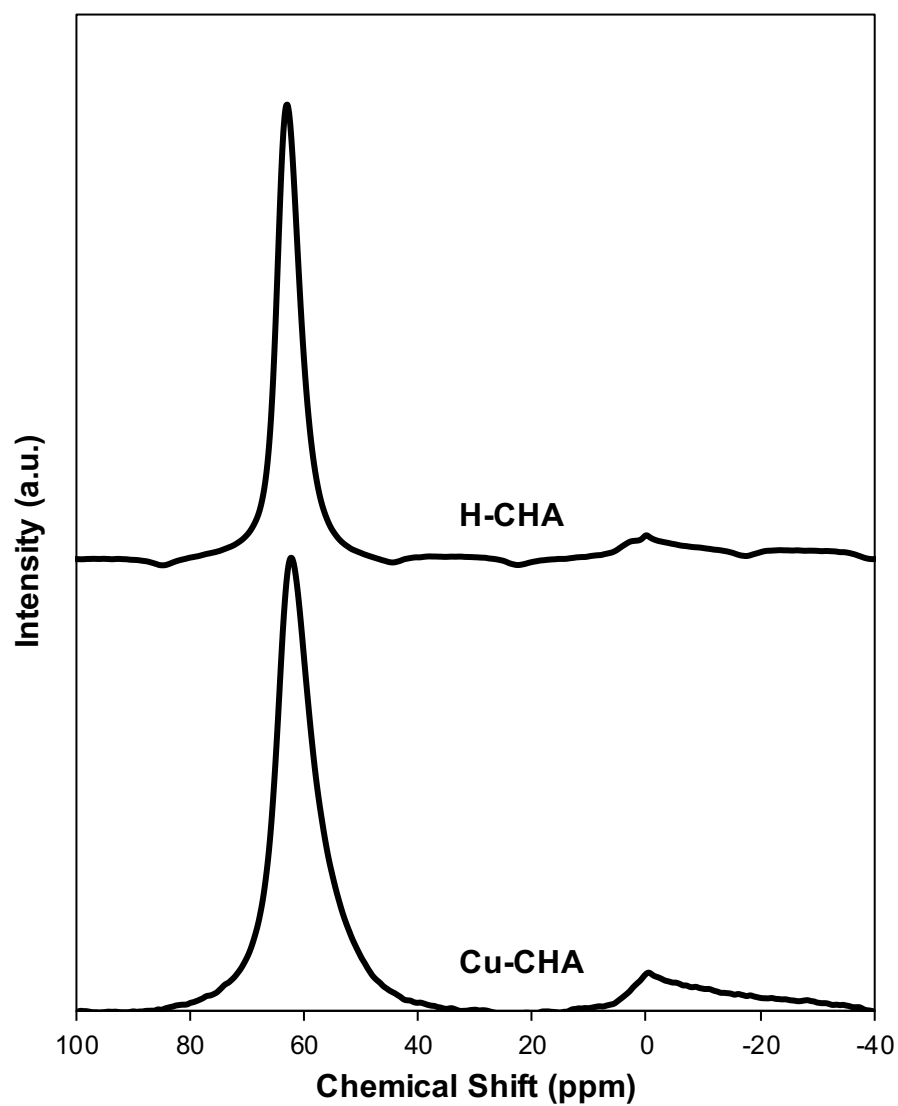Figure E3. ^{27}Al MAS NMR spectra of H-AEI and Cu-AEI.

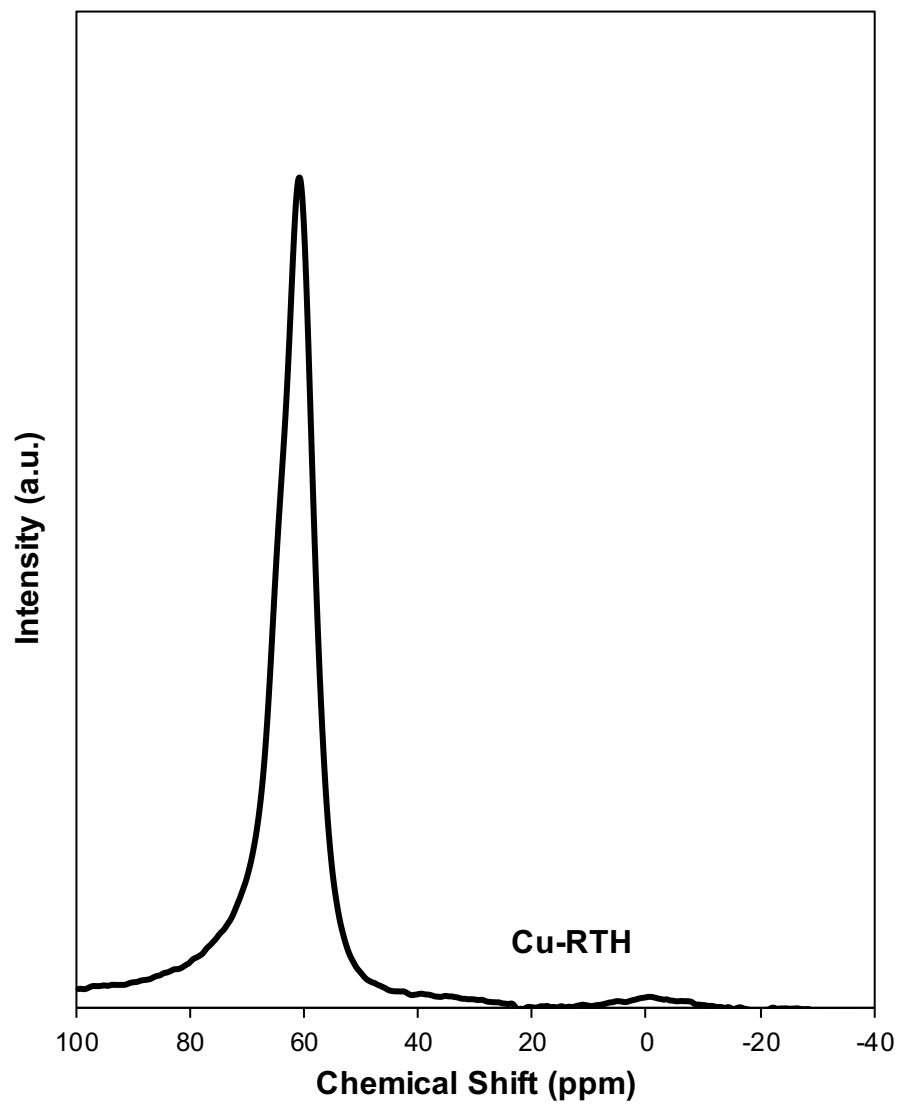Figure E4. ^{27}Al MAS NMR spectra of H-CHA and Cu-CHA.

Figure E5. ^{27}Al MAS NMR spectra of Cu-RTH.

E4. IR Spectra of H-RTH Before and After NH$_3$ Exposure

In situ IR experiments were performed to monitor interactions of H$^+$ sites with NH$_3$ in H-RTH (Si/Al = 15) with NH$_3$. H-RTH was pressed into a self-supporting wafer (~0.40 g) and placed within an *operando* FTIR cell, using a procedure that has been described elsewhere.[7] The sample was heated to 723 K and held for 2 h under 50 mL min^{-1} of 10% O$_2$ (99.5%, Indiana Oxygen) and balance N$_2$ (99.999% UHP, Indiana Oxygen), and then cooled to 433 K under flow (10% O$_2$ and balance N$_2$) to give the dark black spectrum in Figure E6. This IR spectrum shows OH bands for Brønsted acid sites in the 3600 cm^{-1} region. The H-RTH wafer was then saturated in flowing NH$_3$ (350 ppm, 3 h, 433 K), to give the light black spectrum in Figure E6. Brønsted OH bands disappeared completely, and new IR bands for NH$_4^+$ bending vibrations at 1425 cm^{-1} appeared concomitantly (not shown). These data indicate that all H$^+$ sites in H-RTH were titrated by NH$_3$, and that the H$^+$/Al$_f$ value of 0.61 measured in NH$_3$ TPD experiments do not reflect a fraction of H$^+$ sites that were inaccessible to NH$_3$.
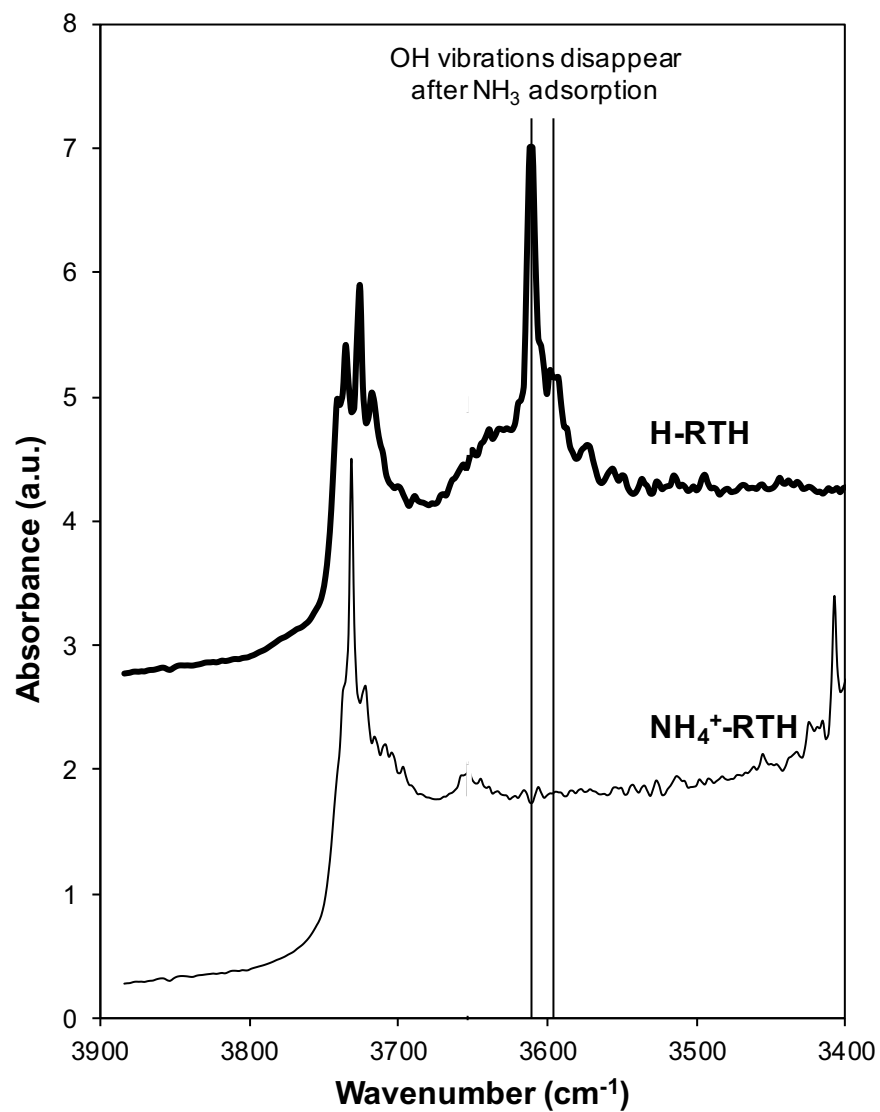
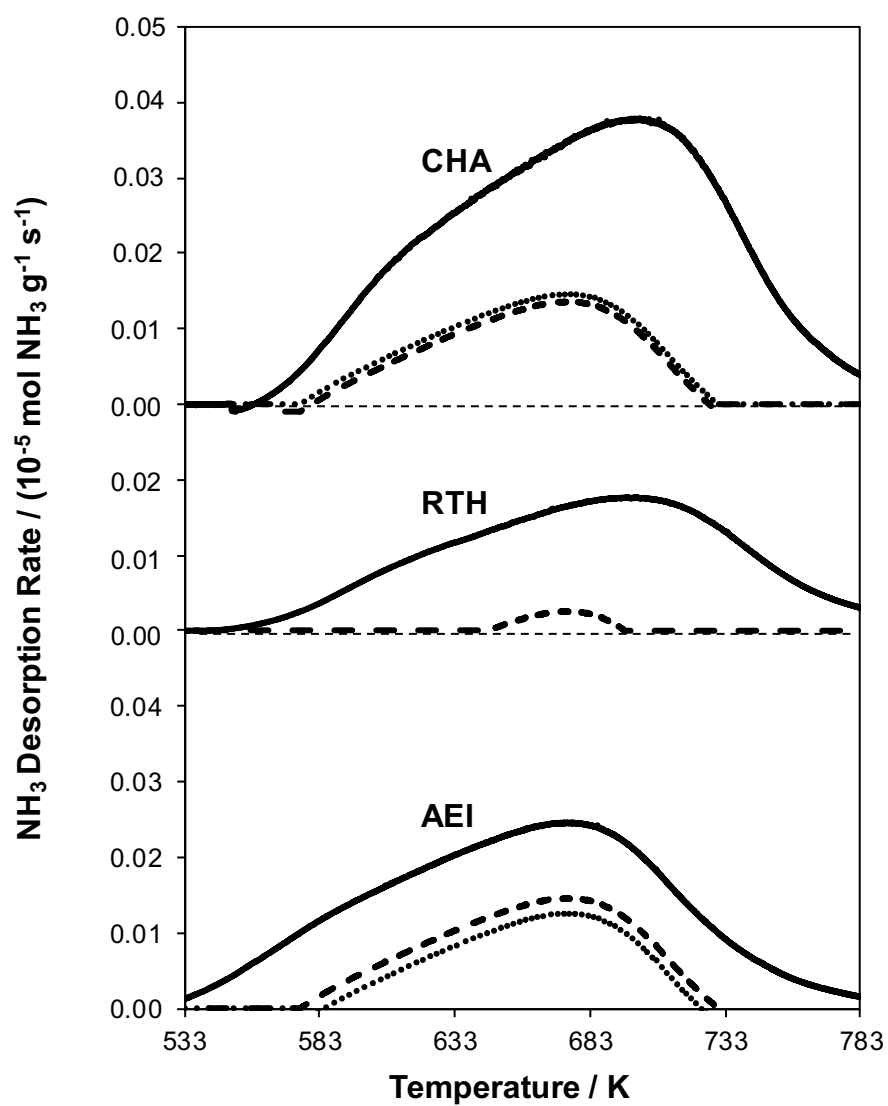Figure E6. IR spectra of H-RTH at 433 K before (dark) and after (light) NH_3 saturation.

E5. NH₃ TPD on Cu-zeolites

Figure E7. NH₃ desorption rates as a function of temperature on fresh Cu-form after SCR (solid), aged Cu-form before SCR (dashed) and aged Cu-form after SCR (dotted) on CHA, RTH, and AEI zeolites.

E6. References

1   J. Klinowski, *Prog. NMR Spectrosc.*, 1984, **16**, 237–309.
2   J. H. Kwak, J. Z. Hu, D. H. Kim, J. Szanyi and C. H. F. Peden, *J. Catal.*, 2007, **251**, 189–194.
3   A. Omegna, J. A. van Bokhoven and R. Prins, *J. Phys. Chem. B*, 2003, **107**, 8854–8860.
4   A. Omegna, R. Prins and J. A. Van Bokhoven, *J. Phys. Chem. B*, 2005, **109**, 9280–9283.
5   R. Gounder, A. J. Jones, R. T. Carr and E. Iglesia, *J. Catal.*, 2012, **286**, 214–223.
6   Z. Luv and A. J. Vega, *J. Phys. Chem.*, 1987, **91**, 374–382.
7   J. Wang, V. F. Kispersky, W. N. Delgass and F. H. Ribeiro, *J. Catal.*, 2012, **289**, 171–178.

APPENDIX F. SUPPLEMENTARY MATERIALS TO CHAPTER 9

For the sake of brevity, supplementary material is not inserted here. Refer to supplementary information of my original coauthored article published in Applied Catalysis A: General, 574, 122-131, 2019, titled "Spectroscopic and kinetic responses of Cu-SSZ-13 to SO_2 exposure and implications for NO_x selective catalytic reduction".
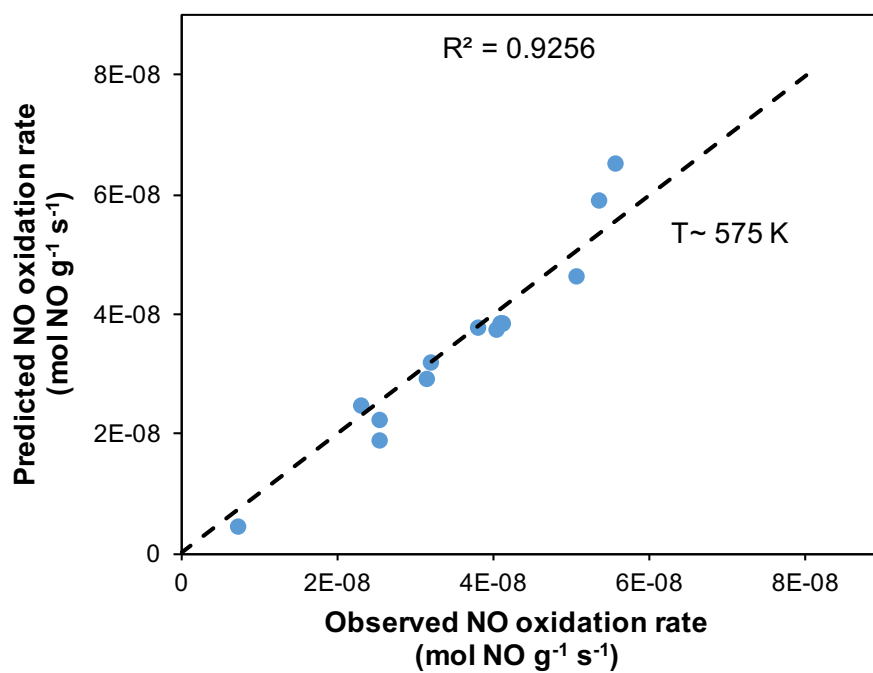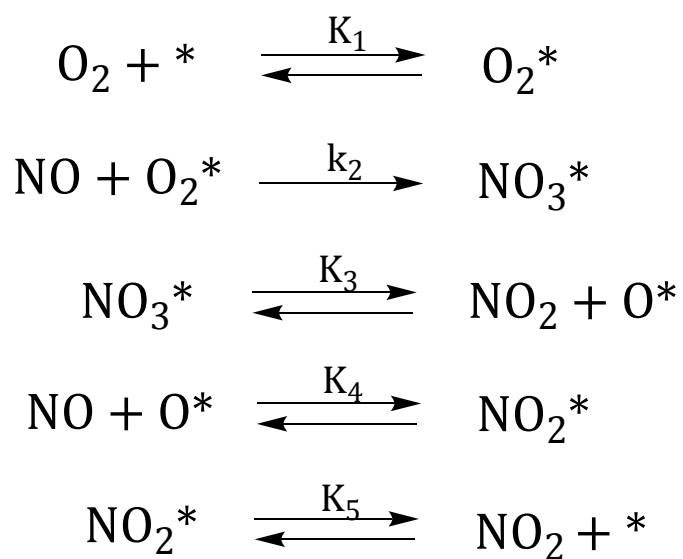
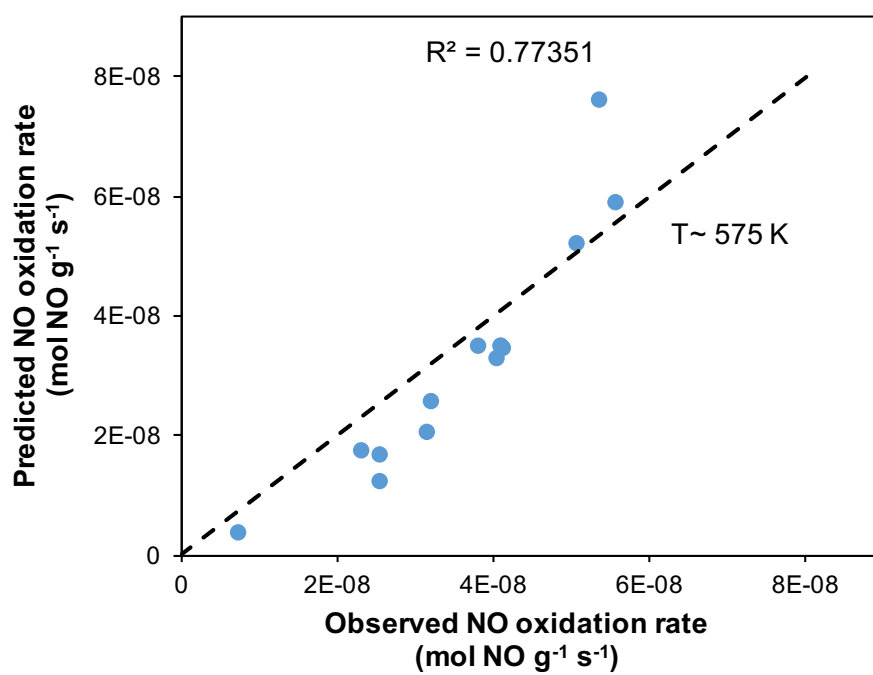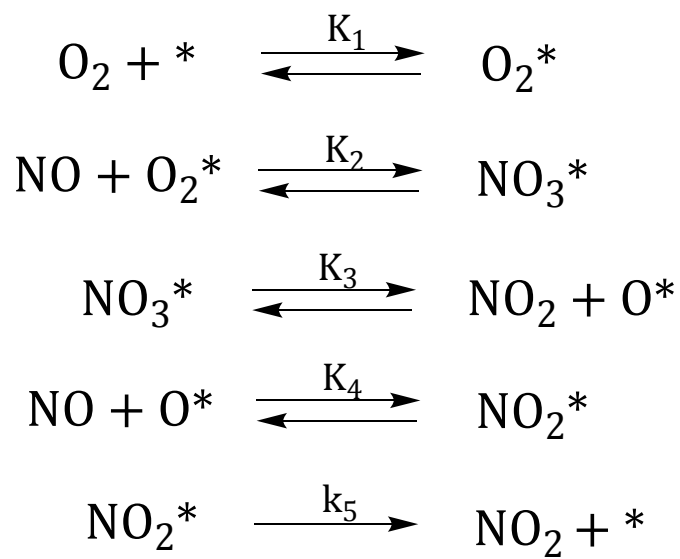# APPENDIX G. SUPPLEMENTARY MATERIALS TO CHAPTER 10

For the sake of brevity, supplementary material is not inserted here. Refer to supplementary information of my original coauthored article published in Chemical Science, 10, 2373-2384, 2019, titled "Consequences of exchange-site heterogeneity and dynamics on the UV-visible spectrum of Cu-exchanged SSZ-13"

APPENDIX H. SUPPLEMENTARY MATERIALS TO CHAPTER 11

$$O_2 + * \;\underset{\longleftarrow}{\overset{K_1}{\longrightarrow}}\; O_2*$$

$$NO + O_2* \;\overset{k_2}{\longrightarrow}\; NO_3*$$

$$NO_3* \;\underset{\longleftarrow}{\overset{K_3}{\longrightarrow}}\; NO_2 + O*$$

$$NO + O* \;\underset{\longleftarrow}{\overset{K_4}{\longrightarrow}}\; NO_2*$$

$$NO_2* \;\underset{\longleftarrow}{\overset{K_5}{\longrightarrow}}\; NO_2 + *$$

$$O_2 + * \xrightleftharpoons{K_1} O_2*$$

$$NO + O_2* \xrightleftharpoons{K_2} NO_3*$$

$$NO_3* \xrightleftharpoons{K_3} NO_2 + O*$$

$$NO + O* \xrightleftharpoons{K_4} NO_2*$$

$$NO_2* \xrightarrow{k_5} NO_2 + *$$

VITA

Ishant Khurana was born in Nagpur, India on October 2nd, 1992 to parents Kishor Khurana and Meena Khurana. He completed his school studies in St. John High School, Pulgaon, followed by completion of junior college (11th and 12th grade) in R.K. Junior College in Pulgaon between 2008 and 2010. He secured admission in Institute of Chemical Technology (ICT) to pursue Bachelor of Chemical Engineering (B. Chem.). During this undergraduate study, he also did internship at Bharat Petroleum Corporation Limited (BPCL), Mumbai. His inquisitive mind and liking for chemistry and problem-solving drove him towards pursuing a Ph.D. in Chemical Engineering at Purdue University, West Lafayette under the supervision of Prof. Fabio H. Ribeiro beginning August 2014 on Catalytic Consequences of Active Site Speciation, Density, Mobility, and Stability on Ammonia Selective Catalytic Reduction over Cu-Zeolites. He successfully defended his PhD thesis in July 2019. During the graduate school, he presented his research work at various renowned conferences like North American Meeting (NAM: 2017), American Institute of Chemical Engineers (AIChE: 2016, 2017 and 2018), regional conferences like the Chicago Catalysis Club's spring symposium (CCC: 2015 and 2016), Michigan Catalysis Society's spring symposium (MCS: 2016) and Cross-Cut Lean Exhaust Emissions Reduction Simulations (CLEERS: 2017 and 2018). He co-authored five research publications, along with three more manuscripts about to be submitted. He was also awarded with Centennial Fellowship, Bisland Dissertation Fellowship, Outstanding Graduate Student Research Award, Best Research Poster Awards and Conference Travel Grants. During his graduate studies at Purdue, he served as a Graduate Student Organization Sustainability Officer, Vice-President and Treasurer of an on-campus student organization viz. SKY at Purdue. Upon graduating from Purdue University, he will be working full-time as a Senior Scientist I in the field of Heterogenous Catalysis with Braskem in Pittsburgh, PA.

PUBLICATIONS

Catalytic Consequences of Condition-Dependent Cu Site Speciation in SSZ-13 Zeolite on Standard SCR Kinetics:
Paolucci, C.; Parekh, A. A.; Khurana, I.; Iorio, J. R. Di; Albarracin, J.; Shih, A.; Anggara, T.; Nicholas, W.; Miller, J. T.; Ribeiro, F. H.; Gounder, R. *J. Am. Chem. Soc.* **2016**, *138*, 6028-6048, 1–63.

Catalytic Consequences of Cu Spatial Density and Mobility in SSZ-13 Zeolite on Standard SCR Kinetics:
Paolucci, C.; Khurana, I.; Parekh, A. A.; Li, S.; Shih, A. J.; Li, H.; Di Iorio, J. R.; Albarracin-Caballero, J. D.; Yezerets, A.; Miller, J. T.; Delgass, W. N.; Ribeiro, F. H.; Schneider, W. F.; Gounder, R. *Science (80-.).* **2017**, *357* (6354), 898-903.

Mechanistic Pathways of Binuclear Copper Complexes in Cu-SSZ-13 During Low Temperature Standard SCR
In Process

Exploring the Dependence of Standard SCR Kinetics over Cu-SSZ-13 on Reactant Gas Pressures
In Process

Catalytic Consequences of Framework Al Spatial Density in Cu-SSZ-13 Zeolite on Standard SCR Kinetics
In Process

Catalytic Consequences of Stability of Small Pore Cu-Zeolites against Hydrothermal Deactivation on Standard SCR Kinetics:
Albarracin-Caballero, J. D.; Khurana, I.; Di Iorio, J. R.; Shih, A. J.; Schmidt, J. E.; Dusselier, M.; Davis, M. E.; Yezerets, A.; Miller, J. T.; Ribeiro, F. H.; Gounder, R. *React. Chem. Eng.* **2017**, 7–10.

Catalytic Consequences of Stability of Cu-SSZ-13 against Sulfur Poisoning on Standard SCR Kinetics:
Shih, A. J.; Khurana, I.; Li, H.; González, J.; Kumar, A.; Paolucci, C.; Lardinois, T. M.; Jones, C. B.; Albarracin Caballero, J. D.; Kamasamudram, K.; Yezerets, A.; Delgass, W. N.; Miller, J. T.; Villa, A. L.; Schneider, W. F.; Gounder, R.; Ribeiro, F. H. *Appl. Catal. A Gen.* **2019**, *574*, 122-131.

Consequences of Exchange-Site Heterogeneity and Dynamics on the UV-visible Spectrum of Cu-Exchanged SSZ-13:
Li, H.; Paolucci, C.; Khurana, I.; Wilcox, L. N.; Göltl, F.; Albarracin-Caballero, J. D.; Shih, A. J.; Ribeiro, F. H.; Gounder, R.; Schneider, W. F. *Chem. Sci.* **2019**, *10* (8), 2373-2384.

Multinuclear Cu-Oxo Sites from Mononuclear Cu Sites in Cu-SSZ-13: Characterization by Selective Titration and NO Oxidation Probe Reaction
In Process